

Cornell Caltech Atacama Telescope

Feasibility/Concept Design Study

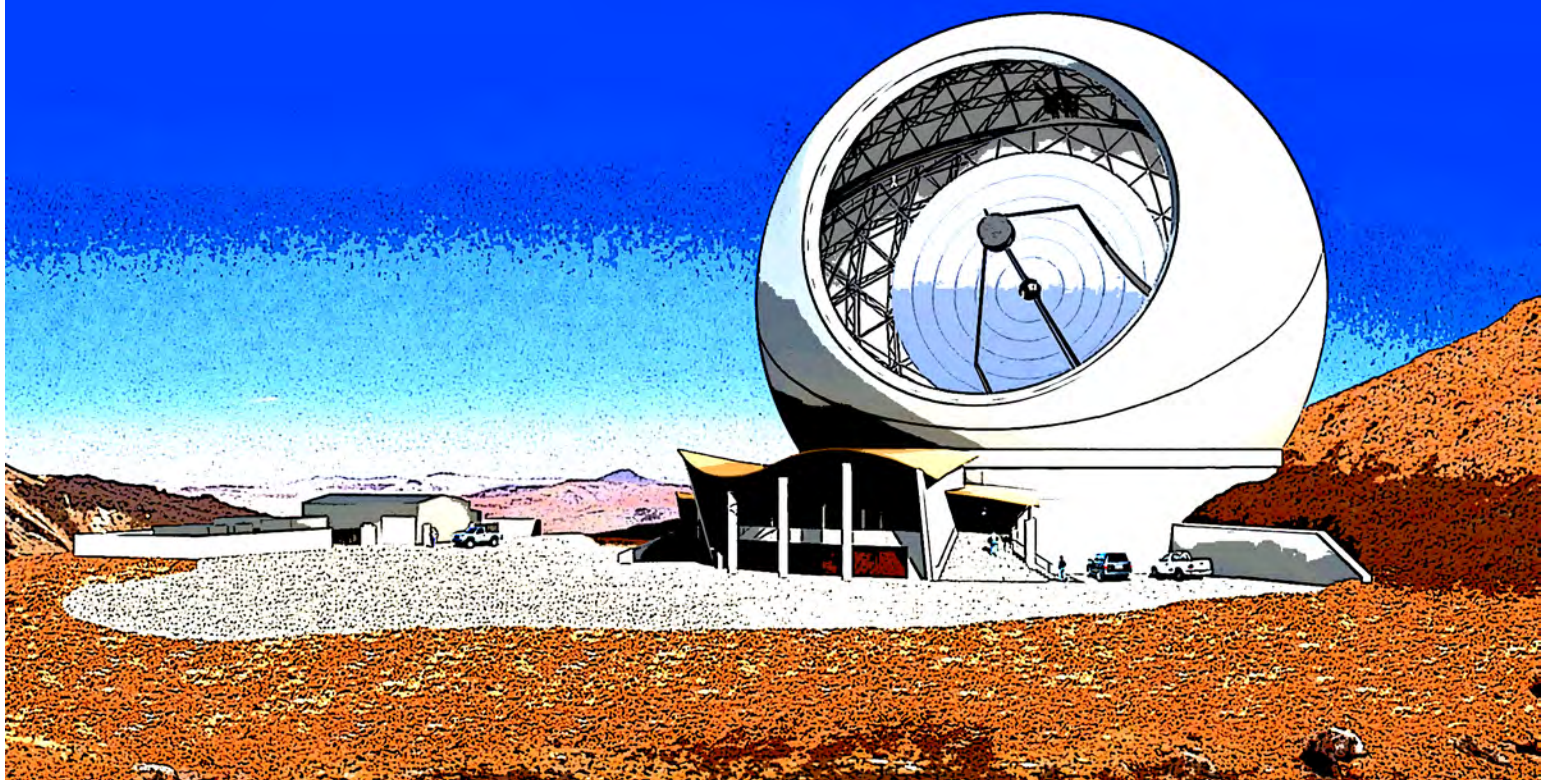
Final Report January 2006



Cornell University

California Institute of Technology

Jet Propulsion Laboratory

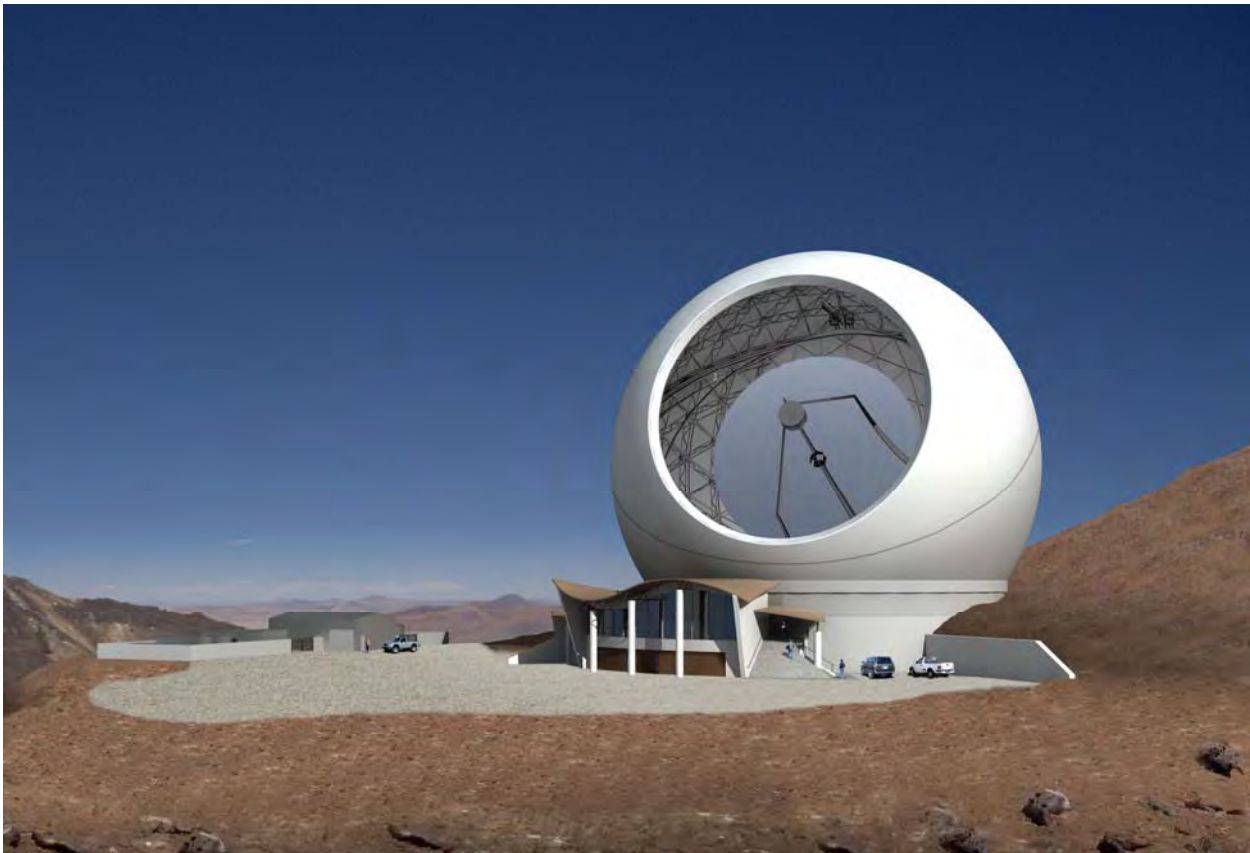


Cornell Caltech Atacama Telescope (CCAT)

Feasibility/Concept Design Study

Final Report

January 2006



Cornell University
California Institute of Technology
Jet Propulsion Laboratory

Table of Contents

| | |
|------|---|
| | Contributors |
| 1.0 | Executive Summary |
| 2.0 | The CCAT Vision |
| 3.0 | Introduction |
| 4.0 | CCAT Science |
| 5.0 | Top-Level Requirements |
| 6.0 | Instrumentation |
| 7.0 | CCAT Concept Design Overview |
| 8.0 | CCAT Baseline Optical Design |
| 9.0 | Systems Engineering |
| 10.0 | Site Selection |
| | 10.2 <i>Geotechnical Report, GEO Consultores</i> |
| 11.0 | Site, Architecture, and Civil Engineering |
| | 11.2 <i>M3 Engineering and Technology Corporation Report</i> |
| 12.0 | Enclosure Dome |
| | 12.2 <i>AMEC Dynamic Structures Ltd. Report</i> |
| 13.0 | Telescope Mount |
| | 13.2 <i>VertexRSI Report</i> |
| 14.0 | Primary Mirror |
| | 14.2 <i>Molded Borosilicate Panels, ITT Industries</i> |
| | 14.3 <i>CFRP Al Panels, Composite Mirror Applications</i> |
| | 14.4 <i>Mandrel Manufacturing, Goodrich</i> |
| 15.0 | CCAT Telescope Alignment and Guiding |
| | 15.2 <i>Calibration and Wavefront Sensing</i> |
| | 15.3 <i>Laser Metrology</i> |
| | 15.4 <i>Shack Hartmann Alignment System, Adaptive Optics Associates</i> |
| | 15.5 <i>Optical Guiding with CCAT</i> |
| 16.0 | Secondary and Tertiary Mirror Systems |
| | 16.2 <i>CSA Engineering Report</i> |
| 17.0 | Observatory Control System |
| 18.0 | Integration Plan |
| 19.0 | Operations Concept |
| 20.0 | Project Plan |
| 21.0 | Summary |
| | Acronyms |

CCAT Project Management

Director: Riccardo Giovanelli
Project Manager: Thomas Sebring
Deputy Project Manager: Simon Radford
Project Scientists: Terry Herter, Jonas Zmuidzinas
Instrument Committee Chair: Gordon Stacey
JPL Lead: Paul Goldsmith

Contributors

Andrew Blain, Caltech
Matt Bradford, JPL
Robert Brown, Cornell University
Don Campbell, Cornell University
German Cortes, Cornell University
Darren Dowell, JPL
Mark Dragovan, JPL
Neal Evans, Univ. of Texas
Duncan Farrah, Cornell University
Sunil Golwala, Caltech
Paul Harvey, Univ. of Texas
Chuck Henderson, Cornell University
Shardha Jogee, Univ. of Texas
Teresa Jordan, Cornell University
William Langer, JPL
James Lloyd, Cornell University
Jean-Luc Margot, Cornell University
Thomas Nikola, Cornell University
Thomas Phillips, Caltech
Shanti Rao, JPL
Anthony Readhead, Caltech
Eugene Serabyn, JPL
Michael Werner, JPL
Harold Yorke, JPL
David Woody, Caltech
Feng Zhao, JPL

Contractors

Adaptive Optics Associates
Ten Wilson Road
Cambridge, MA 02138-1128

AMEC Dynamic Structures Ltd.
1515 Kingsway Ave.
British Columbia, V3C1S2

CSA Engineering
2565 Leghorn Street
Mountain View, CA 94043-1613

Composite Mirror Applications
1638 S. Research Loop, #100
Tucson, AZ 85710

General Dynamics/Vertex RSI
1217 Digital Drive
Richardson, TX 75081

GEO Consultores
6 1/2 Oriente 169
Viña del Mar, Chile

Goodrich Optical and Space Systems
100 Wooster Heights
Danbury, CT 06810-7589

ITT Industries
Space Systems Division
800 Lee Road
Rochester, NY 14606-0488

M3 Engineering & Technology Corp.
2440 W. Ruthrauff Rd., Suite 170
Tucson, AZ 85705

Polytec PI
16 Albert Street
Auburn, MA 01501

1 Executive Summary

Cornell University, the California Institute of Technology (Caltech), and Caltech's Jet Propulsion Laboratory have joined to study the development of a 25 meter telescope to be built above 5000 meters in the Atacama region of northern Chile. The Cornell-Caltech Atacama Telescope (CCAT), operating to the shortest submillimeter wavelengths at which the atmosphere is transparent, will enable astronomical research that no other telescope on earth or in space can perform. Compared to currently existing single-aperture submillimeter telescopes, CCAT will:

- Be substantially larger (25 m vs. 10-15 m) to yield images more quickly and see deeper into space
- Have a more accurate surface (rms. error of 10 μm vs. 15-25 μm) to provide high resolution images
- Employ a site with better atmospheric transmission (Above 5000 meters altitude)
- Employ larger, more capable instruments capable of imaging larger areas of the sky.

The CCAT will enable the partner institutions to maintain and enhance their positions at the forefront of astronomical research and will substantially advance our understanding of the universe.

Over the past year astronomers at Cornell and Caltech have worked to identify the most significant areas of submillimeter research and derive the requirements these programs place on the telescope and instrumentation. The research programs proposed include surveys of galaxy formation in the early universe, galaxy clusters, planetary origins, and the regions within molecular clouds where stars form. The wide field of view of the telescope will make it the best instrument in the world to survey large areas of the sky at submillimeter wavelengths, providing an excellent scientific complement to the Atacama Large Millimeter Array, an interferometer array being built by the US and Europe in the same region of Chile.

During the course of this study we have used the resources of the partner institutions, science and instrumentation committees, and experienced commercial vendors to define a baseline telescope concept design and to evaluate the feasibility and risks associated with its development. Building on technologies developed for the most recent optical and radio telescopes, approaches have been identified which can make the CCAT cost effective, reliable, and robust in operation. This report presents details of architectural and mechanical design of the telescope buildings, dome, and telescope mount together with studies of two possible approaches to mirror panel fabrication and testing. Analysis to assess the first order risks associated with development of the telescope is provided and these risks have been found to be manageable. The total Project has been designed to a target of \$100m and detailed cost estimates developed during the study show that this is a reasonable project budget.

This study constitutes the first phase of development of the Project. The next phase, Engineering Concept Design, is scheduled to begin in June of 2006 and to last one year. This work will significantly advance the design and provide a more detailed assessment of the approaches chosen. When completed, the majority of technical issues will have been thoroughly analyzed, the configuration of all the subsystems chosen, and the cost for construction and operations known to a high degree of accuracy. Detailed design, manufacturing, and construction will follow over a six year Development Phase. First Light is planned in 2012, to be followed by a one year Commissioning Phase to optimize performance of the telescope.

The results to date show the development of CCAT is strategically important and technically feasible. The concept developed is viable, the cost is within expectations, and the scientific goals are compelling. CCAT has the potential to substantially advance astronomical science and significantly enhance the stature of the partner institutions.

2 The CCAT Vision

The Cornell-Caltech Atacama Telescope, CCAT, is specifically designed as a surveyor of cosmic origins. Operating at the far infrared and submillimeter wavelengths at which radiation from distant sites of cosmic birth reaches us, it will be the prime instrument to provide large scale surveys of primeval galaxies, of forming stars, and of the circumstellar disks within which planets aggregate and which may, eventually, lead to the development of life.

The detection and study of cosmic radiation at far infrared and submillimeter wavelengths presents some of the hardest challenges of any region of the electromagnetic spectrum. The Earth's atmosphere absorbs and emits profusely at those wavelengths, both removing valuable photons from the line of sight to cosmic sources and adding unwanted noise. That and the rapidly varying conditions of our dynamic atmosphere make the treatment of data a difficult exercise. In order to minimize the difficulty of that task, the CCAT will be built on a site at which the atmosphere will be minimally intruding: a desert location as high as we can drive a truck. Many good reasons can explain why telescopes of previous generations were not built at extreme elevations, not last being the desire to breathe and think clearly while observing. Advances in communications technology do make it now possible to operate complex facilities remotely and we can dare to place our telescope as high as it is practical to build it. Moreover, advances in forecasting of atmospheric conditions, possible with increasing accuracy and look-ahead times, will make it possible for CCAT to be scheduled in a dynamic manner to optimize the match between science and observing conditions.

The technology of far infrared and submillimeter detectors is undergoing a rapid development. Only a few years ago the most advanced bolometer array cameras had no more than a few dozen pixels. The first light camera intended for CCAT will have several tens of thousands pixels and the telescope is being designed to accommodate megapixel cameras in its field of view. Size, site, and a design that will take advantage of the fast-moving technological wave will make the combination of CCAT's sensitivity, resolution, and survey speed unmatched in its wavelength range by any other telescope on Earth.

CCAT will have a primary mirror 25 m in diameter. That size is determined by the desire to avoid confusion limits for integration times of practical interest, a goal impossible to achieve with the smaller telescope sizes imposed by deployment in the atmosphere-free environment of outer space.

Sites under consideration for the CCAT are all located in the vicinity of the Chajnantor Plateau in the Atacama Desert of northern Chile. Geography, meteorology, availability of services, and Chilean legislation combine to make this region ideal for the pursuit of far infrared/submillimeter astrophysical research. At the latitude of the Tropic of Capricorn, most of the sky is accessible and the center of the Milky Way transits nearly straight overhead. The high altitudes near a western coastline yield extremely low water vapor content in the atmosphere. The proliferation of astronomical initiatives in the region has prompted the government of Chile to establish a National Science Preserve, guaranteeing protection from a variety of potential man-made threats. The region is well endowed with high quality services and good communications due to the presence of intense, technically advanced mining activities. Chile has a long-standing record of excellence as a host to international research facilities. Operational synergies will result from operating in vicinity of other large-scale observatories.

Most important in the latter respect is the scientific complementarity between CCAT and the Atacama Large Millimeter Array (ALMA). ALMA is an international project with large US federal participation, scheduled for completion on a similar timescale as CCAT. ALMA is being built at an altitude of 5000 m at the center of the Chajnantor National Science Preserve. As an array, it will deliver images of unparalleled angular resolution but on relatively tiny fields of view. ALMA will be the natural instrument of choice for follow-up observations of sources discovered by CCAT. As a national facility, ALMA will be accessible to the US astronomical community. Those institutions with access to CCAT will enjoy an important comparative advantage in seeking ALMA time.

In 2003, scientists from Cornell University and the California Institute of Technology met to investigate commonality of long term goals, both scientific and technical, in the area of far infrared/submillimeter astronomy. In early 2004, a Memorandum of Understanding was signed by administrators of the two institutions established a partnership to develop a feasible concept for a 25 m telescope that would operate with high efficiency at wavelengths of 200 μm and longer on a very high site, with the long-term goal of commissioning such facility by the year 2012. As part of Caltech, the Jet Propulsion Laboratory became an important part of the partnership, contributing outstanding science and technology resources to the Project. The robustness of the partnership relies on the combination of those resources with Caltech's experience with forefront mm and submillimeter facilities, such as CSO and CARMA, and in the development of advanced technologies, and Cornell's infrared instrumentation talent and operational experience with NAIC. Moreover, the partnership is built upon nearly two decades of fertile collaboration between Caltech and Cornell in the operation of the 5 m Hale telescope at the Palomar Observatory.

The organization that will eventually operate the CCAT may not be restricted to the current partners. It is arguable that the ideal association would include a few partners with compatible goals, complementary expertise, and similar administrative modes and operational experiences. Because CCAT will be a unique facility and because of its scientific complementarity with ALMA, access to CCAT by the national community through special operation arrangements may not be excluded. It is foreseen CCAT will devote a substantial fraction of its operation to large scale surveys, especially of primordial galaxies. This activity will have an important impact on the operational mode of the telescope, not only in terms of the scheduling and conduct of observations, but in the formal structure of ad hoc, survey-specific partnerships, as successfully implemented within the framework of the Sloan Digital Sky Survey.

While the operational modes of CCAT remain to be firmed up in the future phases of the Project, it is clear the leadership of Cornell and Caltech will provide an initial imprint strongly flavored by the successful experiences of those two institutions through their involvement in CSO, CARMA, CBI, and NAIC.

The results of the Feasibility Study reported in this document indicate the scientific goals of the Project can be realistically met within the timescale indicated in the 2004 MOU and within reasonable financial boundaries. While the Project presents a rich list of technological challenges, no showstoppers have emerged during the Feasibility Study Phase. We look forward optimistically to the realization of the scientific goals that drive CCAT, as well as to the unpredicted discoveries this unique facility will certainly deliver.

3 Introduction to the Study

This section introduces a Concept/Feasibility Study of a 25 m telescope operating down to 200 μm wavelength and sited in the high Atacama Desert of northern Chile performed by Cornell University and the California Institute of Technology (Caltech). The study represents Phase I of a multi-phased effort intended to result in first light by 2012 and completion of the telescope in early 2013.

3.1 Background

In February 2004, Cornell University and the California Institute of Technology (Caltech) signed a Memorandum of Understanding (MOU) on the study phase of a Project to build and operate a 25 m class telescope for submillimeter astronomy. Caltech's Jet Propulsion Laboratory is also participating in this study. The Cornell/Caltech MOU calls for the following:

- A technical design for the telescope, its housing, and associated electronics,
- A technical evaluation of proposed sites within the Atacama area,
- A proposed suite of initial instruments for the telescope,
- Detailed cost estimates and schedules for the above,
- An operating plan and an estimate of the yearly costs of operating the completed facility,
- A proposed management structure for the Atacama telescope during the construction, testing, and operational phases,
- An assessment of the legal and technical issues associated with operating the facility in a foreign country, and
- A plan for raising the funds needed to complete the Project.

3.2 Governance

An oversight committee composed of four representatives of Cornell University, four representatives of Caltech, and the Project Director supervises the Project activities. A Study/Project Manager and a Deputy Study Manager report to the Project Director. The Study/Project Manager is Thomas Sebring. The Deputy Study Project Manager is Simon Radford. Riccardo Giovanelli is the Study/Project Director. The Oversight Committee is composed of the Project Director, Bob Brown, Don Campbell, Gordon Stacey, and Joe Veverka of Cornell, Tony Readhead and Tom Phillips of Caltech and Michael Werner and William Langer (replaced by Paul Goldsmith in October 2005) of Caltech-JPL.

3.3 Approach to Study

Work for this study has been accomplished in three ways:

Project Committees:

The Science Committee has been formed to define the scientific objectives of the CCAT (Section 4), develop analyses of telescope performance parameters, and establish science driven requirements for the observatory (Section 6). The Science Committee is co-chaired by Terry Herter and Jonas Zmuidzinas.

An Instrumentation Committee, chaired by Gordon Stacey, was formed to investigate the requirements for instruments needed to perform the science targeted by CCAT (Section 5). This work includes a survey of development of large area arrays and development of concepts for the two first light instruments for CCAT.

The Operations Committee is charged with development of a plan for operations including staffing, logistics, operational modes for observing, and draft operations budgets. This work resulted in the Operations Plan (Section 19). This Committee is chaired by Simon Radford.

Task Managers:

Several tasks were identified by the Project Office and were undertaken by scientists, engineers, and other technical specialists within the Partner institutions. This has resulted in studies of such technical issues as system

engineering and error budgets (Section 9), analysis of wavefront sensors for telescope calibration and of interferometric sensors for panel alignment maintenance (Section 16), and optical design analysis (Section 8).

Study Contracts:

The Project Office identified the major telescope subsystems that would best be addressed by conceptual studies performed by industrial contractors or architects capable of performing detailed design and/or manufacture, test, and delivery of these subsystems. These subsystems, which include the facility, dome, telescope mount, and components for mirrors within CCAT, were defined by brief draft specifications based on the Science Committee's initial requirements definition. Contractors were identified who had proven track records in development of such systems. After a series of visits, those with the most applicable skills were chosen. In some cases multiple parallel studies were performed to assess differences in performance, cost, and risk between alternative approaches. The contractors were required to review requirements, develop concepts, perform analysis of key performance issues, perform a risk assessment, and develop an initial cost estimate for development of each subsystem. The results of these studies are included in this report.

A series of Status and Technical Exchange Meetings were conducted over the past year, alternating between Cornell and Caltech to enable the participation of substantial numbers of the scientific and technical staff at the Partner institutions. A major Mid-Term Status Review of progress was conducted at Cornell on July 13 and 14, 2005.

3.4 Next Steps

This study establishes the scientific desirability and feasibility of developing CCAT and the associated scientific instruments from both technical and cost perspectives. The concept provided requires further development and some changes in approach may result from additional investigation. The Engineering Concept Design is the focus of Phase II of development, scheduled to begin in mid 2006 and to last one year. The work will be performed by individuals and groups within the Partnership and through Concept Design contracts. Results will be provided in mid 2007. The Project then will be ready to start detailed design, construction, and manufacture by late 2007.

4 CCAT Science

This section highlights the core science objectives established for CCAT, and uses these to derive requirements for the telescope and instruments.

4.1 Introduction

CCAT will be substantially larger and more sensitive than existing submillimeter telescopes, and it will also be the first large submillimeter telescope designed specifically for wide-field imaging. As such, it will provide an unparalleled ability to map large areas of the sky and enable unique approaches to a number of key astronomical problems. The scientific thrusts of the observatory will include:

- How did the first galaxies form?
 - CCAT will detect hundreds of thousands of primeval galaxies from the era of galaxy formation and assembly ($z = 2 - 4$ or about 10-12 billion years ago) providing for the first time a complete picture of this process.
 - CCAT will probe the earliest bursts of dusty star formation as far back as $z \sim 10$ (less than 500 million years after the Big Bang or when the Universe was $\sim 4\%$ of its current age).
- What is the nature of the dark matter and dark energy which fill the Universe?
 - CCAT will image hundreds of clusters of galaxies selected from current and planned southern-hemisphere cluster searches (via the Sunyaev-Zeldovich Effect).
 - CCAT imaging will be important in understanding how clusters form and evolve, and in interpretation and calibration of the survey data to constrain crucial cosmological parameters (Ω_M , Ω_Λ , dark energy equation of state) independently of other techniques (Type Ia supernova and (direct) CMB measurements).
- How do stars form?
 - CCAT will survey molecular clouds in our Galaxy to detect the (cold) cores that collapse to form stars, providing for the first time a complete survey of the star formation process down to very low masses.
 - In nearby molecular clouds, CCAT will be able to detect cold cores down to masses well below that of the lowest mass stars ($0.08 M_\odot$).
- How do conditions in circumstellar disks determine the nature of planetary systems and the possibilities for life?
 - In concert with ALMA, CCAT will study disk evolution from early (Class I) to late (debris disks) stages.
 - CCAT will image the dust resulting from the collisional grinding of planetesimals in planetary systems around other stars allowing determination of the (dynamical) effects of planets on the dust distribution, and hence the properties of the orbits of the planets.
- How did the Solar System form?
 - The trans-Neptunian region (Kuiper Belt) is a remnant disk that contains a record of fundamental processes that operated in the early solar system (accretion, migration, and clearing phases).
 - CCAT will determine sizes and albedos for hundreds of Kuiper belt objects, thereby providing information to anchor models of the planetary accretion process that occurred in the early solar system.

The simplest atoms, hydrogen and helium, make up over 98% of the *baryonic* matter in the Universe, however, in many cases it is the heavier components (carbon, oxygen, silicon, iron, etc.) which allow us to discover and study distant objects. These elements bind together to form complex molecules and small dust particles that in many astrophysical environments obscure optical and ultraviolet photons, and radiate predominantly at wavelengths between 0.1 and 1 mm – the submillimeter waveband. Many of the most powerful and interesting phenomena in the universe are dominated by dust and are completely inaccessible to optical astronomy, from star-forming regions in our own galaxy to entire galaxies. This makes the submillimeter a particularly valuable probe of many astrophysical sources.

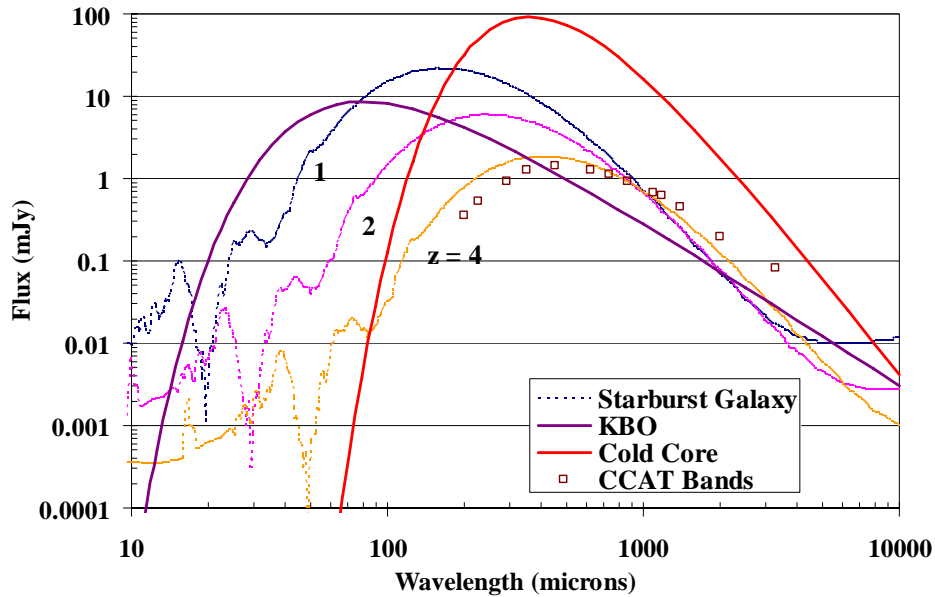


Figure 4.1: Flux density vs. wavelength for several example sources that peak in the far-infrared/submillimeter – a $10^{12} L_{\odot}$ starburst galaxy at redshifts of 1, 2, and 4, a $T = 8\text{K}$, $0.03 M_{\odot}$ cold cloud core located in a nearby (140 pc) star forming region, and a 300 km diameter Kuiper Belt Object located at 40 AU. The CCAT bands are indicated by the open squares (which are the 5-sigma, 30-beams/source confusion limit for CCAT).

Figure 4.1 shows example spectra of three classes of objects detectable with CCAT: distant star forming galaxies, the cold cores of star forming clouds, and Kuiper Belt Objects (KBOs). Each source shows significant (and in many cases its primary) emission in the submillimeter. Figure 4.2 illustrates three views of an interacting galaxy system, the Antennae. Interactions between galaxies stimulate massive amounts of star formation which, because of obscuration by dust at shorter wavelengths, is best seen in the far-infrared and submillimeter. Galaxies such as these can be seen at large distances in the Universe since the peak of their spectra shifts through the submillimeter as the redshift (distance) increases (Figure 4.1).

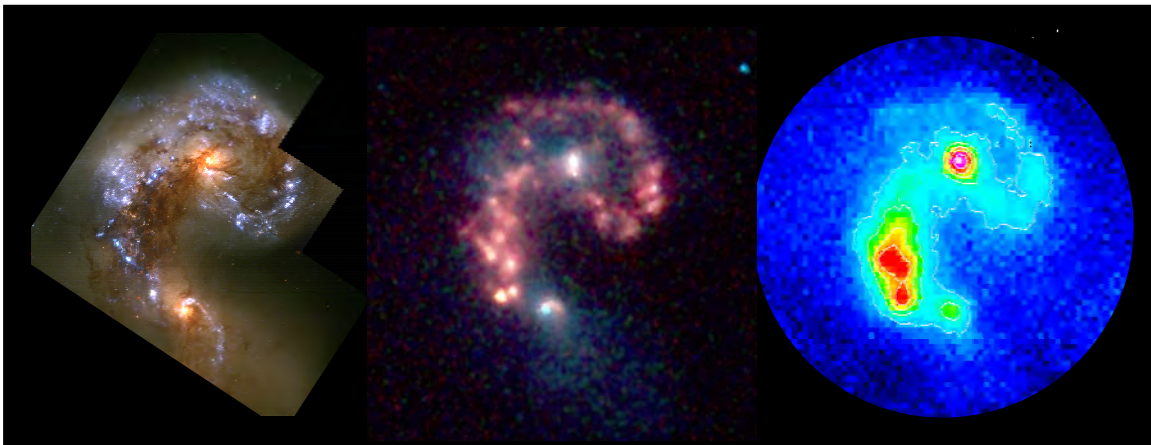


Figure 4.2: Images of the Antennae (NGC 4038/4039) in the visible (left), infrared (center), and submillimeter (right) showing how the submillimeter reveals regions hidden at shorter wavelengths. For this galaxy and many like it, the submillimeter represents the bulk of the energy output of the galaxy, and reveals the real luminosity production regions which are otherwise hidden. CCAT will have 2.5 times better resolution in the submillimeter giving a spatial resolution like that of the infrared image (center). Credits: visible (HST), infrared (Spitzer), and submillimeter (Dowell et al.)

Cold cloud cores, the direct precursor to stars, also emit strongly at CCAT wavelengths (Figure 4.1). CCAT will be sensitive to very small gas masses in nearby star forming regions – masses well below that corresponding to

the smallest hydrogen-burning stars. Figure 4.3 shows a comparison between an optical view and a submillimeter view of the Orion star forming complex, demonstrating how the submillimeter probes regions invisible in the optical. KBOs contain primordial material left from the formation of our solar system. Because of their distance from the Sun they are relatively cool and hence emit significantly in the far-infrared/submillimeter (Figure 4.1). CCAT will be able to measure sizes and albedos for a significant sample of KBOs.

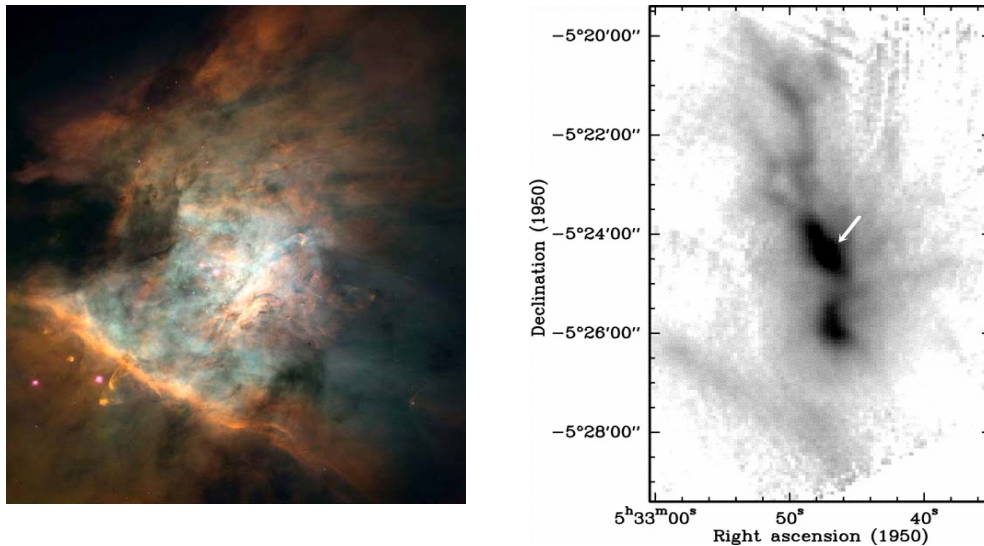


Figure 4.3: Orion Molecular Cloud – Left: Optical image. Right: 350 μm map. The arrow points to a region invisible to optical probes. CCAT will map star forming regions with 2.5 times better spatial resolution and much greater sensitivity than this image.

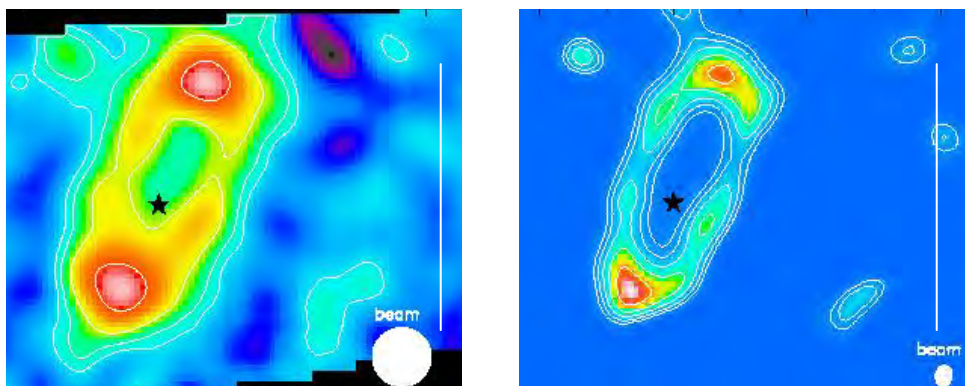


Figure 4.4: Image of Fomalhaut debris disk acquired with the CSO/SHARC II (Marsh et al. 2005, ApJ, 620, L47). Left: The observed image which has 10'' resolution and shows a complete ring of debris around the star. Right: A resolution enhanced image with 3'' resolution. CCAT will have this resolution intrinsically, with the capability to achieve $\sim 1''$ resolution through image enhancement techniques. From the CSO image, we can already infer the presence of a planet due to the asymmetry of the ring. CCAT imaging should show substructure which will pinpoint the location of the planet. The vertical bars in each image are 40'' in length.

An impressive example of the power of the submillimeter waveband is shown in Figure 4.4 which shows an image of the nearby star, Fomalhaut. Fomalhaut is surrounded by a “debris disk” consisting of asteroidal and cometary debris associated with a planetary system. Detailed imaging will allow determination of the effects of planets on the dust distribution, and hence the properties of the orbits of the planets. CCAT is the perfect complement to ALMA, the submillimeter interferometer under joint construction by the United States and Europe. ALMA will be the premier international ground based facility of the next decade, bringing high spatial resolution and sensitivity to the submillimeter. ALMA will offer the ability to examine individual objects with

unprecedented detail. However, ALMA has a very limited instantaneous field-of-view view and is not efficient at surveying the sky or finding sources. CCAT will be able to map the sky at a rate hundreds of times faster than ALMA, finding galaxies by the tens of thousands, and mapping galaxy clusters, Milky Way star-forming regions, and debris disks.

In the next section we discuss the expected sensitivity of CCAT. This is followed by a discussion of some of the main science drivers for CCAT. These science drivers are used to outline the telescope and instrumentation requirements.

4.2 Sensitivity

The radiation received by a millimeter or submillimeter camera operating on a ground-based telescope is completely dominated by thermal emission from the atmosphere, the telescope, and the instrument itself. In contrast, the astronomical signal is much smaller, typically by 6 to 7 orders of magnitude. The fundamental, irreducible limit to sensitivity is set by the random arrival of the background photons, as discussed in more detail in Section 4.2.1 below. This is often referred to as the “BLIP” limit. However, the atmosphere is not entirely stable, and the fluctuations of the atmospheric emissivity would lead to a large degradation of sensitivity unless special measures are taken. These measures may include subtracting the instantaneous common-mode background level seen across the detector array or scanning the telescope across the sky in some pattern and at some rate, as well as other, more complex strategies and algorithms. With these techniques, existing cameras have been able to approach the fundamental BLIP limit under favorable conditions. In the section below, we calculate and discuss the CCAT's BLIP sensitivity, but it must be kept in mind that this carries implications for the scanning performance of the telescope, and that unfavorable atmospheric conditions may at times preclude the BLIP limit from being reached.

4.2.1 Formulae

The sensitivity of a system operating at wavelengths longward of 100 μm must take into account the Bose-Einstein statistics of photons. For systems that are limited by the background (BLIP), the sensitivity of CCAT for detecting the continuum of point sources is given by

$$f_\nu = \frac{(S/N)}{\sqrt{t}} \frac{1}{\tau_A \tau_T} \frac{D_L}{g_f g_R} \frac{h\nu}{\tau_I} \frac{2}{A_T} \sqrt{\frac{\bar{n}_r(1+\bar{n}_r)}{N_p \Delta\nu}} \sqrt{\frac{A_T \Omega}{\lambda^2}} \sqrt{1 + \frac{1}{p^2}}$$

with

$$g_R = e^{-(4\pi s_{rms}/\lambda)^2} \quad \bar{n}_r = \tau_I \left[\frac{\epsilon_A}{e^{h\nu/kT_A} - 1} + \frac{\epsilon_T}{e^{h\nu/kT_T} - 1} \right]$$

where

- f_ν = Point source flux density (mJy or Jy)
- $S/N, t$ = Signal-to-noise ratio in integration time t
- D_L = Losses do to differencing (typically 1.414 or 2)
- $h\nu$ = Energy of the photon at frequency ν (and wavelength, λ)
- τ_A, τ_T = Atmospheric and telescope transmissions, $\tau_A = \exp(-\kappa_a A)$ where κ_a is the extinction per air mass and A is the air mass
- g_f = Fraction of flux in extraction region (~ 0.70)
- g_R = Ruze factor, s_{rms} = root-mean-square surface roughness
- τ_I = Instrument throughput including the detector response
- A_T, Ω = Telescope collecting area and solid angle used for source extraction, $A_T \Omega = 1.075\lambda^2$ for optimal extraction of diffraction limited beam
- \bar{n}_r = Average photon occupation number

- $\Delta\nu$ = Spectral bandwidth of the observation
- N_p = Number of polarizations measured (typically 2)
- ϵ_A, ϵ_T = Atmospheric and telescope emissivities ($\epsilon_A = 1 - \tau_A$)
- T_A, T_T = Atmospheric and telescope temperatures
- p = Pixels across extraction region (roughly accounting for pixilation noise). $p = 2$ for Nyquist sampling.

For direct detection of lines, the sensitivity is given by

$$f_l = f_\nu \Delta\nu$$

where the line flux is in units of W/m^2 and $\Delta\nu$ (in Hz) is matched to the line width (either intrinsic or set by the spectrograph). The optimal extraction flux is modified slightly from the above formulation but not enough to make a significant difference.

For external galaxies, the velocity widths of spectral lines are usually dominated by the rotation of the galaxy and are of order $\Delta V = 100\text{-}1000$ km/s. Thus, a spectral resolution of order $R = c/\Delta V \sim 1000$ is sufficient for optimal detection, and is not difficult to achieve in the submillimeter using a grating or Fabry-Perot spectrometer. However, for clouds within our galaxy, the linewidths are dominated by the internal motions of the gas and are much narrower, of order $\Delta V = 1$ km/s, and so the lines are best studied using a spectrometer with a resolution of $R \sim 10^6$. This value would lead to impractically large direct-detection spectrometers, but is well within reach of compact radio-style (heterodyne) spectrometers, in which the Terahertz-frequency telescope signal is first downconverted to the Gigahertz-frequency (microwave) band and then amplified and spectrally analyzed.

Heterodyne spectrometers operate with large photon number gain and are therefore subject to an extra source of noise, called the quantum noise. The quantum noise is equivalent to the photon noise from a thermal background with an occupation number of unity. For CCAT, the occupation number for the background generated by losses in the atmosphere and telescope will substantially exceed unity for all but the longest wavelength atmospheric windows. Thus, the quantum noise limit for heterodyne instruments is not a significant limitation. In this case, the CCAT sensitivities predicted by the formulae above for direct-detection instruments may also be used to predict the ultimate sensitivity of CCAT when using heterodyne instruments that operate near the quantum limit. Because heterodyne instruments are single-mode, the $A_T \Omega / \lambda^2$ factor is set to unity. One also omits the pixilation noise term since heterodyne spectrometers usually sample the line profile quite well.

Unfortunately, existing submillimeter heterodyne systems do not yet reach the quantum limit, especially at higher frequencies, and so the BLIP sensitivities must be degraded by some factor depending on the receiver performance and the background level. Figure 4.5 shows the current laboratory performance measured for a variety of systems, including those employing tunnel junction mixers (SIS and NbTiN points) as well as hot-electron bolometer mixers (HEB points). These results are plotted as a double-sideband (DSB) noise temperature. This is the relevant quantity for continuum radiation, which enters both the upper and lower sidebands of the receiver. Spectral lines appear in only one sideband, and so the single-sideband (SSB) noise temperature is more appropriate, which in most cases is just twice the double-sideband value. The best receiver results above 1 THz are around 20 times the quantum limit, corresponding to double-sideband noise temperatures of 0.5 K/GHz. More typically the results are around 1 K/GHz.

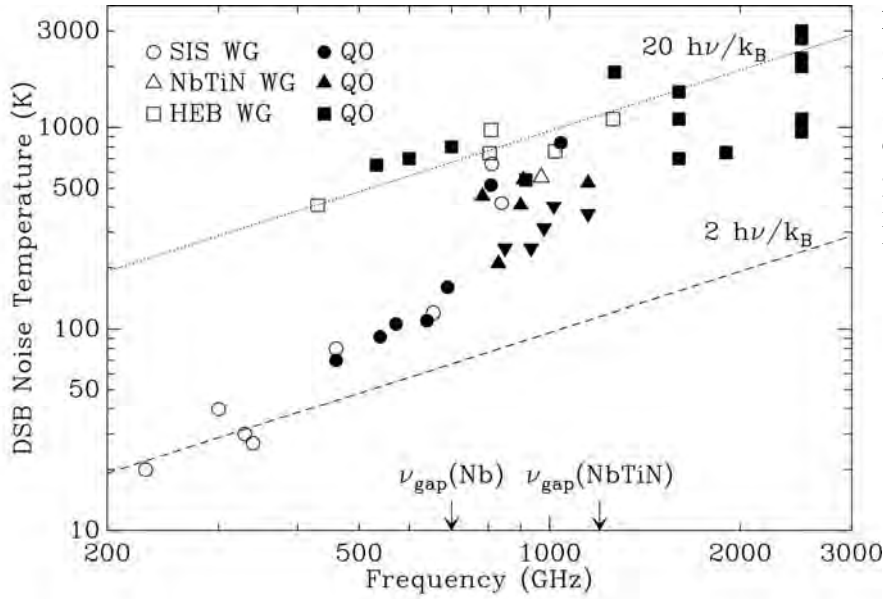


Figure 4.5: The measured sensitivities (expressed as a double-sideband noise temperature) of submillimeter heterodyne systems. The dashed and dotted lines correspond to sensitivities which are 4x and 40x worse than the quantum noise limit (Zmuidzinas and Richards 2004, Proc. IEEE, 92, 1597).

Heterodyne spectroscopy using CCAT is most interesting above 1 THz, where ALMA will not operate. At these frequencies, the atmospheric transmission will typically be 20% for “usable” weather and will very rarely exceed 50%. Figure 4.6 shows that in some cases the transmission does reach 50%. Under these conditions, the background will be dominated by atmospheric emission, and we may neglect emission from the telescope. In this case, the system noise temperature may be calculated using:

$$T_{sys}(SSB) = 2[\varepsilon_A T_A + T_{rec}(DSB)] / \tau_A$$

where ε_A and τ_A are the atmospheric emissivity and transmission, as before. For an ideal BLIP-limited direct-detection system, the equivalent expression reads

$$T_{sys}(BLIP) = \varepsilon_A T_A / \tau_A$$

where the approximation $h\nu \ll k_B T_A$ has been made. The sensitivity degradation factor associated with the use of a double-sideband heterodyne receiver is

$$T_{sys}(SSB) / T_{sys}(BLIP) = 2[1 + T_{rec}(DSB) / \varepsilon_A \tau_A]$$

Given the current receiver sensitivities at 1.5 THz, this degradation factor is in the range 9-16 for 20% atmospheric transmission, and in the range 13-24 for 50% transmission. Thus, a good order-of-magnitude estimate is that THz heterodyne spectroscopy using CCAT will be 10-20 times less sensitive than the BLIP limit. Note that the relevant BLIP limit is calculated using the spectral resolution $\Delta\nu$ corresponding to the heterodyne receiver, which is typically several orders of magnitude smaller than the resolution of an incoherent spectrometer. Therefore, coherent spectrometers still enjoy a sensitivity advantage for narrow lines, as expected. Over time, as the receivers improve, the sensitivities should approach the BLIP limit.

4.2.2 The Atmosphere

Atmospheric conditions will have a profound impact on CCAT's sensitivity. In the submillimeter, observing is only possible in discrete windows bracketed by molecular absorption lines (Figure 4.6). The atmospheric transmission is primarily a function of the water vapor content, although the altitude and temperature are also important. Observations at the shortest wavelengths, $< 500 \mu\text{m}$, are only possible under exceptional conditions.

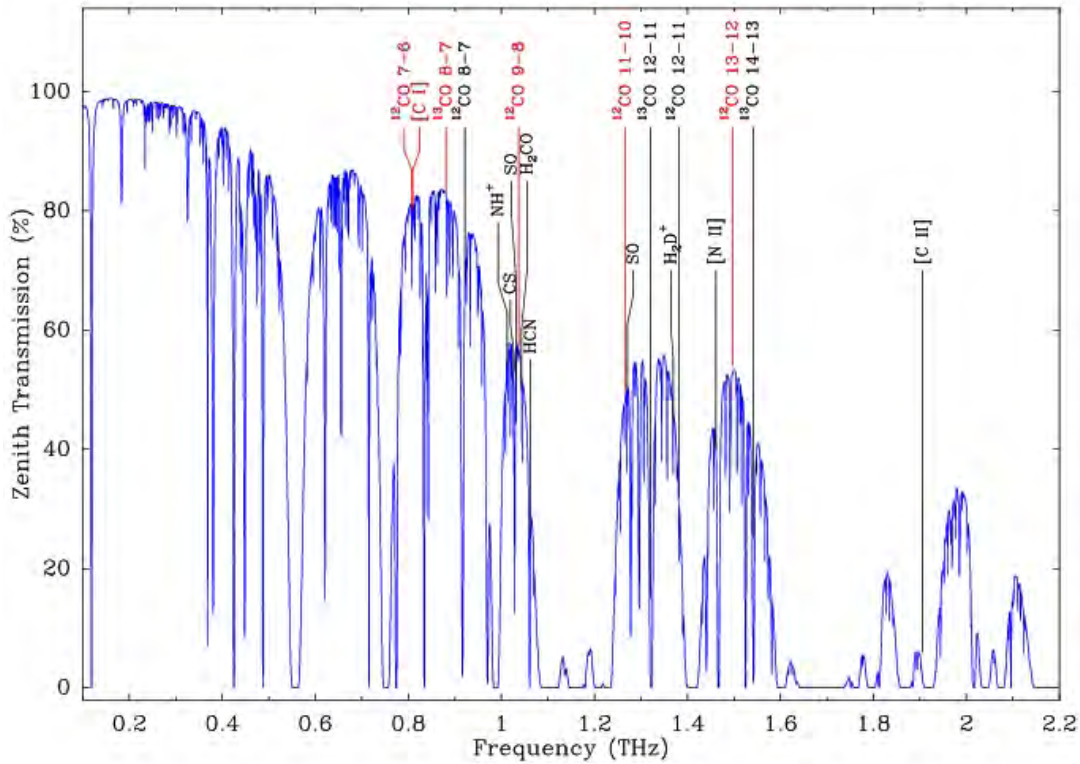


Figure 4.6: Measured atmospheric transmission at Cerro Sairecabur on 2005 January 24 with an Fourier Transform Spectrometer. The inferred precipitable water vapor is only 93 μm . The lines and labels show some of the interesting spectral lines available in the submillimeter and Terahertz windows (Marrone et al. 2005, astro-ph 0505273).

High altitude sites in the Atacama Desert of northern Chile enjoy consistently superb conditions for submillimeter observations (Section 10). Figure 4.6 shows the measured transmission in this region under the very best conditions. Long term atmospheric transparency measurements show the ALMA site on the Chajnantor plateau (5050 m) has twice as much time for submillimeter observations as Mauna Kea (4100 m). Moreover, higher peaks in the vicinity enjoy even better conditions. The differential water vapor distributions on Cerro Sairecabur (5500 m) and the ALMA site illustrate the advantage of the higher site (Figure 4.7).

Weighting the water vapor distributions by the relative integration times indicates the relative value of observing conditions for different bands (Figure 4.8). For example, even though times when PWV < 0.3 mm are rare, three times more observing at 200 μm can be done under those conditions than under the relatively more common circumstances when PWV = 0.5 mm because the higher sensitivity in drier conditions more than compensates for the scarcity of time.

Although the allocation of observing time to different wavelengths must ultimately rest on scientific priorities, the weighted water vapor distribution allows an estimate of the “optimal” time allocation. Starting with the band most sensitive to observing conditions, i. e., 200 μm , an optimal range of conditions is assigned where the effective observing time is greatest. Then optimal ranges are assigned in turn to the remaining bands (Figure 4.8). Table 4.1 summarizes the times available for these bands separately for the ALMA site and Sairecabur. Because observations at some wavelengths require similar conditions, i.e., 350 μm and 450 μm , they share a common range. Note the water vapor ranges adopted here are considerably more stringent than those used at the CSO, where observations at 350 μm are made when the PVW < 0.9 mm (Section 10).

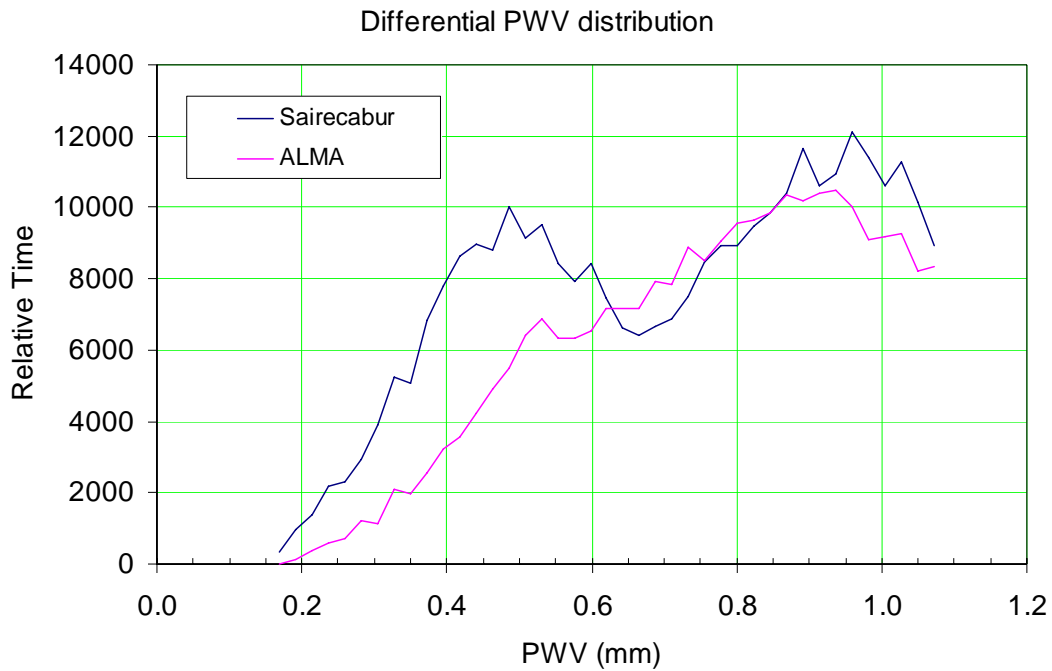


Figure 4.7. The differential distributions of the precipitable water vapor (PWV) column at the ALMA site on the Chajnantor plateau (5050 m) and at Cerro Sairecabur (5500 m) inferred from FTS measurements of the 1.35 THz transmission (Blundell et al. 2002). Integrating the distributions indicates the total amount of time available. For the ALMA site and Sairecabur, respectively, about 58% and 72% of the time (5100 and 6300 hr yr^{-1}) has $\text{PWV} < 1.1 \text{ mm}$. Because of saturation at the measurement frequency, these distributions are incomplete; much of the remaining time at either site has $\text{PWV} < 3 \text{ mm}$.

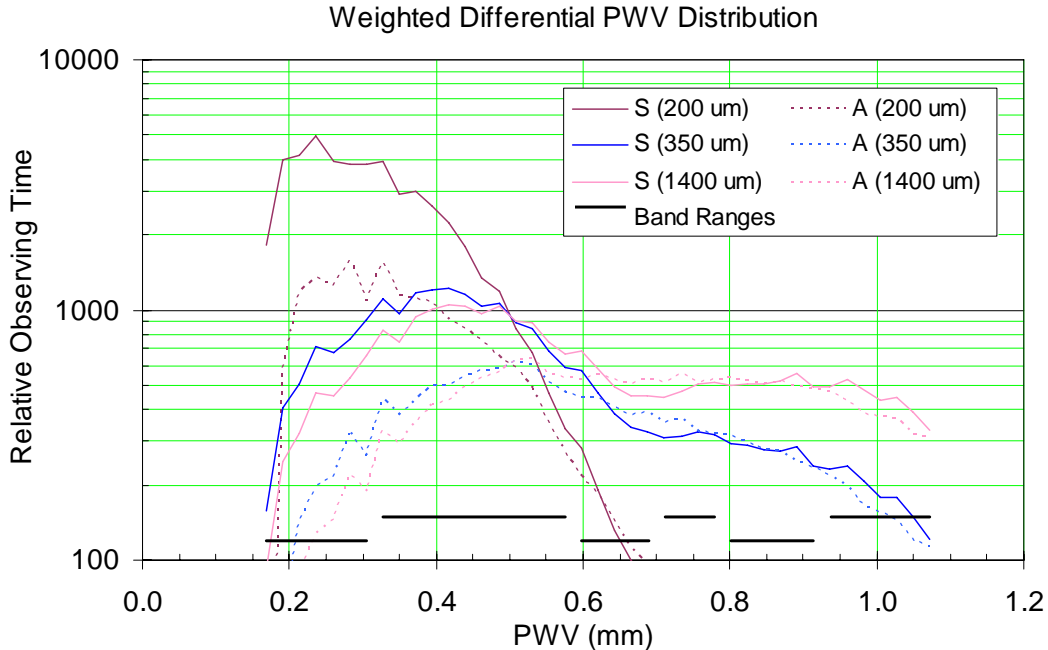


Figure 4.8. Differential precipitable water vapor (PWV) distributions for the ALMA site (dashed) and for Sairecabur (solid) weighted by relative integration time. The distributions are normalized relative to 0.5 mm water vapor. The horizontal bars represent the optimal PWV ranges for observing in different bands. From left to right, these bands are 200 , $350/450$, 620 , 740 , 865 , and $> 1000 \mu\text{m}$.

Table 4.1 indicates the mapping speed of CCAT and emphasizes the advantage of locating the telescope at the best site possible. CCAT sensitivity calculations that follow use the optimal water vapor range for each band.

Table 4.1 Available Observing Time

| Band | | Time to CL [hr] | Ref. PWV [mm] | Sairecabur (5500 m) | | ALMA (5050 m) | | | |
|--------------------------------|----------------|--------------------|---------------------|--|------------------|--|------------------|----------------------------------|------|
| λ [μm] | ν [GHz] | | | Time Available [hr yr ⁻¹] | CL fields [%] | Time Available [hr yr ⁻¹] | CL fields [%] | CL fields [yr ⁻¹] | |
| 200 | 1500 | 1248 | 0.26 | 281 | 3 | 84 | 1 | | |
| 350 | 857 | 0.86 | 0.47 | 1936 | 22 | 2244 | 1084 | 12 | 1257 |
| 620 | 484 | 1.14 | 0.64 | 716 | 8 | 629 | 723 | 8 | 634 |
| 740 | 405 | 0.43 | 0.75 | 639 | 7 | 1488 | 690 | 8 | 1607 |
| 865 | 347 | 0.28 | 0.86 | 1223 | 14 | 4413 | 1205 | 14 | 4348 |
| 1400 | 214 | 0.30 | 1.00 | 1517 | 17 | 5093 | 1299 | 15 | 4361 |
| Time (PWV < 1.1 mm) | | | | 6312 | 72 | 5084 | 58 | | |

4.2.3 Confusion

The ultimate sensitivity of CCAT will be set by the blending together of (unresolved) sources. These sources will be faint galaxies spaced through the Universe. This type of noise is referred to as confusion noise and a rough rule of thumb is that the confusion limit occurs at 30 beams/source. The levels of confusion noise are set by the source counts derived at the relevant wavelengths of submillimeter atmospheric windows using the models described in detail by Blain et al. (1999, MNRAS 302 632), updated by Blain et al. (2002; Physics Reports, 369, 111; astro-ph/0202228).

These use a fitted SED template for distant far-IR luminous galaxies, and an evolving luminosity function based on IRAS to account for the measured counts of galaxies from 60 to 2800 microns, including data from Spitzer, ISO, SCUBA, MAMBO and BIMA. The overall background intensity from COBE is also fitted, and the redshift distribution of SCUBA sources is described adequately.

The model requires a temperature of order 40K for the population, which is consistent with that measured for the typical submillimeter galaxy (Blain et al. 2004; ApJ, 611, 52), and strong evolution of their luminosity, in the sense of pure luminosity evolution, as $(1+z)^n$ with $n \sim 4$ to $z = 1$, with a peak in the global form of evolution at close to $z = 2$, followed by a gradual decline (see Fig 21 in the Physical Reports paper).

The models provide a good account of existing data at 1.3, 1.1, 0.85 and 0.45 mm, and so the resulting confusion estimates are unlikely to be wrong by more than a factor of 2. Figure 4.9 shows the expected cumulative source density as a function of flux density while Table 4.2 gives the flux density limit when the 10 and 30 beams/source limits are reached for a 25-m telescope. The 30 beams/source limit is the most conservative while one might picture reaching the 10 beams/source limit under selected conditions (such as using deconvolution techniques).

Table 4.2: CCAT 5 σ Confusion Limits

| λ (μm) | Flux (mJy) | | λ (μm) | Flux (mJy) | |
|-----------------------------|--------------|--------------|-----------------------------|--------------|--------------|
| | 10 beams/src | 30 beams/src | | 10 beams/src | 30 beams/src |
| 200 | 0.042 | 0.356 | 870 | 0.529 | 1.112 |
| 250 | 0.103 | 0.529 | 1100 | 0.461 | 0.922 |
| 350 | 0.242 | 0.926 | 1400 | 0.359 | 0.670 |
| 450 | 0.372 | 1.293 | 2000 | 0.329 | 0.610 |
| 650 | 0.530 | 1.450 | 3300 | 0.248 | 0.447 |
| 740 | 0.559 | 1.277 | | | |

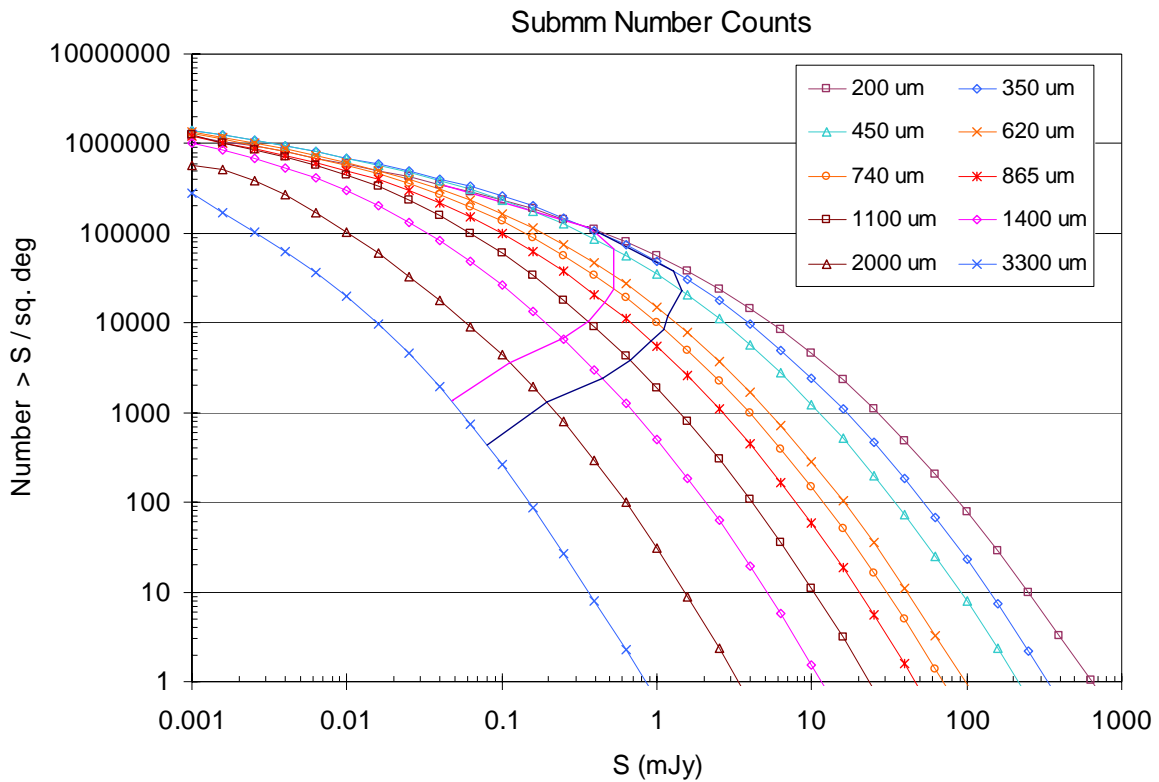


Figure 4.9: Submillimeter galaxy counts vs. flux density (number of sources with flux greater than S vs. S) for different wavelengths (after Blain et al. 1999, 2002). Crossing lines show 30 (lower) and 10 (upper) beams/source confusion limits for a 25 m diameter telescope.

4.2.4 Sensitivity/System Performance

The continuum sensitivity of CCAT is computed according to Section 4.2.1 using the optimized precipitable water vapor for each band (Table 4.1) to compute the appropriate atmospheric transmission (Section 10). Figure 4.10 and Table 4.3 summarize the resulting continuum sensitivity of CCAT. The sensitivity of ALMA (taken from the ALMA web site) is also given. ALMA's sensitivities have not been optimized for each band, and thus ALMA's performance at 350 and 450 μm will be better than indicated. This means that ALMA will be capable of follow-up observations of sources found in CCAT surveys. Also included in Figure 4.10 are the confusion limits (Section 4.2.3) for CCAT and several other current or planned facilities (APEX, Herschel, JCMT, LMT, and Spitzer).

Estimates of the line sensitivity of CCAT are given in Table 4.4 assuming a spectral resolution of $R = \Delta\nu/\nu = 1000$.

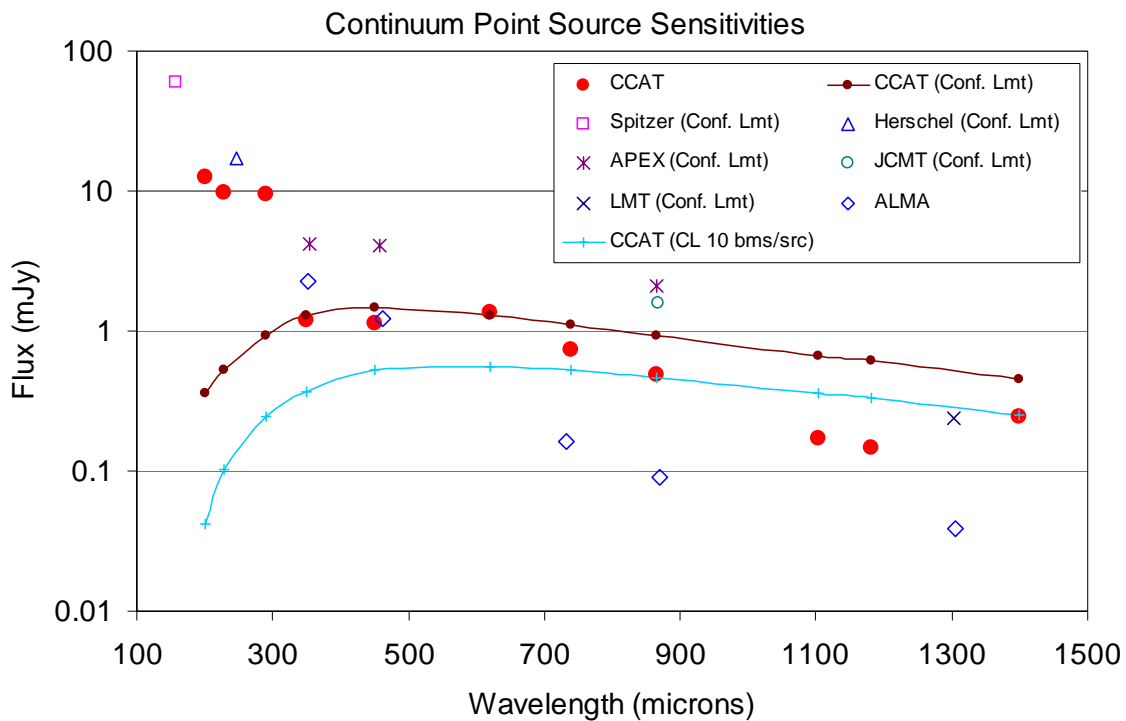


Figure 4.10: A comparison of the sensitivity of CCAT with other facilities, including ALMA. The vertical axis gives the minimum flux for a 5σ detection after a 1-hour integration... All confusion limits assume 30 beams/source, except for the alternative 10 beams/source case shown for CCAT. This case is displayed to illustrate the potential gain of using aggressive deconvolution techniques.

Table 4.3: CCAT Continuum Sensitivity*

| λ (μm) | ν (GHz) | PWV (mm) | NEFD (mJy) | Conf. Limit (mJy) | Time to CL (sec) | Density at CL (#/sq-deg) |
|--------------------------------|----------------|-------------|---------------|-------------------------|------------------------|--------------------------------|
| 200 | 1500 | 0.3 | 150.96 | 0.356 | | 115935 |
| 228 | 1317 | 0.3 | 116.67 | 0.529 | | 89409 |
| 291 | 1030 | 0.3 | 114.17 | 0.926 | | 54677 |
| 350 | 857 | 0.4 | 14.41 | 1.293 | 3106 | 37856 |
| 450 | 667 | 0.5 | 13.80 | 1.450 | 2262 | 22901 |
| 620 | 484 | 0.5 | 16.35 | 1.277 | 4100 | 12064 |
| 740 | 405 | 0.7 | 8.74 | 1.112 | 1545 | 8469 |
| 865 | 347 | 1.0 | 5.83 | 0.922 | 998 | 6198 |
| 1100 | 273 | 1.0 | 2.06 | 0.670 | 236 | 3833 |
| 1180 | 254 | 1.0 | 1.74 | 0.610 | 204 | 3325 |
| 1400 | 214 | 1.5 | 2.93 | 0.447 | 1072 | 2366 |
| 2000 | 150 | 1.5 | 2.30 | 0.196 | 3458 | 1159 |
| 3300 | 90.9 | 1.5 | 2.82 | 0.080 | 30773 | 426 |

*The NEFD is the flux density required to achieve a signal-to-noise ratio of 1 in 1-second. The sensitivity calculated on the basis of the appropriate PWV for that wavelength. The time to the confusion limit is for S/N = 5 and 30 beams/source.

Table 4.4 CCAT Line Sensitivity*

| λ (μm) | Freq (GHz) | PWV (mm) | NEFD (mJy) | Line Flux (W/m ²) |
|--------------------------------|---------------|-------------|---------------|----------------------------------|
| 200 | 1500 | 0.3 | 1627.0 | 2.44×10^{-17} |
| 228 | 1317 | 0.3 | 1760.3 | 2.32×10^{-17} |
| 291 | 1030 | 0.3 | 1182.5 | 1.22×10^{-17} |
| 350 | 857 | 0.4 | 253.4 | 2.17×10^{-18} |
| 450 | 667 | 0.5 | 231.7 | 1.54×10^{-18} |
| 620 | 484 | 0.5 | 272.4 | 1.32×10^{-18} |
| 740 | 406 | 0.7 | 111.1 | 4.50×10^{-19} |
| 865 | 347 | 1.0 | 91.1 | 3.16×10^{-19} |
| 1100 | 272 | 1.0 | 61.4 | 1.67×10^{-19} |
| 1180 | 254 | 1.0 | 62.1 | 1.58×10^{-19} |
| 1400 | 214 | 1.5 | 62.3 | 1.33×10^{-19} |
| 2000 | 150 | 1.5 | 58.4 | 8.34×10^{-20} |
| 3300 | 91 | 1.5 | 64.6 | 5.87×10^{-20} |

* $R = \Delta\nu/\nu = 1000$ spectroscopic sensitivity for CCAT. Continuum (NEFD) and Line fluxes are for 1-sigma in 1-second assuming a transmission equal to the band average. The sensitivity calculated on the basis of the appropriate PWV for that wavelength.

4.2.5 Comparisons with other telescopes

The mapping speed for CCAT is greater than other survey telescopes (Figure 4.11), due to the combination of high sensitivity and wide field of view, partly enabled by the site and partly by the unique optical design. CCAT can thus map faster than any existing or planned submillimeter-wave facilities, and uniquely has the available focal plane area to accommodate improvements in instrumentation, especially in detector format, over the lifetime of the facility. The mapping speed advantage extends over a wide variety of observing depths, and typically exceeds an order of magnitude for a conservative 32x32 detector, providing a factor of 10 over SCUBA-2 at 450 microns, and a factor of 30 at 850 microns.

The reach of CCAT crucially extends beyond more rapid surveying at the same depth but includes better spatial resolution. Thus CCAT is capable of detecting sources that are intrinsically fainter than can be detected using any other facilities except ALMA. These detections could be readily followed up using ALMA. For example, in the case of distant galaxies, luminosities of a few $10^{11} L_{\odot}$ will be detectable. This luminosity range allows CCAT to identify a much larger overlap with high-redshift galaxies found in other wavebands, and to allow ALMA to prioritize its precious resources to efficiently reveal the internal structure of a representative range of galaxies, identified primarily using CCAT. CCAT can thus reach detection limits across the available submillimeter atmospheric windows of a few 100 μJy , exploiting the aperture size to overcome confusion limits more effectively than any existing or planned space-borne or ground-based facilities. At the shortest wavelengths, CCAT is able to probe considerably deeper, providing a unique survey facility.

A far future (2020-2030) 10-m class cold space telescope would be necessary to exceed the detection rate for CCAT. CCAT will continue to provide a resolution advantage and growth potential in detector format.

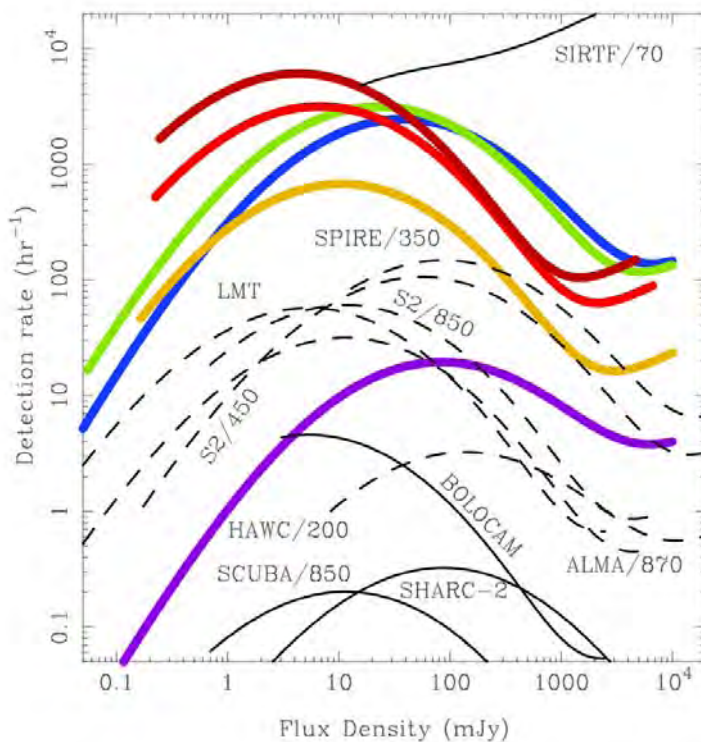


Figure 4.11: Source detection rate estimates, folding together fields of view, sensitivities, the density of sources on the sky and the confusion limit (cutoff to curves on the left) for a variety of ground-based and space-based facilities, including SCUBA-2, Herschel and ALMA. Note that CCAT has greater detection rates than the other facilities, even assuming a modest 32x32 detector for CCAT. The CCAT bands are denoted by spectral colors, 200 (violet), 350 (blue), 450 (green), 620 (orange), 750 (red) and 850 (red-brown) microns.

4.3 Distant Galaxies

4.3.1 Science Goals

The core goal of the distant galaxies project is to understand star and galaxy formation in the first few billion years after the Big Bang, and to place this within the context of the formation of large-scale structures such as clusters, filaments and voids. Only by making observations at far-infrared and submillimeter wavelengths can a full account of these processes be presented. The observed presence of dust in even the highest redshift objects means that continuum observations in the submillimeter can probe its thermal emission to redshifts before reionization at $z > 6$ and as far as $z = 10$ (less than 500 million years after the Big Bang). Far-infrared spectral lines can reveal the details of the galaxies' astrophysics over the same redshift range.

4.3.2 Motivation/Background

Among the most important cosmological results of the last few decades was the discovery by the COBE satellite of a substantial level of background radiation at FIR/submillimeter wavelengths. This background is at least equal in intensity to the optical/near-IR background, suggesting that the global star formation rate at $z > 1$ was much higher than it is now, and that most of this star formation was shrouded in gas and dust. Later surveys at submillimeter wavelengths using first- and second-generation instruments resolved the bulk of this background into a huge population of heavily obscured star-forming galaxies in the redshift range $1 < z < 5$, signposting the peak epoch of galaxy assembly over the history of the Universe. Clearly therefore, a complete picture of the processes of galaxy formation cannot be obtained without submillimeter/FIR observations – submillimeter /FIR observations may in fact provide *most* of the picture.

Very recent results from both large-area surveys, and semi-analytic and hydrodynamical modeling (e.g. Figure 4.12), have shown that these distant submillimeter sources may hold the answers not just to key questions in the area of galaxy formation, but also to the formation of large-scale structures. Modern structure formation models describe the evolution of the total mass distribution via the evolution of initially Gaussian density fluctuations, which means that the evolution of the total mass distribution should be traced by the formation and evolution of galaxies. Density fluctuations or 'haloes' in the dark matter distribution are predicted to undergo successive mergers over time to build haloes of steadily increasing mass. Within this framework, the largest concentrations of baryons are expected to be found within the most massive haloes. A basic verification of this idea can be seen in the local Universe, where massive elliptical galaxies are almost invariably found within rich galaxy clusters. The "naive" expectation from hierarchical theory would be that massive galaxies form relatively late and over a long period of time, representing successive mergers between dark matter haloes, building up the required large baryon reservoirs. There is however observational evidence that high redshift FIR-luminous sources are very massive systems forming on rapid timescales, and serious theoretical difficulties have arisen in trying to explain this result; proposed solutions include a top-heavy initial mass function for the stars formed in bursts, so that the same submillimeter flux can be produced with lower star formation rates, modified treatments of virialization and the survival of sub-haloes to solve the "overmerging" problem in the standard Press-Schechter formalism and make the star formation rates high enough, and modifications to gas cooling and supernova feedback.

Fundamentally however, virtually all structure formation models have one prediction in common, namely that the very massive haloes hosting these distant FIR-luminous systems should cluster together strongly on the sky, usually characterized by the 2-point angular correlation function, $\alpha(\theta)$. Different models however make very different predictions for the amplitude and functional form of $\alpha(\theta)$, and how it evolves with redshift. The characterization of the development of structure in the high z Universe is therefore intimately linked to our ability to study large samples of galaxies in the submillimeter to measure these parameters. Existing ground-based facilities are however assembling samples of, at most, a few hundred submillimeter galaxies, giving us just a glimpse of the most luminous objects. Surveys in multiple submillimeter bands using a substantially larger, more sensitive telescope, such as CCAT, would uncover samples of several thousand sources, allow a rough measurement of each source redshift by photometric means (the accuracy of photometric submillimeter redshifts can be as good as 20% if the range of SEDs is accurately quantified), and probe deeper into the luminosity

function to find more “typical” systems. The improvement in angular resolution which accompanies the larger telescope size is also crucial to overcome spatial confusion (see Section 4.2.3), and the mapping speed of a large-format camera is essential to generate large catalogs of galaxies. The CCAT sample is the ideal training set for this study of representative high-redshift galaxies. This method will allow us to map the history of the star formation of the Universe, as well as the evolution of its clustering properties by monitoring the functional form and amplitude scaling properties of $\omega(\theta)$ at different redshift intervals.

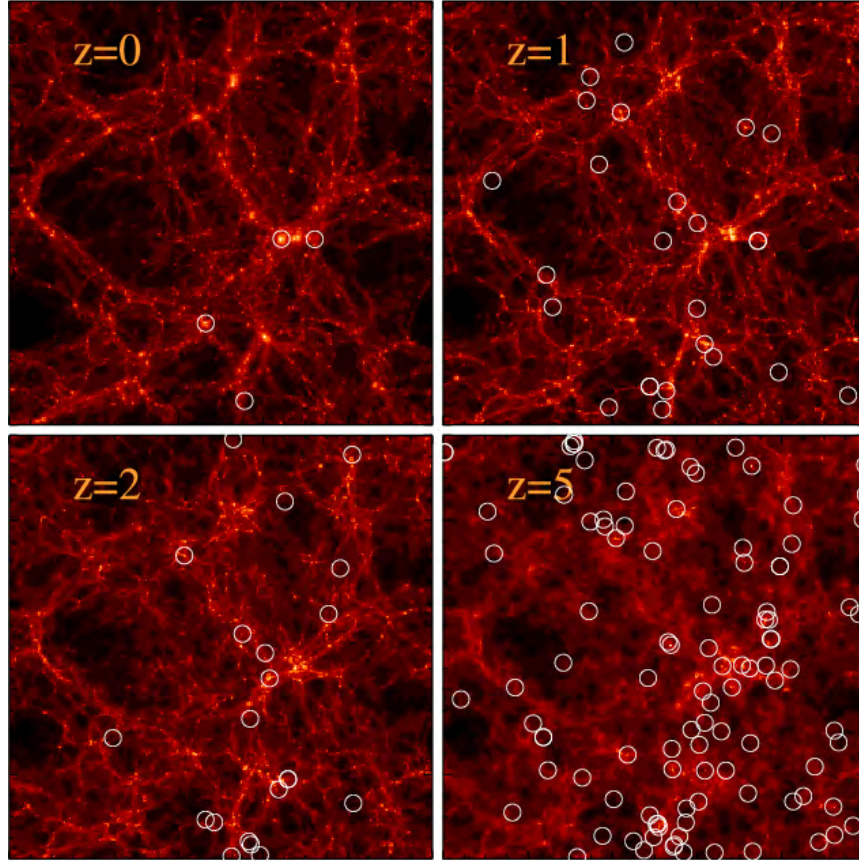


Figure 4.12: An example of modern cosmological hydrodynamic simulations (Nagamine et al 2005). Each panel has a comoving size of 143 Mpc on a side, and the star forming galaxies with instantaneous star formation rate greater than $100 M_{\odot}/\text{yr}$ at each epoch are indicated by the circles.

Finally, access to spectral lines, such as high rotational quantum number transitions of carbon monoxide (CO) and, especially, the fine structure transition of ionized carbon [CII] (rest wavelength of $158 \mu\text{m}$), will play a very important role in yielding accurate redshifts for the most extreme galaxies, providing dynamical information about massive and merging systems and insights in the physics of the star-forming gas.

4.3.3 Technique

1) The number counts of submillimeter galaxies at low flux levels are unknown and are in fact an important aspect of the science to be explored. Ultra-deep surveys located on best studied fields (e.g. GOODS-S etc) will be imaged until the confusion limit is reached. This will require tens of hours per field in two colors ($350 \text{ \& } 450 \mu\text{m}$) to allow confusion to be quantified very securely and exploit the reduced confusion limit to push our knowledge of dusty high-redshift galaxies far beyond the level of current work. Note that determining the confusion limit at $200 \mu\text{m}$ is an important goal for CCAT, but that extensive surveys from the ground at this wavelength are not practical.

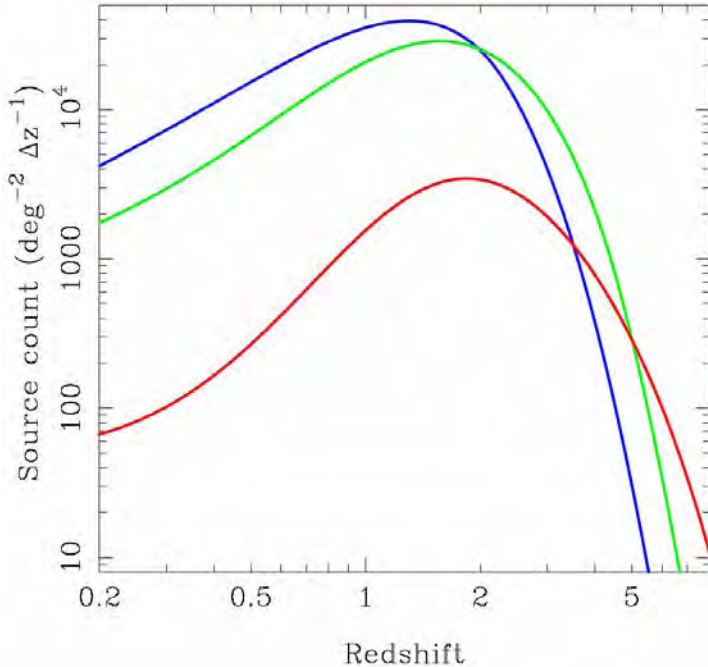


Figure 4.13: Estimated redshift distribution of galaxies that will be detected by CCAT at 1 mJy for 200 (blue), 350 (green), and 850 (red) μm .

2) A major goal is to obtain a significant sample of galaxies spaced in (logarithmic) redshift and luminosity bins. This is accomplished with a 350/450 micron survey covering all accessible well-studied fields (to $\sim 10\text{-}20 \text{ deg}^2$) in best weather. Using the CCAT sensitivity, confusion limits, and field of view from Section 4.2.4, about 500 hours/ deg^2 will be required. This, of course, will only be fully quantified when the ultra-deep surveys are done. Reaching the confusion limit and yielding 1,000,000 galaxies in 10 square degrees will require probably 5000 hours per band. This survey will generate a large sample of galaxies that bridge the luminosity gap at several 10^{11} solar luminosities between the hundreds of luminous submillimeter galaxies currently known and more typical luminous optically-bright galaxies. Existing deep far-infrared surveys of the sky cover 10's of square degrees. Herschel Space Observatory will likely expand this coverage to several hundred square degrees. The estimated redshift distribution of detections by CCAT is shown in Figure 4.13

3) Longer wavelength (620/740/870 micron) surveys can occur in parallel with the above survey, and can be carried out alone in worse weather. A confusion limited map will require about 10 hours per square degree. The goal is to cover a large fraction of the sky in a few years, starting with the best-surveyed regions at complementary wavelengths, to find extreme objects and remove CMB foregrounds.

4) Moderate resolution ($R \sim 1000$) spectroscopy will be used to follow-up selected sources from the survey. The [OI] 63 μm , [OIII] 88 μm , [NII] 122 and 205 μm and, especially, [CII] 158 μm emission will be used to verify the rough photometric redshifts generated from CCAT continuum colors and give very accurate redshifts of selected galaxies. These lines will also allow the study of gas cooling, the physical conditions in the star forming gas, the properties of the interstellar radiation field, the internal dynamics of primeval galaxies and of their merger histories. In 10,000 seconds of integration time the [CII], [OIII], and [OI] lines will be detectable out to $z = 4.8$, 4.1, and 6.1 for galaxies with luminosities $> 5 \times 10^{10}$, 2×10^{11} , and $7 \times 10^{11} L_{\odot}$ (at the most highest redshifts) respectively as the lines redshift across the submillimeter telluric windows. Characterizing thousands of galaxies will require thousands of hours depending on the multi-object capability of the spectrograph.

4.3.4 CCAT Requirements

For the photometric survey field-of-view and sensitivity are of paramount importance. The survey baseline assumes a 5×5 arcmin field-of-view. The time for the survey will scale with sensitivity and array area. For an array with N pixels on a side and a point source sensitivity S , the time to complete the survey scales as $S^2 N^2$. The

chosen field of view matches the resolution of the Planck Surveyor survey, allowing rapid localization of these objects. Galaxy survey science is favored by the largest field of view, and is enabled by the baseline value.

Photometric redshifts require observations in at least two bands. The current baseline is to use 350 and 450 μm combined with a longer wavelength band. Based on the typical SED of a distant dusty galaxy, and the sensitivities of CCAT these bands should achieve the highest signal to noise ratio in a given integration time. The ultra-deep survey will use these same bands.

Follow-up spectroscopy requires access to all the submillimeter windows to obtain a range of galaxy redshifts. Each band should be covered in a single setting to optimize the redshift search (with a first guess based on the photometric redshift). Low redshift identifications can be ruled out with data from Sloan and existing deep survey data in key survey fields. Best sensitivity is achieved when the spatial resolution is at its highest, so the slit size should scale with wavelength (diffraction limit). The shortest wavelengths will provide the most severe constraints. The requirement is to operate at 350 μm where the slit will be ~ 3.5 arcseconds with a goal to reach 200 μm (2 arcseconds slit). The telescope must be able to point and track to $\sim 1/5$ of this size. Follow-up of the brightest Spitzer, Herschel, and Planck Surveyor sources will be an important project making good pointing and spatial resolution important.

Key Instruments:

- 350 & 450 μm camera with greater than 5×5 arcmin field-of-view. A parallel longer wavelength band through the same atmospheric column would be useful for photometric redshifts.
- R ~ 1000 spectrograph with full coverage over each submillimeter window
- 620, 740, 870 μm and 1.2mm cameras with greater than 5×5 arcmin field-of-view. Note that sensitivities in terms of signal-to-noise ratios are likely to be comparable at these wavelengths.

Key Telescope Requirements

- Greater than 10 arcmin field-of-view (to accommodate larger field-of-view instruments as they become available)
- Pointing and tracking to enable spectroscopy with 3.5" (2.0" goal) slits.

4.3.5 CCAT Uniqueness and Synergies

The combination of band coverage, sensitivity, spatial resolution, and sky coverage make CCAT uniquely suited to approaching this problem. Smaller telescopes, including space telescopes (Herschel, SPICA and SAFIR), will be either limited by confusion or sensitivity while ALMA has a limited field of view. For Nyquist sampling four pixels of CCAT will cover the field of view of ALMA. Thus for a 100×100 pixel imaging system, CCAT will be over 600 times faster for large area surveys than ALMA (assuming similar point source sensitivities). However, "interesting" sources detected in the CCAT surveys will be prime candidates for resolved imaging with ALMA. CCAT will complement the LMT working at 1mm since CCAT can reach shorter wavelengths which are important for spectroscopic follow-up and for photometric redshift determination. The larger aperture of LMT at wavelengths longer than 1mm means that in good conditions it would perform as well as CCAT for detecting galaxies at these wavelengths; however, it would not match the detection rate and diagnostic power of CCAT in the submillimeter.

4.3.6 Star Formation in the Early Universe

The [CII] line to far-IR continuum luminosity ratio, R, is a sensitive indicator of the strength of the ambient interstellar radiation field parameterized by G (Figure 4.14). Therefore, the [CII] line detection yields the concentration of any starburst. In regions with the highest UV fields ($G > 10^4$ as for young starbursts and AGNs), the [CII]/far-IR continuum ratio is relatively small ($R \sim 10^{-4}$) due to both the reduced efficiency of photoelectric effect (from increasing grain charge), and to the increased cooling in [OI] 63 μm line. For more diffuse radiation fields ($G \sim 10^3$ like M82) the [CII]/far-IR ratio is significantly larger. For normal galaxies like the Milky Way, $G \sim 1$ to 100, and R is larger still ($R \sim 10^{-3} \rightarrow 10^{-2}$). When compared with the far-IR continuum, the derived G yields

the source beam filling factor, hence physical size of the emitting regions. Therefore, *detecting [CII] from highly redshifted galaxies probes star formation in the epoch of galaxy formation.*

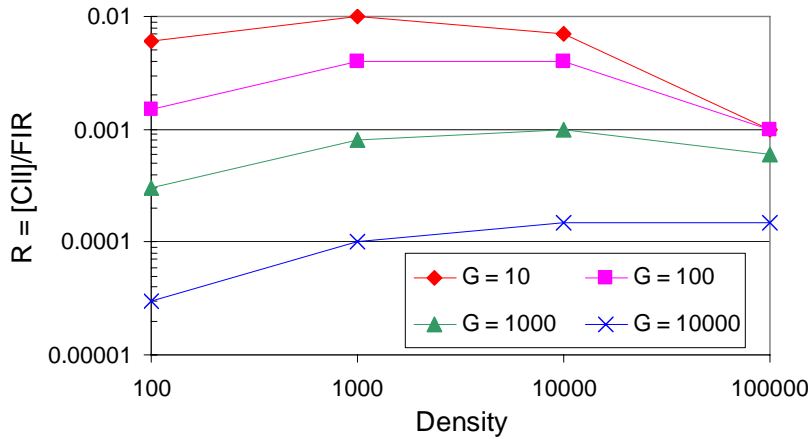


Figure 4.14: The [CII]/far-IR continuum ratio as a function of G, the strength of the ambient interstellar radiation field (from Kaufmann et al 1999).

If the distant sources are powered by starbursts, then G, as measured by R, can measure the age of galactic mergers, or of the starburst itself. In the early merger stage there may be very localized, intense starbursts with very high G. As the merger progresses, other regions are stimulated to burst either by the dynamics of the collision, or by gas compression by supernovae explosions in the original burst. As the burst propagates it will tend to lower the overall G, raising the [CII] line to far-IR continuum ratio.

The [CII] line is uniquely bright so that its detection alone is somewhat unique as a redshift indicator. However, redshifts can be verified, with a gain in the physical understanding, by detecting other bright far-IR lines. The [OI] 63 μm line can serve as a substitute diagnostic for [CII] in PDRs exposed to strong radiation fields, while the [NII] line can help discriminate the origins of the observed [CII] emission. The combined [OI], [CII], and [NII] lines well constrain the photodissociated molecular, atomic, and low density ionized gas in galaxies. Since O^{++} requires 35 eV photons to form detection of the [OIII] line indicates a large scale, *young* starburst headed by early type ($\sim \text{O}6$) stars. The line flux is related to the numbers of early type stars. If one can observe the cm wave free-free continuum, one can relate the numbers of Lyman continuum photons to the harder UV required to form O^{++} , so that the hardness of the UV radiation field is probed as well.

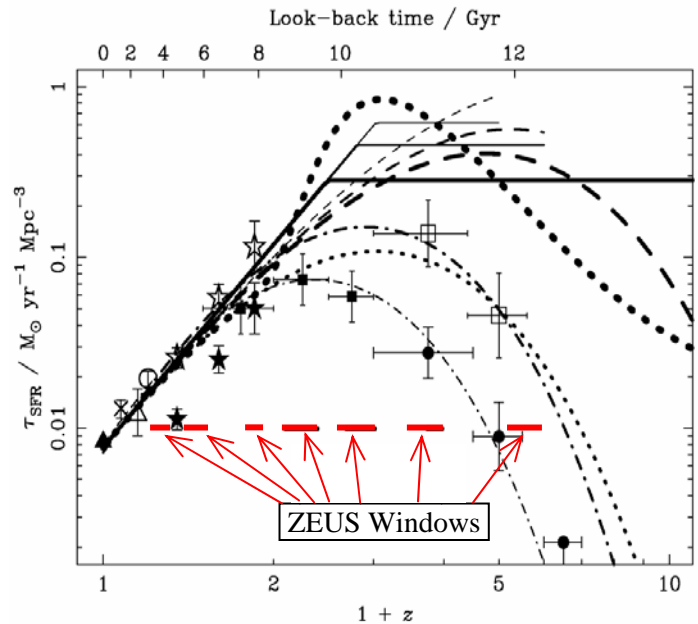


Figure 4.15: Estimates of the comoving star formation history (Blain et al). Filled squares and circles toward the bottom represent the original Madau plot based on optical/UV HDF observations (Madau et al). Open squares correct this data for dust extinction (Pettini et al). The 7 upper curves are models that are consistent with the SCUBA data. The solid lines beneath the curves mark the [CII] redshft ranges accessible to ZEUS.

A long slit echelle grating spectrometer already exists (ZEUS) that can be adapted to the CCAT telescope for detecting the [CII] in the important regions of redshift space (0.2 to 5) where the most evolution per co-moving volume occurs (Figure 4.15). The [CII] line is detectable at redshifts in excess of 5 for $L_{\text{far-IR}} > 3 \times 10^{11} L_{\odot}$ (Figure 4.16), where we have assumed $R \sim 3 \times 10^{-3}$ as for local moderate luminosity systems. ULIRGS ($L > 10^{12} L_{\odot}$), typically have $R \sim 6.6 \times 10^{-4}$, so that the [CII] line is readily detectable from these systems as well. We are particularly interested in detecting the lower luminosity systems since these are important for galaxy assembly.

[CII] Limits in Terms of $L_{\text{Far-IR}}$

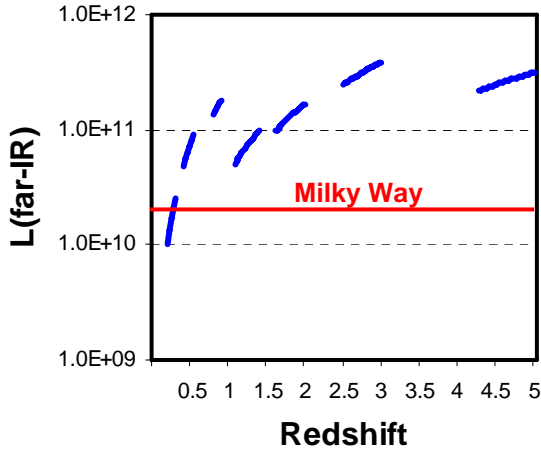


Figure 4.16: Detectability of [CII] line emission from distant galaxies. All limits are 5σ in 4 hours of integration time, using the sensitivity values appropriate for the telluric band into which the $157 \mu\text{m}$ line is redshifted. At redshifts beyond 5, suitable spectrometers on CCAT can detect the [CII] line from galaxies with $L_{\text{far-IR}} < 3 \times 10^{11} L_{\odot}$. Galaxies with only twice the [CII] luminosity of the Milky Way (e.g. NGC 891) can be detected at redshifts of 1.4. This calculation assumes the [CII]/far-IR luminosity ratio, $R = 3 \times 10^{-3}$, suitable for moderate luminosity systems, $H_0 = 71 \text{ km/s/Mpc}$, $\Omega_M = 0.27$, and $\Omega_\Lambda = 0.73$.

4.3.6.1 Contrast and Synergies with Other Facilities

The CCAT spectrometers promise to be more than a factor of a 100 more sensitive than the SPIRE spectrometer on Herschel in the telluric windows. In the higher frequency bands, the CCCAT spectrometers will deliver sensitivity comparable to ALMA for broad line extragalactic point sources, so that with the implementation of spatial multiplexing, the CCAT system will be the best available for detecting redshifted fine-structure lines from galaxies. Again there is strong synergy with ALMA in that once a strong emitter is detected with CCAT, ALMA can much better resolve the underlying spatial structure.

4.4 Cosmology — Sunyaev-Zeldovich Effect

4.4.1 Science Goals

The Sunyaev-Zeldovich (SZ) effect will become, over the next decade, an important probe of cosmology and cluster formation astrophysics via wide-area blind surveys for galaxy clusters using the SZ effect. CCAT can play a significant complementary role to these surveys by pursuing the following SZ observations:

- Detailed thermal SZ (tSZ) effect mapping of clusters detected by wide-area blind tSZ surveys such as APEX-SZ, ACT, SPT, and Planck. CCAT will provide high-resolution SZ profiles to aid in calibrating and interpreting these surveys.
- Blind tSZ surveys reaching lower mass limits than wide-area surveys.
- Measurement of the tSZ anisotropy power spectrum at very high angular multipole number, $\ell \sim 2000 - 20000$.
- Low-resolution tSZ spectroscopic follow-up of clusters to aid in measuring relativistic effects and to possibly provide SZ-based gas temperatures.

We have considered other science goals (primary CMB anisotropy, kSZ searches in known clusters, kSZ anisotropy, SZ polarization) but judged that they are marginal based on conservative confusion-limit estimates, better accomplished by other instruments, or beyond the reach of CCAT.

4.4.2 Motivation/Background

The Sunyaev-Zeldovich effects consist of scattering of cosmic microwave background (CMB) photons by the hot electrons in the intracluster medium (ICM) of galaxy clusters. The thermal SZ (tSZ) effect is a Compton-scattering-induced spectral distortion of the CMB. The kinetic SZ (kSZ) effect is a Doppler shift of the CMB due to scattering by a moving cluster.

The tSZ effect has been detected in tens of clusters; John Carlstrom and collaborators dominate the count, having used the BIMA and OVRO interferometers to image about 60 clusters at 1 cm. The SuZIE experiment has the largest millimeter-wave sample, with a total of 11 clusters with measurements at 1.1, 1.4, and 2.1 mm. No cluster has been found "blindly" in the tSZ yet. The kSZ effect has not been detected. A significant deficiency of the existing data is their relatively poor angular resolution (about 1 arcmin) and their lack of ability to probe extended structure (because the sample is dominated by interferometric measurements).

We believe that the tSZ will provide an important new probe of galaxy clusters in the coming years. Historically, free-free X-ray emission has been the primary probe of intracluster gas, but it is a complicated observable: it scales with the product of the square of the electron density, n_e^2 , and the nontrivial electron-temperature dependent emissivity function, $\Lambda(E_X, T_e)$. While Chandra and XMM have taught us a great deal, they have also highlighted the complexity of the ICM, with cold fronts, bubbles from AGN, evidence of mergers, etc. tSZ would provide another, simpler ICM observable, the line-of-sight integral of the pressure. tSZ profiles of clusters would enable more detailed study of the thermodynamic state of the gas, including the level of entropy injection by star formation or other heating processes, the importance of radiative cooling, and cluster merger histories. tSZ may also give us more information about the shape of the gravitational potential well – the dark matter – because it will extend to larger radius.

Regular observation of the kSZ effect, while extremely challenging, would provide a new and unique observable for cosmology: a probe of the peculiar velocity field at high redshift (z up to 2 or 3). It may also be possible to study internal bulk motions in galaxy clusters using the kSZ effect.

An exciting prospect is the advent of wide-area "blind" surveys in the tSZ. The tSZ provides a largely redshift-independent method for detecting galaxy clusters; a flux-limited tSZ survey is, to a factor of 2, a mass-limited survey. Thus, measurement of cluster abundance as a function of redshift via the tSZ would be free of the extremely redshift-dependent selection functions of optical or X-ray surveys. Such an abundance measurement would constrain cosmological parameters, in particular Ω_m , Ω_Λ , and the equation of state parameter w . Many such

surveys will be undertaken in the coming years by the Atacama Pathfinder Experiment-SZ (APEX-SZ — MPIfR and Berkeley), the Atacama Cosmology Telescope (ACT — Princeton, Penn, Goddard), the South Pole Telescope (SPT — Chicago, Case Western, and Berkeley), and the Planck satellite.

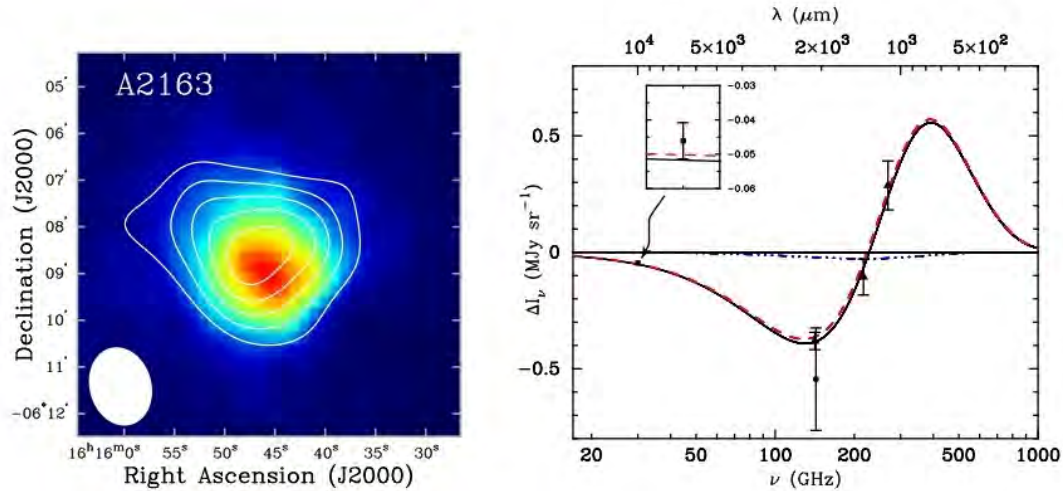


Figure 4.17: Sunyaev-Zeldovich observations of Abell 2163. The left plot shows the ROSAT X-ray map (color) overlaid with contours of SZ obtained with the BIMA interferometer at 30 GHz. The right plot shows the spectrum of the SZ effect in A2163 from combined measurements with BIMA (30 GHz), SuZIE (1.1, 1.4, and 2.1 mm), and Diabolo (2.1 mm).

Interpretation of these surveys will require careful characterization of the tSZ mass determination. The surveys intentionally leave the emission spatially unresolved in order to maximize survey efficiency. Thus, they obtain little information about the tSZ emission aside from its total flux. Follow-up imaging using CCAT would provide 3 to 4 times finer angular resolution. This detailed tSZ information will be useful for understanding how cluster astrophysics affect the tSZ mass determination, whose scatter and bias dominates cosmological interpretation of survey yields.

4.4.3 Technique

There is a large literature on calculating the abundances of clusters, the expected dark-matter and gas profiles of galaxy clusters, and the resulting tSZ and kSZ profiles. We have reviewed this literature in a technical note¹, calculated simple approximate formulae for quantities of interest, made judgments about what projects are feasible and efficient uses of CCAT time, and outlined a set of key projects. We list some of the basic assumptions and parameters and a summary of key projects here.

Table 4.5: Cluster abundances

| Mass [$10^{14} M_\odot$] | Abundance [deg^{-2}] | Number in 20000 deg^2 |
|-------------------------------|------------------------------------|-----------------------------------|
| 1 | 40 | 10^6 |
| 3.5 | 6 | 10^5 |
| 10 | 0.25 | few $\times 10^3$ |
| 35 | 0.012 | 10^2 |

Table 4.6: Assumed beam sizes

| wavelength | beam FWHM |
|------------|-------------------------|
| 1.1 mm | 0.24 arcmin = 14 arcsec |
| 1.4 mm | 0.30 arcmin = 18 arcsec |
| 2.0 mm | 0.44 arcmin = 26 arcsec |
| 3.0 mm | 0.66 arcmin = 40 arcsec |

4.4.3.1 Assumptions

The fiducial cluster we will study is one at the mass limit of the wide-area tSZ surveys such as APEX-SZ, ACT, and SPT, with $M \approx 3.5 \times 10^{14} M_\odot$. Other fiducial targets are clusters with masses of $10^{14} M_\odot$, $10^{15} M_\odot$, and $3.5 \times 10^{15} M_\odot$. The Planck all-sky survey will detect clusters above a mass limit of $M \approx 8 \times 10^{14} M_\odot$. We list the integral cluster abundances ($N > M$) at these fiducial masses in Table 4.5.

¹ This technical note is available at <http://gabba.astro.cornell.edu/twiki/bin/view/Main/Cosmology>.

Minimizing excess optical loading is critical in the long-wavelength SZ bands, so we assume a Gaussian illumination of the 25-m diameter primary with a conservative -10 dB edge taper ($\sigma = 5.8$ m, FWHM = 13.7 m). This results in the beam sizes given in Table 4.6, which are coarser than those usually quoted in these bands for CCAT.

4.4.3.2 Expected Sensitivity

- **Photometric Sensitivity**

A background-limited 150 GHz photometric camera, at a site as good as CCAT's, will be limited by telescope optical loading. Neglecting the factor of 1.414 (square root of 2) chopping/sky-subtraction degradation that is included elsewhere in sensitivity estimates, such a camera would achieve $2.3 \text{ mJy-s}^{1/2}$ ($310 \mu\text{K}_{\text{CMB-s}}^{1/2}$) assuming 10% telescope emissivity and 1.5 mm PWV conditions. If the telescope emissivity is reduced to 5%: the sensitivity improves by 1.414 to $1.6 \text{ mJy-s}^{1/2}$ ($220 \mu\text{K}_{\text{CMB-s}}^{1/2}$). To provide the desired edge taper, we assume $\sim 2(F/\#)\lambda$ pixels, where the $F/\#$ is referenced to uniform illumination of the primary. At that pixel size, a 1000-pixel focal plane covers a $20 \text{ arcmin} \times 20 \text{ arcmin}$ field-of-view.

If we include other frequencies under the same conditions, we obtain the sensitivities given in Table 4.7. The 100 GHz and 150 GHz sensitivities are telescope-limited. The 220 GHz and 275 GHz bands would improve by about 1.414 if either the telescope emissivity were reduced by 2 or if the atmospheric opacity were reduced by 2.

Table 4.7 Background-limited sensitivities for SZ bands*

| frequency [GHz] | atmospheric transmission | NET _{RJ} [$\mu\text{K}_{\text{RJ-s}}^{1/2}$] | NET _{CMB} [$\mu\text{K}_{\text{CMB-s}}^{1/2}$] | NEFD [$\text{mJy-s}^{1/2}$] |
|-----------------|--------------------------|---|---|-------------------------------|
| 275 | 0.86 | 190 | 1000 | 2.5 |
| 220 | 0.905 | 170 | 530 | 2.2 |
| 150 | 0.93 | 180 | 310 | 2.3 |
| 100 | 0.93 | 210 | 270 | 2.7 |

*assuming 10% telescope emissivity and 1.5 mm PWV conditions.

- **Spectroscopic Sensitivity**

A background-limited waveguide spectrometer operating near 150 GHz with 3 GHz resolution should achieve a sensitivity of $\approx 5 \times 10^{-19} \text{ Wm}^{-2}\text{s}^{1/2}$ for the conservative 10% emissivity assumption. A reduction to 5% emissivity would improve this by about 40%, again a significant gain.

- **Confusion Limits**

The dominant source of confusion at SZ frequencies is extragalactic infrared point sources. We present confusion limits in Table 4.8. The confusion limit at 150 GHz is higher than the tSZ signal level in the wings of $3.5 \times 10^{14} M_{\odot}$ and $10^{15} M_{\odot}$ clusters and is comparable to the tSZ signal level at r_g (the geometric mean of the core and virial radii) in $3.5 \times 10^{14} M_{\odot}$ clusters. Confusion is clearly a challenge.

Table 4.8: One-source-per-beam confusion limits*

| Frequency [GHz] | Flux density [μJy] | Temperature [μK_{CMB}] | Compton y parameter |
|-----------------|---------------------------------|--|-----------------------|
| 275 | 66 | 27 | 1.1×10^{-5} |
| 220 | 89 | 21 | N/A |
| 150 | 44 | 6 | 2.3×10^{-6} |
| 100 | 21 | 2.1 | 5.1×10^{-7} |

*for the conservatively large beam sizes in Table 4.6. Limits provided by A. Blain.

We will subtract confusion noise using maps made by CCAT at higher frequencies. In the table of key projects, we list, for the desired key project flux limit, the number of confusing sources per 490 GHz beam at that flux limit when the flux limit is scaled to 490 GHz. This gives a rough estimate of whether sources are removable to the desired flux limit. ALMA follow-up is too slow to do point source removal.²

4.4.3.3 Candidate SZ Key Projects

A number of key SZ science projects suggest themselves, listed in Table 4.9. We have aimed for a number of programs that each require no more than 100 to 200 hours per year and are conducted over 5-year periods. Based on the observed PWV distributions, it would be reasonable to have about 5 of these projects running at any given time.

Table 4.9: Candidate SZ key projects*

| Science Target | Per beam sensitivity | | | # of objects per year | # of hours per year | # of objects in 5 years | # of hours in 5 years | confusion (# srces/ 490 GHz beam) |
|--|----------------------------|----------------|-------|--------------------------------|------------------------------|----------------------------------|--------------------------------|--|
| | μK_{CMB} | μJy | S/N | | | | | |
| tSZ profiles | | | | | | | | |
| High-mass ($> 3.5 \times 10^{15} M_{\odot}$) | | | | | | | | |
| mapping | 2 | 15 | 5 | 10 | 130 | 50 | 650 | 1 / 30 |
| Medium-mass ($1 \times 10^{15} M_{\odot}$ to $3.5 \times 10^{15} M_{\odot}$) | | | | | | | | |
| mapping | 1 | 7.5 | 3 | 3 | 160 | 15 | 800 | $\sim 1 / 10$ |
| radial profile | 10 | 75 | 0.3 | 200 | 100 | 1000 | 600 | $\ll 1 / 30$ |
| Low-mass ($3.5 \times 10^{14} M_{\odot}$ to $1 \times 10^{15} M_{\odot}$) | | | | | | | | |
| radial profile | 3 | 23 | 0.3 | 20 | 120 | 100 | 600 | $< 1 / 30$ |
| tSZ pt-src survey, $S/N = 5$ at $1 \times 10^{15} M_{\odot}$ on 10 deg^2 fields | | | | | | | | |
| | 10 | 75 | 5 | 1 | 50 | 5 | 150 | $\ll 1 / 30$ |
| tSZ spectroscopy, one beam, $S/N = 5$ per $\Delta\nu = 3 \text{ GHz}$ bin | | | | | | | | |
| High-mass ($> 3.5 \times 10^{15} M_{\odot}$) | | | | | | | | |
| 9 pos, $\theta < \theta_g$ | 14 | 100 | 5 | 4 | 140 | 20 | 700 | $< 1 / 30$ |
| Medium-mass ($1 \times 10^{15} M_{\odot}$ to $3.5 \times 10^{15} M_{\odot}$) | | | | | | | | |
| 1 pos, $\theta < \theta_g$ | 3 | 20 | 5 | 2 | 140 | 10 | 700 | $\sim 1 / 30$ |
| kSZ at r_g , $S/N = 1$ per 150 GHz beam (for $4 \mu\text{K}_{\text{CMB}}$ signal level) | | | | | | | | |
| 150 GHz | 4 | 30 | 1 | 5 | 17 | 25 | 80 | $< 1 / 30$ |
| 220 GHz | 5.9 | 25 | 0.7 | 5 | 20 | 25 | 110 | 1 / 10 |
| 275 GHz | 7.3 | 18 | 0.6 | 5 | 50 | 25 | 260 | $\sim 1 / 1?$ |
| tSZ anisotropy survey, $S/N = 5$ at $1 \times 10^{15} M_{\odot}$ on 0.5 deg^2 fields | | | | | | | | |
| | 1.4 | 10 | 5 | 1 | 120 | 5 | 600 | 1 / 10 – 1 / 30 |
| kSZ anisotropy survey, $S/N = 1$ per 150 GHz beam, FoV-side fields | | | | | | | | |
| 150 GHz | 2 | 15 | 1 | 1 | 13 | 1 | 65 | 1 / 30 |
| 220 GHz | 2.9 | 12 | 0.7 | 1 | 19 | 5 | 95 | $\sim 1 / 1?$ |
| 275 GHz | 3.7 | 9 | 0.6 | 1 | 40 | 5 | 200 | $\sim 1 / 1?$ |

*The "confusion" column refers to the number of sources per 490 GHz beam at the flux level obtained by scaling the low-frequency per-beam sensitivity to 490 GHz using $\nu^{3.7}$. θ_g = angle corresponding to r_g , which is the geometrical mean of the core radius and the virial radius.

² The field-of-view of ALMA is too small to cover the bulk of a cluster to sufficient depth in a reasonable time (see the technical note¹ for integration times, as well as Section 4.2.4 of this note).

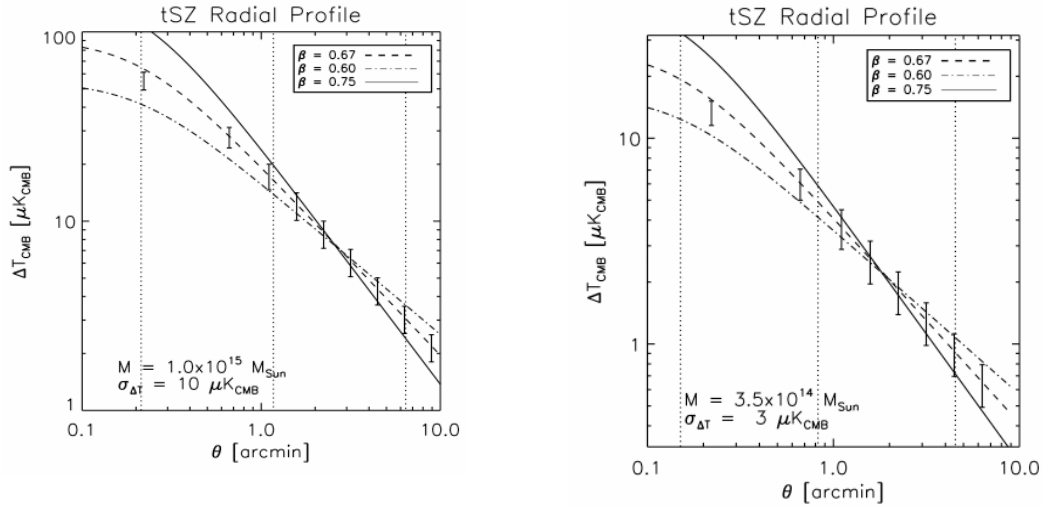


Figure 4.18: Expected errors on tSZ radial profiles. Cluster masses and assumed per-beam sensitivities are indicated. Each plot also shows three different β profiles that would yield the same integrated SZ Comptonization parameter within the virial radius. Profiles are shown for gas concentration factor $c_g = 5$; c_g is the ratio of the dark-matter halo NFW scale radius to the gas β -profile core radius. The vertical dotted lines indicate the three characteristic radii r_c , r_g , and R_v (core, geometrical mean of core and virial, and virial). The radial binning of the data is linear at small radius and logarithmic at large radius; no bin is allowed to be smaller than the beam FWHM at 150 GHz. The increase with radius of the area per bin yields approximate constant $S/N \approx 5$ at large radius.

In addition to full mapping projects, we will also undertake two tSZ "radial profile" key projects using azimuthal averaging for large catalogs of sources. The per-beam sensitivity needed to obtain these radial profiles is a factor of 10 less demanding than what is needed for full mapping, enabling the study of 100 times as many clusters. Expected profiles with uncertainties are shown in Figure 4.18. The choice of sensitivities for these projects was made to achieve $S/N \approx 5$ in each radial bin at large radius. To illustrate the use of such profiles, we have overlaid three different β gas profiles with exponents $\beta = 0.6, 0.67, \text{ and } 0.75$; we can easily distinguish them.

Quantitative evaluation of the scientific merit of these projects awaits detailed simulation work during the ongoing CCAT study. But one can reach some basic conclusions:

- The most worthwhile programs are pure tSZ mapping and radial profile studies because the number of objects obtained is large and confusion is negligible.
- Blind tSZ surveying down to $M = 10^{14} M_\odot$ ($S/N = 5$) over many square degrees is feasible and not limited by confusion noise.
- tSZ spectroscopy is fast enough that we can observe a reasonable sample of objects. Because it requires a special-purpose low- R spectrometer, we view spectroscopy as a follow-on project to tSZ profiles.
- The kSZ studies are stymied by confusion noise. The raw sensitivity is more than sufficient, but confusion will be limiting at 220 GHz and 275 GHz, even with shallow surveys ($S/N = 1$ per 150 GHz beam) and higher-frequency bands to remove confusing sources. Even using ALMA for subtraction, kSZ detection seems very difficult.³⁴
- For similar reasons, attempts to confirm tSZ signals using 220 GHz and 275 GHz are difficult except for the most massive clusters.

³ Observing down to $10 \mu\text{Jy}$ at 275 GHz over 10 arcmin^2 — the size of the core of a cluster out to θ_g — would require about 1 Msec. The 100 arcmin^2 needed to observe kSZ anisotropy would take 10 Msec. Even covering 1 arcmin^2 would require 100 ksec.

⁴ For an explanation of why CCAT seems to suffer worse confusion limitations than APEX, ACT, or SPT, see the companion technical note¹.

One should not take the last two conclusions as the final word because: 1) They depend critically on the infrared galaxy number counts, which are not yet precisely constrained — part of the reason to build CCAT!; 2) More detailed and accurate predictions of tSZ and kSZ signal levels may result in larger values; we have expressly been conservative; 3) Multi-frequency simulations may indicate that confusion is more removable than we have estimated here; and 4) Gravitational lensing by the clusters will mitigate confusion, but has not been taken into account. But, given the large uncertainty in the ability to do SZ work at 220 GHz and 275 GHz, it seems safe to conclude that the initial focus should be on 150 GHz tSZ observations.

4.4.4 CCAT Requirements

The telescope requirements for SZ observations are summarized in Table 4.10.

Table 4.10: Telescope requirements arising from science goals.

| Item | Req'ment | Goal | Notes |
|-------------------|--------------------------------|------------------------------------|--|
| Aperture | ≥ 20 m | — | Uniqueness |
| Surface roughness | < 30 μm | — | $\lambda/20$ at 620 μm |
| Blockage/loading | $< 10\%$ | $< 5\%$ | goal: telescope loading no worse than atmosph. and dewar loading |
| Wavelength range | 2 mm 620, 850 μm | 1 – 2 mm same | SZ obs IR pt src removal |
| FoV (diameter) | 10 arcmin | 20 arcmin | contain entire cluster |
| Pointing | | | |
| on-the-fly | 25 arcsec | 12 arcsec | 1 beam @ 1–2 mm |
| reconstructed | 1.25 arcsec | 0.6 arcsec | beam/20 @ 1–2 mm |
| on-the-fly | 6 arcsec | same | 1 beam @ 620 μm |
| reconstructed | 0.3 arcsec | same | beam/20 @ 620 μm |
| Tracking | | | |
| one hour | 1.5 arcsec | same | do 1 hour obs w/o added pointing jitter |
| 20 min | same | same | |
| 10 sec | same | same | |
| Elevation limits | >30 | — | Planck sources |
| Scan speed | 10 arcmin/sec | 30 arcmin/sec | sky noise, on FoV-sized fields (Lissajous) |
| acceleration | 10 arcmin/sec ² | 30 arcmin/sec ² | |
| Spectroscopy | — | $\Delta\nu = 3$ GHz, 120 – 325 GHz | 2 bands, 120 – 180 GHz and 200 – 325 GHz |
| Pol. capability | — | — | |

4.4.5 CCAT Uniqueness and Synergies

SZ observations with CCAT will probe a unique combination of angular scales and frequencies and would complement other SZ projects:

- For a significant subsample of clusters detected in wide-area surveys, CCAT will provide spatially resolved SZ profiles to aid in the characterization of the tSZ-mass relationship and consequently in cosmological interpretation. SZ data may be critical for such work, as the Chandra and XMM-Newton missions will end ~2010 and Constellation-X will launch no earlier than 2016.
- A CCAT blind tSZ survey would have a lower mass limit, $10^{14} M_{\odot}$, than the wide-area surveys, enabling a check of these surveys' detection efficiencies.
- The Sunyaev-Zeldovich Array (SZA) is an interferometer designed for blind tSZ surveying at 30 GHz and for high-resolution studies at 90 GHz. It is sited at CARMA and is currently taking survey data. The SZA, being an interferometer, will have better control of instrumental and observing systematics than CCAT but likely will have poorer instantaneous sensitivity. Together, SZA and CCAT will provide SZ spectral coverage at high angular resolution from 30 GHz to 150 GHz (and possibly 275 GHz).
- The Penn Array will be a 64-pixel 90 GHz bolometric array to make use of the Green Bank Telescope (GBT) with angular resolution 0.13 arcmin FWHM and 0.5 arcmin FoV. It will complement CCAT by investigating SZ substructure on 0.1 to 0.5 arcmin scales (larger scales will be lost to sky noise).
- The Large Millimeter Telescope (LMT) will provide information on scales comparable to GBT or midway between CCAT and GBT. The LMT design provides a 4-arcmin field-of-view, and currently planned instrumentation (AzTEC) will cover a 1.5-arcmin field-of-view. The angular resolutions of the LMT at 150 GHz and the GBT at 90 GHz are comparable. Atmospheric conditions may favor 90 GHz operation instead, in which case LMT provides angular resolution midway between that of CCAT and GBT. The better angular resolution of the LMT in the 150 – 300 GHz range as compared to CCAT is cancelled by CCAT's ability to remove confusion using the 350 GHz and 490 GHz bands, which are inaccessible to LMT.
- Interferometers like CARMA and ALMA will have exquisite point-source sensitivity over a field-of-view of a fraction of an arcmin² at the frequencies of interest for SZ. They will provide high angular resolution probes of substructure in the SZ, but will have poor fidelity on scales much larger than 1 arcmin, as well as being too slow to map fields appreciably larger than 10 arcmin².

Lastly, we note that SZ observations make the least stringent demands on telescope performance and weather, except on telescope optical loading, and so may be most effective in delivering cutting edge science from the earliest commissioning phase and during the poorest weather periods.

4.5 Nearby Galaxies

In order to understand the properties of the distant galaxies detected by the CCAT telescope, it is necessary to study the submillimeter properties of galaxies in the nearby Universe. Here we broadly group nearby galaxies into two categories (1) those that generate the bulk of their energy through fusion processes in stars (starforming galaxies) and (2) those that generate the bulk of their energy through accretion onto supermassive black holes (active galactic nuclei, AGN). CCAT studies in the submillimeter continuum and spectral lines can lead to much improved understanding of both these processes.

4.5.1 Motivation

The studies proposed here are motivated by two major advantages that submillimeter observations have over other spectral regimes. Firstly, the submillimeter bands are not affected by extinction that plagues optical observers. Stars form in the dusty cores of molecular clouds, so that observations of the starformation process, and newly formed early type stars are limited to the longer wavelength bands. In addition, galactic nuclei are often extinguished by many magnitudes in the visible. For example, only about a visible photon in 10^{10} from the Galactic Center is detectable from the Earth, while more than 90% of the 200 μm photons are transmitted. Secondly, interstellar gas clouds must cool to collapse and form stars, and the far-infrared and submillimeter bands dominate the cooling of much of the ISM. The light from young stars is absorbed locally by dust, and reradiated in the submillimeter bands. The Milky Way Galaxy radiates about a third of its energy in the far-IR and submillimeter bands via this mechanism, while starbursters and ultraluminous infrared galaxies (ULIRGs) emit most (up to 99%) of their light in these bands. The gas cools through collisional excitation of low lying energy levels of abundant molecules, atoms, and ions. These lines also trace the physical conditions (e.g. temperature, density, column density) of the gas. Are the clouds cooling to form stars, or being dissipated by starlight? What are the effects of the interstellar radiation field on the ISM in galaxies? For nearby galaxies, CCAT can study the interstellar medium on size scales of giant molecular clouds (~ 25 pc). What are the effects of bars, spiral arm potentials, and cloud-cloud collisions on star formation and the ISM?

4.5.1.1 The Extragalactic Niche

The CCAT telescope will be the premier facility in the world for fine scale studies of low surface brightness in the short submillimeter windows. This is especially true for continuum studies. Extragalactic studies of spectral lines requires only the modest resolving powers ($R \equiv \lambda/\Delta\lambda \sim \text{few thousand}$), that are readily achievable with direct detection spectrometers. Direct detection spectrometers have significant sensitivity advantages at the highest frequencies. Furthermore, at present it is much easier to design large format imaging spectrometers with direct detection systems

4.5.2 Cold Dust in Galaxies

The far-IR continuum emission from galaxies traces the deposition of optical starlight from nearby OB stars, or the diffuse ISRF so that it traces regions of star formation in an extinction free manner. The submillimeter bands are tracers of the mass of cold ($T < 20$ K) dust. For warmer dust, the submillimeter colors are insensitive to T , since they are in the Rayleigh-Jeans tail. However the warm dust properties are constrained by examining the apparent emissivity law. Combining temperature and emissivity law yields the dust column (mass). Combining with shorter wavelength observations (e.g. 38 or 60 μm SOFIA, or 70 μm Spitzer) yields the far-infrared luminosity of the system.

The far-IR and visible morphologies of galaxies are often quite different (Figure 4.19). For example, in the optical M31 is a quiescent Sb galaxy, while in the far-infrared there is a prominent ring of cool dust, with little or no evidence for spiral structure. There also is warm dust, indicating star formation activity in the nucleus.

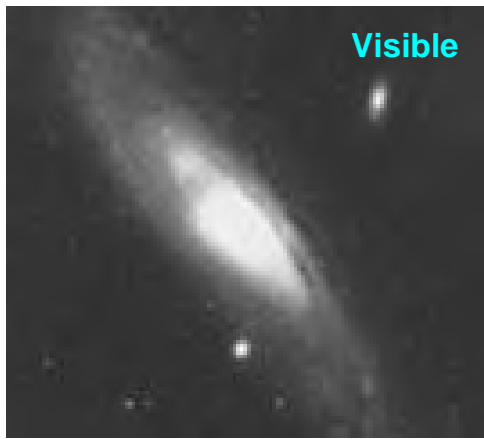
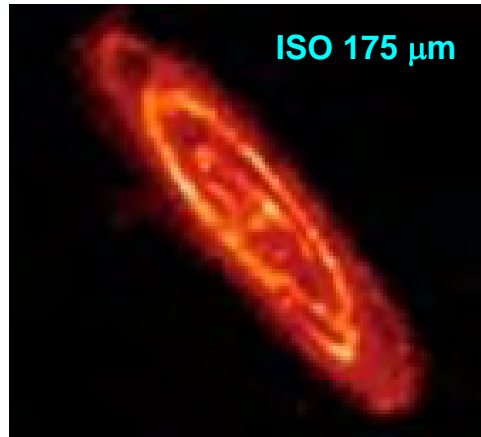
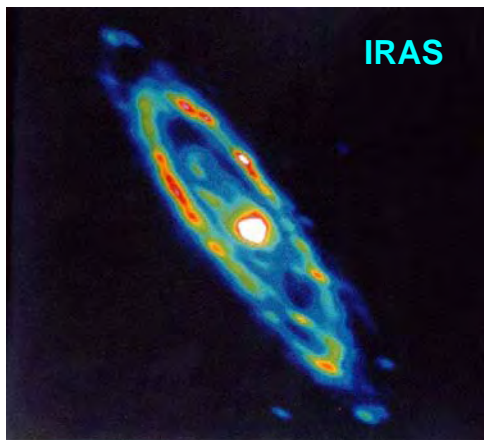


Figure 4.19: (left) M31 in the visible tracing starlight (below, left) M31 in a composite (12, 24, 60 and 120 μm) IRAS map, tracing warm dust near starformation regions (below, right) M31 as seen by ISO at 175 μm , tracing cold dust (Haas et al. 1998)



The longer wavelength (175 μm) ISO image of Haas et al. (1998) reveals that most of the dust in M31 is quite cold, with $T \sim 16$ K, much cooler, and ten times more massive than the warmer dust that was detected through IRAS studies. The warm dust to cold dust ratio varies little across the galaxy, so that it appears to be two distinct dust populations, not just differing heating mechanisms. The cold dust mass is large ($\sim 3 \times 10^7 M_{\odot}$), so that if distributed uniformly across the galaxy it would make M31 moderately opaque ($A_V \sim 0.5$) in the visible.

The edge-on Sb galaxy, NGC 891 has been imaged in the submillimeter continuum using both the SCUBA (450 and 850 μm) camera on the JCMT (Alton et al. 1998, Israel et al. 1998), and the SHARC (350 μm) camera on the CSO. The cold dust in the disk is well delineated by these efforts (Figure 4.20), but the angular resolution is insufficient to reveal the super bubbles and galactic chimneys apparent in the visible lines that trace the expulsion of gas and dust from the disk. With 3 to 4 times better angular resolution, CCAT should easily resolve these features at 200 and 350 μm .

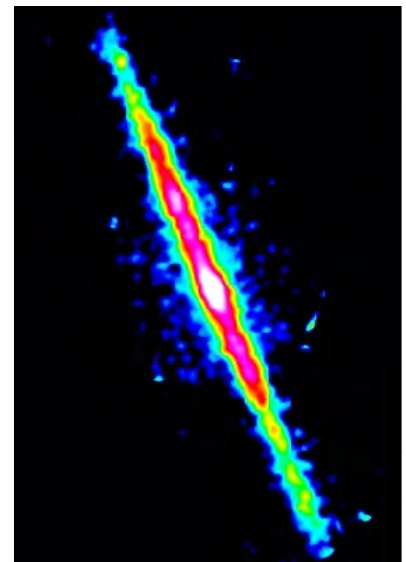


Figure 4.20 850 μm continuum image of NGC 891 (Alton et al. 1998, SCUBA/JCMT)

CCAT images the far-IR and submillimeter luminosity in an extinction free manner. For example, the Spitzer IRAC mid-IR images of the NGC 4038/4039 (Antennae Galaxy) system reveal a pearly inverted S shaped string of star formation. However, it is only in the submillimeter band that the most massive sites of star formation in the interaction zone are revealed (Figure 4.21).

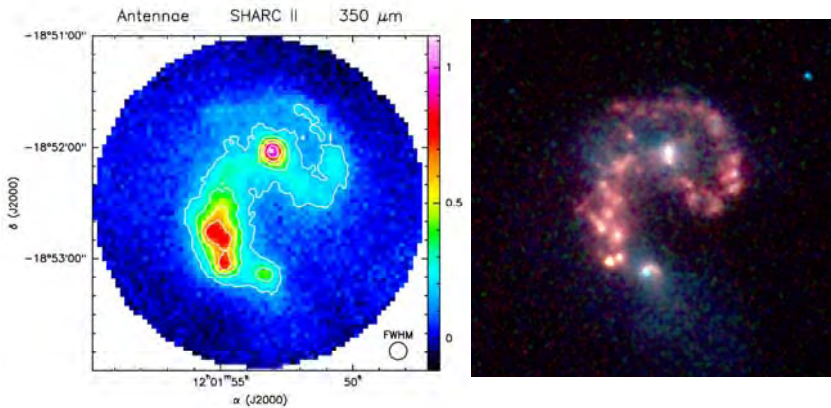


Figure 4.21 (left) SHARC image of the Antennae galaxy at 350 μm (Dowell et al.).

(right) IRAC/Spitzer composite of the Antennae system.

4.5.2.1 Time to Image Galaxies in the Submillimeter Continuum

Nearby interacting systems like the Antennae can be imaged quite rapidly with the cameras proposed for CCAT. At 350 μm , the extended emission is ~ 0.2 Jy per $10''$ CSO beam. This scales to 20 mJy per $3.5''$ CCAT beam. In 200 seconds, CCAT attains a flux limit of 1 mJy per beam, so that the signal-to-noise ratio (SNR) is ~ 20 . At 850 μm , the flux is 10 times smaller per beam. However, since the CCAT system is twice as sensitive at 850 μm , and the beam solid angle is 6 times larger, we estimate a SNR ~ 24 per beam in 200 seconds at 850 μm . Even at 200 μm , the Antennae system is easily detectable (SNR ~ 10) in a modest integration time of 1.6 hours. Therefore, with CCAT, we can image the Antennae in 4 bands (200, 350, 450, and 850 μm) in less than 2 hours, or in only 10 minutes without the 200 μm band!

For the less intense M83 system, a typical flux per beam is ~ 4 mJy at 350 μm , so that it would take ~ 1.3 hours to reach SNR > 20 in a typical beam over the $5'$ FoV of the SW-Cam. To image M83 in 3 bands (350, 450, 850 μm) requires ~ 4 hours.

The sensitivity is such that we could survey the brightest 100 nearby galaxies including quiescent spirals, starbursters, and ULIRGs in approximate 400 hours. This would provide a statistically significant sample of the submillimeter continuum emission from nearby systems forming templates to which the emission from distance systems can be compared.

4.5.2.2 Contrast and Synergies with Other Facilities

CCAT continuum sensitivities and the SW-Cam field of view ($5' \times 5'$) is such that it maps a $4' \times 4'$ region 100 times faster than Herschel to the same sensitivity. In addition, CCAT delivers a factor of 7 better spatial resolution. Point source sensitivities for CCAT are similar to that of ALMA, but the $5' \times 5'$ field of view of SW-Cam ensures mapping speeds that are 10,000 times larger for extended regions. ALMA provides great synergy with CCAT in that the most interesting regions detected with CCAT can be resolved with vastly superior spatial resolution of the ALMA array.

4.5.3 Cooling the ISM and the Generations of Star Formation

The 158 μm [CII] line is the dominant coolant for UV exposed molecular cloud surfaces, and atomic clouds, and is an important coolant for low density HII regions. It is therefore among the brightest, if not the brightest, single emission line from starforming galaxies. In the Milky Way the line amounts to some $6 \times 10^7 L_{\odot}$ (Stacey et al. 1985, Wright et al. 1991), or about 0.3% of the far-IR luminosity. Nearly as bright are the 122 μm and 205 μm lines of N^+ that the COBE satellite mapped from the Galaxy with luminosities $\sim 1/6$ and $1/10$ that of [CII] respectively. The [NII] lines are important coolants for diffuse ionized gas. Their line ratio is density sensitive, and it can be shown that their brightness is proportional to the ionizing photon rates for ionization bounded HII

regions. Furthermore, the 205 μm line emission has the same density dependence as [CII] for ionized gas, so that its intensity constrains the fraction of the observed [CII] emission that arises from HII regions.

The COBE satellite also detected strong mid-J CO rotational line emission from the Galaxy, up to $J = 8 \rightarrow 7$. The strength of these lines indicates substantial amounts of warm ($T > 40$ K), dense gas exists in the Galaxy, particularly towards the Galactic Center. The primary CO cooling lines are the submillimeter (mid-J) transitions. Furthermore, COBE detected ubiquitous 609 and 370 μm [CI] line emission from the Galaxy. The ratio of the [CI] lines is sensitive to the gas temperature (40 K for the Galaxy), and the combined cooling of the [CI] lines (most of which is in the 370 μm line) equals the total cooling of all the CO rotational lines.

The [NII] 205 μm , the [CI] and several submillimeter CO (e.g. $J = 4 \rightarrow 3$, $6 \rightarrow 5$, $7 \rightarrow 6$, $11 \rightarrow 10$, $13 \rightarrow 12$), and isotopic CO (e.g. $^{13}\text{CO}(6 \rightarrow 5)$) lines are available to the CCAT telescope. These lines are the primary cooling lines for much of the ISM, and important astrophysical probes of ionized gas, molecular clouds, photodissociation regions, shocks, and astro-chemistry.

The CO molecule is typically the dominant coolant for molecular gas. The run of line intensity with J constrains the gas temperature, density and mass. CO studies are quite important, as it is the molecular gas reservoir that constrains future episodes of star formation. The low- J line CO and isotopic lines cool the cold cores of molecular clouds, and trace their mass. The mid- J line emission signals the presence of PDRs associated with newly formed OB stars, while the high J lines trace molecular shocks associated with outflows from these stars or from cloud-cloud collisions.

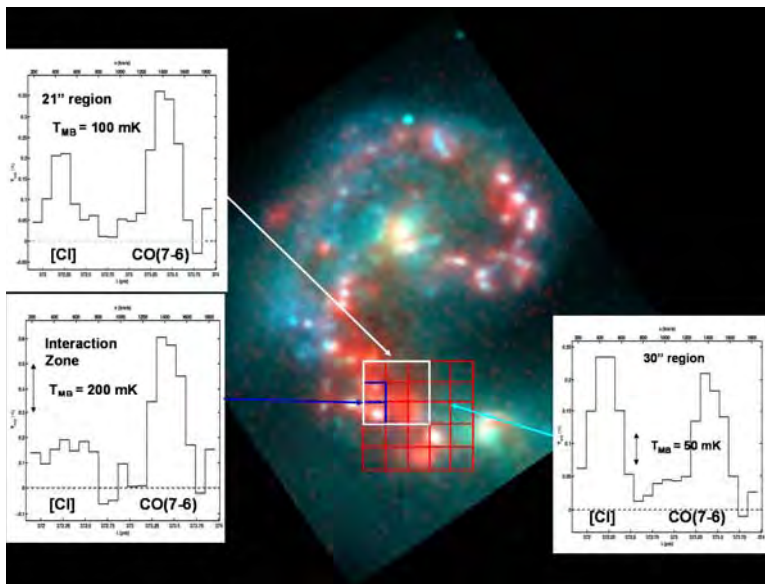


Figure 4.22: Simultaneous mapping of CO(7→6) and [CI] 370 μm line emission from the Antennae system obtained using SPIFI on the JCMT. The squares indicate the positions of the various pixels in SPIFI’s imaging array. Averaged over a 16 pixel ($28'' \times 28''$) footprint the [CI] line is somewhat brighter than the CO line (right-most spectrum). As one zooms into a $21'' \times 21''$ region, the CO line becomes brighter than the [CI] line (top-left spectrum). At the position of the starburst (lower-left spectrum), the CO line is greatly enhanced, reflecting the higher gas densities there.

Of particular interest are the [CI] 370 μm line and the CO(7→6) line pair. Since they lie only 2.7 GHz (1000 km/sec) apart, they are easily observed simultaneously in one extragalactic spectrum yielding excellent relative calibration and “perfect” spatial registration. The line ratio is very density sensitive, and can be used to rapidly pick out heavily extinguished star formation regions via their enhanced CO(7→6) line emission (Figure 4.22 and Figure 4.23).

Mid- J CO line emission has been detected from about a dozen nearby starforming galaxies showing the preponderance of warm dense gas. For example, the CO(7→6) line was mapped from the starburst nucleus of NGC 253 using an imaging Fabry-Perot interferometer, SPIFI on the JCMT (Bradford et al. 2003). The run of ^{12}CO , and ^{13}CO line emission with J is consistent with *all of the molecular gas* residing in a single warm ($T \sim 120$ K), dense ($n \sim 4.5 \times 10^4 \text{ cm}^{-3}$) component. This component also can account for the observed H_2 rotational line emission as well. The mass of this warm molecular gas is 10 to 30 times larger than that in PDRs as traced by their [CII] and [OI] line emission. PDR models fail by an order of magnitude to account for this much warm CO.

However, the cosmic ray flux (~ 800 times the Milky Way value) can heat the molecular gas and also provides a natural mechanism for heating the entire volume of molecular gas. Nikola et al. (2005, see also Gerin et al. 2005), have detected the $370 \mu\text{m}$ [CII] line from the nucleus of NGC 253 confirming the high gas temperatures. The added heat at the cloud cores from the cosmic rays will inhibit cloud collapse, so that the starburst in NGC 253 is self-limiting.

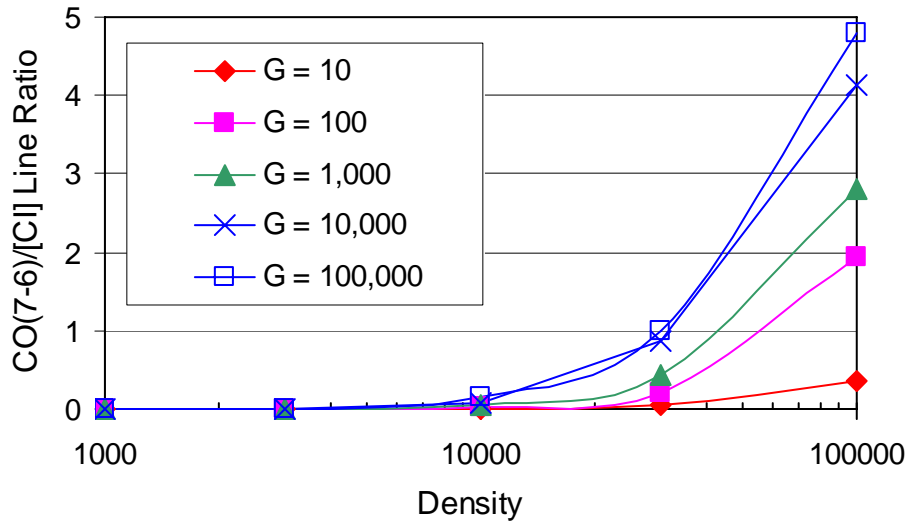


Figure 4.23: CO(7→6)/[CI] $370 \mu\text{m}$ line ratio as a function of density for various values of the strength of the interstellar far-UV radiation field, G (from Kaufman et al. 1999).

4.5.3.1 Examples: M83 and NGC 891

We will map several dozen of the nearby galaxies in their far-infrared continuum and submillimeter spectral line emission. Perhaps the best example is M83 a bright barred Sc galaxy presented to us nearly face on (see Figure 4.24). M83 was extensively mapped in the bright far-IR fine structure lines ([OI], [NII] $122 \mu\text{m}$, [OIII], [NIII], and [CII]) with the ISO LWS ($70''$ beam). The spiral arm/inter-arm contrast is highest for the [OIII] $88 \mu\text{m}$ line, and at the bar-spiral arm interfaces, the [OI], [OIII], and [CII] lines are all quite bright indicating star formation rates triggered by orbit crowding collisions of molecular clouds. With CCAT, one can easily resolve the far-IR continuum, the ionized gas {[NII]}, the atomic/molecular gas ([CI]) and the dense molecular gas (mid-J CO) as they cross the spiral arms. Can we trace the compression of gas and subsequent “ignition” of the next generation of stars?

M83 makes an excellent target for CCAT observations. At a distance of 5 Mpc, the $370 \mu\text{m}$ [CI] beam ($3.7''$) subtends 90 pc. The peak [CI] line flux is $2 \times 10^{-17} \text{ W/m}^2$ per beam, so that $\text{SNR} \sim 50$ is achieved in 30 seconds of integration time. The brighter regions of the galaxy subtend about $4' \times 5'$ (5300 points at full beam spacing). The total time required to map this region down to a $\text{SNR} \sim 5$ at the 10% contour level is ~ 100 hours assuming 75% efficiency with a single pixel spectrometer. A long slit spectrometer would reduced the required time by the number of beams along the slit (probably ~ 16), so that the whole project would then take only about 6 hours. With a modest array format along the dispersion direction (> 12 pixels), we would have a map in the CO(7→6) line as well.

One could also quickly map the edge-on galaxy NGC 891 in the lines and continuum tracers, thereby tracing the scale height of the ISM, and the injection of energy into the ISM via imaging of super bubbles and chimneys. Scoville et al. find the CO(1→0) scale height of the order of 200 to 300 pc (4 to $6''$) so that the galactic plane will be well resolved.

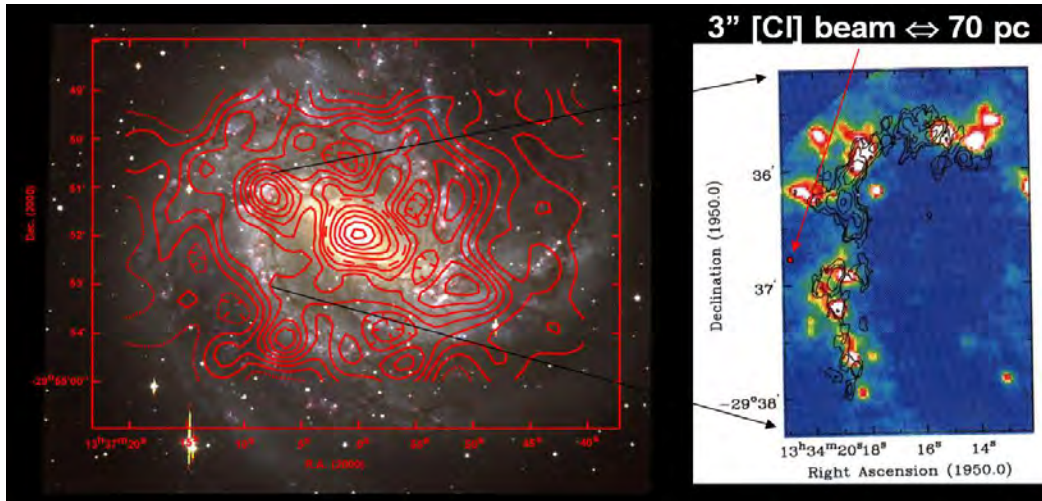


Figure 4.24: (left) KAO map (55'' beam) of the [CII] line emission from M83 superposed on an optical image (N. Geis private communication). (right) 6'' resolution CO (1-0) Map on false-color HI (Rand, Lord, and Higdon 1999)

4.5.3.2 Contrast and Synergies with Other Facilities

CCAT will be more than a factor of 100 more sensitive than Herschel for point source spectroscopy, and provides a factor of 7 better spatial resolution. CCAT cannot compete with the spatial resolution offered by ALMA, but it does deliver comparable sensitivity for point broad line point sources, plus access to the 200 μm window. With the implementation of spatial multiplexing, CCAT spectrometers will be the best method for mapping extended ($> 7''$ or so) regions in galaxies. Again, the natural synergy is with ALMA where CCAT can find the most interesting regions to be examined at high spatial resolution with ALMA.

4.5.4 Active Galactic Nuclei: Revealing the Confining Torus

Galaxies for which much of their luminosity is not derived from nucleosynthesis in stellar interiors are termed "active galaxies". These galaxies include the active galactic nuclei (AGN) of Seyfert, and Markarian galaxies, radio galaxies, quasars, LINERS, BL Lac objects, etc. Energy generation and its outward expression is ordered under the "unification model" for AGN, whose principal characteristics are: (1) energy is derived from accretion onto a super massive black hole at the center of the galaxy, (2) there is an accretion disk enveloping the black hole that is fed by a circumnuclear torus, or the tidal disruption of stars in a nuclear star cluster, (3) the jets often seen emanating from AGN are confined by a parsec scale molecular torus, (4) the broad lines come from gas (up to 1000 M_{\odot}) photoionized by a very hot accretion disk within 1 pc of the supermassive black hole, (5) the narrow lines come from a great deal of gas (up to $10^9 M_{\odot}$) in regions 10 to 1000 pc from the nucleus.

The model proposes that the primary difference between Seyfert 1 and Seyfert 2 nuclei as a geometric selection effect. Seyfert 1 nuclei are viewed face-on so that the broad line region is visible, while Seyfert 2 nuclei are viewed edge-on so that the broad line region is obscured by the torus (Figure 4.25).

4.5.4.1 Surveys for Seyfert Tori

The confining torus should be both very warm (1000 K), and very dense ($\sim 10^7 \text{ cm}^{-3}$) so that it strongly emits in the far-IR dust continuum and in far-IR and submillimeter line emission (e.g. CO, [OI], H_2O ; Krolik & Lepp, 1989). For example, the CO rotational line emission is predicted to peak near $J \sim 58$, or 48 μm at a line luminosity of $L_{58-57} \sim 7 \times 10^{40} f_{\text{abs}} L_{X44} \text{ ergs-s}^{-1}$, and $L_{17-16} \sim 2 \times 10^{39} f_{\text{abs}} L_{X44} \text{ ergs-s}^{-1}$, where f_{abs} is the fraction of hard x-ray emission absorbed by the torus ($\sim 10\%$), and L_{X44} is the ionizing luminosity in units of $10^{44} \text{ ergs-s}^{-1}$ (Krolik & Lepp, 1989). For a typical source at 100 Mpc, the predicted line flux is $\sim 6 \times 10^{-18} \text{ W-m}^{-2}$ in the CO (13 \rightarrow 12) (200 μm) line – easily detected (SNR ~ 100) in 20 minutes of integration time with direct detection spectrometers on CCAT. The CCAT sensitivity is such that for the first time, a systematic survey for high-J line emission can be undertaken.

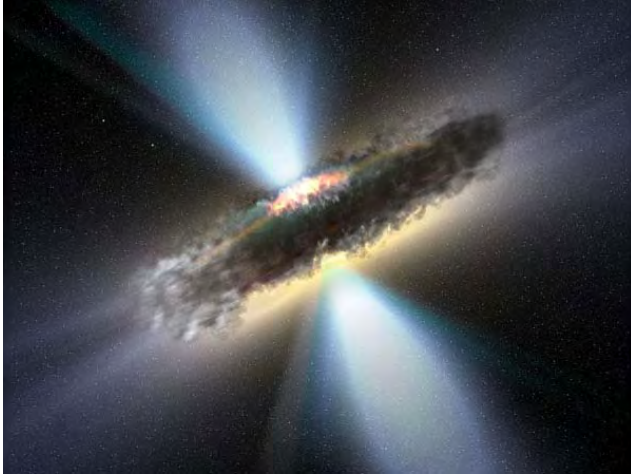


Figure 4.25: Artist's conception of the doughnut shaped torus that obscures the broadline region in Seyfert 2 nuclei (credit ESA).

4.5.4.2 Contrast and Synergies with Other Facilities

The CCAT telescope is uniquely positioned to detect line emission from the torus. Observed low and mid-J line emission may be difficult to uniquely ascribe to the torus due to strong emission from the intervening molecular ISM that is heated by a nuclear starburst. The key to detection is both the high spatial resolution offered by the 25 m telescope (2" at 200 μm), and the uniqueness of emission in the $J = 13 \rightarrow 12$ (200 μm) line. Detectable CO(13 \rightarrow 12) line emission can only arise in the extreme excitation conditions of the confining torus. Furthermore, the high J lines are *very* sensitive to its physical conditions, and the primary coolant for the torus – for a warm, optically thick cloud, the luminosity is proportional to J^3 . ISO did not detect high J CO lines from the torus since they are both too weak, and washed out in the large (70") ISO/LWS beam. The ALMA site does enable efficient 200 μm (1.5 THz) operations, so that ALMA will not operate in the 200 μm window in the foreseeable future. Clearly the high spatial resolution of ALMA is critical for spatially resolving the torus: CCAT detects the lines that constrain the physical conditions, while ALMA can reveal the structure.

Some of this science can be done with the Herschel telescope, but its 15" beam will substantially dilute the torus emission with ISM emission. The much smaller CCAT beam at 200 μm (2") covers only the inner 200 pc regions for the closest Seyfert 2 nucleus (NGC 1068) (see Figure 4.26). Furthermore, CCAT is about 100 times more sensitive than SPIRE/Herschel in spectral lines, so that many more sources become available.

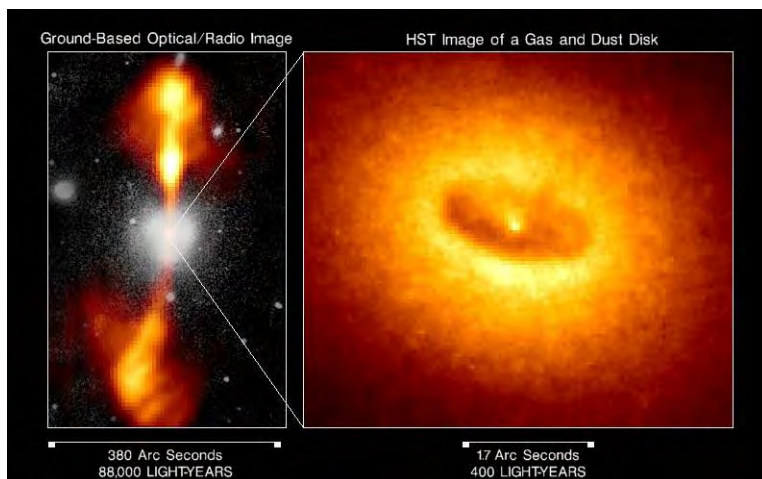
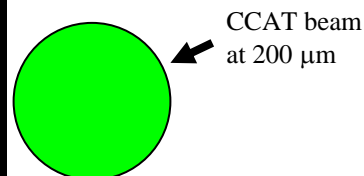


Figure 4.26: CCAT beam size (2") at 200 μm superposed on an HST image of the core of the radio galaxy NGC 4261.



4.6 Sagittarius A*

4.6.1 Science Goals

CCAT operating at its highest frequencies has a niche in studying Sagittarius A*, the radio source corresponding to the supermassive black hole at the center of the Milky Way galaxy. The peak of the spectrum of this source can be measured for the first time, and the time variability of the flux and polarization can be studied with unprecedented sensitivity on timescales faster than orbiting relativistic particles.

4.6.2 Motivation/Background

Sgr A* is the only radio source surrounding a supermassive black hole where we can cleanly probe the matter only a few Schwarzschild radii from the event horizon at the peak of its spectrum (Figure 4.27). At radio wavelengths, where high angular resolution is available, the innermost matter is optically thick to synchrotron absorption. In the submillimeter, however, the source is optically thin, and the emission is believed to originate from within 10 Schwarzschild radii (Falke et al. 1998, ApJ, 499, 731; Liu & Melia 2001, ApJ, 561, L77). Furthermore, the surrounding $\sim 10''$ appears to be remarkably free of compact dust emission (Marrone et al. 2005, astro-ph/0511653), affording both CCAT and ALMA an excellent opportunity to study this source.

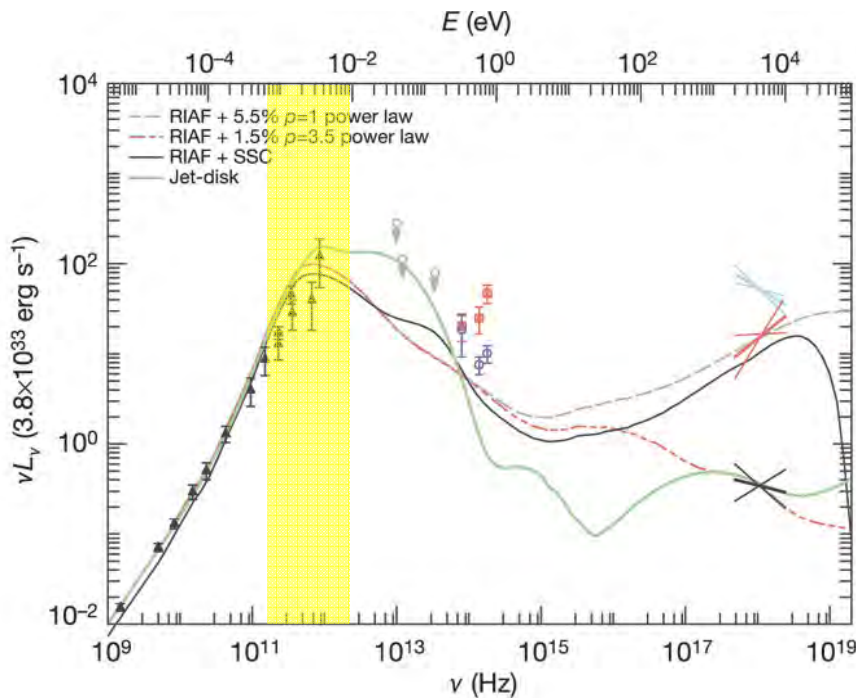


Figure 4.27: Broad-band spectrum of Sagittarius A* from the radio through the X-ray (Genzel et al. 2003). The wavelength coverage of CCAT and ALMA (shaded yellow band) nicely straddles the peak of the spectrum predicted by most models but not confirmed with direct measurement. As illustrated by the plot, the variability in the X-ray is dramatic – two orders of magnitude. Variability at (sub)millimeter wavelengths has been shown to be a more modest factor of 2 (Yusef-Zadeh et al. 2005; Marrone et al. 2005).

Sgr A* has been studied intensively across the electromagnetic spectrum (Figure 4.27). Intense flaring (one or two orders of magnitude) has been observed in the X-ray and near-infrared (Baganoff et al. 2001, Nature, 413, 45; Genzel et al. 2003, Nature, 425, 934), and in many models these flares should be related to variability in the submillimeter. For example, the X-rays may be generated by the upscattering of submillimeter seed photons (which are the most common in the inner accretion zone) off relativistic particles. Coincident X-ray and

submillimeter events have not yet been reported; however, there is a first detection of a simultaneous near-infrared and submillimeter flare (Yusef-Zadeh et al. 2005, astro-ph/0510787; Figure 4.28)

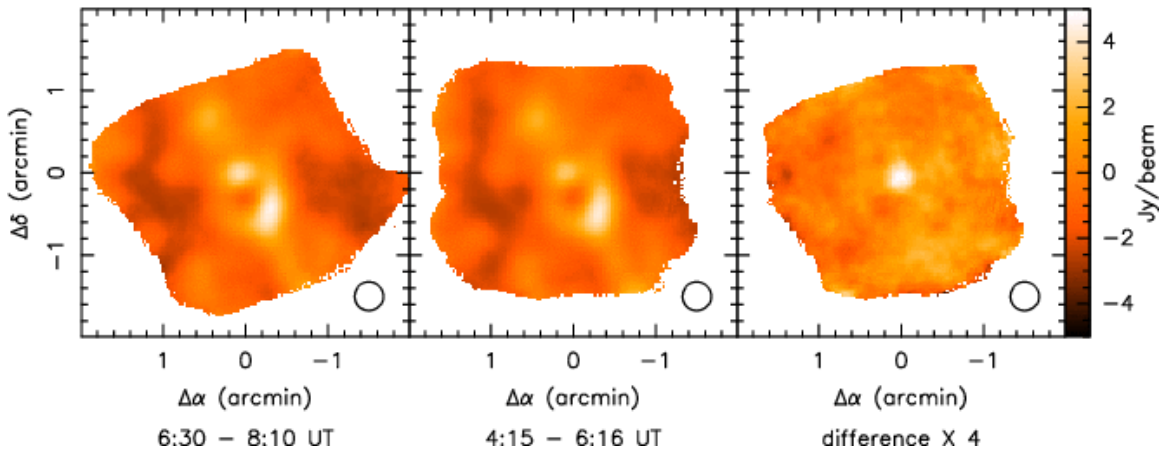


Figure 4.28: Submillimeter flare observed with the CSO at 850 μm (Yusef-Zadeh et al. 2005). The image during the flare is shown at left, and the image two hours prior is shown in the middle. The difference image at right highlights the time variable point source at center and the canceling of the surrounding dust emission which can be used for calibration. The flare amplitude was approximately $\times 1.35$.

4.6.3 Technique

Our approach will be to use precision measurement of the flux and polarization to downselect models for the accretion zone of Sgr A*, where spherical infall, a disk, jet outflow, relativistic physics, and magnetic fields are all believed to play a role (Melia & Falcke, 2001, ARAA, 39, 309). The current state of the art for submillimeter measurements made with the SMA and CSO is the detection of 10% flux variations on >30 minute timescales and the detection of polarization variations on >2 hour timescales (Marrone et al. 2005; Yusef-Zadeh et al. 2005). With outstanding angular resolution and sensitivity, ALMA will cleanly detect Sgr A* with *signal-to-noise in excess of 200 in 1 second* at $\lambda = 450 \mu\text{m}$ and longer. CCAT has similar sensitivity to ALMA at 450 μm , better sensitivity at 350 μm , and the only coverage at 200 μm where the spectrum is expected to peak. With the combination of ALMA and CCAT, we can therefore obtain outstanding time resolution of flare events and easily search for periodicities in the emission from the innermost stable disk orbit (~ 10 minutes) to the outer radio disk (~ 100 days).

With the CSO, the use of surrounding dust emission to perform relative calibration of Sgr A* to better than 10% at 450 μm has been demonstrated (Yusef-Zadeh et al. 2005). With CCAT, we expect this can be pushed to the 1% level due to the greater sensitivity and contrast.

The degree of polarization of the submillimeter synchrotron emission from Sgr A* ($\sim 5\%$, but variable; Marrone et al. 2005) is a measure of the overall magnetic field order in the source, and the Faraday rotation measure derived from multi-wavelength polarimetry yields the product of the magnetic field strength and electron density. The 350 and 450 μm polarization of Sgr A* can be measured with CCAT and ALMA with 0.5% precision in under 1 minute, allowing the study of the polarization on all relevant timescales. Polarization systematic errors must be reduced to the same 0.5% level.

4.6.4 CCAT Requirements

ALMA will make the most important measurements of Sgr A* at 450-1000 μm . However, CCAT operating at 350 μm and 200 μm will have the most power in discriminating models based on the spectral energy distribution (Figure 4.27). A large, accurate telescope is the key requirement (Table 4.11). With diffraction-limited 40 μm imaging, even with only a subset of panels, it may be possible to detect Sgr A* in the mid-infrared with CCAT.

Table 4.11 Required characteristics for CCAT for the study of Sagittarius A*

| Item | Req'ment | Goal | Notes |
|--------------------------------|---------------------------------------|---------------------------------------|---|
| Aperture | 25 m | >25 m | confusion from dust emission |
| Aperture efficiency | 20% at 200 μm | 40% at 200 μm | sensitivity at the peak of the Sgr A* spectrum |
| Wavelength range | 200 - 450 μm | 200 - 450 μm | CCAT niche; ALMA at longer wavelengths |
| Field of view | 3' | 3' | Coverage of surrounding dust emission for calibration |
| Pointing cameras | 0.4" | 0.2" | reconstructed |
| Tracking | one hour 20 min 10 sec | n/a n/a n/a | imaging only |
| Elevation limits | 30-85° | 30-85° | full coverage |
| ($\lambda < 40 \mu\text{m}$) | none | diffraction-limited image | first 40 μm detection? |
| Polarization capability | 1' FoV, $\lambda=200-350 \mu\text{m}$ | 3' FoV, $\lambda=200-350 \mu\text{m}$ | $\sigma(P) < 0.5\%$ |

4.6.5 CCAT Uniqueness and Synergies

Since Sagittarius A* is bright (3 Jy level in submillimeter), but surrounded by dust emission, aperture – whether single dish or synthesized – is the most important characteristic determining detectability at THz frequencies. A 10 m telescope is required to distinguish Sgr A* at 350 μm with a 30% absolute uncertainty from dust confusion (Yusef-Zadeh et al. 2005), and a 25 m telescope is required at 200 μm for a 10% absolute uncertainty. Of projects on the horizon, only ALMA and CCAT have this aperture and THz capability. CCAT will cover higher frequencies than ALMA and make the first detection of the peak of the spectrum.

4.7 Cold Cloud Cores and Star Formation – The “CCC” Survey

4.7.1 Science Goals

The Cold Cloud Core (or CCC) survey is intended to provide a complete inventory of cloud cores – the regions within molecular clouds where stars form – in a number of nearby molecular clouds and throughout a large fraction of the Galactic plane. By exploiting the good angular resolution and unequalled mapping speed of the CCAT equipped with large-format submillimeter cameras, we expect to be able to detect cloud cores having a mass greater than a fraction of a solar mass throughout entire clouds and cloud complexes. This data will allow

- a complete census of the mass distribution of cloud cores down to masses that can form brown dwarf stars;
- assessment of the total gravitationally bound mass available for star formation and greatly improved accuracy of determining the star formation efficiency;
- extensive and unbiased comparison of cloud cores with embedded young stars detected by Spitzer and other facilities;
- analysis of multiple-wavelength images to determine dust temperature distribution and the external radiation field, both of which are essential for understanding the dynamics of these regions and the star formation process;
- high resolution studies that can determine the basic structure of these cores and help understand the role of thermal pressure and magnetic fields;
- identification of prime candidates for extremely high resolution studies using the ALMA synthesis instrument

4.7.2 Background

Star formation is a fundamental process in astronomy, as it determines the structure and luminosity of galaxies, as well as their chemical evolution. It also is intimately connected with the formation of planetary systems including our own. Stars form within molecular clouds, but these very large (size up to 50 pc), massive (up to 10^6 solar mass) objects are not at all uniform. Within them are dense region called “cloud cores”. It is within these condensations that the youngest stars are found, and from which we believe that both isolated and multiple stellar systems are formed. These range in mass at least over a range of 0.3 to 3000 solar masses.

Figure 4.29 shows an image of a dense core in a molecular cloud. The image is of the intensity of the thermal emission at 350 μm wavelength from the dust in the core, which in this case has a temperature between 15 K and 20 K. This core has an overall morphology which is highly filamentary. Within this, however, there is considerable substructure which may be a result of fragmentation into subcores of masses of a few solar masses.

The low mass end of the distribution of cloud core masses is still limited by sensitivity in surveys of nearby clouds, while the high mass end is uncertain because the massive clouds are very rare and hence distant. The low mass cores will reveal information on the low end of the mass function, including brown dwarfs. The most massive cores are the nearest examples of the kinds of regions that lead to starburst galaxies. Understanding these regions provides connections to both the formation of planetary systems and the origin of the stellar content of galaxies.

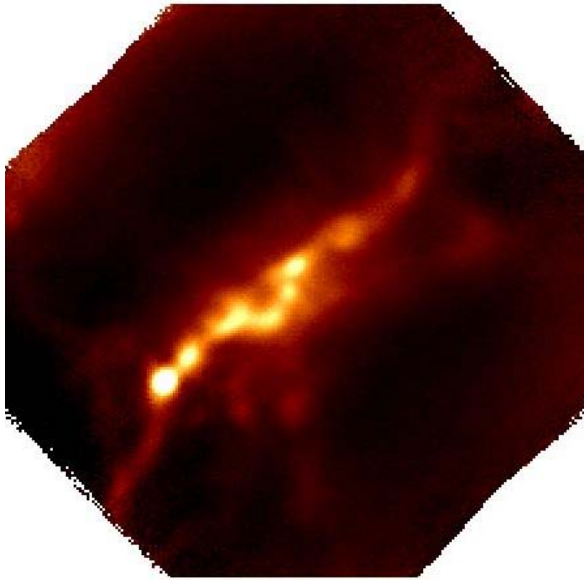


Figure 4.29 Image of the core ORI1 in the OMC3 region of the Orion Molecular Cloud at 350 μm wavelength obtained with the Caltech Submillimeter Telescope (CSO). The condensations are $\leq 10''$ in size and have masses \leq few solar masses. (Image courtesy of Di Li, Harvard-Smithsonian Center for Astrophysics)

However, although the basic connection between cores and stars has been established, many critical aspects of the astrophysics which transforms these regions from cold ($T \sim 10\text{K}$) regions with $\sim 10^6$ molecules cm^{-3} to stars that are thousands to millions times hotter and a factor 10^{17} higher density remain mysterious. These include the redistribution and significance of angular momentum. While considerable work in recent years has revealed that rotating disks are common around very young stars, and that these disks are the precursors of planetary systems, the connection between the angular momentum of a rotating protostellar core and the star-plus-disk system remains elusive. The role of the magnetic field is also largely not understood, beyond agreement that can play an important or even a critical role in controlling the collapse of the core and defining the process by which the young star clears out the material surrounding it by means of stellar jets which in turn drive molecular outflows. And another important question is the role of turbulence – in forming these cloud cores, in their internal support, and whether dissipation of turbulence is (as some have suggested) a key factor in controlling the rate of core contraction and star formation.

To make progress in unraveling this complex problem, we need data on molecular cloud cores as well as on young stars. Observations of the young stars are being produced by facilities such as the Spitzer observatory, and will also be enhanced by observations made using JWST. To understand the statistics of the overall problem as well as details of core structure, we need to have a large unbiased sample of cores in a variety of regions. It is this data set that CCAT should be able to deliver, and it should have a major impact on unraveling the core-star connection in unprecedented detail.

The challenge of detecting and mapping dense cloud cores comes from the fact that the gas and dust within them is extremely cold, due to the shielding from visible-UV heating sources and the lack of any significant internal energy source from either gravitational contraction or nuclear reactions. As a result, dust temperatures are generally between 6 and 12 K. The dust emission is generally optically thin, with the dust optical depending on frequency as $\tau \sim \nu^\beta$, with β in the range between 1 and 2. The result, as shown in Figure 4.30, is that the emission peaks in the submillimeter portion of the spectrum. For the coldest dust with $\beta = 1$, the peak can be as long as $\lambda = 800 \mu\text{m}$ wavelength, while for 10 K dust with $\beta = 2$, the peak is at 300 μm wavelength.

The wavelength of peak emission is a good guide to the optimum wavelength for searching for cores, but there are a number of factors to be considered. The angular resolution of the telescope increases at shorter wavelength, affording better capability of studying the internal core structure, but the atmospheric attenuation is worse, making observations more difficult. Thus, it is difficult at this point to state exactly what will be the “best” wavelength for CCC surveys, but it is almost certainly between 850 and 350 microns wavelength. Beyond this, dense starless cores are heated from the outside and thus have an outward directed temperature gradient. In this

case, the ratio of the fluxes at 350 and 850 microns, for example, constrain the strength of the external radiation field. Such constraints are vital for extracting detailed information from observations of both dust and gas.

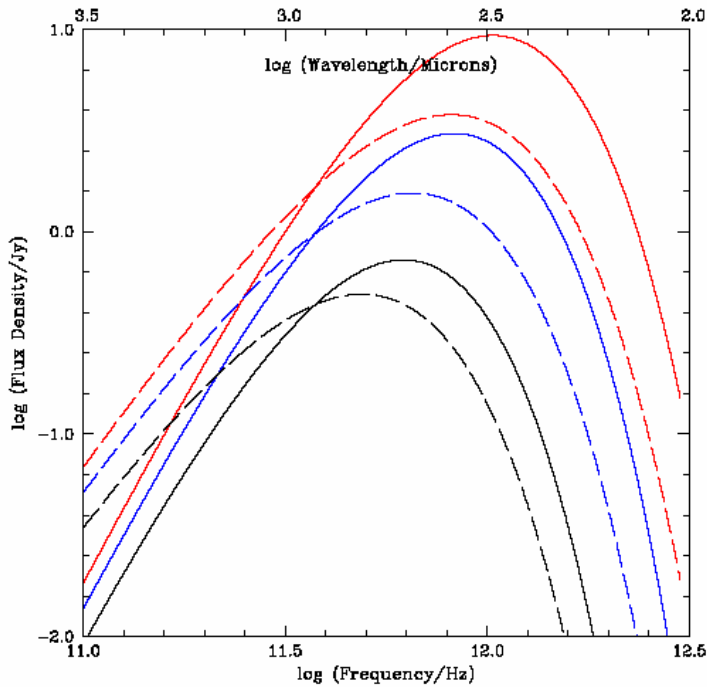


Figure 4.30 Flux density (in Jy) produced by 1 solar mass cloud with nominal dust parameters at a distance of 140 pc. The red curves are for dust at 10 K, the blue curves for dust at 8 K, and the black curves for dust at 6 K. The solid curves are for dust emissivity spectral index $\beta = 2$, and the dashed curves for $\beta = 1$, values which bracket the expected and observed ranges in dense interstellar clouds.

In any case, it is essential to obtain reliable data at a number of wavelengths to constrain the combination of external heating, density distribution, and dust properties.

The above figure indicates that the dust emission is on the order of 1 Jy/solar mass, depending primarily on dust temperature, but also on the spectral index of the emissivity. We are of course interested in detecting masses considerably less than one solar mass, but the sensitivity of the CCAT with anticipated detector performance is better than $0.1 \text{ Jy}/\sqrt{\text{Hz}}$. Thus, we are expecting integration times on the order of seconds, and with large-format cameras, it is evident that extensive but very sensitive surveys are feasible with reasonable total telescope time.

For the massive cores that are precursors to clusters, the emission should be quite strong, despite their great distance. The problem is to find them, since they are rare. Indeed, no clear cases of truly massive starless cores have been found, though studies of infrared dark clouds found with the MSX mission are promising. What is really needed is a survey of the entire Galactic plane. This survey will complement the GLIMPSE survey with Spitzer, which will reveal essentially all the regions of massive star formation in the Galaxy. This survey should cover the entire Galactic plane visible from Atacama, covering at least ± 1 degree in latitude. This will be the most demanding project in terms of mapping speed, observing time, and data handling.

4.7.3 Technique

In order to assess feasibility of any particular observing project, we have compiled Table 4.12 which follows. In it, we include, as a function of wavelength throughout the submillimeter range, the expected noise equivalent flux density (NEFD), which is the incident flux in mJy, which produces a signal to noise ratio of unity in 1 second of integration time. The NEFD is very sensitive to the precipitable water vapor (PWV) above the telescope at the shorter wavelengths, so we have used the values for the values of PWV (in mm) indicated in the fourth column. These are thought to represent “likely” conditions for effective observations as each given wavelength. Only the wavelengths shortward of $700 \mu\text{m}$ require better than average conditions for the Atacama site.

In columns 5 to 10 we indicate the flux density and signal to noise ratio with one second integration time, produced by a 1 solar mass cloud at a distance of 140 pc (as appropriate for e.g. the Taurus or Ophiuchus dark clouds), and assuming a standard dust to gas ratio, dust emissivity spectral index $\beta = 2$, and dust temperatures of 6 K, 8 K, and 10 K, respectively.

Table 4.12 CCAT Sensitivities and Dust Continuum Flux Densities*

| ν (GHz) | λ (μm) | NEFD (mJy) | PWV (mm) | $T_d = 6 \text{ K}$ | | $T_d = 8 \text{ K}$ | | $T_d = 10 \text{ K}$ | |
|----------------|--------------------------------|---------------|-------------|---------------------|-----|---------------------|-----|----------------------|-----|
| | | | | S_ν (mJy) | S/N | S_ν (mJy) | S/N | S_ν (mJy) | S/N |
| 150 | 2000 | 2.0 | 1.0 | 37 | 19 | 58 | 29 | 88 | 41 |
| 220 | 1420 | 2.5 | 1.0 | 120 | 48 | 211 | 84 | 309 | 124 |
| 250 | 1200 | 1.7 | 1.0 | 172 | 101 | 315 | 185 | 472 | 278 |
| 350 | 860 | 5.8 | 1.0 | 342 | 66 | 823 | 142 | 1350 | 233 |
| 410 | 730 | 8.7 | 0.7 | 508 | 58 | 1220 | 140 | 2110 | 243 |
| 670 | 450 | 14.0 | 0.5 | 715 | 51 | 2770 | 198 | 6330 | 452 |
| 860 | 350 | 14.0 | 0.4 | 543 | 39 | 3050 | 218 | 8650 | 618 |
| 1310 | 230 | 114.0 | 0.3 | 121 | 1 | 1670 | 15 | 8050 | 71 |
| 1500 | 200 | 151.0 | 0.3 | 52 | 0.3 | 1050 | 7 | 6460 | 42 |

*for a one solar-mass cold cloud at a distance of 140 pc with $\beta = 2$ and an integration time of one second

There is an “optimum” wavelength (in terms of S/N ratio) that depends primarily on the dust temperature. The optimum λ is 1200 μm for $T_d = 6 \text{ K}$, $\sim 450 \mu\text{m}$ for $T_d = 8 \text{ K}$, and 350 μm for $T_d = 10 \text{ K}$. Note that this optimum depends on the interplay between emission and sensitivity. At this optimum, the S/N ratio for 1 solar mass of dust is large, and increases rapidly with increasing dust temperature, being ~ 100 for $T_d = 6 \text{ K}$, ~ 200 for $T_d = 8 \text{ K}$, and ~ 600 for $T_d = 10 \text{ K}$. This of course confirms that cold dust is more difficult to detect than warmer dust. It also indicates, however, why multi-wavelength observations are extremely valuable, which is connected with the question of contrast. Considering emission at 1200 μm , for example, the emission increases only by a factor ~ 2.5 in going from 6 K to 10 K dust, while at 350 μm the emission increases by a factor ~ 16 . Thus, if one is interested in distinguishing an enhanced column density of really cold dust from irregularly distributed extended emission, it is far more effective to work at the longer wavelengths. If the dust in a condensation is slightly heated, however, the situation is dramatically different, and the shorter wavelength part of the CCAT range is much more promising.

We feel that the most effective way to find and to study cold cores embedded in more extended cold clouds will be to use multi-wavelength CCAT maps. At this point, a minimum of two wavelengths appear necessary, but it seems likely that three wavelengths will be yet better, plausibly $\lambda = 1200, 450$ or $350, \text{ and } 200 \mu\text{m}$.

We will adopt as our nominal survey requirement to detect 0.1 solar mass of dust at 6 K, characteristic of a very cold core that might form a brown dwarf. We will need detections at three widely separated wavelengths in order to maximum detectability in terms of contrast as well as flux, and also to determine the dust temperature to extract the most accurate information on source mass and structure.

From the above Table, we see that in one second of integration time, the signal to noise ratios are 10, 7, and 4, at wavelengths of 1200, 860, and 350 μm , respectively. Thus, an integration time of 4 second per pointing is necessary to have a reasonable signal to noise ratio at the shortest wavelength.

The most simplistic estimate of mapping speed can be obtained as follows. If we assume that we do Nyquist-sampled mapping at 350 μm wavelength, the Nyquist sampling interval is $\lambda/2D = 7 \times 10^{-6}$ radian = 1.44 seconds of arc. A square degree of the sky thus includes 6.2×10^6 samples. Assuming that we have a camera with 10^4 pixels, each square degree of sky corresponds to 620 telescope pointings (this is obviously optimistic since it assumes

perfect tessellating of pointings, and no other overhead). If we devote a nominal integration time of 4 seconds per pixel, this corresponds to 2480 seconds per square degree. Allowing for overhead, a more realistic number might be 1 hour/square degree.

A moderate - sized nearby star forming region such as Ophiuchus might require observing an area of 20 square degrees, which would take only 20 hours with above parameters. A larger region such as Taurus - Perseus requiring 100 square degrees of coverage, would need 100 hours. Similarly a good fraction of the Galactic plane could be covered in approximately 300 hours of telescope time. The area covered by GLIMPSE and a likely follow-up project is 260 square degrees. Note that the numbers in Table 4.12 are not appropriate due to greater typical source distance; this is offset to some degree by the anticipated higher dust temperature.

Also, we would be looking for higher mass cores in the Galactic Plane survey. A full survey of 300 square degrees would provide nearly 2×10^9 data points. Each of these projects has dramatic synergy with ongoing studies at other wavelengths, from millimeter-wavelength spectral line studies, to mid - IR Spitzer mapping.

4.7.4 CCAT Requirements

The CCAT requirements that are evident at this time are that

- There be the large – format cameras with indicated numbers of pixels and sensitivity in order to carry out this project in reasonable time. To a large extent, sensitivity and number of pixels can be traded off as we are mapping objects far larger than the field of view of the telescope.
- The telescope can take data with accurate pointing while moving at the rate of 1/4 diffraction-limited beam per second. This “On The Fly” (or OTF) type of mapping is finding almost universal acceptance and should be a baseline part of telescope pointing system as well as data taking and other software.
- The software for taking such maps be carefully designed and tested so that it properly handles partially completed maps, averaging maps taken under different conditions, integrating pointing tests as needed automatically with data taking.
- It would be desirable to carry out simultaneous multiband observations. This might be considered less important than previous topics. It actually is most beneficial for observation of somewhat warmer dust for which the S/N ratio is comparable for several bands and the gain in efficiency is thus maximized. For very coldest dust, it should also be more valuable than indicated by Table 4.12 since to really exploit the contrast advantage at the longer wavelengths requires the higher signal to noise ratio that occurs for integration time equal to that needed simply for reliable detection at the shortest wavelength.

4.7.5 CCAT Uniqueness and Synergies

Surveying large areas of individual molecular clouds as well as the Galactic plane takes full advantage of a large-aperture single antenna equipped with submillimeter wavelength cameras. This is the most evident strength of CCAT, and one that the CCC survey will exploit to the fullest. The angular resolution of CCAT of 3.5 to 8 arcseconds at 350 m to 850 m wavelength is very well suited to identifying even the most distant cold cores, and allowing considerable structural information to be obtained on those closer to the Earth. A further enhancement of the CCC survey project would be to exploit the capability of simultaneous multi-wavelength imaging, something that CCAT (and probably only CCAT) should be capable with appropriate instrument design.

The cold cloud cores and star formation project will have important synergies with a number of other projects using both ground- and space-based facilities. Several of these involve ongoing projects using the Spitzer spacecraft.

The TAURUS project (D. Padgett PI) is mapping approximately a 50 square degree area in Taurus with the primary motive to identify protostars including those of relatively low luminosity. This will be the first unbiased large-scale survey of this region. The resulting catalog of low-mass protostars will be a vital complement to the inventory of cold cloud cores that the CCC project with CCAT will identify.

The GLIMPSE Legacy project on Spitzer has mapped a 220 square degrees of the Galactic Plane, finding many more sources of star forming activity. A likely follow-up will fill in the missing 20 square degrees around the

Galactic Center. We will also have the full HI Galactic Plane map, showing the locations of diffuse gas. Clearly, the missing link is a fully sampled map with high resolution of the dust emission at submillimeter wavelengths, which traces the dense molecular gas that is the direct antecedent of the forming stars. This database could be provided by a CCC Galactic Plane Survey carried out with CCAT at both 850 and 350 microns wavelength. In addition to their relevance for the formation of isolated stars, this is the best way to find the precursors of the massive dense cores that form clusters of stars before they form stars. We currently lack information on this vital step in the formation of massive star clusters. Understanding the initial conditions for massive, clustered star formation is important for understanding the formation and evolution of galaxies, as well as stars in our Galaxy.

The cold cores identified in the CCC project, both local and in the Galactic Plane, will constitute a major catalog for high-resolution studies using ALMA. The enormous mapping speed of CCAT equipped with large-format submillimeter cameras gives a great advantage in identifying cores, some of which will be selected for more detailed studies using the synthesis array.

4.8 Interstellar Medium Studies

4.8.1 Introduction

The submillimeter and far-infrared bands contain spectral lines from a large number of molecular and atomic species which are physically and chemically important in the interstellar medium. For instance, the fine-structure electronic transitions of light atoms and ions, such as carbon, nitrogen, and oxygen, lie in this band, and often play an essential role in the energetics of interstellar gas. A good example is the C^+ line at 1900 GHz, which often dominates the cooling of entire galaxies, but this line will be accessible using CCAT only for objects with suitable redshifts. Another example is the N^+ line at 1461 GHz, which should be accessible with CCAT (see below).

Hydride molecules, radicals, and ions (e.g. H_2O , OH , and H_3O^+) are particularly interesting. Their small moments of inertia generate fundamental rotational transition frequencies that often fall above 1 THz, and therefore these species have traditionally been difficult to study. The hydrides are important because they play key roles in the gas-phase chemical reaction networks that produce many of the observed interstellar molecules. In addition, their abundances are sometimes high enough so that they dominate the energetics of dense regions. Some species, such as H_2D^+ , which has a ground-state transition at 1370 GHz, appear to remain in the gas phase even in the densest regions, while other molecules have been frozen onto the surfaces of interstellar dust grains, and may prove to be very valuable for studies of protostellar disks and the early stages of star formation

In the past, observations of many of these key species required airborne, balloon-borne, or space observatories. Over the past decade, it has become clear that ground-based observations at frequencies above 1 THz are indeed possible at a high site in Atacama. A group from the Harvard-Smithsonian Center for Astrophysics (CfA) is carrying out pioneering ground-based THz spectroscopy using a small submillimeter telescope on Sairecabur, along with a heterodyne receiver using a hot-electron bolometer (HEB) mixer. Figure 4.6 shows some of the transitions which may be accessible with CCAT. The atmospheric transmission curve is calculated based on FTS measurements, and demonstrates that the THz windows can be quite good. More detailed plots of the available atmospheric windows and spectral lines are given on the project web site, along with a table which provides details of selected transitions (<http://gabba.astro.cornell.edu/twiki/bin/view/Main/Atacama>).

4.8.2 The 1.3 THz window

The atmospheric window at 1.3 THz is especially interesting because it contains the 1370 GHz ground-state line of H_2D^+ , which is a key species for interstellar chemistry since it is a deuterated version of the H_3^+ ion which initiates the ion-molecule reaction scheme. However, H_2D^+ has an electric dipole moment and therefore has observable rotational transitions. Also, H_2D^+ should be a useful probe of highly depleted regions. Note that the HIFI instrument on the Herschel Space Observatory does not cover this frequency.

4.8.3 Absorption Spectroscopy

An impressive number of species have ground-state or low-lying transitions that will be accessible with CCAT, including HDO, D₂O, HCL, DF, H₂S, C, CH⁺, NH, NH⁺, H₂D⁺, and CH. This opens up the possibility of observing these species in absorption, where the submillimeter continuum from a bright source is used as a “backlight” to measure the abundances of these species in foreground material. Observations of this type have been carried out in the past and have proven to be very valuable, because column densities and abundances can be measured accurately, often without having to resort to using complex numerical radiative transfer codes. However, such observations have often been restricted to the very brightest submillimeter sources such as Sgr B2 and W 49. With CCAT's large aperture, many more submillimeter sources should provide a continuum that is readily detectable at high spectral resolution, enabling a much broader program of absorption spectroscopy.

4.8.4 Excited-state lines

The CO molecule is very abundant and has been widely observed using the low-lying J=1-0 and 2-1 transitions at 115 and 230 GHz. These transitions primarily sample gas with temperatures of 10-20 K and with densities of order 10³ cm⁻³. The higher frequency transitions allow one to probe regions that are successively warmer and denser as one moves up in frequency. Such observations allow useful constraints to be placed on the quantity and excitation conditions for the warm gas associated with regions of active star formation, both in our galaxy and in external galaxies. With CCAT, it will be possible to observe transitions up to J=13-12 at a spatial resolution of 2”, which will provide essential information on the densest and warmest gas in these regions. Other heavier species, such as HCN, should also produce lines that are readily detectable, providing complementary physical and dynamical information.

Of course, ALMA should achieve angular resolutions substantially better than 2”, and will have excellent sensitivity in the lower frequency windows. Nonetheless, 2” resolution is comparable to the capability of the current generation of millimeter interferometers, and so CCAT THz observations should provide useful information on relatively small scales – e.g. protostellar disks, and the nuclei of starburst galaxies. It will be especially interesting to see how the information provided by the spectral probes that are available in the higher frequency windows can be used to complement ALMA observations.

4.8.5 Array Receivers

Recent advances in coherent receiver technology – mixers, local oscillators, and especially the digital electronics for spectrometers – make the construction of array receivers both practical and affordable. Array receivers would be especially powerful on a large telescope such as CCAT. Again, this is an area in which CCAT can complement ALMA, providing large-area maps at moderate angular resolutions, which can then be used to find interesting targets for deep ALMA follow-up at high angular resolution.

4.9 Circumstellar Disks

4.9.1 Science Goals

The primary goals of the CCAT circumstellar disk program are:

1. to perform unbiased surveys of young star clusters at 100-500 pc for the prevalence of protoplanetary disks from the time in which protostellar envelopes are first dispersed until the completion of planet formation,
2. to measure the mean magnetic field orientation of protoplanetary disks, and to better constrain the size of the dust grains, both via polarimetry,
3. to survey stars within 500 pc for previously unknown cold debris disks, in order to provide a complete assessment of disk evolution,
4. to provide high-fidelity images of debris disks around stars within 30 pc, suitable for identifying the location and actions of otherwise undetected planets.

This program will be accomplished through continuum imaging at $\lambda = 200 - 1000 \mu\text{m}$ using the facility cameras and multi-wavelength polarimetry in the submillimeter bands not suitably measured by ALMA.

4.9.2 Motivation/Background

Current understanding of low mass star formation indicates that a circumstellar disk is present at the **protostellar** (Class 0⇒Class I) phase, but that the disk is embedded in a dense envelope. By the end of the Class I phase, infall onto the disk and bipolar outflow have dispersed the envelope, exposing the disk which can be studied throughout the next Gyr's of its evolution with CCAT. Accretion to build the mass of the star and then the planets proceeds for ~10 Myr during the **protoplanetary** (Class II) phase. When the disk mass becomes insufficient, accretion terminates, and the star enters the **transitional disk** (Class III) phase. Left on its own, the dust in the disk collects into planetesimals, spirals in to the star, or is blown out by stellar radiation and winds. However, the disk is occasionally replenished with debris from the collision of planetesimals in asteroid or Kuiper belts. Gas-poor **debris disks** have been detected around main sequence stars as old as 10 Gyr (Greaves et al. 2004, MNRAS, 351, L54); a handful can be imaged with existing telescopes (Figure 4.31). The debris is one of the few detectable tracers of evolutionary processes in other solar systems.

Present-day knowledge of disk lifetime statistics comes from work primarily in the infrared. Near-infrared surveys have been able to take a census of protoplanetary disks containing hot dust (>500 K, located within ~1 AU of the star) over entire stellar clusters (e.g., Haisch et al. 2001, ApJ, 553, L153). These “infrared excess” measurements are sensitive to the Wien part of the dust spectrum, so mass estimates are difficult. (Sub)millimeter measurements with, e.g., CCAT, are more suitable for the determination of mass since on the Rayleigh-Jeans side of the spectrum, the temperature dependence of the flux density/mass ratio is minimized ($\propto T$). Existing submillimeter surveys have detected ~100 sources with disk masses as low as the mass of Jupiter (Andrews & Williams 2005, ApJ, 631, 1134); these surveys are toward pre-selected stellar targets. CCAT will be able to perform *unbiased* surveys for protoplanetary disks over many square degrees. With sensitive observations over many wavelengths, we can measure the timescales for dissipation of the inner and outer parts of the disk as it enters the transitional phase. CCAT submillimeter observations are especially important since observed (short) infrared disk lifetimes are difficult to reconcile with the apparent widespread formation of planets.

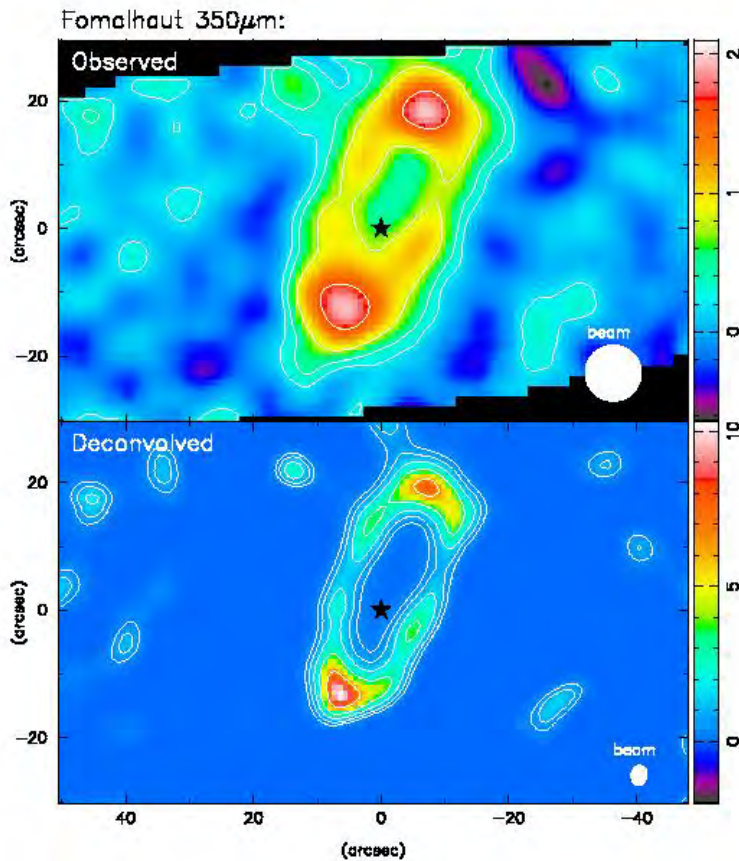


Figure 4.31: Image of Fomalhaut debris disk acquired with the CSO/SHARC II (Marsh et al. 2005, ApJ, 620, L47). The observed image above has 10" resolution and shows a complete ring of debris around the star. The resolution is enhanced to 3" below with a Richardson-Lucy algorithm; CCAT will have this resolution intrinsically, with the capability to achieve ~1" resolution through deconvolution. From the CSO image, we can already infer the presence of a planet due to the asymmetry of the ring. CCAT imaging should show substructure which will pinpoint the location of the planet.

The protoplanetary disks are bright enough that their submillimeter linear polarization can be measured accurately. The ~3% polarization from two of the brightest disks has been detected with the JCMT to infer mean magnetic fields which are toroidal (Tamura et al. 1999, ApJ, 525, 832), and CCAT has the sensitivity to quickly measure mean magnetic directions in hundreds of protoplanetary disks. If multi-wavelength polarimetry with systematic errors <0.5% is not available with ALMA, it will be a priority to add this capability to CCAT. Since disk grains can be comparable in size to submillimeter wavelengths of emission, we can expect their emitted degree of polarization to increase with increasing wavelength at a rate which constrains the grain size (B. Draine, private communication).

Since debris disks have generally lower mass than protoplanetary disks, their emission is best studied at $\lambda > 10 \mu\text{m}$ due to the better contrast with the more luminous star. The Spitzer Space Telescope has now surveyed several hundred stars at 24 μm and 70 μm (e.g., Beichman et al. 2005, ApJ, 622, 1160; Rieke et al. 2005, ApJ, 620, 1010); approximately 30% have detectable disks. Since debris disk hosts include the local, older stellar population, many of these stars are within 30 pc of the Sun and can be spatially resolved. In comparison with Spitzer, CCAT offers angular resolution better by a factor of 3 or more and superior sensitivity to colder disks (Figure 4.32)

Probably the most important contribution of CCAT in the study of circumstellar disks will be in the imaging of nearby debris disks. The matter in debris disks is sculpted by the underlying system of planets, and resolved submillimeter images can be used to derive their locations (Ozernoy et al. 2000, ApJ, 537, L147; Wilner et al. 2002, ApJ, 569, L115; Marsh et al. 2005). Since the "dust" results from a collisional cascade of planetesimals, the particles can be large. There is theoretical and observational evidence that the larger particles have different spatial distributions (Wyatt 2005, astro-ph/0511219; Marsh et al. 2006, in prep.), so multi-wavelength imaging is key

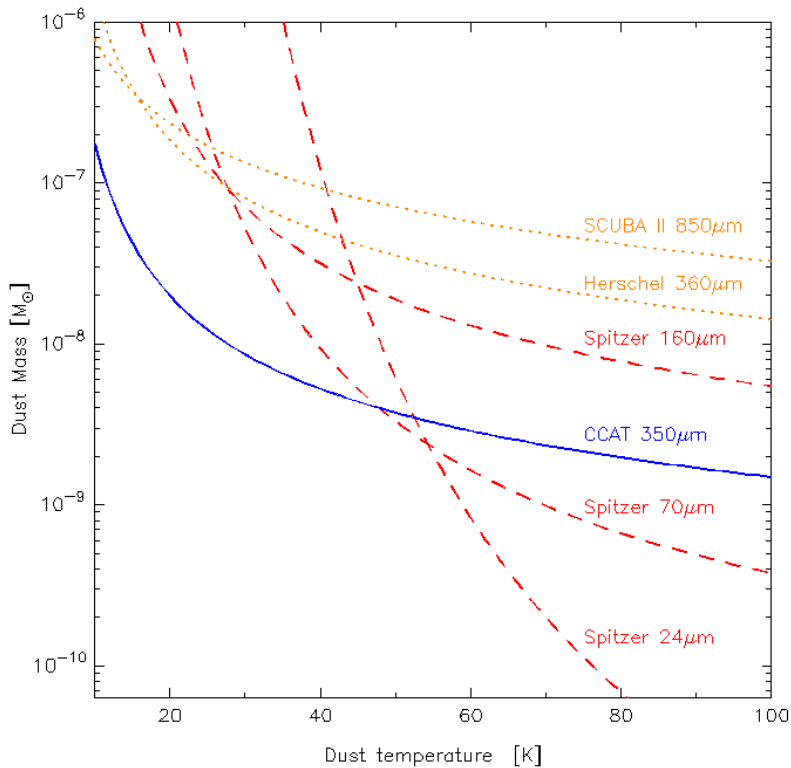


Figure 4.32 Sensitivity of various telescopes to tenuous disk emission. The Spitzer Space Telescope is sensitive to small amounts of dust if it is heated above 50 K by proximity to the star. If, however, the majority of the disk mass lies outside ~ 50 AU, its emission may be too faint for detection by Spitzer but will be detected by a CCAT camera operating at $350 \mu\text{m}$. Although typical far-infrared-selected disks have characteristic temperatures of 80 K (Sheret et al. 2004, MNRAS, 348, 1282), that selection is biased towards warmer disks. Disks with temperatures as low as 40 K are known (Liu et al. 2004, ApJ, 608, 526; Chen et al. 2005, ApJ, accepted), and especially around lower mass stars and brown dwarfs we can expect dust of yet lower temperature to be discovered.

With a typical diameter of 300 AU and distance of 20 pc, a debris disk has an angular extent of $\sim 15''$, which is easily resolved by CCAT. The outer envelope of some systems is substantially larger (Su et al. 2005, ApJ, 628, 487). We therefore expect that with CCAT the number of debris disks with resolved submillimeter images will be increased from ~ 8 at present to ~ 50 – a statistical sample covering a variety of stellar masses. CCAT mapping is synergistic with ALMA imaging. ALMA will detect the fine dust concentrations, and CCAT will excel at the detection of extended structures, and both are present in theoretical models (Ozernoy et al. 2000; Wilner et al. 2005; Wyatt 2005).

Surveys for previously unknown debris disks within clusters of stars with approximately the same age will be a later goal for CCAT, requiring 100,000 pixel arrays operating at $350 \mu\text{m}$. With these surveys, we will explore the timescales of debris disk evolution by counting the number of Vega-like systems probably resulting from recent, spectacular planetesimal collisions as well as the number of more ordinary disks. In addition, we will provide new target lists for high-resolution study with ALMA.

4.9.3 Technique

The circumstellar disk program will consist of surveys for previously unknown disks and detailed study of known disks, as summarized in Table 4.13. The first three programs are to be carried out with the first-light instruments. The secondary surveys require a second-generation camera with a larger field of view.

The sources of confusion in the disk programs are in fact of scientific interest to other programs to be carried out with CCAT. For example, the extended emission that will be detected in the Taurus survey is of value to the star formation/cold cores program. The old star cluster surveys are expected to uncover relatively rare debris disks, but will detect many more distant galaxies which can supplement the high-redshift program.

Table 4.13 Key Surveys for Circumstellar Disks Program

| Target | Observing Strategy | 5 σ depth (mJy/beam) | Mass Sensitivity | Time Required (hr) | Comment |
|--|--------------------|--|---------------------|--------------------|--|
| Taurus protoplanetary disks | 10°×10° | 1 mJy, $\lambda = 1100 \mu\text{m}$ | 0.05 M(Jupiter) | 50 | LWCam, 13' FoV |
| protoplanetary disk polarization survey | 100@ 1'×1' | 2, 0.2 mJy; $\lambda = 350, 1100 \mu\text{m}$ | M(Jupiter) | 150 | $\sigma(P) \leq 0.4\%$; single pol. inst. |
| debris disks at $d < 30$ pc | 100@ 3'×3' | ~1 mJy, $\lambda = 350\text{-}1100 \mu\text{m}$; ~10 mJy, $\lambda = 200 \mu\text{m}$ | 0.2 M(Eps Eri disk) | 500 | SWCam and LWCam; resolved images |
| Primary Goals | | | | 700 | |
| debris disks in Pleiades, 130 pc, 100 Myr (coeval) | 1°×1° | 0.25 mJy, $\lambda = 350 \mu\text{m}$ | M(Eps Eri disk) | 200 | second-generation camera, 20' FoV |
| debris disks in NGC 752, 500 pc, 1.1 Gyr (coeval) | 1°×1° | 0.25 mJy, $\lambda = 350 \mu\text{m}$ | M(Fomalhaut disk) | 200 | second-generation camera, 20' FoV |
| Secondary Goals | | | | 400 | |

4.9.4 CCAT Requirements

The first-light circumstellar disk science goals for CCAT are imaging of nearby debris disks, surveys of young stellar clusters for accretion disks, and multi-wavelength polarization surveys of protoplanetary disks. Dust grains in disks can be as large as the submillimeter wavelengths of emission, as evidenced by disk spectral energy distributions (Beckwith, Henning, & Nakagawa 1999, *astro-ph/9902241*). Furthermore, the appearance of a debris disk changes with wavelength due to the effects of temperature and grain size (Fomalhaut: Stapelfeldt et al. 2005, *ApJS*, 154, 458; Marsh et al. 2005, *ApJ*, 620, L47. Vega: Marsh et al. 2006, in prep.) To explore these effects, we therefore require images at all CCAT wavelengths, *including the critical 200 μm window* which gives the best angular resolution and handle on the dust temperature. In order to achieve adequate image fidelity and sensitivity on debris disks of low surface brightness surrounding a point-source photosphere, we require an aperture efficiency of at least 50% at 350 μm and a filled focal plane. To resolve a statistically significant sample of 50 debris disks, we require an angular resolution approaching 3" and hence a telescope aperture of 25 m. We expect that almost all debris disks would be contained within a field of view of 3', and the same field of view would be adequate for surveys of young star clusters for protoplanetary disks since they are relatively bright. A polarization survey of protoplanetary disks can be carried out with a modest 1' field of view and targeted observations.

The disk science goal for second-generation CCAT instruments is the survey of old stellar clusters for debris disks. Old stellar clusters which may harbor debris disks can be as large as a few degrees in angular extent, which pushes the limits of CCAT mapping speed. To survey large areas to the confusion limit, we require short-wavelength detector arrays filling as much of the 20' field of view as possible.

Table 4.14 Required characteristics for CCAT for the study of circumstellar disks

| Item | Req'ment | Goal | Notes |
|--------------------------------|---|--|--|
| Aperture | 25 m | >25 m | debris disk substructure; confusion |
| Aperture efficiency | 50% at 350 μm | 70% at 350 μm | sensitivity and fidelity |
| Wavelength range | 200 - 1100 μm | 200 – 1100 | grain size and temperature |
| Field of view | 3' | 20' | imaging vs. surveys |
| Pointing cameras | 0.35" | 0.2" | @ 350 & 200 μm , reconstructed |
| Tracking | one hour 20 min 10 sec | n/a n/a n/a | imaging only |
| Elevation limits | >30 | >20 | overlap with northern hemisphere telescopes |
| ($\lambda < 40 \mu\text{m}$) | none | none | SOFIA IR matches CCAT submm resolution |
| Polarization capability | 1' FoV, $\lambda=350,1100 \mu\text{m}$ | 1' FoV, $\lambda=200-$ 1000 μm | $\sigma(\text{P}) < 0.4\%$; protoplanetary disks; dust physics |

4.9.5 CCAT Uniqueness and Synergies

Herschel and SOFIA will provide complementary $\lambda \approx 50 \mu\text{m}$ images of nearby debris disks, but will have poor angular resolution and sensitivity (confusion-limited) in comparison to CCAT at the longer wavelengths. SAFIR would be the first far-infrared facility to match CCAT capability in the study of all but the coldest disks.

As discussed in Section 4.9.2, we anticipate a synergistic study of nearby debris disks with CCAT and ALMA. CCAT will be the preferable facility for finding new disks within stellar clusters due to its greater survey speed.

Multi-wavelength submillimeter polarimetry (not available with Herschel) is a diagnostic of grain size in protoplanetary disks. If ALMA does not have sufficient capability, it will be important to implement it for CCAT.

4.10 Kuiper Belt Objects

4.10.1 Science Goals

Kuiper Belt observations with CCAT will consist primarily of a dedicated program to obtain the sizes and albedos of hundreds of Kuiper Belt Objects (KBOs), thereby providing an essential data set to further our understanding of planet formation. CCAT's unique capability to measure the true size distribution and the albedo variability of an original (accretional) population will anchor models of the planetary accretion process that occurred in early solar system history. In addition, CCAT observations may reveal large, undiscovered minor planets at large heliocentric distances, and may detect periodic variations in the thermal emission that will constrain the spin states of KBOs.

4.10.2 Motivation and Background

A massive disk of small bodies orbiting beyond Neptune has become a key element in our understanding of solar system formation and evolution. The so-called Kuiper belt was discovered in 1992 (Jewitt and Luu, 1993,

Nature, 362, 730) and represents a major scientific frontier in solar system exploration. Almost 1000 Trans-Neptunian Objects (TNOs) have been identified to date, but their most basic properties such as mass, size, shape, spin, rock-ice fraction, surface properties, and interior properties remain essentially unknown (apart from the TNOs Pluto and Charon). The Kuiper belt is a remnant disk that contains a record of fundamental processes that operated in the early solar system (accretion, migration, and clearing phases). As such, its characterization is of very high scientific priority. Understanding the circumsolar disk is also essential as we start to explore similar disks around solar-type stars.

The trans-Neptunian region is a prime example of an area where progress is limited not by theoretical understanding but by a lack of observational data. Current theoretical models are poorly constrained because the size distribution, total mass, radial extent, and spin characteristics of the Kuiper belt population are poorly known. A TNO size-albedo survey will make an essential and long-lasting contribution: it will provide the observational constraints that we need to further our understanding of the origin and evolution of the solar system.

Current understanding of the Kuiper belt suggests that a massive disk of planetesimals - perhaps totaling a few tens of Earth masses - accreted in the first 10^8 - 10^9 years of solar system history. This resulted in a large population of minor planets with a steep size distribution (Elliot et al. 2005, *AJ*, 129, 1117) report a differential power law exponent $q \sim 5$) such that there is a small number of Pluto-sized bodies and a very large number of small bodies. Characterizing the details of the size distribution is quite important in order to constrain the accretion phase in the disk, which is a critical component of the planet formation process. Because TNOs larger than about 100 km diameter have not been significantly altered by collisions over the age of the solar system (Farinella et al., 2000, *Protostars and Planets IV*, p. 1255), the Kuiper belt provides an invaluable picture of the original (accretional) population.

Size measurements can be obtained from occultations/eclipses in a binary system (e.g. Pluto and Charon). Lower limits on a TNO size can also be placed when the TNO occults a star and when the shadow path happens to be observable at a suitable telescope. However neither of these techniques are practical for the measurement of a large sample of TNOs. The best way to determine the sizes and albedoes of a large number of objects is to compare the reflected and emitted light of minor planets, as was done very successfully in the early 1980's for ~2000 main-belt asteroids with the IRAS all-sky survey at 12 and 25 μm (Tedesco et al., 2002, *AJ*, 123, 1056). The reflected light is proportional to the albedo of the object and the object size, while the emitted light is proportional to the complement of the albedo and the object size. Via the assumption of thermal equilibrium, simultaneous reflected and emitted flux measurements therefore yield both the albedo and the size. Because the solar flux at the distance of the Kuiper belt is less than 1 W/m^2 , TNOs are cold ($\sim 40 \text{ K}$) and emit very little light, with a peak in the emission at wavelengths near 70 μm . Even with the most sensitive telescopes like Spitzer, TNO size measurements are challenging and limited to a few of the largest TNOs. CCAT will have the sensitivity to measure the emitted light of hundreds of TNOs, enabling astronomers to establish the true size distribution of a primordial population of protoplanets. In addition, size measurements of binary TNOs will provide density estimates, which are fundamental indicators of the composition. These data on the composition of TNOs will assist in determining the chemical and physical conditions at the time of formation.

Apart from characterizing known TNOs, CCAT will be capable of discovering large objects at heliocentric distances beyond 50 AU. Although current observations suggest an outer edge to the classical TNOs near 50 AU, an extended scattered disk is known to exist with objects at large heliocentric distances (Gladman et al., 2002, *Icarus*, 157, 269). Both our understanding of the accretion process and observations of disks around other stars indicate that large bodies should exist beyond 100 AU. This represents an important discovery space for CCAT.

CCAT observations of TNOs may also reveal periodic variations in the emitted flux related to the rotation of the body. A statistically meaningful set of measurements of spin periods and spin orientations would provide invaluable information about the collisional evolution (or lack thereof) since the accretionary phase.

4.10.3 Observables

We design the TNO size-albedo survey for all known TNOs with radius larger than about 150 km (Figure 4.33) which is about the CCAT 5-sigma detection limit for an hour of integration. This corresponds roughly to several hundred objects and to a thousand hours of observing time. The cumulative number of TNOs with red magnitude $m_R < 22$ and $m_R < 23$ is about 0.25 and 1.8 per square degree along the plane of the Kuiper Belt, respectively (Elliot et al. 2005). The number density is roughly constant within 3 degrees of latitude of the plane, so that there are ~500 bodies with $m_R < 22$ and ~3500 bodies with $m_R < 23$ in a ± 3 degree latitude band symmetrical about the Kuiper belt plane (2160 square degrees). At the present time, the known object population represents ~150 objects with $m_R < 22$ and ~350 objects with $m_R < 23$ but newly discovered TNOs are constantly and rapidly added to the sample as search programs strive for completeness. For instance, the Deep Ecliptic Survey searched about 550 square degrees to a limiting magnitude $m_R < 22.5$ and the CFHT Legacy Survey searched about 200 square degrees within 2 degrees of the ecliptic to a limiting magnitude $m_R = 23.5$. Obviously most $m_R = 24$ bodies remain undiscovered. Such objects may well exceed 1000 km in size at distances larger than 100 AU.

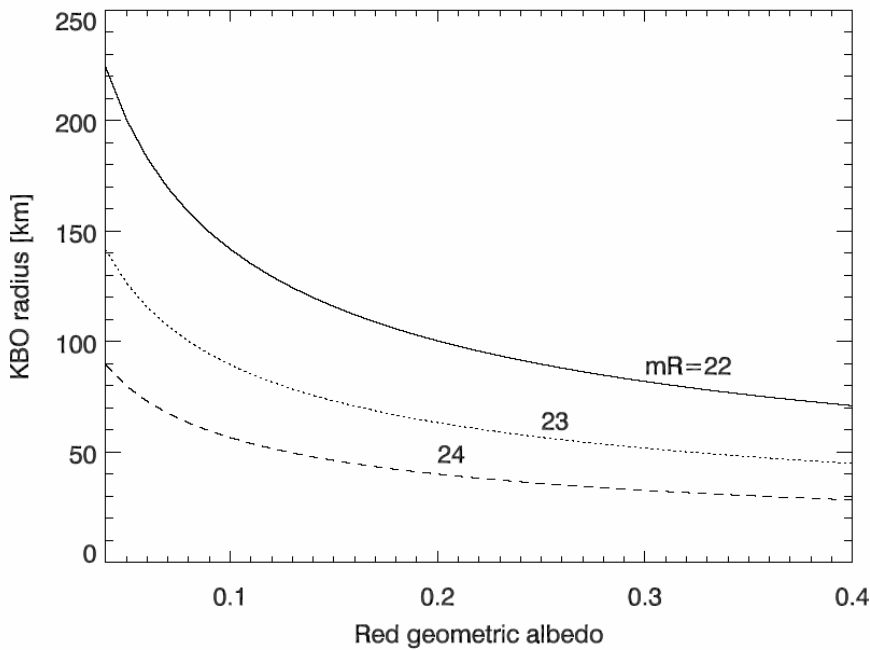


Figure 4.33: Relationship between magnitude, size, and albedo for TNOs at heliocentric distance $R = 45$ AU (solid: $m_R = 22$ dotted: $m_R = 23$ dashed: $m_R = 24$). For $R=100$ (140) AU, multiply sizes by a factor of 5 (10).

4.10.4 Size and Albedo

Thermal models of small bodies balance solar insolation with re-emitted thermal radiation (Lebofsky and Spencer, 1989, *Asteroids II*, p. 128):

$$\pi r^2 (1 - A) F_{sun} / R^2 = \varepsilon \sigma \int_0^\pi \int_0^{2\pi} T(\phi, \theta)^4 r^2 \sin \theta d\theta d\phi \quad (1)$$

where r is the radius of the object assumed spherical, A is the bolometric Bond albedo, $F_{sun} = 1368 \text{ Wm}^{-2}$ is the solar constant at 1 AU, R is the heliocentric distance [AU], ε is the bolometric emissivity, σ is the Stefan-Boltzmann constant, and $T(\phi, \theta)$ is the temperature at longitude ϕ and co-latitude θ . The temperature distribution of various end-member models can be represented in terms of a characteristic temperature:

$$T_x = \left(\frac{(1 - A) F_{sun}}{\chi \varepsilon \sigma R^2} \right)^{1/4}, \quad (2)$$

where $\chi = 1$ represents the temperature at the sub-solar point of a non-rotating body, $\chi = 2$ represents the disk-averaged equilibrium temperature of a non-rotating body, $\chi = \pi$ represents the maximum temperature of a fast-rotating body with the subsolar point on the equator (isothermal-latitude), and $\chi = 4$ represents the disk-averaged equilibrium temperature of the isothermal-latitude model.

A numerical estimate of the temperature is

$$T = \frac{394}{\sqrt{R[\text{AU}]}} \left(\frac{1-A}{\chi \epsilon} \right)^{1/4} \text{ K.} \quad (3)$$

Plausible extremes of the bolometric Bond albedo ($A = pq = 0.01 - 0.25$) are obtained from the observed range of geometric albedos $p = 0.04-0.4$ and likely range of the phase integral $q = 0.3-0.6$.

The thermal flux density [$\text{W m}^{-2} \text{ Hz}^{-1}$] measured by an observer at distance Δ [AU] is

$$F_\nu = \int \epsilon_\nu B_\nu [T(\phi, \theta)] d\Omega, \quad (4)$$

where B_ν is the Planck function and $d\Omega$ is the elemental solid angle [sr]. In the Rayleigh-Jeans approximation ($B_\nu(T) \sim 2KT/\lambda^2$) brightness is proportional to temperature and the integration is easily carried out:

$$F_\nu = \frac{2K\bar{T}}{\lambda^2} \epsilon_\nu \frac{\pi r^2}{\Delta^2} \quad (5)$$

where \bar{T} is an effective emission temperature (temperature distribution weighted by solid angle). In the non-rotating case \bar{T} corresponds to $\chi = 1.6$, and in the isothermal-latitude case \bar{T} corresponds to $\chi = 3.8$. However the Rayleigh-Jeans approximation breaks down for submillimeter observations of TNOs, and the Planck function must be integrated with the relevant temperature distribution. Figure 4.34 shows the submillimeter flux of TNOs of various sizes near opposition ($\Delta = R - 1$, phase angle ~ 0), assuming the standard thermal model.

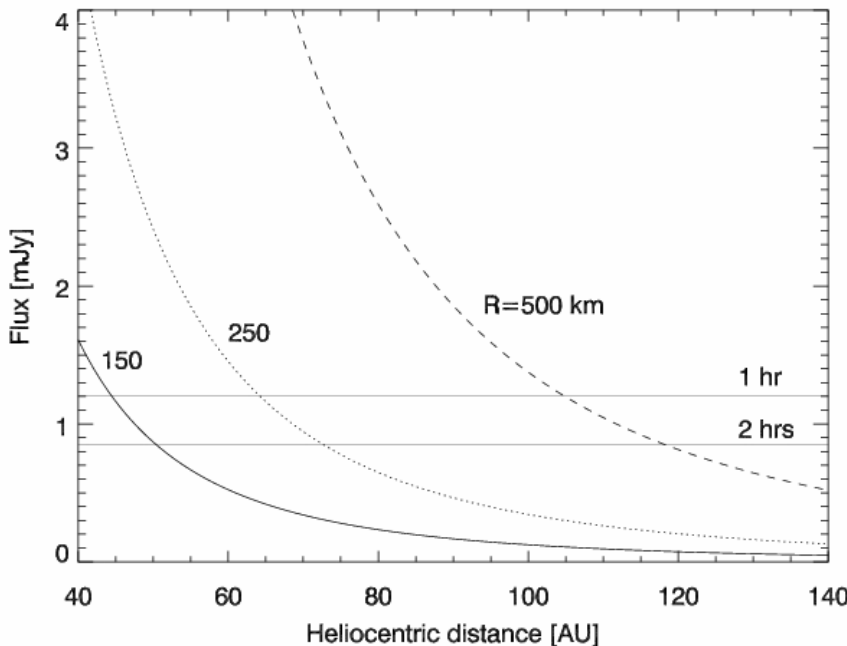


Figure 4.34. Predicted 350 μm submillimeter flux for TNOs assuming the standard thermal model, i.e. non-rotating. Bodies with radii of 150 km, 250 km, and 500 km are shown with the solid, dotted, and dashed lines, respectively. We assume a geometric albedo $p = 10\%$, phase integral $q = 0.45$, bolometric and submillimeter emissivity $\epsilon = \epsilon_\nu = 0.9$. The horizontal lines show the CCAT 5-sigma detection limits for

one hour and two hours of on-source integration at 350 μ m, respectively.

4.10.5 Serendipitous Discoveries of Large, Distant Minor Planets

Detection of TNOs at large heliocentric distances is advantageous in the submillimeter regime. For a given magnitude, the surface area of a TNO scales as $R^2\Delta^2$, all other things being equal. Hence the solid angle subtended by the TNO at the observer's location scales as the square of the heliocentric distance R^2 . The temperature of the TNO is proportional to $R^{-1/2}$. In the Rayleigh-Jeans approximation, the submillimeter flux depends on the product of temperature and solid angle (5), i.e. it scales as $R^{3/2}$. For any given magnitude, there is therefore in principle a distance beyond which detectability becomes easier in the submillimeter regime. The situation is not as favorable as this calculation suggests due to the breakdown of the Rayleigh-Jeans approximation at low temperatures and high frequencies. Nevertheless, Figure 4.35 illustrates that there is an important discovery space for CCAT. Most $m_R = 24$ bodies remain undiscovered since optical surveys typically do not reach that depth. Low-albedo objects in that magnitude range and at distances beyond 80 or 100 AU would be easily detectable by CCAT.

The apparent motion of TNOs across the sky is primarily due to parallax, with a rate at opposition given approximately by $150/R$ in arcseconds per hour. Detection of moving objects at distances larger than 100 AU will therefore require integrations spanning several hours and multiple images. This program is particularly efficient in that it can be undertaken in a piggy-back mode, in which fields obtained during other observing programs are searched for moving sources. Because the latitude distribution of TNOs is broad, discoveries tens of degrees from the Kuiper belt plane are likely.

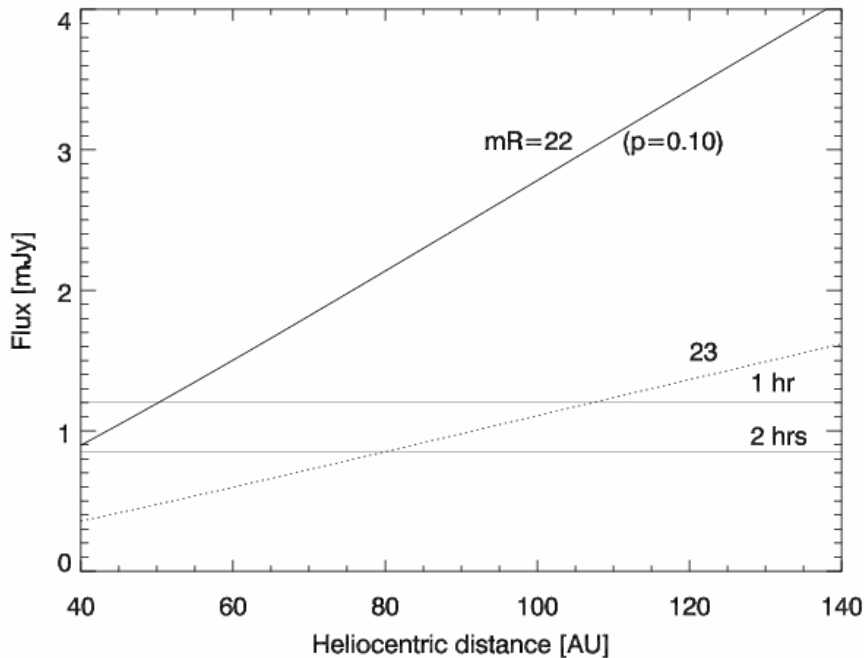


Figure 4.35: Predicted 350 μ m submillimeter flux for TNOs assuming the standard thermal model. The solid line corresponds to bodies with $m_R = 22$ and red geometric albedo of 10% or equivalently bodies with $m_R = 23$ and red geometric albedo of 4%. The dotted line corresponds to bodies with $m_R = 23$ and red geometric albedo of 10% or equivalently bodies with $m_R = 24$ and red geometric albedo of 4%. The horizontal lines show the CCAT 5-sigma detection limits for one hour and two hours of on-source integration at 350 μ m, respectively.

4.10.6 Lightcurve Observations

The rotational signature of TNOs may be detectable if periodic variations in the thermal flux are measurable. This would provide a powerful tool for the statistical study of spin states in the Kuiper belt, something that has been difficult to achieve so far at optical wavelengths due to the intrinsic faintness of most TNOs. Studies of correlations between lightcurve periods and sizes, colors, dynamical class, and orbital parameters can yield profound insights into the origin and evolution of the minor planets, their dynamical evolution, and even into their interior structure and mechanical properties. In the case of the Main Belt of asteroids, this important body of

knowledge has been accumulated by painstakingly measuring asteroid lightcurves at manually-operated telescopes over the past ~30 years. A TNO lightcurve survey is an important endeavor that would be best accomplished by a ~2.5 m robotic telescope at a site with exceptional seeing. If such programs have not been carried out by the time CCAT comes on-line, there will be another important discovery space and insights to be gained.

Lightcurve analysis ideally requires tens of data points within a spin period, and observations spanning at least a full spin period. Since TNOs are likely to have period of order 10 hours, the lightcurve observations may require roughly ten times longer than the size-albedo measurements, and may be limited to TNOs for which adequate SNR can be obtained in a fraction of an hour ($m_R < 22$). Lightcurve analyses may also be sensitive to confusion with background sources at a flux level ~2 mag below the TNO (10% variations).

4.10.7 Telescope Requirements

As far as TNO thermal flux measurements with nominal CCAT sensitivities are concerned, little is gained by observations at 200 μm compared to 350 μm . There is a rather strict requirement on telescope size. At sizes less than 25 m, the sample of detectable TNOs is no longer statistically meaningful for the establishment of the size distribution. There is no particular constraint on field of view for TNO studies as most targets will be known in advance and are scarcely distributed on the sky, except that piggy back searches will be more effective with a large field.

5 Top-level Requirements

This section presents the CCAT technical requirements that follow from the science objectives and the instrument concepts. In this context, CCAT encompasses the entire observatory including both the telescope and the facility.

The following definitions are used:

Requirements describe the design or performance capabilities needed to meet the science goals of the Project. These requirements are judged to be necessary and technically feasible.

Goals are desirable performance capabilities that should be included if feasible and compatible with the established requirements. If such goals cannot be met due to technical or programmatic concerns, this shall be identified during the course of the design. Goals are labeled with a [G]. A [G] at the head of a subsection or category indicates that all the requirements included in the subsection or category are goals.

When the Project becomes subject to change control, alterations in requirements or goals shall be regulated according to procedures established by the Project office.

5.1 Requirements Summary

| | Requirement | Goal | Remarks |
|-------------------------|--|----------------------------|---------------------|
| Wavelength range | 350 – 1400 μm | 200 – 3500 μm | |
| Aperture | 25 m | | |
| Field of view | 10' | 20' | |
| ----- | | | |
| Half Wavefront Error | < 12.5 μm rms | < 9.5 μm rms | |
| Site conditions | < 1 mm | < 0.7 mm | Median pwv |
| Polarization | 0.2% | 0.05% | After calibration |
| Emissivity | < 10% @ > 300 μm < 20% @ 200 μm | < 5% @ > 800 μm | |
| ----- | | | |
| Pointing, blind | 2" | 0.5" | rms |
| offset | 0.3" | 0.2" | within 1° |
| Repeatability, one hour | 0.3" | 0.2" | rms |
| Elevation range | 15–90° | | from horizon |
| Azimuth range | $\pm 270^\circ$ | | from north |
| Scanning rate | 0.2° s ⁻¹ | 1° s ⁻¹ | slow and fast modes |
| acceleration | 0.4° s ⁻² | 2° s ⁻² | |
| point. know. | 0.2" | 0.1" | rms |
| Secondary nutation | $\pm 2.5'$ @ 1 Hz | | azimuth only |

5.2 Radiometric Requirements

These requirements summarize the radiometric and optical requirements for the telescope.

5.2.1 Wavelength range

The CCAT science objectives (section 4) are addressed by observations at submillimeter wavelengths, 300 – 1400 μm , so the telescope is required to operate at these wavelengths. Important additional capabilities are provided by operation at 200 – 300 μm and at 1400 – 3500 μm , so these are goals. Limited performance in the infrared, < 40 μm , in particular for non-redundant mask interferometry, is also a goal.

5.2.2 Aperture

The CCAT science objectives require a primary aperture of 25 m diameter. The principle issues are sensitivity and source confusion (section 4). Angular resolution is an important corollary.

5.2.3 Field of View

Wide field surveys are an important component of the science program. For large format cameras, a large field of view is essential. This is a unique capability of CCAT. The requirement is 10' and the goal is 20' diameter unvignetted field of view.

5.2.4 Wavefront Error

The wavefront error budget sets the requirements for the telescope in the absence of atmospheric effects or instrumental degradation and pre-allocates limits to the sources of image degradation to guide the design of the telescope (sections 8 and 9).

For CCAT the increase in integration time for point source detection because of degradation telescope performance caused by surface imperfections and other errors must be less than 50% relative to the ideal case for observations at 350 μm . The goal is less than 25% for the integration time increase. In terms of the half wavefront error, or rms surface error, $\text{WFE}_{0.5}$, the integration time requirement and goal correspond to $\text{WFE}_{0.5} = 12.6$ and 9.3 μm , respectively. Figure 5.1 shows the trade between relative integration time and $\text{WFE}_{0.5}$ for different wavelengths.

Except for field curvature, the wavefront error requirement applies over the entire field of view. In addition, the telescope performance should not degrade more than 10% over the elevation range.

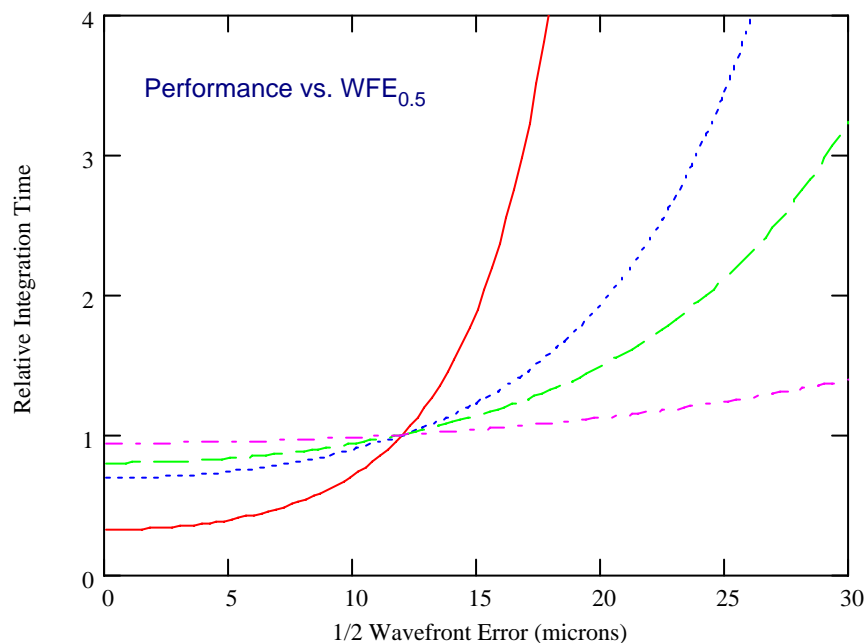


Figure 5.1: Relative integration time change vs. half wavefront error at 200, 350, 450 and 850 μm . This is the factor needed to get the equivalent signal-to-noise ratio on a source for background-limited performance for a change in surface rms while other parameters are kept constant. The integration time is normalized at $\text{WFE}_{0.5} = 12 \mu\text{m}$.

5.2.5 Site

Consistently superb observing conditions are crucial to the CCAT's scientific success. A site is required with substantially conditions than encountered on Mauna Kea. Suitable sites exist at high altitude in the Atacama region of northern Chile (sections 4.2.2 and 10). The precipitable water vapor (PWV) is a convenient measure of site quality. For CCAT, the requirement is the median PWV < 1 mm and the goal is the median PWV < 0.7 mm.

5.2.6 Polarization

For accurate polarimetry, the intrinsic telescope polarization must be calibratable to 0.2%. A goal shall be 0.05% (section 6).

5.2.7 Emissivity

The total telescope emissivity must be less than 10% for wavelengths longer than 300 μm and less than 20% at 200–300 μm . A goal is for the total telescope emissivity to be less than 5% for wavelengths longer than 800 μm . Sources of emissivity include, but is not limited to, surface emission, scattered light, primary and secondary obscuration, secondary supports, and segment gaps. Any variations in emissivity must contribute less than 10% of the noise from this background (section 4).

5.3 Motion Requirements

To accomplish the science objectives, the telescope mount must support all sky coverage with the following specifications.

5.3.1 Range of Motion

| | |
|-----------------------------|-----------------------|
| Azimuth, from north | $\pm 270^\circ$ |
| Elevation, from horizon | $15^\circ - 90^\circ$ |
| Zenith blind spot, tracking | $\leq 5^\circ$ |

The lower elevation limit, 15° , corresponds to an airmass of 4. Below this elevation, the atmosphere renders observations impractical. For sites near the tropic of Capricorn around -23° S, the corresponding northern declination limit is about 52° .

5.3.2 Slewing

Slewing is gross motion for rough pointing. Data will not be recorded during slewing. The rate and acceleration are applicable to elevation motions and to azimuth motions at elevations $< 60^\circ$ from the horizon.

| | |
|--------------|---|
| Maximum rate | 3° s^{-1} |
| Acceleration | $1^\circ \text{ s}^{-2}; 2^\circ \text{ s}^{-2} [\text{G}]$ |

5.3.3 Pointing Accuracy

| | |
|------------------------------------|---|
| Blind, all sky | $< 2'' \text{ rms}; < 0.5'' \text{ rms} [\text{G}]$ |
| Offset, within 1° of target | $< 0.3'' \text{ rms}; < 0.2'' \text{ rms} [\text{G}]$ |

A guider system may be used to meet these requirements.

5.3.4 Track Rates

Tracking is following a source for long integrations. In addition to sidereal tracking, faster tracking is required for Solar system targets. Data is recorded during a track.

| | |
|--------------|----------------------------|
| Maximum rate | 0.5° s^{-1} |
|--------------|----------------------------|

5.3.5 Pointing Repeatability

| | |
|--------------------------------|---|
| Within one hour after pointing | $< 0.3'' \text{ rms}; < 0.2 \text{ rms} [\text{G}]$ |
|--------------------------------|---|

5.3.6 Nodding

Nodding is rapid repointing of the telescope to a nearby position for subtraction of sky emission. Data is not recorded during the nod.

| | |
|-----------------|-------|
| Nod distance | < 20' |
| Nod time | < 2 s |
| Nod settle time | < 1 s |

5.3.7 Scanning

Rapid scanning is required to overcome fluctuations in sky emission during wide field observations (Section 6). There are two regimes, slow and fast, for short and long wavelength observations, respectively. The rates and accelerations are applicable to elevation motions and to azimuth motions at elevations < 60° from the horizon. Data is recorded during scanning, including accelerations.

| | | |
|--------------------|----------------------|--------------------|
| | <i>Slow</i> | <i>Fast</i> |
| Field | 2° | 10° |
| Rate | 0.2° s ⁻¹ | 1° s ⁻¹ |
| Acceleration | 0.4° s ⁻² | 2° s ⁻² |
| Pointing knowledge | 0.2" | 1" rms |

5.3.8 Secondary Mirror Nutation

Secondary mirror nutation (chopping) is required to overcome fluctuations in sky emission when observing point sources or with single pixel receivers or slit spectrometers. Data is recorded during the dwell phases.

| | |
|-----------------|--------|
| Amplitude | ± 2.5' |
| Rate | 1 Hz |
| Transition time | 100 ms |

Smaller beam displacements with proportionally faster transitions are a goal. During the dwell phases, the telescope pointing must be maintained within 0.1".

5.4 Instrument Support Requirements

5.4.1 First Generation Instruments

To address the science objectives, these first generation instruments will be developed as part of the Project (section 6). They will be operable at telescope commissioning. Other, previously existing instruments will likely also be available.

| Instrument | λ range | $\lambda/\Delta\lambda$ | FOV | Type |
|------------|------------------------|-------------------------|-----------|-----------------------|
| SWCam | 350–620 μm | ≈ 10 | 5' × 5' | TES bolometers |
| LWCam | 750–2000 μm | ≈ 10 | 15' × 15' | Antenna coupled MKIDs |

5.4.2 Instrument Locations

The principal instrument mounting locations will be the two Nasmyth foci. Each Nasmyth location will have the provision for mounting up to three instruments in a common envelope. These three instrument clusters will allow rapid (< 30 min) switching between instruments. The telescope will be bilaterally symmetric up to the two instrument flanges so instruments can be mounted at either mount. Smaller instruments will be allowed at one bent Cassegrain focus with a goal of smaller instruments being allowed at both bent Cassegrain foci.

No provision is required for instruments at either the prime focus or the direct Cassegrain focus.

5.4.3 Instrument Optical Requirements

All instruments shall operate at the nominal focus position. The following are the optical requirements for the instruments. Further details are in section 8.

| | |
|---------------|--------------------------|
| Focal ratio | $f/8$ |
| Field of view | 20' unvignetted diameter |

5.4.4 Tertiary Rotator

The Nasmyth and bent Cassegrain foci require three reflections. Switching between foci will be accomplished by rotating the tertiary mirror (M3) to direct the beam to the desired focus.

| | |
|---------------------|-------------------------------|
| Number of Positions | No limit within 180° (360° G) |
| Time to switch beam | < 2 min for 180° switch |
| Repeatability | < 0.1" on sky after motion |

5.4.5 Instrument or Field Rotators

No facility instrument or field rotators are required. If these are deemed necessary they will be provided as part of the instrument.

5.4.6 Instrument Interface

Standard interfaces will provide seamless mounting for instruments. Details, including but not limited to mass, volume, and cantilever, will be defined in the next phase of the Project.

5.4.7 Instrument Utilities

The instruments will require various support utilities, including but not limited to electrical power, network connections for data, control and timing, vacuum, cryogenics, and compressed gasses. These details will be defined during the next Project phase.

5.4.8 Instrument Preparation Room

A room adjacent to the telescope will be needed to support the installation of new instrumentation on the telescope and the repair and maintenance of existing instruments (section 6). This room shall be about about 50 m² and have enhanced O₂ for comfort and safety. The movement of instruments from storage to this prep room and then to the focal plane position must be handled seamlessly. Adequate cranes, hoists, elevators, etc., to move all instruments are required.

5.4.9 Instrument Storage

Storage space for up to 10 (TBD) instruments must be present. Instruments will be stored in their shipping cases but they must be protected from moisture, wind, and dust during all observatory operations, both maintenance and observing. The necessary volume can be estimated from the instruments discussed in Section 6.

5.5 Remote Operations

The facility will be remotely operable, i.e., no manned presence at the telescope will be necessary for routine observations. This can be implemented in a phased approach involving the following steps.

| | |
|---------|--|
| Phase 1 | Operator and observer both at telescope for instrument commissioning, etc. |
| Phase 2 | Operator at telescope with remote observer at base facility or home institution. |
| Phase 3 | Operator at base facility with remote observer elsewhere. |

5.6 Environmental Requirements

These are derived from the meteorological data recorded on or near candidate sites in Chile (section 10). The requirement is operation under the 75th percentile conditions and the goal is 90th percentile conditions.

5.6.1 Operating Conditions

The following represent the range of environmental conditions expected during operation. All CCAT systems must remain fully functional during the worst case combination of these conditions.

| | |
|-------------------|--|
| Air pressure | 495–565 kPa (7.2–8.2 psi) |
| Wind speed | < 10 m s ⁻¹ (33 ft s ⁻¹) with 15 m ⁻¹ (50 ft s ⁻¹) gusts |
| Temperature | -20 to +15 °C (-4 to +59 °F) |
| Relative humidity | 0% to 95% |

5.6.2 Survival Conditions

The following represent the maximum non-operating environmental conditions the CCAT is required to withstand. The dome shall be in the fully closed stationary configuration when considering the worst case combination of these conditions.

| | |
|---|--|
| Wind | 65 m s ⁻¹ (215 ft s ⁻¹) |
| Temperature | -30 to +25 °C (-22 to +77 °F) |
| diurnal variation | 30 °C (54 °F) |
| Snow load | 100 kg m ⁻² (20 psf) on horizontal surface |
| Uniform ice buildup on snow free surfaces | 25 mm (1.0 in) or 22 kg m ⁻² (5 psf) |
| Annual precipitation | Up to 300 mm (up to 12 in) |
| Precipitation | 25 mm hr ⁻¹ (1 in hr ⁻¹) in 30 m s ⁻¹ (100 ft s ⁻¹) wind |
| Seismic ground acceleration | Zone 4 per the Uniform Building Code |

5.6.3 Daytime Operations

Daytime operations will necessary to take advantage of good observing conditions (section 10) and maximize CCAT's science return. Daytime operations will be allowed so long as sunlight does not directly strike the primary mirror.

5.7 Safety Requirements

Working around an observatory inherently involves risks associated with large moving equipment, high platforms and ladders, etc., circumstances likely to be exaggerated by high altitude. All parts of the telescope and facility will be designed to ensure safety for personnel and vulnerable equipment. The safety policies shall conform to applicable standards, e.g., OSHA.

Particular attention will be given to operating in a high altitude environment. Telescope operations will be generally performed remotely and most observers will use facility instruments designed for remote operation. There will be an oxygenated control room and workroom so necessary maintenance and on site observing can be done when necessary, for example during instrument commissioning, can be done safely.

5.8 Servicing and Maintenance [G]

Good observing conditions throughout the day (section 10) so the time required for routine service and maintenance operations has a direct impact on scientific observations. The examples here are goals for some typical operations.

5.8.1 Typical Time for Routine Periodic Operations

| | |
|------------------------------------|---------|
| Remove or install primary segment | < 2 hrs |
| Remove or install secondary mirror | < 2 hrs |
| Remove or install tertiary mirror | < 2 hrs |
| Mount and cable instrument | < 2 hrs |
| Collimate telescope | < 2 hrs |

5.8.2 Time to Perform Servicing and Maintenance Operations

| | |
|---|---------|
| Service/Replace dome truck or drive | < 7 hrs |
| Replace telescope encoder and electronics | < 7 hrs |
| Replace telescope drive and amplifier | < 2 hrs |

5.8.3 Optics Cleaning

Cleaning may be necessary to maintain the system emissivity discussed above. Provisions will be made for regular manual CO₂ or other cleaning of M1 and smaller optics. A goal is to clean as often as required to ensure dust scattering does not limit telescope photometric performance and sensitivity.

6 Instrumentation

6.1 Introduction

The primary science goals of the CCAT are to (1) Explore the origins of the Solar System through surveys of Kuiper Belt objects (2) Explore the origins of stars and planetary systems through surveys for protostellar condensations and through pointed observations of stellar debris disks in the dust continuum, (3) Explore the origins of galaxies through submillimeter surveys of distant “protogalaxies” and (4) Explore the structure of the Universe through the Sunyaev-Zeldovich Effect.

These science topics emphasize wide field imaging and surveys; hence the first light instruments will be cameras. Two cameras, one for the submillimeter wavelengths and the second for near mm wavelengths, are part of the baseline Project. It is more practical to build two cameras rather than one combination instrument. The short wavelength camera (SWCam, section 6.3) has 32,000 TES silicon bolometers that, at 350 μm , fully sample a 5' \times 5' field of view (FoV). The long wavelength camera (LWCam, section 6.4) uses a slot dipole antenna coupled bolometers with various bands separated by microstrip bandpass filters. Plate scales and pixel counts are wavelength dependent. The larger plate scales cover the entire 20' \times 20' FoV. These cameras are challenging, but achievable through modest advances in the current array technologies. Polarimetry (section 6.5) is a natural addition to the first light cameras. Section 6.6 covers data taking strategies and sky noise removal.

Existing, previous generation instruments, including direct detection and heterodyne spectrometers developed for other facilities, will be brought to CCAT to enhance the scientific yield of the two cameras. Although these existing instruments can not accomplish all the primary CCAT science objectives, they will provide important supplementary capabilities, especially in the early years of operation. Looking into the future, foreseeable instrument developments will greatly extend the CCAT science return for many years. Existing instruments and future instruments, such as a polarimeter and a 40 μm camera, are outlined in Sections 6.7 and 6.8, respectively. We finish with a brief discussion of the laboratory facilities that are necessary at the telescope (section 6.9).

Table 6.1a. CCAT First Light Instruments

| | Band Center | Resolving Power | Number of pixels | Arcseconds/pixel | Field of View |
|-----------------|--------------------|------------------------|-------------------------|-------------------------|----------------------|
| SWCam | 200 μm | 23 | 32,000 | 1.75" | 5.05' \times 5.05' |
| | 350 μm | 8 | | | |
| | 450 μm | 8 | | | |
| | 620 μm | 7 | | | |
| LWCam | 740 μm | 13.5 | 16384 | 4.7" | 10' \times 10' |
| | | | 3072 | 19" | 20' \times 20' |
| | 870 μm | 8.8 | 16384 | 4.7" | 10' \times 10' |
| | | | 3072 | 19" | 20' \times 20' |
| | 1.1 mm | 5.5 | 4096 | 19" | 20' \times 20' |
| | 1.4 mm | 5.5 | 1024 | 37" | 20' \times 20' |
| | 2.0 mm | 5 | 1024 | 37" | 20' \times 20' |
| Total Detectors | | | 45,056 | | |

| Table 6.1b. CCAT Existing Instruments | | | | | |
|--|---|---|---------------------|-------------------------|------------------------|
| | Bands | Resolving Power $R \equiv \lambda/\Delta\lambda$ | Available Bandwidth | Instantaneous Bandwidth | Number of beams on sky |
| ZEUS: echelle grating spectrometer | 200, 225, 300, 360, 450, 600, & 900 μm | 2000, 1800, 1450, 1100, 900, 700 & 450 | 13% | 6% | 6 |
| Z-Spec waveguide grating spectrometer | 1 to 1.6 mm | 200 to 400 | 165% | 165% | 1 |
| Heterodyne receivers | 180 – 950 GHz | Up to 10^7 | Up to 20% | 1 -4 GHz | 1 |

6.2 Overview

6.2.1 Current State of the Art Detector Arrays

At present, there are a handful of 10 to 15 m diameter submillimeter telescopes in very good submillimeter sites. These facilities have delivered paradigm changing science using relatively modest format submillimeter bolometer array cameras including the 384 pixel SHARC-2 (Figure 6.1, Dowel et al. 2003 SPIE 4855, 73) on the CSO and the 128 pixel SCUBA on the JCMT. These capabilities will soon be upgraded by the large format TES arrays in SCUBA-2, with 5120 pixels at both 450 and 850 μm (Figure 6.2, Holland et al. SPIE 4855,1, Audley et al. 2004, SPIE 5498, 63).

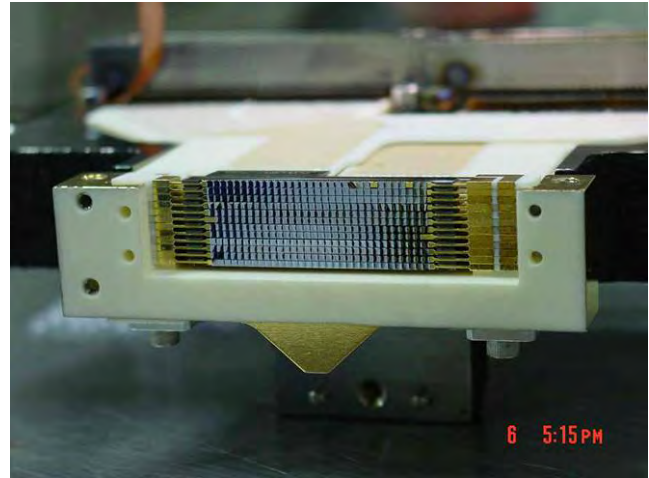


Figure 6.1. SHARC-2 bolometer array manufactured by GSFC using the “pop-up” detector technology. The arrays are sensed with implanted thermistors. There are 12 rows of 32 pixels. Each pixel is 1 mm \times 1 mm.

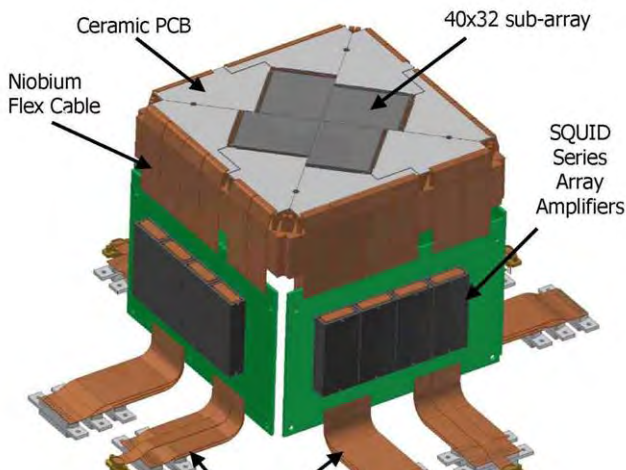


Figure 6.2. Functional layout for the 5120 element arrays in SCUBA-2. The array is composed of 4 - 32 \times 40 pixel sub-arrays butted together. These arrays employ TES readouts and a SQUID multiplexer. The arrays are manufactured by NIST.

Our baseline submillimeter camera employs the SCUBA-2 architecture arrays modified so that to fully populate a 5' \times 5' field of view with 1.75" pixels. The subarray unit cell is 32 \times 40 pixels so the completed focal plane will consist of 25 subarrays, for a total of 32,000 pixels, a factor of more than 6 larger than the SCUBA-2 focal plane. Combined with the larger aperture of the CCAT, its better surface accuracy, and its better site on a high Atacama peak, we expect 10 to 40 times better sensitivity per beam than prior facilities at 350 μm . Combined with the larger format arrays, we expect factors of thousands improvement in mapping speed.

6.2.2 Overall Instrument Requirements

All facility instruments on the CCAT must be remotely operable and use only closed cycle refrigerators. The

SWCam and LWCam cameras will couple to the telescope at the $f/8$ Nasmyth focus, one on each arm. This arrangement maximizes the efficiency of use of prevailing weather conditions. The cameras require re-imaging fore-optics that could be used for other instruments as well. Other instruments will likely be coupled through a quarternary flat at each focus, in which case there will be 3 ports times 2, or 6 positions. Other instrument requirements are stated in sections 5.9 and 5.17.

6.2.3 Telescope Pointing and Jitter Requirements.

The pointing and tracking jitter requirements for the CCAT can be calculated in a straight forward manner (Bradford, C.M., CCAT Website). Here we define pointing as the error in the boresight position, caused by, for example, an error in a slew from a pointing source or an incorrect guider offset. Jitter is random deviations in the pointing that may occur on short (seconds) timescales. Examples are jitter in the tracking mechanisms or atmospheric “seeing”. For a fully sampled camera, pointing errors need not affect sensitivity but jitter will. For slit spectrometers, such as ZEUS and Z-spec, or heterodyne spectrometers, both types of errors will degrade performance. To not degrade sensitivity by more than 10%, the pointing requirement is 0.61" in each dimension for a 350 μm slit spectrometer. The jitter requirement is similar: the RMS jitter must be less than 0.66" for 90% of peak performance. If both of these errors contribute equally, a mean offset and RMS jitter error of 0.45" (each) degrades the 350 μm performance by 10%. The requirements naturally scale with wavelength: with no jitter, pointing requirement = $0.61'' \cdot (\lambda/350 \mu\text{m})$, with jitter pointing requirement = $0.46'' \cdot (\lambda/350 \mu\text{m})$.

6.2.4 Why Two Cameras, Instead of One?

It can be argued there is a science advantage to creating an instrument that can image at 350 and 850 μm simultaneously. This would ensure near perfect registration between the two wavelengths and immediately yield two points on the spectral energy distribution (SED) for astrophysical sources. However, we rejected this idea because:

- The expected sensitivities and SEDs are not well matched. The confusion limit is reached three times faster at 850 μm than at 350 μm so that the 850 μm exposure would be “finished” much sooner than the 350 μm exposure.
- The technologies for detector arrays are different at the two wavelengths. An optically coupled array appears best in the submillimeter while antenna coupled arrays have better promise at the longer wavelengths.
- The image quality requirements are much more stringent at the shorter wavelengths. Transmissive reimaging optics easily deliver the requisite image quality with acceptable losses in the submillimeter. However, transmissive optics would have unacceptably large emissivity for work in the near mm bands.
- Array costs are the largest single capital item for the instruments describe here. Folded in with the different array technologies, it is logical to construct separate instruments for work at 350 and 850 μm .

6.3 Short Wavelength Camera

The Short Wavelength Camera (SWCam) will deliver diffraction limited imaging in the short submillimeter (200, 350, 450, and 620 μm) telluric windows. Each of these windows is accessible via a cryogenic filter wheel containing bandpass filters well matched to the telluric windows. The baseline design has a 5' \times 5' field of view, is fully sampled at 350 μm , and is coupled to the telescope through a Germanium lens re-imaging system.

6.3.1 Instrument Requirements

To accomplish our primary science goals, the SWCam requirements are:

1. Broadband photometry in the 350, 450, and 620 μm telluric windows. Bandpass filters to be optimized for greatest sensitivity to continuum sources as determined by the telluric and instrument transmission.
2. Diffraction limited imaging at the primary survey band (350 μm) in order to maximize the science return in the interplay between array size (numbers of pixels), field of view, and source confusion.
3. Total instrument throughput requirement is 20% (goal is 40%) including detector quantum efficiency.
4. Background limited performance at each wavelength even under the best observing conditions.

6.3.2 Field of View

The telescope is designed to deliver a 20' FoV. However, to fully populate this field at 350 μm would require ~ 500,000 pixels, which would be extremely expensive using current technologies. Next generation technologies will likely reduce this cost significantly so development of a mega-pixel camera is logically postponed. We are designing our baseline submillimeter camera to have a 5' FoV for four reasons.

1. Much of the primary science can be delivered with a 5' FoV camera within the first 3 years of operation.

2. The telescope delivers a 1.17 meter image for a 20' FoV, which is quite challenging to couple into a 350 μm diffraction and background limited camera.
3. The current and near future technology suggests 32,000 pixels is a reasonable goal for array size. This delivers Nyquist sampled images over a $5' \times 5'$ FoV at 350 μm .
4. Much of the 20' FoV could be imaged through clever arrangement of 4 identical cameras covering 5' each, providing a natural growth path (Section 6.8.1, below).

6.3.3 Detailed Design

6.3.3.1 Fore-optics

A focal plane that Nyquist samples a diffraction limited image must have a final $f/\#$ given by $1.22 \times f/\# \cdot \lambda/2 = x$ where x is the physical dimension of individual pixels. The proposed NIST detector arrays have 1mm pitch so at 350 μm , the final $f/\#$ must be $f/4.6$. The telescope delivers $f/8$ so we must re-image the focal plane. The re-imaging process also enables formation of a pupil (image of the primary mirror) within the camera itself. A cold Lyot stop is placed at this pupil minimizing extraneous background power.

We have investigated both fully reflective and transmissive optics for the re-imaging fore-optics. The reflective design has the advantage that it maximizes throughput, and minimizes emissivity. An optical design was attained using the ZEMAX ray-tracing program that delivers the requisite image quality over the entire 20' FoV of the telescope. However, this design requires 4 m class off-axis paraboloids and results in a dewar that is roughly 8 m \times 3 m in size. For the first light instrument, the more modest 5' FoV focal plane can be properly imaged into a more modest 3 m \times 1.5 m dewar, but the reimaging mirror is still a formidable 3 m class paraboloid. We therefore investigated the use of transmissive optics.

A transmissive system is easily designed with the 5' FoV imaged into a compact 0.7 \times 1.0 m dewar with a 25 cm dewar window. Lens diameters are modest at about 44 cm or less. However, selection of lens materials is challenging, as bulk absorption lessens system transmission and increases system emissivity. Unfortunately, in the short submillimeter bands system emissivity will never be less than about 30% due to contributions from the sky, so that modest ($\sim 10\%$) emissivity of the lens material is acceptable, and we can use transmissive optics. We found a variety of materials that would work as lenses including polyethylene, quartz, sapphire, silicon, and germanium. The selection criterion was essentially the extinction coefficient, but other important issues include material properties (environmental [water damage], structural [use as a window]), cost, and the availability of suitable anti-reflection coatings.

6.3.3.2 Optical Design

The baseline design employs germanium lenses with expected transmissions greater than 90%. Germanium lenses are commercially available with standard sizes to 35 cm diameter with diamond AR coatings (e.g., Umicore Corp: www.optics.umicore.com).

The system is quite simple (Figure 6.3): the first element takes the f-cone of the 5' FoV of the telescope and collimates it with a beam size of 13.5 cm. The second element is near the pupil of the first element, and takes the collimated light and images it at the focal plane at $f/4.8$. The first element is a 44 cm diameter plano-convex lens, with a radius of curvature of 350 cm and a center thickness of 2.5 cm. This lens is placed 1.10 m back from the Nasmyth focus and sends a collimated beam to the entrance window of the dewar 1.05 m downstream. The second element serves as both the entrance window to the dewar and the camera. The second lens has a diameter of 22 cm, and needs to be at least 0.64 cm thick to serve as a pressure window. It is plano-convex, and we specify a thickness of 1.5 cm. The second lens images the field of view onto the array 69.5 cm further downstream. The combined transmission of the two lens AR coated system is estimated at 85%.

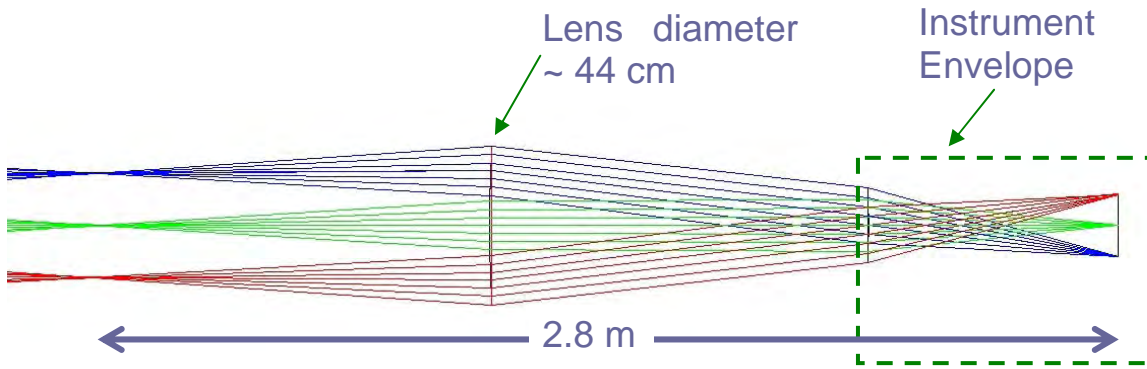


Figure 6.3. SWCam Fore-optics with schematic instrument

A ZEMAX raytrace indicates excellent image quality with this system (Figure 6.4). The spot sizes have an rms radius of less than 0.3 mm (30% of a pixel) even for the most off-axis beams. The image plane is curved, so that the outer pixels can be improved significantly by adjusting the tiling of the focal plane accordingly. One can also do significantly better by letting the lens diameters grow modestly, although this is not deemed necessary.

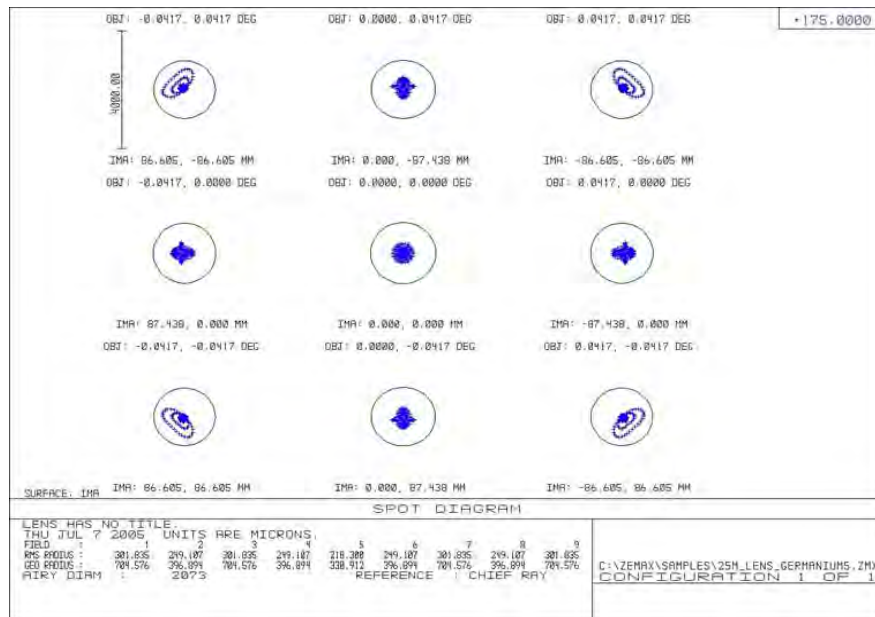


Figure 6.4. ZEMAX spot diagrams for the optical system outlined in the text. The circles are λ/D in diameter at 350 μm .

6.3.3.3 Optical Path within the Cryostat

The requisite optics, filters, electronics, cryocoolers, and array for the submillimeter camera can be enclosed in a cryostat with a diameter of about 0.8 m and a length of 1.2 m (Figure 6.5). The beam enters the dewar through the germanium entrance window. Most of the power of the thermal background is reflected back out of the window by an AR coated crystal quartz filter located within 10 cm of the window. This filter needs to be about 20 cm in diameter. The Lyot stop has a diameter of 12 cm and is formed 21 cm from the entrance window. We place a 4 position filter wheel immediately behind the Lyot stop. This wheel will contain filters for work at 200, 350, 450, and 620 μm (available from P. Ade). The image focal plane is 80 cm from the entrance window.

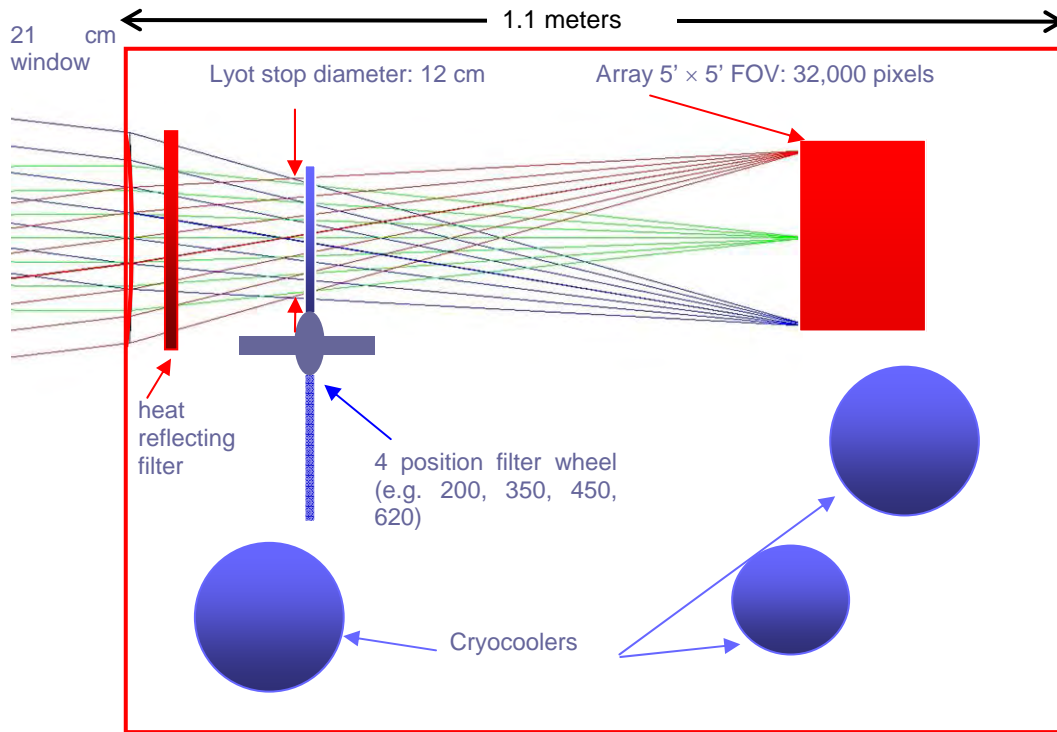


Figure 6.5. Submillimeter camera layout

6.3.3.4 Cryocoolers

We have baselined closed cycle refrigerators for all CCAT instrumentation both to eliminate cryogenic maintenance and to enable remote operations. Bolometers are susceptible to microphonics induced by mechanical vibrations. Sterling and Gifford-McMahon cycle coolers have moving parts that will likely induce unacceptable microphonics. Pulse tube coolers, however, which have no moving parts in their cold heads, demonstrate acceptable vibration levels and are now commercially available with a so called “vibration free” option ($\ll 1 \mu\text{m}$ at 4 K, Cryomech Inc.). Bolometers must operate with very stable base temperatures. The end stage coolers will therefore likely be closed cycle ^3He systems or adiabatic demagnetization refrigerators (ADRs) that provide the requisite temperature stability and are vibration free. The temperature isolation system for the array (e.g. Kevlar thread) will further shield against 4.2 K temperature fluctuations and residual vibrations. An important feature of TES bolometers, which will be used in CCAT instrumentation, is they are less susceptible to microphonics than thermistor sensed devices since they are low impedance devices. The cooling chain of choice therefore consists of pulse tube coolers to bring the system down to 4.2 K, closed cycle ^4He cooler to bring the detector package and requisite filters down to 2 K, and a closed cycle ^3He system or ADR to bring the detector itself down to 250 or 60 mK, respectively.

The first cold stage would be at about 45 K. A rough estimate of the heat load from room temperature to the 45 K stage (taking only radiative load from the background and thermal conductivity through wires and G10 mounting struts into account and assuming cryostat dimensions given in section 6.3.3.3) results in a total power of about 30 W: 25 W of radiative heat load and about 3 W of conductive heat load dominated by the $\sim 12,000$ wires necessary to read out the TES arrays. Similarly, the total heat load from the 45 K stage onto the 4.2 K stage is ~ 0.5 W, about 2/3 of which is from the wires. Between the 4 K electronics and the detector we will likely use Cu/Ni clad Nb/Ti wires, the cores of which become superconducting below a temperature of about 9.8 K, so heat is only conducted through the Cu/Ni clad, greatly reducing the heat load to the array. Even if all 12000 wires go to the detector array (via a 2 K stage, dumping about $200 \mu\text{W}$) the heat load is reduced to about $25 \mu\text{W}$ at 300 mK. It is likely that the future large submillimeter arrays will use a different multiplexing scheme than the current small arrays thereby reducing the number of wires and therefore also the heat load.

The PT410 pulse tube cooler available from Cryomech, Inc., is compatible with the envisioned cryostat size and provides a cooling power of about 40 W at 45 K and about 1 W at 4.2 K (PT410, Cryomech Inc). The dual stage ^3He refrigerator in of our ZEUS instrument delivers 100 μW of cooling power at 300 mK, and $\sim 50 \mu\text{W}$ of cooling at the ultra-cold head at 250 mK. For the baseline camera, the sensitivity is achievable with cold head temperatures of 250 mK. For example, we are achieving detector NEPs better than $10^{-16} \text{ W/Hz}^{1/2}$ with our ZEUS spectrometer with a cold head of 250 mK.

6.3.4 Array

The baseline array is based on SCUBA-2 technology and will be procured from NIST. The array consists of 25 edge-butteted sub-arrays of 32×40 pixel format, or 32,000 pixels. The pixel pitch is the same as for SCUBA-2: 1 mm square. The first of the SCUBA-2 subarrays have been delivered and tested by members of the SCUBA-2 consortium and they are delivering the expected optical NEPs (Figure 6.6). These arrays will certainly deliver the requisite NEPs for the SWCam at 60 mK and will likely deliver the requisite NEPs at 250 mK.

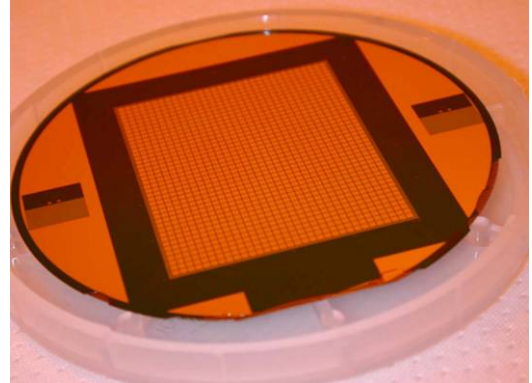


Figure 6.6. 32×40 pixel subarray component of SCUBA-2 array (K. Irwin, personal communication)

6.4 Long-Wavelength Camera

A wide-field, long-wavelength continuum camera (LWCam), covering frequencies from 150 GHz to 405 GHz ($740 \mu\text{m}$ to 2 mm) over a field-of-view (FoV) as large as 20' diameter, would provide the means for CCAT to accomplish many of its science goals and make use of time when short-wavelength ($\leq 620 \mu\text{m}$) observations are not feasible. A strawman design for such a camera is presented here, including an assessment of the current status of various necessary technologies.

The decision of the upper frequency for the LWCam requires discussion. It is, in general, scientifically advantageous to include more bands if different detector arrays can be used simultaneously and to optimize sensitivity for each band separately, which would suggest to including $620 \mu\text{m}$ also (where antenna-coupling would still work). But the $620 \mu\text{m}$ band provides the most challenging pixel count, so the strawman design presented here does not include it, though some discussion is given to including it in future upgrades.

6.4.1 Design Principles

A number of guiding principles have directed our strawman design.

6.4.1.1 Maximal Use of the FoV

The telescope provides a 20' diameter FoV, we should do everything possible to make use of it, or at least not preclude filling it as technology advances.

6.4.1.2 Simultaneous Multifrequency Coverage

There are a number of motivations:

- For all of the science topics for which LWCam will be used, observations at multiple frequencies are necessary to do any kind of detailed astrophysics: spectral energy distributions are key. In general, fluxes rise quickly with frequency, so the degradation of sensitivity with frequency due to decreasing atmospheric transparency is not necessarily a problem. Certainly, when possible, simultaneous multifrequency observations greatly increase observatory efficiency by obviating multiple observations of the same fields at different frequencies.
- Sky noise removal can be significantly aided by simultaneous observations in multiple bands. The SED of atmospheric emission is well-studied and can likely be very well characterized *in situ*. It should be a very robust function of transparency. The spatial correlation function of atmospheric noise is, on the other hand,

neither as well known (on short length scales < 25 m) nor as stable. Spatial decorrelation of sky noise presents a fundamental obstacle to imaging of large, extended structures. Sky noise removal using both spectral and spatial information will be far more effective than simple techniques using spatial averaging to construct sky templates.

- Observatory efficiency is also improved by a single LWCam because it minimizes the number of instrument switches. In fact, if the short-wavelength and long-wavelength cameras (SWCam and LWCam) can occupy the two Nasmyth foci, then all the continuum science goals of the telescope can be met without instrument changes. Furthermore, maximally efficient use of prevailing weather conditions can be made by having access to all continuum bands at any given time.

6.4.1.3 Use of Antenna-Coupled Bolometric Designs

To obtain large pixel counts (reaching 10^4 for $740\ \mu\text{m}$), feedhorn-coupled bolometric receivers are clearly not feasible. Bare-absorber arrays are one possible choice, but each array can cover only a single wavelength band at a time. (It is possible to use filter wheels to switch between bands using the same focal plane array; the SWCam will use such a design). At longer wavelengths (> 1 mm), bare-absorber arrays present problems from the point of view of precise beam definition and stray light. Antenna-coupled arrays, on the other hand, present the possibility of multifrequency coverage using a single focal plane array and accurate beam definition by the phased array antennae. Antenna-coupled single pixels are in the demonstration stage but it is expected the technology will mature sufficiently quickly to be used in CCAT. It should be noted such designs become substantially more difficult to implement in the SWCam bands because the photon energy exceeds the superconducting gap energy of the niobium used in the antenna structures ($2\Delta \approx 725$ GHz $\approx 410\ \mu\text{m}$), hence the choice of bare absorbers there.

6.4.1.4 Use of a Highly Multiplexable Bolometer Technology

With the pixel counts under consideration, multiplexing as close to the array as possible is necessary, especially for simultaneous multifrequency coverage. Transition-edge sensors (TESs) currently have been coupled to time-domain SQUID multiplexers with a \sqrt{N} multiplex advantage (N^2 pixels read out with $2N$ lines, approximately). Such SQUID multiplexers are currently being implemented for SCUBA-2 (pixel counts of 10^4). Frequency-domain TES multiplexing has also been demonstrated, with multiplexing factors of 8 to 16; larger multiplex factors are expected. Microwave kinetic inductance detectors (MKIDs) promise frequency-domain multiplexing with multiplex factors of as high as 10^3 (N pixels read out by 2 lines). Some aspects of MKID multiplexing have been demonstrated in multiplex ratios of ~ 50 -100, though simultaneous data has to date only been taken on 2 pixels. Power considerations for the room-temperature electronics needed for MKID multiplexing should also enter the discussion.

6.4.1.5 An Optical Train that Provides Minimal Optical Loading

At the longest wavelengths, the telescope itself dominates over the atmosphere in providing optical loading on the detectors. A 5% telescope emissivity criterion is required to ensure maximal use of the high-quality site for wavelengths longer than 1 mm.. This criterion implies that all warm optics must be reflective, and transmissive elements must be implemented at low temperature (4 K, most likely).

6.4.2 Strawman Design

With the above principles in mind, we present the following strawman design. It should be emphasized this design has had significantly less study put into it than the SWCam (because that instrument is the prime motivator for CCAT). Much work is still needed to ensure the design is fully feasible and within budget.

6.4.2.1 Optical Design

A few basic constraints and considerations lead us to a first-pass optical design.

- The F/# at the Nasmyth focus of the telescope is F/8.
- A reasonable F/# at the focal plane is roughly F/2, for two main reasons:
 - Pixel size: at the longer wavelengths, we would like to use $2(F/\#)\lambda$ pixels to obtain high optical efficiency and good control of primary illumination (and hence spillover and beam shape). A

$2(F/\#)\lambda$ pixel at $F/2$ and $\lambda = 2$ mm is 8 mm across. This is a very reasonable size for an antenna-coupled pixel at 2 mm; single pixels of this size have already been produced. The proportional decrease in pixel size at shorter wavelengths can in principle be accommodated; further details are provided in the section on the detector array.

- Focal plane size: the plate scale at $F/2$ is $4''/\text{mm}$, so a 20' FoV requires a 30-cm diameter focal plane. This is a very reasonable size for a focal plane: 16 tiles produced on 4-inch semiconductor wafers would fill this focal plane. The cold optics and windows will be of order the same size, and such elements have already been built for the BICEP CMB polarization receiver.
- The relay optics that reduce the $F/\#$ from $F/8$ to $F/2$ will likely be a pair of ellipsoidal (or possibly aspheric) mirrors:
 - Reflective elements are needed to minimize optical loading.
 - A single ellipsoid produces distortion, but a second ellipsoid, placed in conjugate fashion, can in principle cancel much of this distortion (Serabyn 1996). Use of aspherics may result in even better image quality.
 - It is desired to have an image of the primary just inside the dewar window so a cold stop may be used to terminate the sidelobes of the beam radiated by the phased-antenna array.
- A telecentric design is desired in order to have a flat focal plane. While one can imagine tilting different focal plane tiles to accommodate some focal curvature, it is obviously undesirable.
- Since the mirrors may be warm, the overall length of the system need only be short enough that it can fit at a Nasmyth focus. Distances between optical elements as large as a few meters are acceptable and optical elements as large as 2-3 m may be acceptable, especially if they can be light-weighted.
- All transmissive optical elements – windows, radiation filters, lenses – must be anti-reflection coated so as to be reasonably efficient across the entire wavelength range of $740\ \mu\text{m}$ to 2 mm, with maximal efficiency at the longest wavelengths where undesired reflections or absorption can most affect the system sensitivity. This will be a challenge.

A strawman design that results from these considerations is shown in Figure 6.7. This design is far from optimized, yet has a Strehl ratio of $> 90\%$ across the 20' FoV except at two extreme corners. The field distortion is not satisfactory – 15% at the corners of the FoV, which corresponds to approximately two pixel spacings – but it is hoped this can be reduced significantly in an optimized design. Nevertheless, it is clear a design with reasonably sized optical elements, inter-element spacings, and dewar and filter sizes is within reach.

6.4.3 Focal Plane Detectors

There are two aspects of the focal plane design: how the light is routed from free space to detectors, and what kind of detectors are used. Inextricably linked to the type of detectors are the readout electronics, including multiplexing.

6.4.3.1 Optical Architecture

The first consideration is the architecture for receiving light and routing it to detectors. The obvious technical advance to take advantage of is the development of antenna-coupled focal plane architectures. The most advanced and promising of these efforts is the one underway at Caltech-JPL, led by Bock and Zmuidzinas. A prototype antenna array is shown in Figure 6.8. This design uses an array of slot dipole antennae, each with its own subarray of taps. Details are provided in the figure caption. It suffices to say here the phased array is sensitive to a single polarization for wavelengths ranging from approximately $\sqrt{\epsilon}$ times the tap spacing to the slot length ($\epsilon =$ substrate dielectric constant, $\epsilon = 11.5$ for silicon). The design is fundamentally wide bandwidth and in principle can cover the desired $740\ \mu\text{m}$ to 2 mm frequency range by using slots of length ~ 8 mm with 64 taps each, spaced by $\sim 125\ \mu\text{m}$, with 64 slots across a single 2 mm pixel. Different bands are separated using microstrip bandpass filters placed at the end of the binary summing tree. All $64^2 = 4096$ taps in a single pixel are summed to obtain a $\lambda = 2$ mm band pixel of size $\sim 2 \cdot (F/\#) \cdot \lambda$. For shorter wavelength bands, one would sum only subarrays; for example, at $\lambda = 740\ \mu\text{m}$, one would sum up $8^2 = 64$ taps to obtain a $\sim 0.7 \cdot (F/\#) \cdot \lambda$ pixel. Each $\lambda = 2$ mm pixel of size $2 \cdot (F/\#) \cdot \lambda$ would thus comprise $8^2 = 64$ pixels at $\lambda = 740\ \mu\text{m}$ of size $0.7 \cdot (F/\#) \cdot \lambda$. This use

of the same antenna array to form pixels of different sizes can be termed “multiscale pixellization”. The challenge comes primarily in the routing of all the microstrip from the taps out to the microstrip filters and detectors. While difficult, it is expected that such a design can indeed be implemented.

The actual pixel distribution requires some discussion. Filling the entire 20' FoV with multiscale pixels across the entire wavelength range would require about 140,000 pixels. While this is not unthinkable, it is certainly a challenge for a first-light instrument. It is the shortest wavelength bands of course that drive this pixel count. A natural way to reduce our ambitions for the first version of this camera is to include high-frequency pixels in only the central portion of the array. The FoV would naturally be filled with 16 tiles, of which only the central four would be populated with multiscale pixels covering up to 405 GHz. This provides a 10' × 10' FoV at 740 μm and 865 μm with 16,384 pixels in each band. The remaining 12 tiles would not, however, totally dispense with the high-frequency bands. Instead, the 740 μm and 865 μm bands would use the same pixel size as 1.1 mm, resulting in only 256 pixels in each band in each tile, or an additional 3072 pixels in each of these bands over the entire array. This provides the benefit of multifrequency sky subtraction to the entire FoV, yet maintains a reasonable detector count: this scheme yields 45,056 detectors summed over all bands. This design may also be sensible if 740 μm optical quality cannot be obtained in the outer parts of the focal plane due to optical aberrations. The pixel count is summarized in Table 6.2. Future, more ambitious upgrades are listed in Table 6.4.

| Observing Band GHz (μm) | Bandwidth (GHz) | Pixel Size (F/#) λ | Number of Spatial Pixels |
|----------------------------|--------------------|-----------------------|---|
| 150 (2000) | 30 | 2.3 | 16 tiles × 64 = 1024 |
| 220 (1400) | 40 | 3.2 | 16 tiles × 64 = 1024 |
| 275 (1100) | 50 | 2.1 | 16 tiles × 256 = 4096 |
| 350 (870) | 40 | 0.7 2.8 | 4 tiles × 4096 = 16384 12 tiles × 256 = 3072 |
| 405 (740) | 30 | 0.8 3.2 | 4 tiles × 4096 = 16384 12 tiles × 256 = 3072 |
| Total | | | 45,056 detectors |

Prospective band parameters, pixel sizes, and pixel counts for first-light LWCam. The focal plane is composed of 16 tiles. At the shortest wavelengths, the central 4 tiles use the full multiscale design to obtain pixels that are only slightly larger than the $0.5 \cdot (F/\#) \cdot \lambda$ Nyquist-sampling criterion. The remaining 12 tiles use the $\lambda = 1.1$ mm pixels at 740 μm and 850 μm. This provides a full-resolution 10' × 10' FoV at shorter wavelengths and a 20' × 20' FoV at longer wavelengths.

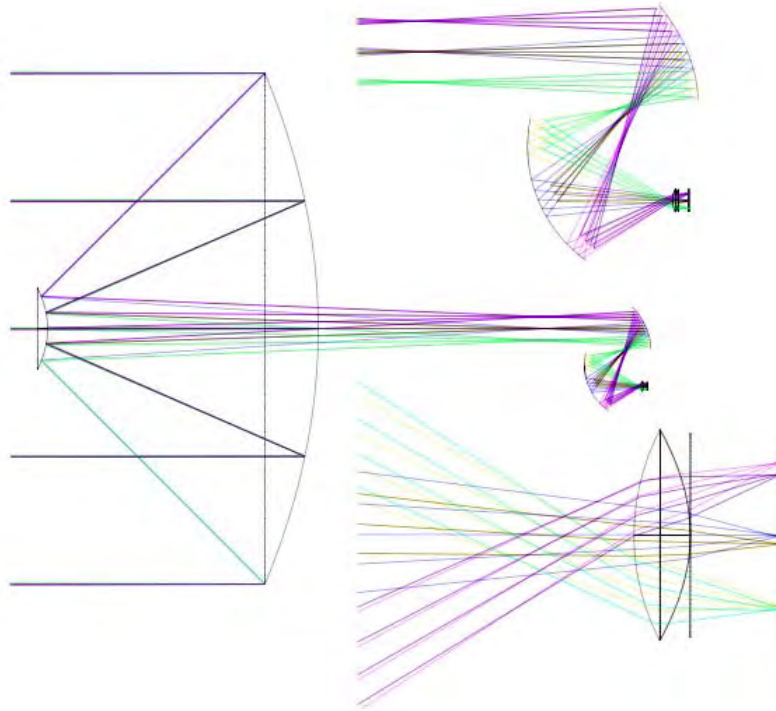


Figure 6.7. Strawman optical design for LWCam. (M3 flip mirror has been removed for simplicity.) The distance from Cassegrain focus to first ellipsoid is 5 m, the distance from the first ellipsoid to the second is 4 m, and from the second ellipsoid to the dewar window is 2 m. The first ellipsoid is 2 m in size, the second is 3 m. The fold angle at each ellipsoidal mirror is 45 degrees. $F/\#$ is reduced from 8 to 3 by the first mirror, largely unaffected by the second mirror, and reduced to $F/2$ by the cold lens. The focal plane, cold lens, and primary image (location of cold Lyot stop) are 30 cm, 45 cm, and 20 cm, respectively. The distances between focal plane and lens midline and lens midline and cold stop are 25 cm and 20 cm, respectively. The warm optics fit inside a 4 m x 5 m x 3 m box, and the dewar itself need only be approximately 1 m in length. The cold lens as drawn is high-density polyethylene (for which Teflon anti-reflection coatings have been made); a silicon lens would be much thinner (but more difficult to AR coat).

The antenna-coupled architecture has seen a first demonstration in the lab; beam maps at 110 GHz are shown in Figure 6.9. The beam shape meets expectations. The expected bandwidth has been confirmed. The antennae have reasonable cross-polarization, $\sim 1\%$.

The microstrip filters that define observing bands have seen initial implementation in concert with the antenna architecture. The Caltech-JPL group will soon be producing a small 16-pixel array of 4-color pixels – bands at 220, 270, 350, and 420 GHz – using filters of this kind.

A collaboration led by Jason Glenn of University of Colorado and including the Caltech-JPL group is proposing to build a prototype multicolor camera for the CSO using these bands. This first prototype uses the same pixel size at all frequencies – there is no subdivision of pixels in a frequency-dependent fashion – and so will suffer somewhat from imperfect matching of pixels size to $(f/\#)\cdot\lambda$ at the longest and shortest wavelengths. Wide-bandwidth optics will be developed as part of this effort (covering the entire 740 μm to 2 mm range desired for the CCAT camera). Work will continue in parallel to develop the multiscale pixels needed to cover the large bandwidth range desired for CCAT.



Figure 6.8. Antenna-coupled focal plane architecture prototype device. The vertical lines are slots in a niobium ground plane. Incident light with its electric field perpendicular to the slots will be absorbed. The pie slice shaped structures are connected to microstrip taps that cross over the slot; the absorbed power is directed into these taps. The power from all the taps is summed using a binary tree microstrip structure and the line is terminated with a lossy load at a power detector. The maximum wavelength to which the array is sensitive is set by the slot length and the minimum wavelength by the tap spacing along the slots and the interslot horizontal spacing. This prototype antenna used only 16 taps per slot, 16 slots, tap spacing $620\ \mu\text{m}$, and slot length $9920\ \mu\text{m}$, resulting in a band covering only 75-120 GHz; much larger bandwidths are possible by reducing the tap spacing (and size). The beam pattern is defined by the coherent addition of the dipole slots given the tap placement and results in a beam with a ~ 20 degree FWHM (F/2.8) at 110 GHz and first sidelobes of magnitude -13 dB at 25 deg. Beam maps are shown in Figure 10. (Figure provided by R. LeDuc (JPL).)

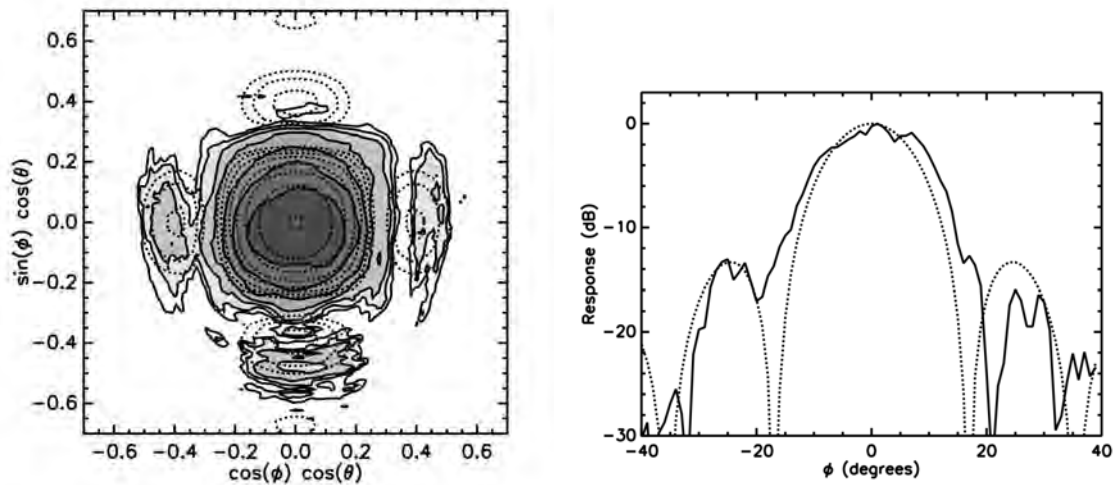


Figure 6.9. Measured beam profile of antenna-coupled pixel of the architecture shown in Figure 8. The profile was measured at 110 GHz using a coherent source and coupling the output of the antenna array to a SIS mixer. In both plots, the dashed lines indicated the expected pattern. The missing upper sidelobe in the 2D map is due to limitations in travel during beammapping; the lobe is not truly missing. Similar measurements have been undertaken using a broadband thermal source and with an antenna array coupled to a TES detectors via a microstrip filter and are consistent.

6.4.3.2 Detectors

The best candidates for the detectors placed at the ends of the microstrip are superconducting transition-edge sensors (TESs) or microwave kinetic inductance detectors (MKIDs). The advantages and disadvantages of the two detector types are as follows:

- **Sensitivity. Advantage: TESs, but only slightly.** TES detectors operating at 300 mK already provide sufficiently good NEP to be background limited on CCAT, even with ambitious loading goals of 10 K sky + 10 K telescope at $\lambda = 2$ mm. MKIDs currently have NEPs that would be background limited in the shorter wavelength bands, but probably not longward of 1 mm. This current noise performance is far from

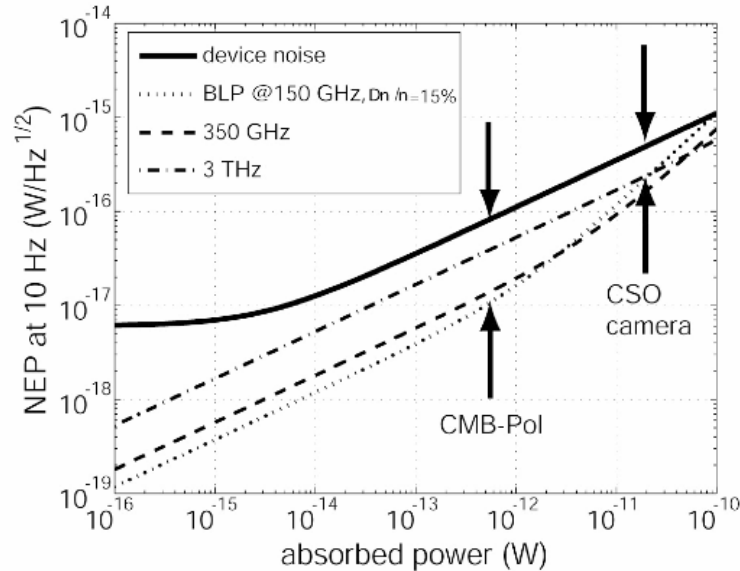


Figure 6.10: MKID sensitivity vs. optical loading power. The solid line is based on currently achieved device performance. The various dashed lines indicated background-limited sensitivities as a function of optical loading for three different frequencies: 150 GHz, 350 GHz, and 3 THz. The sensitivity at CSO optical loadings is within a factor of 2 of the background limit. CCAT optical loadings will be factors of 1 to a few lower; the sensitivity remains within a factor of a few of the background limit. (Figure provided by P. Day (JPL).)

fundamental limits ($\text{NEP} \sim 10^{-20} \text{ W}/\sqrt{\text{Hz}}$). MKID development is progressing quickly and will likely reach the necessary sensitivities on the timescale that the LWCam would be built.

- **Degradation under optical loading. Advantage: MKIDs, but only slightly.** TESs degrade less gracefully under optical loading because, above a certain optical power, the device is pushed into its normal state and is blind. One must build in a “safety factor” in optical loading to prevent this from happening. A pair of series TESs, one with higher T_c , can, in principle, solve this limitation. MKID sensitivity degrades more gracefully, simply due to the approximately linear increase in quiescent quasiparticle density with optical power (Figure 6.10). But a safety factor of 5 in a TES is probably sufficient; if the loading is more than 5 times worse than expectations, then the loss of sensitivity is probably so great that one is in trouble even if the detectors are not blind.
- **Fabrication. Advantage: MKIDS.** Both TESs and MKIDs are simple films of superconductor, though TESs are frequently made in bilayers to tune the transition temperature T_c . T_c reproducibility is the main challenge with TESs, especially when they are incorporated into complex arrays and thus suffer many later processing steps. MKIDs are much less sensitive to variations in T_c because they operate at $T \ll T_c$. MKID-based designs also require fewer photolithographic mask layers and hence fewer processing steps. But current MKID designs do seem to show significant noise dependence on the quality of the edges in the coplanar waveguide structure and on the presence of two-level defect impurity systems in the dielectric. These problems may be mitigated by alternative architectures, but could prove a significant fabrication

challenge. We also note that the fabrication of the SQUID arrays used for TES multiplexing is a complex process itself.

- **Multiplexing. Advantage: MKIDs.** There exist demonstrated time-domain and frequency-domain multiplexing schemes for TESs. The multiplexing advantages demonstrated to date are 32×40 pixels \Rightarrow 64 lines for time-domain and multiplex factors of 8 for frequency-domain. The time-domain scheme is rather complex, requiring two stages of SQUID amplifiers, one first-stage SQUID for each array pixel, active (though multiplexed) flux feedback to the first-stage SQUIDs, and FPGA-based room-temperature electronics to control the addressing and feedback to the SQUIDs. The routing of the lines between the array and the first-stage SQUIDs and between the first and second stage SQUIDs is challenging; the former provides no multiplexing advantage and will almost certainly require a custom first-stage SQUID chip that is hybridized with the focal plane array. The frequency-domain scheme requires only a single SQUID array to read out N pixels ($N = 8$ has been demonstrated), but each pixel must have a custom LC filter placed in-line to isolate its IF band from that of the other pixels. MKIDs, on the other hand, are very easily frequency-multiplexed. A MKID in a notch resonator structure (whose resonant frequency is set by the length of the MKID) is inherently narrowband. A set of MKIDs can be attached to a single feed line without interacting with each other. Room temperature electronics can be used to construct a frequency comb to bias the resonators; that bias is sent down the single feed line. A HEMT at the output of the feedline amplifies the transmitted signal, which can then be frequency-demultiplexed at room temperature. Emergent software-defined radio techniques promise to make bias generation and demultiplexing almost entirely digital and buildable using commercial electronics. A multiplex advantage of 10^3 is entirely feasible.
- **Cold electronics power dissipation: Advantage: TESs.** In the time-domain SQUID multiplexing scheme, the first-stage single-SQUID chips dissipate about 2 nW per detector pixel. Using ^3He closed-cycle refrigeration, this becomes challenging at the 10,000 pixel level, but Kent Irwin (NIST) has indicated first-stage SQUID power dissipation could be reduced significantly (especially because large detector response bandwidth is not necessary for bolometric cameras). The SQUID arrays that reside at 4 K dissipate about 1 μW each, but only one array is needed per “column” in this multiplexing scheme, currently 40 pixels. Even at 40,000 pixels, one only dissipates 1 mW at 4 K, which is quite reasonable. In the frequency-domain scheme, no first-stage SQUIDs are used, and the SQUID arrays again sit at 4 K. The multiplex factor may be somewhat lower ($N = 8$ has been demonstrated), but the 4 K load remains small. MKID readout power dissipation is significantly larger because of the use of HEMTs. These reside at 4 K and dissipate 10-20 mW each there. The power dissipation could thus approach 1 W for a 50,000 pixel array. However, Sandy Weinreb (JPL) indicates that HEMTs with sufficiently good noise temperatures could be obtained at 10 to 100 times smaller power dissipation, reducing the heat load to a level that is small compared to quiescent loads on 4 K.
- **Microphonic Susceptibility: Advantage: MKIDs.** Because cryocoolers are the baseline for all CCAT instruments, sensitivity to vibrations is an important consideration. MKIDs offer an important advantage here: because they are non-thermal detectors, they are rather insensitive to thermal fluctuations in the refrigerator base temperature stage. The gap energy in aluminum, for example, corresponds to 4 K. Vibrations reaching the base temperature stage must be made much less than this typical energy in order for the refrigeration itself to function, so it is very unlikely that vibrations will be so large as to break Cooper pairs. It should be noted the operation of TES bolometers with cryocoolers has been demonstrated, in particular for APEX-SZ and SCUBA-2. It is certainly possible to implement TESs on a cryocooler platform; it just requires additional engineering care.

Antenna-coupled TES and MKID receivers are being prototyped by the Caltech-JPL group: proposals have been submitted for SPIDER, a balloon-borne CMB polarization receiver that will use dual-polarization, single-color focal planes in bands from 40 GHz to 275 GHz and for a MKID-based multicolor camera for the CSO as described above. These projects, if successful, will leave only two specific technology challenges for CCAT: multiscale antenna-coupled pixel design and very wide-bandwidth optics. This is an acceptable level of technical risk.

6.5 Polarimetry

Measurement of linear polarization in the submillimeter allows the study of magnetic fields in interstellar clouds and active galactic nuclei. A common characteristic of successful polarimeters operating at (sub)millimeter wavelengths in the presence of the bright and variable atmosphere is their ability to reject unpolarized emission on short timescales (>1 Hz). This has been done with chopping secondary mirrors (SCUBA – Greaves et al. 2003, MNRAS, 340, 353), simultaneous dual-polarization imaging of the field of view (Boomerang – Masi et al. 2005, astro-ph/0507509; QUAD – Church et al. 2003, NewAR, 47, 1083; BICEP – Keating et al. 2003, SPIE 4843, 284; SHARP – Novak et al. 2004, SPIE, 5498, 278), both of those techniques (Hertz – Dowell et al. 1998, ApJ, 504, 588), and rapid polarization modulation (POLKA – Siringo et al. 2004, A&A, 422, 751).

For first-light CCAT polarimetry, we will adopt the rapid polarization modulation approach due to its cost effectiveness and the expected $\ll 1\%$ instrumental polarization of the telescope, despite the $\sqrt{2}$ sensitivity penalty compared to dual-polarization imaging. The baseline plan will be a constantly rotating quartz half-wave plate – which can be warm without significant noise penalty – followed by a wire polarizer at the window of SWCam and LWCam. The newer Martin-Puplett polarization modulation concept (Chuss et al. 2004, SPIE, 5492, 1487) is another option for implementation in reflective relay optics.

More options are available for second-generation CCAT polarimetry. Some promising detector architectures have dual-polarization sensing, and polarization-splitting foreoptics could be built to feed multi-array cameras. Both of these approaches will recover the full polarization sensitivity available with CCAT.

6.6 Data Taking Strategies and Sky Noise Removal

Following the introduction of ~ 100 pixel (sub)millimeter detector arrays on existing telescopes and the development of readout electronics with low $1/f$ noise, the traditional submillimeter observing technique of chopping and nodding is being replaced with pure scanning techniques. For both wide field $350\ \mu\text{m}$ mapping and detection of faint, compact sources with CSO/SHARCII, it has proven sufficient to scan the telescope without chopping the secondary mirror, and fundamental $(\text{time})^{-1/2}$ noise limits are sustained over integrations of several hours on compact sources (Marsh et al. 2005, ApJ, 620, L47; Kovacs et al. 2006, in prep.). This technique requires a detection system free of $1/f$ noise on timescales as long as the scan modulation frequency (10-30 seconds at CSO), a dynamic range of ~ 1000 in that period to detect fundamental photon noise in the presence of a variable atmosphere, and an inversion algorithm to separate the source and background emission based on their different time signatures during the scan.

Two scan strategies are used with CSO/SHARC II, both having the following desirable attributes:

- even coverage of a chosen rectangular map
- multiple crossings of scan trajectories within the map
- minimized accelerations at map edges

Compact sources (< 1 arcminute) are mapped using a Lissajous pattern (sinusoidal motion in azimuth and elevation with non-commensurate periods; Figure 6.11) with a scan envelope comparable to the size of the detector array. This strategy is appropriate for mapping of specific point sources such as debris disks and galaxies at 20-100 Mpc. Large fields are mapped with a “billiards scan” (Figure 6.11 (right) in which the telescope “bounces” off the walls of a virtual rectangular boundary. Accelerations at the boundaries are minimized by curving the trajectory.

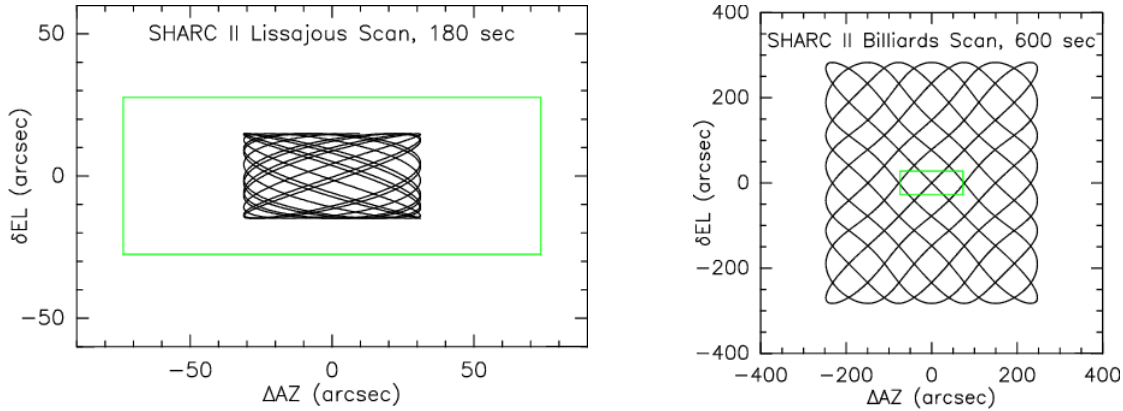


Figure 6.11. Telescope scan patterns used successfully with CSO/SHARC II. In both figures, the size of the rectangular detector array is shown in green, and the trajectory of the center of the array is shown in black. The Lissajous scan (left) is used for detection of compact sources and the billiards scan (right) is used for wide-field mapping. (The low-order approximation to triangle-wave motion during the billiards scan that softens the edge reflections also results in a slightly wavy trajectory.)

It is demonstrated with CSO/SHARC II that, at $350\ \mu\text{m}$, scan rates under 1 arcmin/sec and accelerations under 1 arcmin/sec² are sufficient for a majority of mapping experiments undertaken to date. It should be noted, however, background-limited performance has been obtained only on length scales of up to about 1 arcmin. On larger length scales, it is difficult to obtain sufficient coverage of the map area over a short enough time to separate sky noise and astronomical structure. Background-limited performance on 1 arcmin length scales at scan speeds of 0.5 arcmin/sec implies that residual 1/f sky noise begins to appear at timescales of 2 seconds and longer. This is confirmed qualitatively by PSDs of bolometer timestream differences.

Despite the different 1.1 mm and 2.1 mm observing wavelengths of CSO/Bolocam, residual sky noise is also seen on > 2 second timescales. In the context of the frozen-screen model of sky noise, we can associate that timescale with an angular scale. For a typical atmospheric drift rate¹ of 30 arcmin/sec, the residual sky noise appears on scales of > 1 degree. For both CSO/SHARC II and CSO/Bolocam, the scan rates are well below the atmospheric drift rate, which is confirmed by CSO/Bolocam scanning experiments at rates up to 4 arcmin/sec.

To obtain scan speed criteria for CCAT, we conservatively assume the residual sky noise will be seen on the same $t > 2$ sec timescales as seen at the CSO. To measure a spatial scale L with background-limited sensitivity, we need to scan the telescope at a rate $> L/t$. Science programs requiring the recovery of very extended emission push the limits of CCAT scanning, but we can put an upper limit on the scan rate by noting that there is no sensitivity benefit to scanning faster than the atmospheric drift rate of 30 arcmin/sec, at which one has hope of recovering $L = 1$ degree scales. A scan speed goal of 30 arcmin/sec is quite challenging. We instead set an *ad hoc* requirement of recovering $L = 20$ arcmin scales corresponding to the CCAT field of view, requiring a 10 arcmin/sec scan rate, leaving 30 arcmin/sec as a goal. For acceleration, we make the requirement that scanning be 50% efficient on a field of size L , which requires 2 sec turnarounds, or an acceleration requirement of 10 arcmin/sec² and a goal of 30 arcmin/sec².

6.7 Existing Instruments for CCAT

Budget and schedule will necessarily limit the first light instrumentation to the two cameras described above. These cameras will deliver most of the fundamental science goals of the Project. It is clear, however, that the science can be enhanced through the addition of other capabilities such as submillimeter spectroscopy both with direct detection and heterodyne receivers. Members of the consortium have constructed a wide variety of such instrumentation for both the JCMT and CSO telescopes. These instruments continue to evolve and be replaced by

¹ At the scale height of the water vapor of 1 km, the typical wind speed is 10 m/s, corresponding to about 30 arcmin/sec.

better instruments as technological improvements are attained. For modest resolving powers, direct detection spectrometers are the instruments of choice since they can have very large instantaneous bandwidths and operate near the photon noise limit. As a snap-shot of current technology, we outline two direct detection spectrometers below.

6.7.1 ZEUS

The redshift (z) and Early Universe Spectrometer (ZEUS) is a long slit echelle grating spectrometer designed for use in the 350, 450, and 610 μm telluric windows on large submillimeter telescopes (Figure 12, Nikola et al. 2003 SPIE 4855, 88, Stacey et al. SPIE 5498, 232). At present ZEUS has a 1×32 pixel thermistor sensed bolometer array held at ~ 250 mK with a dual stage ^3He refrigerator. This array yields an instantaneous spectrum of 32 spectral elements for a single beam on the sky. In the future, the ZEUS array will be enlarged to facilitate multibeam imaging. The largest format array ZEUS can accept is $\sim 12 \times 64$ pixels which will yield a 64 element spectrum typically covering a total bandwidth of 6.4 % at 12 positions on the sky. The long slit configuration is very useful for resolved galaxies. In the future, we anticipate construction of a “fiber optics” system that would enable multiple sources distributed in the focal plane to be brought into a line on the spectrometer entrance slit. In this way, ZEUS could be modified to become a multi-object (6 independent beams) spectrometer.

ZEUS is an R2 echelle (blaze angle 63.43°) with a blaze wavelength of 359 μm in 5th order (groove spacing 992 μm). ZEUS can access all of the submillimeter windows by tuning to different orders of the echelle, as selected by bandpass filters (Table 6.3). The resolving power is typically ~ 1000 and with a 64 element, $f\lambda$ pixel size array.

| Echelle Order | Blaze λ (μm) | Spectral Range (μm) | Resolving Power |
|----------------------|--|--|------------------------|
| 9 | 199.4 | 185 - 211 | 1280 – 2700 |
| 8 | 224.4 | 208 - 237 | 1140 – 2400 |
| 6 | 299.2 | 278 - 316 | 850 – 1800 |
| 5 | 359.0 | 333 - 379 | 710 – 1500 |
| 4 | 448.8 | 416 - 474 | 570 – 1200 |
| 3 | 598.3 | 555 - 632 | 430 – 900 |
| 2 | 897.5 | 832 - 948 | 285 – 600 |

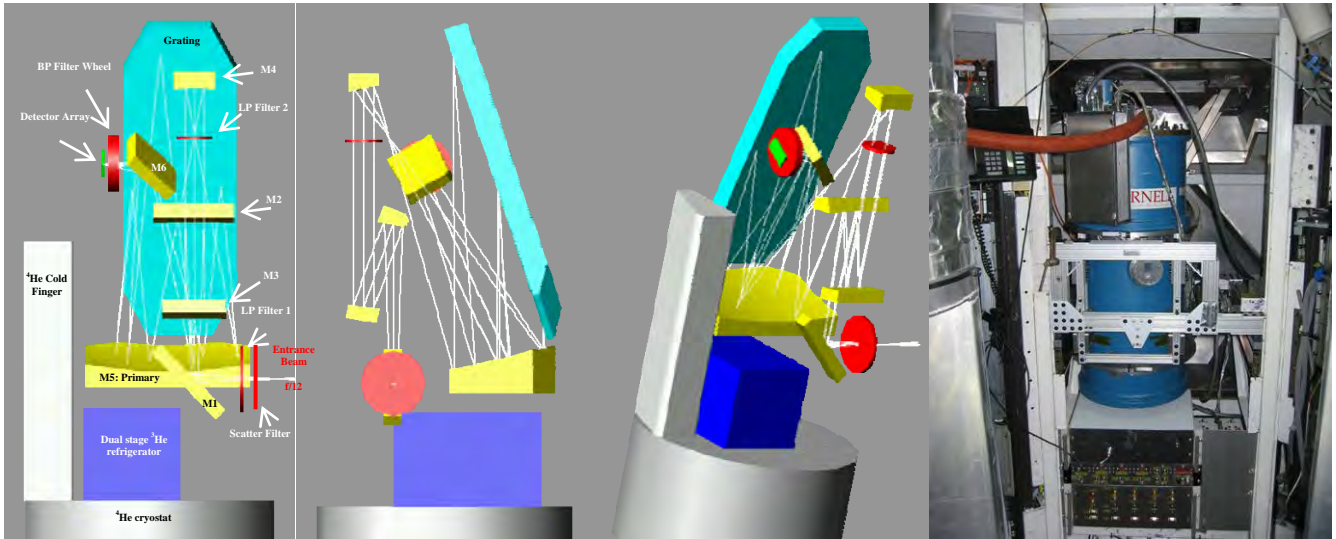


Figure 6.12. Three views of the optical layout for ZEUS (left). ZEUS mounted on the JCMT (right).

6.7.2 Z-SPEC

As an alternative to conventional long-slit grating instruments, a new architecture was recently developed that uses curved grating inside parallel plate waveguide to provide nearly an octave of instantaneous bandwidth in a small size. The Waveguide Far-IR Spectrograph (WaFIRS) concept is shown in Figure 6.13, along with the millimeter-wave version, Z-Spec, recently commissioned at the CSO. In this concept, light from a single spatial mode propagates through the waveguide region to the curved grating which both focuses and diffracts the light to an array of detectors. As with any grating spectrometer, the size of a CCAT WaFIRS instrument will be driven by the $R \cdot \lambda$ required grating size. WaFIRS is, however, much smaller than comparable conventional designs because the propagation is confined to a 2-D planar waveguide and there are no additional focusing or collimating optics. Thus the size of the resulting instrument is not much larger than the required $R \cdot \lambda$.

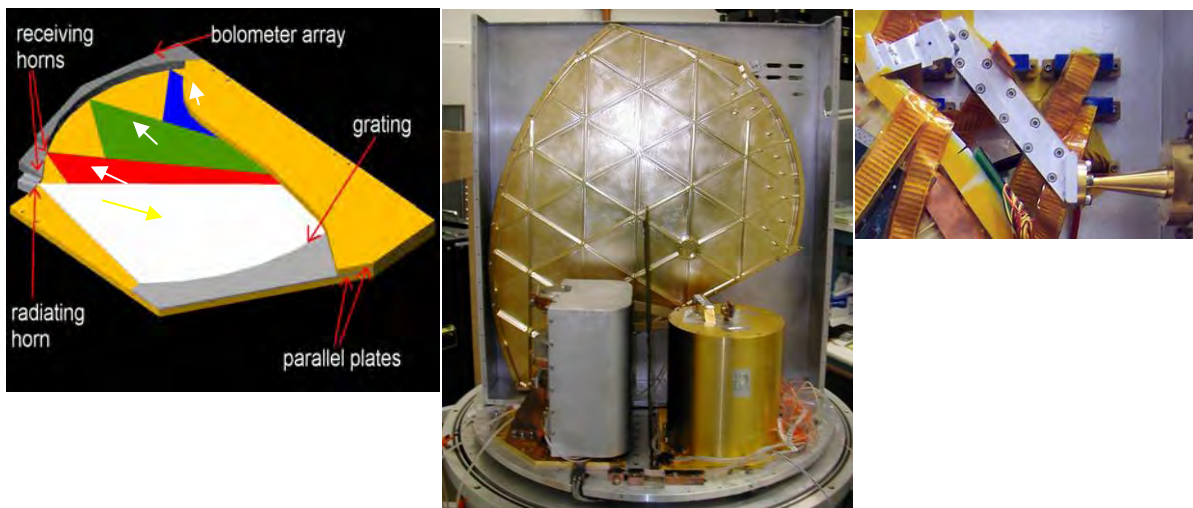


Figure 6.13 WaFIRS Spectrometer architecture (LEFT), with Z-Spec instrument (center, right) based on this principle. Z-Spec provides instantaneous coverage from 190 to 310 GHz at moderate resolving power (250-400) and is used for spectral surveys in this band (Bradford et al. 2004, SPIE 5498, 257).

Each WaFIRS module provides an instantaneous bandwidth of at least 1:1.7 for a single beam on the sky. The 2-D geometry, however, lends itself to stacking multiple modules in a single instrument. Scaling from Z-Spec, it is possible to stack a few modules which provide $R\cdot\lambda$ of 500 mm in a 1 meter cryostat. These modules can multiplex in frequency band on the same source through use of dichroic filters. This approach offers the potential to provide simultaneous spectral coverage across all CCATs atmospheric windows for a single galaxy. Alternatively, multiple modules could be stacked to provide the same spectral coverage on multiple sky positions.

6.7.3 Heterodyne Receivers

Heterodyne receivers currently on the CSO enable access to all of the submillimeter windows (except 200 μm). These receivers have excellent sensitivity – typically within a factor of 5 of the quantum limit. These are the receivers of choice for high resolution spectroscopy, such as is required for detailed investigations of Galactic star formation regions. Very sensitive HEB terahertz devices exist and have been used in receivers at the South Pole and at Atacama sites with good success. The receivers are compact and easily transportable to the CCAT facility. Near future developments promise multi-pixel arrays at all frequencies.

6.8 Future Instruments for CCAT

There are significant upgrade paths for both the SWCam and LWCam instruments outlined above. In addition, we plan significant new instrumentation to exploit the niches available to the CCAT, including a 40 μm camera and large format direct detection spectrometers.

6.8.1 SWCam

The SWCam design is constrained by image quality concerns to be an on-axis transmissive optics system. The lens system is feasible and has good transmission at its current dimensions. However, to image the entire 20' field of view of the telescope would require unrealistically large and thick lenses (~ 1.7 meter aperture) that would have unacceptable losses due to bulk absorption. The entire field of view can be imaged into a single cryostat with off-axis parabolic mirrors. However, these mirrors need to be quite large (4 m class) to deliver good image quality, and the cryostat itself would be of the order 8 m in size. A far simpler upgrade path is to make several copies of the proposed SWCam including the fore-optics. These multiple cameras can be nestled in a close – packed configuration to give good coverage of the 20' FoV (Figure 6.14). The total coverage of the 4 cameras would be 102 square arcmin, or 1/3 of the total area in the 20" diameter FoV.

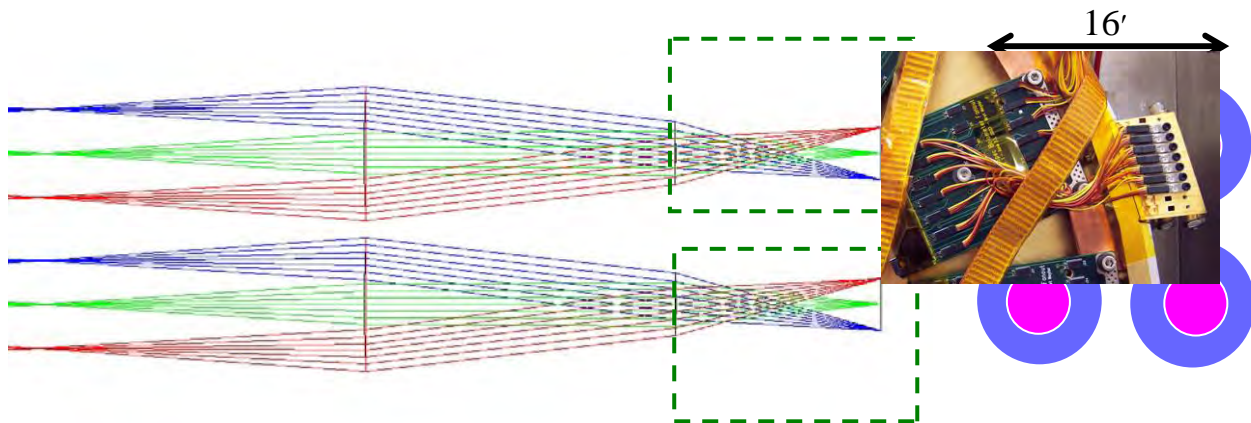


Figure 6.14. Four identical SWCam and fore-optics systems can deliver good field coverage for CCAT. The total field covered would be ~ 102 square arcmin.

6.8.2 LWCam

Various upgrade paths would allow full coverage of the focal plane at shorter wavelengths and extend coverage to 620 μm :

- Cover entire FoV with \sim Nyquist-sampled pixels at 740 and 865 μm , resulting in a total of 137,216 pixels.
- In addition, cover the entire FoV with \sim Nyquist-sampled pixels at 620 μm , adding 262,144 pixels *in addition to* the 137,216 pixels in the first upgrade.

It is not yet clear whether these upgrades are scientifically well motivated. It is also not clear whether it is possible to design a relay optics system that will provide sufficient image quality at the edges of the field of view at the shortest wavelengths. It may turn out it is possible to do so, but only by increasing the size of the optics unreasonably. We neglect the optics upgrade in this discussion.

- **Focal plane arrays:** The upgrade to \sim Nyquist-sampled coverage over the entire FoV at 740 μm and 865 μm would only require fabrication of additional arrays of existing designs; the process will have already been developed to provide the \sim Nyquist-sampled innermost tiles. The upgrade to \sim Nyquist-sampled coverage of the FoV at 620 μm requires both development of a 620 μm band and fabrication a full set of 16 new tiles incorporating the 620 μm band, a much larger investment.
- **Cold Readout Electronics:**
 - **TES:** Upgrading to \sim Nyquist-sampling over the entire array will simply make use of the SQUID array design used for the inner four tiles for the entire array. We should only incur fabrication costs. Upgrading to use 620 μm pixels will be a much greater challenge. The number of pixels per tile would increase by about a factor of 4, which may run into fundamental limitations in SQUID packing density.
 - **MKID:** Scaleups as described would require approximately 140 and 400 HEMTs, respectively. These pose a challenge primarily because of the HEMT heat load at 4K. This is probably a surmountable problem with the use of very low power-dissipation HEMTs and addition of cooling power at 4K.
- **Warm Readout Electronics**
 - **TES:** The number of digital feedback channels for the two scaleups would be \sim 4500 or \sim 12500 (total) for the future upgrades. The scale-ups will likely require some significant architecture change that greatly increases the number of detectors per feedback circuit. This would feed back to the cold electronics, requiring an increase in the number of first-stage SQUIDs connected to a single second-stage array.
 - **MKID:** Since the challenge is almost entirely computational – generation of the frequency comb and digitization and de-multiplexing – it is likely that this problem will become tenable over the next decade. One will still require one block up-converter and down-converter per HEMT, but that is a relatively small part of the warm electronics.

It appears that a MKID-based focal plane is more easily scaleable, another argument in its favor.

| Observing Band GHz (μm) | Pixel Size (F/#) λ | Number of Spatial Pixels |
|---|---|---|
| 350 (870) | 1.4 (inner tiles 0.7) 0.7 | 28672 (16384 + 12288) 65536 |
| 400 (740) | 1.6 (inner tiles 0.8) 0.8 | 28672 (16384 + 12288) 65536 |
| 490 (620) | 2.0 (inner tiles 0.5) 1.0 (inner tiles 0.5) 0.5 | 77824 (65536 + 12288) 114688 (65536 + 49152) 262144 |

Future expansion/upgrade options for LWCam. A modest upgrade option would be to reduce the size of the high-frequency pixels in the outermost 12 tiles from ~ 3 (F/#) λ to ~ 1.5 (F/#) λ . This is shown as the first sub-row of each row. A more ambitious upgrade would be to reduce the pixel size to ~ 0.7 (F/#) λ across the entire focal plane, which is shown as the second row of each sub-row. Finally, one could consider adding a 620 μm band; pixel counts for various options are provided. This is the most ambitious and least well-motivated upgrade option, as 620 μm will be provided by SWCam, but we list it for completeness.

6.8.3 Far-IR Camera

Some of the panel technologies that have been discussed for CCAT would likely support some modes of infrared observing. Infrared guiding may be used to achieve maintenance of the telescope tracking at the required level, which will also require the telescope primary to maintain an infrared specular surface. If this is the case, the large aperture and high, dry site of CCAT offer unique scientific opportunities for high spatial resolution imaging in the IR. The system wavefront error budget of 12 μm rms will not support diffraction limited imaging short of ~ 200 μm with the full pupil. On the individual panel scale and smaller, however, the wavefront error is significantly diminished. A sparse aperture imaging mode, similar to the non-redundant aperture masking technique used on the Keck 10 m telescope (Tuthill et. al.) requires only that the overall telescope phasing is to within the coherence length of the light, not to a small fraction of a wavelength. For example, if the panels meet a 5 μm RMS specification, then subapertures of the size of a panel each are $\lambda/8$ rms at 40 μm . Two panels separated by the diameter of the telescope would then form a long baseline interferometer achieving a resolution of 0.4". A Fizeau beam combination of many such subapertures spread over the disk in a non-redundant pattern enables interferometric image reconstruction with the full resolution of a 25m telescope over a narrow field of view. Such a capability would be uniquely complementary for high spatial resolution follow-up to the current and future capabilities of space based instruments such as Spitzer and JWST. This is further a unique niche in terms of ground based capabilities as the currently planned large aperture optical/IR telescopes (e.g. TMT, GMT, GSMT) are unlikely to be placed at a site with as low PWV as CCAT, and therefore will not be capable of observations at the longer IR wavelengths. Long baseline interferometers such as the Keck Interferometer and VLTI suffer a large sensitivity penalty due to high emissivity and low throughput and lack dense Fourier coverage for imaging complex objects. This niche is therefore likely to be unique to CCAT and provide unique scientific opportunities for high resolution imaging in the IR of galaxies, AGN, star formation and debris disks.

6.8.4 Future Spectrometers

The next generation spectrometers would likely include improved versions of both the ZEUS and Z-Spec spectrometers outlined above. An improved echelle would have larger collimating optics and a larger echelle grating to provide a wider field of view (longer slit). An improved waveguide spectrometer would offer $R \sim 1000$ for the submillimeter bands and could be a multiple beam version (created by cloning the instrument), or a version that covers multiple bands (dichroic mirrors feeding differing wavelength version of the instrument). One could also envision large field of view imaging Fabry-Perot spectrometers (heritage of the SPIFI instrument, Bradford et al. 2002 Applied Optics 41, 2561) for imaging large targets in a single line, or image slicing grating spectrometers

for deep imaging of small, but resolved targets. More detailed discussions of these concepts are available on the CCAT Website.

6.9 Lab Facilities

For instrument installation, commissioning, and maintenance, labs will be needed both at the telescope and at the base facility in Chile. As part of observatory construction, these labs will be furnished with standard furniture and equipment but specialized lab equipment is considered part of the instrument. Labs will also be necessary at the partner institutions for instrument construction, but these are not considered here.

6.9.1 Telescope Facility

The architectural concept for the telescope facility includes a 50 m² instrument lab adjacent to the telescope. This allows enough space for work on one major instrument at a time. Beyond standard amenities, the lab will have oxygen enriched air, easy access to a loading dock, and access to a lift or crane for installing instruments on the telescope.

6.9.2 Base Facility

A similar lab is included in the concept for the support facility near San Pedro. This allows checkout of instruments after receipt and prior to installation the telescope.

7 CCAT Concept Design Overview

7.1 Introduction

This section provides an overview of the current concept design for the CCAT. The concept has evolved over the duration of the Project to date. In some cases design approaches were decided after trade analysis and in other cases designs were chosen to build on recent prior radio or optical telescope development activities. In some cases requirements were established by the Project and provided to contractors who were responsible to develop designs in response to them. In others, the Project has developed concepts and turned to contractors and people within the Project consortium to supply approaches for supporting components and subsystems. The objective has been to develop systems that are comfortably within the state-of-the-art with respect to technical risk, offer robust solutions to requirements, and are efficient both with respect to design and cost.

7.2 Background

The Feasibility/Concept Design Study phase of CCAT was constituted to provide initial definition of requirements, design, and potential for CCAT to be constructed within acceptable cost and risk envelopes. Additional development and analyses of design approaches to the telescope will be performed during the Engineering Concept Design phase to follow.

7.2.1 Overview

To fulfill the radiometric requirements, the basic design is a Ritchey Chretien telescope on an azimuth elevation mount with $f/8$ Nasmyth foci for instruments. The primary mirror has a 25 m diameter with a 0.6 focal ratio. The telescope will be capable of operating at wavelengths as short as 200 μm . A major goal of the observatory is to take advantage of the unique, low water vapor observing conditions prevalent at high altitude sites in the Atacama region of Northern Chile. The optical design is discussed by German Cortes in Section 8.

To achieve the wavefront error and other requirements, the telescope may employ “active optics” so pointing, tracking, and image quality are maintained. These active optics may include the primary, secondary, or tertiary mirrors.

7.3 Major Telescope Systems

This section provides a uniform overview of the current CCAT concept.

7.3.1 Site

A number of peaks in the Atacama region are under consideration. Over the past several years Cornell and other groups made measurements of atmospheric transparency and weather at some of these. Factors involved in site selection include observing conditions, site logistics and infrastructure, proximity to ALMA and other telescopes, permission to build, topography, and soil load bearing conditions. A final site selection will be made before mid 2007. Detailed information is presented in Section 10.

7.3.2 Facility

Two facilities are required for CCAT, the mountain top telescope facility and a support facility at lower altitude and nearer to San Pedro de Atacama.

7.3.2.1 CCAT Telescope Facility

Requirements for the Telescope Facility were developed iteratively by working with the Science, Instrument, and Operations Committees. This process involved making broad decisions regarding the minimum facility that would provide adequate and efficient support to observing, telescope and instrument maintenance and repair, and personnel. The likely high cost of construction at the planned altitude mandates a smaller facility. The experience being accumulated by APEX and ASTE, which operate with minimal mountain facilities, will have an important impact on our final decisions. At the same time, it was judged to be very important to be able to partially

disassemble instruments for repair and modification at the telescope. The transport road to the site will not be paved and some level of re-alignment, final assembly, removal of transport locking mechanism, etc., will have to be performed at the observatory. The resulting facility design utilizes common Chilean construction technologies, has minimum space for the currently specified range of activities, and provides for oxygen enrichment in the routine work areas within the facility. Portable oxygen systems will be provided for work outside these areas. The Telescope Facility scope extends from the foundations to the rotating interface with the dome and includes all utilities, buildings, and finishes. M3 Engineering of Tucson, AZ has developed the initial concept for this facility (Section 11).

7.3.2.2 CCAT Base Facility

The CCAT Base Facility concept follows the approach taken by the APEX observatory. The location is a balance between a site in or adjacent to the village of San Pedro and a more remote site closer to the telescope in the unpopulated high desert. San Pedro is crowded, carefully guards its architectural motifs, has very narrow dirt streets, and generally lacks adequate utilities (electricity, water, and communications) to support a facility of the size we require. Remote locations, such as ALMA has chosen, are far from town and can be expensive to develop. The CCAT Facility is tentatively designed as a compact enclave located on the outskirts of San Pedro. APEX purchased some agricultural land at a favorable price close enough to San Pedro to receive irrigation water and communications from the village. The CCAT facility incorporates housing units, a remote control room, offices, laboratories, a workshop, kitchen, and sufficient recreation spaces to house workers on turno for eight day shifts. Architecture is chosen to blend with that prevalent in and around San Pedro. The facility must provide its own electric power from generators as San Pedro lacks adequate capacity. Details regarding this facility are provided in Section 11.

7.3.3 Dome

The necessity of a dome was discussed at the start of the study; it was apparent that meeting the CCAT's surface accuracy requirement of $\leq 10 \mu\text{m}$ would require protection of the telescope from the deleterious effects of wind and solar heating. The challenge of providing a dome would be the cost and engineering feasibility. Work on dome design was performed by AMEC Dynamic Structures of Port Coquitlam, BC, who previously designed and built both the Keck and Gemini telescope domes. Analysis of three types of domes indicated that the Calotte style chosen for CCAT is the most structurally efficient, would have the lowest weight, and would require the least power to drive it. On the other hand, a large dome of this type has never been built and reservations on this option have been raised by other telescope project reviews.. That said, the large moving shutter type domes built for Gemini, Keck, and Subaru have all had problems generally associated with wear and binding of shutter and vent mechanisms. The concept design effort was enhanced by AMEC's concurrent conceptual design work on a dome for the Thirty Meter Telescope (TMT) project. Analysis and design efforts for the two domes are strongly complementary. The largest technical challenge is the design of the tilted rotation stage required for movement of the upper "cap" portion of the dome. During the next phase of work, the dome design will be refined, the possible use of aluminum geodesic structures for the shells investigated, and the effects of thermal and wind driven distortion of the dome will be analyzed. The dome design is structurally efficient. All structural members will be bolted for easy transport to the summit and for assembly with a minimum of field welding, alignment, and adjustment. AMEC's study is found in Section 12.

7.3.4 Telescope Mount

The telescope mount conceptual design (Section 13) has been developed by Vertex RSI (now part of General Dynamics). Their Richardson, Texas, office has led the effort as they previously built a substantial number of radio telescopes and radars ranging from smaller to much larger than CCAT. They have the particular advantage of an in-house division that designs, manufactures, and sells servo control systems specifically directed at telescope and radar mount positioning.

7.3.4.1 Configuration

Some alternate configurations were investigated including directing images to a location between the elevation bearings and/or down to a receiver cabin beneath the center of the elevation axis. This approach was not

acceptable owing to the desire to have multiple hot instruments and the overall size of instruments and the limited space envelope in these locations. Next, a conventional optical telescope type Nasmyth design was investigated with the instrument locations outside the outer diameter of the primary mirror. Analysis of this configuration showed that the final image diameter at this back focal distance would be about 2.5 m, too large for anticipated focal plane development. Refinement of this design brought the Nasmyth foci inward, behind the primary mirror. The distance between the elevation bearings was reduced to the minimum thought necessary to provide adequate stiffness, and sufficient space for instruments outside the elevation bearings preserved. This resulted in acceptable final image sizes.

7.3.4.2 Bearings

There are substantially different load conditions on the elevation and azimuth bearings. Hydrostatic azimuth bearings were chosen, based on the smoothness of translation, lack of Coulomb friction, and simple load case (straight axial loads.) Control of radial runout will be controlled by a rolling element pintle bearing as the loads are much smaller and implementation of a second axis of hydrostatic bearing at the outer diameter was judged unnecessary and too expensive. The elevation axis will have much lower loads and an addition requirement for almost 2 m of clear inner diameter to allow large beam diameters to pass through unvignetted. Rolling element bearings, custom made but not of unprecedented size or precision, were chosen for this axis. These bearings will most likely feature recirculating and filtered oil supplies to keep them clean and lubricated.

7.3.4.3 Drives

Initially it was hoped that DC servo motors could be implemented on both axes, torque motors in elevation and curvilinear motors in azimuth. Investigation proved these to be too expensive at the required power levels. Consequently a sector gear drive was designed for elevation that follows common radio telescope practice. A gear drive was also designed for azimuth, with the gear located on the inner diameter of the azimuth hydrostatic bearing ways and the motors rotating with the telescope. Helical gears were specified for each axis to minimize residual gear ripple. One pair of motors for elevation and two for azimuth are included each pair counter-torqued against each other to minimize backlash and hysteresis. Controls incorporate VRSI's extensive experience and existing products.

7.3.4.4 Encoders

The use of Heidenhain tape encoders on each axis is planned. This is common practice with large optical telescopes and the 0.2 arc sec pointing precision required for CCAT demands such accuracy. The azimuth encoder is located high in the azimuth base structure, with the static portion, a disc with the encoder tape, mounted to a separate pier from ground to obviate the effects of structural wind up. The four encoder heads are mounted to the structure. One tape each with four read heads are incorporated at each elevation bearing, the two encoders capable of deciphering any twist in the elevation structure.

7.3.4.5 Structure

Both space frame and monocoque approaches to the mount structure were considered. The nature of the point loads at the drive locations and elevation bearings as well as considerations of structural and manufacturing efficiency pointed toward a monocoque design. The major downside is the need to break the mount into subassemblies that can be transported to Chile and to the site and re-assembled by bolting. This might be better addressed by a space frame structure, but the majority of considerations favored the monocoque approach, so it was chosen. The azimuth structure was developed to be asymmetrical to allow the telescope to point within 15 degrees of the horizon without interference between the PM and the azimuth structure. The loads will remain centered over the azimuth bearing.

7.3.5 Primary Mirror

Development of a functional 25 m primary mirror achieving better than 10 μm rms figure at an acceptable price is one of the major technical challenges to the CCAT Project. In addition to segments of necessary precision, the mirror requires metrology and actuators capable of achieving and maintaining accurate segment alignment over the full range of gravity loading and thermal conditions. The instrumentation required for sensing mirror segment

position as well as M1/M2 alignment is discussed in Section 15. The Primary Mirror (Section 14) includes the truss, segments, actuators, and coating. The following design choices have led to the current configuration of the CCAT Primary Mirror:

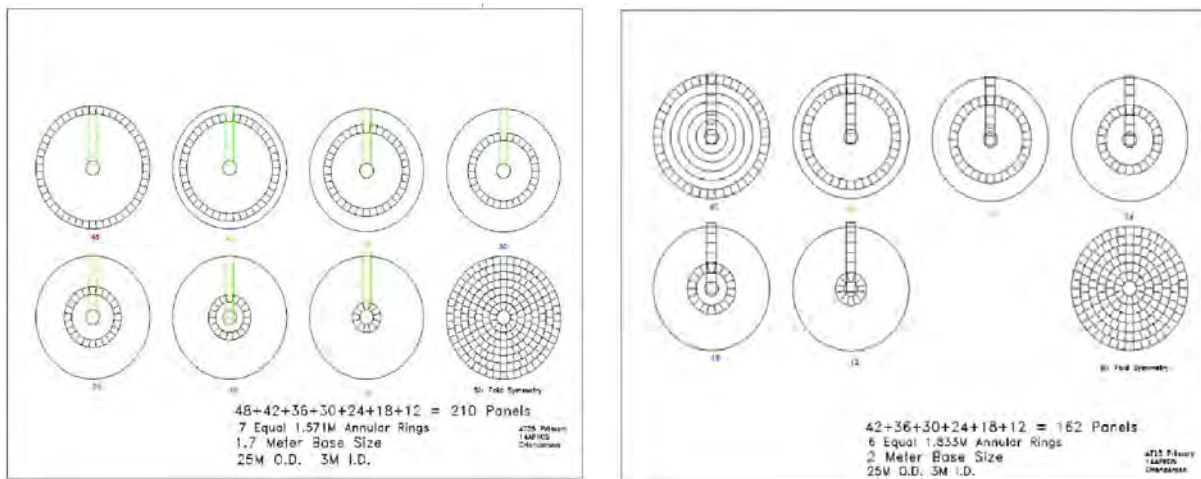
7.3.5.1 Segmented vs. Monolithic

There was little point in discussing the merits of monolithic versus segmented mirrors at the 25 m size, as no recognized approach for manufacture of a monolithic mirror at this size is known. So the choice of a segmented primary mirror was obvious.

7.3.5.2 Segmentation Scheme

There are several potential arrangements for segmentation. Circular mirrors with large gaps were ruled out by the emissivity requirements. That left us with annular rings of roughly trapezoidal segments or hexagons.

- Hexagonal Segments:** An initial assumption was made that it would be desirable to mount segments kinematically on only three points, without the need for load spreading via whiffle tree type mounts, as with optical telescopes with segmented primaries. This favored hexagons as their six-fold symmetry implies less gravity deformation when supported on three points. On the other hand, hexagonal segments do not generate smooth inner and outer edges of the array and across the entire array only six segments are identical of each segment type. Hexagonal segments do not smoothly tile a parabola and hence perimeter shapes need to also be varied to maintain uniform interstitial spacing. This implies additional effort in fabrication and, depending on the approach to manufacture, more complicated tooling and testing. Hexagonal segments have the advantage of prior implementation on the Keck, the HET and the CSO.
- Radial Rings of Segments:** With segments arranged in an annular ring, all segments in a given ring are identical. The inner and outer apertures can be smooth circles. Several segmentation schemes were investigated with different numbers of annular rings and a segments angular extent chosen to maintain a roughly square envelope. It is assumed that replication might be a suitable manufacturing approach, given the large number of identical segments in this approach. Final selection of a segmentation arrangement depends on a number of factors including: maximum size compatible with manufacture and structural performance, number of segments and attendant sensors and actuators, arrangement of segmentation to optimize edge sensor performance, diffraction effects, and/or structural load bearing design of the support truss. The final segmentation arrangement will be decided during the Engineering Concept Design phase of CCAT. The two illustrations show the increase in panel number when segment major dimension goes from 2 m to 1.7 m.



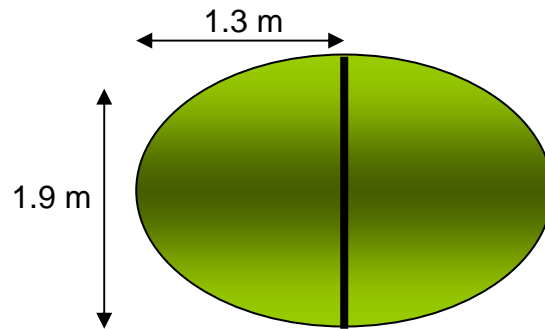
- Number & Sizes of Segments:** As segment size increases the number of segments goes down. Infrastructure required for positioning segments (actuators and edge sensors, for example) varies with the number of segments. Manufacturing cost in general goes up with segment size. These two offsetting factors, when considered in a first-order analyses indicated that there is an intermediate segment size (approximately

between 1 and 2 m) over which the varying costs of infrastructure and segment fabrication offset each other and little difference in array cost results. Consideration of machine size capacity also directs this decision.

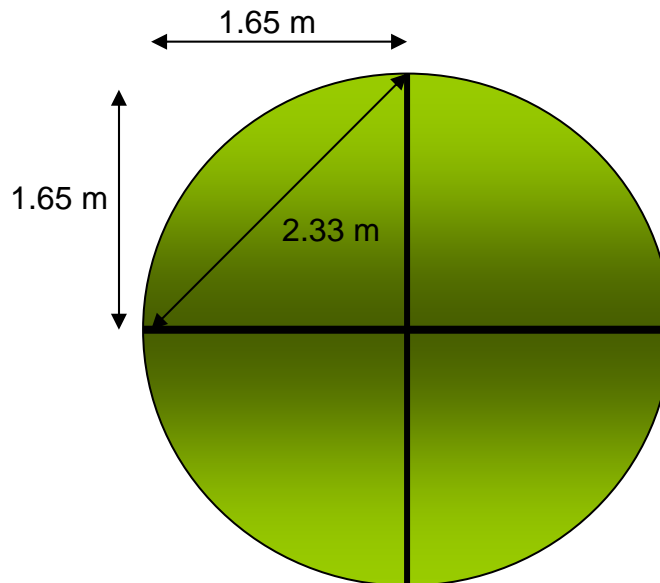
- **Manufacturing:** First consideration was given to the two methods utilized for the ALMA prototype antenna segments. This included Media Lario's electrodeposited Ni with Al honeycomb core panels and machined Al panels. Al panels do not extrapolate well to sizes larger than the ~0.75 m sizes used with ALMA owing to machine size, ability to cast segments, and thermal and mechanical performance. The Ni/Al panels remain of interest and will be further investigated in the next Project phase. Both ALMA panel types derive their fundamental stiffness from and are figure-adjusted by manual actuators in their overconstrained mounting to the composite PM backup structures. Casting and machining Al panels to larger sizes is problematic and the stresses imparted by successive machining passes result in unpredictable low order warping of panels. Vertex RSI was queried on whether they believed that the ALMA approach of CFRP backup structure and multi-point mounted panels could be made to deliver precision of ~5-6 μm rms for the primary and their answer was an unequivocal no. They felt that ALMA had taken this technology as far as it would go. Further investigation was carried out three of possible alternate approaches for replicated panels, CFRP, SiC, and borosilicate glass.
- **Panel Mounting:** Building a dimensionally stable PM truss of 25 m did not seem feasible (or affordable) owing to the large likely gravity-driven distortion and the total amount of carbon fiber material that would be required. It also seemed unlikely that we would be able to improve the ALMA approach, sufficiently to obtain the order of 2.5X improvement in figure. Hence we resolved that CCAT would have an active controlled panel positioning system. This would enable use of a cost effective steel PM truss and allow active control algorithms to be optimized to attain best telescope performance. Prior experience with whiffle tree type mounts indicated these assemblies are disproportionately expensive, have high part count and are machining intensive; they are also prone to driving low order panel deformation, owing to residual strain from imperfect force equalization. We thus investigated whether simple three point kinematic mounting of segments could be successful. From a mechanism and attachment standpoint this type of mounting has been successfully implemented in many optical systems, in particular flight systems. The configuration would likely be three bipod flexures attaching the segment to the actuator. The actuator is intended to accommodate both axial and lateral loads. The question would be whether the large amount of gravity distortion and the mismatch of panel perimeter shape with three point mounting could be overcome by high stiffness of the panels themselves or integral reinforcement of panels.
- **Panel Actuators:** Two potential vendors were contacted with respect to the panel actuators. These vendors looked at whether the technical requirements could be met and considered strawman designs. Requirements included 10mm range and 0.1 μm resolution and the ability for the actuators to accommodate the segment gravity loads, axial and lateral, at all elevation angles. Polytec PI of Auburn, Mass. has provided a Section on their study of actuators. The other vendor, Danaher Precision Motion of Hudson, NH has indicated interest and a belief that they could produce the systems, but failed to provide any study materials. The actuator system is specified to include all electronics, cabling, and control system as well as the electro-mechanical actuators themselves. While a variety of actuator approaches could be considered, we felt strongly that we wanted a commercial solution, available as a complete turn-key system. Hence the reliance on commercial motion control vendors.

7.3.6 Secondary & Tertiary Mirrors

The secondary and tertiary mirrors of CCAT will be significantly larger than those of other submillimeter telescopes. The tertiary mirror is elliptical, 1.9 m \times 2.6 m.



The secondary mirror is 3.3 m in diameter.



These sizes are within scope for manufacture as monolithic glass mirrors, but would be quite expensive. Lightweight glass substrates alone could cost several million dollars. For this reason, we have elected to study the development of these mirrors as segmented optics. In the case of the tertiary, two segments of 1.9 m \times 1.3 m would make up the optic and for M2, four segments of quarter circles, 1.65 m in length on the flat sides would suffice. These sizes are compatible with the processes being studied for primary mirror segments, and hence we propose that the same process would be used to make these segments. This would yield segments at approximately 10kg/m² areal density compatible with three point mounting.

7.3.6.1 Tertiary Mirror

For the tertiary, we anticipate mounting the two segments to a stable, likely carbon fiber (though invar alloy could also be considered) space frame. The segments would be mounted using invar manual adjusters, and the mirror could be set up using a large spherometer and manual adjustment.

7.3.6.2 Secondary Mirror

We considered a number of approaches for mounting M2 segments, including manually mounting them to a rigid carbon space frame, using a plano carbon/aluminum raft structure, and mounting them on actuators to enable adjustment. M2 is complicated by the requirement that the system chop at or near 1 Hz., and that it also be capable of rigid body positioning in 5 degrees-of-freedom for M1/M2 alignment purposes. This being the case, we considered stacking a hexapod for rigid body alignment, a nutator capable of the chopping motion, and then

the backing structure with the segments fastened atop it. This seemed awkward from a packaging standpoint as well as heavy, with the weight of M2 cantilevered well out from the spider mounting point. As an alternative, we considered mounting each segment separately on three active positioning actuators capable of coordinated high bandwidth motion. In this way the segments could be co-aligned, aligned as a group with M1, and chopped through concerted motions, hence yielding all positioning requirements through a single set of actuators. This was studied by CSA Engineering of Mountain View, CA and the results of their study are found in Section 16.

7.3.7 Telescope Alignment

Section 15 discusses the various systems required to achieve telescope calibration alignment, maintenance alignment, and tracking/guiding. The approach to each is discussed. We have elected to view this system, including the Calibration Wavefront Sensor, M1 panel Edge Sensors, and Absolute Laser Distance Sensors as a complete system that JPL's Metrology and Optics Group will study in the next Phase of the CCAT Project. This will enable a systems approach including modeling and analysis which will ultimately take all sources of error into consideration and provide information regarding the optimal deployment and operation of the complete system to obtain best performance.

7.3.7.1 Calibration Wavefront Sensor

Preliminary alignment of segments at installation will be achieved initially by mechanical metrology and subsequent position scanning to bring them within capture range of a Calibration Wavefront Sensor (CWS.) Several approaches to Calibration Wavefront Sensing were considered. The Caltech Submillimeter Observatory (CSO) uses shearing interferometry to align segments for their telescope to precision comparable to that we require. This system was developed by Gene Serabyn of JPL and he studied an upgrade to this system, using an extended focal plane rather than a single point detector. This sensor is intended to operate using the image of a distant planet and provide information necessary to position all mirror segments and rigid bodies appropriately to form the best images. His report is found in section 15.2.

7.3.7.2 Edge Sensor System (ESS)

The ESS is conceptually modeled after the systems employed on Keck, HET, and SALT which use either capacitance or inductance sensors to measure panel-to-panel displacements and, in the case of Keck, dihedral angles between panels. Initial analyses by (Section 9.3.5) indicate care must be taken in implementation of this system owing to error magnification, degeneracy in the matrix solution linking the sensed data to positioning requirements, and spurious errors resulting from panel deformations. There are also issues relating to the design of the segmentation scheme and orientation of panel joints. The details of implementation will be worked out in the next Phase of CCAT development. An interesting aside is the identification of lateral effect photodiodes as a potential source for cost effective edge sensors. These opto-electronic devices cost only a few dollars apiece and offer the resolution we require over limited ranges. JPL will be studying optimization of this technology as part of the study on overall mirror sensing and control. This approach has the potential to substantially reduce the cost of the overall edge sensor system.

7.3.7.3 Maintenance Alignment

JPL has developed an absolute distance measuring laser approach to mirror position control for various programs needing large segmented mirrors in space. This system has the potential to mitigate the shortfalls of the ESS noted above. Section 15.3 includes a report of the preliminary study of this system and illustrates the concept for implementation in conjunction with edge sensors. This system has the additional capability of providing accurate start-up positions for the optics, substantially reducing the time required to bring the system to optimal alignment following shut down. A second approach using a Shack Hartmann type sensor is provided in a white paper from Adaptive Optics Associates (Section 15.4).

7.3.7.4 Wavefront Sensing Guider

The high resolution of this telescope drives a requirement for precise pointing and tracking. The telescope is specified to perform offset pointing of 0.2 arcsec. This requirement will be more easily met for such a large telescope if there is a capability for guiding using stars. We consider the possibility that the telescope have mirror

surfaces that are specular at IR wavelengths, enabling IR guiding on images either in the periphery of the science field or using pick-off probes which extend into the science field. This cannot be done at submillimeter wavelengths owing to the scarcity of suitable objects at these wavelengths. Jamie Lloyd of Cornell has provided the initial study of a guider, and has concluded such a guider is best implemented as a Shack Hartmann type wavefront sensing device. In addition to providing the required mount control information, the guider may also provide information on low order aberrations, assisting in mirror alignment and control as well as automated focus correction on a real-time basis. The guider study is found in Section 15.4.

7.3.7.5 Mirror Control Law

In addition to determining the best arrangements for mechanical deployment of the sensors and optimizing design of the sensors themselves, it is critical that the entire system be developed to achieve optimal performance. For this reason, JPL is developing a system model which will permit variations of all the critical parameters which affect mirror control performance and can serve as a test bed to optimize mirror control algorithms. It is anticipated that each subsystem will have its own control computer, but that the integration of sensor data and calculation of appropriate actuator commands will be addressed in a central, mirror control computer.

7.3.8 Controls & Software

There are many options for platforms, communications protocols, operating systems, and software environments which have been used successfully for astronomical telescope control systems. Among the things that are important in configuration of such a system are:

- Robust and Cost Effective Platforms with a wide range of available “plug-in” hardware such as motion control cards, data acquisition cards, GPS Timing hardware, etc.
- Stable architectures which will have a high probability of being continued and supported well into the future
- Communication protocols which will support the highest data bandwidths required and be compatible with the wide variety of devices which will need to be connected to the bus.
- Software environments which are simple, well known, stable, commercially supported, easily documented, and capable of cross operability on a variety of platforms and operating systems.

For the purpose of the current Feasibility/Concept Design Study and cost estimation, we favor a system which employs the following:

- PC Platforms: Cost effective, easily modified to provide capabilities specific to the node in the system where used, wide range of available hardware, well understood architectures, capable of operating either Windows or Linux OS
- Fast Ethernet Communications: Cost effective distribution hardware (routers, switches, etc.) Acceptable bandwidth, Multiple backbones possible to separate data from control from support communications.
- Linux OS: Most nodes in the control system will run stable Linux OS. Selected nodes may run Windows depending on contractor/instrumentalist preferences and required capabilities.
- National Instruments LabVIEW Software: Graphic programming language, rapid development of GUI, capable of rapid implementation of legacy code, developed specifically for instrument, process, machine control.

During the next phase of work this trade will be more formally addressed, but with respect to providing an adequate cost estimate, assessing risk and feasibility, and addressing the full range of telescope subsystem requirements, this strawman system approach meet established requirements.

Further discussion is presented in Section 17.

7.4 Risk Assessment

The assessment of risk is a principal objective of this Study. The system defined above has been developed to provide initial definition of subsystems which when integrated provide an observatory that will meet established requirements. Risk is not uniformly distributed through these subsystems. Some are well with the state-of-the-art

and others are at the very edge of it. The objective has been to remain comfortably within this limit where possible, and address new technologies and/or systems approaches only when proven and existing solutions fail to meet performance or cost objectives. Taken as a whole, the defined concept serves the purpose of risk assessment and cost estimation well and the next phase of work, Engineering Concept Design, will provide the further development and additional trades between alternate competing designs required to bring the Project to the next level of definition.

8 CCAT Baseline Optical Design

8.1 Telescope Optical Parameters and Design

The baseline design for CCAT is a symmetric Ritchey-Chretien (RC) reflector system with dual Nasmyth focus. The frequency of operation of CCAT will be from 150 GHz up to 1.5 THz, The design system focal ratio is $f/8$, with an aperture diameter of 25 m. The main reflector focal ratio is $f_p/D = 0.6$ with a back focal distance of $B = 11.0$ m. These four parameters in conjunction with a specified Field of View (FoV) of 20.0 arc minutes determine the main optical design of the CCAT sub-millimeter telescope (see Table 8.1).

Table 8.1. CCAT Optical Design Parameters

| | Symbol | Value | Units |
|---|---------------|--------------|--------------|
| Primary reflector (M_1) diameter | D_1 | 25.000 | (m) |
| Primary reflector (M_1) focal ratio | f_1/D | 0.6 | |
| System focal ratio | $f/\#$ | $f/8$ | |
| Back focal distance | B | 11.000 | (m) |
| Field of View diameter | FoV | 20.0 | (arcmin) |

8.1.1 Ritchey-Chretien Design

In a RC design both primary and secondary reflector surfaces are hyperboloids whose vertex radius of curvature and distance between surfaces are the same as the correspondent Cassegrain design. By imposing the condition to cancel both coma and spherical aberration up to 3rd order, we obtain the eccentricities of the primary and secondary reflectors [1]:

$$\epsilon_1^2 = 1 + \frac{2(1 + \beta)}{m^2(m - \beta)}, \quad (1)$$

$$\epsilon_2^2 = \frac{2m(m + 1)}{(m - \beta)(m - 1)^3} + \left(\frac{m + 1}{m - 1}\right)^2. \quad (2)$$

Where, $m = f/f_1$, f is the system focal length, and $\beta = B/f_1$.

The final set of derived parameters is presented in Table 8.2; notice that, since the calculations involving conic surfaces are very sensitive to round-off errors, we have included several decimal places in those related values.

The CCAT sub-reflector diameter, including provisions for the FoV, is 3.2 m. This corresponds to a 1.6% blockage of the total aperture, not including the quadripod contribution.

Figure 8.1 shows the optical layout of the CCAT RC design, including a ray-tracing scan of the telescope and optical dimensions of M_2 and M_3 for a 20 arcmin field of view.

Table 8.2. Derived RC Optical Design Parameters

| Primary Reflector M₁ | Symbol | Value | Units |
|---|------------------|-----------------|-------------------|
| Reflector Type | | Hyperboloid | |
| Eccentricity | ϵ_1 | 1.0007735103647 | |
| Vertex radius of curvature | Rc_1 | 30.000000000 | (m) |
| Equivalent Focal distance ¹ | f_1 | 15.000000000 | (m) |
| Edge angle from prime focus | θ_1 | 45.23973 | (deg) |
| Secondary Reflector M₂ | | | |
| Reflector Type | | Hyperboloid | |
| Eccentricity | ϵ_2 | 1.1690982278146 | |
| Radius of curvature | Rc_2 | 3.922061596 | (m) |
| Diameter (on axis design) | D_2' | 3.063000000 | (m) |
| Diameter with provisions for FoV ² | D_2 | 3.198000000 | (m) |
| Edge angle from secondary focus | θ_2 | 3.57982 | (deg) |
| Reflector M₃ | | | |
| Reflector Type | | Flat | |
| Shape | | Ellipse | |
| Minimum size ² | axb | 2.60 x1.84 | (m) |
| Distance: M ₃ to M ₁ vertex | | 3.000 | (m) |
| Distance: M ₃ to Nasmyth Focus | | 8.000 | (m) |
| Miscellaneous System Parameters | | | |
| Magnification | m | 13.3333333 | |
| System Focal Length | f | 200.000000000 | (m) |
| Minimum Operating Wavelength | λ_{\min} | 200.0 | (μm) |
| Diffraction Limit at 200 μm | | 1.980 | (arcsec) |

8.1.2 The Nasmyth Focus

The telescope pedestal assembly is a counterbalanced elevation-over azimuth design. In the current structural design, the telescope elevation axis passes 3 m behind the main reflector vertex, allowing enough room for the back-structure of the main reflector. In the same way, the elevation bearings location and accessibility to the focal region place the two Nasmyth focus at 8 m radii on either side of main optical axis, on the elevation axis, as shown in Figure 8.1.

A flat mirror (M₃), 3m behind the main reflector vertex, inclined 45° with respect to the main optical axis provides the optical path relay to either of the two Nasmyth platforms, and to a bent Cassegrain focus that will be used for calibration.

¹ Focal distance of an equivalent paraboloid with the same radius of curvature as of M₁

² This size does not account for chopping or beam spillover.

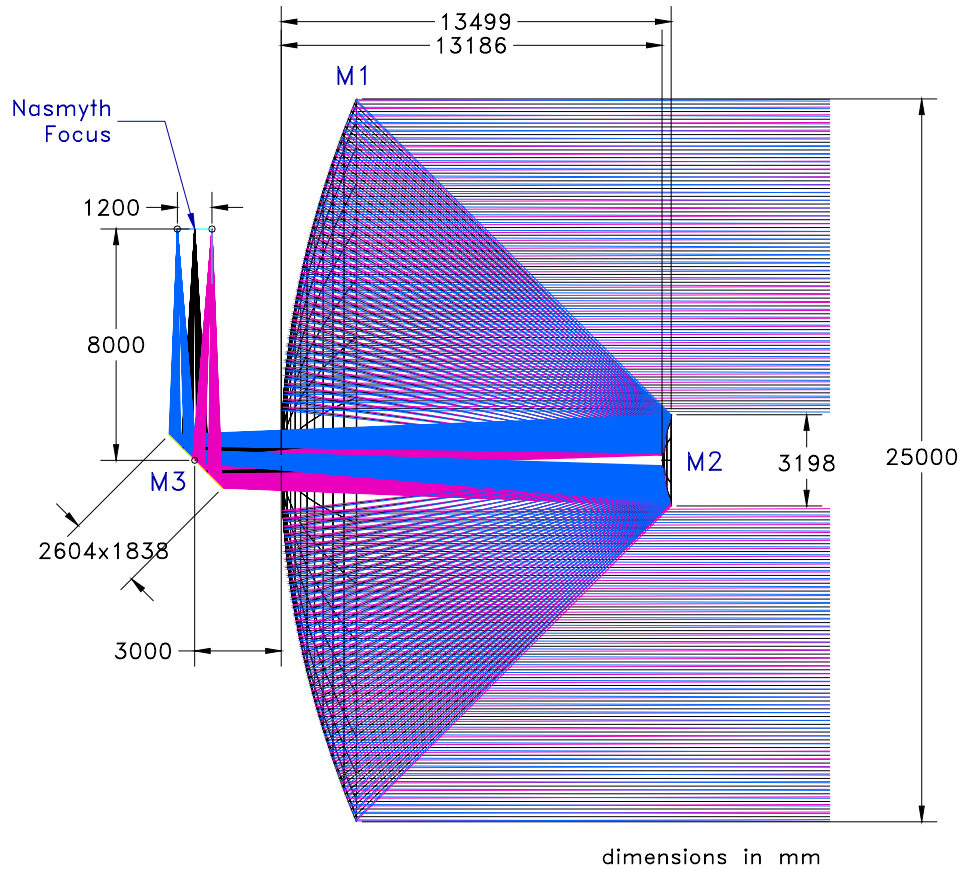


Figure 8.1. Optical layout and ray-tracing of the f/8 Ritchey-Chrétien CCAT design, including overall dimensions for the primary, M_1 , secondary, M_2 , (with FoV oversize), and flat mirror M_3 .

8.1.3 Field of View Characteristics

The image scale at the CCAT f/8 Nasmyth focus is 1.0313 arcsec/mm. Therefore, the size of CCAT's 20 arcmin FoV is 116.4 cm in diameter, as shown in Table 8.3

Table 8.3. CCAT Field of View Parameters

| | Symbol | Value | Units |
|--|-----------|--------|-------------|
| Focal Plane | | | |
| Specified FoV Diameter | FoV | 20.0 | (arcmin) |
| Image Scale at Nasmyth focus | IMS | 1.0313 | (arcsec/mm) |
| Optimum Radius of curvature ³ | $R\omega$ | 1.9381 | (m) |
| Size of 20 arcmin FoV | | 116.40 | (cm) |
| Diffraction Spot Size at 200 μm | | 1.920 | (mm) |

The focal surface has an estimated radius of curvature of 1.91185 m using the convention of minimum wave-front error [1]. On the other hand, by optimizing the Strehl ratio response as a function of Δz at various radial points in the focal plane we obtained a best fitted value of the optimum radius of curvature $R\omega$ of 1.938 m, at 200 μm , (see Figure 8.2).

³ This is the best-fitted value for optimum Strehl ratio at 200 μm .

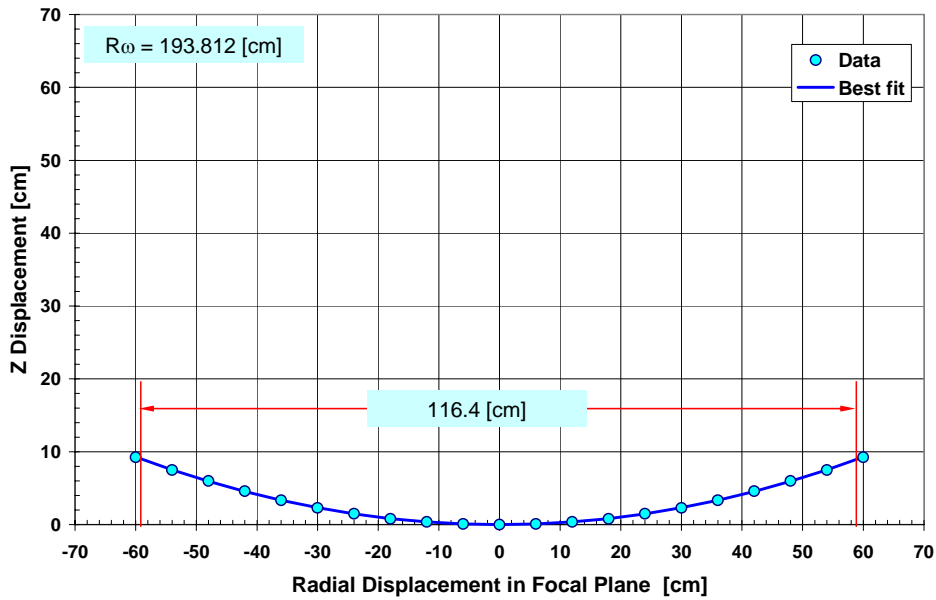


Figure 8.2. Optimum Focal Surface Geometry

The calculated maximum Δz displacement at the edge of the FoV, on the optimum focal surface, is 8.7 cm.

8.2 Antenna Performance

8.2.1 Methodology

In order to analyze the optics of CCAT we use a forward electromagnetic ray tracing method. This method uses a point source feed at the focal plane of the antenna that launches a pre-determined spherical field radiation pattern, with a specified polarization. The fields are then traced forward, in amplitude, phase and polarization, to the antenna aperture.

The fields in the aperture, both Co-polar and Cross-polar, are then integrated over the aperture to obtain corresponding Co/Cross-polar far field radiation patterns of the telescope.

In the analysis we use two types of feeds at the focal plane, both with azimuthally symmetric field distributions and linear polarization: the first one has a uniform field radiation pattern, and the second has a Gaussian illumination pattern, typical of a corrugated feed horn, with an edge taper of -11 dB at the edge of the secondary reflector M_2 .

8.2.2 Preliminary Design Evaluation

Table 8.4 shows the calculated angular aberration [1] of CCAT aplanatic design at the edge of the 20 arcmin FoV.

Table 8.4. Calculated Angular Aberrations of the CCAT Optical Design

| | Symbol | Value | Units |
|-------------------------|--------|-------|----------|
| Field of View diameter | FoV | 20.0 | (arcmin) |
| Angular Tangential Coma | ATC | 0.00 | (arcsec) |
| Angular Astigmatism | AAS | 2.83 | (arcsec) |
| Angular Distortion | ADI | 0.48 | (arcsec) |

Since the RC design cancels-out up to 3rd order the spherical aberration and tangential coma, the only residual main contribution is astigmatism followed by the field distortion.

Table 8.5. RMS Spot Sizes (from [2])

| Δx (arcmin) | Δy (arcmin) | RMS (arcsec) | Minimum rms (arcsec) |
|--------------------------|--------------------------|-------------------|---------------------------|
| 0.0 | 0.0 | 0.16 | 0.05 |
| 0.0 | 10.0 | 0.31 | 0.31 |
| 10.0 | 10.0 | 0.71 | 0.62 |

Figure 8.3 (left) shows a spot diagram for the CCAT optical system using a curved focal surface. RMS spot sizes are given in Table 8.5 from [2] for displacements (Δx and Δy) of 0, 10, and 14 arcmin).

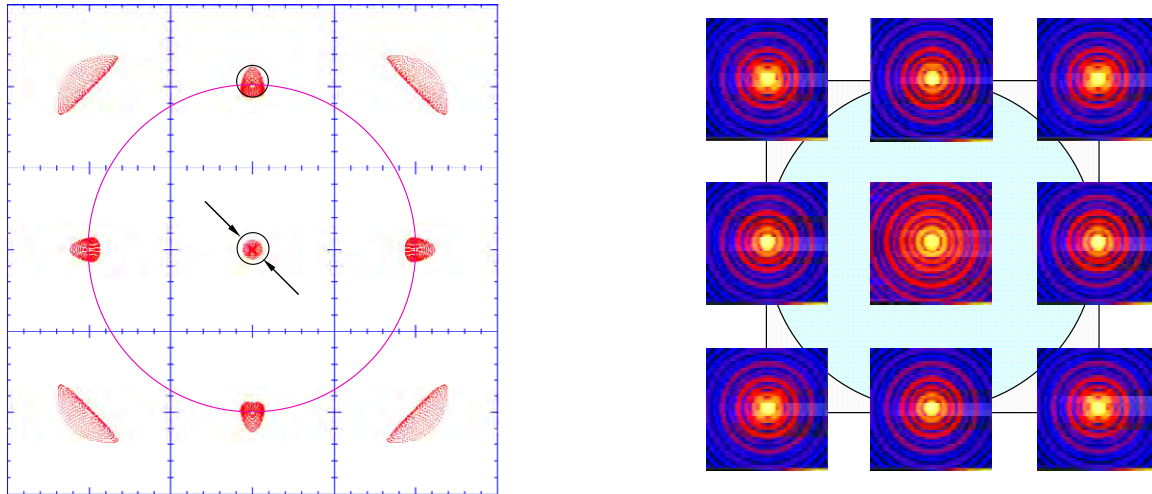


Figure 8.3. **Left:** Spot diagram for CCAT for the locations given in Table 8.3. The focus has been adjusted to roughly equalize the RMS in the center and at 10 arc minutes from field center. The corner spots are for 14.1 arc minutes off-axis, which is beyond the nominal field-of-view requirement for CCAT. The black circle at the center is 2 arcsec in diameter, (from [2]). **Right:** For comparison, the corresponding far field radiation patterns maps (each 51" x 51" in size, with a logarithmic color scale), on the optimum focal surface.

The image surface has been refocused to give the best RMS at a 10 arcmin FoV radius.

On the right of Figure 8.3 we present for comparison the corresponding 51" x 51" far field radiation maps of the telescope, (shown in a logarithmic color scale), obtained at 200 μm , on the optimum focal surface.

In these maps, it is possible to appreciate more clearly the astigmatism present in the beams at 200 μm , particularly at the corners of the field, (past the FoV radius specified for CCAT).

8.2.3 Figure of Merit

As we mentioned earlier, CCAT will operate from a wavelength of 1 mm down to 200 μm ; therefore, it is important to express its performance in a form consistent with both the optical and antenna figures of merit.

We chose the Strehl ratio as one of these unifying parameters, since is well established in the optical community as performance criteria in terms of RMS wave-front error, and it simultaneously connected with the aperture efficiency, within the antenna community, through the Ruze's formula and the structural rms surface errors. In addition, we have included other antenna parameters such as the beam width, beam efficiency polarization efficiency, side lobe level and Cross-Polarization levels, which are important figures that serve to characterize further the telescope performance.

Summarizing, we use the following set of parameters as the figure of merit of the optical and electromagnetic performance of CCAT:

- Strehl Ratio
- RMS wave-front error.
- Ruze's formula and structural surface rms error.
- Antenna Gain and Aperture Efficiency
- Beam width and Beam efficiency
- Polarization efficiency
- Far field Side Lobe Level (SLL)
- Far field Cross-Polarization level

Next, we will define more precisely these parameters.

Strehl Ratio

Defined as the ratio of the central irradiance of its aberrated and unaberrated *point-spread* functions [3], which in the aperture plane is expressed by,

$$Strehl = \frac{\left| \int_{AP} E_a(\mathbf{r}') e^{j\Phi_{ab}(\mathbf{r}')} dS' \right|^2}{\left| \int_{AP} E_a(\mathbf{r}') dS' \right|^2}, \quad (3)$$

Here, E_a is the amplitude field distribution, and Φ_{ab} is the field phase (aberration) distribution in the aperture.

A good approximation to the Strehl ratio, valid for Strehl ratios $> 10\%$, is given in [4], and is expressed, either in terms of the E-field *phase covariance*, σ_ϕ^2 , or the *rms wave-front error*, ω_{rms}^2 , in the aperture, i.e.,

$$Strehl = e^{-\sigma_\phi^2} = e^{-(2\pi\omega_{rms})^2} \quad (4)$$

Phase Covariance

The phase covariance is defined by,

$$\sigma_\phi^2 = \int_{AP} \left(\Phi_{ab}(\mathbf{r}') - \langle \Phi_{ab} \rangle \right)^2 W_n(\mathbf{r}') dS' \quad (5)$$

Where, $\langle \Phi_{ab} \rangle$ is the average phase error in the aperture, $W_n(\mathbf{r}')$ is a weighting function which in this case is the normalized illumination power in the aperture.

RMS Wave-Front Error

Likewise, the rms wave-front error is defined as,

$$\omega_{rms}^2 = \int_{AP} (s_\lambda - \langle s_\lambda \rangle)^2 W_n(\mathbf{r}') dS' \quad (6)$$

Here, s_λ is the total path-length, in wavelengths, traveled by the ray in the optical system from the feed source to the aperture. $\langle s_\lambda \rangle$ is the average value of s_λ in the aperture.

Ruze's Formula and Structural RMS Surface Errors

Ruze's formula is the equivalent to the Strehl ratio in antenna analysis. Structural deformations of the antenna optics change the resultant phase distribution in the aperture, or similarly the rms wave-front error. Ruze's formula connects the variation in phase distribution with the *structural rms surface errors*, ϵ_{rms} [5]

$$\eta_{RUZE} = e^{-\left(\frac{4\pi\epsilon_{rms}}{\lambda}\right)^2} \quad (7)$$

In fact, the connection between all these is the following:

$$\frac{\epsilon_{rms}}{\lambda} = \frac{1}{4\pi} \sigma_{\phi} = \frac{1}{2} \omega_{rms} \quad (8)$$

Antenna Gain and Aperture Efficiency

The antenna gain is a measure of the coupling of the antenna to an incoming plane wave field, and is normally expressed in terms of the *Effective Aperture*, A_{eff} ,

$$G_{ain} = \frac{4\pi}{\lambda^2} A_{eff} = \frac{4\pi}{\lambda^2} \eta_A A_g \quad (10)$$

or, in terms of the geometric aperture, A_g , by means of the *Aperture efficiency*, η_A .

The aperture efficiency includes contribution from Ohmic losses, spillover, blockage, diffraction, and illumination, taper and phase distribution in the aperture of the telescope.

Our calculations do not include ohmic losses and strut or edge diffraction contributions to the aperture efficiency.

Beam Width and Beam Efficiency

The beam width is the *Half Power Full Width* (HPFW) angular size of the beam. The beam efficiency is the ratio of the amount of power contained up to some specified power level (-10 dB, in our case) in the beam to the total power in the far field radiation pattern⁴ power.

Polarization Efficiency

Is the ratio of the Co-polar power to the total (Co-polar + Cross-polar) power in the radiation pattern?

Far Field Side Lobe Level

In the Co-polar radiation pattern, it is the value in dB of the first peak next to the main beam. It is a function of the taper illumination in the aperture.

Far Field Cross-Polarization Level

It is measured in the Cross-polar radiation pattern of the antenna. It is defined as the peak Cross-polar value in dB with respect to the main (Co-polar) beam; as such, and with an ideal spherical feed source, it is a measure of the intrinsic cross-polarization introduced by the optics of the telescope.

We have included in this document Co-polar and Cross-polar image maps of the radiation pattern of the telescope in which, both the far field side lobe level and the cross-polar level, are measured in different test of performance contained therein.

8.2.4 CCAT Performance

Table 8.6 presents the calculate performance of CCAT at 200 μm , using the parameters we just described. As we mentioned, we use two different sources that produce a uniform aperture illumination and a Gaussian illumination respectively.

⁴ The radiation patterns of a receiving and transmitting antenna are identical by reciprocity

The table shows the performance on axis as well as at the edge of the FoV, on the optimum radius of curvature surface.

Table 8.6. Calculated Performance of CCAT Design at 200 μm (1.499 THz)

| | Uniform Illumination | | (-11dB) Gaussian Illumination | | Units |
|-----------------------------|-----------------------------|----------------|--------------------------------------|----------------|--------------|
| | On Axis | At Edge | On Axis | At Edge | |
| HPFW Beam Width | 1.86 | 1.89 | 1.98 | 2.01 | (arcsec) |
| Strehl ratio | 100.00 | 96.75 | 100.00 | 98.39 | (%) |
| Polarization Efficiency | 100.00 | 99.99 | 100.00 | 99.99 | (%) |
| Beam Efficiency | 76.21 | 74.41 | 85.97 | 84.65 | (%) |
| Aperture Plane Efficiency | 98.73 | 95.59 | 87.58 | 85.41 | (%) |
| Spillover Efficiency | ----- | ----- | 88.37 | 88.37 | (%) |
| Overall Aperture Efficiency | ----- | ----- | 77.40 | 75.48 | (%) |
| Antenna Gain | ----- | ----- | 110.76 | 110.66 | (dB) |
| Side Lobe Level (SLL) | -16.70 | -15.71 | -22.27 | -20.89 | (dB) |
| Cross-Polarization Level | -327.30 | -51.21 | -326.73 | 52.63 | (dB) |

The HPBW beam sizes increase at the edge of the FoV in both, the uniform and Gaussian illumination cases. The Gaussian illumination reduces the effective area of the telescope hence the HPFW beam sizes are larger than the uniform illumination instance. This can be appreciated more clearly in the far field co-polar image maps in Figures 8.4 and 8.5.

The Strehl ratio is better than 96% with uniform illumination and better than 98% with Gaussian illumination. The reason behind this may be found in the aperture phase distribution map in the top of the left column of both Figure 8.4 and 8.5. At the edge of the FoV, the phase distribution in the aperture is dominated by astigmatism, with peak values at the rim of the aperture. A Gaussian illumination tends to minimize phase errors closer to the edge of the aperture than to the center, hence we obtain a better Strehl at the expense of a wider beam.

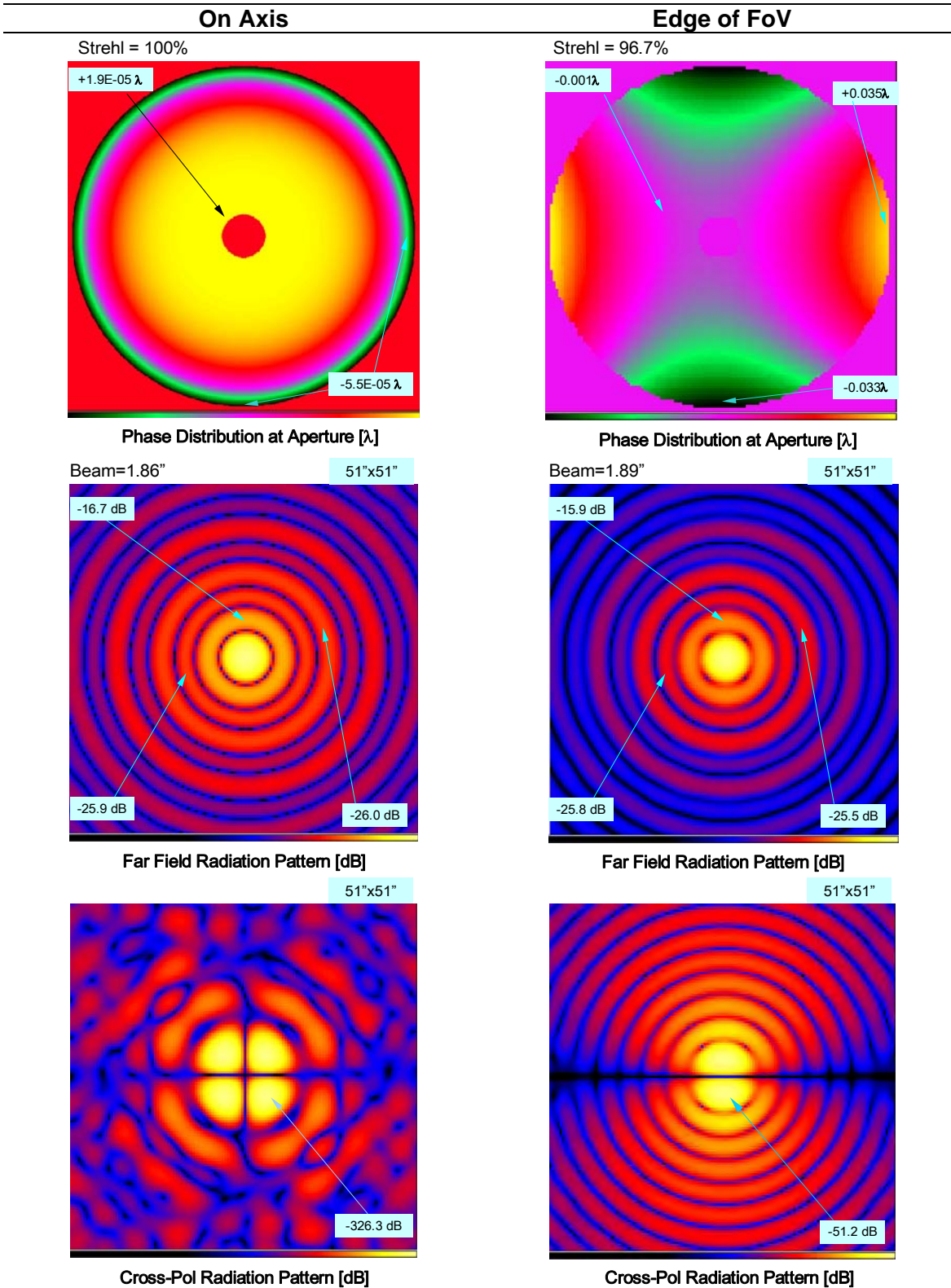


Figure 8.4. From top to bottom: CCAT Aperture phase distribution, 51" x 51" map of far field co-polar and cross-polar radiation pattern, with *uniform illumination* at 200 μm , for both: on axis (**left**) and at edge of the FoV (**right**)

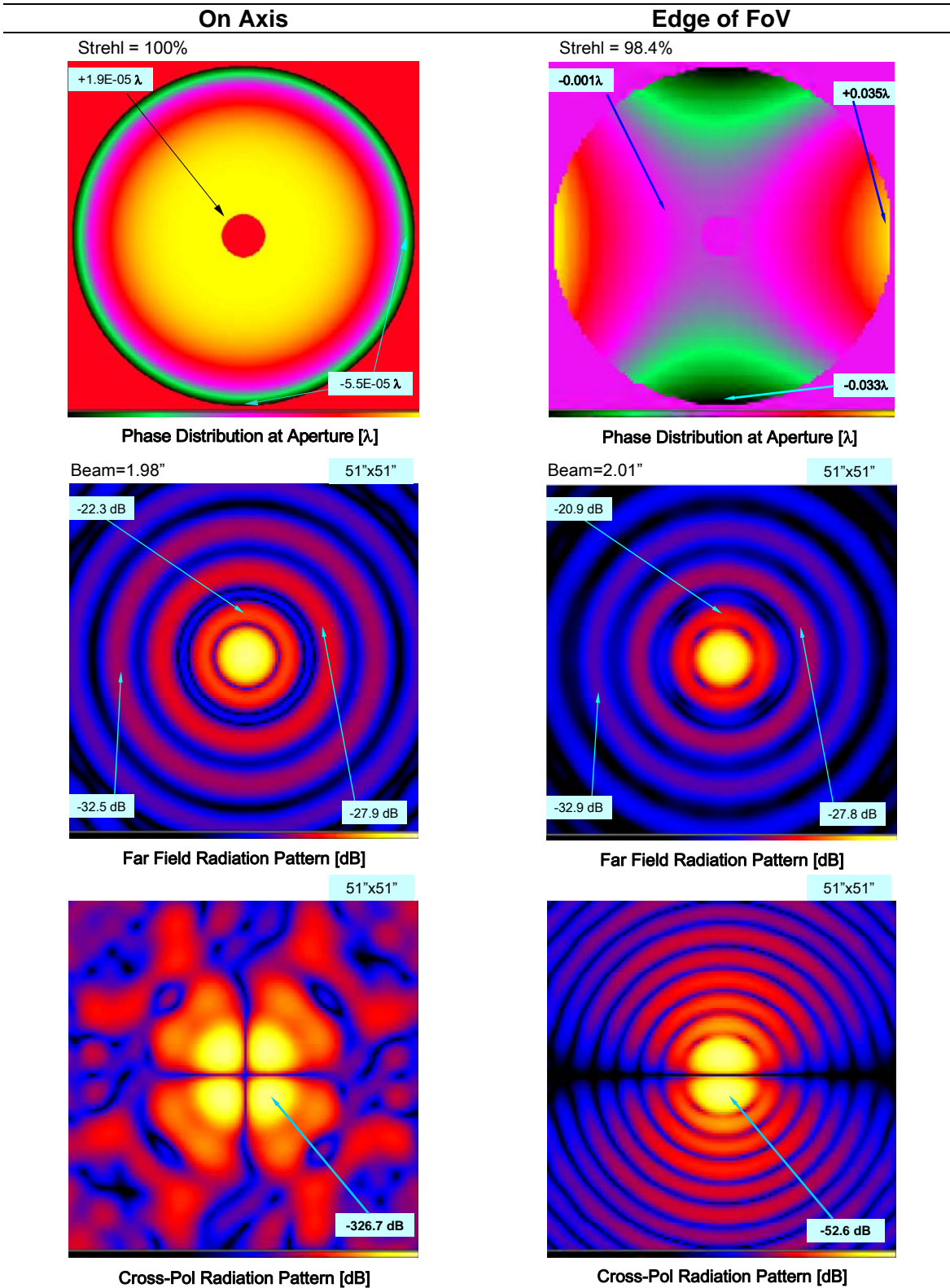


Figure 8.5. From top to bottom: CCAT Aperture phase distribution, 51" x 51" map far field co-polar and cross-polar radiation pattern, with a -11 dB taper Gaussian illumination at 200 μm , for both: on axis (left), and at edge of the FoV (right)

Figure 8.6 shows the Strehl variation in the FoV at 200 μm , as function of beam deviation, on both the optimum focal surface⁵ and the focal plane scan, with uniform illumination.

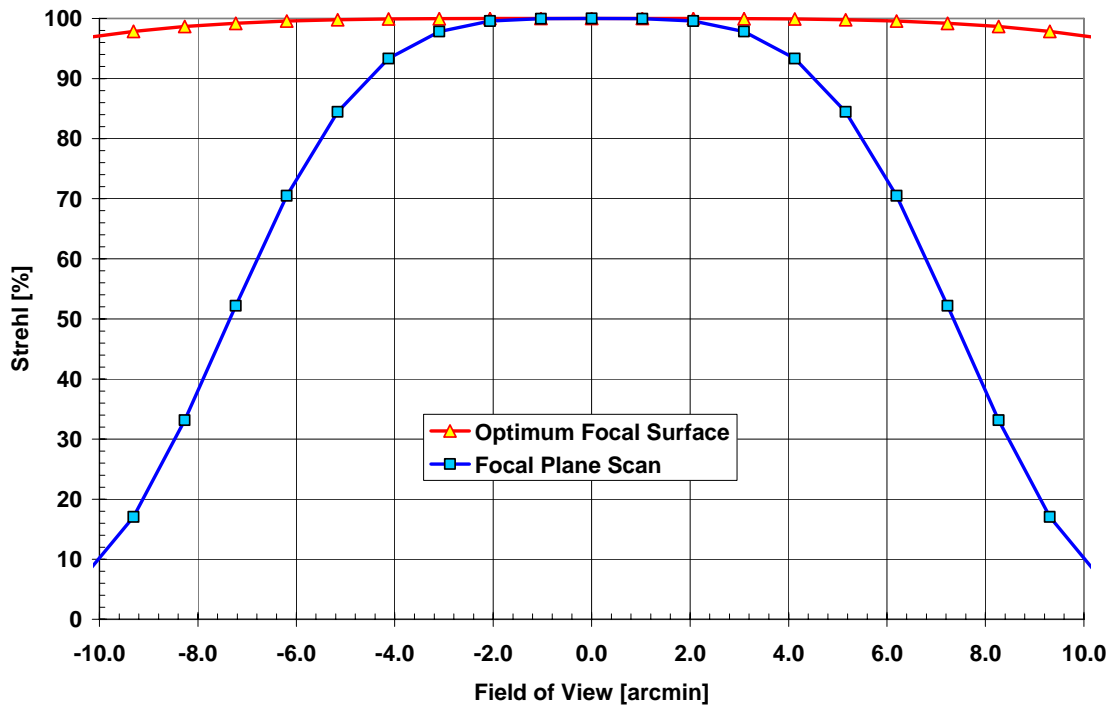


Figure 8.6. Strehl ratio variations on the FoV on the optimum scan surface and for a focal plane scan with uniform illumination. (At 200 μm).

Accordingly, the CCAT 20 arcmin FoV is able to accommodate up to 1200×1200 (Nyquist Sampled) Pixels at 200 μm , with better than 96% Strehl ratio.

Polarization efficiencies are quite high over the FoV, for both types of illumination. Beam efficiencies are higher with Gaussian illumination because of the wider beam; in general the beam efficiencies tend to be lower at the edge of the FoV.

The aperture plane efficiency does include blockage contribution from the sub-reflector but not from the quadripod leg support. The aperture efficiencies are better of 95% with uniform illumination and better than 85% with Gaussian illumination over the FoV.

With uniform illumination there is no spillover efficiency information, and hence there are no overall aperture efficiency or gain calculations. With Gaussian illumination the spillover efficiency is 88% for an -11 dB taper at the sub-reflector edge, and the overall aperture efficiency of the Gaussian case is better than 75% over the 20 arcmin FoV. Figure 8.7 shows the scanning losses over the FoV, with Gaussian illumination at 200 μm , for both, scanning on the optimum focal surface and on the focal plane.

⁵ With radius of curvature R_0 in Table 3

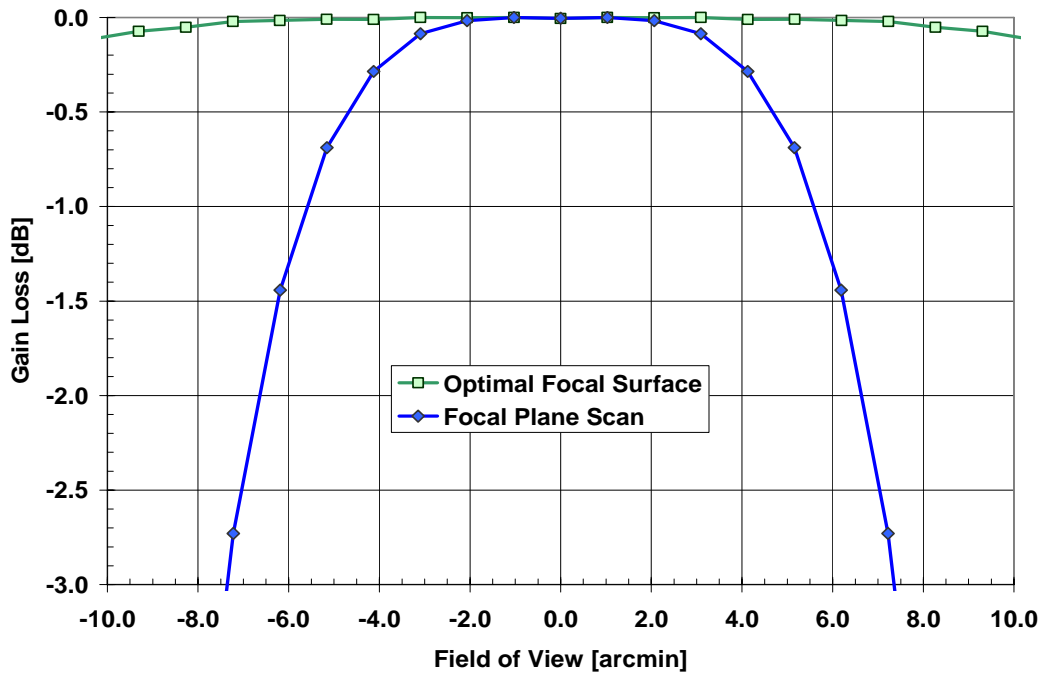


Figure 8.7. Gain losses across the FoV for scanning on the optimum focal surface and on the focal plane. With -11 dB edge taper Gaussian illumination at 200 μm .

The maximum scanning loss is -0.1 dB when on the optimum focal surface. When scanning of the focal plane (not the optimum focal surface), we found scanning losses as high as -1.0 dB at 5.5 arcmin radius from the field center.

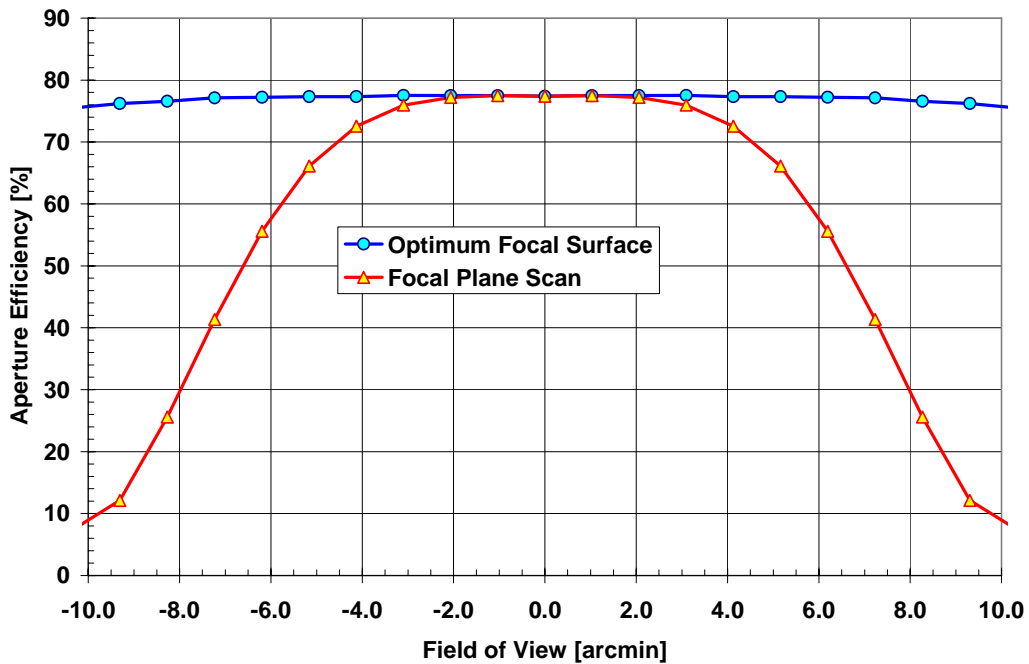


Figure 8.8. Aperture Efficiency variations across the FoV for scanning on the optimum focal surface and on the focal plane. With -11 dB edge taper Gaussian illumination at 200 μm .

Figure 8.8 shows the aperture efficiency variation over the FoV, with Gaussian illumination at 200 μm , for both, scanning on the optimum focal surface and on the focal plane. While the aperture efficiency is better than 75% on the optimum focal surface, it is as low as 9% when at the edge of the FoV when scanned on the focal plane.

The SLL of the uniformly illuminated aperture is -16.7 dB at the center of the field and -15.7 dB at the edge of the FoV, as shown in the Co-polar maps Figure 8.3, (middle). In contrast, SLL values for the Gaussian illumination are better than -20.8 dB over the FoV.

Cross-polarization levels at the center of the FoV are practically non-existent as it can be appreciated at the bottom left of Figures 8.3 and 8.4. The maximum intrinsic Cross-polar level introduced by the optics on the FoV is -51 dB for uniform illumination and 1dB lower for Gaussian illumination.

8.3 Sub-Reflector Sensitivity Analysis

We obtained the telescope performance sensitivity to sub-reflector (M_2) motion in terms of variations in Strehl ratio and beam pointing under uniform illumination at 200 μm .

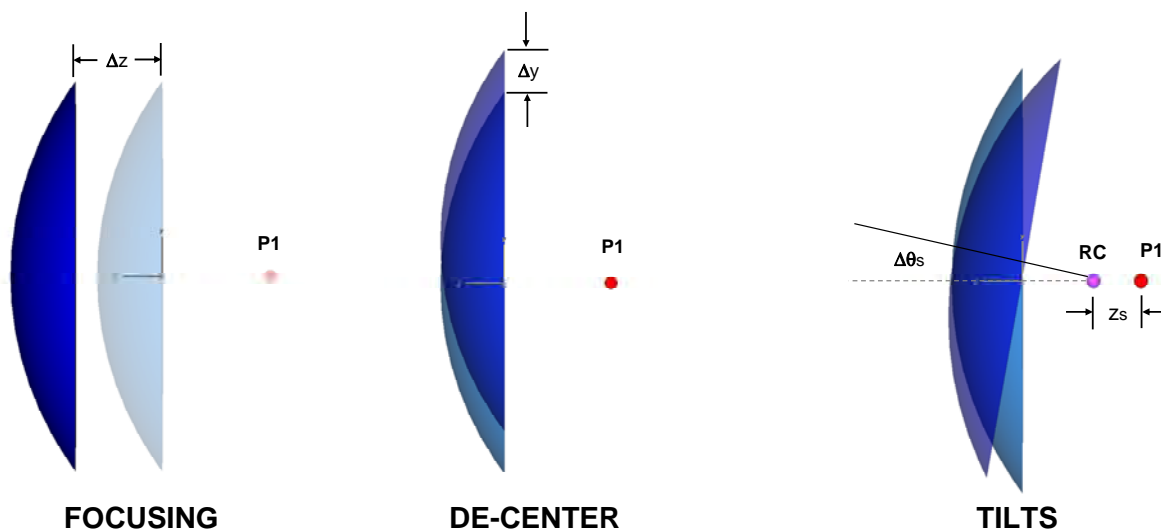


Figure 8.9. Simulated sub-reflector motions: (left) focusing, (center) de-centering, and (right) tilt. The system (equivalent) prime focus is at P1; The sub-reflector rotation (nutating) center is RC, located at a distance of z_s from P1. The sub-reflector tilt (nutating) angle is $\Delta\theta_s$.

We simulated three types of sub-reflector motion: *focus*, *de-center* and *tilt (or nutation)*. We show in Figure 8.9 the geometry and notation used in these sub-reflector motions. Figure 8.10 shows the variations in Strehl ratio of CCAT as a function of sub-reflector displacements for the three types of sub-reflector motion just mentioned. For focusing (or piston) motion we move the sub-reflector along the optical axis of the telescope by an amount $|\Delta z| \leq 2.5\lambda$. For de-center, we displaced the sub-reflector, perpendicularly with respect to the optical axis from its nominal position, by $|\Delta y| \leq 10.0\lambda$. For tilts (or nutation), we rotate the sub-reflector around a rotation (nutating) center z_s (see Figure 8.9 right), located between the telescope (equivalent) prime focus and the sub-reflector vertex. In particular, sub-reflector Tilt Strehl variations in Figure 8.10 correspond to the case for $z_s = 120\text{ cm}$, and the maximum sub-reflector tilt angle is $|\Delta\theta_s|$ such that $|\Delta\theta_s \times D_2| \leq 20.0\lambda$.

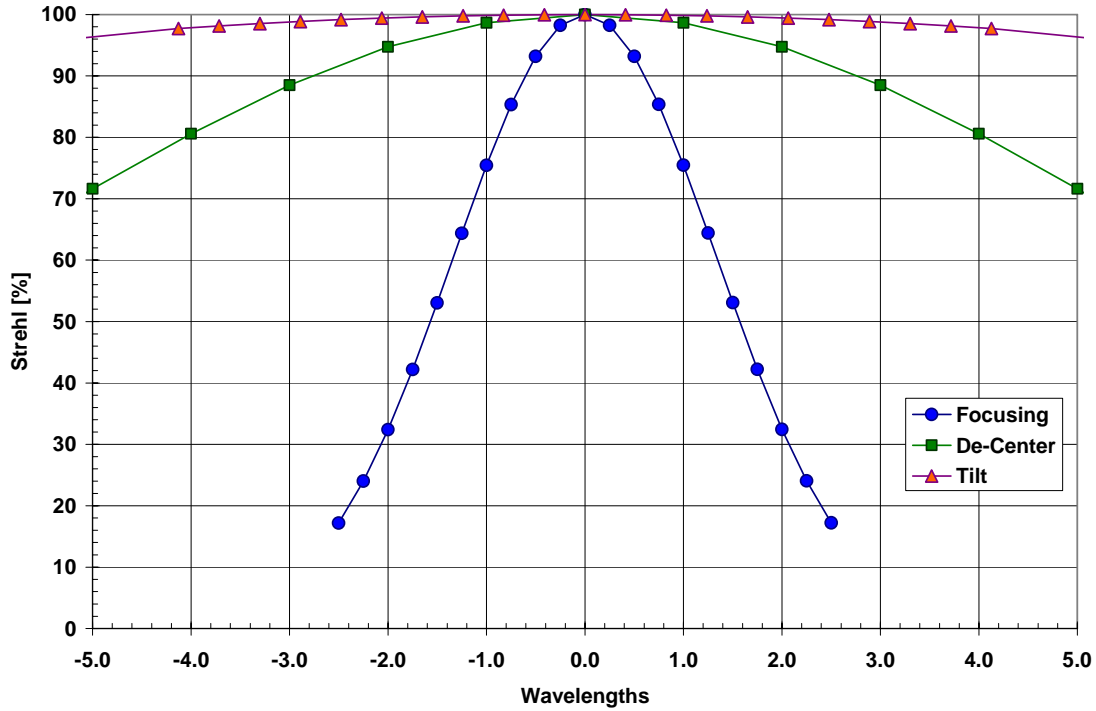


Figure 8.10. Sub-Reflector Positioning Sensitivities: Strehl ratio variation as a function of sub-reflector displacements for focusing (piston), de-center and tilt. The center of rotation is at $z=120$ cm from prime focus. (All calculations at $200 \mu\text{m}$.)

There are two considerations regarding sub-reflector positioning sensitivities, the first one has to do with loss in performance of the telescope due sub-reflector motion; and the second, has to do with the antenna pointing requirements at the highest frequency of operation.

8.3.1 Sub-reflector Sensitivities and Optical Performance

In terms of optical performance, the highest sensitivity corresponds to sub-reflector focusing. More specifically, in order to sustain an operational Strehl ratio better than, e.g., 95% at $200 \mu\text{m}$, and assuming no other contributions from the rest of the antenna optics, we have to maintain the sub-reflector focus within $\pm 80 \mu\text{m}$ from its nominal position. Similarly, sub-reflector de-centering should be kept within $\pm 350 \mu\text{m}$, and edge-to-edge displacements, due to sub-reflector tilt should be within ± 1.07 mm, (equivalently, sub-reflector tilts should be $|\Delta\theta_s| < 70$ arcsec for a M_2 diameter of 3.115 m), respectively, for the same Strehl ratio requirement.

From Figure 8.10 we see that the Strehl has a Gaussian dependence with respect to M_2 displacements of the form:

$$\text{Strehl}(\Delta\xi) = e^{-\alpha_\xi \Delta\xi^2} \quad (11)$$

Where, α_ξ is the Gaussian coefficient, and $\Delta\xi$ the respective displacement in wavelengths. The best fitted coefficients from Figure 8.9 data are presented in Table 8.7.

Table 8.7. Best Fitted Positioning Sensitivities for M_2 . ($\Delta\xi$ in wavelengths, and for tilts, $|\Delta\theta_s \times D_2| \leq 20.0\lambda$)

| | | Value |
|--------------|--------------------------|----------------------|
| Focus | α_{Focus} | $0.281753/\lambda^2$ |
| De-Centering | α_{Center} | $0.013174/\lambda^2$ |
| Tilt | α_{Tilt} | $0.001350/\lambda^2$ |

8.3.2 Sub-reflector Sensitivities and Antenna Pointing Requirements

The second consideration regarding sub-reflector positioning is the antenna pointing. The pointing requirement is one tenth of a beam; which, at 200 μm , translates to 0.2 arcsec. Both, sub-reflector de-centering and tilts affect the antenna pointing.

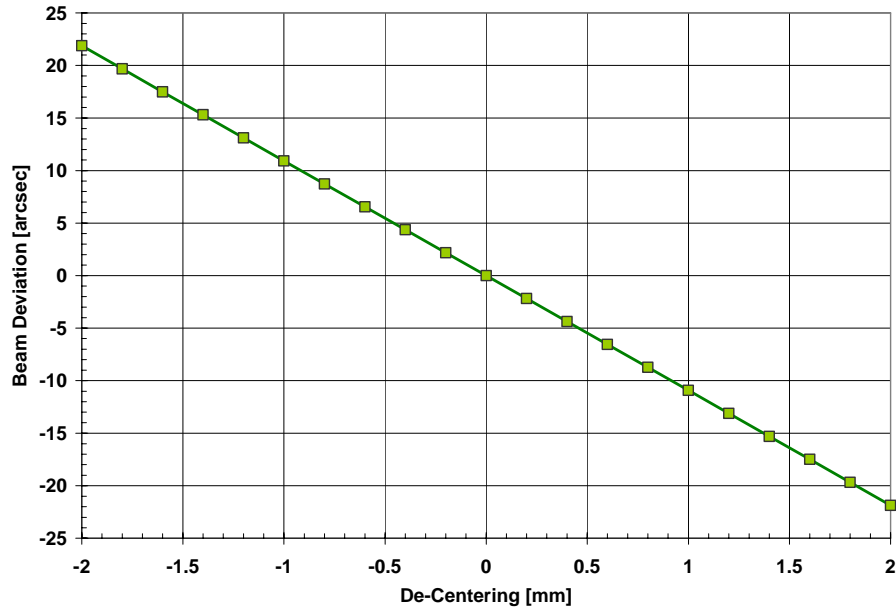


Figure 8.11. Antenna beam deviation vs. M_2 De-centering (at 200 μm .)

The telescope beam pointing varies linearly with sub-reflector de-centering (for de-centering errors of the order of 10λ at 200 μm) as shown in Figure 8.11. The corresponding factor or beam deviation sensitivity for M_2 is given in Table 8.8

Table 8.8. Beam Deviation Sensitivity for M_2 de-centering.

| | Value | Units |
|---|--------|-------------|
| $\frac{\Delta\theta_{BEAM}}{\Delta C_{center}}$ | -10.94 | (arcsec/mm) |

Therefore, to comply with the pointing requirement of one 10^{th} of a beam at 200 μm , we need to maintain the sub-reflector de-centering errors within 18 μm .

As expected, sub-reflector tilts also affect the telescope beam pointing direction, furthermore, the resultant sensitivity depends on the location of the center of rotation (nutation), z_s . Let's define,

$$\beta(z_s) = \left| \frac{\Delta\theta_{BEAM}}{\Delta\theta_s} \right| \tag{9.12}$$

where, $\Delta\theta_{BEAM}$ is the telescope beam deviation in the sky, and $\Delta\theta_s$ is the sub-reflector tilt. A plot of β as a function of z_s is presented in Figure 8.11.

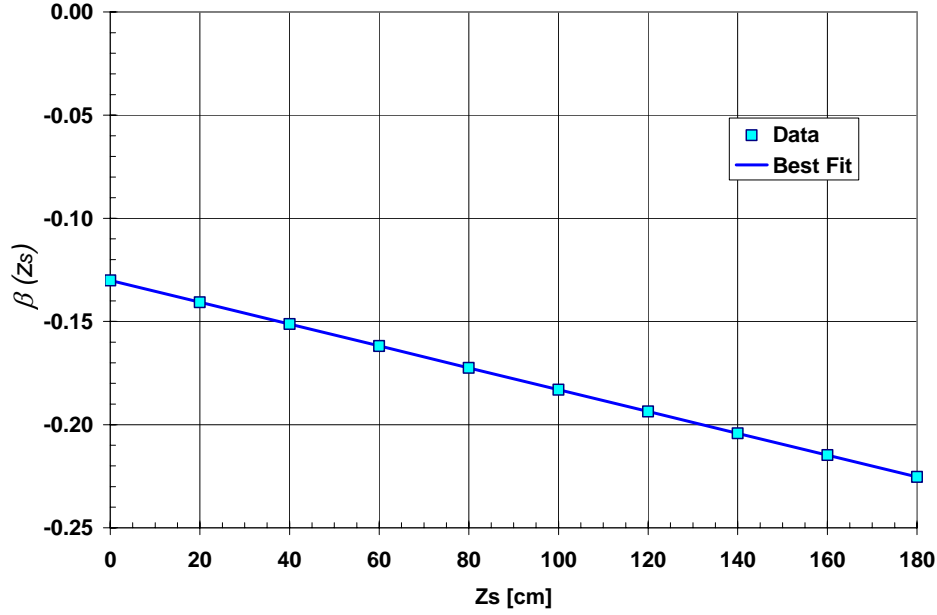


Figure 8.12. Beam deviation/Sub-Reflector tilt as a function of M2's rotation center location with respect to prime focus (at 200 μ m).

In this graph, Prime focus is at $z_s = 0.0$ cm, and the sub-reflector vertex is at $z_s = 181.4$ cm. $\beta < 0$, indicates that as the sub-reflector tilts in one direction with respect to the telescope optical axis, the beam in the sky deviates in the opposite direction.

We parameterized $\beta(z_s)$ in the following form [6]:

$$\beta(z_s) = - \left[\frac{a}{f} + b \left(\frac{1}{f_1} - \frac{1}{f} \right) z_s \right] \quad (9.13)$$

Where, f , and f_1 are the system and primary reflector focal length, shown in Table 8.2. The best fitting parameters are: $a = 26.0204$ m, and $b = 0.858306$.

The sub-reflector pointing sensitivity varies between $0.1301 \leq |\beta(z_s)| \leq 0.2261$ when z_s runs from prime focus to the secondary vertex. Consequently, a 10th of a beam pointing requirement at 200 μ m implies that sub-reflector tilts should be maintained within $|\Delta\theta_s| \leq 1.537$ arcsec, (for $z_s = 0$), or $|\Delta\theta_s| \leq 0.885$ arcsec, (for $z_s = 181.4$ cm). If we translate these to equivalent, edge-to-edge displacement of M2, we obtain $|\Delta\theta_s \times D_2| \leq 23.51$ μ m, with the center of rotation (nutation) at prime focus, and $|\Delta\theta_s \times D_2| \leq 13.53$ μ m, at the vertex of M2.

Summarizing, the positioning requirements for CCAT's sub-reflector are driven by the pointing sensitivities not by the optical performance sensitivities. From these, tilt sensitivity for pointing is the most stringent, requiring that the sub-reflector equivalent edge-to-edge displacements be less than 13.53 μ m, in the worst case. In terms of optical performance, focus sensitivity is the most relevant, requiring to maintain the sub-reflector focusing within 80 μ m for a 95% or better Strehl ratio, at 200 μ m.

8.3.3 Sub-Reflector Chopping and Optical Performance

The final aspect considered in the sub-reflector positioning sensitivities is the telescope performance for beam chopping operation. We calculated the telescope performance in terms of Strehl ratio for different values of beam throw as a function of the location of the sub-reflector center of rotation (nutation) as shown in Figure 8.12

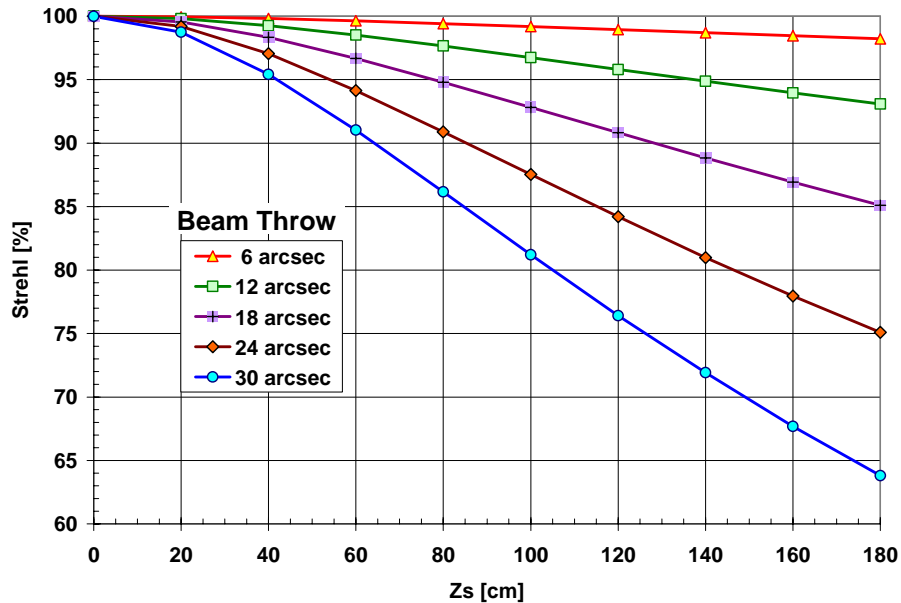


Figure 8.13. Sub-Reflector Chopping : Strehl ratio variation for five different beam throw values as a function of the center of rotation (nutation) at 200 μm

The chopping amplitude is measured in terms of beam throw in the sky, rather than the actual sub-reflector rotation angle.

We found that a 95% Strehl ratio is achievable for beam throws between 3 to 6 beam widths when the center of rotation (nutation) is less than 120 cm away from prime focus.

Further details about the sub-reflector nutator may be found in [7].

8.4 Active Surface Segmentation Analysis

8.4.1 Active surface layout and segmentation effects

The current active surface concept uses pie shaped segments; each segment has three actuators that provide piston and tilt/tip control for positioning and orientation. There are two possible segmentation layouts under consideration for the active surface of CCAT as shown in Figure 8.14; both with six-fold symmetry.

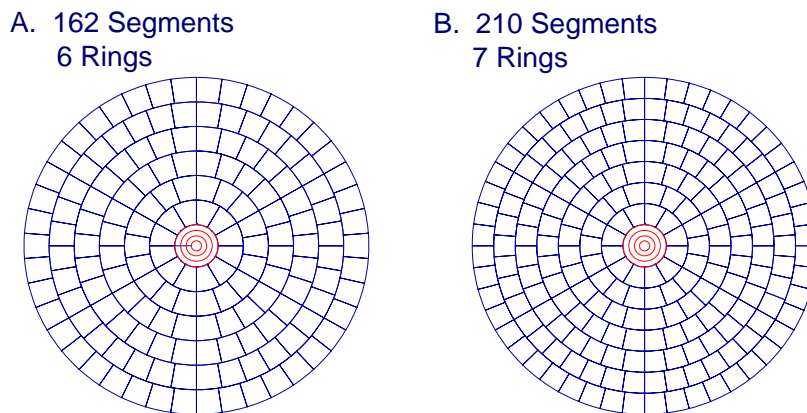


Figure 8.14. Layouts under consideration for the primary active surface of CCAT. Layout A, on the (left), has 6 rings with 162 segments. Layout B, on the (right), has 7 rings with 210 segments.

Layout-A consists of six rings and 162 segments with a 2 m base size; Layout-B consists of 210 segments with a 1.7 m base size. There are 12 segments in the first ring and six additional segments in each subsequent ring. In general, the number of segments with this type of symmetry is given by:

$$N_s = 3n(n+3) \tag{14}$$

Where, n is the total number of rings.

For purpose of analysis of the effects of segmentation of CCAT active surface we are considering only Layout-A.

Figure 8.14 shows, on the top-left, the full aperture phase distribution of the CCAT with segmented primary active surface and on the top-right a close-up. Figure 8.14 (bottom-left) shows a 6.8' x 6.8' far field radiation pattern map of the antenna; and on the right, an inset of 3.4' x 3.4'. In this simulation we use uniform aperture illumination at 200 μm .

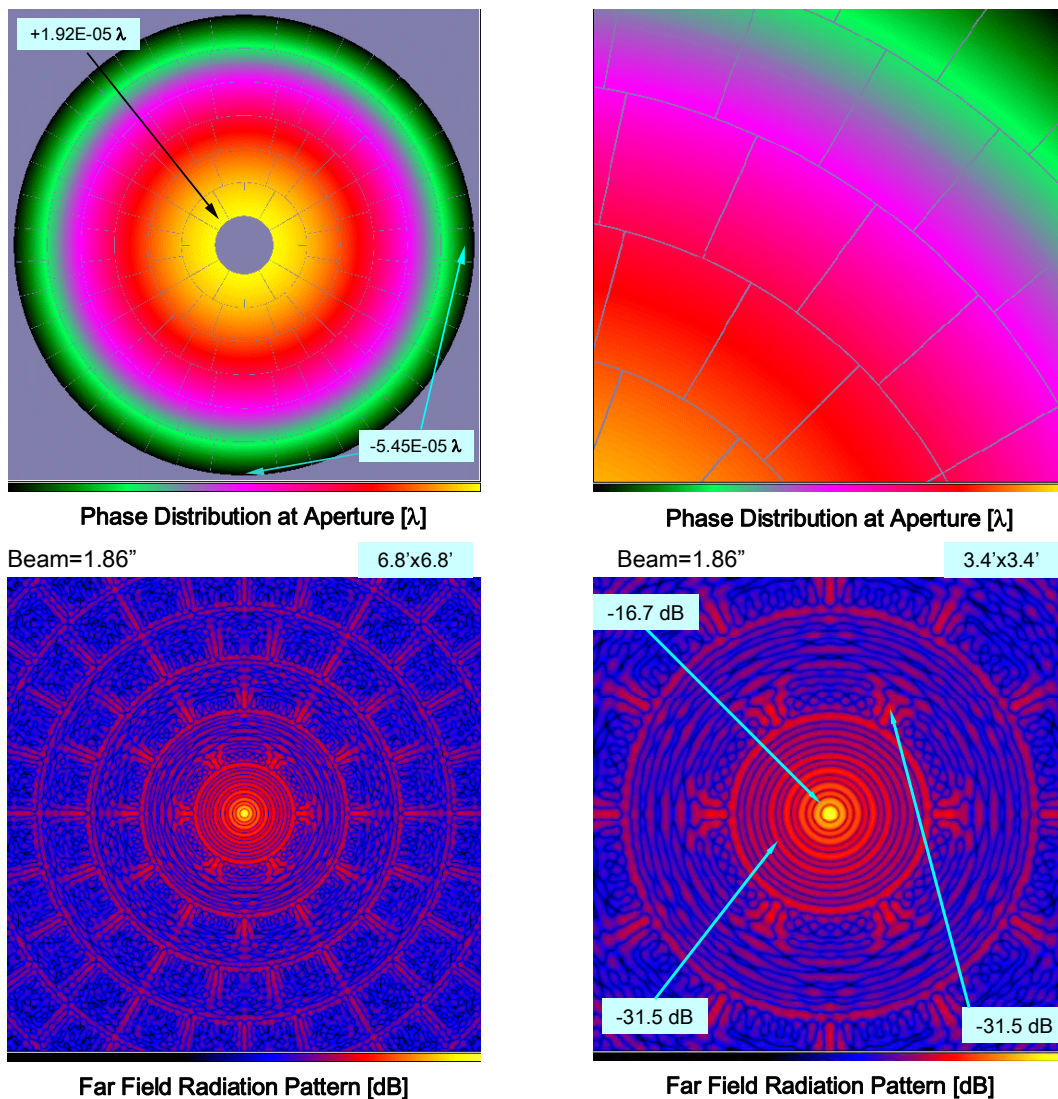


Figure 8.15. On the top we show the aperture phase distribution of CCAT with segmented active surface, full aperture (left) and a close-up (right). On the bottom-left we show a 6.8' x 6.8' map of far field co-polar radiation pattern of the CCAT with the segmented active surface; and on the right, a 3.4' x 3.4' inset of the previous map. (uniform aperture illumination at 200 μm).

The six-fold symmetry of the active surface layout is noticeable in the grating lobes of the radiation pattern. The first set of grating lobes⁶ has a power level of -31.5 dB with respect to the main beam.

The first grating lobes are located at a radius of approximately 10 times the First Null Full Width (FNFV) of the beam, which is related to the scale length of the telescope aperture and average segment size.

8.4.2 Active Surface Segment Positioning Errors and Strehl

This section presents the results of a study relating the active surface segment positioning errors with the optical performance of CCAT in terms of Strehl ratio.

In general, the CCAT active surface control system will sense and correct piston and tilt/tip segments errors and even possible large scale errors distributed over the main aperture of the telescope⁷. Nevertheless, segment setting errors will occur during the construction some of which the active surface control system may not be able to directly sense or control. Therefore, a set of specifications, in terms of positioning standard deviation, has to be given for the initial placement of the segments on the active surface.

In order to make this study very comprehensive, in addition to segment piston and tilt/tip errors, we included also radial, azimuth and segment twist positioning errors. Figure 8.15 shows details of these positioning errors and the variables used to describe them.

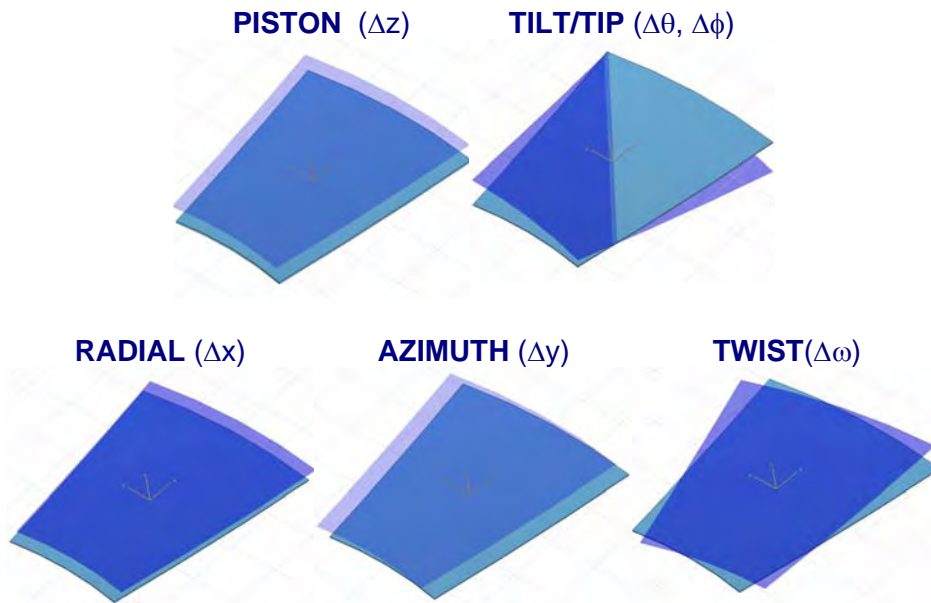


Figure 8.16. Types of segment positioning errors considered for this study.

Methodology

For the study, we made a Monte Carlo simulation in which we generated a statistical ensemble, of active segmented surface telescopes with random positioning errors, for each particular type of segment error and within a specified range. Segment positioning errors within a given telescope sample have a Gaussian distribution with *standard deviation* σ_i , all with the exception of segment tilt/tip errors, which use two random distributions instead of one. A summary of the random positioning errors variables and parameterization used in the simulation is presented in Table 8.9.

⁶The nominal gap size between segments is approximately 5 mm. Nevertheless, we used a 4 cm gap between segments in order to make more apparent the effects of the segmentation in the far field radiation pattern.

⁷ For example: large scale residual manufacturing errors of the sub-reflector [8].

Table 8.9. Parameters used in CCAT random segment positioning errors simulation.

| Segment Positioning Error | Random Variable | Standard Deviation | Distribution (zero mean) |
|----------------------------------|------------------------|---------------------------|------------------------------------|
| Piston | Δz | σ_z | Gaussian |
| Tilt/Tip | $\Delta\theta$ | σ_θ | Gaussian |
| | $\Delta\phi$ | σ_ϕ | Uniform $[0, 2\pi]$ |
| Radial | Δx | σ_x | Gaussian |
| Azimuth | Δy | σ_y | Gaussian |
| Twist | $\Delta\omega$ | σ_ω | Gaussian |

We define *piston errors* as displacements along the *normal* to the surface at the geometric center of the segment. These displacements are Gaussian distributed with zero mean.

For *tilts/tips errors* the *center of rotation or tilt* is located at the middle of the segment. As we mentioned, this particular case uses two random distributions: one for the actual segment tilt/tip, which is Gaussian distributed with zero mean with respect to the *surface normal* direction of segment, and the other for the orientation of the tilt/tip, which is *uniformly distributed* over the interval $[0, 2\pi]$.

Radial, azimuth and twist errors correspond to segment displacements on a plane tangent to the geometric center of that particular segment. Each of these errors has a Gaussian distribution with zero mean.

It is important to notice that, while segment piston errors and tilt/tip errors are directly controlled by the segment actuators of CCAT active control surface, lateral segment displacements, nor twist errors, on the other hand, can be directly controlled by the active surface of CCAT.

After setting the segmented surfaces, all telescope samples within the ensemble are then analyzed at a wavelength of 200 μm using forward electromagnetic ray-tracing with uniform illumination, and their performance characterized, in terms of Strehl ratio, for that particular type of segment positioning error.

In order to make the connection between the standard deviation of a particular type of segment error distribution with the optical performance of the telescope sample, we use a non-linear fit model of a modified form of Ruze's formula:

$$\eta_{RUZE_i} = e^{-\left(\frac{4\pi \kappa_i \sigma_i}{\lambda}\right)^2} \quad (15)$$

Here, κ_i is the Ruze's *coefficient* associated to the mean value of *structural rms surface error* produced by a random distribution of segment positioning errors of i^{th} type and standard deviation σ_i , i.e.,

$$\varepsilon_{rms_i} = \kappa_i \sigma_i \quad (16)$$

is the associate structural rms surface error.

Segment Piston Errors

This ensemble consisted of main reflectors with Gaussian distributed segment piston errors, and standard deviation running from 0 to 20 μm , in discrete steps. For each standard deviation we generated five samples. A graph of the Strehl ratio obtained in this simulation as a function of standard deviation is presented in Figure 8.16. The best fitted Ruze's coefficient is 0.9542.

The three left images in Figure 8.19 show a sample of this piston error ensemble corresponding to a standard deviation of 6 μm , and a Strehl ratio of 89.6%. The top-left image corresponds to the phase distribution on the

aperture, where the maximum and minimum piston errors in wavelengths are $+0.1196\lambda$ and -0.3763λ respectively. The structural rms surface error of this case is $\epsilon_{\text{rms}} = 0.0264\lambda$ or $5.7 \mu\text{m}$.

Figure 8.19 (middle-left) is a close-up of a small region in the aperture phase distribution showing a more detail variation of the phase across single segments. In particular, we show two segments with an average piston error of $+0.1081\lambda$ and -0.3707λ respectively, with a very small phase gradient across the segment face of the order of $0.04 \mu\text{m}$. Finally, Figure 8.19 (bottom-left) shows a $3.4' \times 3.4'$ map of the far field co-polar radiation pattern of this case with a SLL of -15.1 dB .

Segment Tilt/tip Errors

We generated an ensemble of CCAT's main reflectors with Gaussian distributed tilt/tip errors with standard deviation ranging from 0 to 8 arcsec and zero mean. While we mentioned earlier, that the actual tilt orientation of each segment is uniformly distributed from 0 to 2π , we use only the Gaussian standard deviation as the parameter of the sample. The best fitted Gaussian parameter⁸ is $0.152014 \text{ arcsec}^{-1}$, which expressed as *equivalent linear edge* displacement of a 2 m base-size (1 m radius) segment gives the Ruze's coefficient: 0.4990, i.e., half of what we obtained for segment piston errors. Figure 8.17 shows the Strehl ratio variation as function of Tilt/tip *equivalent* standard deviation in micrometers.

The right column in Figure 8.19 shows a sample of the tilt/tip error ensemble data corresponding to a standard deviation of $\sigma_0 = 3 \text{ arcsec}$, or equivalent linear standard deviation of $\sigma_{\text{tilt}} = 14.5 \mu\text{m}$, and a Strehl ratio of 80.7%. The aperture phase distribution map in the top-right shows the characteristic segment phase signatures for random orientation tilts.

The structural rms surface error of this case is $\epsilon_{\text{rms}} = 0.0369\lambda$ or $7.4 \mu\text{m}$. Figure 8.19 (middle-right) is a close-up of the aperture phase distribution showing a more detail variation of the phase across single segments. In particular, we show the phase gradient variation across two segments, one with $\Delta\phi = 0.0278\lambda$ ($5.5 \mu\text{m}$), and other with a larger variation of $\Delta\phi = 0.2123\lambda$ ($42.5 \mu\text{m}$), respectively. Lastly, Figure 8.19 (bottom-right) shows the far field co-polar radiation pattern for this sample with a SLL of -16.8 dB .

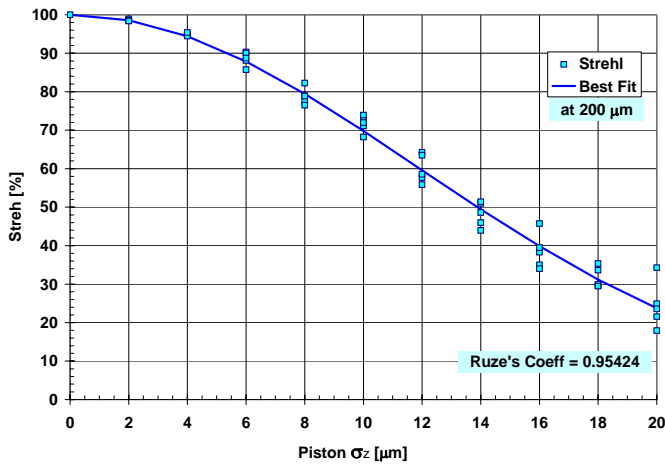


Figure 8.17. Segment Piston Errors: Strehl ratio vs. standard deviation at 200 μm

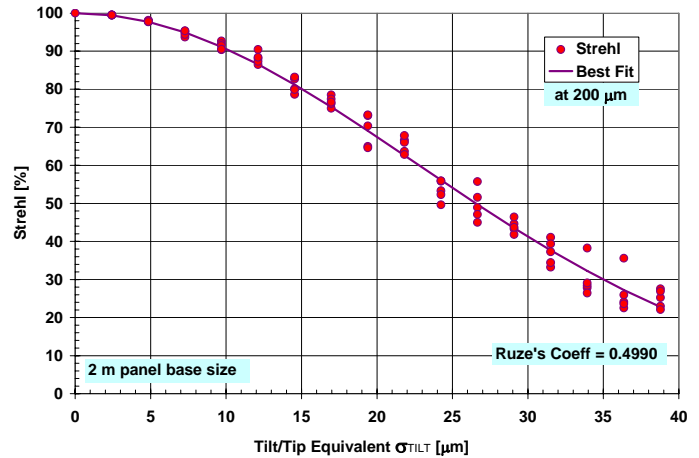


Figure 8.18. Segment Tilt/tip Errors: Strehl ratio vs. *equivalent* standard deviation for a 2 m panel-base size at 200 μm

⁸ Just a simple Gaussian fit to the tilt/tip angle.

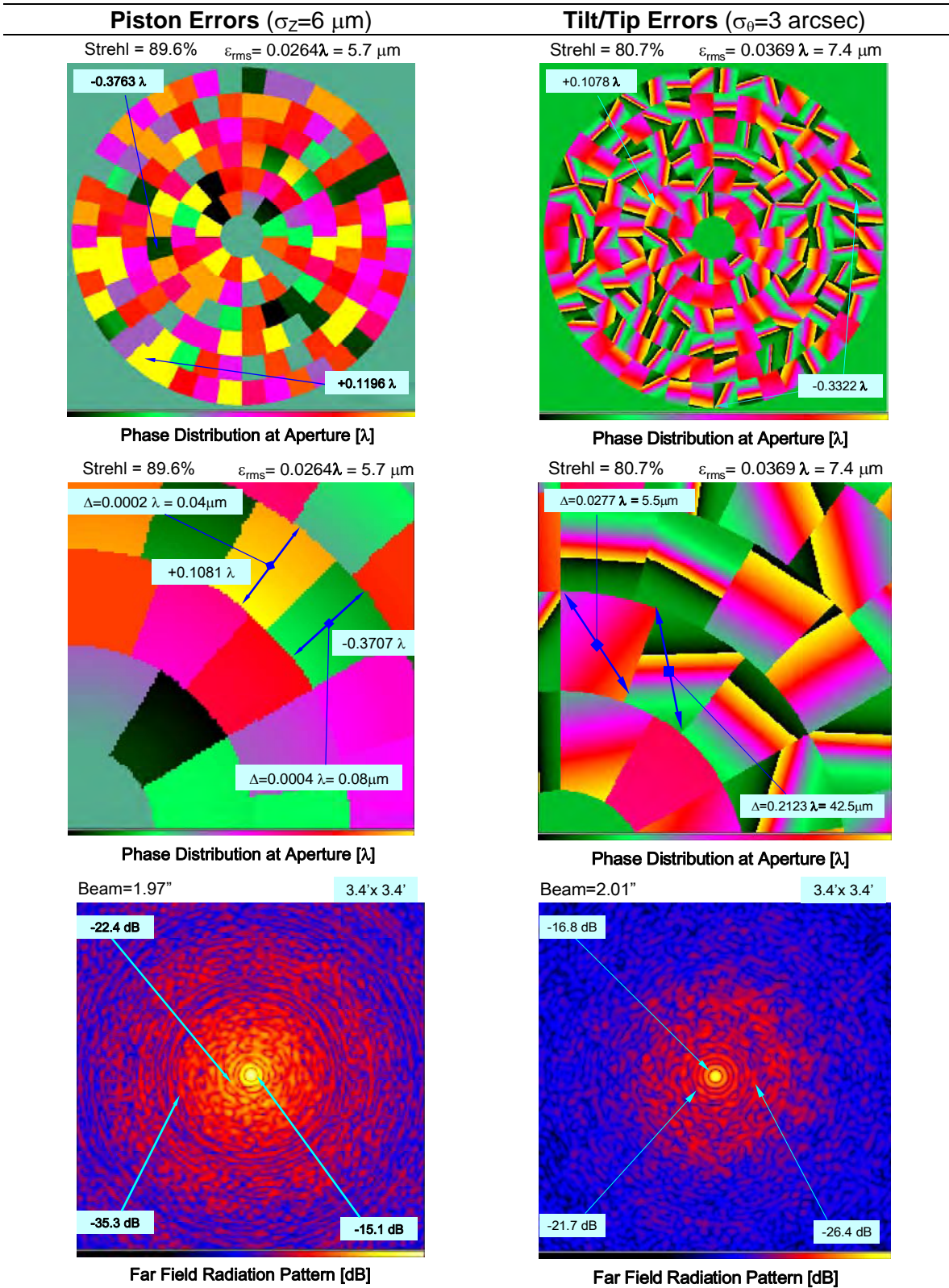


Figure 8.19. CCAT Segmented active surface errors. Piston (left), and Tilt/Tip errors (right). From top to bottom: aperture phase distribution, close-up of the aperture phase, and a 3.4' x 3.4' map of far field radiation pattern (*Uniform illumination at 200 μm*).

Segment Radial Errors (Δx)

This is the first non-directly controllable type of segment positioning error using only three actuators per segment that we analyzed. For this simulation ensemble we generated samples of CCAT's segmented active surface with Gaussian distributed radial segment positioning errors with standard deviation varying from 0 to 1mm, and zero mean. We move the segments along the tangent plane that passes through the center of the segment (i.e., perpendicular to the normal there). A graph of the Strehl ratio variation as a function of standard deviation is shown in Figure 8.20. The best fitted Ruze's coefficient for radial segment displacements is 1.543×10^{-2} .

The left column in Figure 8.22 corresponds to a sample of radial segment errors with standard deviation of $\sigma_x = 0.3$ mm, and a Strehl ratio of 91.9%. The top-left image corresponds to the phase distribution on the aperture; notice the characteristic *circular* shape of the radial displacement errors. The structural rms surface error of this case is $\epsilon_{\text{rms}} = 0.0231\lambda$ or $4.6 \mu\text{m}$. Figure 8.22 (middle-left) is a close-up of a small region in the aperture phase distribution showing a more detail variation of the phase across single segments. In particular, we show the radial gradient phase variation across two segments, one with a large phase variation of $\Delta\phi = 0.0792\lambda$ ($15.9 \mu\text{m}$), and other with a very small variation of $\Delta\phi = 0.0151\lambda$ ($3.0 \mu\text{m}$), respectively. Figure 8.21 (bottom-left) shows the far field co-polar radiation pattern for this sample of radial segment errors with a SLL of -16.2 dB. Notice the circular features of the radiation pattern in contrast with the tilt/tip far field pattern.

Segment Azimuth Errors (Δy)

This is the second non-directly controllable segment positioning errors. For this case we generated a Gaussian distributed azimuth segment displacement errors with standard deviation varying from 0 to 1mm and zero mean. A graph of the Strehl ratio variation as a function of standard deviation is shown in Figure 8.21. The best fitted Ruze's coefficient for azimuth segment displacement errors is 1.468×10^{-2} , i.e., slightly lower than for radial displacement errors which means that the optics is less sensitive to azimuth of errors than to radial, as expected.

The right column of Figure 8.22 shows a sample of azimuth segment errors corresponding to a standard deviation of $\sigma_y = 0.3$ mm, and a Strehl ratio of 90.8%. The top-left image corresponds to the phase distribution on the aperture with a characteristic *radial* shape of the azimuth displacement errors. The structural rms surface error of this case is $\epsilon_{\text{rms}} = 0.0247\lambda$ or $4.9 \mu\text{m}$.

Figure 8.22 (middle-right) is a close-up of a small region in the aperture phase distribution showing a more detail variation of the phase across single segments. Specifically, we show the azimuth-oriented gradient phase variation across two segments, one with a large phase variation $\Delta\phi = 0.1008\lambda$ ($20.2 \mu\text{m}$), and other with a very small variation of $\Delta\phi = 0.0289\lambda$ ($5.7 \mu\text{m}$), respectively. Lastly, Figure 8.21 (bottom-right) shows the far field co-polar radiation pattern for this sample of radial segment errors with a SLL of -17.1 dB. Notice the *radial* features of the radiation pattern in contrast with the radial segment error displacement far field pattern sample, on the left.

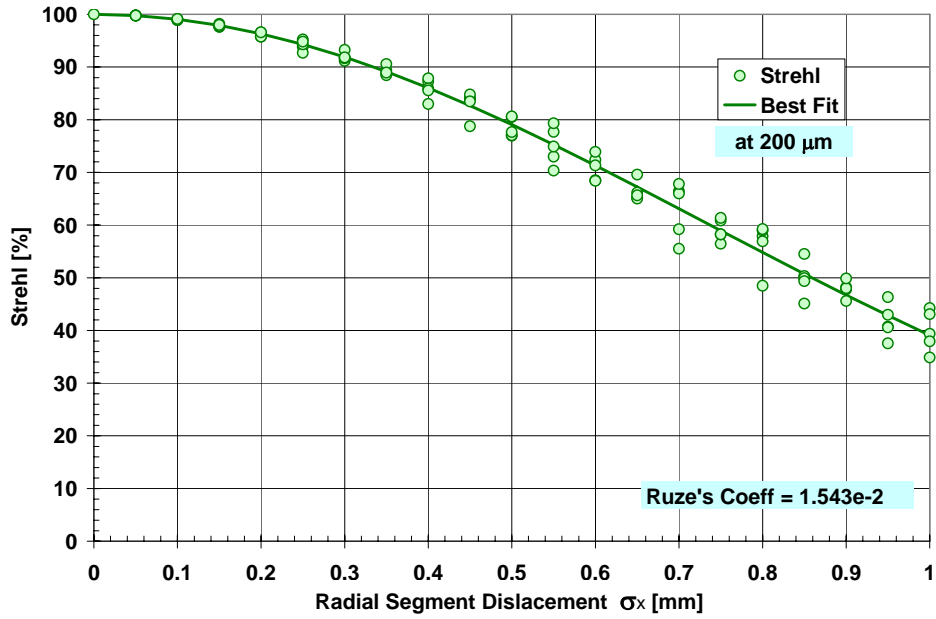


Figure 8.20. Segment Radial Errors: Strehl ratio vs. standard deviation at 200 μm

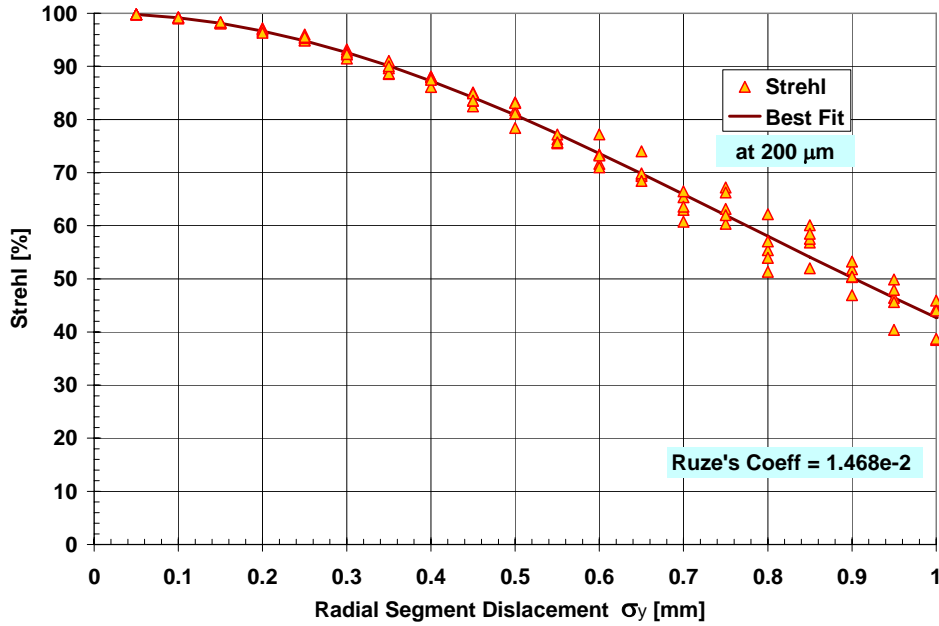


Figure 8.21. Segment Azimuth Errors: Strehl ratio vs. standard deviation at 200 μm

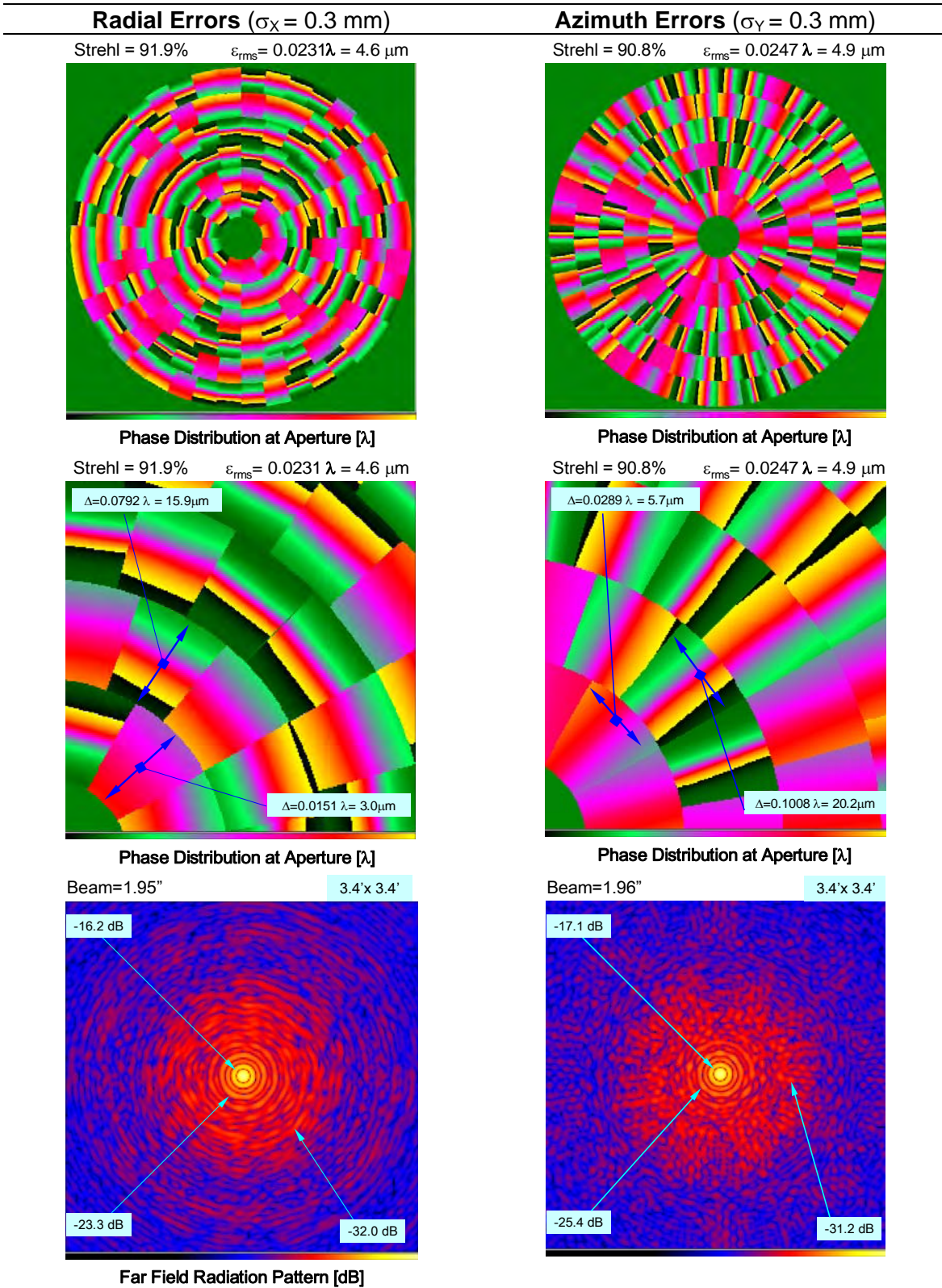


Figure 8.22. CCAT Segmented active surface errors. Radial (left), and Azimuth errors (right). From top to bottom: aperture phase distribution, close-up of the aperture phase, and a 3.4' x 3.4' map of far field radiation pattern (*Uniform illumination at 200 μm*).

Combined Radial and Azimuth Segment Errors ($\Delta x + \Delta y$)

We also made a simulation of combined radial and azimuth segments errors. Gaussian distributed in both directions, with standard deviations varying from 0 to 1mm, and zero mean. The resultant graph of Strehl ratio variation as a function of standard deviation is presented in Figure 8.23. The best fitted Ruze's coefficient for combined radial + azimuth segment displacements is 2.123×10^{-2} , essentially the RSS of the individual radial and azimuth Ruze's coefficients. We also show in the same figure the individual radial and azimuth Strehl ratio variation vs. standard deviation for comparison purposes.

The left column in Figure 8.25 shows a sample of the combined radial + azimuth segment errors that corresponding to a standard deviation of $\sigma_x = \sigma_y = 0.3$ mm, and a Strehl ratio of 83.9%. The top-left image is the phase distribution on the aperture, practically indistinguishable from a segment Tilt/Tip error case. Which means that, all thought this type of error is not directly controllable by three linear actuators per segment, it may be *compensated* by tilting the segments. The structural rms surface error of this case is $\epsilon_{\text{rms}} = 0.0333\lambda$ or $6.7 \mu\text{m}$.

Figure 8.25 (middle-left) shows a close-up of the phase distribution across single segments. In particular, we show the gradient phase variation across two segments, one with phase variation of $\Delta\phi = 0.0905\lambda$ ($18.1 \mu\text{m}$), and other with a smaller variation of $\Delta\phi = 0.0418\lambda$ ($8.4 \mu\text{m}$), respectively, which is of the same order of a pure segment Tilt/Tip error case. Figure 8.25 (bottom-left) shows the far field co-polar radiation pattern for this sample of combined radial and azimuth segment errors.

Segment Twist Errors ($\Delta\omega$)

The third case of non-directly controllable segment positioning errors is segment twists. For this case we generated a Gaussian distributed segment twist errors with standard deviation varying from 0 to 100 arcmin and zero mean. A graph of the Strehl ratio variation as a function of *equivalent* twist standard deviation in mm, for a 2 m base-size segment, is shown in Figure 8.24. The best fitted Ruze's coefficient for segment twist errors is 7.24×10^{-4} .

The right column of Figure 8.25 illustrates one sample of azimuth segment errors corresponding to a standard deviation of $\sigma_\omega = 1^\circ$, and a Strehl ratio of 43.5%. The top-right image shows the phase distribution on the aperture; notice the characteristic shape signature of segment *twist* errors. The structural rms surface error of this case is $\epsilon_{\text{rms}} = 0.0726\lambda$ or $14.5 \mu\text{m}$. Figure 8.25 (middle-right) is a close-up of a small region in the aperture phase distribution showing a more detail variation of the phase across single segments. Particularly, we show the non-linear *saddle shaped* phase variation across two segments, one with total a phase variation of $\Delta\phi = 0.1558\lambda$ ($31.1 \mu\text{m}$), starting at the top-right corner of the segment, down to the segment center and then down (in phase) to the segment upper left corner. In the same fashion, the other segment has a smaller phase variation of $\Delta\phi = 0.0107\lambda$ ($2.1 \mu\text{m}$). Clearly this type of non linear errors cannot be corrected or compensated by three linear actuators per segment. Finally, Figure 8.25 (bottom-right) shows the far field radiation pattern for this sample of segment twist errors with a SLL of -17.2 dB.

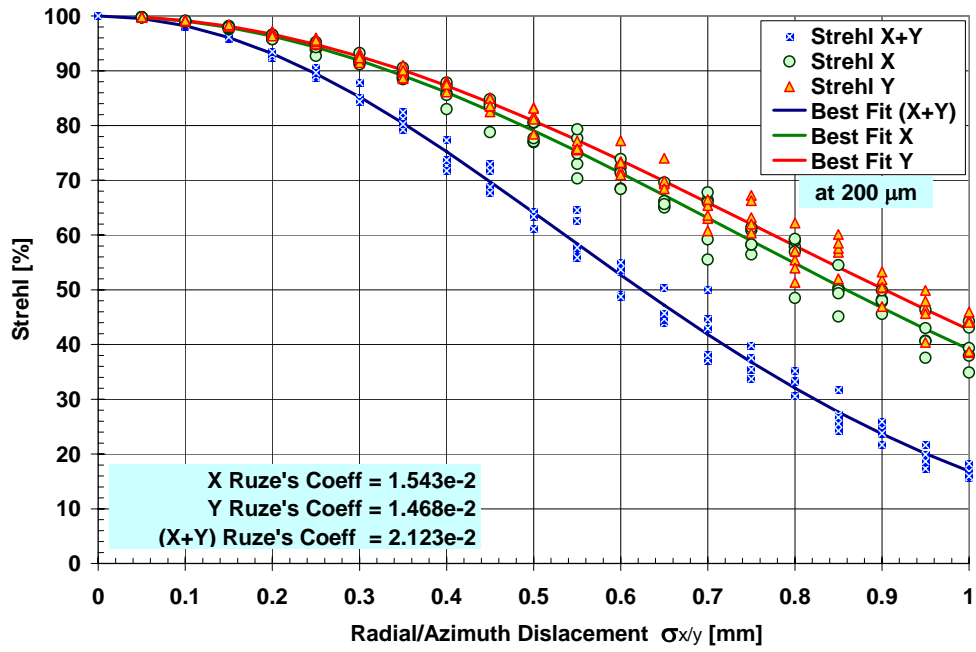


Figure 8.23. Combined Segment Radial and Azimuth Errors: Strehl ratio vs. standard deviation at 200 μm . For comparison, the figure includes the individual Strehl ratio vs. standard deviation.

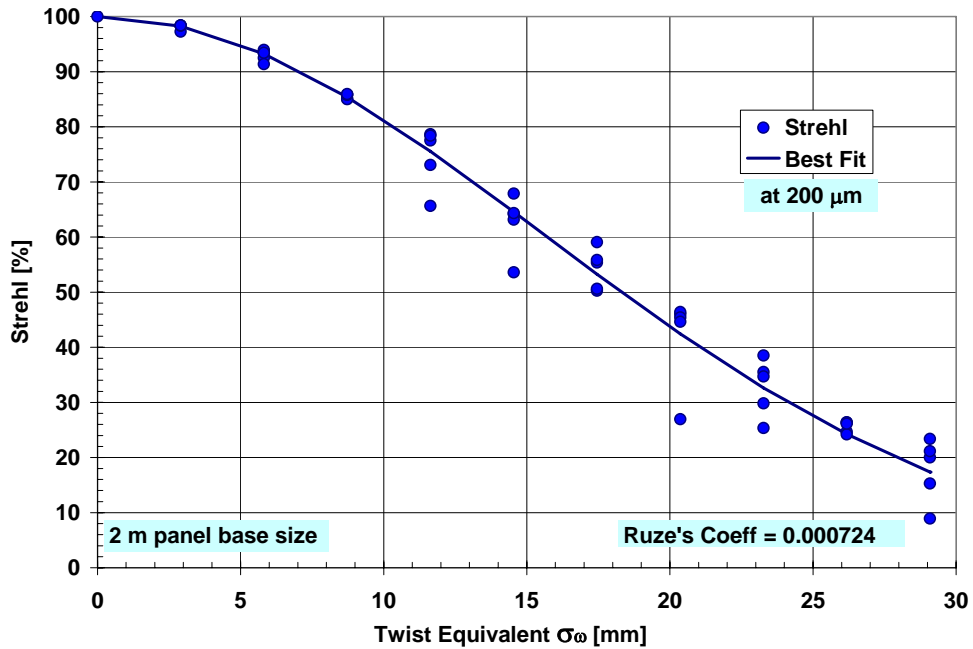


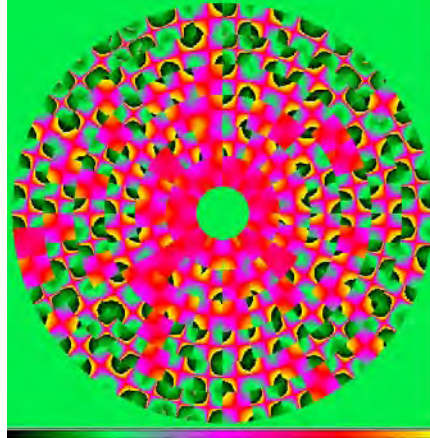
Figure 8.24. Segment Twist Errors: Strehl ratio vs. equivalent standard deviation at 200 μm for a 2 m panel base size.

Radial + Azimuth Errors ($\sigma_X = \sigma_Y = 0.3 \text{ mm}$)

Twist Errors ($\sigma_\omega = 1^\circ$)

Strehl = 83.9% $\epsilon_{\text{rms}} = 0.0333\lambda = 6.7 \mu\text{m}$

Strehl = 43.5% $\epsilon_{\text{rms}} = 0.0726\lambda = 14.5 \mu\text{m}$

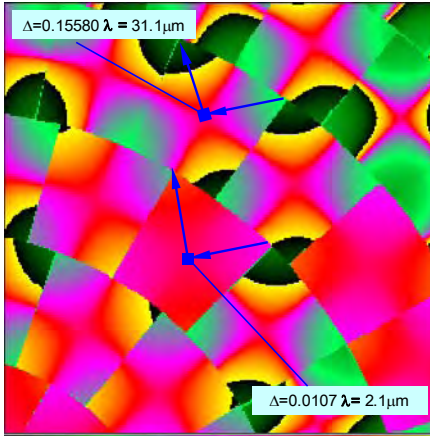
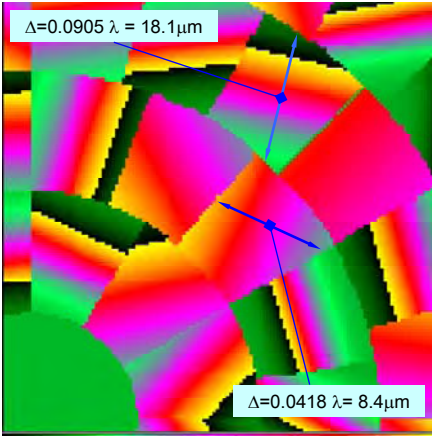


Phase Distribution at Aperture [λ]

Phase Distribution at Aperture [λ]

Strehl = 83.9% $\epsilon_{\text{rms}} = 0.0333\lambda = 6.7 \mu\text{m}$

Strehl = 43.5% $\epsilon_{\text{rms}} = 0.0726\lambda = 14.5 \mu\text{m}$

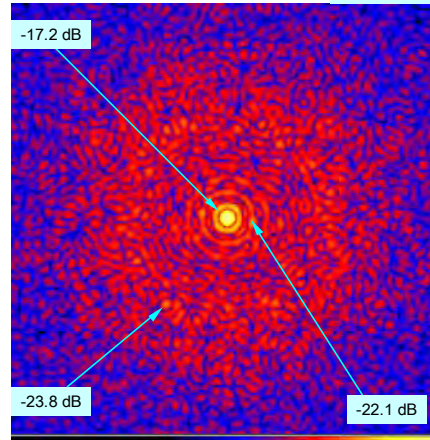
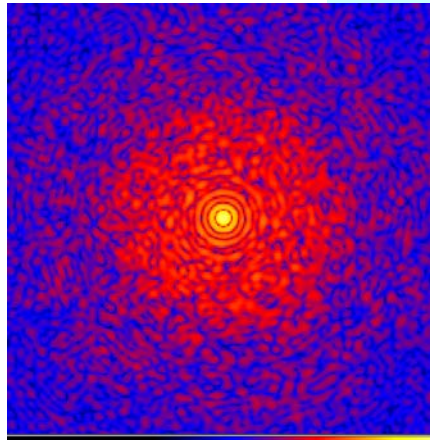


Phase Distribution at Aperture [λ]

Phase Distribution at Aperture [λ]

Beam=2.04" 3.4'x3.4'

Beam=2.35" 3.4' x 3.4'



Far Field Radiation Pattern [dB]

Far Field Radiation Pattern [dB]

Figure 8.25. CCAT Segmented active surface errors. Radial and Azimuth (**left**), and Twist errors (**right**). From top to bottom: aperture phase distribution, close-up of the aperture phase, and a 3.4' x 3.4' map of far field radiation pattern (*Uniform illumination* at 200 μm).

Table 8.10. Best fitted Ruze’s coefficients for random segment positioning errors (200 μm)

| Ruze’s Coefficient | Symbol | Value | Controllable ⁹ |
|--|------------------|---------|---------------------------|
| Segment Piston Displacement | κ_z | 0.95424 | Yes |
| Segment Tilt/Tip (Equiv. Edge Displacement*) | κ_{TILT} | 0.49903 | Yes |
| Segment Radial Displacement | κ_X | 0.01543 | Indirectly |
| Segment Azimuth Displacement | κ_Y | 0.01468 | Indirectly |
| Segment Twist (Equiv. Edge Displacement*) | κ_{TWIST} | 0.00073 | No |

* For a 2 m panel base-size

8.4.3 Summary

Table 8.10 presents the best fitted Ruze’s coefficients for CCAT segment positioning errors for all the cases studied.

The combined structural rms surface error is given simply by,

$$\varepsilon_{rms} = \sqrt{(\kappa_z \sigma_z)^2 + (\kappa_{tilt} \sigma_{tilt})^2 + (\kappa_x \sigma_x)^2 + (\kappa_y \sigma_y)^2 + (\kappa_\omega \sigma_\omega)^2} \quad (17)$$

The dominant error is piston displacement, which indicates that the overall active surface structural rms surface error depends directly on residual segment piston errors. Segment tilt/tip errors are half as important.

Combined radial and azimuth segments errors have less impact and can be indirectly compensated by segment tilt/tip corrections.

Segment twist errors produce non-linear phase distribution errors across the segment faces, which can not be compensated by the current active surface concept; fortunately, their impact is very small to the overall structural rms error: twist errors producing a 10 mm of equivalent edge segment displacement standard deviation result in 80% Strehl ratios, (see Figure 8.24).

Lastly, Figure 8.26 illustrates the Strehl ratio variations vs. segment piston errors that we could expect for CCAT at two different wavelengths: 350 μm and 200 μm respectively.

⁹ With an active surface that senses and controls segment piston and tilt/tip errors only.

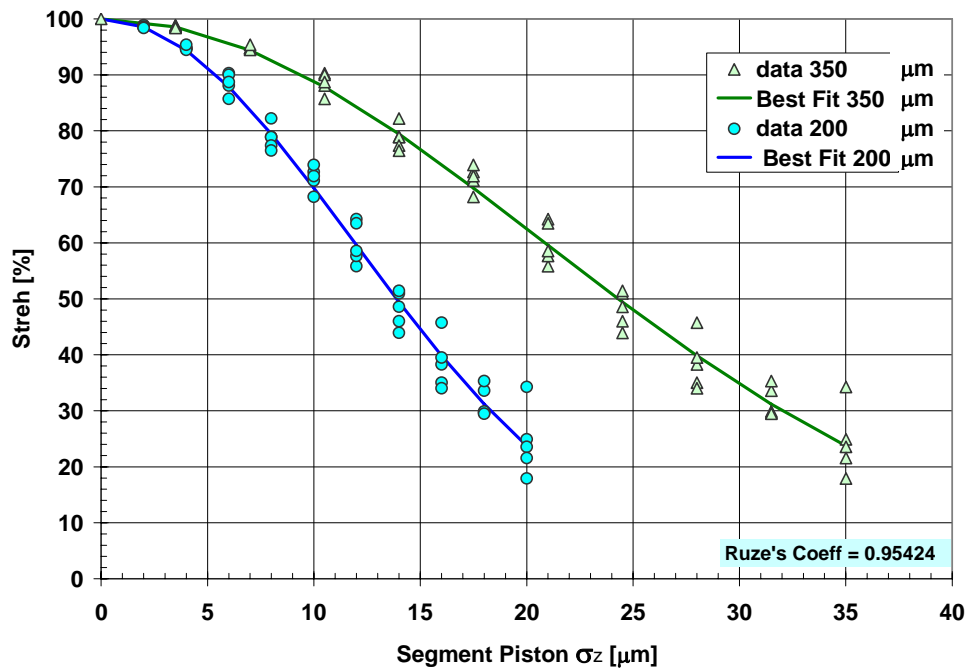


Figure 8.26. Strehl ratio vs. standard deviation for piston errors at 350 μm and 200 μm

8.5 References

- [1] D. J. Schroeder. *Astronomical Optics*. San Diego, Academic Press, 1987.
- [2] Terry Herter and Germán Cortés, “CCAT Optical Design”, *CCAT-Technical Memo TM-005*, May 9, 2005.
- [3] M. Born and E. Wolf, *Principles of Optics, Electromagnetic Theory of Propagation, Interference and Diffraction of Light*. Cambridge University press, 7th Ed. ch. 9, 1999.
- [4] V. N. Mahajan, “Aberrated Point Spread Functions for Rotationally Symmetric Aberrations”. *Applied Optic*, Vol. 22, No. 19, pp. 3035-3041, Oct. 1983
- [5] J. Ruze, “Antenna Tolerance Theory”. *Proc. IEEE*, Vol. 54, pp. 633-640, Apr. 1966.
- [6] Lamb, J. W, “Optimized Optical Layout for MMA 12m Antennas”, *MMA Memo 246*, NRAO, 1999.
- [7] Simon .J.E. Radford and Germán Cortés, “Considerations for a Secondary Mirror Nutator”, *CCAT-Technical Memo*. Aug. 2005.
- [8] Germán Cortés, Rogerio Enriquez, Amy Lowell and David R. Smith. “Using an Active Primary Surface to Correct for low-order Manufacturing Errors in Secondary Mirrors of Large Reflector Antennas”. *Astronomical Structures and Mechanisms Technology*, edited by Joseph Antebi, Dietrich Lemke, *Proceedings of SPIE Vol. 5495* (SPIE, Bellingham, WA, 2004) pages 126-136.

9 Systems Engineering

9.1 Introduction

System engineering addresses the Wave Front Error (WFE), image quality, pointing/tracking accuracy and other design issues that will affect the operations and quality of the science obtained with CCAT. The WFE budget includes the primary, secondary, and tertiary, optics and achieving the specified telescope WFE is anticipated to be one of the most challenging aspects of the Project. As such it will receive most of the attention in this section.

Both top-down and bottom-up error budgets are being developed to ensure the final CCAT design will meet the demanding science driven image quality requirements. These can be summarized by a few dominant design specifications. Efficient operation at 200 μm implies the net effective surface error be less than 10 μm and that you be able to find and track a source with an accuracy of better than 0.2 arcsec. In addition, high aperture efficiency and low receiver noise and background detector loading require that the optical losses and beam blockage be less than $\sim 3\%$. CCAT will push the performance of radio telescopes operating at sub-millimeter further towards the infrared than previous telescopes.

Fabricating, setting and maintaining a 10 μm half WFE on a 25 m diameter radio telescope is probably the most difficult challenge for this Project. Figure 9.1 shows the standard vonHoerner plot for telescope distortions versus size for gravity and thermal loads. CCAT will be in a dome so the effect of wind is significantly reduced. The performance of various radio telescopes is shown in this plot. (Note the CSO has implemented an active adjuster system based on a lookup table that has improved the half WFE to $\sim 16 \mu\text{m}$.) Although CCAT is required to operate during the daytime, direct solar illumination of the primary surface is not allowed and modest temperature gradients of 1 K across the primary mirror are assumed in this plot. As this plot shows, the scaling laws for the various gravitational and thermal distortions indicate building a completely passive 25 m diameter telescope operating efficiently at 200 μm is not feasible using the best proven materials and techniques. This implies active surface control will be necessary.

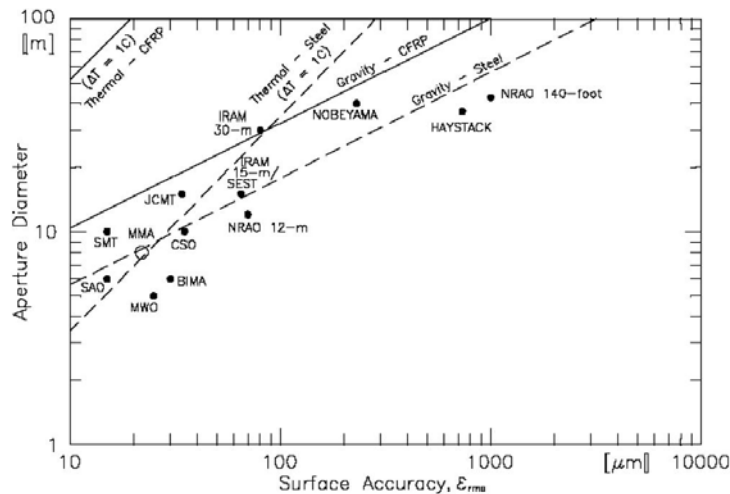


Fig. 9.1. vonHoerner diagram showing achievable surface accuracies as limited by thermal and gravitational effects [ref. ALMA memo by James Lamb]

Active surfaces are now common for optical and infrared telescopes but are relatively new for radio telescopes. The 100 m GBT operating at wavelengths longer than 3 mm and the CSO operating at 350 μm both have active adjusters that use look up tables to correct for gravitational distortions. Because the thermal distortions will be critical for CCAT it will be necessary to implement a more dynamic closed loop control system using sensors and feedback. This is commonly done at optical/infrared wavelengths using edge sensors and optical instruments that measure the wavefront errors in real-time. The requirement that CCAT be able to operate during the daytime and also in the presences of thin cloud cover makes it desirable to have a surface maintenance and control system that can function without an infrared wavefront measuring instrument.

Comparing the CCAT requirements to recent advanced telescope designs is useful for understanding the developments that are required beyond the current state-of-the-art. The 12 m telescopes being built for ALMA have been designed for operation at 350 μm using the latest materials and technology and have successful prototypes in operation. The estimated error budget presented in the request for proposals for these telescopes is given in Table 9.1. A preliminary top-down CCAT error budget is also provided. This top-down error budget is generated to help itemize the potential sources of error and to initially allocate the net error among subsystems so that more detailed design efforts can proceed. These detailed designs will then yield the errors to use in a realistic bottom-up error budget.

The magnitude of the challenge for CCAT is apparent. CCAT is twice the diameter of an ALMA antenna with a net half WFE half as large. The active surface control will obviously decrease the errors from the support structure and panel mounting but also contributes its own residual errors. The panel fabrication and distortion probably represent the largest challenge and risk to the Project, especially because of the desire to use relatively large panels to minimize the cost, part count, and complexity. The active control of the surface is also challenging because of the increased number of panels relative to existing optical telescopes with active control and the lack of full time wavefront measuring instruments at millimeter or sub-millimeter wavelengths. Most of this section is aimed at addressing these issues.

Table 9.1. Error budget from ALMA RFP plus a preliminary top-down error budget for CCAT.

| 1/2 Wavefront Error Budget | | | |
|--|-------------------|-------------|-------------------------|
| | ALMA RFP template | CCAT | |
| | [microns] | [microns] | [microns] |
| Panels | | | |
| Manufacturing (Including measurement errors) | 8.5 | | |
| Aging | 2.0 | | |
| Gravity | 4.0 | | |
| Wind | 4.0 | | |
| Absolute Temperature | 4.0 | | |
| Temperature Gradients | 4.0 | | |
| Total Panel (RSS) | | 11.8 | 5.0 |
| Backing Structure | | | |
| Gravity (Ideal) | 5.5 | | |
| Gravity (Departure From Ideal)* | 3.0 | | |
| Wind | 2.0 | | |
| Absolute Temperature | 2.0 | | |
| Temperature Gradients | 2.3 | | |
| Aging | 2.0 | | |
| Total Backing Structure | | 7.5 | 4.0 |
| Panel Mounting | | | |
| Absolute Temperature | 2.0 | | |
| Temperature Gradients | 2.0 | | |
| Panel Location in Plane | 2.0 | | |
| Panel Adjustment Perpendicular to Plane*** | 2.0 | | |
| Gravity | 3.0 | | |
| Wind | 2.0 | | |
| Total Panel Mounting (RSS) | | 5.4 | 4.0 |
| Secondary Mirror | | | |
| Manufacturing | 5.0 | | |
| Gravity | 2.0 | | |
| Wind | 2.0 | | |
| Absolute Temperature | 2.0 | | |
| Temperature Gradients | 4.0 | | |
| Aging | 3.0 | | |
| Alignment | 3.0 | | |
| Total Secondary Mirror (RSS) | | 8.4 | 3.5 |
| Total Tertiary Mirror (RSS) | | 0.0 | 3.5 |
| Surface Measurement and Setting | 10.0 | | Astro. WFE & Holography |
| Total Measurement and Setting (RSS) | | 10.0 | 4.0 |
| Other Errors not Included Above | | 2.0 | 1.5 |
| TOTAL (RSS) | | 20.0 | 10.0 |

9.1.1 Baseline Design and Analysis Approach

The baseline CCAT design consists of precision panels mounted via flexures on three actuators on a steel support truss with a control system using a set of sensors to maintain the surface figure. It is anticipated edge sensors that measure both the surface continuity as well as the dihedral angle between panels will be used. The lowest order distortion modes are to be controlled using a modest number of devices to measure the distance or angles from selected nodes on the primary to reference targets near the secondary. This control system would operate independently of astronomical observations and atmospheric conditions. The task of the initial setting of the surface and periodically verifying the absolute surface accuracy for astronomical observations will be done using a wavefront sensor or holography system (Section 15).

The key parameters that define the primary reflector configuration are: the size of the panels, the number of distance measuring stations, and the segment tiling geometry, i.e., keystone shaped panels in rings or a regular grid of hexagons. A large number of telescope configurations are possible within this baseline design and it is too early to embark on a detailed bottom-up error budget based on full engineering calculations and FEA at this point in the Project. But it is possible to undertake a systematic physics based bottom-up error analysis to determine the useful design parameter space for the next step of detailed engineering design. This parameterized model is described in the next few sections along with some examples that demonstrate the feasibility of building CCAT with modest improvements from the existing state-of-the-art technologies.

The desired scale up in panel size and reduction in allowed manufacturing errors represents a significant risk to the Project. For this reason an alternate approach using CFRP sub-frames to combine many smaller panels into passive segments in place of the large monolithic panels is described in Section 9.4. This would increase the surface weight and complexity but has a larger margin in meeting the surface half WFE budget.

9.2 Half Wave Front Error Analysis

9.2.1 Primary Reflector Panels

A parametric model of a generic panel has been developed that allows selection of the construction materials and accounts for most of the distortions caused by gravity, thermal environment, and wind. This generic panel consists of front and back face sheets of the same material and thickness t and a core material of depth h . The fractional density of the core is a parameter that can be adjusted to vary from a few percent, corresponding to a low density aluminum honeycomb, to 100% for a solid core of the same material as the face sheets. The material properties for the various materials that might be considered are given in Table 9.2. These are standard materials, but some can be engineered with a range of parameters and costs. Two typical CFRP materials are given in the table.

Table 9.2. Panel material properties.

| parameter | units | carbon | | | | | CFRP | CFRP | borosilic | Cerform | | ULE |
|---------------|-------------------|--------|------|-------|------|-----|---------|--------|-----------|---------|-----|------|
| | | steel | Al | invar | Be | Ni | low CTE | high Y | ate | SiC | SiC | |
| Y-modulus | Gpa | 210 | 70 | 141 | 128 | 214 | 100 | 250 | 63 | 450 | 450 | |
| density | Mg/m ³ | 7.85 | 2.71 | 8 | 1.85 | 8 | 1.8 | 1.8 | 2.23 | 2.95 | 3.2 | 2.21 |
| CTE | ppm/C | 12.7 | 22.7 | 0.9 | 11.4 | 13 | 0.1 | -1 | 3.3 | 2.44 | 4 | 0.03 |
| conductivity | W/m°C | 52 | 155 | 16 | 180 | 94 | 4.2 | 4.2 | 1.14 | 156 | 110 | 1.31 |
| specific heat | J/kg°C | 433 | 879 | 503 | 1925 | 433 | 710 | 710 | 750 | 670 | 670 | 766 |

The panel is treated as uniform plate of known stiffness supported at three points. The stiffness is a simple function of the thickness of the face sheets and core as well as the material elastic modulus. The gravity and wind loads are then treated as a uniform pressure (derived from the panel surface density and local wind speed respectively) applied to the front surface. The first line in Table 9.3 gives the scaling of the gravitational distortions as a function of these parameters. The gravity distortions effectively scale as the d^4/h^2 and if you keep the aspect ratio d/h constant as you change the diameter, d , then the scaling becomes d^2 .

The detailed distortions depend upon the panel outline and where the support points are located. The model used here is a circular disk optimally supported at three points to give the minimum rms distortion. This calculation can be applied to other outlines and support positions by defining an effective diameter. For a rectangular panel

with optimally placed support points, the effective diameter is approximately the diagonal distance between the corners.

The thermal distortions can be calculated if the temperature distribution in the panel is known. Two prominent thermal distributions are treated: 1) a uniform temperature change for the panel, 2) a uniform front-to-back temperature difference, and 3) a random lateral thermal distribution across the panel. The scaling for these cases is given in table 9.3. In case 1) the radius of curvature of a panel changes with the absolute temperature proportional to the CTE. This is a quadratic effect and increases as the d^2 . The distortions in case 3) are caused by thermal expansion of the core and depend upon the CTE of the core material and its thickness. The rms of the temperature distribution translates directly into a surface rms.

Table 9.3. Scaling of deformation for different load cases.

| Load case | Scaling formula |
|------------------------------------|---|
| Gravity | $\frac{\rho_{plate} \cdot t + \rho_{core} \cdot f_{core} \cdot h}{E_{plate} \cdot t \cdot (h + t)^2} \cdot d^4$ |
| Temperature change | $\Delta T \cdot CTE \cdot \frac{d^2}{R_{curve}}$ |
| Front to back temperature gradient | $\Delta T \cdot CTE \cdot \frac{d^2}{h}$ |
| Lateral temperature gradients | $\Delta T_{rms} \cdot CTE_{core} \cdot h$ |
| Segment manufacturing | d^2 |

The distortions in thermal case 2) depend upon the CTE of the face sheets and the core thickness; the temperature difference essentially changes the radius of curvature of the panel producing a “thermal cupping” of the surface. This is a quadratic effect so that for a given gradient the surface error increases as d^2 and inversely with the core thickness h . If the front-to-back gradient is caused by a fixed thermal flux through the core material, then the effect of the thicker core leading to larger temperature differences is canceled by the fact that the face sheets are farther apart and the curvature does not change. These effects are encapsulated in the scaling laws for the generic panel. If the conductivity through the panel is dominated by radiative transfer between the front and back face sheets, as is the case for glass panels, then the temperature difference is only weakly dependent upon the core thickness h and the rms distortions from thermal cupping of a panel with a constant aspect ratio, d/h , increases linearly with d .

Predicting the temperature distribution during operation depends upon many difficult to determine environmental parameters. A thermal model of the surroundings including the air, insulation, and the radiative environment is required. In the parametric modeling used here, the lateral temperature gradients are assumed to grow as $d^{1/2}$, i.e., a random walk in temperature across the surface. This is characterized as the rms temperature over a 1 m patch. A typical value of 1 K is assumed.

Estimating the temperature gradient from front-to-back of the panel is more complicated. The model includes an insulating layer between the panel and support structure as well as air temperatures and radiation to the cold sky. There are parameters for the difference between air in the support structure and the open dome, the thickness of the foam insulation, the effective boundary layer thickness for heat exchange to the air, the radiative emissivity of the front and back surfaces, and the effective fraction of the cold sky seen by the front of the panels. The thermal conduction through the panel includes radiative exchange between the front and back face sheets (assuming an emissivity of one), conduction through the air, as well as simple conduction through the core material. This is all

combined into a calculation that yields the front-to-back temperature difference in the panel that in turn produces a calculable “thermal cupping” of the surface. Typical results produce ~1 K gradients in glass panels, even with 5 cm of insulation, while panels with aluminum honeycomb cores have gradients of ~0.1 K for the same environment. It is assumed the surface properties of all of the various types of panels are similar enough that they will all see the same radiative, convective, and conductive thermal environment. Thus the relative performance of various panel designs can be compared although the predicted distortions have a larger uncertainty.

The last scaling error in Table 9.3 is the manufacturing error. The most difficult errors to control during fabrication are the large scale errors principally because of the same error sources discussed above for the panels also affect the fabrication process. It is expected the manufacturing errors will scale something like d^2 , although more time and money can usually reduce the manufacturing error for any given panel size. The manufacturing errors for a particular size will depend upon the processing details and will have to await measurements on full size prototype panels. In absence of such measurements we are assuming that a 1 m size panel can be manufactured with an rms error of 1 μm . This is roughly consistent with the design studies done for this report by commercial companies.

The parametric design methodology is very useful for exploring a wide range of parameter space quickly and helps identify feasible panel technologies. The largest risks for the Project are probably the cost and manufacturing error for the large panels. This is one of the primary reasons for developing the parametric models for the panels and the whole telescope (see later in this section). The ramifications of any reported manufacturing accuracies and cost vs. size can be quickly evaluated for the full system.

The various contributions to the surface error for the three promising panel options are given on the plots shown in Figures 9.2, 9.3, and 9.4. These panels are subjected to the same thermal environment with a 5 K difference in the air temperature between the support structure and the open dome air with 5 cm of foam insulation. The panel surfaces have 7% thermal emissivity and their front surfaces see 50% of the cold sky. The CFRP panels are dominated by the manufacturing errors while the thermal cupping caused by heat flow through the panel is the dominant error for borosilicate glass panels. Note the dominant heat transfer through the glass panel is by emissivity of 1 radiation between the facing surfaces of the front and back face sheets. This leads to a temperature difference that is ~1 K independent of the core thickness and a net linear scaling of this error with size when the aspect ratio is kept constant. The thermal cupping error is similar to the assumed manufacturing error for the Ni-Al-Ni panels.

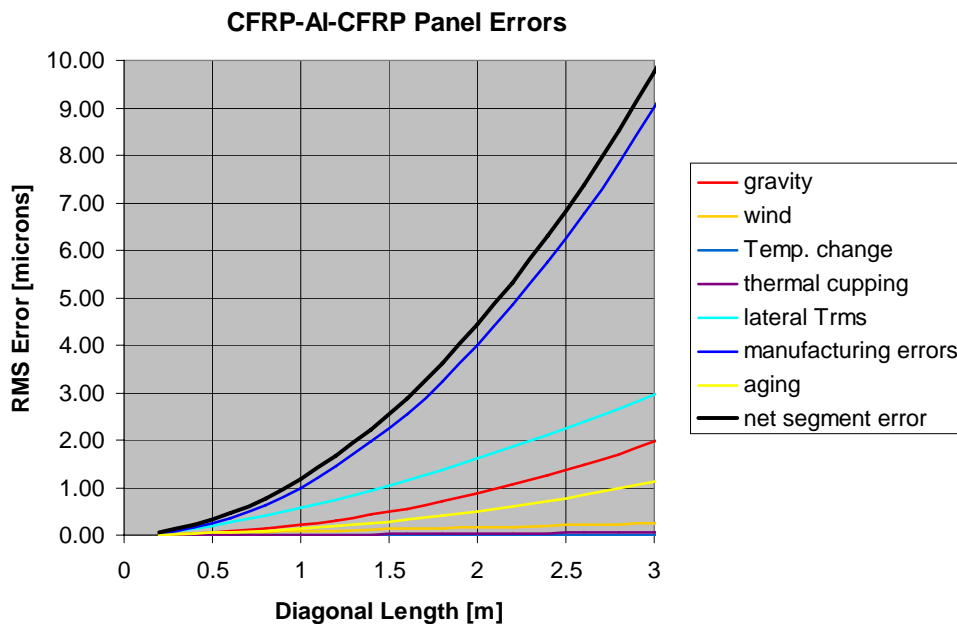


Fig. 9.2. CFRP panel with an Al honeycomb core. The face sheet and core thicknesses are 0.0006 and 0.05, respectively, of the diagonal length.

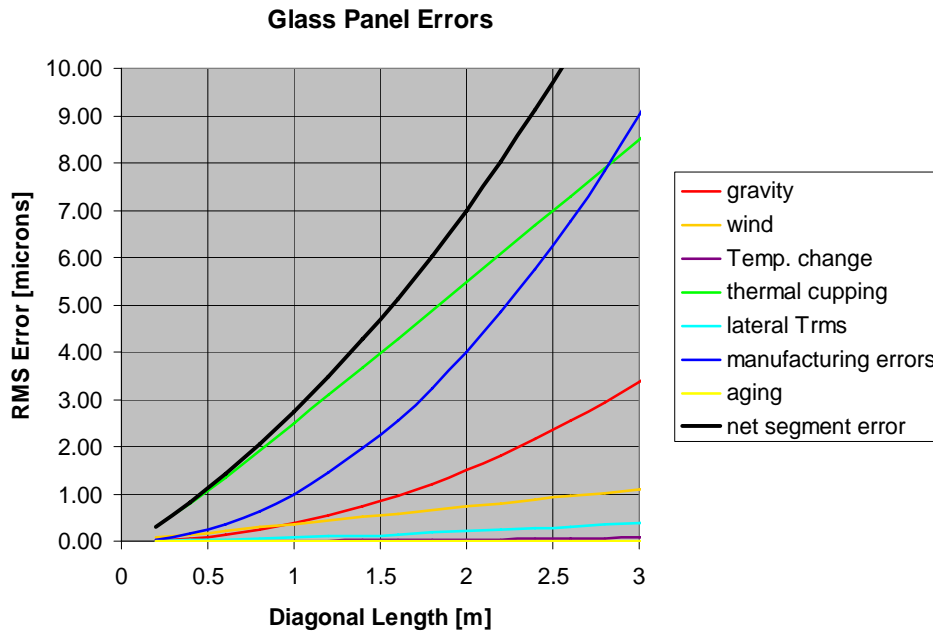


Fig. 9.3. Panel with borosilicate face sheets and core. The face sheet and core thicknesses are 0.001 and 0.045, respectively, of the diagonal length.

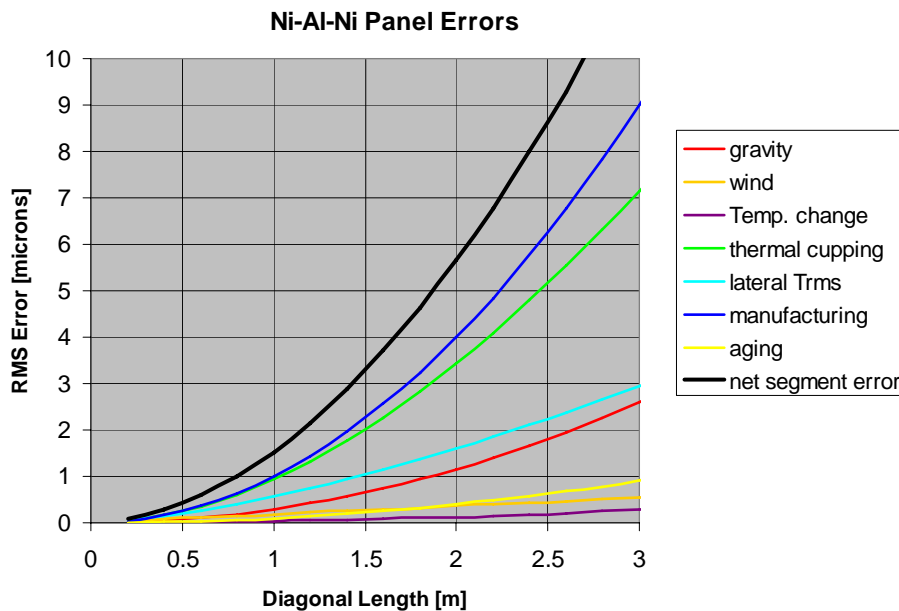


Fig. 9.4. Panel with Ni face sheets and an Al honeycomb core. The face sheet and core thicknesses are 0.0005 and 0.05, respectively, of the diagonal length.

It may be feasible to mitigate some of the thermal cupping error by readjusting the focus of the telescope. This relies on all of the panels experiencing the same thermal environment, including the degradation of the thermal emissivity with time, and that you have a method for measuring the amount of cupping as the sky and thermal environment change. This correction is not currently treated in the parameterized error budget.

9.2.2 Distance Metrology

The ability to stably measure the distance from a few dozen points on the primary surface to several fixed points on or near the secondary greatly facilitates maintaining the primary surface figure. A couple of such devices are

being developed with more than the required accuracy. In particular, a group at JPL is developing a system for space borne interferometry (Section 15). That would be well suited to CCAT. This system provides absolute point A to point B distance measurements. Standard commercial laser interferometers have the required precision and stability but can't tolerate interruption of the laser beam. There are other schemes that could be developed for this purpose, although none of them are commercially available with the precision required by CCAT.

The problem of interrupted beams for the commercial interferometric distance measuring instruments is not serious if only a few beams are interrupted for short periods of time. There is a lot of redundant information from the edge sensors and the remaining distance measuring instruments so this can be used to reset the distance on the interrupted beams. The surface figure would degrade slowly as a consequence of many beam interruptions and it may be necessary to measure and tune the surface using astronomical holography.

9.2.3 Edge Sensors

Edge sensors that measure the continuity and the dihedral angle between segments is a powerful method for maintaining the surface figure of a segmented reflector. This technique has been used successfully on optical telescopes like the Keck and HET. A complete control algorithm is required to fully evaluate the performance of this technique for any given telescope segment and edge sensor configuration. A major part of developing such an algorithm is the singular value decomposition of the matrix relating the sensor readings to actuator motion. Such an analysis for other telescope designs indicate there can be very large magnifications of sensor errors into resulting surface errors, that is some of the eigenvalues from the singular value decomposition are small. The lowest order modes, such as focus, can have a sensor error magnification of several hundred for primaries with 125 segments.

The magnification of sensor errors can be very detrimental when it is realized the thermal and gravitational distortions of the panels need to be included in the sensor error. Although sensors suitable for the high accuracy requirements of optical telescopes are available, the performance of the edge sensor system will most likely be dominated by distortions in the panels themselves.

A preliminary analysis of a surface control system for CCAT was undertaken by simply calculating the ratio of the rms of the sensor readings to the rms of the surface distortion for each of the first 90 Zernike polynomial distortions. This is a proxy for the mode sensitivity, or 1/magnification, obtained from a full singular value decomposition calculation and gives a lower limit for the magnification. Again, a parametric model was developed to quickly evaluate the dependence of these ratios upon the primary configuration and the number of segments. Figure 9.5 shows the results of for a nominal 36 segment Keck configuration while Figure 9.6 shows the results for CCAT constructed from 162 keystone segments. The dips correspond to small eigenvalues and hence large sensor error magnification. The corresponding calculations for distance and tip-tilt measurements are plotted in Figure 9.7. As expected, adding distance measurements greatly improves the detection and correction of the low order aberrations.

The sensitivity to a given low order mode decreases roughly linearly with the number of segments, or at best as one over the square root of the number of segments. Thus given a constant sensor error you want to have fewer segments by increasing their size. But the segment distortions contribute to the sensor error roughly in proportion to the segment diameter squared. Increasing the segment size can degrade the performance of the edge sensor system as well as increase the segment error contributions as seen in the previous section.

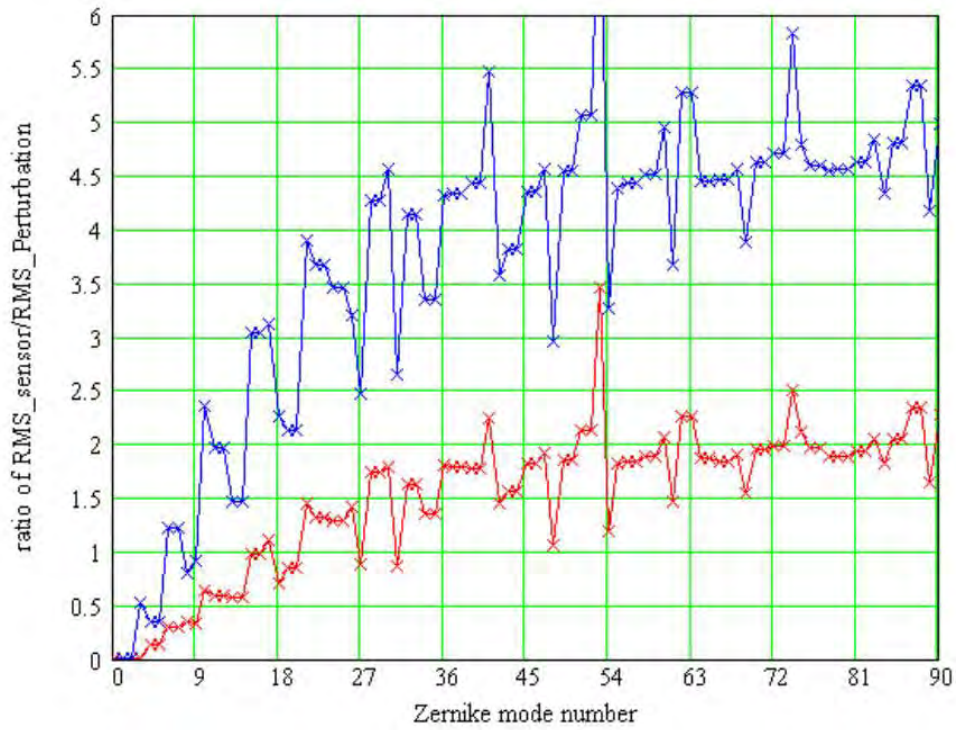


Fig. 9.5. Sensitivity of edge (red) and dihedral angle (blue) sensors for 36 hexagonal panels. The dihedral sensitivity is in [$\mu\text{radians}_{\text{rms}}/\mu\text{m}_{\text{rms}}$].

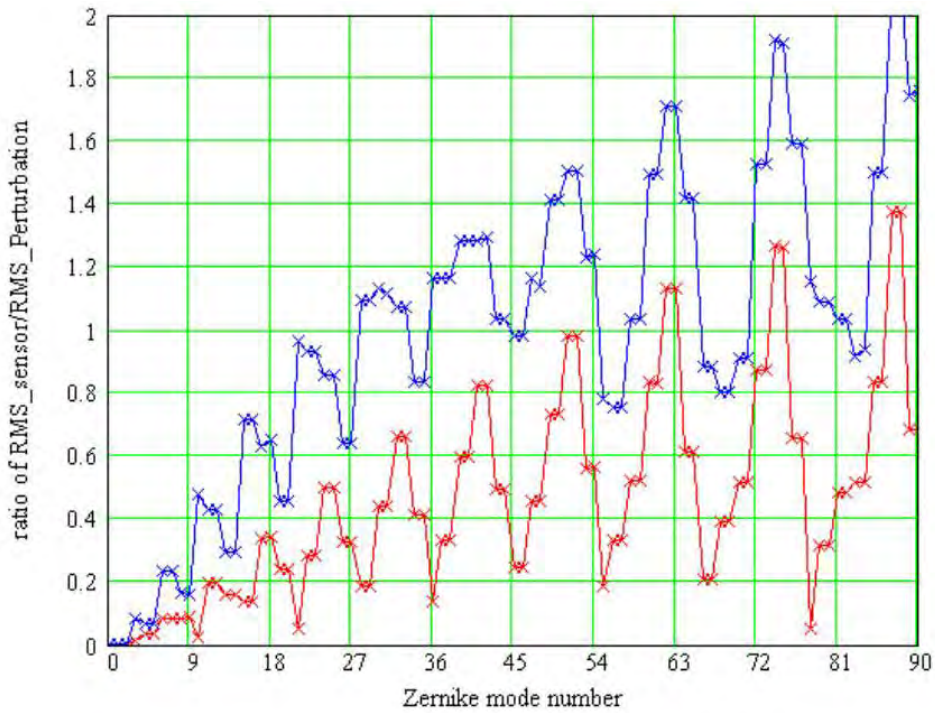


Fig. 9.6. Sensitivity of edge (red) and dihedral angle (blue) sensors for 162 keystone panels in rings. The dihedral sensitivity is in [$\mu\text{radians}_{\text{rms}}/\mu\text{m}_{\text{rms}}$].

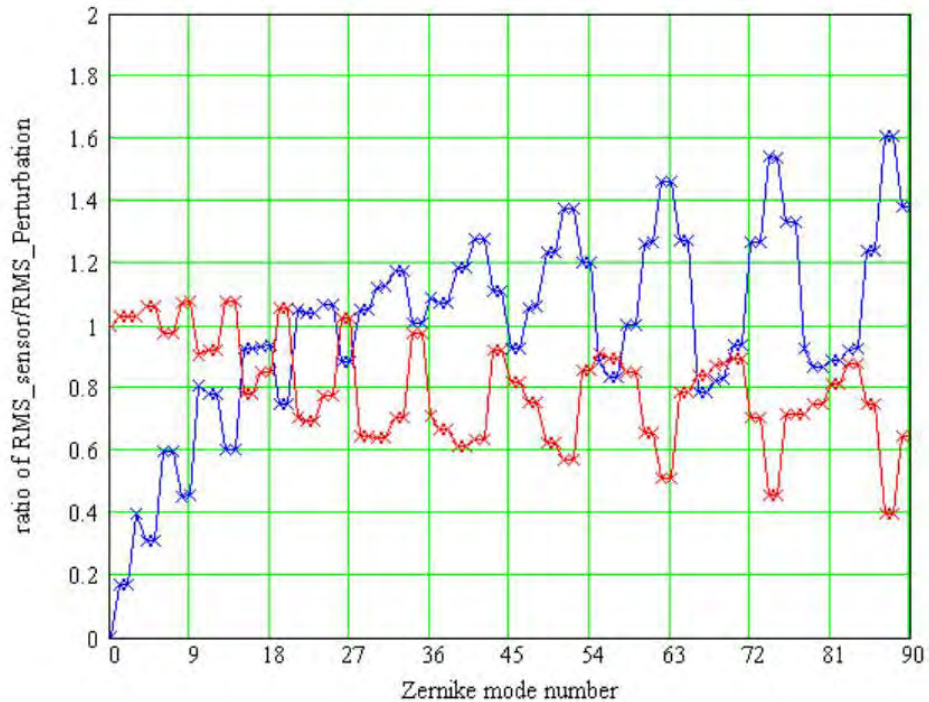


Fig. 9.7. Sensitivity of distance (red) and tip-tilt (blue) sensors for 162 keystone panels in rings. The tip-tilt sensitivity is in [micro-radians_rms/ μm_rms].

9.2.4 System Error Budget

Detailed parameterized errors for the panel errors, primary surface maintenance system, support structure, and other optical elements are root sum squared together to give the total telescope half WFE. Examples of the error budget for four different panel configurations are given in Table 9.4. The panel aspect ratios are close to the configurations suggested or previously used by manufacturers of each type of panel. The thermal environment is the same for all panels and is described in Section 9.2.1. The manufacturing errors for the CFRP-Al-CFRP, Ni-Al-Ni, and borosilicate glass panels are all assumed to be $1\ \mu\text{m}$ for a 1 m sized panel, while the all Al panel is assumed to have much larger fabrication errors of $4\ \mu\text{m}$ for a 1 m panel. This is intended to reflect the high replication accuracy that should be achievable for the first three types of panels and the current state-of-the-art for a machined aluminum panel. The continuity and dihedral sensors can be independently used to calculate the surface corrections. The error analysis assumes the results from these sensors are optimally combined to minimize the resulting surface error. Thus the net surface maintenance error budget in Table 9.4 can be less than the errors associated with each of these types of sensors. The primary support error includes wind and vibration outside the bandwidth of the surface maintenance system. It also includes errors arising from lateral location tolerance for the panels and hence has a weak dependence on the panel size. The weak dependence of the measurement and setting accuracy on panel size arises from the loss of accuracy when more pixels are required to set smaller panels.

Table 9.4. Sample 1/2 WFE for various panel options.

| CCAT 1/2 WFE from parameterized model | | | | |
|--|--------------|--------------|--------------|--------------|
| segments | CFRP-AI-CFRP | Ni-AI-Ni | borosilicate | Aluminum |
| size, diagonal [m] | 2.07 | 1.82 | 1.30 | 1.07 |
| number of segments | 147 | 190 | 370 | 542 |
| areal density [km/m ²] | 8.94 | 18.45 | 8.41 | 13.10 |
| errors [microns] | | | | |
| gravity | 0.93 | 0.95 | 0.63 | 0.60 |
| wind | 0.16 | 0.32 | 0.48 | 0.29 |
| thermal cupping | 0.03 | 2.87 | 3.39 | 0.64 |
| lateral Trms | 1.68 | 1.39 | 0.11 | 0.63 |
| manufacturing errors | 4.26 | 3.29 | 1.69 | 4.61 |
| aging | 0.53 | 0.33 | 0.00 | 0.58 |
| net segment error | 4.71 | 4.70 | 3.87 | 4.78 |
| primary figure maintence | | | | |
| number of distance measurements | 6 | 36 | 58 | 36 |
| distance measuring error | 1.00 | 1.00 | 1.00 | 1.00 |
| surface error from edge sensors | 10.32 | 3.80 | 4.89 | 4.46 |
| surface error from angle sensors | 3.48 | 10.46 | 14.91 | 6.78 |
| net surface maintenance error | 3.45 | 3.71 | 4.75 | 3.86 |
| total primary 1/2WFE | 5.84 | 5.99 | 6.13 | 6.14 |
| other non-primary surface 1/2WFE | | | | |
| primary support | 4.91 | 4.72 | 4.50 | 4.46 |
| secondary | 3.49 | 3.49 | 3.49 | 3.49 |
| tertiary | 3.49 | 3.49 | 3.49 | 3.49 |
| wavefront measurement | 4.18 | 4.19 | 4.22 | 4.26 |
| total non-primary surface 1/2WFE | 8.12 | 8.0 | 7.90 | 7.90 |
| total telescope 1/2WFE | 10.00 | 10.00 | 10.00 | 10.00 |

The panel size and number of distance measurements were adjusted until the total half WFE reached the goal of 10 μm . Generally the net error decreases when smaller panels are used or more distance measurements added and these can be traded against each other.

The error budgets in Table 9.4 indicate there are several possible panel and sensor configurations that should be able to meet the demanding requirements for CCAT. More detailed results from manufacturers, particularly replication results for large panels, are required to verify the viability of any particular panel technology.

9.3 Setting and Tuning

The “gold standard” for measuring radio telescope surfaces has been holography using ground based or satellite transmitters. Holography on astronomical sources, mainly the planets, has also been used very successfully for measuring the large scale errors on millimeter and sub-millimeter telescopes. Gene Serabyn describes a method that will use the next generation of large format bolometer arrays to extend this technique down the small scale size required for setting and tuning the CCAT primary in Section 15.2. This technique will be used to fine tune the surface after an initial setting to an accuracy of $\sim 30 \mu\text{m}$ using photogrammetry or precision laser surveying. Although special astronomical objects, mainly Neptune and Uranus, are required and hence not always available, it should be possible to monitor and retune the surface often enough to maintain surface figure for all observations if the techniques described in the previous section for maintaining the surface are successful.

9.4 Sub-frame Concept

The main driver for large segments is to decrease the complexity and number of panel actuators and their associated cost. Fabricating large segments, 2 m diameter and larger, that meet the CCAT specifications is likely to be a difficult and expensive task. The manufacturing error appears to be the dominant error in such large panels.

This limitation can be removed if the structural stiffness and stability are separated from the fabrication of the surface accuracy. The idea is to construct low precision but stiff thermally stable sub-frames from CFRP and load this sub-frame with accurate small segments. The segments would be small enough that their gravity and thermal distortions are negligible and they would be attached with manually adjustable standoffs. The small segments would be attached to the sub-frame and set to the required accuracy in the factory using any of a number of appropriate measuring techniques. This is essentially what is done for any telescope with segment and a passive support structure. This sub-frame would then be mounted on the large primary support structure with three motorized actuators to be used by the surface control system. Sub-frames in the range of 2-4 m diameter are feasible using standard inexpensive CFRP construction and even larger sub-frames are possible with careful design.

Two sub-frame constructions are considered: 1) CFRP top and bottom plates with a low density aluminum honeycomb core and 2) an all CFRP box type construction. The performance is then determined by the diagonal length and thickness of the sub-frame. The generic panel analysis can also be applied to calculate the deformations in the sub-frames and included in the error budget. The adjusters that attach the segments to the sub-frame are invar with manual fine setting capability.

This concept has the system advantage of measuring and controlling a much smaller number of large panels without incurring the expense and difficulty of manufacturing monolith segments larger the ~1m diameter comfort range that segment manufacturing techniques may have. It also adds another dimension to the cost performance trades that will have to be made and could lead to a very cost effective solution to the CCAT primary. The sub-frame does add complexity in itself, but it is a well defined component that can be treated as a deliverable with a set of specifications and a simple interface to the rest of the system.

Table 9.5 shows a sample error budget using 1 m Ni-Al-Ni panels with the manufacturing error increased to 2 μm and using 2.79 m CFRP sub-frames. So despite the added error from the panel manufacturing and more error terms from the sub-frames you can still satisfy the requirements using only six distance measuring devices.

Table 9.5. Error budget including sub-frames using Ni-Al-Ni panels.

| | |
|--|--------------|
| Telescope 1/2 WFE | |
| segments | |
| size, diagonal [m] | 1.00 |
| number of segments | 625 |
| areal density [km/m ²] | 10.17 |
| errors [microns] | |
| gravity | 0.29 |
| wind | 0.18 |
| Temp. change | 0.03 |
| thermal cupping | 0.93 |
| lateral Trms | 0.57 |
| manufacturing errors | 2.00 |
| aging | 0.10 |
| net segment error | 2.31 |
| sub-frames | |
| dia [m] | 2.79 |
| number of sub-frames | 80 |
| number of segments per sub-frames | 7.8 |
| areal density | 22.60 |
| stiffness | 2.8E+06 |
| gravity, including segment wt. | 2.72 |
| wind | 0.52 |
| Temp. change | 0.00 |
| thermal cupping | 0.17 |
| lateral Trms | 0.01 |
| adjuster temp & gravity | 0.21 |
| segment setting errors | 1.56 |
| aging | 0.78 |
| net subframe error | 3.28 |
| primary figure maintenance | |
| number of distance measurements | 6 |
| distance measuring error | 1 |
| surface error from edge sensors | 4.61 |
| surface error from angle sensors | 3.09 |
| net surface maintenance error | 2.75 |
| total primary 1/2WFE | |
| | 4.86 |
| other non-primary surface 1/2WFE | |
| primary support | 5.89 |
| secondary | 3.49 |
| tertiary | 3.49 |
| wavefront measurement | 4.17 |
| total non-primary surface 1/2WFE | 8.7 |
| total telescope 1/2WFE | 10.00 |

9.5 Image Quality

The image quality is taken to mean the central beam profile, sidelobes, and optical efficiency. These three items can be roughly attributed to the WFE, optical configuration, and aperture loss, respectively. A highly quality central beam, essentially a diffraction limited Gaussian, is ensured by maintaining a better than $\lambda/20$ half WFE, i.e., better than 10 μm effective surface error for observations at 200 μm wavelength. The optical configuration

includes the primary panel shapes and gaps between the panels as well as the secondary and tertiary sizes, shapes and positions as well as the structure supporting these structures. Physical optics and ray tracing calculations are used to calculate the image distortions for off-axis pixels as well as the diffraction sidelobes from these optical configuration details. The same configuration details are also used to calculate the light throughput or aperture loss. The aperture loss enters into the telescope performance not only as a loss in signal but also as an added source of detector loading and noise to detectors. Thus there is a strong driver to minimize these losses, including optics emissivity, and strive to keep the nominal aperture losses to below 3%.

9.6 Pointing and Tracking

The diffraction limited beam for observations at 200 μm is only ~ 2 arcsec and pointing and tracking a 25 m telescope with $1/10^{\text{th}}$ beam accuracy is a challenging task. Achieving this goal will require careful attention to all aspects of the mount and drive system. As with most radio telescopes it is anticipated that a pointing model will be developed that allows blind pointing anywhere on the sky that is within one or two beam widths to allow for quick source acquisition and refinement of the pointing using bright sub-millimeter sources. The telescope must then be able to track the target source to within about $1/10^{\text{th}}$ of the beam for an hour or so before correcting the pointing on a nearby strong source. Because of the requirement to observe during the day and with thin clouds, it is desirable to achieve this pointing and tracking performance without a dedicated special offset guiding system. An offset guiding system will be part of the system design and possibly part of individual instrument packages and may be required for the highest fidelity imaging and other demanding observations.

The pointing model would incorporate the various mount and bearing distortions that are determined from the FEA and any stable measurable deviation from ideal bearings, encoders, etc. Precision tiltmeters mounted on the alidade and concentric with the azimuth axis can provide instantaneous measurements of the gravitational vertical referenced to the alidade as input to the pointing model. This has proven to be very useful for accurate pointing on existing sub-millimeter telescopes such as the CSO.

The preliminary non-repeatable pointing and tracking error budget for CCAT is shown in table 9.6 along with the template from the ALMA RFP. This divides the errors among the many possible contributions but is not based on detailed analysis or engineering studies of those contributions. The ALMA pointing specifications were considered to be one of system drivers for the design of those telescopes and were successfully met by the prototype versions of the antennas. CCAT requirements are several times smaller but CCAT has the distinct advantage of being in a dome and never subjected to full solar illumination, or unmitigated wind.

It is anticipated that one of the more difficult challenges will be keeping the servo-errors within tolerance. The errors associated with torque ripple in the motors and gears are outside of the servo bandwidth and hence not easily controlled using feedback from the encoders. Care will be taken in the design and selection of these components to minimize these sources of error. A detailed telescope and servo design will be undertaken to address these issues during the next phase of the Project.

Observations that can use offset guiding may be able to use the active control of the secondary or a separate tip-tilt corrector to improve upon the performance of the basic servo system. This might be done at infrared wavelengths if the primary surface has the requisite surface finish and accuracy. Such a system would also correct for the dry air component of the seeing, but correcting for the seeing arising from the fluctuations in the water vapor will require a system operating at millimeter or sub-millimeter wavelengths. There are several novel techniques that have been proposed that might measure the water vapor seeing and provide the necessary information to make corrections. This is another topic that will be pursued during the next phase of the Project.

Table 9.6. Preliminary non-repeatable pointing and tracking error budget.

| Nonrepeatable Pointing and Tracking Errors | | | |
|---|-------------------|-------------------|------|
| | ALMA RFP template | | CCAT |
| | Day [arcsec] | Night [arcsec] | |
| Wind, steady component | 0.20 | 0.45 | 0.04 |
| Wind, gusty component | 0.10 | 0.10 | 0.02 |
| Structure temperature gradients | 0.35 | 0.00 | 0.05 |
| Ambient temperature changes | 0.20 | 0.00 | 0.05 |
| Inertial forces | 0.15 | 0.15 | 0.10 |
| Encoder errors | 0.20 | 0.20 | 0.10 |
| Servo error | 0.10 | 0.10 | 0.10 |
| Bearing errors | 0.20 | 0.20 | 0.05 |
| Other errors | 0.19 | 0.19 | 0.05 |
| Total RSS error | 0.60 | 0.60 | .020 |

10 Site Selection

10.1 Introduction

Consistently superb observing conditions are crucial to the CCAT's scientific success. Observations at 350 μm and, when possible, shorter wavelengths are the telescope's primary scientific objectives. At these submillimeter wavelengths, the atmosphere is only partially transparent. Molecules, particularly water vapor, absorb and emit submillimeter radiation. The absorption attenuates astronomical signals and the emission adds a deleterious background. Together these effects present a natural limit to the telescope sensitivity.

The global distribution of water is very inhomogeneous and water vapor is concentrated in the lower atmosphere. Hence, high altitude sites in dry climates offer the best observing conditions. At present, the 4100 m summit of Mauna Kea, Hawaii, is the best developed location. The CSO, the JCMT, the SMA and numerous optical telescopes are located there. Over the past decade, sites with superb observing conditions have been identified in the Andean highlands near the village of San Pedro de Atacama in northern Chile. There the high (> 5000 m) altitude and extreme aridity produce exceptional atmospheric transparency and permit observations at wavelengths as short as 200 μm . Extensive measurements demonstrate observing conditions at these sites surpass those on Mauna Kea. The area is rapidly becoming an important center for astronomy with several telescopes already operating or under construction. This is the region selected for CCAT.

10.1.1 The Vicinity of San Pedro de Atacama, Chile

The Atacama Desert of northern Chile is among the driest places on Earth. The combined effects of a high pressure belt over the southeast Pacific, the cold Humboldt current, and the moisture barrier of the Andean cordillera normally prevent both winter storms, from the ocean, and summer tropical convection, from the Amazon, from penetrating the area. The lack of glaciers, even on the highest peak in the region, Volcán Lullailaco (6740 m), is unique for these altitudes and attests to the aridity (Messerli et al. 1993). The annual 0° C isotherm is about 4400 m altitude and vegetation is extremely sparse. The precipitation that does fall, mainly during the austral summer, amounts to less than 200 mm year⁻¹ in the highlands (Núñez et al. 2002). Significant interannual variations in summer precipitation are correlated with the El Niño Southern Oscillation, with warm years drier than cool ones (Garreaud et al. 2003).

Northern Chile is sparsely populated but has tremendous mineral reserves and mining is the major economic activity. Several large towns, mostly near the coast, support the mines (Figure 10.1). At the foot of the mountains is a small settlement at the oasis of San Pedro de Atacama. This village, which thrives on tourism, provides a convenient base for telescope operations. It is about 100 km from Calama, a large regional mining support town with good commercial air service. Over the last decade, several groups have explored sites and installed telescopes near San Pedro (Table 10.1). Extensive measurements demonstrate these sites enjoy some of the best observing conditions in the world. The latitude of 23° S provides excellent sky coverage, including near zenith transit of the Galactic center. Recognizing the importance of the region, the Chilean government has declared the area surrounding Cerro Chajnantor, including a large plateau at 5000 m altitude, as a scientific preserve. This status protects astronomical observatories in the preserve from potential threats posed by such activities as mining or broadcasting.

For the CCAT, there are several candidate sites near San Pedro (Table 10.2, Figure 10.2–10.5). As a result of the ALMA Project and other telescopes, the Chajnantor plateau will soon be well developed, offering significant logistical advantages to nearby observatories.

Although observing conditions at the ALMA site are extremely good, even better conditions are found on the nearby peaks, which are about 500 m higher. Measurements on Cerro Sairecabur, about 35 km north of the science preserve, demonstrate the atmospheric transmission there is significantly higher than at the ALMA site. Cerros Chajnantor and Chascón, inside the preserve, should enjoy conditions comparable to Sairecabur because their altitudes are similar. Direct measurements of observing conditions on Cerro Chajnantor will begin as soon as access permission is secured.

For the purpose of the Concept Feasibility Study, a site near the summit of Cerro Chajnantor has been selected for the CCAT. Because it is 500 m higher, observing conditions there should be better than at the ALMA site. On the other hand, it is only about 5 km from the ALMA, maintaining the logistical advantages of advantages to that Project.



Figure 10.1. Northern Chile. San Pedro de Atacama is 100 km from Calama, which has a commercial airport with service to Santiago several times daily.

Table 10.1. Astronomy projects near San Pedro de Atacama.

| Project | Institutions | Science | Location | Altitude | Dates |
|---------|------------------|-----------|--------------------|----------|------------------|
| MAT | Princeton, Penn | cosmology | Cerro Toco | 5200 m | 1997, 1998, 2001 |
| CBI | Caltech, et al. | cosmology | Chajnantor plateau | 5050 m | 1999 – present |
| MINT | Princeton | cosmology | Cerro Toco | 5200 m | 2001 |
| ASTE | NAO Japan | mm/submm | Pampa la Bola | 4800 m | 2002 – present |
| RLT | SAO | THz | Sairecabur | 5500 m | 2002 – present |
| APEX | MPIfR, OSO, ESO | mm/submm | Chajnantor plateau | 5100 m | 2003 – present |
| NANTEN2 | Nagoya | THz | Pampa la Bola | 4800 m | 2004 – present |
| ACT | Princeton, Penn | cosmology | Cerro Toco | 5200 m | 2006 |
| ALMA | NRAO, ESO, Japan | mm/submm | Chajnantor plateau | 5050 m | 2013 completion |

Table 10.2. Candidate CCAT Sites

| Site | Alt. [m] | Lat. [S] | Long. [W] | N [m] | E [m] |
|----------------------|----------|-------------|-------------|-------------------------|---------|
| Cerro Chajnantor | 5590 | 22° 59' 8" | 67° 44' 24" | 7457 900 | 629 350 |
| Cerro Chascón | 5650 | 23° 0' 41" | 67° 41' 25" | 7455 000 | 634 400 |
| Cerro Sairecabur | 5500 | 22° 43' 58" | 67° 53' 34" | 7486 000 | 613 900 |
| Chaj. plateau (ALMA) | 5050 | 23° 1' 22" | 67° 45' 18" | 7453 773 | 627 772 |
| datum | | WGS 1984 | | UTM Zone 19, PSAm. 1956 | |



Figure 10.2. View northeast across the Chajnantor plateau toward Cerros Toco (center) and Chajnantor (right). The CBI and the APEX telescopes are visible. A candidate CCAT site is the summit of Cerro Chajnantor (5590 m). (J. Dietrich)



Figure 10.3. View to the east of Cerro Chajnantor (5600 m). On this mountain, the candidate CCAT site is behind the summit skyline.



Figure 10.4. View southwest toward Cerro Chascón (5650 m). Here the candidate CCAT site is the right summit.



Figure 10.5. View south past the SAO equipment on Cerro Sairecabur (5500 m) toward Volcán Llullaillaco in the far distance. Here the candidate CCAT site is near the existing equipment. (D. Marrone / CfA)

10.1.2 Observing Conditions

Characterization of observing conditions at potential CCAT sites has benefited from previous work in the vicinity by other groups. Atmospheric transparency is the fundamental concern. Astronomical observations will be futile if signals cannot penetrate the atmosphere. Techniques and objectives of site characterization for mm/submillimeter astronomy are reviewed elsewhere (Radford 2002). Tipping radiometers, pioneered by Dicke et al. (1946), are the standard tools for measuring atmospheric transparency. Measurements with 225 GHz radiometers have been made at several sites, providing historical baselines and global comparisons. Conditions in the submillimeter have been evaluated both with submillimeter tippers and with Fourier transform spectrometers. Different sites in the region have been compared sequentially, with an FTS, and simultaneously, with two submillimeter tippers.

10.1.2.1 225 GHz Transparency

For more than a decade, NRAO has operated instruments on the Chajnantor plateau for the ALMA project, including a heterodyne tipping radiometer that measure the 225 GHz optical depth (τ_{225}) every 10 min. A functionally identical radiometer has operated since 1989 at the CSO on Mauna Kea. These measurements demonstrate the ALMA site enjoys much better observing conditions than Mauna Kea (Figure 10.7). At the CSO, observations at 350 μm wavelength are made when $\tau_{225} < 0.055$ and at longer wavelength otherwise (Golwala 2005). At the Chajnantor plateau, conditions this good occur more than twice as often as on Mauna Kea. Because these measurements now span more than a decade, the comparison shows long term stability.

On the Chajnantor plateau, the diurnal transparency variations are less pronounced than at Mauna Kea (Figure 10.7). Although conditions are generally better at night than during the day, the transparency variation lags solar time in both places. At the ALMA site, the offset is about 6 h so the best conditions occur from local midnight until late morning and the best transparency is seen shortly after sunrise. The morning hours after sunrise are better than the evening hours after sunset. This places a premium on daytime operations.

Seasonal variations are more pronounced than the diurnal variations (Figure 10.7). At the Chajnantor plateau, conditions are consistently good from April to December when westerly winds prevail. The best conditions occur during the winter and spring, June through November. In comparison, conditions deteriorate during the summer, January through March, when the circulation pattern allows incursions of moist air masses from east of Andes (the *inveirno Boliviano*). There is

considerable annual variation in the severity of these summertime conditions. Even in summer, however, there is a substantial amount of time suitable for observing in the mm, if not the THz, especially from local midnight until late morning.

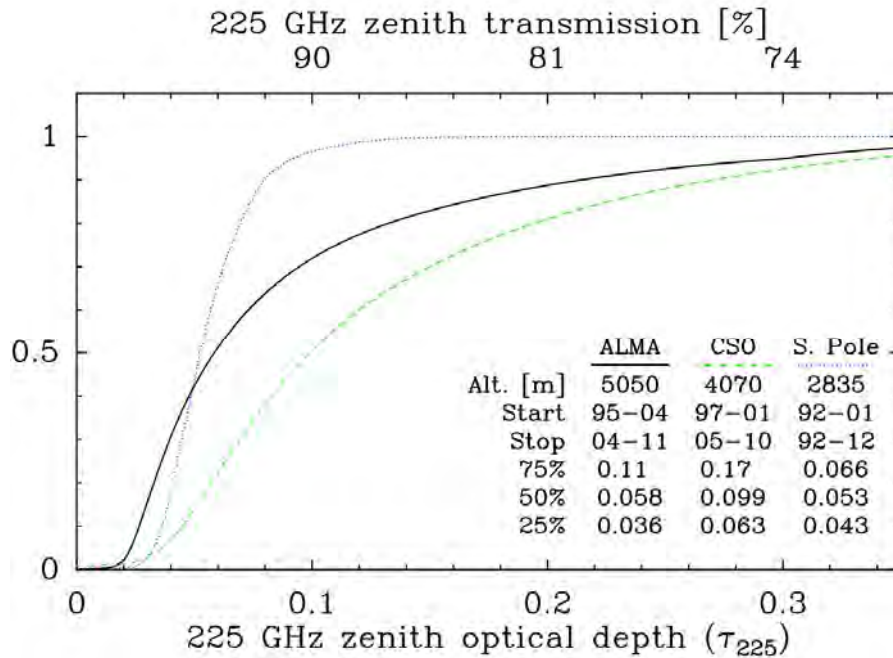


Figure 10.6. Cumulative distributions of the measured narrowband 225 GHz zenith optical depth (τ_{225}) show the Chajnantor plateau enjoys much better conditions than Mauna Kea. The South Pole is also a good site. Adapted from Radford and Chamberlin (2000).

10.1.2.2 Water Vapor

With an atmospheric model, the water vapor column can be inferred from the 225 GHz measurements. Calculations show the linear relation between the water vapor column depth and the optical depth changes depending on the altitude and temperature (Table 10.3). There is a dry air term, $\tau_{225}(\text{dry}) = -b/a$, that decreases with altitude. The slope, a , on the other hand, increases with for the higher sites, meaning more water is needed to cause the same optical depth. For Mauna Kea and the ALMA site, the regression coefficients differ by less than 10%, so an average is appropriate for comparing these sites. (The regression for the South Pole is very different.) Then the relative distribution of the water vapor column depth is the same as the distribution of 225 GHz transparency. The first quartile water vapor column at Mauna Kea and the median at the ALMA site are about the same, 1 mm. At the CSO, the threshold for observations at $350 \mu\text{m}$, $\tau_{225} < 0.055$, corresponds to a water column depth < 0.9 mm. Because conditions at candidate CCAT sites are much better, considerably more stringent water vapor ranges are anticipated (section 4.2.2).

Table 10.3. Regression between 225 GHz optical depth and water vapor column, w [mm] = $a\tau_{225} + b$, in the interval $0.02 < \tau_{225} < 0.3$, calculated with the ATM model (Pardo et al. 2001) for different sites.

| Site | Altitude | Temp. | a | b | $\tau_{225}(\text{dry})$ |
|---------------------|----------|-------|------|--------|--------------------------|
| Mauna Kea | 4100 m | 273 K | 21.4 | -0.30 | 0.014 |
| ALMA | 5000 m | 270 K | 23.2 | -0.31 | 0.013 |
| Sairecabur | 5500 m | 270 K | 24.9 | -0.28 | 0.011 |
| South Pole | 2835 m | 225 K | 13.7 | -0.27 | 0.019 |
| average (MK & ALMA) | | | 22.3 | -0.305 | |

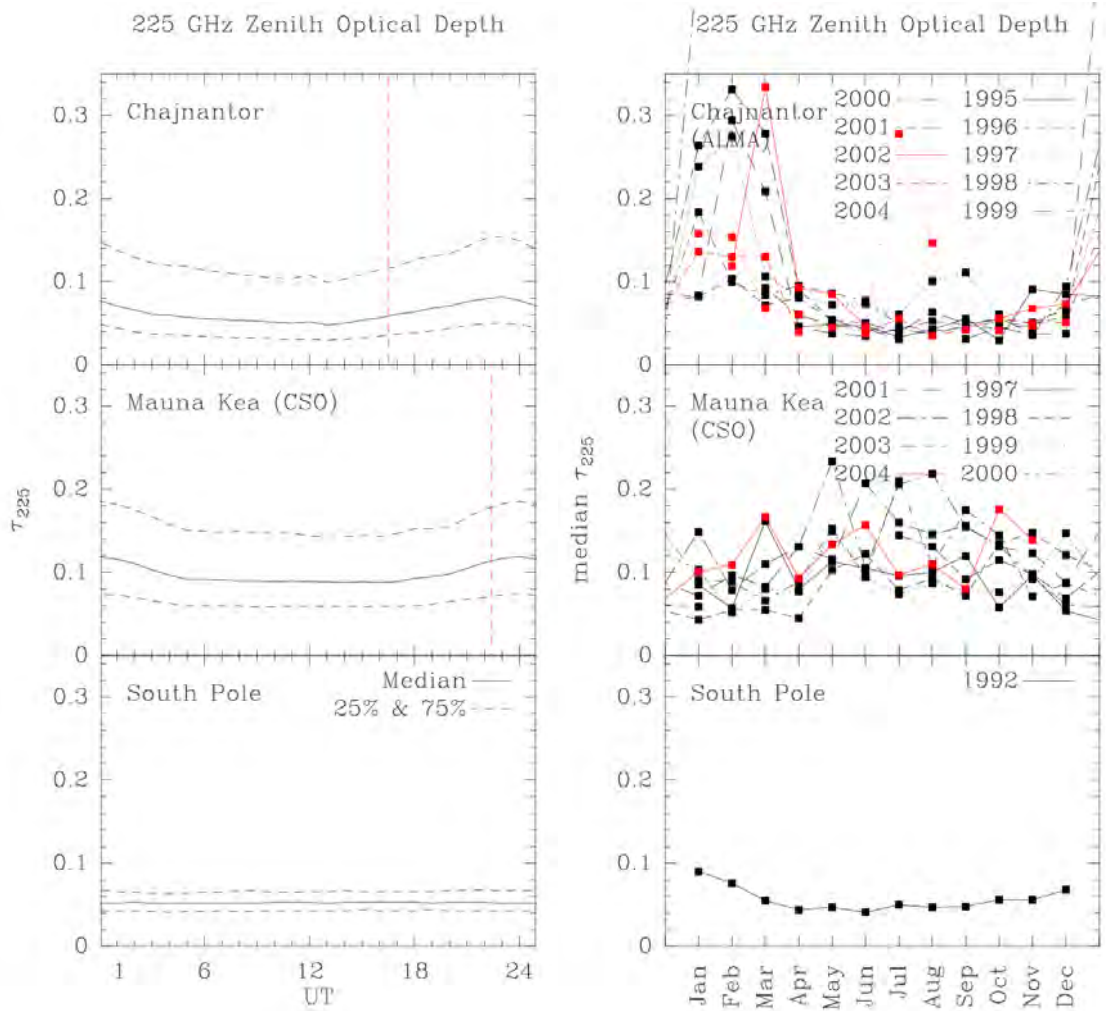


Figure 10.7. Diurnal (left) and seasonal (right) variations of the measured 225 GHz zenith optical depth (τ_{225}) at the ALMA site (Chajnantor plateau), at Mauna Kea, and for interest the South Pole. Local solar noon is indicated by the vertical dashed line. Local solar time is UT – 4 h 31 m at Chajnantor and UT – 10 h 22 m at Mauna Kea.

10.1.2.3 Submillimeter Transparency

Three approaches have been taken to characterizing observing conditions at shorter wavelengths. These efforts have occurred simultaneously, so the situation is much better understood now than a decade ago. In the vicinity of the ALMA site, two groups have fielded wide band spectrometers and simultaneous measurements have been made with 225 GHz and 350 μm tipping radiometers. Theoretical efforts produced reliable models.

In 1997 and 1998, Matsushita et al. (1999) operated a Fourier transform spectrometer (FTS) at Pampa la Bola, about 8 km NE and 250 m lower than the ALMA site, for short periods of time (Figure 10.8). They demonstrated there is significant transparency in several windows between 1.0 and 1.5 THz during dry conditions. By linking their empirical correlations between the transparency at 220 GHz and at higher frequencies to the long term 225 GHz measurements, they estimated conditions at Pampa la Bola are suitable for submillimeter observations about 50% of the winter time.

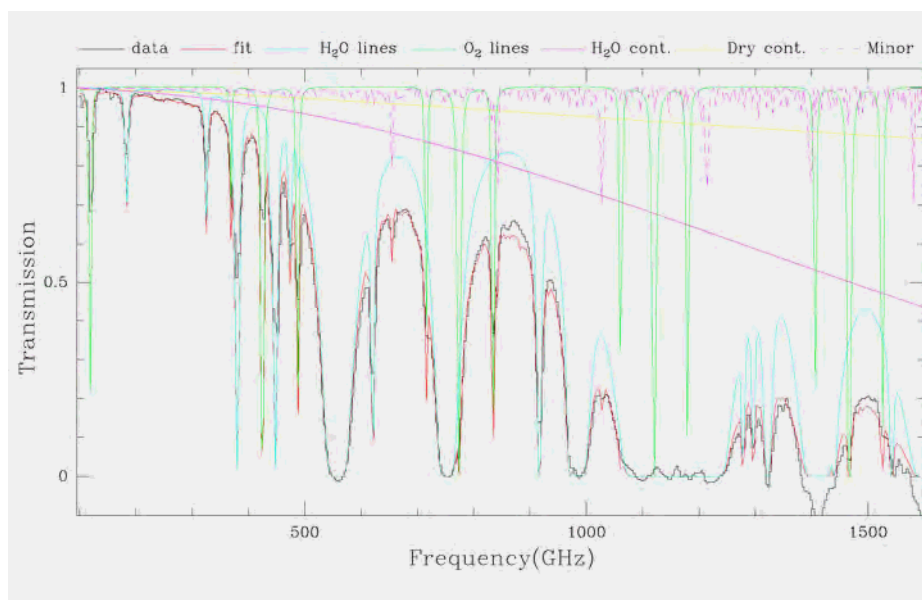


Figure 10.8. Atmospheric spectrum measured at Pampa la Bola (4800 m) on 1998 June 17 at 14:20 UT overlaid with the components of the best fit ATM model. The inferred water vapor column is 0.25 mm. (Matsushita et al. 1999)

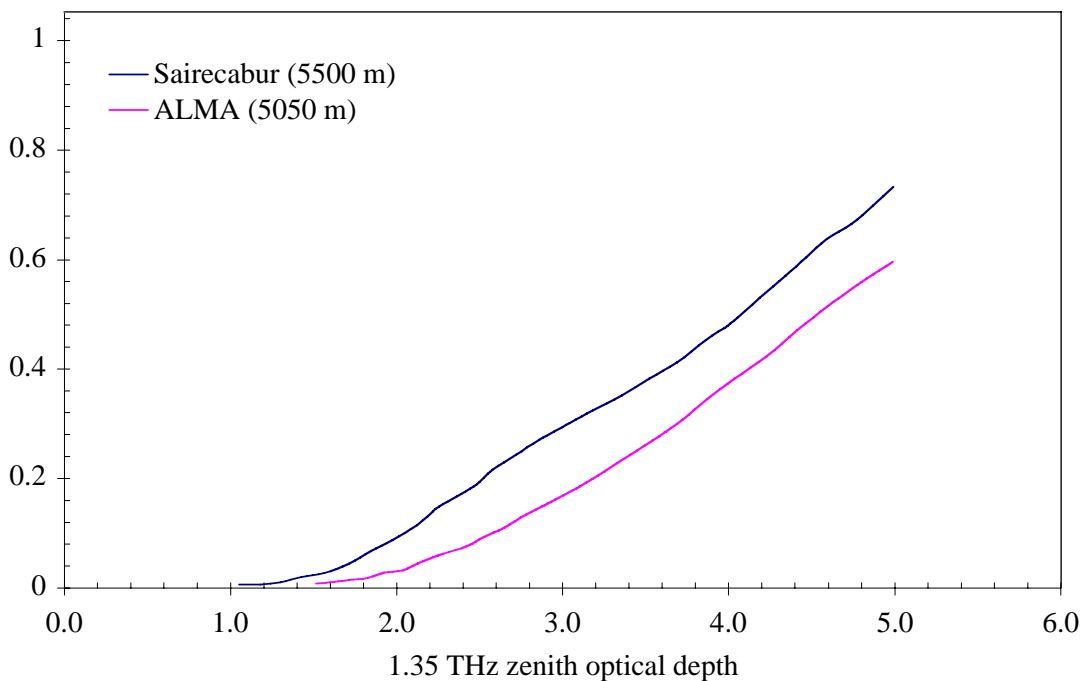


Figure 10.9. Cumulative distributions of the measured 1.35 THz zenith optical depth (τ_{1350}) show Cerro Sairecabur enjoys better conditions than the ALMA site on the Chajnantor plateau. Adapted from Blundell et al. (2002).

Blundell et al. (2002) have operated an FTS for long periods at the ALMA site (1997–1999) and at Sairecabur (2000–present). Their instrument has a resolution of 3 GHz and records spectra every 10 min (Paine et al. 2000). These long term, sequential measurements provide direct evidence of conditions suitable for short wavelength ($< 300 \mu\text{m}$) observations (Figure 10.9).

For direct, model free comparison of conditions at different sites, identical broadband tippers were deployed to the ALMA site, Mauna Kea, and the South Pole (Radford 2002). These instruments measure the 350 μm zenith optical depth every 15 min. At the ALMA site, simultaneous measurements at 350 μm and at 225 GHz heterodyne tippers show a strong correlation (Figure 10.10).

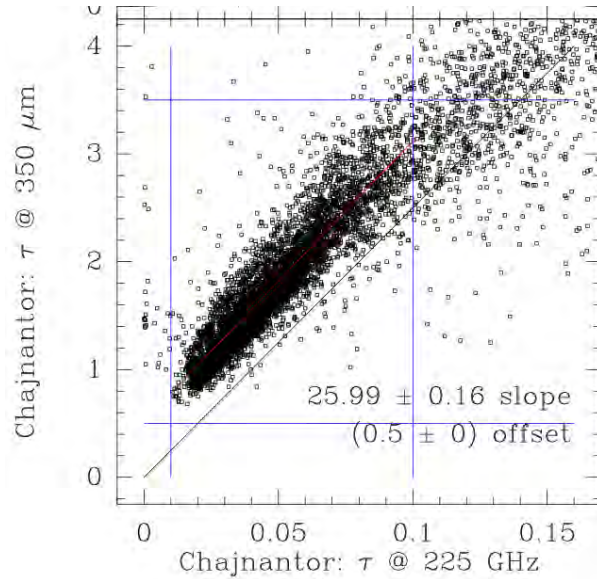


Figure 10.10. Simultaneous measurements of the narrowband 225 GHz and broadband 350 μm zenith optical depths on the Chajnantor plateau (ALMA) during 2004 show a strong correlation.

In concert with FTS measurements at the CSO, Pardo et al. (2001) developed an improved model (ATM) of atmospheric transmission at submillimeter wavelengths. Paine (2004) has developed an equally good model (*am*). These models agree in all but the finest details and fit all existing observations. Looking to the future, then, the models are sufficient with observations at only one frequency.

10.1.2.4 Site Altitude

Other things being equal, there are a few reasons to expect better observing conditions at higher altitude sites. Pressure broadening is less at higher altitude so for the same water vapor column, the skirts of the atmospheric lines are weaker and the windows between the lines are more transparent. Water is concentrated in the lower atmosphere so higher sites generally have less water above them. Furthermore, atmospheric water may be trapped below inversion layers, so a site above an inversion will enjoy even better conditions than expected from the altitude alone.

During 1998–2001, a consortium of Cornell, NRAO, ESO, SAO, and NAOJ launched a series of over 200 radiosonde flights from the Chajnantor plateau. These measured the temperature, humidity, and wind profiles from the surface to the tropopause (Figure 10.11). The water vapor density declines rapidly with altitude above the Chajnantor plateau with a typical, time averaged, scale height of 1.1 km. In addition, an inversion layer often traps most of the water vapor below its altitude. An altitude increase of 500 m is sufficient to rise above a significant fraction of the water so high sites are expected to enjoy better observing conditions (Giovanelli et al. 2001).

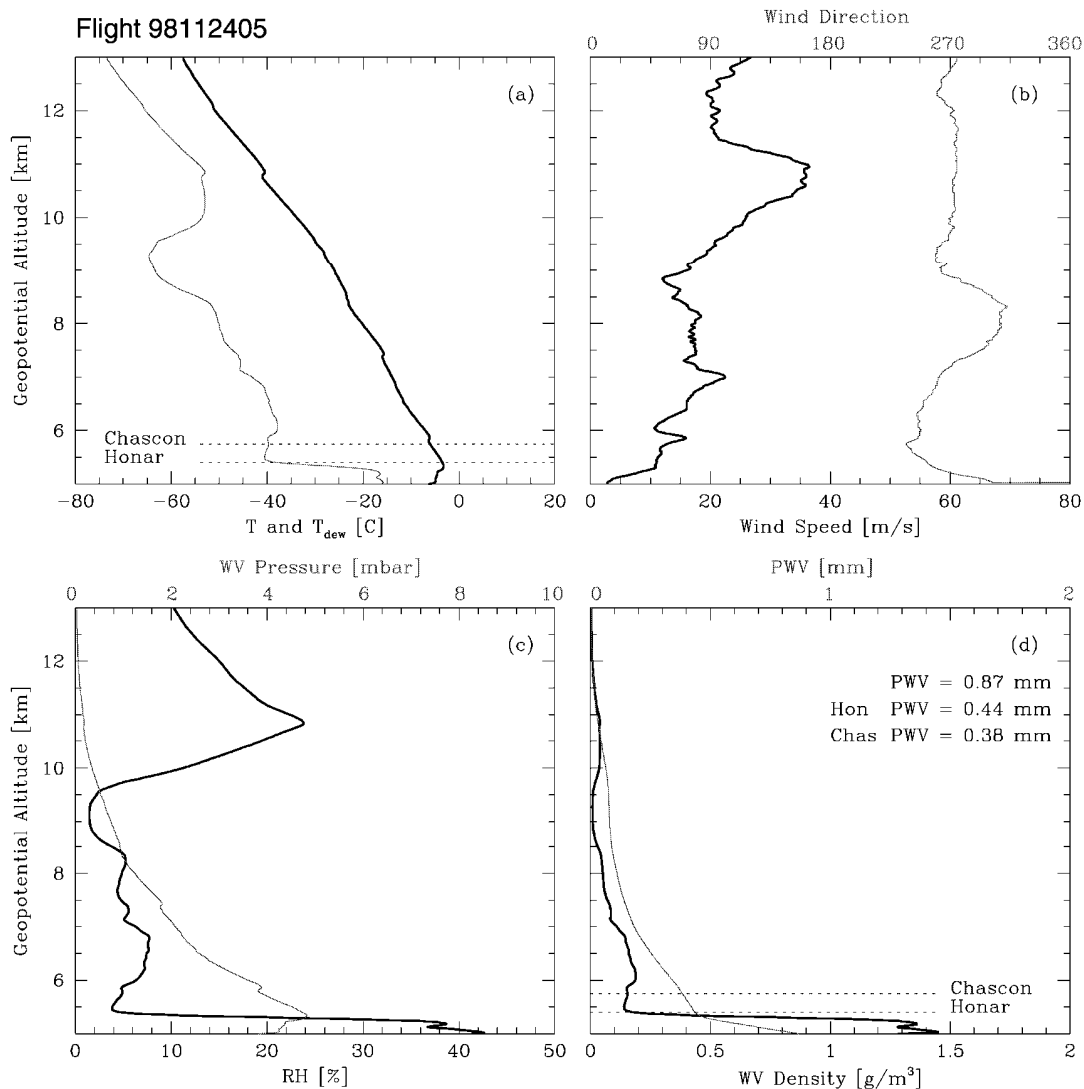


Figure 10.11. Atmospheric profiles measured during a radiosonde flight from the Chajnantor plateau on 1998 November 24 at 5 UT. Upper left: temperature (thick line) and dew point temperature (thin line). Upper right: wind speed (thick) and direction (thin line). Lower left: relative humidity (thick line) and water vapor pressure (thin line). Lower right: water vapor density (thick line) and PWV (thin line). Note the inversion layer traps much of the water vapor below the altitudes of Cerro Honar (5400 m) and Cerro Chascón (5650 m). (Giovanelli et al. 2001)

On Cerro Sairecabur, about 35 km north of the ALMA site, an existing road leads to an abandoned mine at about 5500 m altitude. This site provides a direct comparison with the lower ALMA site. Sequential FTS measurements (Figure 10.9) confirm the expected improvement in observing conditions at higher altitude, especially at the shorter wavelengths. With two instruments, simultaneous measurements at different sites are possible, dispelling any doubts about sequential measurements. Because nearby sites are affected by the same regional weather patterns, a short term comparison can reveal the relative quality of the sites before a historical baseline is established for both sites. Measurements at $350\ \mu\text{m}$ during 2001–4 demonstrate Cerro Sairecabur enjoys significantly better conditions than the Chajnantor plateau (Figure 10.12). The threshold $\tau_{225} = 0.055$ corresponds to $\tau(350\ \mu\text{m}) = 1.9$, which occurs 30% more often at Sairecabur than at the ALMA site, confirming the sequential FTS measurements. Seasonal and diurnal variations are similar at both sites and for all wavelengths.

10.1.3 Meteorology

Most of the groups working at the Chajnantor plateau and surrounding locations have operated weather stations. The meteorological records from the CBI are representative (Figure 10.13). At the Chajnantor plateau, the median temperature is slightly below freezing, -2.5°C . The radiosonde data confirm the standard lapse rate, about 7 K km^{-1} , so the expected median temperature on Cerro Chajnantor is about -6°C . The diurnal and seasonal swings in the median temperature are both about 10°C and follow the usual pattern so winter nights are colder than summer noontimes. Winds are generally from the WNW with a median speed of 6 m s^{-1} . Easterly winds occur a small fraction of the time, mostly during the summer, and are weaker than westerlies. The wind speed peaks in the late afternoon. The radiosonde data, corroborated by limited measurements on Cerro Toco (5600 m) and Cordon Honar (5300 m), indicate the wind speed increases with altitude. Hence the wind on Cerro Chajnantor is likely stronger. Surface humidity measurements are consistent with the water column depths inferred from radiometric measurements of the atmospheric transparency. Long term records indicate the weather patterns have been stable over the last half century (Bustos 2000).

10.1.4 Geology

For the ALMA project and its antecedents, a series of reports have characterized the geology of the Chajnantor plateau and its surroundings (Barrientos 1996; Gardeweg 1996; Townsend 1996; Rojas 2000, 2002, 2003, & 2004).

At the ALMA site, competent bedrock lies about 2 m below the surface, providing a firm base for telescope foundations. Cerro Chajnantor, the preferred site for CCAT, is, however, a volcanic peak rising above the plateau and likely has

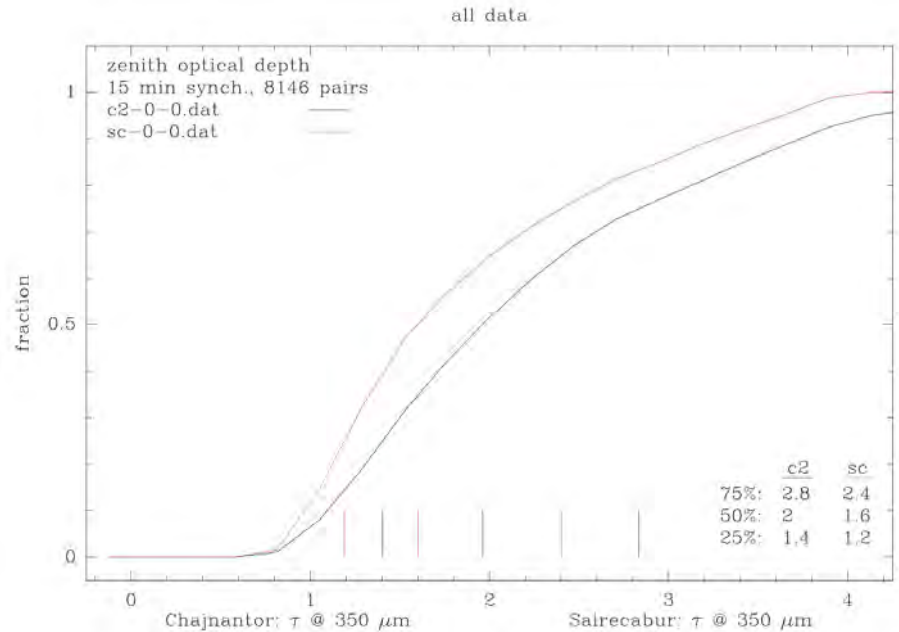


Figure 10.12. Cumulative distributions of simultaneous measurements of the broadband $350\text{ }\mu\text{m}$ zenith optical depth during 2001–4 show Cerro Sairecabur (5500 m) enjoys significantly better observing conditions than the ALMA site on the Chajnantor plateau (5050 m).

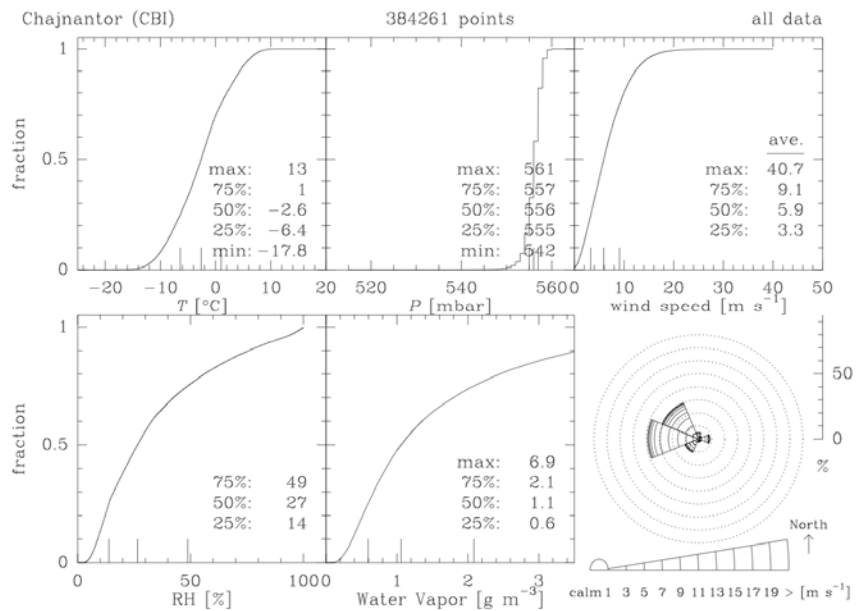


Figure 10.13. Distributions of weather data recorded at the CBI on the Chajnantor plateau, 2001 January – 2005 August.

different geological characteristics from the plateau. As a step to understanding the geology of the higher peaks, CCAT commissioned an evaluation (Section 10.2) of Cordon Honar, a ridge with an existing road that rises to the south 400 m above the ALMA site. Cordon Honar, however, seems more similar to the plateau than to the volcanic peaks. Nevertheless, there is an expectation that competent rock will be encountered at the summit. Further studies will be undertaken once access to the preferred CCAT site is established.

10.1.5 Report of Prof. Teresa Jordan

Prof. Teresa E. Jordan, Chair of the Earth and Atmospheric Sciences department at Cornell, reviewed the reports on behalf of the CCAT Project. Although most of her comments concern the ALMA site, they provide guidance for geotechnical investigations in the next phase of the CCAT Project:

At a gross level, the Geoconsultores [Rojas] reports are all sound. I read through them in the order in which they were prepared (late 1990s through 2005). They progressively improved their treatment of the geology and materials. Here are comments which were not entirely resolved by the time I'd read to the end of the entire set.

1. I would have approached the site assessment by obtaining more information about the distribution of the various types of ignimbrites and collected physical properties data that was tied to the individual types of ignimbrites. It wasn't until the 2002 report that it was finally acknowledged that not all the ignimbrite is welded (Schmitt's Figure 2 of memo 418). By mapping the distribution of the various ignimbrite flow units and tying the core data and rock mechanics data to those flow units, one could project to undrilled locations the engineering properties (degree of fracturing, porosity) with confidence. Perhaps some drilling and some trenching could have been avoided. A geologist experienced in volcanic studies could create a map and project onto cross sections (located wherever you need them) the continuity and depths of the materials of varying rock properties.

2. One part of the studies that is appropriate but perhaps not yet used properly is the geophysical survey (resistivity survey). This survey technique, or other shallow geophysical techniques like Ground Penetrating Radar or refraction surveys, can potentially trace the boundaries between the different ignimbrite flow units. But Memo 418 reports an interpretation of the resistivity survey that is both internally inconsistent (the lowest unit is stated to show lower resistivity when instead the values are higher) and apparently inconsistent with the Schmitt et al. (2001) description of the ignimbrite stratigraphy. The inconsistency with the Schmitt et al. description may be entirely justified (they may describe different locations), but without an explanation it appears that the resistivity is erroneously interpreted.

3. You ought to have a photogeologic (or high resolution satellite image) interpretation of the combined trench, borehole, and geologic data for the Chajnantor Pampa (or whatever other site interests you). This would make it easier to pick the sites with least (or most, if you prefer) thickness of sand above the massive ignimbrite.

4. I would ask for more detailed study of the shallow faults in the area. As noted in the reports, the Pampa Chajnantor site lies along strike of the major young (but uncertain how young) Miscanti fault, and there are very small offset fault scarps both east and west of the site (within a few kilometers distance of the ALMA site). Why be suspicious? Other faults of similar geometry and orientation in the vicinity (Salar de Atacama subsurface) have only very recently been recognized, and one has been shown to have had around 28 m of offset in the last 16,500 years. Both the Geoconsultores reports and Gardeweg (1996) report make internally inconsistent remarks about whether the faults cut the 1.3 Ma Purico (Cajón) ignimbrite (or any younger units). These inconsistencies may be translation errors, but it's important to know whether or not the faults offset the youngest units. Most useful would be to know whether they offset the glacial moraines that Gardeweg refers to.

5. Although Barrientos' 1996 hazard assessment stated that there are no shallow earthquake events known in the region, this is not strictly true if one considers small earthquakes (which are not usually located by the global teleseismic network used by Barrientos). A German-Chilean group recently completed a microseismicity study of the Atacama region. Arturo Belmonte's thesis describes the results. His thesis isn't yet published but I know that he is working on revising a manuscript, and he might be willing to comment on microseismicity in the area of the telescopes. He works in Chile for Codelco conducting seismic studies of the El Teniente mine.

6. Barrientos' 1996 assessment that 100 km deep normal fault earthquakes are the major threat of EQ accelerations at the telescope site appears to be consistent with the 2005 earthquake that struck the eastern part of Iquique province.

7. Referring to the Rojas/Geoconsultores (Section 10.2), I don't know whether Rojas was sufficiently clear in his answer to your question about the similarity in what to anticipate on Cerros Chascón, Chajnantor, Toco and Negro, compared to the Honar ridgeline. There would be very big differences between those peaks and the geology dealt with in the many geotechnical reports. Most of Cerros de Macón and Cerros de Honar are buried by the Purico (Cajón) Ignimbrite, and will have a gross similarity to the ALMA site. But none of those peaks you listed will have the uniformity of rock type that characterizes the "pampa" and will have little of the ignimbrite (which varies little spatially). All the peaks are likely to have a complex mixture of textures and types of volcanic rocks. You'd really have to start over at the beginning to develop reliable site surveys for those areas. If so, it would be very helpful to involve a geologist who would provide a detailed map of the multiple volcanic units, prior to turning to the engineering geologists.

Moyra Gardeweg would be an excellent choice of such a geologist. Other highly qualified geologists could be contracted through SERNAGEOMIN, or I could ask here in Antofagasta at the Universidad Católica del Norte where I'm based now whether one of their faculty members is well suited to this work. There are also a pair of Cornell graduate students who would be very competent. I could describe the obvious features at the surface, but I don't have the training and experience with which to predict the spatial extent and depth of various types of volcanic deposits – and it is this ability to extrapolate that brings value to the geologist in this situation.

10.1.6 Site Access

To meet the Project schedule, formal establishment of CCAT in Chile must be initiated relatively soon. The required legal process is likely to take the better part of a year. Thus, in order to start site preparation activities by late 2007 or early 2008, this process must be initiated by the middle of 2006. In addition, the independent process to obtain permission to use a particular site for construction of an observatory and an access road – should the selected site require one - will require a lengthy legal and technical procedure. Thus site selection and the beginning of the legal steps to obtain site access permission must occur soon.

10.1.6.1 Legal Presence of CCAT in Chile.

A possible model for the establishment of CCAT's legal presence in Chile follows the example of several previous astronomy initiatives in Chile, among them AURA (CTIO and Gemini South), the Carnegie Observatories, AUI (NRAO/ALMA), and Caltech (CBI). This procedure involves the following steps:

1. A non-for profit corporation composed of the CCAT partners is established in the US along lines similar to AUI or AURA. The corporation charter should foresee possible future expansion of the partnership or other possible changes.
2. This CCAT corporation establishes legal presence in Chile and enters into a cooperative agreement with a Chilean academic institution, such as the Universidad de Chile or the Pontificia Universidad Católica de Chile.

3. Invoking the “Astronomy Law” (nr. 15172), the CCAT corporation and its Chilean cooperative partner request the privileges established by that law, including exemption from import duties on Project related goods and equipment, free entry of specialized manpower, exemption from the value added tax on any purchases within Chile, and other benefits.

Upon completion of this procedure, CCAT would be in position to construct and operate an observatory in Chile. It is important to note a revised version of the Astronomy Law has been presented on the floor of the Chilean Congress, where it currently lies dormant. There is no immediate pressure for its passage but this may change with a new administration. It is also thought the bureaucratic path imposed by the revised law may lengthen the times as well as some of the modes for establishing a legal presence for CCAT in Chile

10.1.6.2 Site and Road Access

Legal presence for CCAT in Chile does not, by itself, grant access to a particular site for telescope construction. Separate permission is needed before site development may begin. The process of obtaining permission for any sort of extended activity in the Atacama region -be it site testing, road construction, or site development - has in recent times become lengthier than it was in the past. The increased participation of indigenous groups in decisions at a regional level has had an important impact. Even the simplest of activities, such as deployment of a portable weather station at a previously untested site, requires consideration by local committees appointed by such national bodies as the Corporación Nacional de Desarrollo Idigena (CONADI). Archeological and environmental impact studies will be necessary as well as, ultimately, approval by the Comisión Nacional de Investigación Científica y Tecnológica de Chile (CONICYT), which is the official "concessionaire" for any site within the National Science Preserve centered on the Chajnantor plateau. It is cautiously estimated the process of obtaining permission to construct CCAT will take at least one year.

10.1.7 Future Plans

For CCAT, direct measurements of observing conditions on Cerro Chajnantor are a high priority. Other groups, including the University of Tokyo, are also interested in this peak. The intention is to compare measurements of the 350 μm transparency on Cerro Chajnantor with simultaneous measurements at the CBI on the Chajnantor plateau. Because of the long record of measurements at the lower site, this comparative technique will permit a quick evaluation of the relative quality of the two sites. Because of administrative and technical difficulties, however, these measurements have not been possible to date. The evaluation equipment, including a 350 μm tipper, a weather station, a shelter, a photovoltaic power system, and communication equipment, have been prepared and deployed to test locations on Cerro Toco in 2004 May and on Cordon Honar (Figure 10.14) in 2005 April. The two tippers have been operated side by side at the CBI since 2005 June to confirm their measurements are directly comparable. CCAT recently received permission to install the site evaluation equipment on Cerro Chajnantor and deployment is planned in early 2006 as soon as logistics can be arranged.

10.1.8 Summary

Sites in the high Andes of northern Chile enjoy some of the best observing conditions for submillimeter astronomy in the world. As a result, the vicinity of San Pedro de Atacama in northern Chile is rapidly becoming a major center for astronomy. Of several candidate sites for the CCAT, a location just below the summit of Cerro Chajnantor (5590 m) has been selected as the baseline for the Concept Feasibility Study. This site is within the science preserve surrounding the ALMA project. Because it is higher than the Chajnantor plateau, observing conditions should be better.



Figure 10.14. CCAT site evaluation equipment during test deployment at 5312 m on Cordon Honar in 2005 May. The submillimeter tipper is right of the yellow shelter, which houses batteries and electronics. Cerro Chajnantor is on the skyline immediately left of the yellow shelter.

10.1.9 References

- Barrientos, S. E., 1996, Seismicity and Seismic Hazard at MMA site, Antofagasta, Chile, MMA Memo 250 (NRAO).
- Blundell, R., et al., 2002, Prospects for Terahertz Radio Astronomy from Northern Chile, in Proc. Thirteenth International Symposium on Space Terahertz Technology, ed. Tong, C. E., & Blundell, R. (Harvard) pp. 159-166.
- Bustos, R., Delgado, G., Nyman, L.-Å., & Radford, S. J. E., 2000, 52 Years of Climatological Data for the Chajnantor Area, ALMA Memo 333 (NRAO).
- Dicke, R. H., Beringer, R., Kyhl, R. L., and Vane, A. B., 1946, Atmospheric Absorption Measurements with a Microwave Radiometer, *Phys. Rev.* 70, 340-348.
- Gardeweg P., M. C., 1996, MMA Site East of San Pedro De Atacama, North Chile; Volcanic Hazards Assessment and Geologic Setting, MMA Memo 251 (NRAO).
- Garreaud, R., Vuille, M., and Clement, A., 2003, The climate of the Altiplano: Observed current conditions and mechanisms of past changes, *Palaeogeogr. Palaeoclimatol. Palaeoecol.* 194, 5-22.
- Giovanelli, R., Darling, J., Henderson, C., Hoffman, W., Barry, D., Cordes, J., Eikenberry, S., Gull, G., Keller, L., Smith, J. D., and Stacey, G., 2001, The Optical/Infrared Astronomical Quality of High Atacama Sites. II. Infrared Characteristics, *PASP* 113, 803-813.
- Golwala, S., 2005, Definition of a Cut for Multiplexing between Bolocam and High-Frequency Observations at the CSO (CSO memo).
- Matsushita, S., Matsuo, H., Pardo, J. R., and Radford, S. J. E., 1999, FTS Measurements of Submillimeter-Wave Atmospheric Opacity at Pampa la Bola II: Supra-Terahertz Windows and Model Fitting, *PASJ* 51, 603.
- Messerli, B., et al., 1993, Climate Change and Natural Resource Dynamics of the Atacama Altiplano during the Last 18,000 Years: A Preliminary Synthesis, *Mountain Research and Development* 13, 117-127.

- Núñez, L., Grosjean, M. and Cartajena, I., 2002, Human Occupations and Climate Change in the Puna de Atacama, Chile, *Science* 298, 821-824.
- Paine, S., Blundell, R., Papa, D. C., Barrett, J. W., and Radford, S. J. E., 2000, A Fourier Transform Spectrometer for Measurement of Atmospheric Transmission at Submillimeter Wavelengths, *PASP* 112, 108.
- Paine, S., 2004, The *am* Atmospheric Model, SMA Memo 152.
- Pardo, J. R., Cernicharo, J., and Serabyn, E., 2001, Atmospheric Transmission at Microwaves (ATM): An Improved Model for mm/submillimeter applications, *IEEE Trans. Ant. Prop.* 49/12, 1683-1694.
- Radford, S. J. E., and Chamberlin, R. A., 2000, Atmospheric Transparency at 225 GHz over Chajnantor, Mauna Kea, and the South Pole, ALMA Memo 334.1 (NRAO).
- Radford, S., 2002, Site Characterization for mm/submillimeter Astronomy, in *Astronomical Site Evaluation in the Visible and Radio Range*, ASP Conf. Ser. 266, ed. Vernin, J., Benkhaldoun, Z., & Muñoz-Tuñón, C. (San Francisco: ASP) 148.
- Rojas, L., 2000, Geotechnical Study Chajnantor Site, II Region, Chile, ALMA Memo 408 (NRAO).
- Rojas, L., 2002, Geotechnical Study, Chajnantor Site, 2002 Campaign, II Region, Chile, ALMA Memo 418 (NRAO).
- Rojas, L., 2003, Preliminary Geological/Geotechnical Site Inspection, Chajnantor Area (ALMA).
- Rojas, L., 2004, Excavation and Geological/Geotechnical Assessment; 79 Locations at the ALMA Array Operations Site (ALMA).
- Rojas, L., 2005, Preliminary Geological/Geotechnical Site Assessment, Cordon Honar (CCAT).
- Townsend G., F., 1996, Preliminary Report on Water Supply, Millimeter Array Project, MMA Memo 230 (NRAO).



10.2 Geotechnical Report, GEO Consultores

Report prepared by GeoConsultores, S. A.

10.2.1 Introduction

As part of the Caltech Cornell Atacama Telescope Project (CCAT), it has been proposed that a telescope be installed south of the ALMA project site on the summit of the Honar ridge at an altitude of 5400 m, at the following location (UTM positions on Prov. S. Am. 1956 datum):

| | |
|---|----------|
| N | 7 448500 |
| E | 627800 |

The CCAT meteorological station is installed nearby, at an altitude of 5312 m and:

| | |
|---|----------|
| N | 7 448736 |
| E | 628219 |

This Consultant traveled to the site on June 1st to develop a preliminary geological /geotechnical site assessment, to estimate foundation conditions at the location and to suggest future activities.

This note summarizes the results of the visit and includes some information related to the subsurface that is relevant to the proposed location.

10.2.2 Site Description

The Honar ridge extends from the North East to the South West outside of the South border of the ALMA project site and is part of the CONYCIT Science Preserve. To the North and to the North East, at a distance of approximately 9 km, one can observe the Chajnantor and the Chascon mountains, respectively.

Photo 10.2.1 shows the gentle slope of the ridge, with abundant rock pieces on the surface, whereas Photo 10.2.2 presents a view of the meteorological site on the flat near the bottom of the ridge. Photo 10.2.3 shows the road to the top of the ridge. Again, the surface of the ridge shows abundant rock pieces and debris. Photos 10.2.4, 10.2.5 and 10.2.6 are views around 360° taken at the top of the ridge. Note the surface drainage system of the ALMA flat site covered with snow and the Chajnantor and Chascon mountains on the center and left of the view in Photo 10.2.4. Also, note in Photos 10.2.4 and 10.2.5 the detail of large rock pieces on the surface of the Honar ridge, product of erosion by water, ice and wind.

10.2.3 Geologic Setting

The Honar ridge is located within the Purico ignimbrite sheet as part of the Purico volcanic group. A summary of the geologic site description, which has previously been included in *Geo* reports for the location, follows.

Several stratified units, ranging from Paleozoic to Quaternary, and groups of plutonic rocks, have been distinguished in the overall region. The precordillera and Andean cordillera domain morph structure contains upper Cenozoic volcanic rocks separated into two major groups, the ignimbrites and the volcanoes.

Ignimbrite is defined as a silicic volcanic rock forming thick, massive, compact, lava like sheets covering wide areas. The rock is chiefly a fine grained rhyolitic tuff formed mainly of glass particles, firmly welded. The

deposits are believed to have been formed by the eruption of dense clouds of incandescent volcanic glass in a semi molten or viscous state from groups of fissures.

Ignimbrites are divided into three groups according to their ages, that is: Miocene, Pliocene and Pleistocene. They are constituted by pyroclastic flows, mainly dacitic and andesitic; the Cajon ignimbrite, present at the site, is dated from the Pleistocene-Holocene with 0.8 Million years. Its outcrop covers approximately 450 km² in the Calama sheet, extending another 530 km² to the South. Its thickness ranges from 250 m to a few meters thinning to the West.

To the North-East of the Purico volcano (zone of interest), the unit is composed by tuff moderately to weakly welded with phenocrystals of plagioclase, quartz, biotite and hornblend. Its matrix is composed of pieces of glass. Typically, the flows contain a large number of pumice. From a chemical point of view they are classified as chalcoalcalines.

It is proposed that the Cajon ignimbrite was formed by the emission through concentric fractures around the Purico volcano.

The volcanoes are divided into three groups: Miocene, Pliocene-lower Pleistocene and upper Pleistocene-Holocene, with the Chajnantor and Purico being strato-volcanoes from the later group.

The Purico volcanic group is believed to have evolved around an old strato-volcano (the Purico) having andesitic composition, with a later emission of very viscous lava flows (North-East and South-East of the Purico and on the South-East flank of the Chajnantor). The emission of ignimbritic flows would have come later in the superior Pleistocene. The last stage would be the occurrence of the Toco, La Torta, Chajnantor, and Chascon volcanoes around the Purico.

The tectonic structure shows very little disturbance by recent activity. The only structures known correspond to normal faults and fractures of little magnitude with three main systems: N-S, NW-SE, NE-SW.

The N-S system in line with the N-S volcanic chain, affect the Cajon ignimbrite West of the Purico, but has not produced vertical movement on the rock. It seems that they have been inactive prior to the ignimbrite flows.

The NW-SE and NE-SW systems affect various volcanic units in the area. They are minor structures with local development. These systems appear controlled by the local volcanic activity. They would be the result of E-W extension movements.

A resistivity geophysical study done by NRAO (2001 and 2002 at the Science Preserve) shows the existence of three horizons with specific resistivity: the upper one with a thickness of approximately one meter and a resistivity of 1,513 Ω m corresponds to meteorized cover. The second, with a depth of about 18 m and resistivity of 8,852 Ω m is correlated with sound rock composed by the Purico Superior Ignimbrite. Finally, the lower horizon, with resistivity of 16,184 Ω m is related with the Purico Inferior II Ignimbrite.



Figure 10.2.1. The Honar Ridge

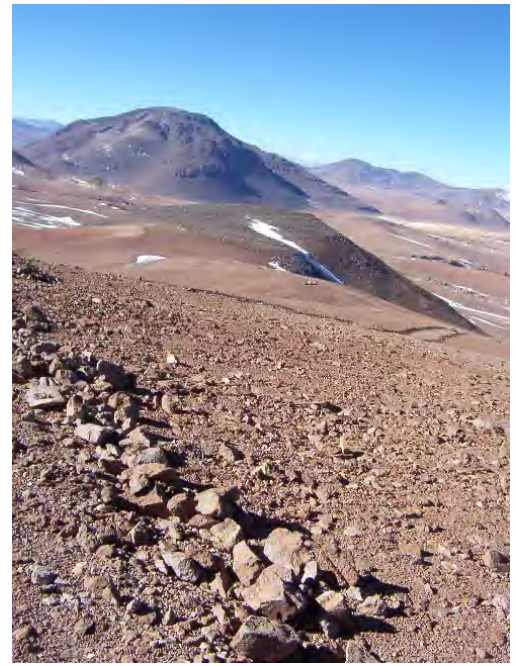


Figure 10.2.2. View of Meteorological Installation from the Honar Ridge



Figure10.2.3. Access Road to the Honar Ridge



Figure 10.2.4. View from the Honar Ridge to the North UJT Chajnantor and Chascon on Front



Figure 10.2.5. View from the Honar Ridge to the West

10.2.4 Site Visit

During the site visit of this Consultant could confirm that the Honar ridge is part of the Cajón ignimbrite field and thus it should have an ignimbrite cover with thickness that could reach up to 30 m at the location. The topography of the ridge itself is gentle, indicating that the ignimbrite cover could very well have a very constant thickness, depending on the direction of deposition travel.

The surface, as it has already been depicted, shows abundant rock pieces, product of weathering and erosion. This cover that could be considered as a residual soil could reach a thickness of approximately one meter.

Under the cover lay the massive ignimbrite horizon. The rock has been shown to be blocky with fractures that create cubical shapes up to various m^3 in volume.

10.2.5 Comments

In general the rock mass underlying the soil/rock upper layer is competent and should be adequate to receive the foundation of an equipment such as a telescope.

The foundation of such equipment should be rather massive to hold the normally large overturning moment loads and to comply with the strict deflection requirements.

The foundation will be located at a depth of 1 to 1.5 m, with the surface of the excavation free of open cracks. It is expected the massive ignimbrite rock be present at a depth ranging from 1 to 1.5 m.

The cerros, Negro, Chajnantor, Toco and Chascon are most likely composed of volcanic rock (andesitas, etc.) with very hard crystalline structure but very broken near the surface.

10.2.6 Recommendations

It is recommended that a trench to the massive rock be excavated as an exploratory step at the specific location once such location has been selected. The trench should be visited and explored to determine that the rock underlying the top soil/rock is sound and that its geotechnical characteristics are adequate to place the foundation of the equipment.

During construction and once the excavation for the foundation has been completed, it should be visited and approved for soundness of the rock and adequacy of bearing capacity.



Figure 10.2.6. View from the Honar Ridge to the south

11 Site, Architecture, and Civil Engineering

11.1 Introduction

This section addresses the conceptual design of site improvements and facilities for CCAT. The site improvements include access roads, grading & leveling, and utilities. Architectural design addresses both the summit facility from the ground up to the azimuth rotation levels of the dome and telescope and the base support facility to be located near San Pedro. To address these issues, we contracted with M3 Architecture and Engineering of Tucson, AZ, to study elements of site and facility development. While negotiations with other institutions may lead to sharing a variety of services and support facilities in Chile, the baseline study assumes that CCAT will be fully self-sufficient.

11.1.1 Background

Previous sections have addressed the requirements established for the facilities by the work of science, instrument, and operations committees. Section 10 (site testing evaluation) provides the results from previous work and some initial geological assessment of what the bearing strata might be. To establish feasibility and cost estimates for the facility we elected to develop a conceptual design for roads, foundations, buildings, and infrastructure. In spite of not being able to definitively determine the actual summit to be used for CCAT, we looked at three likely sites. The site will be chosen during the next phase of work following additional testing and further investigation of access and sources for electrical power. Design of the facilities and infrastructure will also be further developed. Our objective in the next phase will be to have sufficient documentation of site work in hand to obtain bids and begin work as soon as formal approval of the development phase of CCAT is received.

11.1.2 Discussion

Critical Elements of Infrastructure Design: Several key areas of infrastructure would be required to establish and operate CCAT.

11.1.2.1 Roads

Only one peak under consideration, Sairecabur, has a road to the summit, though this road would require some work to be compatible with routine use and the large loads required for telescope development. Either of the other two peaks would require a significant length of new road to be constructed. In order to assess the feasibility and cost of constructing these roads, M3, working from topographic maps, identified road routes and assessed the volumes of cuts and fills and other infrastructure such as culverts and drainage features. This enabled an assessment of the practicality and likely costs for construction.

11.1.2.2 Site Works

The summits of the proposed peaks require work in preparation for construction. This includes leveling, drainage features, locations for required utilities, and consideration of excavation and bearing capacities to support foundations. Assessment of the technical data provided regarding the bearing strata and consideration of the difficulty of excavation and earth moving were considered. Better assessment of the needs of site development (and road construction as well) can be performed when more accurate topographic information is available. CCAT intends to survey the proposed site (aerial or ground TBD) to support more detailed and accurate concept design during the next phase of work.

11.1.2.3 Summit Facility

Initial discussions with M3 indicated our aggressive position with respect to cost and the minimum complement of summit capabilities which would meet operational requirements. The ability to store and work on large complex instruments, appropriate spaces for observing and other work, support of the large rotating dome, and required utilities were considered. Accommodating these requirements using construction approaches that would maximize safety and minimize cost at the extreme altitudes was a key element in design. The resulting facility has a large volume of concrete in construction. This is a proven approach for observatory facilities in Chile, but

careful attention will need to be paid to the logistics and costs implied by the remote location. ALMA will prove an interesting example to watch as we progress into the next Project phase.

11.1.2.4 Base Support Facility

Our proposed operations plan requires both sleeping and working accommodations for modest numbers of personnel at a lower altitude than the summit. ALMA, CBI, and APEX have provided examples of how this requirement may be met, ranging from leasing of space from hoteliers in San Pedro to building large dedicated facilities in close proximity to the summit access roads. Our on-site assessment led us to prefer an approach like APEX, close to San Pedro to take advantage of the infrastructure available there, but independent to allow maximum freedom of operation. Architecture in San Pedro is protected by law, so this provided additional requirements to the design. M3 was asked to develop a reasonably modest yet capable facility that could house workers on turno from their residences. The resulting facility design is similar in scope to that developed by APEX.

11.1.2.5 Critical Issues

Several areas of site, facility, and infrastructure development constitute significant challenges:

- **Road Construction:** This is likely to be a significant project expense. Partnering with another program to share development cost would be desirable. Over the next phase of CCAT we plan to get better cost estimates for the road.
- **Concrete:** There is a large amount of concrete in CCAT, particularly the summit facility. This includes forming, reinforcing steel, and the concrete itself. We will investigate ways to reduce the total volume required and optimize the cost per cubic meter.
- **HVAC and Oxygenation Equipment:** The oxygenation of habitable facilities at the summit is expensive. We plan to revisit the design to minimize the amount of oxygenated space while maintaining functionality and a safe working environment.

11.1.2.6 Summary

The next phase of CCAT work is very important to the ongoing development of operations planning and facility design. Working with local contractors ahead of the bidding process and adjusting designs to use the most cost effective construction approaches will result in the lowest cost. The ongoing development of the science preserve caused by ALMA and other international projects has the potential to significantly affect the approaches to utility and infrastructure development. By the end of the Engineering Concept Design phase, we anticipate having trimmed our needs to the minimum required over the life cycle of CCAT and having identified construction approaches that meet our cost constraints.

11.2 Site, Architecture, and Civil Engineering

Report prepared by M3 Engineering and Technology Corporation

11.2.1 Introduction

M3 Engineering & Technology Corporation (M3) was retained by CCAT to provide a conceptual level design study of the facilities for a 25 m telescope for submillimeter astronomy located in the Atacama region of northern Chile. The major objective of the study is to identify desirable configurations for major subsystems, identify significant risks in the development of the CCAT, and develop initial estimates of cost.

The primary focus of the study is the mountain facility which includes the following:

- Site access road
- Site utilities
- Telescope foundation
- Dome foundation
- Control building

The telescope dome is part of a separate study and cost estimate.

This study also briefly addresses CCAT's support facility planned at a lower altitude (≈ 2500 m) in the vicinity of San Pedro, Chile, and provides a rough order of magnitude of the estimated costs.

11.2.2 Site Options, Road Design and Site Utilities

Three sites, all in the Atacama Desert, are possible locations for the mountain facilities. The study compares elevation, accessibility, soil conditions and costs between the three sites. For the purpose of the conceptual design, CCAT selected Cerro Chajnantor as the preferred site.

11.2.3 Cerro Chajnantor

Cerro Chajnantor is within the CONICYT expanded science preserve at an elevation of 5600 m (18,350 feet) above sea level (Figure 11.2.1). A relatively level plateau just northeast of the peak is the preferred mountain facility location.

The proposed access road to the site is approximately 6.3 km (3.9 miles) in length with 15 switchbacks. The road begins at an existing dirt road on the east side of the mountain and wraps around the northern region to the mountain site.

11.2.4 Cerro Chascon

Located within the CONICYT science preserve at an elevation of 5675 m (18,600 feet), this site is approximately 6.0 km (3.75 miles) southeast of Cerro Chajnantor. The selected mountain facility site is on the ridge west of the summit caldera (Figure 11.2.2).

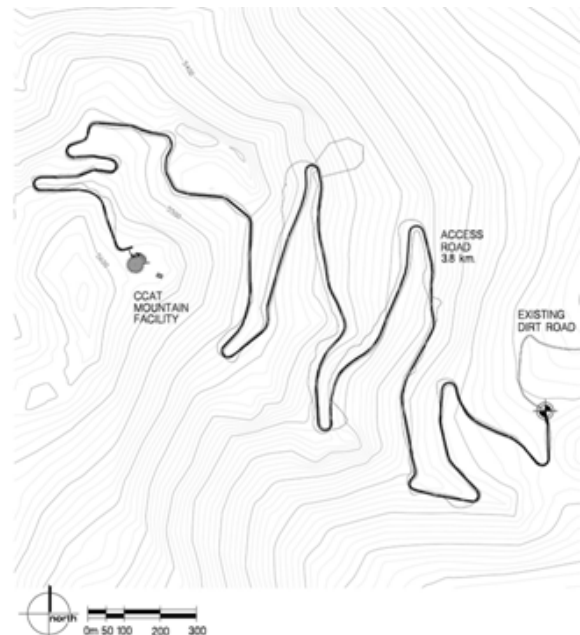


Figure 11.2.1

The selected mountain facility site is on the ridge west of the

The proposed access road begins at an existing road located on the northeast side of the mountain. The total length is approximately 13 km (8 miles) with only 3.0 km (1.80 miles) of road at a 10% grade. There are a total of 5 switchbacks with most of the road located on the southeast side of the mountain.

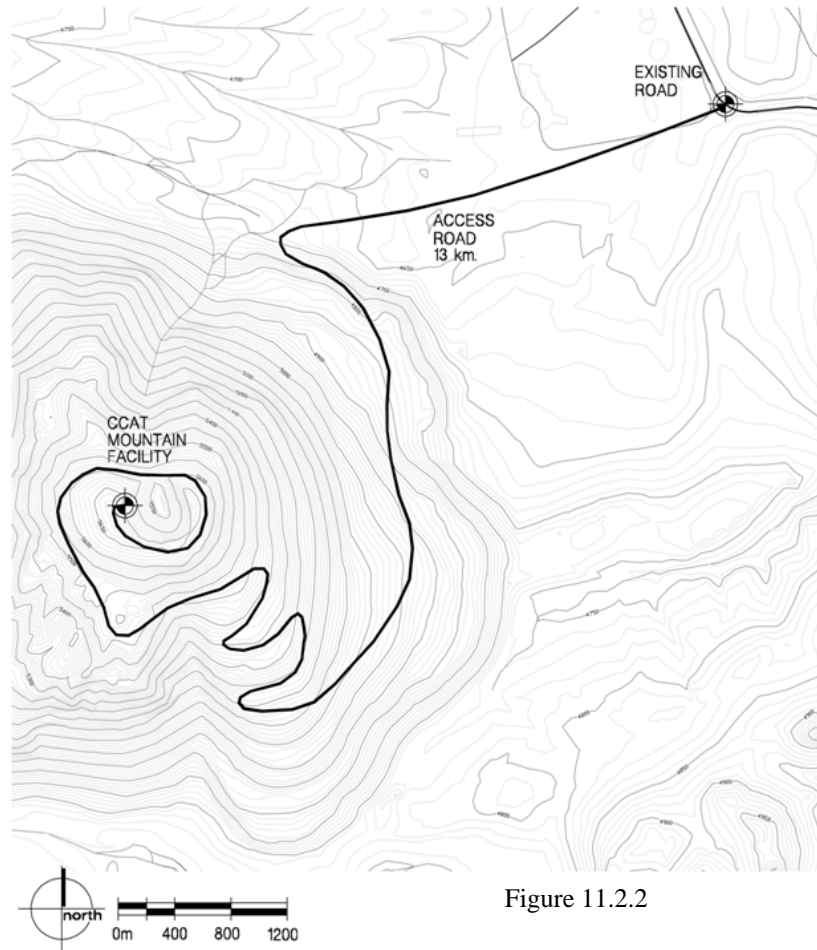


Figure 11.2.2

11.2.5 Sairecabur

Sairecabur is located approximately 25 km (15.5 miles) from San Pedro at an elevation of 5500 m (18,000 feet) above sea level. This site is approximately 35 km (22 miles) north of the other two locations. There is an existing dirt mining road to the site used by the Smithsonian telescope. This road is generally in good condition but needs to be widened and several switchbacks require improvement. The total length of the access road from the El Tatio highway is approximately 21 km (13 miles).

11.2.6 Environmental Conditions

In general all three potential sites are very similar environmentally. All sites are located above 5500 m (18,000 feet) elevation and are on volcanic cones. Environmental testing is planned on all three sites.

For the purposes of this study the following site conditions are the design criteria for the mountain facility:

11.2.6.1 Operating Conditions

The following represent the range of environmental conditions expected during operation. All CCAT systems must remain fully functional during the worst case combination of these conditions.

| | |
|------------------------------|---|
| Air Pressure | 7.2-7.9 psi (495-545 kPa) |
| Wind speed | < 10 m s ⁻¹ (33 ft s ⁻¹) with 15m s ⁻¹ (50 ft s ⁻¹) gusts |
| Temperature | -25 to +20 °C (-13 to +16 °F) |
| Relative humidity | 0% to 95% |
| Maximum uniform ice build-up | 25 mm (1.0 in) or 22 kg m ⁻² (5 psf) |

11.2.6.2 Survival Conditions

The following represent the maximum non-operating environmental conditions the CCAT is required to withstand. The dome shall be in the fully closed stationary configuration when considering the worst case combination of these conditions.

| | |
|---|--|
| Wind speed | 65 m s ⁻¹ (215 ft s ⁻¹) |
| Temperature | -30 to +25 °C (-22 to +77 °F) |
| Diurnal temperature variation | 30 °C (54°F) |
| Snow load on horizontal surface | 100 kg m ⁻² (20 psf) |
| Additional uniform ice build-up on surfaces not covered by snow | 25 mm (1.0 in) or 22 kg m ⁻² (5 psf) |
| Annual precipitation | up to 300 mm (up to 12 in) |
| Design precipitation event | 25 mm hr ⁻¹ (1 in hr ⁻¹) at 30 m s ⁻¹ (100 ft s ⁻¹) wind |
| Seismic ground acceleration | Zone 4 per the Uniform Building Code |

11.2.6.3 Access Road Design

The existing access road to Sairecabur is a single lane dirt road. The proposed access roads to Cerros Chajnantor and Chascon are also single lane dirt roads, with the following design guidelines.

- The proposed road width is 3.65 m (12 feet) with guardrails as required and safety pullouts located throughout the length of the road. This provides a single lane access road with the minimum width required to transport large instruments and telescope parts.
- Minimize switchbacks and design the road width just enough to allow passage of the proper size vehicle with large instruments and components up to the site.
- Slope the road back into the mountains and install culverts as required for proper drainage. This minimizes road erosion and maintenance costs.
- For safety and maintenance concerns it is best to locate the access road on the mountain side exposed to the sun thereby minimizing snow and ice build-up.

11.2.7 Site Utilities

Utilities at the mountain facility are as follows: At this stage, all equipment loads and requirements are notional and subject to refinement during the next phase of the project.

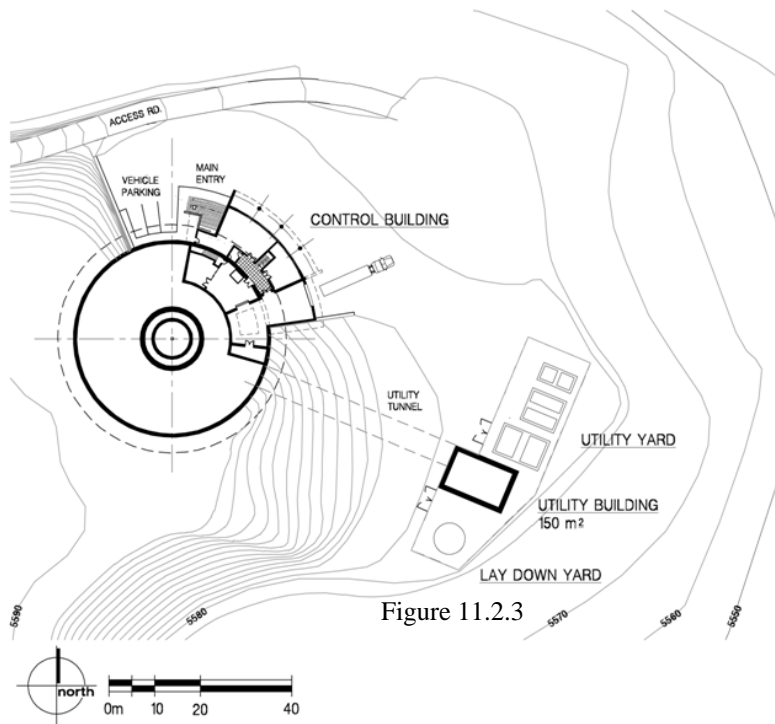
- Two 750 kVA power generators with one unit as a backup.
- 37,800 liter (10,000 gallon) non-potable domestic and fire water tank.
- Communications between the mountain and support facilities by microwave link. A direct line of sight is possible from Cerro Chajnantor or Sairecabur. From Cerro Chascon, a repeater may be necessary.
- All equipment is de-rated for altitude.

11.2.8 Site Design

For the purpose of the conceptual study, Cerro Chajnantor is the selected site. Access to the site is from the northwest along the side of the mountain. The natural terrain at the site slopes approximately 10 m (32 feet) at 10% grade to the east and the prevailing winds are generally from the northwest. The telescope site is below and northwest of the summit. In addition to shielding the telescope from westerly winds, the summit ridge hides the telescope out of view of San Pedro de Atacama, easing some environmental impact considerations. The site has great views of the lower plain, especially to the north northeast (Figure 11.2.3).

The site design and layout incorporates the following parameters:

- Minimize the earthwork and site impact by terracing the facility into the mountain side.
- Keep all major mechanical and electrical equipment away and downwind from the telescope facility eliminating equipment vibration or heat from impeding the telescope performance.
- Locate the control building to take advantage of passive solar design and the views towards the northeast.
- Provide adequate open space around the observatory to allow vehicle maneuvering and a staging area for construction and erection of the facility and telescope.



The telescope facility is located immediately upon approaching the site with vehicle parking and the main entrance in clear view. The enclosure ring wall is used to retain the mountain grade providing insulation to the telescope chamber. Cut and fill of the natural grade along with retaining walls provide a level area adjacent to the observatory.

The utility building is located southeast and downwind of the observatory. The building is lower in elevation to minimize earthwork and allow a direct path of the underground utility tunnel to the observatory. All major electrical and mechanical equipment is located in this building keep noise, vibration and heat away from the observatory. The utility building also provides space for a panel recoating facility, if required.

Adjacent to the utility building is a fenced yard with the primary chillers, underground sewage holding tank and domestic/fire water tank. All equipment is set on concrete footings and gravel base. Heat tape and heat blankets are used to prevent the water tank and pipes from freezing.

11.2.9 Site Design Trade-offs

Several options of how to place the telescope facility on site were studied and compared. Because direct geotechnical studies have not yet been made on the preferred site, Cerro Chajnantor for the purpose of the design M3 assumed similar soil conditions to the nearby ALMA site. In general, the soil condition at ALMA has a top layer of fissured rock and soil approximately 1-2m (3-6 feet) deep, then one-half meter of cracked rock that can be broken up with back hoe easily, and solid rock down from that point. Frost depth is approximately 1.5m (5 feet) below top of grade.

The proposed site design minimizes excavation and earthwork needed to provide a functional site. By providing a terraced layout, the depth of excavation is less and easier to dig. This minimizes costs and is less time consuming than leveling the entire site and dealing with excessive rock excavation and removal from the site.

A terraced site design is not as functional as a uniform level site. There are more constraints and restrictions of access and maneuverability around the enclosure, but financially makes sense. The goal is to minimize the amount of earthwork and the high cost associated with high altitude construction while providing a functional site.

11.2.10 Telescope Facility Design

The purpose of the facility is to provide the necessary infrastructure for the operations and maintenance of the telescope and associated instrumentation. The various spaces that make up the mountain facility are as follows:

- Telescope pier
- Telescope chamber
- Control building
 - Control room
 - Computer and backend room
 - Instrument preparation lab and workshop
 - Office area
 - Conference room
 - Kitchenette, toilets, shower
 - Mechanical/HVAC room
 - Electrical room
 - Receiving area/storage

11.2.11 Telescope Pier

At this stage, there has been no detailed analysis of the telescope pier. The conceptual pier design supplied by Vertex/RSI was integrated into the facility design. The pier cost was estimated from its volume.

11.2.12 Telescope Chamber

The function of this space is to house the telescope and protect it from weather and other environmental elements. The space is defined by a 0.75 m (30 inch) thick cast-in-place concrete ring wall that also acts as a retaining wall on the uphill side. The 43 m (141 foot) diameter concrete ring wall extends up to the base of the telescope dome and down to solid rock, below frost depth (Figure 11.2.4). The dome weighs approximately 500 tons and is continuously supported by the ring wall. This is the interface point between the dome, mechanisms and the ring wall.

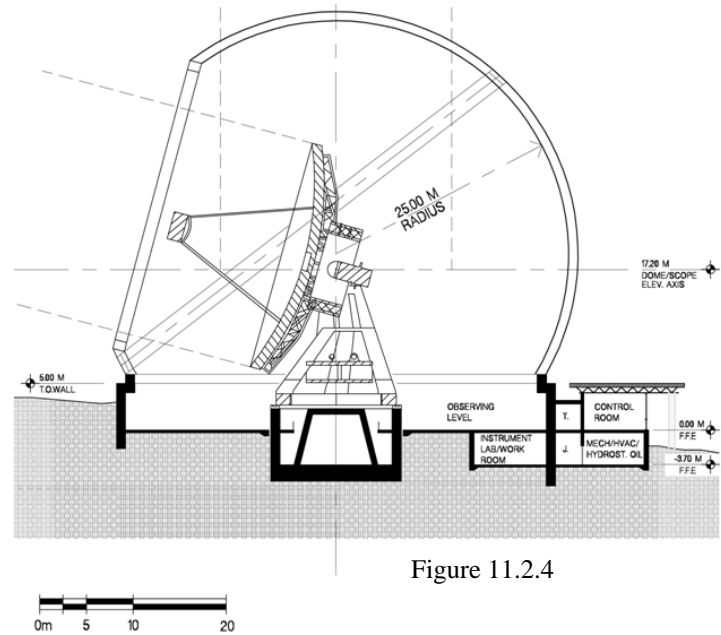


Figure 11.2.4

A steel structure with metal skin in lieu of a concrete ring wall was considered. The ability to fabricate the steel in a shop at a lower elevation and erect on-site minimizes the on-site labor. Due to the dynamic and static loads imposed by the dome, M3 felt that the quantity of steel and required tolerances makes this option less desirable. Concrete is a well-known and commonly used material throughout this region. There are several local contractors that are very capable with concrete making this material a favorable product for the ring wall. Since the telescope pier is also made out of concrete, it makes sense to use concrete for the ring wall since the materials and

contractors are already on site. With the additional concrete for the ring wall, it may justify the use of an on-site concrete batch plant therefore potentially lowering the cost of construction.

11.2.13 Control Building

Adjacent to the telescope chamber is a two-story control building. The top level finish floor elevation is the same as the floor elevation of the telescope chamber and serves primarily as a control room and office work space. The entrance to this level is next to the vehicle parking spaces and through an air lock vestibule (Figure 11.2.5)

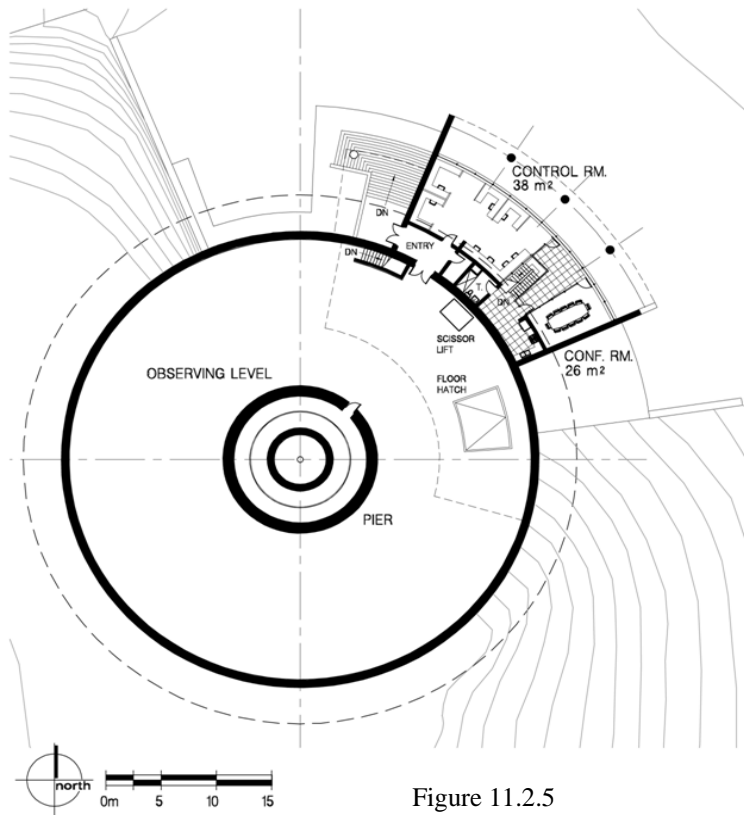


Figure 11.2.5

The layout of the second level is an open plan with minimal interior walls, maximizing the mountain views and flexibility with adjacent spaces. The control room and office areas are within the same space and the conference room is isolated for privacy. The open plan also simplifies the mechanical HVAC system by minimizing ductwork, zones, and the control system required for proper temperature and humidity control.

Also located on this level are the service spaces such as the kitchenette, toilets, etc. These spaces are placed on the inside radius of the control building minimizing the height of the building next to the telescope chamber so the dome can rotate freely without interference.

The finish floor elevation of the lower level is 4.0 m (13.1 feet) below the telescope chamber floor elevation (Figure 11.2.6). Located on this level is a receiving bay with a roll-up door and roof hatch that opens into the telescope chamber above. The dome crane can lift large instruments from the receiving bay into the

telescope chamber. The instrument lab located adjacent to the receiving bay, has a scissor lift to raise smaller instruments and equipment up to the telescope. Depending on the instrument or equipment size that needs to be hoisted into the telescope chamber, the height of the lower level may need to be increased accordingly.

The electrical and mechanical spaces also on the lower level contain equipment such as the oxygen enrichment and hydrostatic oil plants. These spaces are along the outer perimeter of the building to allow fresh air intake and ventilation of the equipment inside.

11.2.13.1 Control Building Systems and Trade-offs

The control building structure is designed to minimize the on-site labor and cost associated with high altitude construction. The goal is to fabricate most of the components in the shop and transport them to the site for erection. Materials such as pre-cast concrete panels, steel structure, metal deck and roof panels are relatively easy to erect on-site and withstand severe environmental conditions and the test of time.

The interior spaces have minimal finishes such as gypsum board walls and lay-in ceiling, decreasing the on-site construction and maintenance. Glass partitions are preassembled at the shop and erected on-site. Exposed ducts and surface mounted wire mold in the control room allow flexibility and ease of construction

The trade-off of having minimal style architecture is that interior spaces are not as inviting but provide a space that is functional, easy to maintain, and less expensive to construct. The goal is to provide an environment that is utilitarian, serves the needs of the occupants, and minimizes on-site construction as well as long term maintenance.

11.2.13.2 Environmental Control

The environmental control system for the telescope chamber is minimal ventilation only. Filtered louvers incorporated along the base of the ring wall flush air out and maintain temperature close to ambient.

The control building environmental system includes air conditioning and heating as required to maintain a comfortable working environment. The system consists of separate air conditioned zones for the upper and lower occupied levels. The mechanical and electrical spaces are ventilated through filtered louvers and dampers located along the exterior wall and heated for freeze protection only. The cooling and heating system is a 45 °F glycol chilled water loop and air handler units with heating coils located in the mechanical room. Ducted supply air and plenum return air circulates the conditioned air throughout the building.

All routinely occupied spaces in the control building are oxygen enriched to a 28% concentration which is the equivalent to 3000 m (9675 feet) elevation above sea level. Since the oxygen is delivered via the HVAC system, it is also zoned between the upper and lower levels. As a cost saving measure, the electrical, mechanical and telescope chamber do not have oxygen enrichment. Occupants in these spaces will use portable oxygen equipment.

Typical building infiltration ranges from 0.1 to 0.3 cfm/ft² with wind velocity as the driving factor. The oxygen enrichment system must provide enough oxygen to compensate for air directly pulled in through the air handler unit and building infiltration. This becomes the largest design factor when sizing the oxygen enrichment system. The control building is designed to minimize air leakage by providing air locks into the oxygen enriched environment and having a double layer vapor barrier along the entire perimeter of the building. All joints between materials and surfaces require sealant throughout for an air-tight environment.

The cost of making the building air-tight is minimal in comparison to the cost of the added capacity to the oxygen enrichment system and air conditioning. The one time cost of sealing the building properly saves operational and maintenance cost for the life of the building.

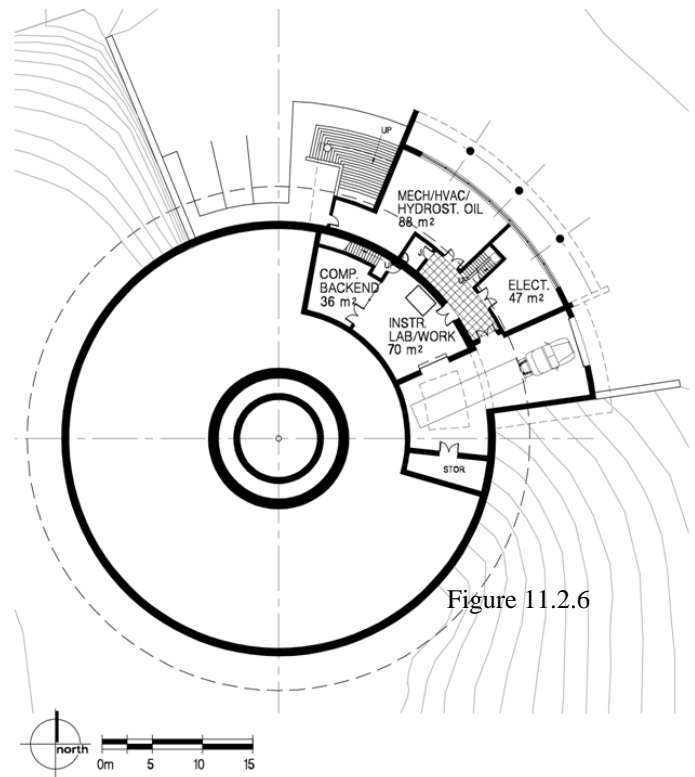


Figure 11.2.6

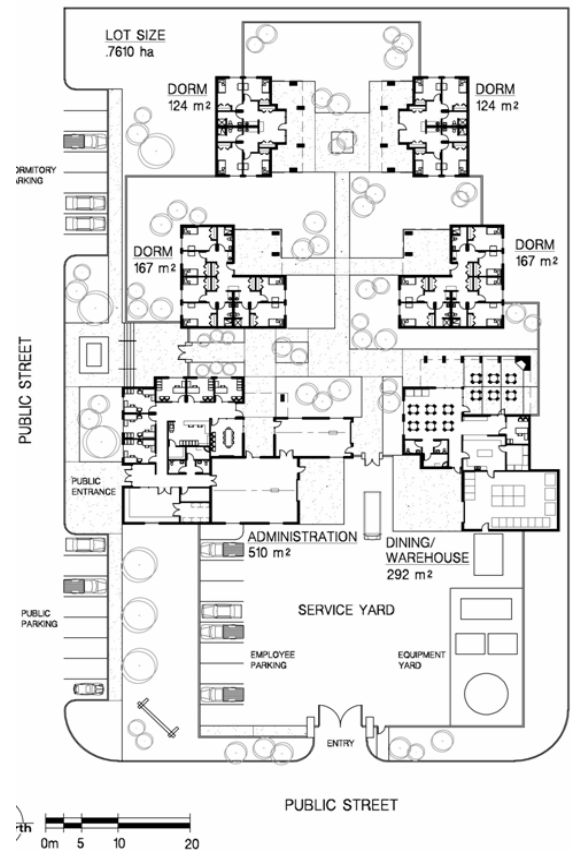


Figure 11.2.7

11.2.14 Electrical Systems

Prime electrical power shall be generated on site using two (2) diesel driven, prime/continuous generators, each rated at 750 kW at 0.8 power factor (850 kVA), 277/480 V, 3 phase, 4 wire operating in parallel. Paralleling type switchgear and controls allow the two (2) prime generators to operate in parallel for a total combined capacity of 1500 kW (1875 kVA) at the telescope altitude. The current rating and capacity of standby generators are estimated, and will be refined as the total electrical loads for the enclosure become available during the next phase of the project.

From the main generator paralleling switchgear to the control building, an underground ductbank consisting of a generator service entrance lateral will be provided to serve the mountain facility's main electrical service entrance equipment located in the electrical room. The main electrical service entrance equipment shall consist of bottom feed incoming section, main disconnect switch with integral ground fault protection, and distribution sections.

Prime power generators and paralleling switchgear are located in the utility building and mounted on concrete housekeeping pads. The generator enclosure/building shall be located as close to the CCAT Enclosure Building as practical, but considering site issues such as prime generator feeder/ductbank lengths, diesel fuel storage tank(s), exhaust direction and prevailing winds, vibration, and noise relative to the enclosure.

The main service entrance equipment shall be rated at 230/480 V, 3 phase, 4 wire, estimated to be 3000 A bus. From multiple feeders fed by the main service entrance equipment, electrical power is provided and distributed throughout the facility using distribution and sub-distribution panels. A second voltage transformation to 120/240 V, 3 phase, 4 wire, if required, is provided using smaller dry type transformers and associated sub-distribution panels located throughout the facility. A central UPS is used and sized as determined by the CCAT electrical UPS type loads being served.



Figure 11.2.8

11.2.14.1 Grounding and Lightning Protection Systems

The enclosure design has an electrical safety grounding system as required by the National Electrical Code (NEC). The grounding system consists of a continuous grounding mat/mesh made using bare stranded copper (SDBC) conductor arranged in 1 m squares and located directly under the enclosure concrete floor and spread foundations. A continuous SDBC ground ring shall be provided around entire building foundation perimeter with ground rods exothermically connected to ground ring at 15 m intervals and minimum of one ground test well. In addition, the enclosure structural steel columns and concrete reinforcing rebar are bonded to grounding ring and grid using exothermic type welds. The entire building grounding system is buried at a minimum depth of 1 m below finished grade.

The lightning protection system consists of an array of copper air terminals located at the top of telescope enclosure dome. The air terminal array shall be bonded together using 28 strand #14 copper down lead type conductor with direct connections to the building buried grounding system made at a minimum of four to six locations via slip ring commutators.

11.2.15 Support Facility

CCAT's support facility is planned at a lower altitude (≈ 2500 m) in the vicinity of San Pedro de Atacama, Chile. At present, no specific site has been selected so therefore M3 assumed a site configuration and size based on the support facility requirements. The space requirements are as follows:

- Remote Control Room
- Offices (6)
- Instrument Lab
- Workshop
- Warehouse
- Cafeteria
- Dormitories
- Support facilities, i.e., toilet, storage, utility room, etc.
- Staff and visitor parking
- Equipment yard

The facility is designed similar to the characteristics and architectural motifs in and around the village of San Pedro. The compound is made up of several smaller buildings with a landscaped courtyard within a perimeter wall providing privacy and security. (Figure 11.2.8) Public access into the facility is through the administration building and an entry gate into the compound near the public parking. Staff parking and equipment access is within the compound wall in the service yard providing access to the site equipment, warehouse, workshop and instrument lab.

The proposed site utilities include a septic tank and leach field, domestic and fire water tank and generator power. The San Pedro power grid is not of adequate capacity to serve as a permanent electrical source.

11.2.16 Architecture

The proposed architecture of the support facility blends with the existing San Pedro architecture. Many of the buildings are made out of rustic adobe walls with wood roof structures and windows (Figure 11.2.8). Most of the building colors reflect the natural earth tones that surround the town.

Structurally the support buildings are reinforced concrete block walls with an adobe veneer. This, along with concrete footings and a steel roof structure, provides the facility the modern materials required to withstand earthquakes and severe winds per today's building codes and maintains the same style of architecture in San Pedro.

11.2.17 Critical Risk Assessment

For construction of both the support and the mountain facility the intent is to keep it simple, follow traditional construction systems, and use materials that are used commonly by local contractors. The proposed material for the support facility such as concrete block, adobe, wood and steel are traditional materials that any contractor is comfortable with. This facility does not have any potential risks in the design or construction.

The mountain facility's materials are poured-in-place and pre-cast concrete, steel, metal panels, etc. These materials are very easy to fabricate and erect on a typical site with an elevation less than 3000 m (10,000 feet) but can be very challenging at a remote site such as Cerro Chajnantor with an elevation above 5500 m (18,000 feet) with low oxygen level. Some of the complications are:

- **Contractor's availability:** Many contractors do not like to work at remote, high altitude sites so they will propose on other projects in the city before they propose on this project.
- **Remote site complication:** Due to the remoteness of the site the contractor needs to provide a contractor's camp, room and board for their workers at a lower elevation and transport them to the construction site every day. Availability of materials and labor needs to be well coordinated and scheduled well in advance. If something does not arrive onsite as scheduled or fabricated properly, it takes a long time to remedy the situation and can potentially stop construction. Why work at a difficult site when there is plenty of work at lower elevation sites?
- **Weather and construction seasons:** Construction at high altitude sites is complicated by severe weather and limited construction seasons. It is difficult to construct a facility when it is windy and cold. Productivity diminishes significantly with unfavorable weather conditions. Construction seasons force the contractor to mobilize onsite several times and the project needs to be phased. There is, therefore, a premium to starting construction in the spring (September) and avoiding exterior work during winter.
- **Lack of oxygen:** At this elevation construction workers may be required to use portable oxygen tanks and masks. This complicates mobility, flexibility and the ability to perform simple construction tasks. The lack of oxygen also makes it difficult to build within typical construction tolerances requiring modifications or rebuilding.
- **Equipment operation and warranty:** Typical mechanical and electrical equipment is rated for sites under 3000 m (10,000 feet) altitude and built to withstand normal environmental conditions. Manufacturers of building equipment such as transformers, chillers, etc. do not guarantee the performance of the equipment at 5500 m (18,000 feet) altitude or higher. They have to modify the typical equipment housing to withstand the severe environmental conditions and require additional anchorage.

All of these factors have a direct impact and risk on the project's schedule and costs. Construction delays, due to weather, labor availability, etc. is additional cost to the contractor and owner and extends the overall construction schedule, possibly into the construction season.

12 Enclosure Dome

12.1 Introduction

This section provides results of a study of the large enclosure dome required for CCAT. A concept design was developed after a parametric assessment of several potential approaches. The approach chosen, known as a “calotte” style dome, has never been built in the size we are contemplating – though this is true for any of the types considered. The results of this study illustrate feasibility sufficient to progress into the next phase of work, Engineering Concept Design.

12.1.1 Background

As discussed in the concept design overview (Section 7) we have concluded an enclosure will be required for CCAT. This is based on a number of major factors:

- **Solar Heating:** At $\sim 1 \text{ kW/m}^2$ direct solar radiation on the telescope would result in large temperature variations across the structure and mirror arrays. This would pose a substantial challenge to mirror figure optimization and would impose requirements for large panel gaps. Constructing a primary mirror array accurate to better than $10 \text{ }\mu\text{m rms}$ will be challenging enough without this additional thermal load.
- **Wind:** The tight pointing and tracking requirements (of order 0.2 arcsec) that result from the resolution of CCAT will be very difficult to meet in the very windy environs of Atacama peaks. The primary mirror is $\sim 483 \text{ m}^2$. Unattenuated wind pressure on this surface would require the structure, truss, motors, and servo controls of the mount to be significantly larger and stiffer. It is anticipated the wind pressure on the primary will be attenuated as much as 10 times inside a dome.
- **Dust:** The Atacama is a dusty region. While there is little we can do to reduce the amount of dust falling on the telescope during operations, an enclosure can substantially reduce the amount when the telescope is out of operation.
- **Snow:** While the Atacama is a dry region, snow precipitation is a fairly common occurrence. Hardening the telescope to survive direct exposure to snow would constitute a significant additional burden. This would be particularly difficult as we may implement mirror surfaces which are specular in the infrared wavelengths.

12.1.2 Scope

The enclosure dome extends from the interface to the facility at the base of the azimuth rotation system and includes the full extent of the dome and shutter. Also included are all mechanisms, bearings, drives, cabling, slip rings, structure, cladding, and computer control of motions. We anticipate the contract for development of the dome will include detailed design, fabrication, procurement of components, and trial assembly at the contractor’s facility. The contractor will be responsible for transport to the nearest deepwater port for shipment to Chile.

12.1.3 Technical Discussion

12.1.3.1 Selection of Dome Type

Initial work for a CCAT sized dome at AMEC was funded by the TMT project. As part of this work, and included in Section 12.2 are parametric evaluations of three potential types of dome. Two of these, the dome-shutter and the carousel types have been built for 10 m class telescopes (Keck/Gemini and Subaru.) No comparable size calotte dome has been constructed. Nonetheless, the calotte offers significant advantages in structural efficiency, balance, uniformity of loading on bearings, mass, and structural loading in wind conditions. For a 30 m clear aperture, determined by the FOV and scanning requirements, the shutters would be very large and heavy for the two alternative types. Finally, the calotte lends itself well to geodesic type structures, which are made up of relatively small parts that can be packed and shipped to the summit easily. While we are aware of the concerns of the TMT project on this type of dome, it appears to us that the calotte solution offers the most promising prospects. We thus use it for our baseline design.

12.1.3.2 Dome Reliability

Examination of a wide range of astronomical domes reveals almost all domes have experienced some problems in operation. These generally fall into three categories:

- **Overconstraint:** Often domes are designed with overconstrained mechanisms. One example is azimuth bogie systems, where the plane of rotation is defined by the three highest bogies and loading on bogies is dependent on load distribution of the ways on which they run and their relative heights. Another concern regards parallel linear or curvilinear bearings for dome shutters, which can bind when the lack of parallelism or differential runout exceeds the compliance of the structure and bearings.
- **Wear & Breakage:** It is difficult to estimate life cycle characteristics of bearings accurately. Overconstraint can lead to conditions where loads are not distributed equally as designed. Alignment of bearings in rotational systems is critical and many domes were not designed to incorporate alignment reference datum for roller pointing angles, resulting in slip wear. Many domes have a history of breaking or wearing one particular part repeatedly owing to poor design or implementation.
- **Alignment Problems.** In addition to the alignment issue identified in the above paragraph, alignment of shutters is a frequent problem with domes. Typical cable or chain drives for shutters become maladjusted allowing shutters to cock and subsequently bind in their ways.

Understanding the ways in which domes fail is important in designing a dome that will be reliable and easy to assemble.

12.1.4 Technical Requirements

The following represents the range of preliminary requirements established at the onset of the study.

12.1.4.1 Dimensions

- **Diameter:** Overall interior dome diameter must be sufficient to clear the swept volume of the telescope over its full range of elevation and azimuth. This will be in the range of 50 m between the largest extent of the telescope swept volume and the dome inside diameter. (Note: This requirement was modified to state the secondary mirror should remain 2 m inside the plane described by the dome aperture in order to keep M2 out of the direct wind.)

12.1.4.2 Motions

The dome shall provide the following motions:

- **Azimuth Rotation:** The dome shall rotate without limit in azimuth in either direction to enable the most efficient slew capability.
- **Calotte Rotation:** The calotte (upper) portion of the dome shall rotate over a range of 200 degrees. This shall provide 10 degrees additional beyond the position where the aperture is at its highest and lowest elevation.
- **Elevation:** The dome shall provide a clear line of sight over the elevation range from 15 degrees above the horizon to 5 degrees from vertical inclusive.
- **Velocity and Acceleration:**

| | |
|---|------------------------------|
| Calotte Velocity Range: | 0 to 2.5°/s |
| Calotte Acceleration Range: | 0.1 to 0.25 °/s ² |
| Calotte Position Accuracy (moves over 2°): | 0.5° |
| Calotte Position Accuracy (moves under 2°): | 0.25° |
| Azimuth Velocity Range | 0 to 2.5°/s |
| Azimuth Acceleration Range: | 0.1 to 0.25 °/s ² |
| Azimuth Position Accuracy (moves over 2°): | 0.5° |
| Azimuth Position Accuracy (moves under 2°): | 0.25° |

Settling Time (Both Axes): The maximum settling time under normal operation conditions shall be 10 seconds from maximum slew speed with maximum deceleration of $0.25^\circ/s^2$.

12.1.5 Structural Approach

The dome shall utilize a geodesic or similar space frame structural approach suitable for bolted assembly and disassembly. The purpose is both to take advantage of the structural efficiency and ease of factory manufacture of the relatively small components required and to result in a dome which can be substantially assembled and tested at the manufacturer's facility. It can subsequently be disassembled and shipped to the telescope site using standard shipping containers, and finally, assembled with minimal requirements for field welding and metrology during final assembly at the site.



Figure 12.1. HET Dome Structure

12.1.6 Assembly Requirements

The concept to be studied should be capable of rapid assembly using powered and un-powered hand tools. Requirements for in-process metrology during assembly should be minimized and the required precision of the final structure should result from the precision of component pieces and joining techniques.

12.1.7 Bearings

12.1.7.1 Azimuth Bearing System

It is anticipated that the azimuth system will rotate on a number of bogey assemblies mounted to either concrete piers or structural steel columns at a height of TBD above grade. The bogey assemblies will be stationary and a continuous ring journal will be part of the rotating azimuth structure. These bogey assemblies may be replicated as required to reach the necessary load bearing capacity.

12.1.7.2 Calotte Bearing System

An initial concept might use a curved track bearing system for the calotte. This would imply a large number of bearing assemblies distributed over the track to achieve the necessary load bearing capability. This also implies significant over-constraint of this system and it is anticipated the calotte would attach to the bearing assemblies via flexures or other approach that would accommodate this overconstraint. This will be one of the challenging design aspects of the calotte approach.

12.1.8 Drives

12.1.8.1 Azimuth Drive

The azimuth drive system would consist of four diametrically opposed and orthogonal rubber tired friction drives. These drives would be mounted on slides allowing constant force against the circular beam/journal and would be servo controlled in a Master/Slave system that would yield constant torque from each drive assembly.

12.1.8.2 Calotte Drive

A cable drive system might be implemented to drive the calotte. The cable system would be tolerant of significant variations in geometry of the assembly and could be replicated to employ two or more drive motors and capstans. Alternatively, rubber tired drives similar to those anticipated for the azimuth drive could be employed.

12.1.8.3 Motor Sizes

During this study an initial effort shall be made to establish the required sizes of drive motors. This is to ensure compatibility with space envelopes defined for drives and to bound cost.

12.1.9 Encoders

Both axes of motion shall be fitted with encoders capable of measuring rotational position to 0.1 degree absolute. It is permissible to have two stage encoders, employing, for example, bar code readers to establish absolute position and to calibrate a second, incremental encoder, such as a friction wheel encoder driven from the rotation journals.

12.1.10 Electronics

Conceptual design shall include a first-order concept for servo drive and other required electronics, their disposition, and packaging.

12.1.11 Cable Wraps & Slip Rings

- Azimuth: As azimuth motion occurs without limits, no cable wraps may be used. A slip ring bringing only power across the rotating interface is to be implemented.
- Calotte: A slip ring will also be used for the calotte motion as packaging envelopes available for a cable wrap are minimal.

12.1.12 Controls

All controls and electronics will be procured with the dome system, but for the purpose of this study no work needs to be done on this aspect of system design.

12.1.13 Summary

The study that follows represents an excellent initial cut at the design of a calotte style dome. Concerns that such a dome has no large scale precursor must be met with a good deal of care in design and analysis. Assessments performed to date indicate the calotte has substantial advantages in structural efficiency, balance, weight, and load distribution on the motion systems. The provision for trial assembly and operation at the vendor's facility will significantly reduce risk at the remote Atacama site. Investigations in the next phase will include the possible implementation of commercially available factory produced aluminum geodesic structures and further development and analysis of all dome subsystems.

12.2 CCAT Enclosure Dome

Report prepared by AMEC Dynamic Structures Ltd.

12.2.1 Introduction

The following chapter describes the CCAT enclosure feasibility study carried out by AMEC Dynamic Structures Ltd. The decisions leading to the selected enclosure design are outlined and supported by analysis results. Areas of high risk are identified, and mitigation strategies are proposed.

12.2.2 Background

Due to the high precision required by the telescope, the CCAT requires an enclosure to reduce the effects of wind and thermal loading on telescope performance. Additionally, the enclosure is needed to ensure that the telescope is not damaged by the high winds, snow, and ice that are anticipated at the site.

AMEC Dynamic Structures has designed and built many of the largest telescope enclosures in the world, including telescope enclosures for Gemini North and South, Keck I and II, Subaru, Starfire Optical Range, Sir William Herschel Observatory, Canada France Hawaii Telescope, and Sir Isaac Newton Observatory.

12.2.3 Scope

The enclosure is defined as everything from the azimuth bogies and rails upwards (essentially everything above the fixed structure). The scope of the enclosure work includes structural, mechanical, drive and control systems. In addition to the main enclosure structural and mechanical systems, the enclosure requires a shutter to open and close the aperture, and an enclosure-mounted crane for telescope maintenance.

12.2.4 Requirements

The major enclosure requirements are as follows:

- Dome diameter: 50 m (governed by wind attenuation on telescope structure)
- Aperture diameter: 30 m
- Aperture zenith range: 0 – 75 degrees
- Azimuth rotation: unlimited
- Calotte rotation: 200 degrees
- Key environmental loads:
 - Wind (survival): 65 m/s
 - Snow load: 100kg/m²
 - Ice load: 25 kg/m²
 - Seismic: 0.4 g ground acceleration

A general requirement is the need to simplify on-site construction due to the extreme altitude. This includes allowing trial assembly at the manufacturer's site, disassembly into components that can be shipped via standard containers, and on-site reassembly procedures that minimize labor intensive activities such as field welding and metrology.

12.2.5 Key Design Trades

The following sections outline key design trades leading to the selection of the enclosure reference design.

12.2.5.1 Enclosure Type

The most basic enclosure design decision is selecting the mechanism that controls the aperture pointing. All conceivable enclosure types rotate about a vertical axis to control the azimuth pointing of the aperture. However, various options exist for controlling the zenith pointing of the aperture. Figure 12.2.1 below shows three alternate enclosure types:

- Conventional dome-shutter enclosure (examples: Keck, Gemini)
- Carousel enclosure (examples: Subaru, JCMT)
- Calotte enclosure

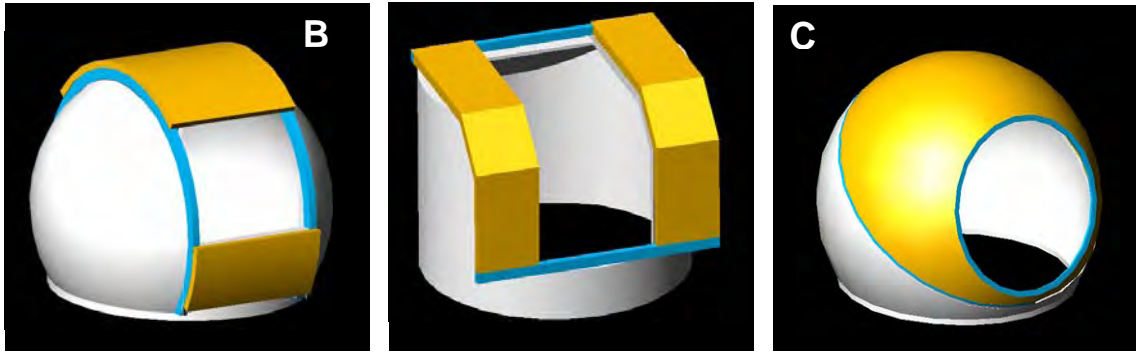


Figure 12.2.1: General form of alternate enclosure types: A) conventional dome-shutter enclosure, B) carousel enclosure, and C) calotte enclosure

As enclosure structures are scaled to the very large diameters required for the CCAT project, the enclosure mass and cost increase rapidly. The calotte enclosure provides a fundamental advantage over alternate existing enclosure types due to its nearly-continuous spherical form (interrupted only by the circular aperture) that results in a highly efficient structure.

12.2.5.2 TMT Enclosure Comparative Studies

Previous studies carried out for the 20 m and 30 m class optical telescopes have indicated that the structural mass of the calotte enclosure is substantially less than the conventional dome-shutter and carousel enclosures. The most recent of these studies was for the Thirty-Meter Telescope (TMT) project. A detailed finite element analysis and mass estimate of various enclosure styles was carried out.

Finite element models for the TMT alternate enclosure styles are plotted in Figure 12.2.2 below. Figure 12.2.3 plots the total base reactions under various load cases. Figure 12.2.4 plots the azimuth bogie load distribution. It is observed that the dome shutter and carousel models exhibit high load concentrations at the base of the arch girders requiring tightly packed bogies at this location; this is not evident in the Calotte model due to the lack of arch girders. Figure 12.2.5 shows the first mode shapes for each of the enclosure styles; the calotte has the highest natural frequency (2.5Hz) followed by the carousel (1.8Hz) and the dome-shutter (1.5Hz).

Figure 12.2.6 plots the element stress utilizations after each enclosure was optimized for minimum weight under survival environmental conditions. The plot shows the 95th and 50th percentile stress utilizations for each element type used in the model in order to gain insight into the efficiency of the optimized model, and to support the claim that all models have been optimized to an equal level.

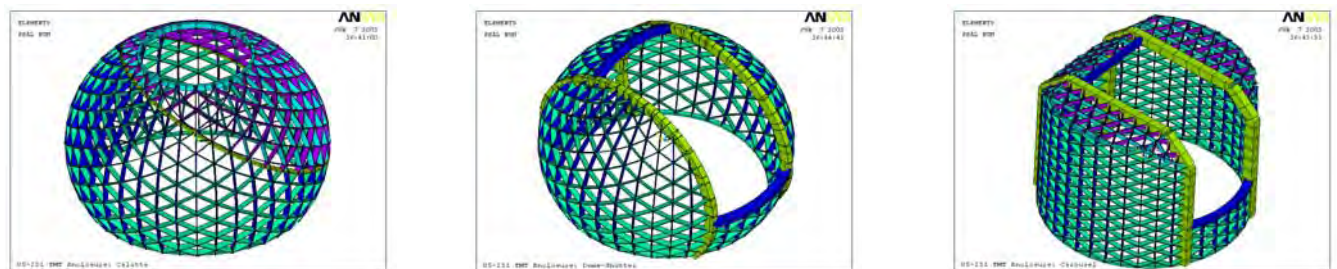


Figure 12.2.2. Finite element models of the TMT enclosure for calotte (left), dome-shutter (center) and carousel (right) style enclosures

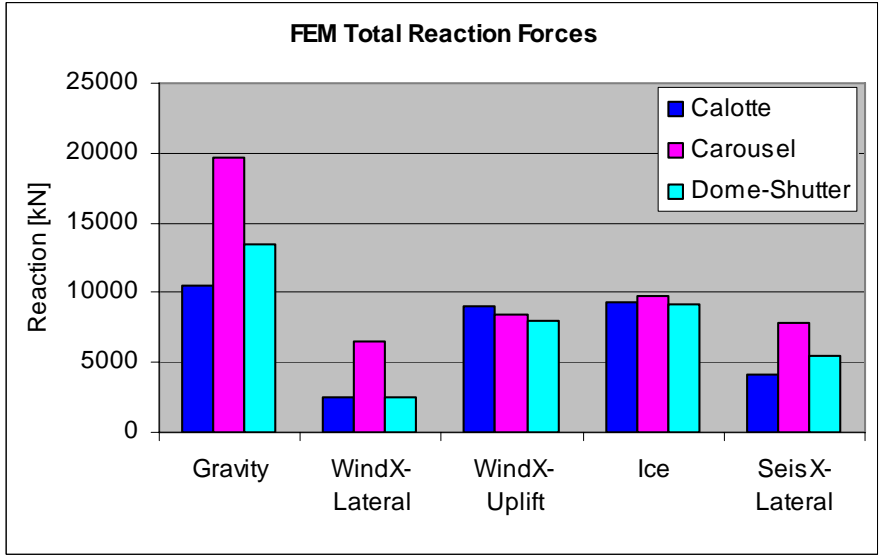


Figure 12.2.3. TMT FEM total reaction forces for various load cases¹

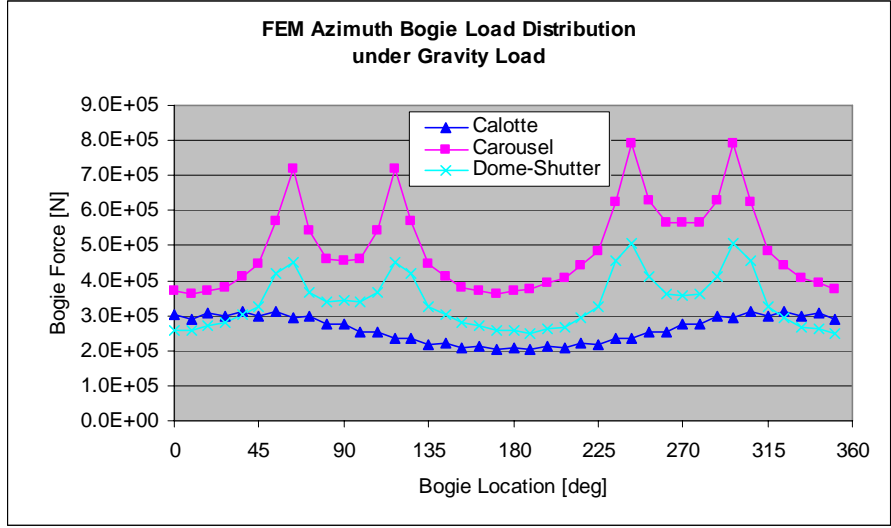


Figure 12.2.4. TMT FEM bogie load distribution under gravity load

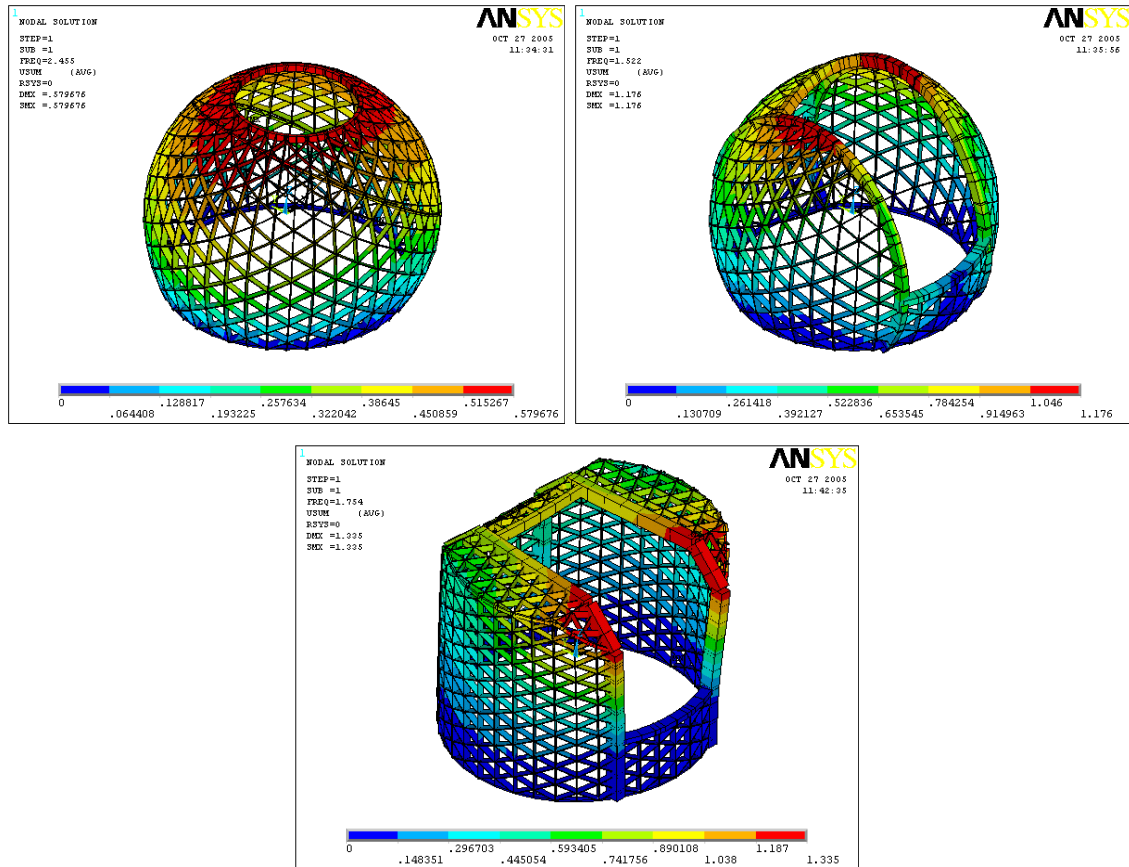


Figure 12.2.5. First mode shapes for calotte (top left, 2.5Hz), dome-shutter (top right, 1.5Hz), and carousel (bottom, 1.8Hz)¹

¹ Drives were set to be very stiff for the modal analysis in order to preclude mode shapes involving rigid body structural modes due to drive compliance; bearings were modeled with realistic stiffness values

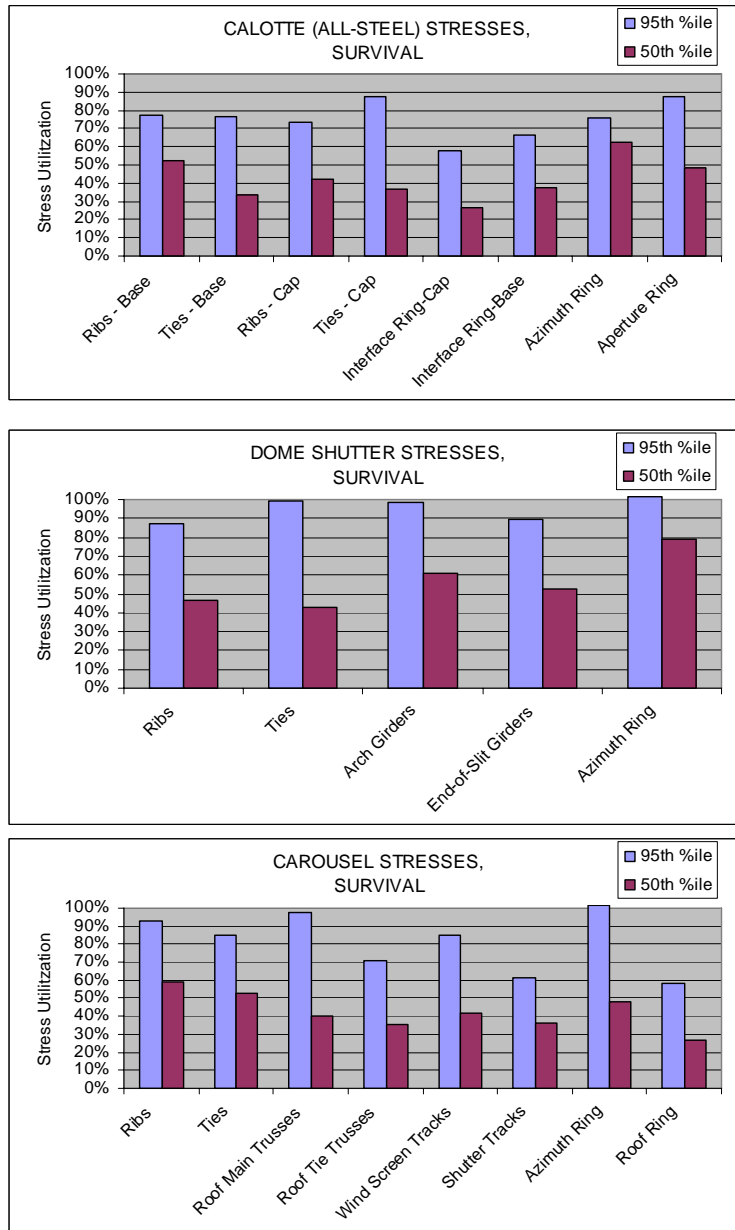


Figure 12.2.6. TMT stress distributions; for each element type, the plots show and 95th and 50th percentile element stress utilizations (i.e. 95 or 50 percent of those element types have a stress utilization at or below the utilization value plotted on the y-axis); stress utilizations are given as a percentage of allowable stress

The estimated total mass of each enclosure was 2300 T for the calotte, 2500 T for the dome-shutter, and 3600 T for the carousel. All moving components of the calotte design are balanced about their axis of rotation, and therefore only minimal power is required to operate the moving components. At the scale of the CCAT, the conventional dome-shutter would require on the order of 1MW of power to operate the shutters, due to the large lifted mass. This has a significant impact on the life-cycle cost of the enclosure. Additional benefits include a lower mass of individual structural components due to the lack of heavy arch girders, which simplifies shipping and erection. The clean, spherical exterior also avoids build-up of snow and ice.

A cost estimate was carried out based on the designs developed, and indicated that capital cost for the dome-shutter and carousel designs would be 21% and 43% higher than the calotte, respectively. The major drawback of the calotte is that it is unprecedented at the scales of the CCAT project, so there is an inherent design risk involved.

However, this does not offset its advantages which are likely required to achieve the project budget. Therefore, the CCAT project, in consultation with AMEC Dynamic Structures, has selected to move forward with a calotte enclosure as the baseline design.

12.2.5.3 Calotte Description

Figure 12.2.7 below defines the major components of the calotte enclosure, and Figure 12.2.8 illustrates the basic mechanism which defines the aperture position. Figure 12.2.9 gives the overall dimensions of the CCAT calotte enclosure.

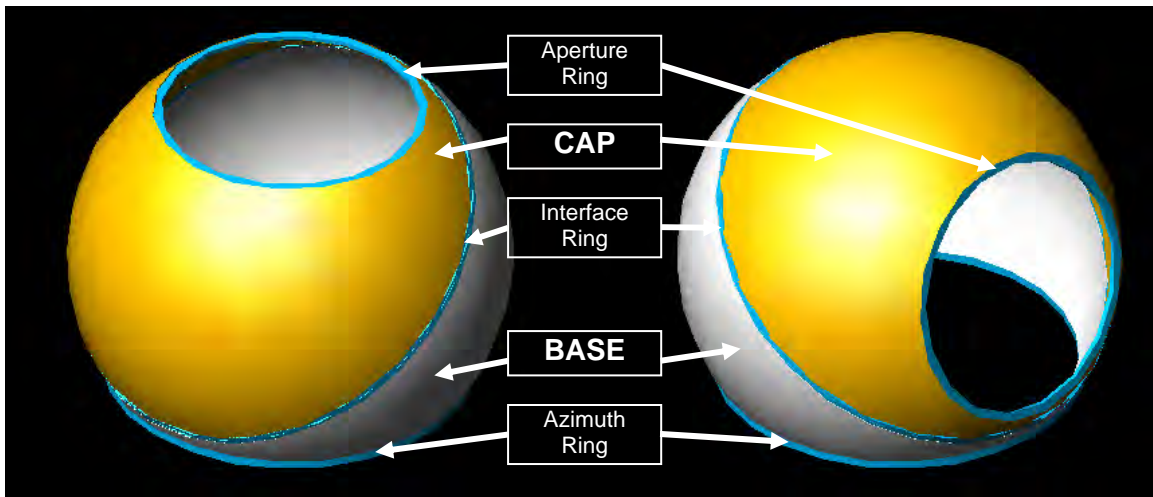


Figure 12.2.7. Major components of calotte enclosure, shown looking at zenith angles of 0 degrees (left) and 75 degrees (right)

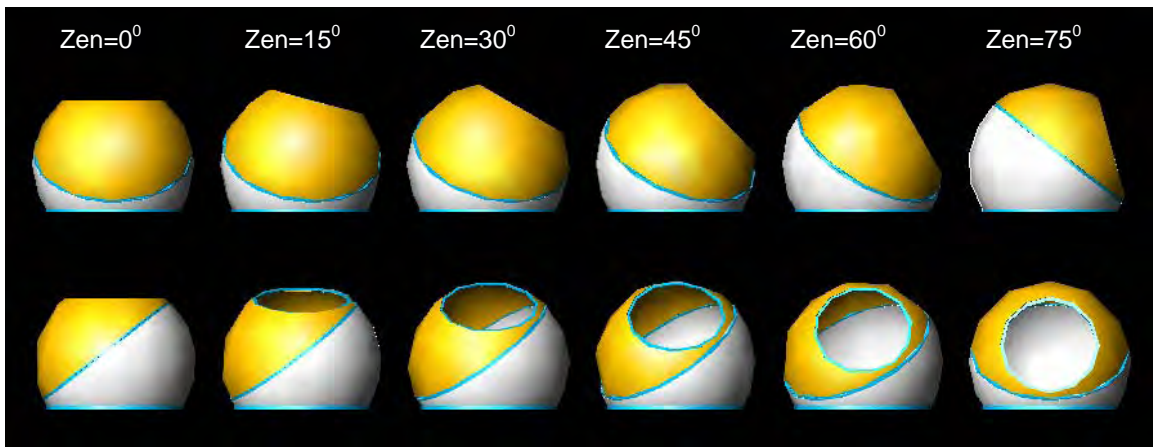


Figure 12.2.8, Elevation view of calotte aperture slewing from zenith angles of 0 to 75 degrees at a constant azimuth pointing

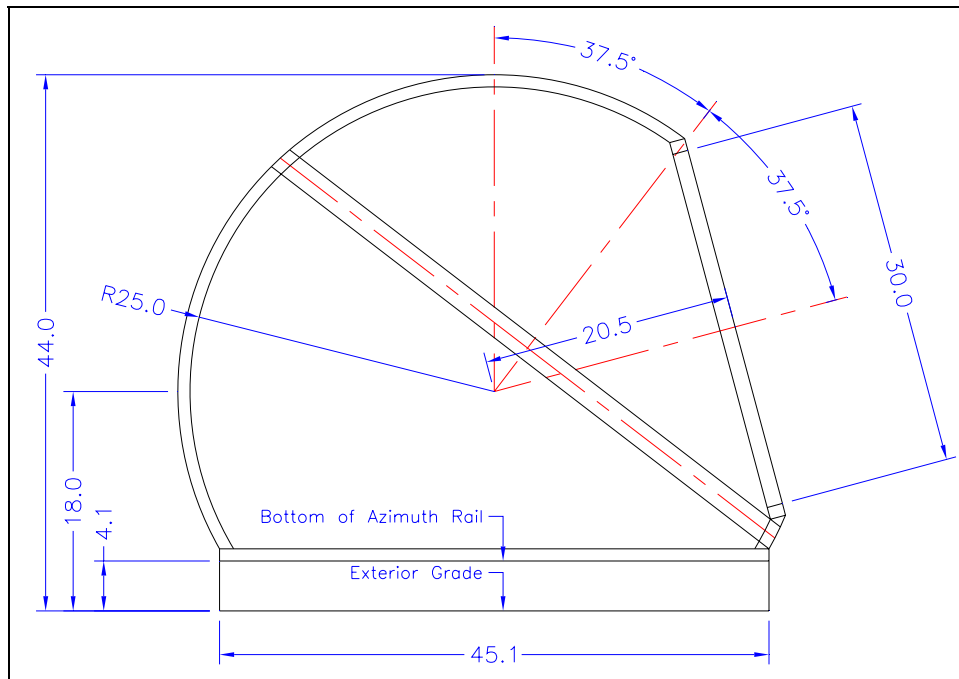


Figure 12.2.9. CCAT calotte enclosure dimensions

12.2.5.4 Geodesic vs. Rib & Tie Structure

A general consideration for the structural form is the geometry of the grid that defines the major structural elements. Geodesic geometry is a well-known geometric form that utilizes only a small number of different size members, the advantage being reduced cost due to repetition in fabrication of members, nodes, and panels. However, typical geodesic domes are not subject to the geometrical constraints of the calotte enclosure due to the aperture ring and sloping interface plane; therefore, many of the benefits of the geodesic form are no longer available. An alternate geometric form referred to as rib and tie geometry has been used on existing enclosures. This consists of ribs that lie in vertical planes with equal angular spacing, which are then triangulated to each other by diagonal tie elements. The rib and tie geometry is readily adapted to the calotte enclosure by triangulating the ties to the required geometric planes, and is therefore selected for the point design.

12.2.5.5 Beam vs. Truss Structure

Another general consideration is whether the triangular structural grid is composed of simple wide-flange beam elements, or open web truss elements. The mass of both systems is estimated to be similar. A beam structure may be more economical due to reduced fabrication labor, but requires complicated moment connections at the nodes. A truss structure would provide additional local stiffness and resistance to buckling, and would minimize the part count due to continuous members. A truss structure is assumed for the feasibility study since this is felt to be a more conservative assumption.

12.2.5.6 Aluminum vs. Steel Structure

It is assumed that steel components will be used in the ring girders at the mechanical interfaces due to the need for locally high strength, fatigue resistance, and compact design. However, the material that forms the structural shell could be either steel or aluminum. Aluminum has the major advantage of yielding a lighter structure (~50% lighter than steel), whereas steel has the advantage of weldability without loss in strength. The overall cost of steel vs. aluminum is similar at this point, and with further work this is likely the determining factor. There may be some complications regarding an aluminum/steel interface relating to differential expansion and galvanic corrosion, and for these reasons an all-steel enclosure is assumed for the feasibility study.

12.2.5.7 Interface Mechanical Configuration

The initial design space for the sloping mechanical interface between the cap and base structures (herein referred to as the “interface”) is very broad since experience with similar systems is not available. Several key design decisions were identified early in the conceptual design process, and these are summarized below.

- **Continuous vs. Discrete Bogie Elements:** Initial concepts for the bogie system included utilizing a relatively continuous curved track recirculating ball bearing system, or alternatively using more conventional discrete bogie assemblies spaced on the order of 5 m. It was concluded that the widely spaced bogie assemblies could better accommodate fabrication and assembly tolerances and deformations due to wind and thermal loading, and therefore this approach was selected for the point design.
- **Bogie Mount Location:** The bogies could either be fixed to the base or cap portion of the structure. The conclusion for the feasibility study was to utilize cap-mounted bogies, since this allows the bogies to be accessed from a single location at the lowest point of the cap/base interface ring by rotating the cap structure. This is perceived to greatly facilitate maintenance of the bogie system compared to a base-mounted bogie system.
- **Interface Bogie Orientation:** The bogie sets could be oriented in a variety of directions relative to the plane of the interface. It was concluded that the bogie orientation should utilize two sets of orthogonal rollers: one set transferring forces normal to the interface plane (the “normal rollers”) and one set transferring forces normal to the axis of interface rotation (the “radial rollers”). The driving factor here was the minimization of conical rail surfaces and wheels, which simplifies fabrication, assembly and alignment of these components.

12.2.5.8 Shutter Configuration

Similar to the interface mechanical configuration, the shutter mechanism (i.e. the structural/mechanical system that allows the aperture to be opened and closed) has a very large initial design space since previous experience is not available. Two major design decisions were identified and are described below.

- **Fixed vs. Movable Shutter:** A shutter structure that was fixed to the ground was initially considered. The fixed shutter would be located such that the aperture would align with the shutter when pointed south at a zenith angle of 75 degrees. However, geometric studies found that a fixed shutter blocked too much of the sky to be considered a reasonable solution. Therefore, a movable shutter that did not block any portion of the sky was selected as a basic requirement for the feasibility study.
- **Interior vs. Exterior Shutter:** Interior or exterior shutters (relative to the enclosure shell) were both initially considered. An interior shutter was selected for two primary reasons. Firstly, the shutter structure could be reduced in mass since it would not be exposed to wind and snow loads except for the circular portion that covers the aperture opening. Secondly, it would maintain a clean spherical exterior structure that would mitigate the buildup of snow and ice, and reduce wind turbulence.

12.2.6 Enclosure Design

The following sections give further description and illustrations of the point design used as the basis for the feasibility study. An overview of the enclosure concept is shown in Figure 12.2.10 below.

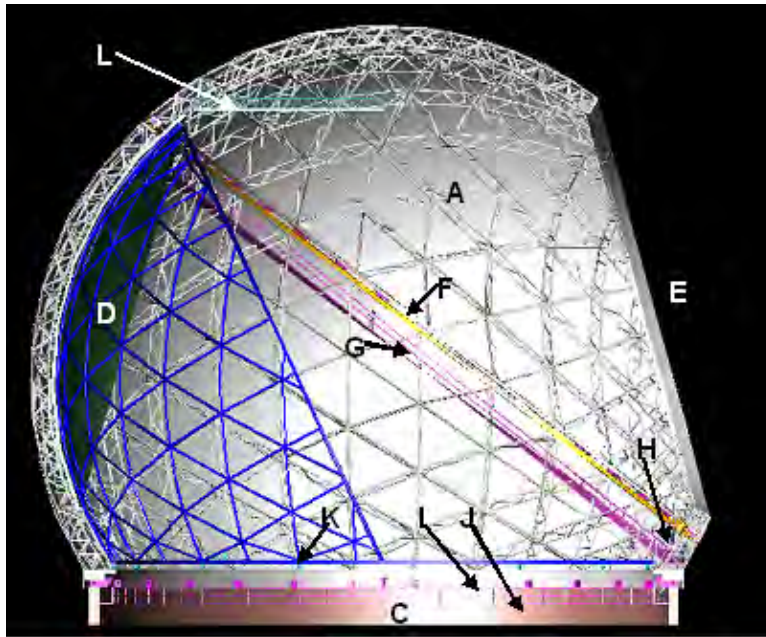


Figure 12.2.10. Cutaway through enclosure showing key components of point design (enclosure is open, and pointing to zenith = 75 degrees): (A) cap structure, (B) base structure, (C) fixed pier, (D) shutter structure, (E) aperture, (F) interface bogie/rail system, (G) interface/crane access walkway, (H) interface maintenance platform and interface drives, (I) azimuth bogie/rail system, (J) azimuth maintenance walkway, (K) shutter bogie/rail system, (L) enclosure crane

12.2.6.1 Structure

Figure 12.2.11 below highlights the structural framework of the enclosure. The main structural shell consists of rib trusses lying in vertical planes spaced at 12 degrees, which are triangulated via diagonal ties. The rib and tie members consist of open web welded trusses that are 1.0 m deep. This structure is triangulated to intersect ring girders at the mechanical interfaces and at the aperture ring.

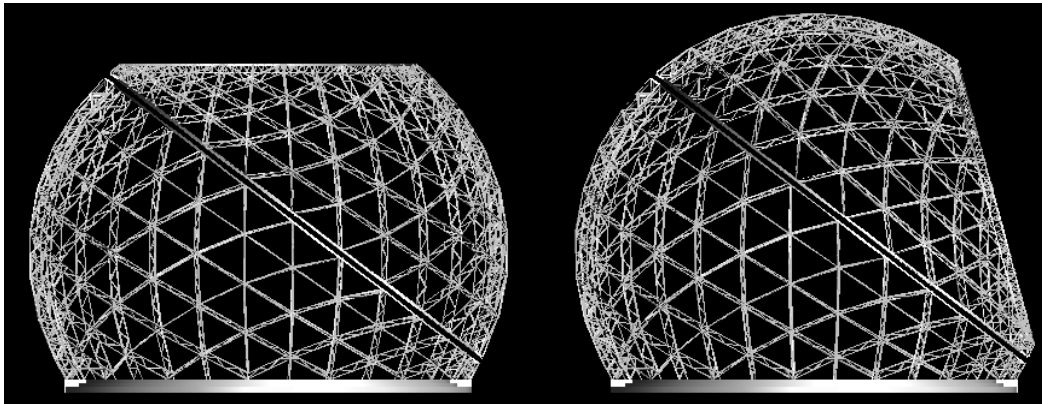


Figure 12.2.11. Enclosure structural framework, shown with aperture pointing to zenith = 0 degrees (left) and zenith = 75 degrees (right)

12.2.6.2 Azimuth Mechanical

The design of the azimuth mechanical system is expected to be similar to that of existing enclosures, and does not present any unique design challenges. Currently it is anticipated that the azimuth bogies and drives will be fixed to the foundation structure and will support/drive a rail on the underside of the azimuth ring girder. This system has been used successfully on the enclosures for the Hobby Eberly and SOAR telescopes.

12.2.6.3 Interface Mechanical

Many alternative design solutions were considered for the interface mechanical system, and the following provides a description of the selected point design. The interface bogie design is shown in Figure 12.2.12 and Figure 12.2.13 below, and is described in detail here due to its unique nature.

30 bogies are evenly distributed around the interface and the bogies are mounted to the cap portion of the enclosure. Each bogie consists of 1 radial roller, 4 normal rollers, and 4 uplift rollers. The radial roller is polyurethane (approximately 24" diameter), and the normal and uplift rollers are steel (approximately 8" and 4" diameter, respectively). The normal roller pair transmits load directly to the cap support frame through a pivot bearing which equalizes the force within the normal roller pair. Preliminary sizing of polyurethane wheels indicates that it is possible to achieve the desired equivalent spring stiffness through compliance in the wheel itself, and therefore no radial suspension system would likely be required. In the normal direction, suspension may be implemented at the pivot bearing, possibly through rubber springs.

The bogie frame connecting the radial and normal rollers is a planar frame which gives it the properties of being torsionally soft and laterally stiff. The torsionally soft property allows the normal rollers to equalize about the pivot bearing, while the laterally stiff property maintains the conical angle between normal roller pairs within the same bogie which controls the turning radius of the bogie

The rails are composed of rolled wide-flange sections, which can be readily rolled to the required curvature within 1/8" tolerance. The rails have hardened steel wear plates tack welded to the flanges and web where radial and normal rollers are in high-duty contact with the rails.

The drives are mounted to the base structure near the low point of the cap/base interface. This facilitates maintenance, and does not require transfer of power across the interface. Multiple smaller drives are used in order to increase system redundancy, and allow operation when a single drive is out of operation. The current drive concept utilizes spring loaded rubber-tired rollers.

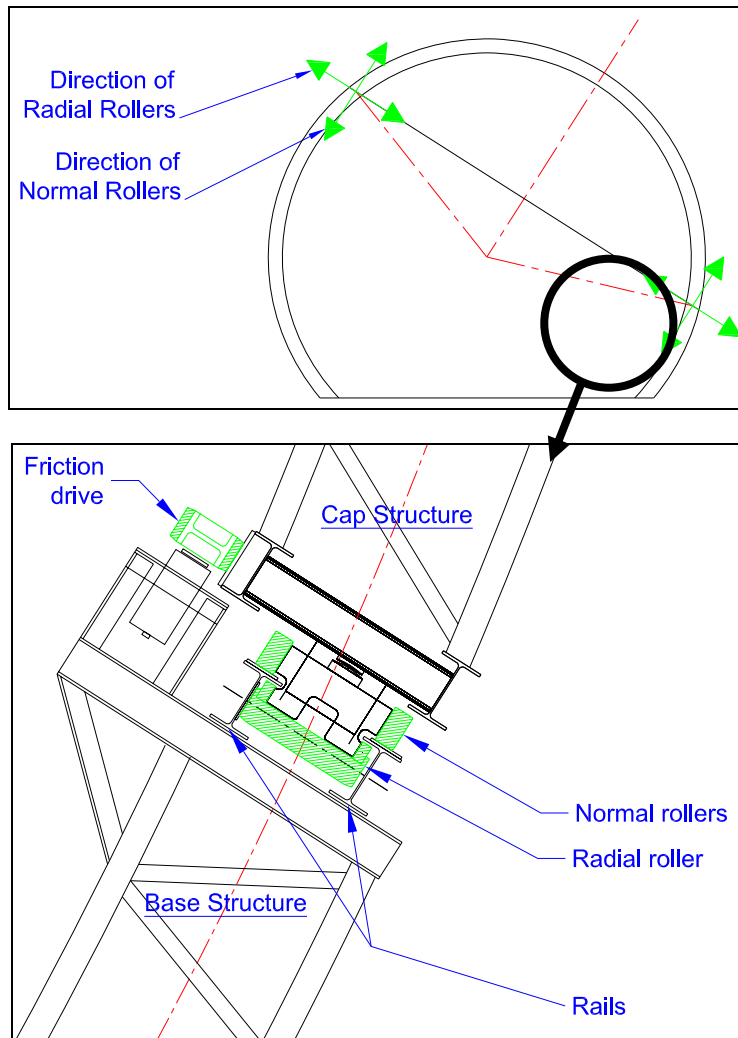


Figure 12.2.12. Interface bogie and drive point design showing location of interface detail (top), and cross section of interface detail (bottom)

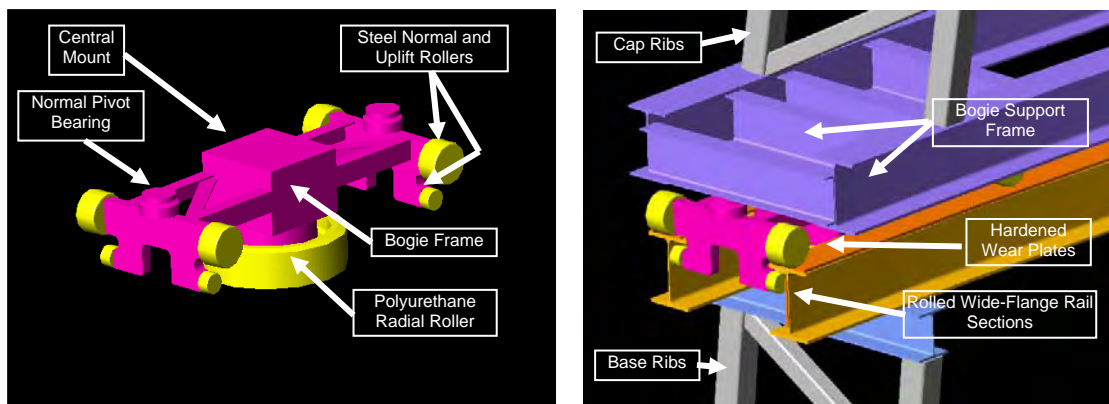


Figure 12.2.13. Interface bogie 3D rendering showing bogie components (left), and interface between bogie, rail, and supporting structure (right)

Figure 12.2.14 illustrates the locations of radial roller contact under gravity load conditions. Analysis has indicated that the structural deformations of the cap are such that the radial rollers will contact the inner rail at the

upper portion of the interface, and contact the outer rail at the lower portion of the interface. There is a transition point near the mid-height of the interface where the rollers will contact neither rail. A section of the inner rail at the low point of the interface is removable to facilitate bogie maintenance.

To eliminate the possibility of wheel binding (during transition between inner and outer rails) the running faces of the bottom section of the inner rail and upper section of outer rail have been offset away from the wheel; the spacing between the radial rail faces is nominally 1" greater than the radial wheel diameter. The radial clearance created by this offset makes the calotte interface less sensitive to fabrication and installation tolerances and it compensates for thermal expansion and operational wear.

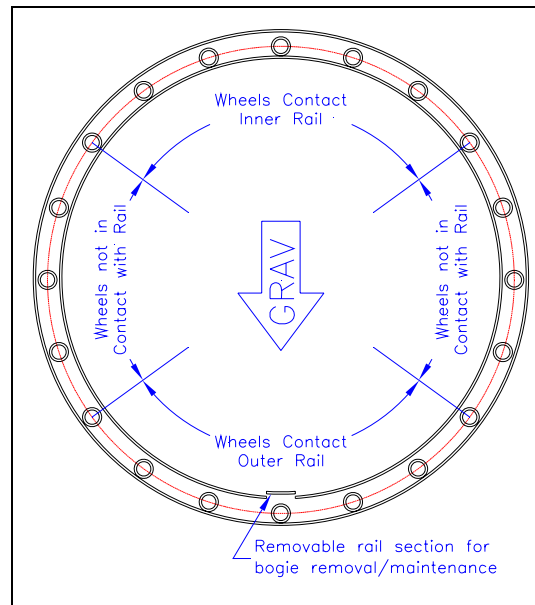


Figure 12.2.14. Interface radial roller contact under gravity loads

Bogie and drive maintenance is carried out at an interior maintenance platform at the low point of the cap/base interface, providing good access to bogies and drives. In the event that emergency access to a bogie is required at a location away from the maintenance platform, an access walkway follows the interface ring along the interior of the enclosure. Figure 12.2.10 shows both the maintenance platform (location H) and access walkway (location G).

12.2.6.4 Shutter

The current shutter concept is based on an azimuthally rotating shutter structure that is supported by a set of bearings on top of the enclosure azimuth ring girder. This enables the shutter to rotate by 180 degrees relative to the base structure to either open or close the aperture. In the open position, the shutter centerline is rotated in line with the high point on the interface ring girder and does not obstruct any viewing position of the aperture. In the closed position, the shutter centerline rotates in line with the low point of the interface, which covers the aperture when the cap is rotated to the zenith = 75 degree position (Figure 12.2.15). The point design utilizes inflatable seals to seal the gap between the shutter structure and the aperture ring.

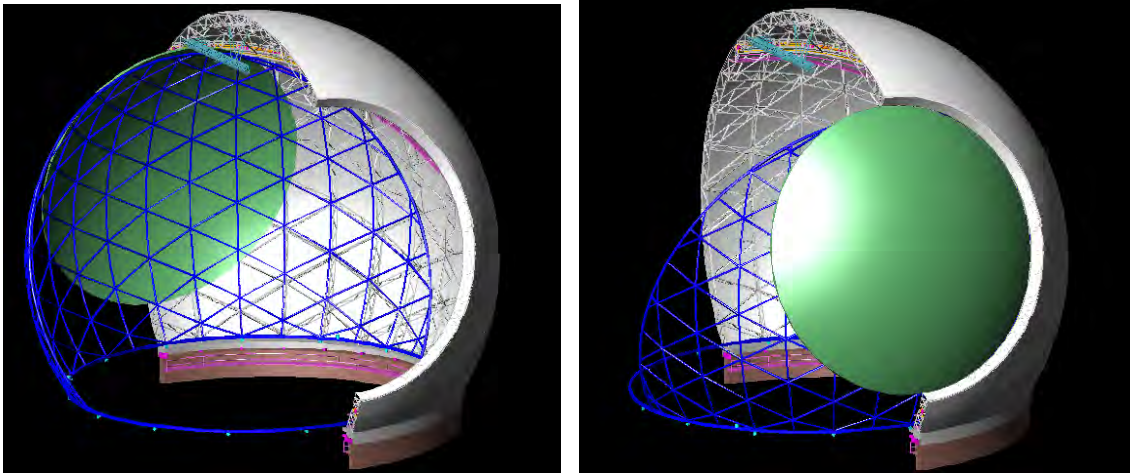


Figure 12.2.15. Cutaway through enclosure showing azimuthally rotating shutter, shown in open position (left) and closed position (right)

12.2.6.5 Enclosure Crane

The enclosure requirements specify a 2-tonne enclosure mounted crane for telescope equipment handling. Alternate crane options were considered, and an enclosure-mounted retractable gantry crane is currently the preferred option (Figure 12.2.16). The crane is mounted to the enclosure cap structure, and is pinned at one end and supported by cables at the other end. When the cap is rotated to the closed aperture position, the crane is located at the centerline of the enclosure, above the high point of the interface. When the telescope is in operation, the supporting cables retract the crane via winch (this may not be required depending on the exact telescope clearance envelope).

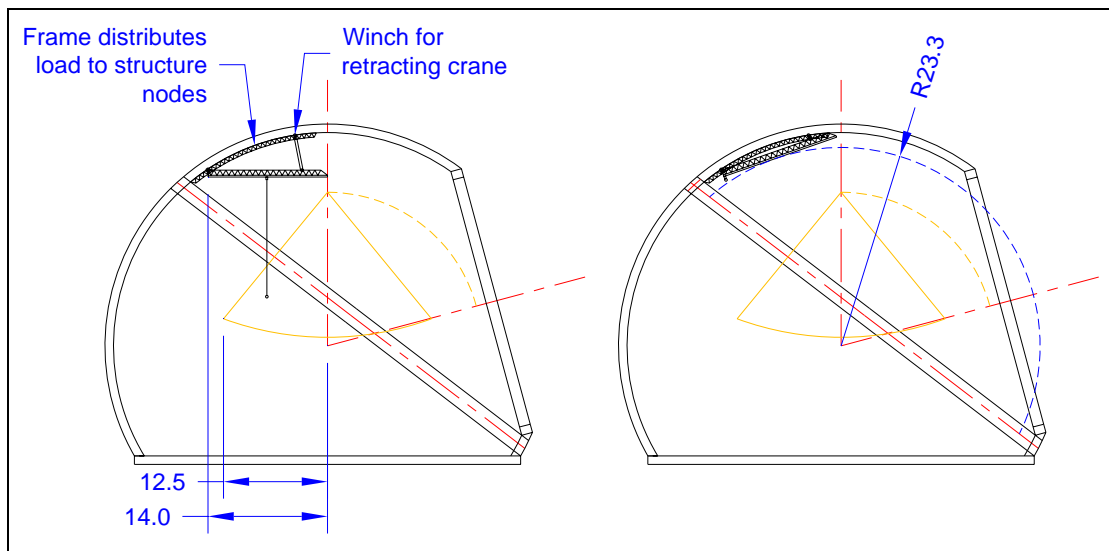


Figure 12.2.16. Enclosure mounted crane shown in operating position (left) and retracted position (right)

12.2.6.6 Manufacturing Approach

The manufacture of the dome utilizes standard steel fabricating procedures. It is possible that the shell structure of the enclosure may be factory produced, and the structure interfacing to the mechanical systems would be built by a fabricator. Companies that exclusively produce dome shell structures out of steel and aluminum have been identified, and this may provide cost savings; however, the associated complexity of integrating structures from multiple manufacturers must be assessed.

It is anticipated that a trial assembly of the major structural framework and mechanical systems will be required at the contractor's site. This is to minimize the fit-up required in the field, and to allow a practice alignment of the critical structural/mechanical components. The structural design is well suited to utilizing small components that can be shipped in standard containers. The field assembly procedure will minimize welding and other labor-intensive activities. It is estimated that a 200 ft telescoping hydraulic crane will be adequate for the on-site construction.

12.2.7 Analysis

The following summarizes the analysis carried out for the feasibility study.

12.2.7.1 Structural Analysis

A structural analysis was run using a finite element model of the entire enclosure, and is briefly summarized here. Sample plots of the element layout, deflected shapes, and wind loading are shown in Figure 12.2.17. The ribs, ties, and ring girders were modeled using beam elements. The bogies and drives at both the azimuth and sloping interfaces were modeled using spring elements oriented parallel to the line of action of the rollers or drives and with equivalent stiffness properties.

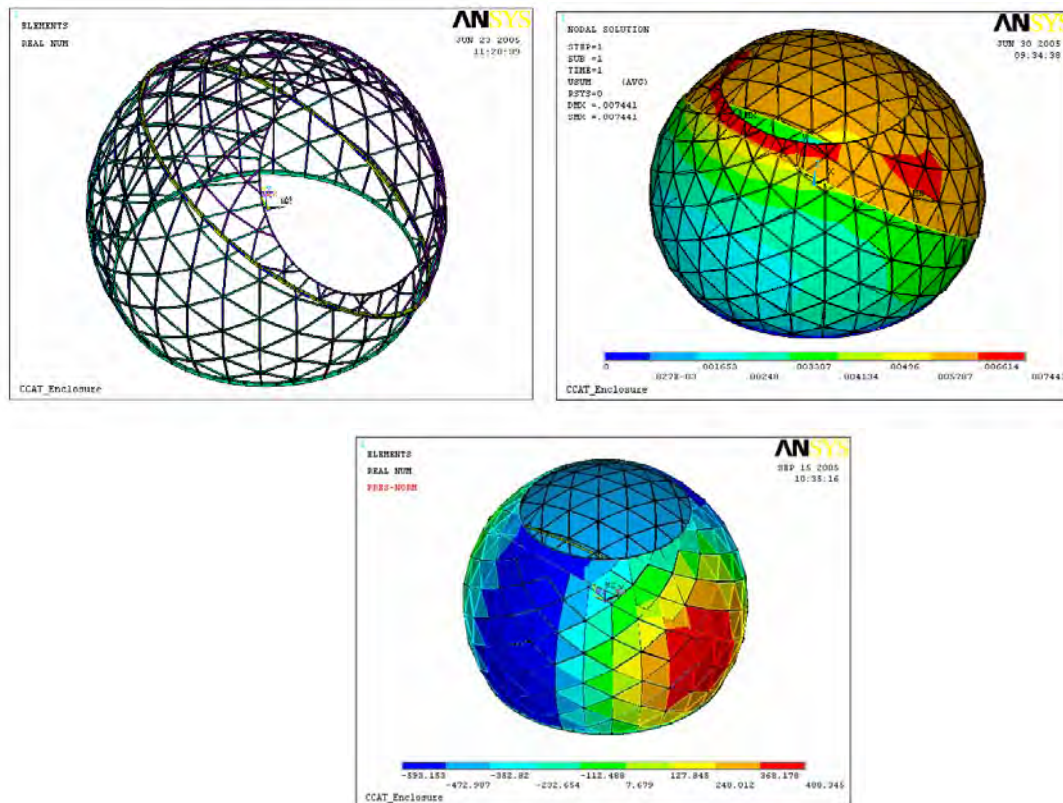


Figure 12.2.17. Enclosure finite element model sample plots showing elements (top left), gravity deflections (top right), and applied wind pressures (bottom)

The analysis included load combinations for gravity, wind, seismic, and snow/ice loads. Member sizes were optimized based on allowable stresses under all load combinations. A modal analysis was also carried out, and the following summarizes the first four modes:

- Mode 1: 1.4 Hz, azimuthal rotation (compliance of azimuth drives)
- Mode 2: 2.0 Hz, ovalization of aperture ring
- Mode 3: 2.0 Hz, ovalization of aperture ring
- Mode 4: 2.9 Hz, cap rotation (compliance of interface drives)

12.2.7.2 Interface Analysis

Due to the high risk associated with the design of the interface mechanical system, an extensive analysis of the forces through this mechanism was carried out using the enclosure finite element model. Results and conclusions are summarized here. Analyses were carried out to determine the bogie forces under following conditions:

- Gravity load with multiple cap orientations (sample results in Figure 12.2.18)
- Gravity load with various initial radial roller gap sizes (sample results in Figure 12.2.19)
- Gravity load with assembly tolerance errors (the interface rail was assumed to be assembled in an elliptical shape with a deviation of +/-13 mm from the perfect circle to estimate the effects of fabrication and assembly tolerances)
- Wind load (including multiple wind directions and aperture orientations, sample results in Figure 12.2.20)
- Thermal load (including both absolute temperature changes, and temperature gradients across the enclosure)

The following conclusions were drawn based on the analyses described:

- Gaps at the radial wheels and rails have a relatively minor effect on gravity load distribution
- Fabrication and assembly tolerances play a key role in governing wheel forces; methods of achieving tight tolerances through design, fabrication, and assembly procedures need to be investigated
- Wind loads result in load reversals in both radial and normal wheels under extreme operational conditions, and the mechanical design must accommodate this
- Thermal loads do not result in significant increase in wheel loads

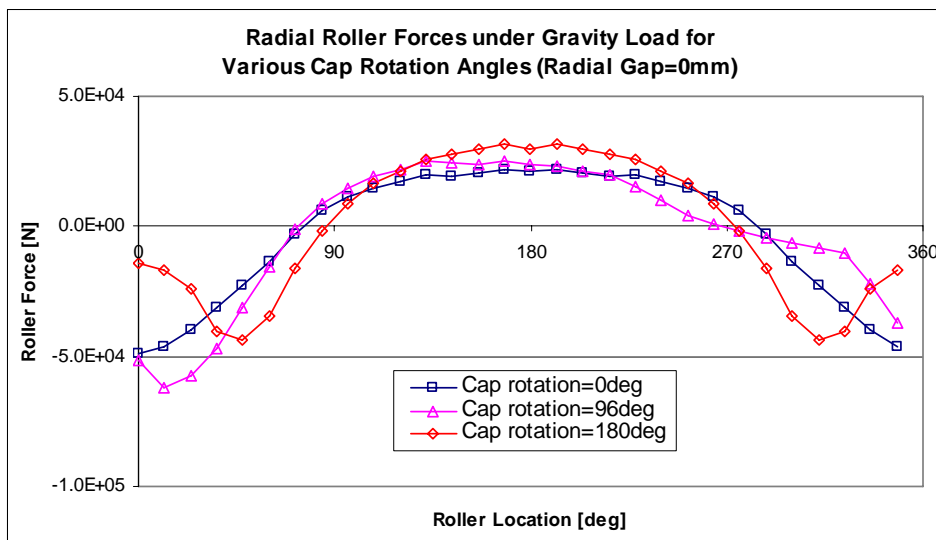


Figure 12.2.18. Interface radial roller forces under gravity loads for various cap rotation angles. Bogies at bottom and top of interface correspond to bogie locations (plotted on x-axis) of 0 and 180 degrees, respectively. Positive and negative forces indicate radial roller is in contact with inner and outer rail, respectively.

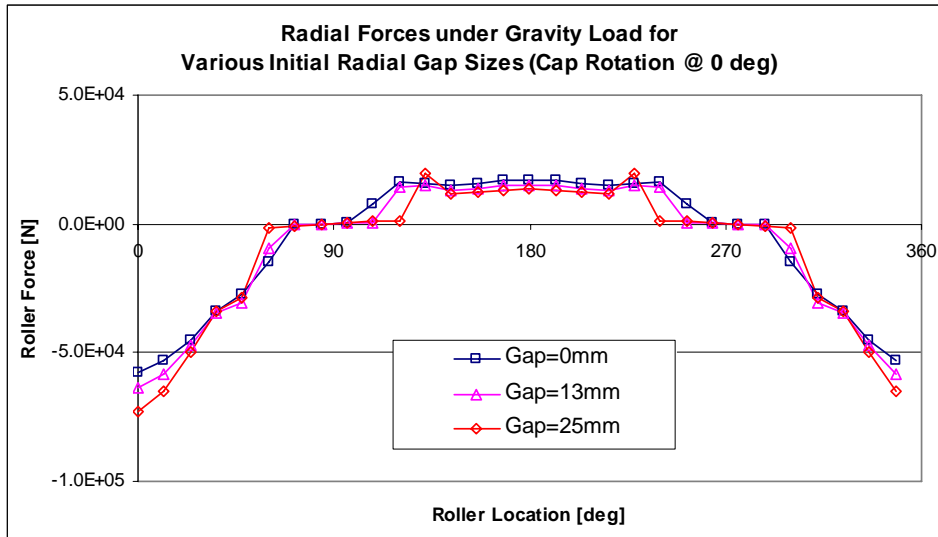


Figure 12.2.19. Interface radial roller forces under gravity loads for various initial radial gap sizes (aperture rotated to zenith)

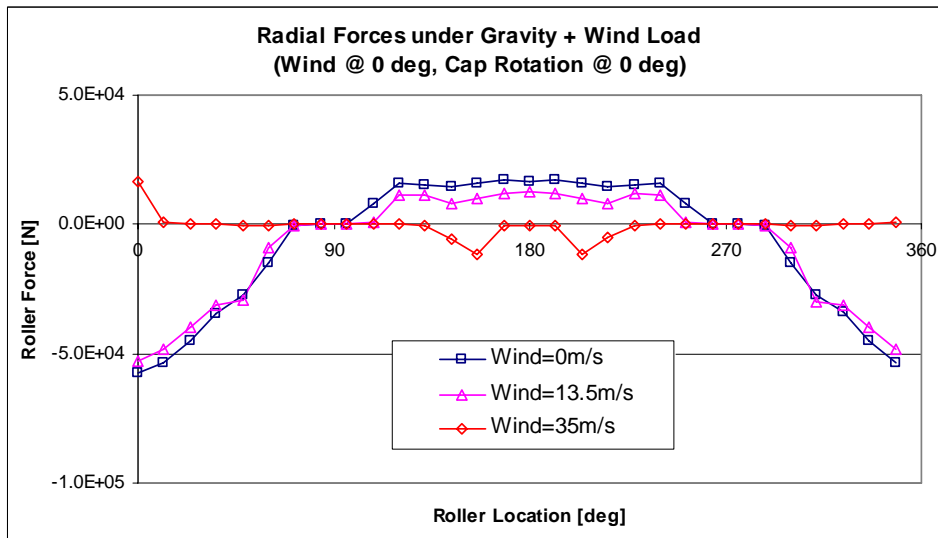


Figure 12.2.20. Interface radial roller forces under gravity and wind loads (wind incoming from 0 degree location on interface, aperture rotated to zenith, initial radial gap = 6 mm)

12.2.7.3 Drive Systems

The total input horsepower requirements for the azimuth and interface drives were estimated to be 110 hp and 90 hp, respectively. The analysis assumed a required slewing time of 2 minutes (for 180 degrees rotation), and accounted for torque due to inertia, friction, and wind. It was assumed that the cap center of mass was balanced to within 50mm of the cap rotation axis. The required input power assumed 50% efficiency due to drive train friction and de-rating for high altitude. Additionally, a service factor of 2 was applied, which includes allowance for enclosure operation if a single drive goes down. Each mechanism is assumed to use 4 motors in the range of 30 hp, which allows system redundancy and motors of a relatively modest size

12.2.7.4 Mass Estimate

Based on the above structural and mechanical analysis results, a preliminary mass estimate for the enclosure was carried out, and is summarized in Table 12.2.1. Masses based on FEA results include allowances for connections, stiffeners, and bracing.

Table 12.2.1. Enclosure mass breakdown

| Component | Mass [Tonnes] |
|----------------------------------|--------------------------|
| Structural - Ribs | 54 |
| Structural - Ties | 101 |
| Structural - Azimuth Ring | 21 |
| Structural - Interface Ring-Cap | 24 |
| Structural - Interface Ring-Cap | 24 |
| Structural - Aperture Ring | 12 |
| Structural - Shutter | 50 |
| Structural - Cladding/Insulation | 81 |
| Mechanical - Azimuth | 76 |
| Mechanical - calotte | 38 |
| Mechanical - Shutter | 15 |
| TOTAL | 496 |

12.2.8 Critical Risk Assessment / Mitigation

The items identified below have been identified as the critical risks associated with the calotte enclosure. For each risk item a level of risk is identified, and mitigation strategies are proposed:

- Interface assembly tolerances – *High Risk*: The analysis of the interface bogie forces indicated that an expected out-of-roundness tolerance of +/- 13mm would approximately double the peak bogie forces, and therefore has a large impact on the mechanical design. Further investigation of alignment procedures would allow this risk to be reduced. The design of more compliant structural and suspension systems may also reduce the loads caused by these tolerances.
- Shutter seal – *Moderate Risk*: Due to the nature of the motion between the shutter and the aperture, the sealing of the shutter for the calotte enclosure is different from existing enclosures. However, initial concepts indicate that robust sealing concepts are likely available, and therefore the risk is considered moderate.
- Mechanical system cost – *Moderate Risk*: The mechanical design is still early in the conceptual phase. The cost of this system is extrapolated from other enclosures based on the supported mass and factors pertaining to design complexity, and is considered to have moderate risk.
- Structural mass/cost – *Low Risk*: The structural mass and cost estimates are based on mature analysis methods and estimating databases, and are therefore considered to be relatively low risk.

12.2.9 Future Work

The conceptual design phase will include the development of structural and mechanical concepts to the level of assembly drawings. This level of detail will allow reliable bottom-up cost estimates to be produced. The critical risks identified above will be paid special attention, and the proposed mitigation strategies will be assessed. It is expected that the overall level of risk at the end of the conceptual design phase will be low.

13 Telescope Mount

13.1 Introduction

The majority of this section is devoted to a report on a funded conceptual design study performed by Vertex RSI.

13.1.1 Background

The telescope mount is a moderately challenging design task. For a 25 m telescope, CCAT has extremely tight pointing and tracking requirements (0.2 arcsec) because of its high resolution at 200 μm wavelength. A second major design driver is the desire to observe in scanning modes. During scanning, while exact pointing is not as important, the knowledge of what the pointing is as each exposure is made is critical if subsequent images of the same field of view are to be added. These requirements drive a need for excellent dynamic structural performance and sophisticated control hardware and algorithms. It also places substantial demands on the design of encoders and the portions of the structure that support them. A final but perhaps the most significant challenge is that of cost. Cost of astronomical telescope structures scale very closely with weight and, since they are designed to be structurally efficient, it is not easy to find ways to hold costs down. In the design of CCAT we have paid close attention to structural design, choice of configuration, choices of bearings, drives, and encoders in an attempt to meet the established requirements at minimum cost.

13.1.2 Scope

The telescope mount extends from the pier, which is considered part of the facility, to the mounting points for the primary mirror truss and the instrument mounting points at the Nasmyth and bent Cassegrain foci. For the purpose of this study, the primary mirror truss was considered part of the mount, but we intend to pursue development of the truss independently and to make it a separate procurement. The mount includes all drives, bearings, cabling, electronics, and controls required to operate all motion and other degrees of freedom in a stand-alone manner and as interfaced to the Telescope Control System.

13.1.3 Design Elements

The following design elements were recommended to VertexRSI at the inception of the study.

13.1.3.1 Azimuth

- Azimuth Bearing (Axial Loads): The choice of hydrostatic bearings for azimuth is fairly simple as the only reasonable alternative is a wheel and track system. While these have been used successfully on radio telescopes, they have not been used for optical telescopes and it was generally felt that the jitter and Coulomb friction of this type of system would not be compatible with the precision pointing requirements. The hydrostatic was deemed much simpler provided that the issue of acceptable flatness of the bearing ways could be accommodated. We believe this requirement can be met by using a method developed for the HET in which the pier was poured to 25 mm short of the finished height. Machined steel forms were then attached inside and outside of the pier and leveled using a Hamar laser to ~ 0.025 mm flatness. A special mix of concrete was then poured in and screened level using the forms. With the HET this resulted in a pier flat to about 100 μm . For CCAT after the pier is sufficiently level, anchor holes would be bored and the hydrostatic bearing ways which had been Blanchard ground to a plane parallel state could be bolted down. Joints would be sealed by gaskets or o-rings and no welding or grinding of these ways would be proposed.
- Azimuth Bearing (Radial Loads): Rather than machine a second very large radius surface on the hydrostatic bearings, we elected to incorporate a pintle bearing. The radial loads are small, and as the drive motors are near the hydrostatic bearing, they have a significant mechanical advantage to overcome any friction in this bearing. This is a standard commercial bearing and hence much less expensive.
- Azimuth Drives: Initially curvilinear torque motors were considered for driving azimuth, but these proved to be much too expensive. Consequently it was decided after trying a number of different arrangements, to use helical gear drive with the gear stationary and mounted to the inside circumference of the hydrostatic ways. Motors would be mounted on the rotating azimuth structure and move with it. We anticipate two pairs of

motors, diametrically opposed. The motors in each pair would be counter torqued against each other which controls hysteresis and backlash.

- **Azimuth Encoder:** A version of the arrangement used for the SOAR telescope (built by VRSI) and as further developed for the VISTA telescope is incorporated. This will be the third iteration of this successful design, and has proven robust and precise. The Heidenhain encoder tape is mounted to a steel disk which is supported by a tower which begins at bedrock. It is therefore impervious to any wind up of the structure. The tower extend through the central hole of the pintle bearing and some ways toward the elevation axis as the closer to the optics the more representative the readings will be of the optical pointing vector. Four readouts are mounted to structure of the azimuth base and move in close non-contact to the tape. There are precision adjustment bases for these readers which enable rapid and accurate adjustment of position.
- **Cable Wrap:** Inside the diameter of the hydrostatic azimuth bearing and the pier there will be a track type cable wrap similar to that used with Keck and optimized for HET. While these types of wraps have caused some problems in the past, it was found that if cable loads are kept light relative to the size of the track, are kept on the center of the track so that length changes when flexed are minimal, and the cables of sufficient flexibility are chosen that the approach can work very well.

13.1.3.2 Elevation

- **Elevation Bearings:** In contrast to the azimuth, the diameter and loads of the elevation axis are well within the capabilities of rolling element bearings. Bearings are commercially available with inner diameters to two meters which provides more than adequate pass through for the beam to Nasmyth at the full specified field of view. In contrast to the hydrostatic bearings, the rolling element bearings can be self aligning, which reduces overconstraint of the mechanical design.
- **Elevation Drives:** Again, the first plan was to use frameless servo motors (Torquers) at this location. Unfortunately in appropriate sizes these were also prohibitively expensive. We considered helical gears at the elevation bearings, which would work, but would require four motors and clutter the space. It was determined that if we used a sector type drive (as is shown) that we would also gain the structural depth that we needed to support the interface to the primary mirror truss. This approach also provides a place to support the M3 turntable assembly as well. The plan would be to, again, use two motors counter torqued against each other.
- **Elevation Encoders:** The arrangement here is, again, similar to that proven on SOAR and VISTA. It uses Heidenhain tapes mounted at the elevation bearings. The two can be used to remove any pointing error related to twist of the elevation axis.

13.1.3.3 Requirements and Design Process

The initial structural concept and space envelopes were worked out iteratively using drawing services provided by Spacemill Design near Ithaca, NY, and performance requirements for the mount were developed by Terry Herter and reviewed on several occasions by members of the scientific staff of the partner institutions. During design a good deal of attention was paid to the scanning motions anticipated and the requirements for pointing and tracking. Space envelopes required for the instruments have been reviewed by the instrument committee and it is anticipated that further development of these interfaces will be accomplished as the concept design for instruments is refined.

13.1.4 Summary

The mount concept appears valid and not particularly risky. That said, there is a good deal of work to do in the Engineering Concept Design phase before the concept has been completely developed and validated. In particular we plan to pay close attention to structural efficiency and the manufacturing process to ensure that the final design can be produced at the lowest possible cost for the specified performance.

13.2 TELESCOPE MOUNT

Report prepared by VertexRSI

13.2.1 Introduction

The following is a description of the CCAT mount and mount control system as shown in Figure 13.2.1. It covers the design of the mount, the reasoning behind our design choices, our assessment of the program's risks, and the next steps necessary to completing the design work.

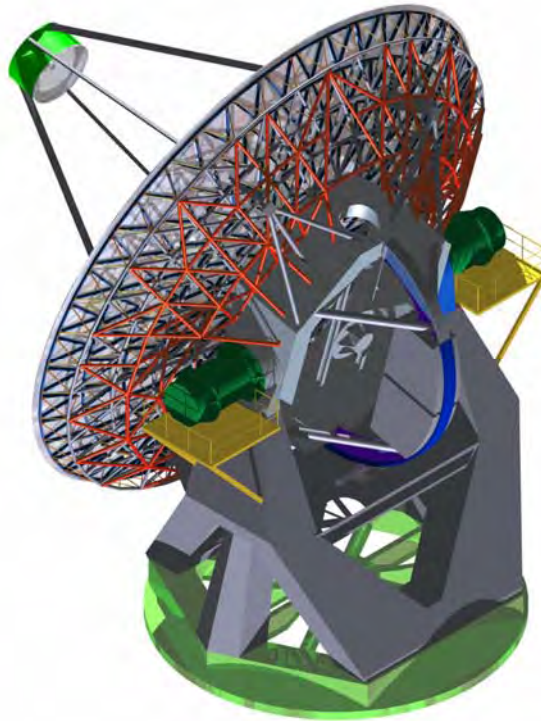


Figure 13.2.1. CCAT Mount

13.2.2 Background of Company

VertexRSI's Control and Structures Division is a supplier of full-motion antennas, telescopes, and other unique control systems and "controlled structure" instruments. We produce structures and controls systems designed to accurately point and track objects. This report will refer to lessons learned from the following projects:

- Southern Astrophysical Research Telescope (SOAR), a 4.1 m alt-az optical telescope located on Cerro Pachon, Chile.
- The Hobby Eberly Telescope, an 11m optical telescope located at the McDonald Observatory.
- The Very Long Baseline Array (VLBA), a network of ten 25m radio telescopes, located across the United States from New Hampshire to Hawaii.
- The Green Bank Telescope (GBT), a 100 m radio telescope located in Green Bank, West Virginia.
- The South Pole Telescope (SPT), a 10 m diameter telescope being constructed for deployment at the NSF South Pole research station. Controls and Structures' contribution to this project is limited to the control system.
- The first Keck telescope, on the summit of Mauna Kea, was installed by a company that is now part of VertexRSI Controls and Structures.
- Various precision radar projects for the US Department of Defense.

13.2.3 Scope

The scope of this study is to provide a mount for the CCAT. The mount structure must be able to accommodate the optical layout and move the optics in azimuth and elevation. It must be stiff enough to allow the servo to point, track, and to support the open loop pointing requirements. It also includes choosing drive components to support telescope scans.

The structure under study is the azimuth rotating structure, the elevation structure less the primary mirror and its backup structure, and the drives for each axis, with the associated control system. This study provided a first order examination of the mount geometry and the requirements to produce it. It covers questions about structural geometry, selection of drive components, and estimates of a performance bounds.

13.2.4 Trades and Design Choices

13.2.4.1 Panel Layout

There were a variety of reflector panel layouts possible for CCAT. The panels were to be a nominal 2m x 2m size. A CAD layout was used to establish the configuration that maintained a uniform panel length for all panels as given in the Outside Radius column in Table 13.2.1. This data was then provided to the system designer for use in our CAD modeling phase of the CCAT study project. Figure 13.2.2 shows the variety of ways in which the panels could be configured. Note the differences in symmetry lines that are possible as well.

Our initial selection used the configuration with 3/6 fold geometry. This geometry provides lines of symmetry along six axes. Final selection of the configuration is dependent upon many factors including panel manufacturing techniques, size, and structural support design.

We assumed the following:

- 2 m ID hole at the center of the reflector
- Panels to be uniform in length (radial away from center)
- For this analysis a spherical surface was considered; final design would be per the required surface shape
- Maximum panel size would be 2 m in both width or length
- There are six tiers, with tier number 1 being the inside tier

Table 13.2.1. Panel Layout Configuration

| Tier Number | Outside Radius (meters) | Circumference (meters) | Potential Number of Panels and Width (meters) (assuming 2m width and less) |
|-------------|-------------------------|------------------------|--|
| 1 | 3.180 | 19.983 | 10@1.99m ; 11@1.82; 12@1.67 |
| 2 | 5.095 | 32.014 | 16@2.00m; 17@1.88; 18@1.78 |
| 3 | 6.991 | 43.928 | 21@2.09m; 22@1.99; 23@1.91; 24@1.83 |
| 4 | 8.862 | 55.683 | 27@2.06m; 28@1.99; 29@1.92; 30@1.86; 31@1.86 |
| 5 | 10.701 | 67.234 | 34@1.98m; 35@1.92; 36@1.87; 37@1.82 |
| 6 | 12.500 | 78.540 | 40@1.96m; 41@1.92; 42@1.87; 43@1.83; 44@1.79 |

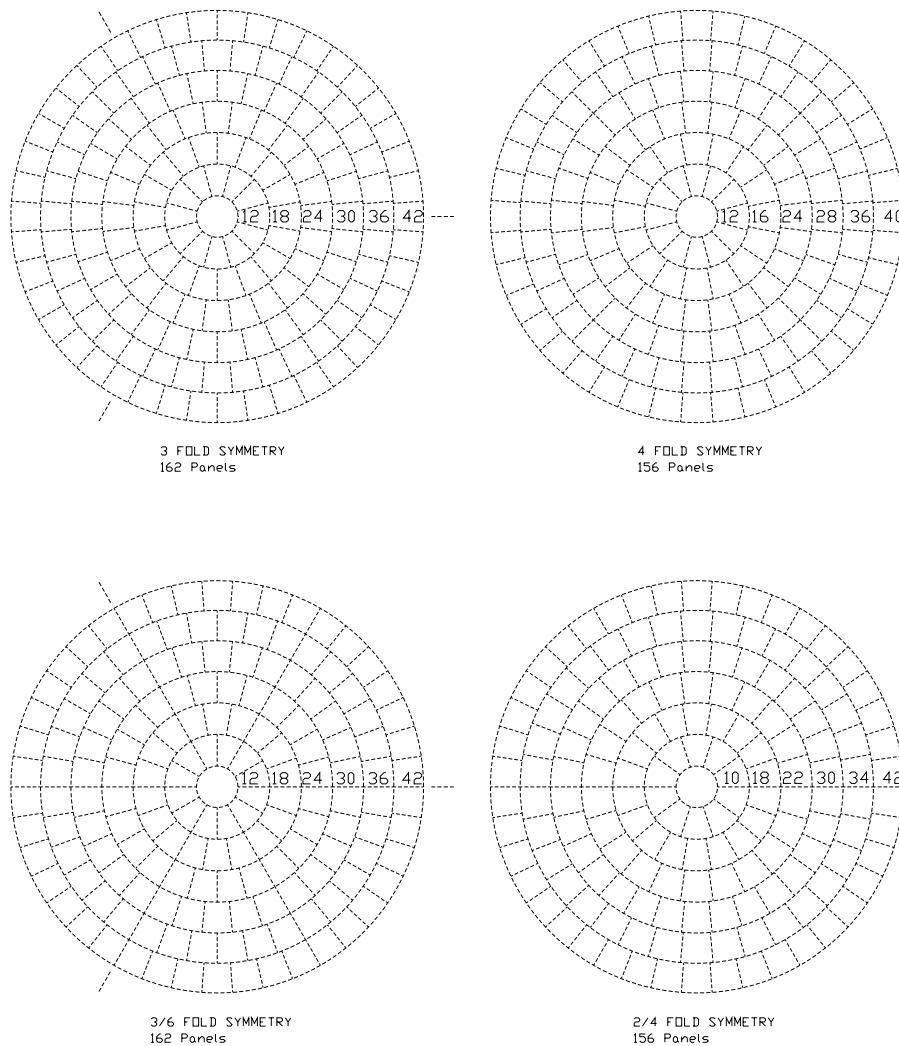


Figure 13.2.2. Various Panel Layout Configurations

13.2.4.2 Azimuth and Elevation Drives

Multiple drive train choices are available, and include friction drives, geared drives, and direct drives. Friction drives have not been used on this class of system. High velocities and accelerations are difficult to obtain, and they are subject to environmental and maintenance issues. Direct drives are feasible, but the large torques required makes them expensive. Geared drives have proven effective on SOAR and GBT and are a mature, low risk technology.

The choices for the drives on each axis are driven by considerations of horsepower needed to carry out the scanning pattern, the number of drives to maintain an acceptable system resonance, and the overall stiffness of the drive. As will be explained in greater detail in a later section, a gear drive offers greater flexibility to adapt to changes as the design progresses. At present, the inertia and axis speeds of the structure are under review, and the best path forward provides a configuration that allows the number and horsepower of the drives to change easily. Locating the drive at a large radius gives higher drive train stiffness. Since the stiffness of a gear tooth is a fixed quantity, locating the gear mesh at a larger radius means the angle created by the deflection of the gear teeth is smaller than a gear mesh at a smaller radius.

13.2.4.3 Monocoque vs. Truss Structure

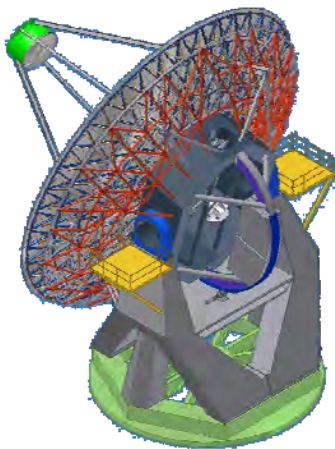
The options for the CCAT structure are a truss or a monocoque structure. Our experience with the two, most involving design of precision radars, has shown that monocoque structures provide greater stiffness for the

weight. For this application, they are also easier to fabricate, assemble, and transport than truss structures, and use larger, fewer sections.

13.2.5 Mount Concept Design Overview

The CCAT mount is shown in Figure 13.2.3. The mount is divided into two major divisions. The Optics Support Structure (OSS), provides support for the primary, secondary, and tertiary mirrors, and comprises that portion of the structure that rotates in elevation. The alidade comprises that portion of the structure that rotates in azimuth and supports the OSS. It also houses the mechanisms for the elevation and azimuth drives and the bearings that make motion about those axes possible.

The starting point for the mount structural design was the optical layout, which established keep out zones for the structural components. The distance between the vertices of the primary and tertiary mirror affects the depth of the primary mirror truss and the depth of the hub on the OSS. This close spacing makes it challenging to put panel actuators, a support truss, and a hub interface structure in that space. In addition, the distance between the tertiary mirror and the Nasmyth foci determine the width of the hub. Finally, the shape of the parabola affects the layout of the alidade, since the front legs of the alidade since the mirror truss must be able to clear the alidade legs at low elevation angles.



To isolate the deflections for the primary and secondary mirrors, the secondary mirror support has its own load path to the OSS hub, without being attached to the primary mirror truss.

On the hydrostatic bearing, the shoes are located as directly under the elevation bearings as possible, to provide the most direct load path from the OSS to the foundation. To prevent a lag between the azimuth drives and the encoder that measures their motion, it is necessary to have a stiff structure between the two. A centering bearing is needed to keep the telescope on an azimuth axis.

The following sections show how the design satisfies these initial conditions.

Figure 13.2.3. Overview of CCAT Mount

13.2.6 Structural Design – Optics Support Structure (OSS)

13.2.6.1 Hub Assembly

The CCAT OSS is shown in Figure 13.2.4. Our scope included all the parts shown except for the primary mirror and the primary mirror truss. The central feature of the OSS is the hub. All the other elements of the OSS are supported from the hub. The primary mirror truss, the secondary mirror quadrapod, and the tertiary mirror support are all supported by the hub. The sector gear for the elevation drive is supported on the back of the hub. Finally, the OSS is supported by elevation axles from the hub. Figure 13.2.4 shows the major subassemblies that make up the OSS.

The hub provides the support for all the subassemblies of the OSS. The design of the hub is based on a torus, a doughnut shaped ring using a hollow box cross section. Toroidal hubs are commonly used in large antenna structures, experience having shown them to possess a number of advantages. The first is in its high stiffness to weight ratio. Since it is a closed box section, the toroidal hub is an efficient means of resisting the twist placed on it from the cantilevered load of the primary mirror backup structure. In addition, it is a clean, simple design that is easy to fabricate, ship, and install.

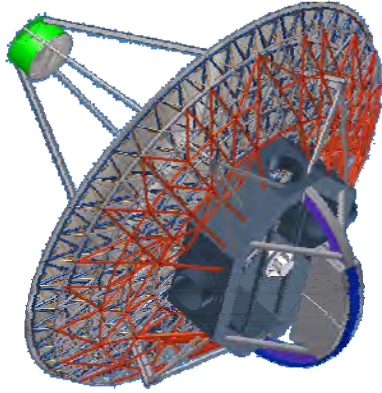


Figure 13.2.4. CCAT Elevation Structure

The hub is an irregular octagon, longer vertically than horizontally. The horizontal dimension is driven by the distance between the optical axis and the Nasmyth focal point. That 7 m distance had to include half the outer diameter of the hub, the elevation bearing supports, and the length of the Nasmyth instrument between the mounting flange and the focal plane. The vertical dimension is driven by the radius of the elevation sector gear. It needs a larger radius to keep the elevation motor size to a reasonable level. Using an oblong hub satisfied both needs.

The elevation axles are placed as close to the reflector side of the hub as possible. This was driven by the distance between the vertex of the primary and tertiary mirror, since the tertiary mirror is on the elevation axis. This allows as much space as possible for primary mirror

support, since it minimizes the distance between the elevation axis and the front of the hub. The elevation bearings are a set of spherical roller bearings, which will establish the elevation axis. Spherical roller bearings of this size have been used on structures as large as the GBT with great success.

13.2.6.2 Secondary and Tertiary Mirror Supports

To separate the load paths between the primary and secondary mirrors, we borrowed a concept used for the VLBA radio telescopes. There are separate support legs coming from the diagonal surfaces of the hub which support the base of the secondary mirror quadrapod. This will require modifications to the panels to allow the quadrapod legs to penetrate the reflector.

Looking into the dish, the quadrapod legs assume an “X” pattern, as opposed to a “+” pattern. This geometry provides clearance between the back of the mirror truss and the alidade arms. Using an “X” pattern gives clear space at the 6 o’clock position on the mirror truss, which prevents interference between the quadrapod and the alidade legs when the primary mirror is pointed at low elevation angles. Figure 13.2.5 shows the clearance allowed with the “X” pattern.

The tertiary mirror mounts in the center of the hub. There is open structure at the elevation sector gear back structure to allow crane access for installation and removal.

13.2.6.3 Sector Gear Support and Counterweights

The elevation sector gear and counterweights are supported off the back of the hub. The center of the arc of the sector gear is the elevation axis. The large radius of the sector gear allows a greater lever arm for the elevation drive. This improves the stiffness on the elevation axis because deflections at the pinion and gear interface resolve to smaller angles when the sector gear radius is larger.

The sector wheel also carries the system’s counterweights. Struts coming out of the hub stabilize the sector wheel and increase its natural frequency.

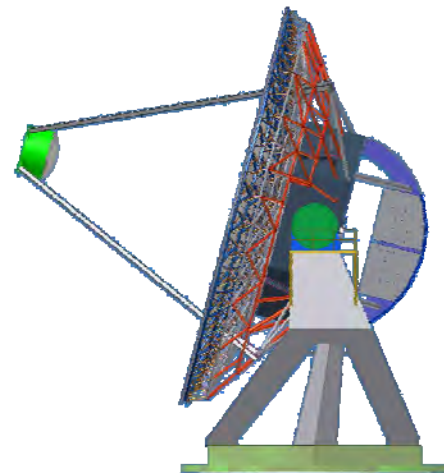


Figure 13.2.5. Clearance between Mirror Truss and Alidade

Additional discussion of the drives is in a subsequent section.

13.2.6.4 Structural Design – Azimuth Structure (Alidade)

The function of the alidade is to provide azimuth motion for the mount and a stiff support for the OSS. The CCAT alidade structure is shown in Figure 13.2.6. It supports the OSS and is supported by the azimuth bearing.

The alidade arms support the OSS and provide a direct load path between the elevation bearing housings and the azimuth bearing. The top of the arms support the OSS at the elevation bearing housings, then branch into three support feet at the bottom, each supported by a hydrostatic bearing pad. The azimuth bearing pads located so that they are centered under the OSS load. The arms are a monocoque structure, made of very large box beams with internal reinforcing for additional stiffness. This gives a structure with a high stiffness for its weight. It is also easy to fabricate, ship, and install.

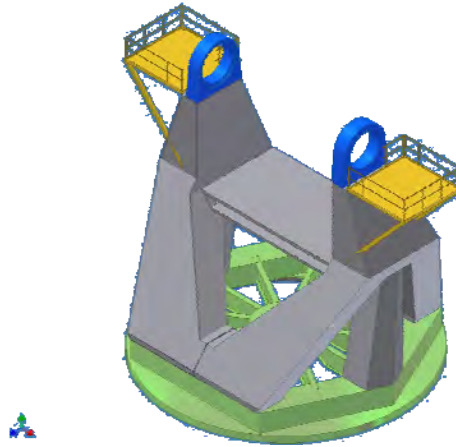


Figure 13.2.6. CCAT Alidade Structure



Figure 13.2.7. Example of Utility Wraps on CCAT Elevation Axis

The elevation bearing housings at the top of the arms support the stub axes coming out of the OSS hub. The bearing housings also provide support for the Nasmyth instruments through interfaces on the outboard side. In addition, the housings support the encoders and utility wraps that service the OSS. An example of these utility wraps is given in Figure 13.2.7.

The elevation drive platform provides support for the elevation drive motors. In addition, it ties the two arms together to increase the overall stiffness of the alidade, increasing the net section available to resist front-to-back and side-to-side loads. This increases the natural frequencies that involve bending of the arms.

The alidade arms are supported by the azimuth base. The azimuth base ring ties all the hydrostatic bearing pads together and provides a stiff structure with a high out of plane stiffness to back up the pads. A flexible backup structure would create load variations in the hydrostatic bearing pads as the CCAT moved. The azimuth base also provides an interface for the azimuth drives and the encoders. The outer and inner diameters are connected by a set of spokes. This limits the lag between the motion of the azimuth drive and the motion of the encoder, a source of pointing error.

The azimuth bearing only provides support vertically, not horizontally. For horizontal support, there is a pintle bearing at the center of the azimuth base, at the center of azimuth rotation. This rolling element bearing that reacts any side loads on the structure to keep the CCAT centered and rotating on a stable azimuth axis. It is mounted to the azimuth base using flexures to insure that the only load path to the bearing is radial. The other side of the bearing is mounted to the foundation.

13.2.7 Foundation Interface

Although not part of the mount, the mount structure interfaces with the CCAT foundation. The pier support provides an interface for the hydrostatic bearing, the pintle bearing, and the stationary part of the azimuth encoder. The foundation includes a cylindrical pier that provides the mount for the azimuth bearing track. The space within that cylinder contains the azimuth cable wrap, a tower for mounting the pintle bearing, and the stationary part of the azimuth encoder. Figure 13.2.8 shows the foundation interfaces.

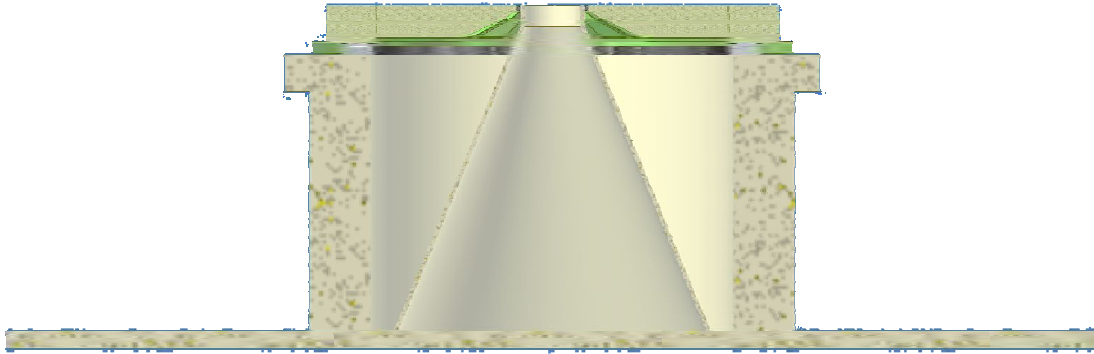


Figure 13.2.8. CCAT Foundation Interfaces

13.2.8 Bearings, Drives, and Encoders

We will use helical gears on this application because they have been proven effective on optical telescope applications. Helical gears provide a stiffer interface than spur gears, since multiple teeth are engaged simultaneously. Having multiple teeth engaged also minimizes the ripple that comes from the pinion meshing with the gears. Spur gears normally impose a tangential and radial load the structure has to react. Helical gears add an axial load at the pinion, which will require special design consideration at the gear supports and elevation motor mounts.

At the concept stage, only rough motor sizing is possible. Both loads and requirements are still being finalized, so the flexible nature of a geared drive is a significant benefit. The azimuth drive system has four drive motors to share load, eliminate drive train backlash, and provide parallel stiffness paths from the motors to the telescope load. The range of motor sizes available is well within off-the-shelf, high performance brushless DC technology. The elevation axis could use either two or four motors. We use four motors for the design baseline, for similar reasons as azimuth.

13.2.8.1 Elevation Drive

The elevation drive gear is mounted to the elevation sector gear support at the back of the hub. Struts coming from the hub provide lateral stability for the gear and the counterweights. The diameter of the sector gear arc requires using an oblong hub. The benefit of a large arc for the sector gear is that smaller motors can be used while increasing the stiffness of the drive.

The elevation bearings are spherical roller bearings, which will define the elevation axis. We use this type of bearing on large projects, including GBT, with great success.

13.2.8.2 Azimuth Drive

Azimuth drives are shown in Figure 13.2.9. The gear here is an internal gear that will be mounted on the inner diameter of the azimuth bearing track. As in elevation, this is a helical gear. The gear will be separate from the bearing track, made in sectors to allow for alignment to the pinions.

There are four drives, mounted to the rotating structure, grouped in pairs. Each drive in the pair is torque biased against the others to eliminate the effects of backlash in the gearsets.

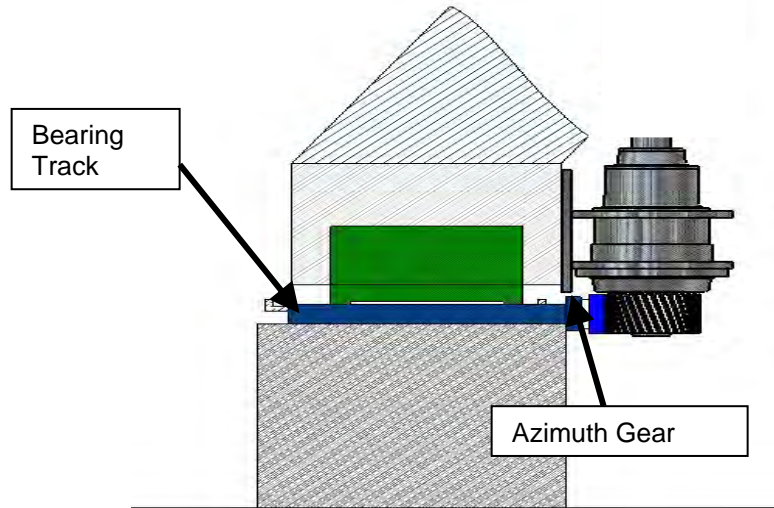


Figure 13.2.9. Typical CCAT Azimuth Drive

13.2.8.3 Azimuth Bearing

The azimuth bearing comprises six hydrostatic bearing pads and a track. The pads are located at the bottom of each foot on the alidade arms. The bearing pads are manufactured by SKF, based on bearing pads for telescopes such as Gemini. The bearing pads are fed by a recirculating oil system, which includes a heat exchanger to cool the oil, to prevent introducing heat into the telescope enclosure. The bearing will have to be protected from blowing dust at the site.

The track will be fabricated by VertexRSI. This is a very precise machining operation, as the pads will produce an oil film thickness of approximately 70 μ m. The track bed will need to be flat enough to accommodate the oil film, but also allow the oil to recirculate. The foundation design and installation will allow the bearing track to be placed directly on it.

13.2.9 Controls and Electronics

13.2.9.1 Encoders

The geometry of the mount and the requirement for on-axis holes for optics means that housed encoders are not feasible. Fortunately, Heidenhain tape encoders have been used with success on numerous optical telescopes, providing pointing accuracy and resolution that meet the specification requirements. There are a small number of other similar technologies and manufacturers, but there is little reason to consider these alternatives at this time.

The azimuth encoder design comes from a concept proven on SOAR. The azimuth encoder is a Heidenhain tape mounted on a horizontal ring that will be mounted to the foundation. There are four read heads mounted to the moving part of the alidade. Multiple read heads provide an extra bit of accuracy, as both encoder and mechanical errors are reduced by the average of the readings.

The elevation encoder concept comes from SOAR as well. This encoder must be an off-axis design, given the optical path requirements for the Nasmyth. In this case, the Heidenhain tape will be mounted to a machined wheel mounted to the elevation axle. The center of the machined wheel is the elevation axis.

13.2.9.2 Controls Requirements

Modes, pointing, safety hardware, and motor synchronization are tasks that have been directly addressed on previous projects. High performance telescopes such as GBT, SOAR, and VISTA have used four to sixteen

motors per axis, using product line hardware. Software interfaces from the Mount Control to the Telescope Control are straightforward, and system safety issues are directly addressed.

Specific performance requirements that fit this topic were addressed as follows. Preliminary error budgets were derived based on vendor specification sheets, field tests from similar systems, and preliminary analysis. Rough derived budgets include: offset pointing, tracking, and jitter. All specifications appear achievable within current technology, as shown in Table 13.2.2.

Table 13.2.2. Control Related Requirements

| Item | Requirement | Comment |
|-----------------------------|---|---|
| Pointing Accuracy | 2 arcsec RMS | Values of 2-4 Arcsec Achievable |
| Offset Pointing 1° To 5° | < 0.5 arcsec RMS | Reasonable Requirement for this Application |
| Tracking Dynamics | 0.25 deg/sec 0.01 deg/sec ² | Achievable |
| Zenith Transit Outage | Nominal 8 minutes | Consistent With Tracking Dynamics |
| Nonguided Image Jitter | < 0.1 arcsec | Consistent with Similar Designs. Wind Load Needs More Study |
| Open Loop Drift | 0.1 arcsec/min | Realistic, SOAR meets this requirement |

Scanning requirements are still in discussion, and affect many aspects of the drive train. At present, the specifications are:

- Axis velocity 1 deg/sec
- Acceleration 2 Deg/sec² (direction reversal)
- Maximum error 1 arcsec, except during reversals
- Performance range Through at least 60 degrees of elevation.

The last point effectively doubles the required azimuth acceleration due to mount geometry. There is little question that the required accuracy can be met during constant velocity scanning. The issues are ensuring accurate communications and expectations; along with understand the effective useful time of the telescope for this mode of operation.

For clarity, then, the specification needs to distinguish between the following performance definitions as they have different behavior and errors:

- Scanning Following Accuracy The ability to precisely follow the desired scan trajectory; the error between the position vector and the commanded position
- Scanning Position Reporting Accuracy The ability to know the precise pointing vector during scanning dynamics; the error between the true pointing vector and the reported pointing vector

It is possible to have a large following error and yet know the on-sky position perfectly. It is also possible to have no following error and not know the on-sky position. This is important in understanding how the telescope is used and referenced to the sky and targets of interest.

For following accuracy, performance is a function of the scanning pattern dynamics, the structure, and the control system. Errors are reduced by lowering scan dynamics, increasing the resonant frequency of the structure, and

increasing the bandwidth of the servo. Figure 13.2.10 and Figure 13.2.11 show example following errors to a 1 deg/sec² ramp to a 2 deg/sec constant velocity. Figure 13.2.10 uses performance similar to the VLBA 25m radio telescopes, while Figure 13.2.11 uses performance similar to the South Pole Telescope design. These were chosen as reasonable approximations to CCAT potential performance; with the VLBA performance representing a reasonable lower bound for CCAT. These also give some initial impressions of the system sensitivity to mount resonant frequency. For this concept model, these errors can be considered as reported by the encoder, ignoring on-sky position reporting errors to be discussed.

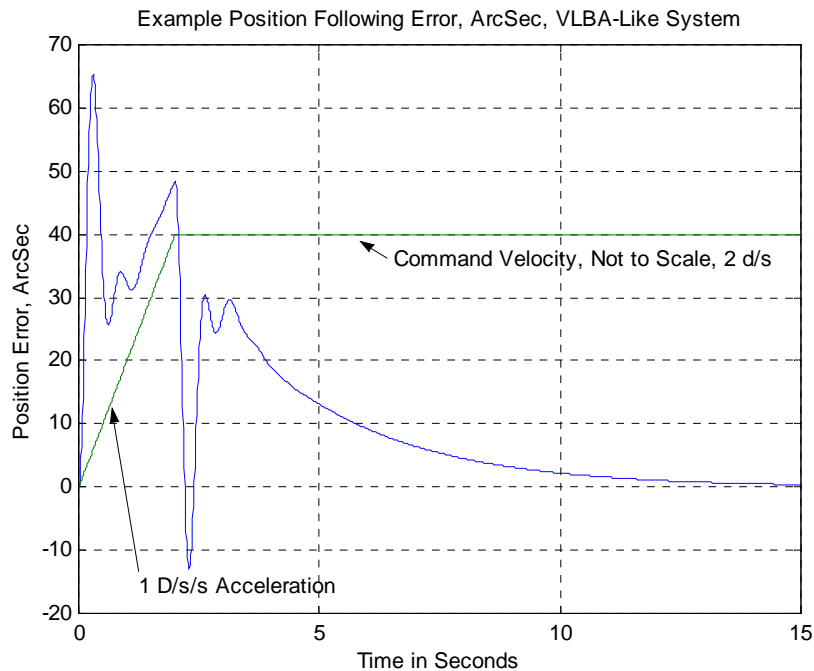


Figure 13.2.10. Error between Commanded and Actual Position, VLBA Type Design

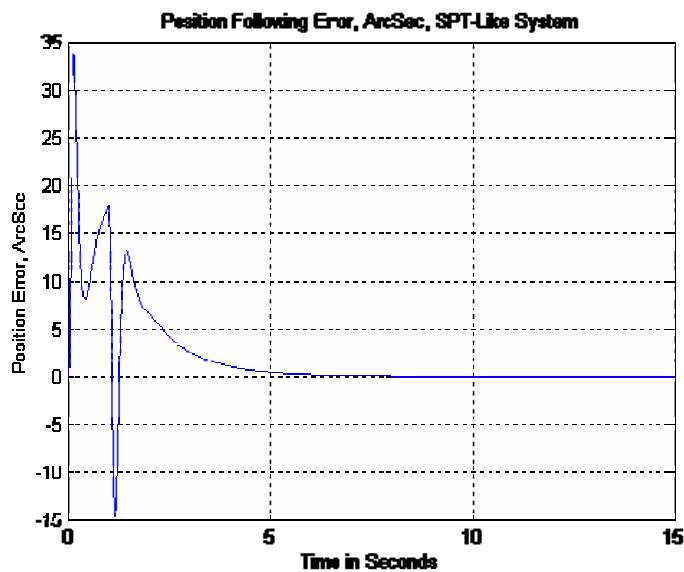


Figure 13.2.11. Error between Commanded and Actual Position, South Pole Telescope Type Design

Rather than increasing resonant frequency, the scan dynamics can be modified to reduce following error. In general, shaping increases axis dynamics requirements and lengthens position move time. The benefit is lower error during the move and frequently this improves settling time. Figure 13.2.12 shows following error to an example shaped step. When compared to Figure 13.2.10, peak following error is about 1/2 of the previous value. Settling time is similar. Selection of a shaping function involves the desired result and can affect axis velocity and acceleration selection. Thus specifications need to be clarified before or during the design stage. This area has been discussed and is part of ongoing efforts.

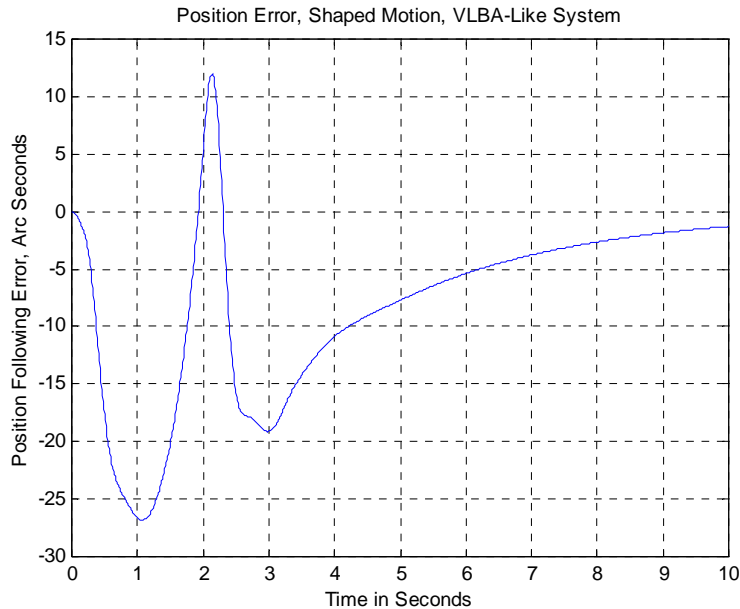


Figure 13.2.12. Shaped Step, VLBA Type Design

Position reporting errors will also be affected by the structure and trajectory shape, but have modest terms from the control system implementation. The dominant error for position reporting is expected to be the structural deflection between the encoder and the reflector optics. Table 13.2.3 shows the steady-state errors for various accelerations and structural stiffnesses. Based on optical and radio telescope historical implementations (1), we would expect resonances in the 3-7 Hz range. Although in steady state disturbances it is theoretically possible to remove this error by calibration, we are unaware of any successful use of this technique. We also caution that the error may be more transient than steady state, making calibration difficult.

Table 13.2.3. Steady State Position Reporting Errors due to Structural Deflection

| Acceleration | 1 °/sec ² | 2 °/sec ² | 3 °/sec ² |
|----------------------|--------------------------------|----------------------|----------------------|
| Structural Resonance | Steady State Error, arcseconds | | |
| 2 Hz | 23 | 46 | 69 |
| 3 Hz | 10 | 20 | 31 |
| 4 Hz | 6 | 12 | 17 |
| 7 Hz | 2 | 4 | 6 |
| 10 Hz | 0.9 | 1.8 | 2.8 |

13.2.10 Risk Assessment and Mitigation

| Risk | Criticality | Mitigation |
|--|-------------|--|
| Space limitations imposed by optical layout | Med | <ul style="list-style-type: none"> • Use of an oblong hub to satisfy optical and drive concerns • Placement of elevation axles near front of hub • Active optical surface |
| Installation at a remote site | Med | <ul style="list-style-type: none"> • A complete factory acceptance test plan • Specific installation risks will be considered as an additional design constraint |
| Using a hydrostatic bearing in the high desert environment | Low | <ul style="list-style-type: none"> • Lessons learned from other hydrostatic installations, especially Keck on Mauna Kea • Covers and seals to keep out dust as part of the bearing housing design • Viscosity of oil chosen for site conditions |
| Scan pattern & science mission undefined | Med | <ul style="list-style-type: none"> • Issue brought to team's attention at the mid point review • CCAT program office dealing with topic |
| Achieving goals for offset and open loop drift | Low | <ul style="list-style-type: none"> • Not necessary to achieve these goals on all missions • On-sky calibration instruments may render these goals obsolete. |

13.2.11 Manufacturing

Most of the work involved in fabrication and shipping of the CCAT follows standard practice and does not pose any extraordinary challenge. Installing this in a remote site does pose a significant challenge, which can be mitigated in the fabrication and testing phases.

13.2.11.1 Fabrication

The alidade would be made in four main pieces: the alidade base, two alidade arms, and the elevation drive platform. These components could be fabricated separately and assembled in the factory on a test foundation.

The alidade base would be assembled on the foundation first and leveled to accommodate the remaining pieces. Any machined interfaces to accommodate the hydrostatic bearings would be aligned first, with the rest of the structure brought up to fit.

The alidade arms would be made in subassemblies, given its size and its bottom branches into three legs. Each of these bottom branches would be made individually and attached to the alidade base. This enables work to occur in parallel and accommodates crane capacity. The elevation drive platform and the top of the alidade arms would be added to the structure in turn.

The elevation bearing housings would be a separate weldment, or possibly a casting. Each of these solutions has been applied on projects of this scale; it would take some further tradeoff studies to establish the best choice.

The OSS would be made in subassemblies as well. The hub, sector gear support, and quadrapod would each be made separately and assembled together according to standard antenna fabrication practice. These components could be assembled separately and installed as a unit on the alidade, or could be assembled piece by piece on the alidade. The tradeoff between the two options would be a matter for study in a future phase.

The elevation axles would depart from typical antenna practice, but follow previously established procedures for other projects. Given the large optical path on the elevation axis, a forging would probably not be appropriate. There are fabricators in the oil industry that can roll thick plates into cylinders. A first order calculation shows that one could roll a plate up to 5 inches thick into an elevation axle. We would have to fabricate two axles and weld each into the hub. Using a total station theodolite, it would be possible to position the first axle and then align the second axle to the first. In addition, pre- and post weld heating would be possible using portable equipment brought to the site. On site machining is also available to assure alignment between the bearing mount surfaces on each axle.

13.2.11.2 Factory Testing

In summary, all subsystems will be installed, tested and integrated with other systems to the largest extent possible. Conditional acceptance testing of all subsystems will be completed at the factory integration. Problems discovered at the site installation phase of the project will be exponentially more difficult to deal with due to the high altitude and remoteness of the site.

The entire structure will be assembled and mechanically aligned. The elevation axis drives will be capable of movement through the entire range of motion. An M1 simulation structure will be required for dynamic and system resonance testing. The azimuth hydrostatic bearing and drive system will be made operational. Segments of the track or track simulation plates will be installed in the foundation so the hydrostatic system can be tested with a limited azimuth travel range.

The complete control system inclusive of the encoder readout subsystems should be factory installed and calibrated. The hydrostatic bearing will be installed, operated, tested and integrated with the control system. All system interlocks and cooling and lubrication systems will be installed and tested.

Any special machining, welding and rigging operations that will be done at site should be proven at the factory integration phase of the project. Mock setups can be used where necessary to facilitate these tests.

After factory testing, the structure will be broken down into shippable units, then painted and packed. The site installation team will participate in the disassembly and packaging of the telescope upon the completion of the factory integration. This familiarizes the field crew with the hardware and packing arrangements.

There are many suitable routes for transporting the pieces of the CCAT to the site. The pieces would be shipped from Mexia to Houston, the nearest deep water port. Large weldments are shipped frequently over that route. In addition, the route from the port of Antofagasta to Cerro San Pedro de Atacama has been surveyed in connection with the ALMA and APEX project. The port and the routes out of the city are large enough to move large weldments without much problem. Once outside of the city, the roads were built to accommodate large mining equipment and are not a restriction.

13.2.12 Continuing the Work

The current study has established a configuration. We dealt with the optical spacing requirements, establishing the basic geometry and load paths, initiating conversations with vendors on purchase parts, and working interactively with the CCAT project team to work out specification requirements. The next phase of the project would focus on structural analysis, servo analysis, clearer definition of major components, and interface work with other subcontractors.

FEA work would include determining natural frequencies, especially for the secondary mirror support, which will be one of the lowest natural frequencies in the system. It would also be important to determine overall frequencies of the mount, for example, the modes of the mount rocking on the hydrostatic bearing and the locked rotor modes.

We need additional information to be able to size the drive motors. As we determine the inertia of the structure with greater accuracy and with a clearer definition of the scan pattern, we can size the motors. The rest of the drive train will follow.

We need to work the hydrostatic bearing design in greater depth. Tasks associated with that include determining the spring rates of the bearing and tolerances on the machining of the track. There is the additional work of the interface between the servo and the hydrostatic bearing shoes. Much of this is in the area of establishing safety requirements for the system, such as establishing when the oil film is sufficient to allow the motion of the unit and detecting faults in the system.

Finally, there will be a great deal of interface work between the subcontractors for the mount, the foundation, the mirror truss, and the secondary and tertiary mirror supports.

13.2.13 References

E. Reese, B. Smith, K. Hermann, "Mechanical Design Considerations Unique to Giant Telescopes" (SPIE 4870-77)

14 Primary Mirror

14.1 Introduction

This section addresses the feasibility and initial conceptual design of the CCAT Primary Mirror. The surface precision required for CCAT exceeds that of any previously constructed radio telescope, though the development of ALMA antennas has provided surfaces that are almost half as good as required. We have looked to both existing submillimeter telescopes and segmented optical telescopes as examples when considering how best to configure the CCAT primary. The resulting concept presented here uses existing technology where possible, but looks to several emerging technologies to provide significant improvements in performance while providing lower costs.

14.1.1 Background

The principal examples studied as background to development of concepts for the CCAT primary are listed below. These were identified as the closest to CCAT requirements in size and precision.

14.1.1.1 Caltech Submillimeter Telescope, Mauna Kea, HI

The M1 of CSO consists of aluminum panels, turned on a custom lathe as a complete assembly. Alignment is implemented by thermal panel position actuators, with open loop control, calibrated for gravity load. Panels are mounted on multiple points on a steel truss. Calibration is done via shearing interferometry. Performance achieved: $\sim 15 \mu\text{m rms}$.

14.1.1.2 Heinrich Hertz Telescope, Mount Graham, AZ

The HHT panels are made of CFRP/aluminum honeycomb sandwich, replicated on borosilicate mandrels, mounted on multiple points, with no active panel control. Calibration is achieved via holography. Performance achieved: $\sim 15 \mu\text{m rms}$.

14.1.1.3 APEX and ALMA Prototype (VertexRSI)

The ALMA M1 panels produced by Vertex are machined cast aluminum (one at a time on 6 axis mill), mounted on multiple points to a dimensionally stable CFRP truss, without active panel control. Calibrated via holography. Performance achieved $\sim 20 \mu\text{m rms}$.

14.1.1.4 ALMA (Alcatel/EIE) Prototype

The ALMA/Alcatel/EIE panels are of nickel/aluminum honeycomb sandwich (Media Lario proprietary process using electro-deposited replicated face and back sheets bonded to aluminum honeycomb core), mounted on multiple points to a dimensionally stable CFRP backup structure. Calibrated via holography. Performance achieved: $\sim 20 \mu\text{m rms}$.

14.1.1.5 Keck Telescopes, Mauna Kea

The M1 of these optical telescopes are zerodur panels (hexagons) stress polished and ion figured, mounted on a steel, actively controlled via tip/tilt/piston positions, loops closed on edge sensors, calibrated via curvature sensing wavefront sensing. Performance achieved $\sim 0.03 \mu\text{m rms}$.

14.1.1.6 Hobby Eberly Telescope, Ft. Davis, Texas

The M1 of the HET consists of zerodur panels (hexagons), fabricated via continuous polishing and ion figuring, mounted on a steel truss, alignment via position actuators (tip/tilt/piston), loop closed on edge sensors, calibrated via Shack Hartmann wavefront sensor. Performance achieved $\sim 0.045 \mu\text{m rms}$.

14.1.1.7 SALT Telescope, Sutherland, South Africa

The SALT M1 has fused quartz panels (hexagons), produced by continuous polishing and ion figuring, mounted on a steel truss, alignment via position actuators (tip/tilt/piston), loop closed on edge sensors, calibrated via Shack Hartmann wavefront sensor. Performance achieved TBD μm rms.

These, the highest performance submillimeter telescopes and the only segmented optical telescopes in the world, represent a good range of approaches to be investigated for CCAT. Note CCAT is specified with a surface of about 9.5 μm rms, a bit more than two times better than the ALMA antennas but about three hundred times worse than Keck. We took these existing samples as the starting point for conceptual trades with the objective of using as much of the proven technology as made sense in the CCAT Primary Mirror concept design.

14.1.2 Scope

The Primary Mirror as a system includes:

- The Primary Mirror Truss, which attaches to the telescope mount at the bottom surface and provides mounting points for panels on the top surface.
- Actuators or Adjusters that attach mirror panels to the truss.
- Mirror Panels that provide the front reflective surface of the primary mirror.
- Sensors: Any sensors required for sensing primary mirror panel positions while in operation
- Calibration Sensor that enables the simple and routine setup of the panel positions whether manually or electro-mechanically adjusted.
- Controls: Any required electronics, wiring, and computer control required if electro-mechanical actuation is chosen.

14.1.3 Trade Discussion

This section tracks the logical process that resulted in selection of a conceptual primary mirror design for study purposes.

14.1.3.1 Architecture

Both cost and mechanical limitations would most likely prevent using the ALMA approach of a dimensionally stable backup structure (Section 9.1). It would involve a good deal of CFRP material and in all probability the structure could not be made stiff enough to eliminate the effects of gravity distortion over the range of elevation angles. Hence actuators will be required to position panels and we have less need for truss dimensional stability as we can adjust panel positions instead. Hence the decision was taken to mount panels to a steel truss and adjust panel position by actuators under computer control. While CSO operates close to our required figure quality in an open loop architecture using lookup tables to set actuator length as a function of elevation angle and calibrations performed earlier, it seemed unlikely this would work over a 25 m aperture as opposed to their 10.4 meter aperture or to the $\sim 2X$ better surface accuracy required. Hence the decision was taken to investigate closed loop control of panel position. This basically leads us to the Keck/HET/SALT architectures of steel trusses and electro-mechanical closed loop panel positioning. Hence we conclude taking the more precise paradigm and making it simpler and more cost effective would be more fruitful than trying to optimize the submillimeter telescope approaches.

14.1.3.2 Segmentation Scheme

Segmentation schemes fall basically into two categories: hexagonal segments and circumferential rings of segments. Several trade studies were performed by CCAT staff looking at different geometries of each. The hexagonal arrangement used by the optical telescopes has inherent advantages with respect to segment support (six fold symmetry of segments) and operation with edge sensors (less degeneracy and error magnification.) There are, however, only six identical segments of each type in the entire array because of the six fold symmetry. In addition, hexagons do not regularly tile a surface of revolution so there are variations in the external shapes of the hexagons in order to maintain uniform interstitial gaps throughout the array. With circumferential rings of segments and a segment size of about ~ 2 m, we need only ~ 145 segments for the entire mirror. Since every

segment in each ring is identical, we need only six types of identical segments. If the segment size is ~1.5 m, there are ~210 segments of 7 types. We chose the circumferential arrangement of segments because it would enable panel fabrication by replication, such as the panels on the HHT, all panel mounts would be largely identical, and all segments in a given ring would be interchangeable. It also provides circular inner and outer edges of the aperture and doesn't waste any mirror surface such as apodizing an aperture formed of hexagonal segments would.

14.1.3.3 Mirror Truss



Figure 14.1. HET Truss Node

The truss would need to be shipped and trucked to the telescope site, assembled on the telescope mount at the extreme altitude, and meet the dimensional requirements with a minimum of on-site adjustment. A meeting with the US Mero affiliate indicated the dimensional precision, cost, and feasibility were all reasonable. Other vendors have comparable systems, but neither they nor the US MERO affiliate have the German Mero's robotic equipment that provides the superior precision and low cost. More detailed design and analysis of the PM truss is planned for the next phase of CCAT.

14.1.3.4 Panel Mounting

There are two basic choices in panel mounting and many variations beyond. Optical telescopes use kinematic mounting in which panels are fully constrained in all position degrees of freedom, but not overconstrained. Radio telescopes typically uniformly employ non-kinematic, overconstrained mounting in which some modes of panel shape as well as rigid body positioning can be affected by adjustment. Since we have chosen not to employ a dimensionally stable truss, using the non-kinematic mounting would imply that variations in truss geometry due to gravity, thermal effects, or truss mounting to the mount could affect the panel figure. Hence we employ kinematic mounting because then only panel position can be affected by changes in truss geometry and we have chosen electro-mechanical segment positioning to address this.

Optical telescopes employ multi-point supports that distribute panel loads from a number of contact points on the

Industrial producers of mirror trusses indicated a CFRP mirror truss at 25 m aperture would be approximately 5 times more expensive than steel. Since we can actively control the panel position, dimensional stability of the truss is less of an issue. Truss dimensional stability is not negligible as issues of in-plane panel location and segment gap control still need to be considered. HET and SALT both use bolted steel trusses. In the case of HET the truss was robotically manufactured by Mero Structures of Wurzburg, Germany, at a cost of \$436,000 for a 10 m diameter truss. The approach provides for assembly using only one wrench size, packs down to a single half height tractor trailer load, and achieves the required dimensional accuracy as assembled without any adjustment owing the precision of the components.

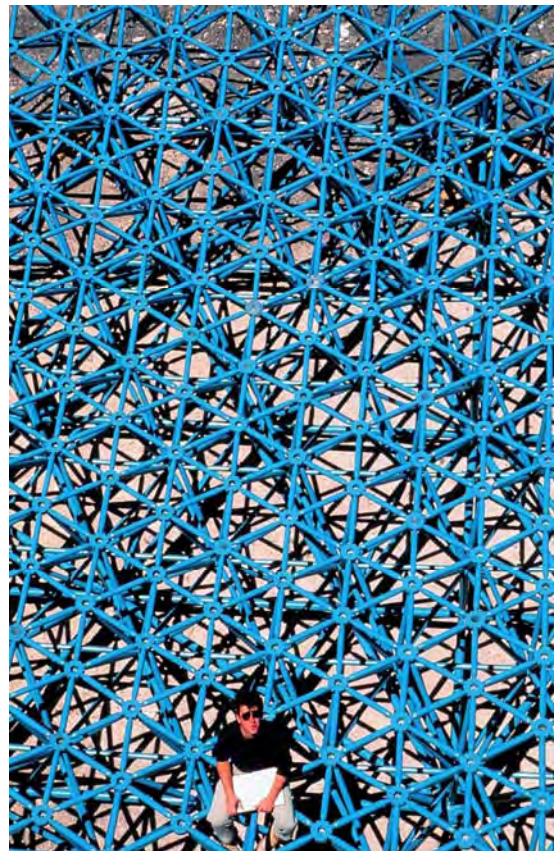


Figure 14.2. HET PM Truss Top View

back via levers and pivots/flexures in “whiffle tree” configurations to three connection points on the mirror truss. This allows the loads to be equalized and independent of variations in truss geometry. For CCAT, we chose to depart from this arrangement as permitted by the greater error tolerance allowed by our observing wavelength. The mirror mounts on Keck/HET/SALT have been problematic, with residual variations and hysteresis in support conditions resulting in compromised segment figure. Keck has also experienced problems in application of warping harnesses that do not follow results predicted by modeling. In addition, mirror mounts are expensive and have extremely high part counts. It is likely the total number of parts in optical telescope mirror mounts exceed the total of all other fabricated parts in the rest of the telescope. For CCAT, we elected instead to pursue simple three point kinematic panel mounting by three bipod flexures mounted to the back surface of the panels and attached to the truss by three actuators. Each actuator is capable of providing piston motion and also accommodating gravity side loads, thereby eliminating the complex and problematic lateral support flexures implemented for the optical telescopes. The gating issue for this approach is whether panels are sufficiently stiff that they would exhibit acceptably low deformation over the elevation range when simply mounted on three points. This is one element considered by panel manufactures during the study.

14.1.3.5 Segment Size

Segment size is bounded on the upper end by gravity distortion on three point mounts. On the other end, toward smaller panels, the number of panels, mandrels (if replicated), actuators, truss nodes, and sensors and the complexity increase. At a segment size of 0.5 m, we would have of order 2000 panels. For a range of sizes in the middle of these extremes, there is a family of solutions of generally equivalent performance and cost. At the upper end there is an additional limitation in the size of available equipment for manufacture of panels and, in particular, mandrels. Since the mandrels are convex, to make concave panels, they do not lend themselves easily to interferometric evaluation. Their figure would need to be measured to a few μm rms to deliver acceptable panels. Since the mandrels would almost certainly be made of a glassy material to enable specular surfaces for mold release and good dimensional stability, this implies the manufacturers would need alternate methods of measurement of sufficient precision. At least two manufacturers in the US (Goodrich and ITT) have equipment that can measure profiles to this precision up to 2 m sizes. Initial discussions with potential panel manufacturers yielded thoughts that panels might perform adequately on three points up to 2 m. We chose to study this size initially with the possibility to go to smaller panels if 2 m would not meet requirements.

14.1.3.6 Panel Surface Finish

One element of the science objectives of CCAT is the ability for the telescope to be used for sparse aperture interferometry at 10 μm wavelength. Additionally, the diffraction limited resolution of the telescope drives tight limits (0.2 arc sec) on accumulated tracking errors over hour long exposures. This precision can be met by current 4 m optical telescopes in unguided tracking, but not by larger telescopes such as Keck and Gemini. Guiding on submm sources is not likely possible because of the scarcity of strong sources. Hence we resolved if panels were made specular in the infrared, we might employ optical guiding at either 2 or 10 μm wavelength. This would also, given that the subapertures of panels offer acceptable surface accuracy, enable interferometric observing modes. This led to a decision to initially pursue that level of panel surface quality. This requirement may be relaxed in the event alternatives in guiding are identified and lower cost can be achieved.

14.1.3.7 Panel Material

Review of ALMA error budgets reveal machined aluminum panels alone can be expected to contribute approximately 12 μm to the error budget as a result of manufacturing errors, aging, gravity distortion (on five or more mounts), absolute temperature, and temperature gradients. While some improvement of panel figure through better machining might be possible, the remainder of the effects are largely material dependent and have no simple solution. The Media Lario Ni/Al sandwich panels may offer better thermal performance. The CFRP/aluminum sandwich panels on the HHT very nearly meet our requirements. These are mounted on multiple points largely to address some bending that appears when they are released from the borosilicate mandrels. Somewhat thicker panels made the same way may have enough increased stiffness to avoid this problem. We found two companies who had successfully made large CFRP panels with specular surfaces to the precision we require. We elected to fund one study here. Extensive polling of the advanced flight optics community and

discussions with JPL personnel led to two other possible alternatives, SiC mated with a nanolaminate facesheet and precision molded lightweight glass. Visits to these contractors seemed promising, so a total of three studies were funded seeking two meter class replicated facesheets, which could provide specular surfaces accurate to ~5 μm rms when supported on only three points.

14.1.3.8 Alternative Concept

An alternative concept was proposed for the PM that employs machined aluminum segments mounted in an over-constrained 5 point arrangement on dimensionally stable CFRP/Al rafts approximately 2 m in extent. The segments would be adjusted using a coordinate measuring machine and then these “Rafted Segments” would be installed on the truss. Initial error modeling indicates this approach will also work, though perhaps not as well as if the panel technologies being studied meet requirements. In any event the solution would have much higher complexity, would weigh roughly three times as much, and offers additional challenges in metrology and segment figure adjustment in operation. Nonetheless, we have this concept in reserve if we find that our baseline concepts fall short of requirements. It is described in more detail in Section 9.4

14.1.4 Summary of Study Results

We funded the following studies the results of which are briefly summarized:

14.1.4.1 Molded Borosilicate Panels, ITT Industries, Rochester, NY

Study of precision molded lightweight cored glass panels (Section 14.2). ITT (formerly Eastman Kodak Government Systems Division) has developed an emerging and novel process that uses heat and forms to create corrugated cores of borosilicate glass approximately 2-5 mm thick. Front and back facesheets of similar thickness are thermally bonded to the core and the resulting sandwich is slumped over a precision mandrel. Design, modeling, and analysis indicate this approach remains a viable panel candidate. The fragility of the panels is offset by the inert nature of the glass, free from effects due to ageing or coating/stripping cycles. Thermal performance must be carefully considered but looks acceptable. Cost also appears acceptable, though higher than CFRP.

14.1.4.2 CFRP Al Panels, Composite Mirror Applications, Tucson, AZ

Study of replication of specular CFRP/aluminum honeycomb panels from glass mandrels (Section 14.3). CMA indicates they believe such panels can be made, will exhibit acceptable gravity deformation on three points, and estimate a cost which is acceptable to the Project. Further study and experimentation is required to determine whether panel warping on removal from the mandrel will be an issue. Accelerated life cycle testing is also needed to determine the long term effects of ageing and coating/stripping cycles. CFRP Panels will meet areal density requirements ($10\text{kg}/\text{m}^2$), exhibit acceptable dynamic structural performance, and have low CTE that offers good thermal performance.

14.1.4.3 SiC Nanolaminate Panels, Xinetics Corp. Devens, MA

A study of a technique developed in partnership with LLNL. LLNL produces a nanolaminate facesheet by magnetron sputtering. Xinetics uses a slip casting technique to produce a SiC substrate that is aggressively lightweighted with cores. The substrate is bonded to the facesheet using a filling/bonding compound and the finished mirror is then released from the mandrel. In general this study revealed the technique is not sufficiently developed to be cost effective. The cost, given the current level of development, is not competitive and the likely time for development of the process is not compatible with CCAT schedules. No further study of this approach will be funded. A formal report was received but is not included.

14.1.4.4 Mandrel Manufacturing, Goodrich, Danbury CT

Mirror Segment Replication Mandrels (Section 14.4): Mandrels for precision replication of segments are a key element of the manufacturing process and have the potential to be a significant cost driver. Segment size is chosen in part to ensure that mandrels can be manufactured using precision profilometry for surface figure

measurement. There are only a few machines in the US which can measure to sub-micron precision over 2 m. It may be possible to re-manufacture mandrels after all the segments and spares for one ring are complete to reuse them for a second ring. This could halve the number of substrates required.

14.1.5 Next Steps

During the Engineering Concept Design we anticipate the following work:

14.1.5.1 Panel Studies and Experimentation

We anticipate further investigation of multiple CFRP vendors. Further analysis and design work are anticipated. We also anticipate that experiments demonstrating subscale (but as large as possible) panels with test to correlate resulting panel figure with mandrel figure, gravity and thermally driven deformation, and mounting techniques. We anticipate receiving fixed price quotes at the conclusion of these activities.

14.1.5.2 Coating Process

Project personnel will study the design of a DC Magnetron sputtering chamber for coating of panels. Multiple approaches to coating both CFRP and glass will be considered. A strawman design and cost will be provided.

14.2 Molded Borosilicate Panels

Report prepared by ITT Industries



14.2.1 Executive Summary

ITT Industries is pleased to provide this engineering study for Cornell Caltech Atacama Telescope (CCAT). We have supplied point designs that meet the specification, given the constraints and geometry outlined in the specification documents. Although not funded by the CCAT engineering study, ITT is also producing subscale sample pieces for CCAT.

We cite previous accomplished projects as testimonials to our experience and manufacturing abilities. The list below enumerates recent previous ground-based projects:

- Southern Africa Large Telescope (SALT) - 91 segments, 10 × 11 m
- Hobby-Eberly Telescope (HET) - hexagonal mirror array made from 91 segments, 9.2 m aperture
- Keck, Keck II - 10 m

In addition to these ground-based projects, ITT also has extensive experience with space-based systems.

ITT offers integrated systems solutions with a single point of contact. Having a single vendor supply mandrels and replications or mirrors and mounts eliminates any questions about responsibility divided between multiple vendors. ITT has existing facilities capable of testing to the CCAT requirements, can build, design and implement mounts and flexures and can coat the finished optics so any interface issues can be dealt with within our company.

ITT's approach to the CCAT program employs ITT's recently developed proprietary manufacturing methods for rapid fabrication and low-cost solutions. The study that follows examined a petal-shaped panel system.

The study concludes with a recommendation for a 3-layer corrugated mirror design. However, mirror system trade-offs between performance, cost, and risk at the system level should be studied in detail in future work. We are pleased to be part of the CCAT team and we believe our experience in large-mirror systems will help the CCAT program be successful.

The CCAT 25 m primary mirror presents significant technical challenges. The CCAT will be the first segmented telescope of this size and precision. The CCAT program requires large, very lightweight, off-axis aspheric primary-mirror segments that must be produced at very low cost. ITT Industries has developed unique manufacturing techniques that enable production of low cost, lightweight segments that meet the CCAT requirements.

ITT Industries has a long history of producing primary mirrors for ground-based astronomical telescopes. This includes the production of the mounted mirror segments for South African Large Telescope (SALT) (Figure 14.2.1) and HET (Figure 14.2.2) as well as figuring of the segments for the Keck telescopes. ITT Industries has either produced or final finished the primary mirror segments for the four largest ground-based astronomical telescopes.

While the primary mirror segments for the CCAT require, by radio telescope standards, high surface accuracy, this surface accuracy is not challenging when compared to astronomical telescope mirrors used for observation in visible wavelengths. The challenge that the CCAT presents is the combination of surface accuracy that is higher than radio telescopes with the requirement that the cost be very much lower than for visible wavelength optical

telescopes. Meeting this combination of requirements mandates new technologies for the production of the lightweight mirror structures and the precision surfacing of the mirrors.

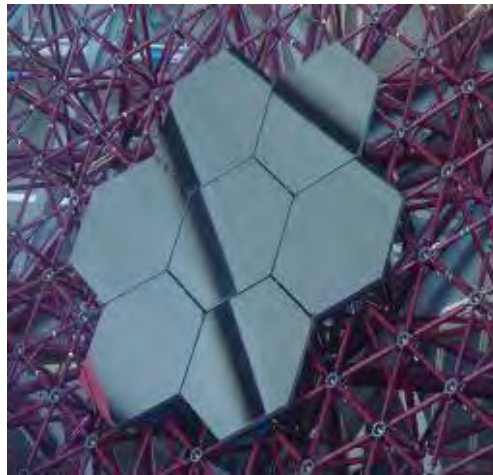


Figure 14.2.1. The South African Large Telescope (SALT) assembly of the first segments. ITT Industries produced all 97 segments for the 11 m SALT.

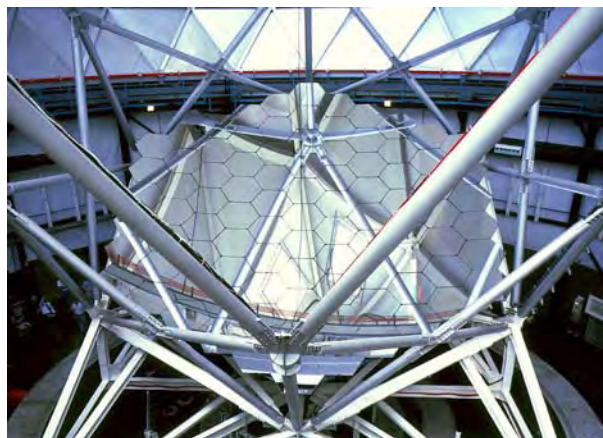


Figure 14.2.2. The Hobby-Eberly Telescope (HET) primary mirror assembled in the telescope. ITT Industries produced all 96 segments for HET.

ITT Industries has developed two new technologies that enable the production of primary mirror segments for CCAT: corrugated glass mirror blanks and optical replication of glass surfaces. The combination of these two technologies allows the production of primary mirror blanks that have the required features for the CCAT:

- low cost
- low areal density
- low gravity sag
- high surface accuracy with low roughness
- high thermal stability
- freedom from stress relaxation
- shape change due to polymerization or outgassing
- the ability to apply, strip, and reapply reflective optical coatings without degradation.

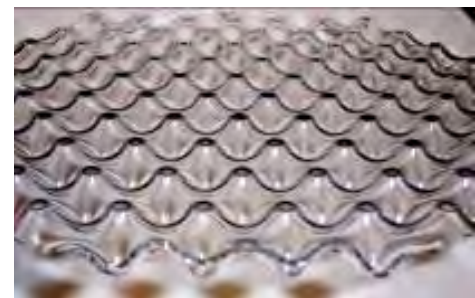


Figure 14.2.3. A borosilicate core for a corrugated mirror. These cores can be fabricated at low cost and low areal density.

Corrugated blank technology allows the production of large, lightweight, high specific- stiffness structures for mirrors. A core for a corrugated mirror is shown in Figure 14.2.3. These cores can be rapidly produced at low cost in industrial volume manufacturing.

A corrugated mirror is assembled from a core and face sheets. An example of a corrugated mirror is shown in Figure 14.2.4. The mirror structure consists of a corrugated core with faceplates fused onto it.

The mechanical properties of corrugated mirrors can be varied by changing the geometry. The geometrical parameters that can be varied include the corrugation depth, the corrugation spacing, and the glass thickness used for both the faceplates and the core. These parameters change the stiffness, the strength and robustness of the mirrors and the fabrication difficulty. For mirrors that have very tight surface requirements, such as those for high-quality visible-wavelength ground-based astronomical telescopes, corrugated mirrors can be designed with additional layers to increase robustness, to increase specific stiffness, or to decrease areal density.



Figure 14.2.4. A corrugated mirror assembled from a corrugated core and faceplates. The assembly has high specific stiffness and thus low gravity sag.

An example of a corrugated mirror with multiple cores is shown in Figure 14.2.5. Adding these additional layers can be thought of as replacing the faceplates of the mirrors with stiff, lightweight assemblies. A 5-layer or 7-layer corrugated mirror should be able to meet high-quality visible-wavelength surface requirements in changing gravity orientations when supported on a simple, kinematic 3-point mount rather than requiring a complex whiffletree assembly.

The material that is used to fabricate corrugated mirrors can also be varied to meet program needs. For the CCAT program, the thermal requirements can be met using borosilicate glass. For visible-wavelength telescopes, the

thermal performance can be improved by using Corning ULE rather than borosilicate glass.

Corrugated mirrors for the CCAT would be made from a borosilicate glass. The mirrors are fused from a single material and are free of adhesives or other joining materials. Because these mirrors would be made of a borosilicate glass, the mirrors will not change shape with time due to outgassing or polymerizing. In addition, glass mirrors can be coated with metal coatings for reflectivity and can survive multiple cycles of stripping and recoating over the lifetime of the telescope.

To meet the CCAT program requirements, the primary mirror segments must be formed with high-accuracy into aspheric shapes at very low recurring cost. The only method that can produce these segments at the costs required is a replication process—a process that makes a nonrecurring investment in mandrels to be able to produce precision aspheric surfaces from those mandrels at high accuracy and low cost.



Figure 14.2.5. The additional layers in this 7-layer corrugated mirror allow a reduction of areal density, an increase in specific stiffness or an increase in the mirror robustness.

ITT Industries is currently developing a process to produce replicated glass optics, such as those required by the CCAT program. Preliminary replication results are shown in Figure 14.2.6 and Figure 14.2.8. These 230 mm hexagonal parts have surface errors <1 and ~ 0.2 μm RMS deviation from the sphere to which they were

replicated. This is a significant improvement over ITT results shown in late 2005, where replicated parts were $<2 \mu\text{m}$ RMS. This process is compatible with the multiple mirror technologies, including the corrugated mirror technology proposed for the CCAT.

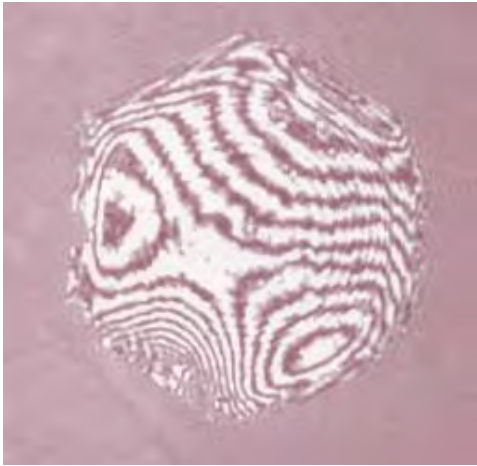


Figure 14.2.6. Interferometric surface measurement of a 230 mm point-to-point replicated optic 3 mm thick. This interferogram was taken at 632.8 nm and the surface is $<5 \mu\text{m}$ p-v and is estimated to be $<1 \mu\text{m}$ RMS. Note: the bull's-eye pattern in the surface error is an interferometer artifact.



Figure 14.2.7. The 230 mm point-to-point, 3 mm thick borosilicate optic demonstrates replication of a specular surface.

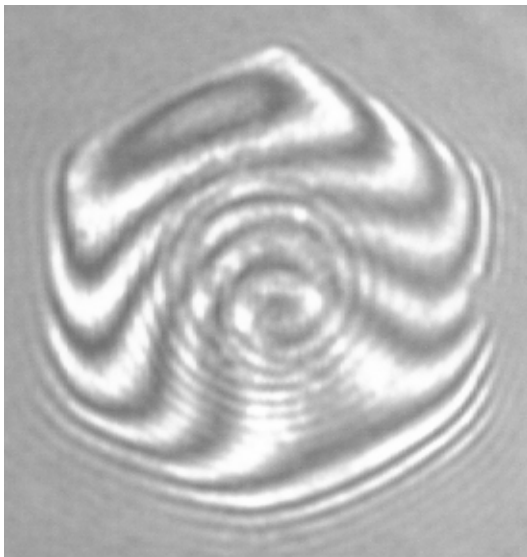


Figure 14.2.8. Interferometric surface measurement of a 230 mm point-to-point replicated optic 19 mm thick. This interferogram was taken at 632.8 nm and the surface is approximately $1 \mu\text{m}$ p-v and is estimated to be approximately $0.2 \mu\text{m}$ RMS. Note: the bulls-eye pattern in the surface error is an interferometer artifact.



Figure 14.2.9. The 230 mm point-to-point, 19 mm thick replicated borosilicate optic. The optical surface shows considerable bubbling due to contamination during the replication process that does not show up in the interferogram because small void areas are not resolved by the interferometer.

ITT Industries is currently scaling both corrugated mirror technology and glass replication technologies to the sizes required for CCAT. Figure 14.2.10 shows a 0.5-meter diameter corrugated mirror blank that is similar to those proposed for CCAT.

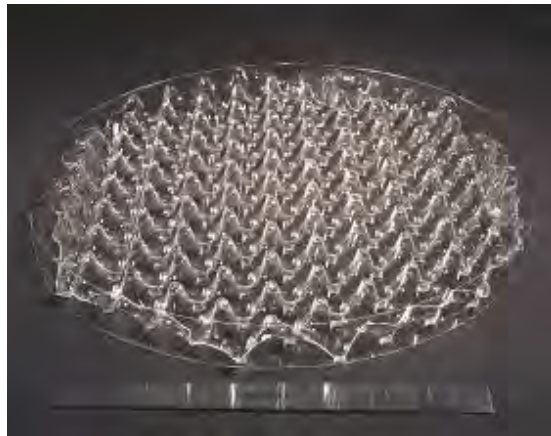


Figure 14.2.10. A half-meter borosilicate corrugated mirror blank. The ruler, included for scale, is 382 mm long.

14.2.2 PM Segment Design Concept

14.2.2.1 Configuration

The ITT proposed configuration is based on a 25 m-diameter telescope with a 3 m center hole. The commercially available sizes of glass sheet drove the number of panels and families (rings of panels). ITT assumed 5 mm wide interstitial gaps. Three-layer corrugated glass panel designs dictated using 2.0 mm thick borosilicate. Discussions with Schott indicated that 2.0 mm thick glass could be made using a float process yielding a 2 m square part. In further discussions with Schott, they indicated that they believed a 2.3 m × 2.15 m sheet could be made in their existing facility.

The panel manufacturing process yields a part smaller than the starting sheet size. The initial layout was based upon a 1.84 m petal shaped (approximately square) panel made from the 2.0 m sheet stock. The 187-panel design with seven families shown in Figure 14.2.1 is based upon this assumption.

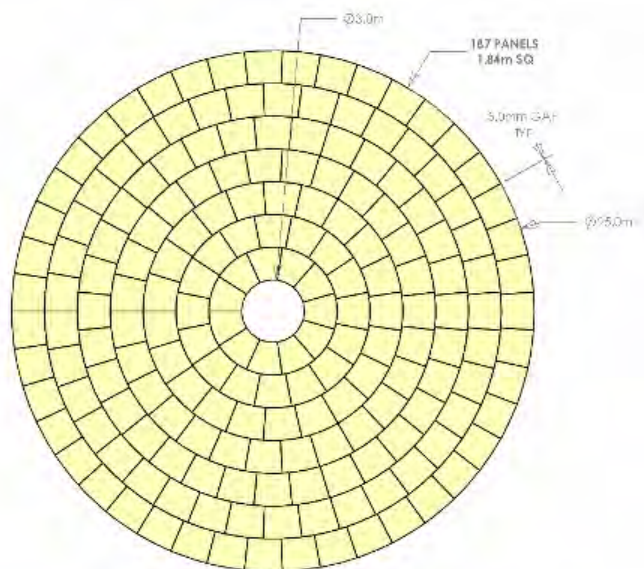


Figure 14.2.11. This layout assumed 2.0 m square glass resulting in 187, 1.84 m, square-like panels in 7 families.

Analysis showed that increasing the size to 1.87 m eliminated the 7th family. Whether this design can be realized depends upon the exact size of the glass available, whether the edges are fully usable and the amount of loss in width when the glass is made into a blank.

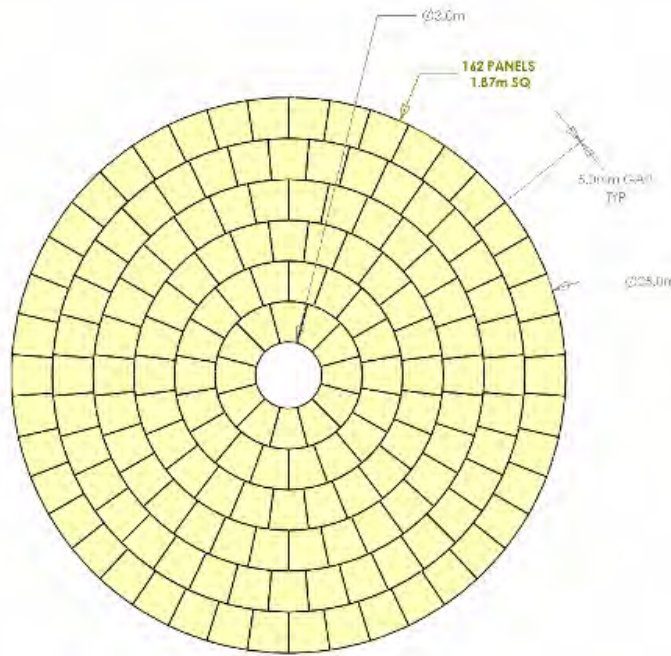


Figure 14.2.12. A 6-family, 162 panel mirror with a 3 m hole and panels that are 1.8702 m, petal shaped can be made if glass, slightly larger than the 2.0 m nominal size, is available.

The layout in Figure 14.2.12 shows a more desirable configuration (saving 1 family). This is dependent on a 2.3 m × 2.15 m sheet available from Schott. We recommend building a demonstrator to the final design to verify the 6-family telescope design is achievable.

In addition to the Schott borosilicate, Corning currently manufactures borosilicate glass in different sizes and thicknesses. Gen-6 glass is 1800 mm × 1500 mm. Gen-7 glass is expected to be 2200 mm × 1800 mm. Gen-7 is currently not yet readily available. Once the Gen-7 becomes readily available, we believe Gen-6 will be discontinued.

In Figure 14.2.17-A (Appendix), we show the layout with Corning borosilicate glass. This orientation resulted in 7-families and 188 panels.

The glasses we have considered for this project are summarized in Table 1 below. The glass properties are in Section 14.2.B. Appendix B.

Table 14.2.1. Available borosilicate glass sizes.

| Width (mm) | Length (mm) | Thickness (mm) | Availability |
|------------|-------------|----------------|---------------|
| 2300 | 2150 | 2.0 | Special Order |
| 2000 | 2000 | 2.0 | Special Order |
| 1700 | 2300 | 3.3 | Standard |
| 1700 | 2300 | 5.0 | Standard |
| 1500 | 1800 | 0.7 | Standard |
| 1500 | 1800 | 0.5 | Standard |
| 1800 | 2200 | 0.7 | Late 2006 |

14.2.3 Error Budget

The several parameters drove the point designs shown in Table 14.2.2 below. In all cases, the parameters were adjusted so the resulting glass thickness was either 2.0 mm thick or 0.7 mm thick. The maximum budgeted RMS delta 1-G gravity sag (on 3 points), based on an error budget, is 2 μm . The total error budget is shown in Figure 14.2.3. The error budget was based on our experience fabricating precision mirrors.

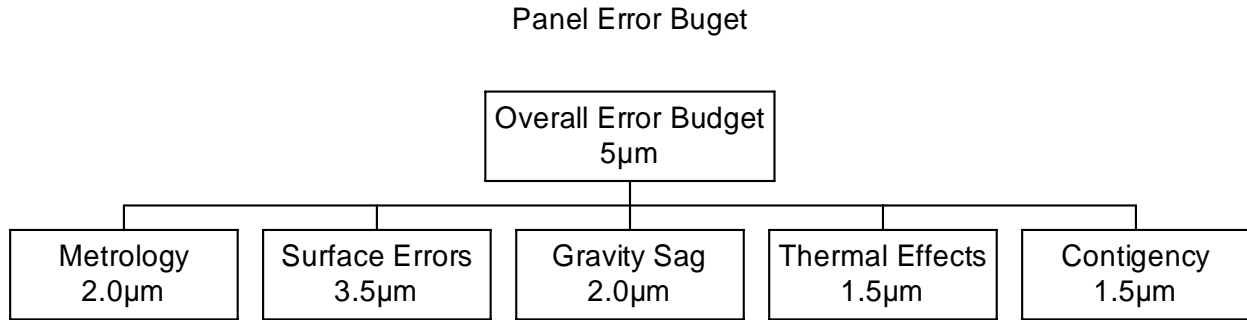


Figure 14.2.13. Panel Error Budget

14.2.4 Segment Design

Several metrics were used to determine whether a specific panel design was acceptable. These include: the 1-G gravity sag, the robustness and the manufacturability.

The 1-G gravity sag measures the gravity-induced deflection on an optimized 3-point mount. The analytical metric is approximate and can be used to select an optimal design, but is not a finite element model and should not be used as the definitive sag of the mirror.

The robustness metric measures the face sheet deflection under load. It gauges the robustness for shipping, for loads applied by handling equipment and from the impacts of small objects. It allows comparison to other mirrors made by ITT.

The quilt depth, spacing, and ratio describe the macro core geometry. The manufacturing difficulty increases as the corrugation depth ratio decreases. A ratio of 1 is the standard ratio for macro corrugations used in most of the demonstrations to date. Designs with a ratio of 0.8 have been demonstrated in micro corrugations, but not in macro corrugations. A ratio of 0.8 is expected to be within process capabilities. A ratio of 0.5 involves considerable risk because no molding data from this configuration is available, however a design with lower ratios would be more robust and would have lower 1-G sag.

Table 14.2.2. Three-layer point designs are shown with color-coding: green for good results, yellow for marginal results, and red for unacceptable. Because the error budget is adjustable and manufacturing capabilities develop over time, marginal results may, with further examination, be found to be acceptable.

| | Glass | 1 G Gravity Sag | Robustness: Deflection | Corrugation | Corrugation | Manufacturability | |
|--------|-----------|-----------------|------------------------|-------------|-------------|-------------------|-------------------|
| | mm | RMS Delta | Under Pressure | Spacing | Depth | Corrugation | Areal Density |
| | Thickness | micro meters | Low=Better | mm | mm | Ratio | kg/m ² |
| Design | | | | | | | |
| 1 | 2.0 | 1.95 | 1.82 | 73.912 | 82.125 | 0.9 | 13.4 |
| 2 | 2.0 | 1.33 | 2 | 75.676 | 100.900 | 0.8 | 13.4 |
| 3 | 2.0 | 1.50 | 2 | 75.718 | 94.650 | 0.8 | 13.4 |
| 4 | 2.0 | 1.79 | 1.75 | 73.228 | 86.151 | 0.8 | 13.4 |
| 5 | 2.0 | 2.18 | 2.2 | 77.513 | 77.513 | 1.0 | 13.4 |
| 6 | 2.0 | 2.28 | 2 | 75.775 | 75.775 | 1.0 | 13.4 |
| 7 | 2.0 | 2.03 | 2.55 | 80.396 | 80.396 | 1.0 | 13.4 |
| 8 | 2.0 | 3.16 | 1 | 63.680 | 63.680 | 1.0 | 13.4 |
| 9 | 0.7 | 4.45 | 5.1 | 43.480 | 54.350 | 0.8 | 4.68 |
| 10 | 0.7 | 1.79 | 5.1 | 43.588 | 87.175 | 0.5 | 4.68 |
| 11 | 0.7 | 1.86 | 31 | 68.360 | 85.45 | 0.8 | 4.68 |

Point design 1 of Table 14.2.2 shows a nearly optimal design. While this design is slightly over the weight budget and is a slight stretch of the manufacturability, it meets the requirements for 1-G sag and robustness. Point designs 2-4 require more development to meet the manufacturability requirement, but have better 1-G sag. Designs 2-4 trade robustness against 1-G sag. Designs 5-7 can be manufactured within the manufacturability of current demonstrations, but cannot quite meet the 1-G sag or robustness requirements. Designs 5-7 trade robustness against 1-G sag. Because many of the analytical models use first mode frequency rather than 1-G sag, a correlation must be established. Figure 14.2.14 compares first mode frequency to 1-G sag for the designs shown in Table 14.2.2.

Designs 9-11 in Table 14.2.2 traded robustness against 1-G sag for 0.7 mm thick glass solutions. There is no acceptable 3-layer solution using 0.7 mm glass. Case 10, however, does show that increasing the ability to manufacture lower ratio corrugations increases the ability to meet the combined 1-G sag and robustness requirements.

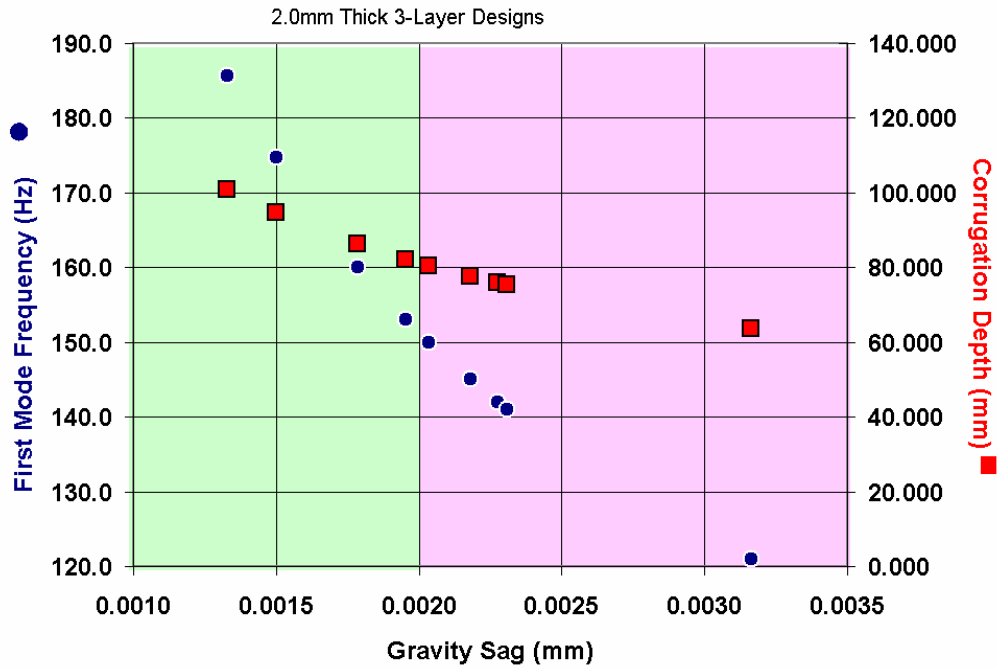


Figure 14.2.14. Corrugation depths, first mode frequencies, and gravity sags are shown for the data in Table 2. The pink area represents gravity sags that are too large. The green area represents possible designs.

The 5-layer designs shown in Table 14.2.3 perform better than the 3-layer solutions shown in Table 14.2.2. This is because the micro core assembly on the front of the 5-layer designs increases the robustness of the solution. While a 5-layer design may not be needed for CCAT, it will be required for visible wavelength applications. For visible wavelength applications, slightly worse (though still acceptable) robustness would be traded for even lower 1-G sag. The increased cost and complexity of a 5-layer design allows lower 1-G sag, greater robustness or lower areal density than 3-layer designs.

Table 14.2.3. Five-layer point designs are shown with color coding: green are good results, white are ok, yellow are mild issues, orange are problems, and red are unacceptable.

| Design | Micro Corrugation | | | | | Macro Corrugation | | | | | RMS Gravity Sag Micro Meter | Areal Density kg/m ² |
|--------|-----------------------|-------------|---------------|--|------------------------------|-------------------|---------------|--|------------------------------|-------|--------------------------------|------------------------------------|
| | Glass Thickness mm | Depth mm | Spacing mm | Manufacturability Corrugation Ratio | Robustness: Plate Deflection | Depth mm | Spacing mm | Manufacturability Corrugation Ratio | Robustness: Plate Deflection | | | |
| | | | | | Low=Better | | | | Low=Better | | | |
| 1 | 0.7 | 14.105 | 11.284 | 0.80 | 0.023 | 151.829 | 151.829 | 1 | 0.238 | 0.651 | 7.81 | |
| 2 | 0.7 | 13.637 | 10.909 | 0.80 | 0.020 | 108.918 | 108.918 | 1 | 0.067 | 1.137 | 7.82 | |
| 3 | 0.7 | 12.271 | 9.816 | 0.80 | 0.013 | 96.226 | 96.226 | 1 | 0.045 | 1.432 | 7.78 | |
| 4 | 0.7 | 12.100 | 9.680 | 0.80 | 0.013 | 79.946 | 79.946 | 1 | 0.024 | 1.977 | 7.80 | |
| 5 | 0.7 | 11.399 | 9.119 | 0.80 | 0.010 | 78.075 | 78.075 | 1 | 0.025 | 2.079 | 7.76 | |
| 6 | 0.7 | 12.350 | 9.880 | 0.80 | 0.013 | 66.426 | 66.426 | 1 | 0.011 | 2.708 | 7.85 | |

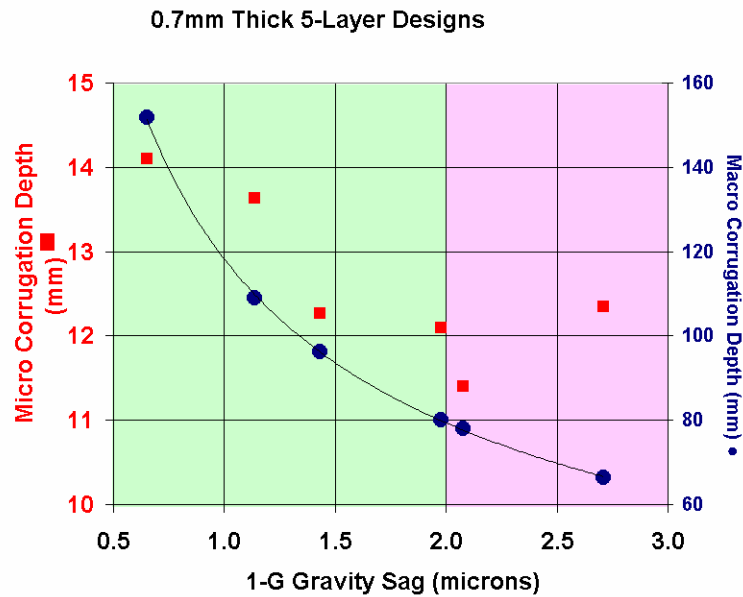


Figure 14.2.15. These 5-layer solutions use 0.7 mm thick glass and are 4.8kg/m². The green area represents possible designs. Red square symbols are micro corrugation depths and blue circles are macro corrugations depths.

14.2.5 Thermal Analysis

Thermal gradients within the mirror blanks in the CCAT telescope will cause distortions of the mirrors. Analysis of the magnitude of these distortions will determine whether the distortions will significantly impact the telescope design and use.

Heat transfer within the mirror blanks controls thermal gradients. There are several mechanisms that transfer heat within a borosilicate CCAT mirror blank. Analysis based upon a model that accounts only for conductive heat transfer within the blank predicts large temperature differences (almost 10 Kelvin) and large amounts of thermal bending. Convection and thermal radiation, however, are much more efficient heat transfer mechanisms and significantly decrease thermal deflections. Details of the thermal calculations are shown in an appendix. From the model that accounts for the most important heat transfer mechanisms, the thermally induced sag change in each segment is roughly 17 μm p-v. This sag will be almost exclusively power. This power can be focused out by moving the segments to make them fit onto the new surface and using the primary mirror with a slightly shorter radius of curvature. The segments will have to be moved less than ± 1.5 mm to accommodate this change. This can be accomplished by actively refocusing the telescope. The amount of active refocusing can be significantly reduced by appropriate design of the telescope support structure, that is, by designing the telescope support structure to bend from thermal gradients in the same way the segments bend.

14.2.6 Recommended Design

Case 1 in Table 14.2.2 is our recommended parametric design for the CCAT mirrors. It uses 2.0 mm thick Schott borosilicate glass made into a mirror blank with 82 mm deep corrugations and 74 mm corrugation periods. This design has less than 2 μm 1-G sag and is mechanically robust. The layout in Figure 14.2.2 with 162 panels in 6 families is our recommended design. This recommendation is based on performance, budget, manufacturing risk, and material availability.

14.2.7 Mount Design

The gravity sag analysis in this proposal was based on a 3-point design approach. ITT would be pleased to propose mounts, adhesive, flexures and other hardware and designs for the telescope.

14.2.8 PM Segment Manufacturing Plan

14.2.8.1 Overview

The manufacturing process starts with sheet glass. This glass is then corrugated to make a core and then high temperature fused to face plates. This corrugated blank is then precision molded to final tolerance. A combination of methods is used to control the front, back, and sides of the high temperature fused panel. This molding process uses precision polished mandrels that are stable at high temperatures.

14.2.8.2 Mandrels

Mandrels are required to be larger than the panel that they mold. A 1.84 m panel will require a 1.9 m square mandrel with a 2.69 m diagonal. The additional surface area will be used to hold fixtures during the molding process. There are several candidate mandrel materials and a final selection will be made by balancing cost and performance. The precision optical polishing of the mandrels will use standard ITT process.

14.2.8.3 Edge Control

ITT has developed methods of edge control and corrugation termination so that there will be no exposed core components. Figure 14.2.16 shows how this 1.5-inch-deep corrugation has ended with a sidewall that supports the face sheets.



Figure 14.2.16. The corrugation and face sheets have been molded together so the interior structure is not exposed or unsupported.

14.2.9 Schedule for Manufacturing

14.2.9.1 Glass Process

ITT anticipates that several trials will be required to tune the production process for the first family of parts. This will be required for the corrugation fabrication process, the assembly process, and the precision molding process. Subsequent families will require fewer tuning runs.

The fabrication of the corrugation and the high temperature assembly of the blank do not require precision annealing, so the cycle times for these operations are very short. A slower cool down cycle, after the precision molding operation, will be required to fine anneal the assembly. This will limit the production rate to approximately one part per week per furnace.

14.2.9.2 Coating

We expect to coat the segments with a SiO₂ protected aluminum coating. This will provide a 95⁺% reflectivity from 250 μm to 3 mm wavelengths and will be strippable. Other metals, such as Au, Ag, and Cr are also possible.

Stress analysis on the coating will be needed. The coating process is shorter than the mirror fabrication process and will not impact the production rates. Capital improvement to our coating facility may be required to ensure efficient production of the segments.

14.2.10 Metrology Plan

Our Off-Axis Generating Machine (OAGM) can be used to probe mandrels and parts for CCAT. Probing is accurate to $\pm 1\mu\text{m}$, which is well within the error budget (per Figure 14.2.13). Because OAGM probing meets all metrology requirements, ITT does not plan to interferometrically test these parts.

14.2.11 System Test

Facilities to test a 25 m telescope are TBD and will be determined in follow-on work.

14.2.12 Capital Equipment

ITT has an extensive base of existing equipment that can be used to manufacture mandrels and segments for CCAT. ITT has existing equipment with the capability to generate, grind, polish and measure the mandrels for CCAT.

ITT currently has a 3 m square furnace. This furnace meets the temperature requirements for production of borosilicate CCAT parts. Although this is an existing furnace, ITT will need to upgrade this furnace for efficient production of the segments.

Coating facilities upgrades will be necessary to ensure efficient production of the segments.

14.2.13 PM Segment System Cost

The cost estimate for this report will be delivered under a separate file.

14.2.14 Critical Risk Assessment

ITT has demonstrated the manufacturing process on 0.25-0.3 m parts and ITT is currently building 0.5 m sizes. The major risks associated with the CCAT production are scale up issues.

14.2.14.1 Scale Up Risk

- **Release from Molds:** Glass that is precision molded against a surface tends to bond with the mandrel surface. A number of techniques are used to control this bonding and several potential mandrel materials are available. Continued development work with these materials will mitigate risks associated with release of the molded parts. The difficulty of releasing the glass from the mandrel increases as the area increases. A demonstration optic built at the CCAT final mirror size will mitigate the risk of releasing from the large parts from the mandrels.
- **Glass Availability:** Larger sizes of borosilicate glass from Schott will require a special run. This run will need to be scheduled into Schott's production schedule. Sufficient material must be ordered to complete the project with some spare glass, but without excessive left over material. A full-scale mirror demonstrator would help us understand exactly how much glass is required.
- **Manufacturing of Corrugations:** Both materials and processes must be developed for the large size corrugations. These processes and materials will be scaled from existing processes at smaller sizes. Some mold materials are not available at the required panel sizes. Significant cost savings could be realized in tooling if the panel size were reduced to fit within a 1.5 m diameter circumscribed circle. While this would decrease the cost of the segments, it would increase the costs of other parts of the telescope system and the size that minimizes overall costs is yet to be determined. Segmenting the molds and building up the tooling with brazing, gluing, and pinning techniques may minimize tooling costs. These joining techniques must be checked at the higher temperatures.
- **Molding Mandrels:** Similar to the corrugation molds, scale up of the mandrels must be demonstrated in follow-on work.
- **Handling Large Sheets:** ITT will need to develop tools to handle large, thin, sheets of glass efficiently for low cost, high yield production. Jigs and fixtures will be built and tested during follow-on work.

14.2.15 Recommended Next Steps

14.2.15.1 Small Scale Demo (20 inch)

This part would demonstrate molding accuracy, edge control, and overall mirror shape. The blank should be made to a specific sphere, or if funding permits, an off-axis sphere.

14.2.15.2 Large Scale Demo (2m)

The 2 m scale demonstrator would be very similar to one panel from the CCAT telescope. The demonstrator size would be determined by balancing tooling and material costs. A slightly smaller demonstrator would not require a very expensive custom run of glass at Schott, but the tooling from the demonstrator would then not be the correct size to use in CCAT production. This demonstration mirror would allow testing of the mold release process from large mandrels, the molding accuracy, and the fabrication of large size mandrels.

14.2.15.3 Coating Stress Analysis

The effects of the coating stress on the prime surface of these optics will need to be analyzed. While the coating stress effects must be examined, the bending is expected to be small compared to CCAT error budget.

ITT Industries is pleased to provide this engineering study for Cornell-Caltech Atacama Telescope (CCAT). Although not funded by the CCAT engineering study, ITT is also producing subscale sample pieces for CCAT. ITT's recently developed manufacturing methods for panels allow rapid fabrication and low cost solutions for CCAT.

The study concludes with a recommendation for a 3-layer corrugated mirror design. However, mirror system trade-offs between performance, cost, and risk at the system level should be studied in detail in future work. We are pleased to be part of the CCAT team and we believe our experience in large-mirror systems will help the CCAT program be successful.

14.2. A. Appendix A

A 5-layer configuration from 0.7 mm thick Corning borosilicate glass is shown below.

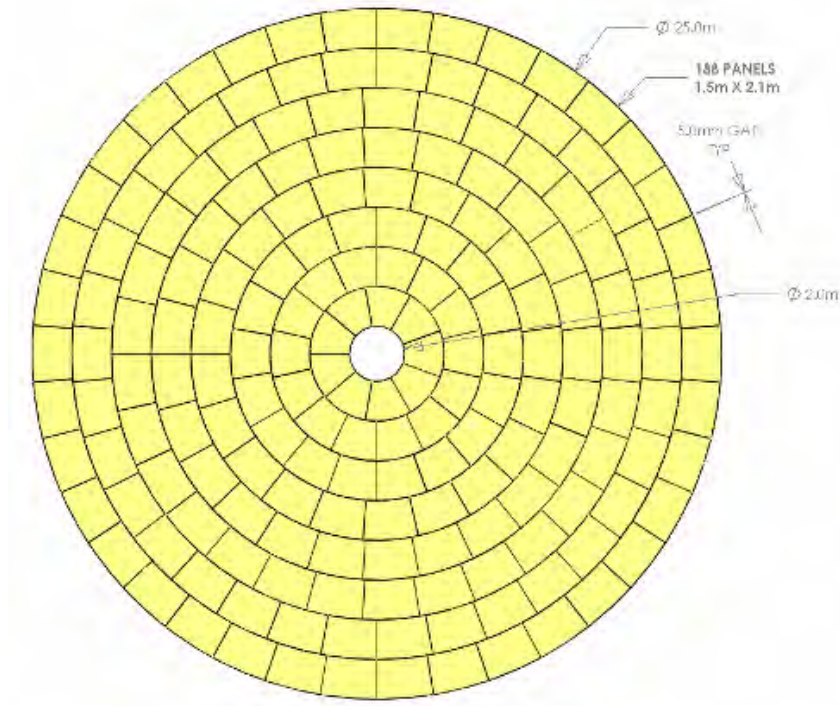


Figure 14.2.17-A. Layout using Corning's borosilicate glass results in 188 panels and 7 families.

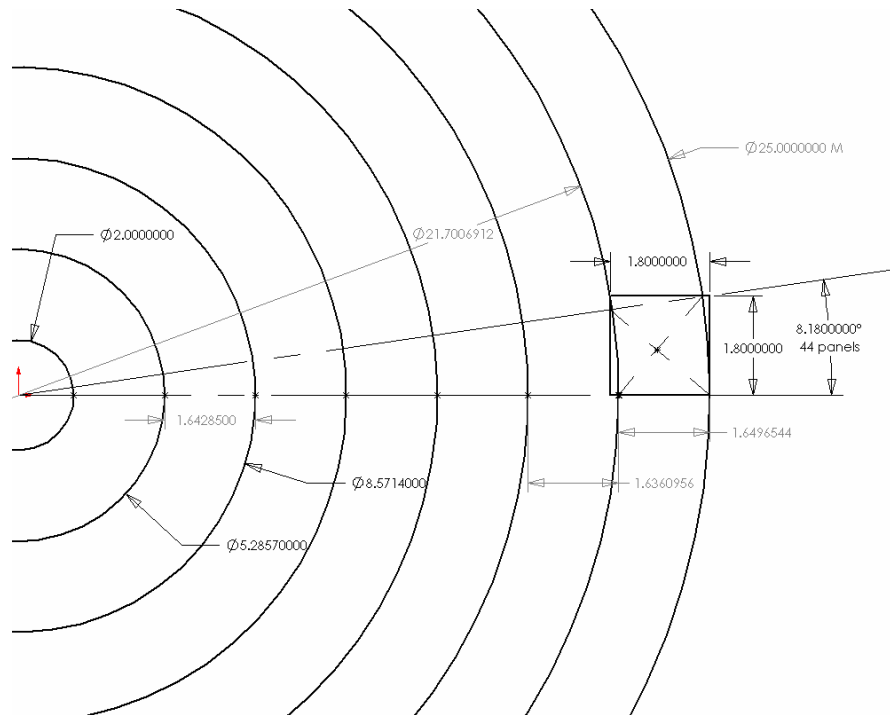


Figure 14.2.18-A. This is the panel layout using 2.0 m square Borosilicate and assuming a 1.84 m square panel.

14.2.B Appendix B

Borosilicate Properties

| | | | |
|---|------------------------|--|--------------------------------------|
| Chemical Data | | Optical Properties | |
| • Hydrolytic Resistance (ISO-719-HGB) | 1 | • Refractive Index (n_d) | 1.472 |
| • Hydrolytic Resistance (ISO 720-HGA) | 1 | • Dispersion ($n_F - n_C$) | 71.9×10^{-4} |
| • Acid Resistance (ISO 1776) | 1 | Thermal Properties | |
| • Alkali Resistance (ISO 695-A) | 2 | • Linear Thermal Coefficient of Expansion α (20-300°C/ 68-572°F) | $3.25 \times 10^{-6}/^\circ\text{K}$ |
| Mechanical Properties | | • Transformation Temperature T_g | 530°C/986°F |
| • Density (@ 25°C/77°F) | 2.23 g/cm ³ | • Annealing Point (10^{13} dPa•s) | 560°C/1040°F |
| • Modulus of Elasticity | 63 kN/mm ² | • Softening Point ($10^{7.6}$ dPa•s) | 815°C/1508°F |
| • Knoop Hardness HK 0.1/20 (according to E DIN/ISO 9385) | 480 | • Thermal Conductivity k @ 90°C | 1.12 W/(m•°K) |
| • Poisson's Ratio | 0.2 | @ 194°F | 0.65 Btu•ft/h•ft ² •°F |
| Electrical Properties | | • Mean Specific Thermal Capacity c_p 20-100°C | 0.83 kJ/(kg•°K) |
| • Dielectric Constant (@ 1 MHz & 25°C) | 4.6 | 68-212°F | 0.19 Btu/lb•°F |
| • Loss Tangent (@ 1 MHz & 25°C) | 37×10^{-4} | • Maximum Operating Temperature (Considering RTD ¹) | |
| • Dielectric Strength(@ 50 Hz & 25°C) | 16 kV/mm | Short term | 500°C/932°F |
| • Electric Volume Resistivity (log ρ) | | Long term | 450°C/842°F |
| @ 250°C | 8.0 | • Resistance to Temperature Differences (RTD ¹) | |
| @ 350°C | 6.5 | Short term exposure | |
| | | (1 hour) | 110°K/198°R |
| | | (1-100 hours) | 90°K/162°R |
| | | Long term exposure | |
| | | (>100 hours) | 80°K/144°R |
| | | • Resistance to Thermal Shock (RTS ²) | |
| | | Thickness <4 mm | 175°K/315°R |
| | | Thickness 4-6 mm | 160°K/288°R |
| | | Thickness 6-15 mm | 150°K/270°R |
| | | Thickness >15 mm | 140°K/252°R |

14.2.C. Appendix C

Thermal Modeling of CCAT Borosilicate Glass Mirrors

Executive Summary

There are several mechanisms that transfer heat within a borosilicate mirror blank for CCAT. Analysis based upon a model that accounts only for conduction predicts large temperature differences and large amounts of thermal bending. Convection and thermal radiation, however, are much more efficient heat transfer mechanisms and significantly decrease thermal deflections. From the model that accounts for the most important heat transfer mechanisms, the thermally induced sag change in each segment is roughly 17 μm p-v. This sag will be almost exclusively power. This power can be focused out by moving the segments to make them fit onto the new surface and using the primary mirror with a slightly shorter radius of curvature. The segments will have to be moved less than ± 1.5 mm to accommodate this change. This can be accomplished by actively refocusing the telescope and can probably be significantly reduced by a thermal design of the telescope, that is, by designing the support structure for the segments such that the same thermal gradients cause it to bend to match the segment radius.

Analysis

Heat flux through the CCAT mirrors in use will cause thermal bending. This bending will impact either the telescope performance or the difficulty in maintaining a phased, continuous primary mirror surface.

To understand the magnitude of these effects, ITT has developed first order models of the heat flux through the mirror segments. The mirror segments were assumed to be well insulated from the primary mirror backing structure. The heat input to the back surface was assumed to be radiated heat from the relatively warm ground and heat loss was assumed to be radiated from the front surface to both the sky and the dome.

The radiative heat flux between two surfaces is modeled using the Steffan-Boltzmann law, modified for the emissivity of two surfaces. Solving the infinite series of reflections yields:

$$\frac{1}{\frac{1}{\epsilon_1} + \frac{1}{\epsilon_2} - 1} \sigma (T_1^4 - T_2^4),$$

where ϵ is the emissivity of the surface and σ is Steffan-Boltzmann's constant. The above equation was used to determine the heat flux from the ground to the back of the segments and from the front of the segments to the sky and dome. Using the solid angle into which radiation is emitted and the obliquity factor for the front surface, the relative amount of radiation exchanged between the front surface and the sky and the front surface and the dome is determined by

$$\int_{\phi_1}^{\phi_2} \text{Sin}(\theta) \text{Cos}(\theta) 2\pi d\theta.$$

The equation above, along with the dome geometry, shows that radiation exchange between the front surface and the sky and the front surface and the dome are each half of the radiation between infinite parallel plates as modeled by the Steffan-Boltzmann Law.

Three mechanisms conduct heat from the front surface to the back surface of the mirror: conduction, radiation and convection. The heat flux from conduction can be calculated from the glass thermal conductivity, accounting for

both the fill fraction of the glass in the middle of the mirror (2-3%) and the average ratio between the blank thickness and the conduction path length (very complicated for this geometry, but is roughly $\sqrt{2}$).

The radiative heat transfer in the blank is determined as above, but the core geometry complicates the model. For some areas, there is a direct radiation path between the front and back plates. In other areas, heat is exchanged between the back plate and the core and then the core exchanges heat with the front surface. Two cases can be analyzed to bound the radiative heat transfer: front and back plates directly exchanging radiation as above and two plates each exchanging radiation with a full core. These two cases result in temperature differences from front to back plates that differ by a factor of two. In the combined model, the average between the two bonding cases was used to approximate the radiative heat transfer.

The convective heat transfer between the front and back plate is modeled as a set of cubical containers with heated bottom surfaces, cooled top surfaces and insulated walls, per Incropera and Dewitt using the heat transfer coefficient

$$\frac{k}{L} \overline{Nu}_L,$$

where the Nusselt number was determined experimentally to be approximately

$$\overline{Nu}_L = 0.18 \left(\frac{\text{Pr}}{0.2 + \text{Pr}} \text{Re}_L \right)^{0.29} \quad \text{and}$$

$$\text{Re}_L = \frac{g\beta(T_1 - T_2)L^3}{\nu\alpha}.$$

The thermal properties of air at a 5000m altitude were taken from an ALMA telescope memo to be

| Property | Value | Units |
|----------|---------|-------------------|
| Pr | 0.71 | Unitless |
| ν | 25.9E-6 | m/s ² |
| α | 35.5e-6 | m ² /s |
| k | 0.0237 | W/mK |
| β | 0.0033 | 1/K |
| g | 9.8 | m/s ² |

The characteristic length is the thickness of the blank and this approximation holds over the relevant Reynolds and Prandl numbers and the 1:1 aspect ratio for the cell shape is a reasonable approximation of the cells in the blank.

The following assumptions were used in these models:

- The ground below the telescope is at 273 K
- The inner surface of the dome is 233 K (a warmer dome would result in less bending)
- The sky has a temperature of 4 K
- The sky has an emissivity of 1.
- The inner surfaces of the blank have an emissivity of 0.92 (a reasonable approximation for glass)
- The top and bottom surfaces of the blank are coated with an emissivity of 0.02 (the emissivity of gold)
- The dome and the ground have emissivity of 0.92
- There is no conductive or convective heat transfer into the air around the telescope – any such heat transfer would decrease the thermal gradients, provided the air is of uniform temperature

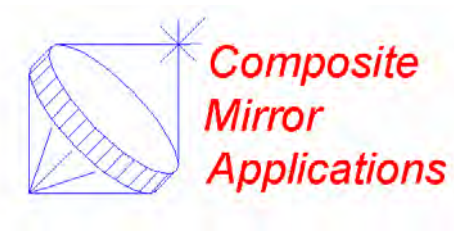
Using these models for heat transfer, the following results can be obtained:

| Heat transfer model | Front Surface Temp (°K) | Back Surface Temp (°K) | Temp Delta (°K) | Radius of Curvature Change (m) | Thermally induced sag in each segment (m) | Thermally induced sag in the primary mirror (m) |
|--|-------------------------|------------------------|-----------------|--------------------------------|---|---|
| Core conduction only | 238.61 | 248.018 | -9.407 K | -0.363 | 0.000204 | 0.0319 |
| Radiation only (no core, over estimates radiation) | 243.038 | 243.857 | -0.819 K | -0.032 | 0.0000178 | 0.00278 |
| Radiation only (full core coverage, under estimates radiation) | 242.634 | 243.449 | -1.62 K | -0.063 | 0.0000351 | 0.00549 |
| Convection only (5000m air) | 242.388 | 244.495 | -2.107 K | -0.082 | 0.0000457 | 0.00715 |
| Convection and radiation (approximated core, 5000m air) | 243.052 | 243.843 | -0.790 K | -0.030 | 0.0000171 | 0.00268 |

From the model that accounts for the most important heat transfer mechanisms, the thermally induced sag change in each segment is roughly 17 μm p-v. This sag will be almost exclusively power. This power can be focused out by moving the segments to make them fit onto the new surface and using the primary mirror with a slightly shorter radius of curvature. The segments will have to be moved less than ± 1.5 mm to accommodate this change. This can be accomplished by actively refocusing the telescope and can probably be significantly reduced by a thermal design of the telescope, that is, by designing the support structure for the segments such that the same thermal gradients cause it to bend to match the segment radius.

14.3 CFRP AI Panels

Report prepared by Composite Mirror Applications



14.3.1 Introduction

This document summarizes the results of the CCAT Panel Feasibility Design Study performed at CMA. This study was undertaken according to the contract issued by JPL to CMA on May 18, 2005 (Appendix I). This is an abridged version of the final report, with the appendices removed for length considerations. The full report can be obtained from the CCAT project office or by contacting CMA.

14.3.1.1 Relevant Documents

This study is based on the specifications and scope of work outlined in the following documents.

- 1) JPL Subcontract No. 1273343 to CMA for this Submm Wavelength Radio Telescope Panel Study.
- 2) Preliminary Specifications - Primary Mirror Panel System; CCAT (Exhibit I to above contract).
- 3) CCAT Memo No. CCAT-TM-005; CCAT Optical Design; 23 May 2005.
- 4) CCAT Primary Mirror Panel Consideration, T. A. Sebring, 8 April 2005 (email report).

14.3.2 Background

14.3.2.1 CFRP Sandwich Panel Technology

Composite reflector (or mirror) panels using CFRP face sheets and honeycomb aluminum core have been used on several high frequency (60-350 GHz), precision, radio telescopes since the early 1980's. The subreflector for the IRAM 30 m telescope was one of the early applications to explore this technology. The IRAM 15 m (and SEST 15 m) telescopes applied this technology to all of the primary and secondary reflector surfaces. Those panels, fabricated by MAN Technologie, were replicated on steel mandrels. The reflective surface layer was a film of teflon coated with a thin layer of aluminum. The teflon layer was bonded to the panel with the aluminum reflective layer protected by the teflon. Since these telescopes are located outside and must withstand the elements, it was thought that the teflon would provide a protection to the reflective surface. This seems to have worked properly for the SEST telescope in Chile, but the layer did not survive for the IRAM telescopes in the French Alps where ice storm particles cut and penetrated the surface layer. Although the sandwich panel technology was sound, the surfacing problem presented a severe problem for the IRAM use.

In the late 1980's, the SMT (Submillimeter Telescope) project (Baars, et al. 1999) further refined this panel technology for higher precision telescope reflectors (frequency range 250-1000 GHz). The panel development results of that project are directly applicable to the CCAT requirements. Glass (pyrex) mandrels were fabricated at the University of Arizona and fabricated the primary and secondary reflector panels under contract to the Max-Planck-Institut fuer Radioastronomie. The mandrels were figured to an accuracy of 3 μm rms and the panels were fabricated to an accuracy of 6 μm rms. The SMT panels are trapezoidal with a dimension of 1.55m on the radial side. The SMT panels are attached to a CFRP backup structure at 5 or 6 points (depending on the ring). There is a slight warp to the panels (on the order of 10-30 μm) during fabrication which is taken out by the over constrained support of the CFRP tubular backup structure. This does not introduce problematic forces or moments to the panels nor the backup structure. The reflective layer of the SMT panels is a 40 μm thick

aluminum foil which is bonded to the panel in the final replication step. The 10m SMT is the most precise radio telescope to date and was the first telescope to make ground based astronomical observations at frequencies above 1 THz (Tong, et al., 2000).

The SMT mandrels were not polished to provide optical, specular surfaces. However, the surface of the panels replicated are still of high enough quality to provide coherent reflection at 10 μm wavelength. During telescope fabrication, measurement tests were made on some of the SMT panels using a 10 μm laser interferometer system. Clean fringes were obtained across the reflective surface and panel surface figure could be evaluated using this method. It is not known what the reflective efficiency was at those wavelengths.



Figure 14.3.1. One of the IRAM 15 m telescopes during assembly on site. **Figure 14.3.2.** SEST 15m in La Silla, Chile.

CMA supplied the tertiary, flat mirror panel for the SMT project in 1992. The 1m x 0.7m oval flat is also a CFRP-aluminum honeycomb sandwich panel. It was replicated on a glass flat and has an accuracy of 0.5 μm rms. This was verified using a 10 μm laser interferometer. The surface coated is vacuum deposited aluminum, similar to an optical glass mirror coating. The mirror was recoated in the mid-1990's after SMT construction was finished. It is still in normal service a decade later.



Figure 14.3.3. Submillimeter Telescope (SMT) on Mt. Graham, AZ.



Figure 14.3.4. SMT panel and pyrex mold during fabrication at MAN Technologie



Figure 14.3.5. SMT panel testing on a 10 μm laser interferometer.

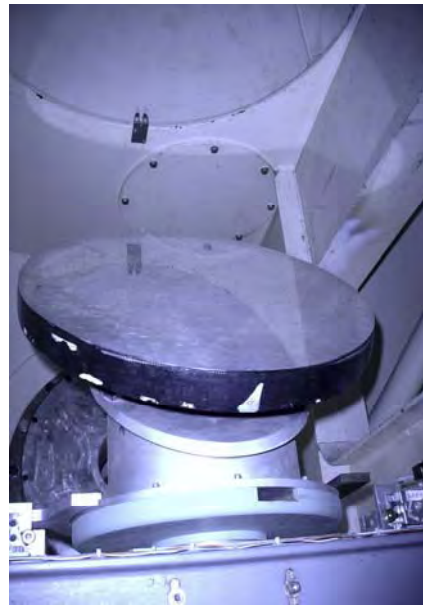


Figure 14.3.6. SMT tertiary mirror built by CMA and in service at the telescope. The surface was verified on a 10 μm interferometer.

It is worth mentioning that the 1.7 m diameter AST/RO submillimeter telescope uses CFRP for the primary mirror reflector surface (Stark et al. 2001). An aluminum reflective layer is vacuum sputtered onto the surface. This telescope is located at the South Pole where the environmental conditions can be harsh. The extreme temperatures at this site are positive statement about the adhesion of the sputtered coating to the polymer surfaces on CFRP.

14.3.2.2 Composite Mirror Applications (CMA)

Composite Mirror Applications, Inc. (CMA) was founded by Robert Romeo in 1991 to design, prototype and manufacture custom lightweight optics. CMA has developed and optimized processes for producing ultra-smooth, high precision lightweight mirrors for use at mm-wavelength up through visible imaging applications and continues to advance mirror technology for UV and x-ray astronomy as well as LIDAR and partial physics applications (Chen et al 2000; Romeo, et al 2000; Romeo and Chen 2002a, 2002b). Mirrors manufactured by CMA are fabricated utilizing a proprietary process which is free of fiber and core print-thru and bond lines. Furthermore CMA manufactures composite mirrors from a wide range of composite materials allowing cost and design flexibility for a given application. CMA is the industry leader in ultra-smooth, extremely lightweight precision composite reflectors.

The CMA client list for past projects includes: Argonne National Laboratory, Academia Sinica Institute of Astronomy and Astrophysics (ASIAA) Taiwan, Bennett Optical Research, Brown University, CalTech, Canadian Space Agency, Carlo Gavazzi Space Center, Efficient Designs Incorporated, Harris Corporation, Harvard CFA, Istituto Nazionale Fisica Nucleare (INFN) Italy, JPL, NASA - Goddard Space Flight Center, National Radio Astronomy Observatory, National Reconnaissance Office, National Science Foundation, Naval Research Lab, Photon Instruments Ltd., Physical Optics Corporation, QinetiQ Ltd., System Specialists Inc., University of Arizona - Steward Observatory, University of Bristol, University of Notre Dame, Vertex Antennentechnik Germany.



Figure 14.3.7. CFRP 0.75 m diameter secondary mirror (built at CMA) for ALMA telescopes.



Figure 14.3.9. CFRP 155 mm diameter secondary mirrors (built at CMA) for the CBI (Cosmic Background Imager) telescopes.



Figure 14.3.8. Two CFRP 320 mm diameter Cassegrain systems built at CMA for the ASIAA AMiBA experiment on Mauna Loa, HI.

Previous CMA projects which are relevant to the CCAT Panel Study include

- Secondary Mirrors for ALMA and APEX antennas (12m diameter submillimeter radio telescopes)
- CFRP components for the ALMA and APEX chopping systems
- CFRP/ Aluminum sandwich tertiary mirror for the SMTO
- CFRP secondary mirrors for CBI dishes (Caltech Cosmic Background Imager)
- 320 mm diameter CFRP Cassegrain mirror telescopes for ASIAA (Academia Sinica Institute of Astronomy and Astrophysics) AMiBA (Array for Microwave Background Anisotropy) system.
- 6m CFRP platform for the ASIAA AMiBA project.
- CFRP 16" optical wave mirrors and OTA (Optical Tube Assembly) for ULTRA (an NSF Major Research Instrumentation program to U Kansas and CMA) and NRL (Naval Research Lab) projects
- 1 m CFRP optical wave mirrors and OTA for ULTRA (in construction)
- 1.4 m CFRP optical wave mirrors and OTA for NRL (in construction)

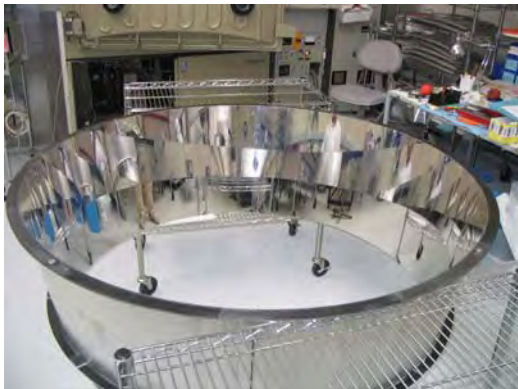


Figure 14.3.10. 1.4 m diameter RICH (Ring Imaging Cherenkov) mirror built by CMA for manned space flight hardware (Carlo Gavazzi Space).

The last 3 (optical telescope) projects on the above list are particularly relevant to the CCAT requirements. CMA has advanced the CFRP mirror development to the point where the surface quality considerations are on the 10's of nm level not the μm level. The 1m diameter optical mirror and OTA will be available for field testing in early 2006.

CMA has just completed the fabrication and delivery of an optical surface (RICH mirror) for the Carlo Gavazzi Space Center in Italy. That mirror will be part of the AMS02 experiment on the International Space Station. That project is scheduled for launch ready in Fall 2007.

CMA has been involved in other development projects with 1-2 m size replication and higher accuracy replication than called for here. Flight simulator mirror segments of 2 m in size have been produced with square shapes and edge matched in assembly to produce a 4 m, continuous projection mirror.

CMA demonstrated their capacity to handle large, CFRP structural projects when fabricating the ASIAA AMiBA platform (Raffin, et al, 2004, Martin & Kingsley, 2000). This 6m diameter platform used CFRP plate construction and required over 1000 Kg of raw CFRP material. CMA tooled up for the project, fabricated all the material on site, and completed the project within about 9 months.

14.3.3 Scope of this Study

The scope of work for this design study is defined in the JPL contract issued to CMA (Appendix I). The main tasks of the study are to

- Review the technical specifications supplied with the contract.
- Develop a panel design (baseline concept).
- Analyze the panel design for performance under various environmental load conditions.
- Optimize the panel concept within the rough boundary conditions supplied.
- Develop a manufacturing plan for a complete set of surface panels.
- Develop a critical risk assessment of all areas related to the panel design and manufacture.
- Provide an initial cost estimate and schedule.
- Recommend steps to be taken in the further development and design of panels.

This initial feasibility study does not include a detailed panel design nor a prototype or test panel fabrication. That would be the scope of future studies.

14.3.3.1 Specifications

The starting configuration specifications relevant to panel designs are summarized below. The specifications were supplied to CMA in (a) the contract and appendix, (b) an April 8, 2005 email document from T. Sebring, and (c) CCAT-TM-005 Memorandum on Optical Design supplied by S. Radford.

- 25 m diameter segmented primary mirror
- 3 m diameter central hole in primary
- f/0.6 primary mirror
- 6 or 7 rings of panels (6 preferred in verbal communications with CCAT management)
- radial panel layout preferred
- 3 point mount for each panel.
- 5 μm rms surface error under all operating conditions
- surface specular on smaller scale
- panel gaps of 5 mm or slightly less
- panel areal density of less than 10 kg/m^2
- panel cost goal of less than \$10,000/ m^2

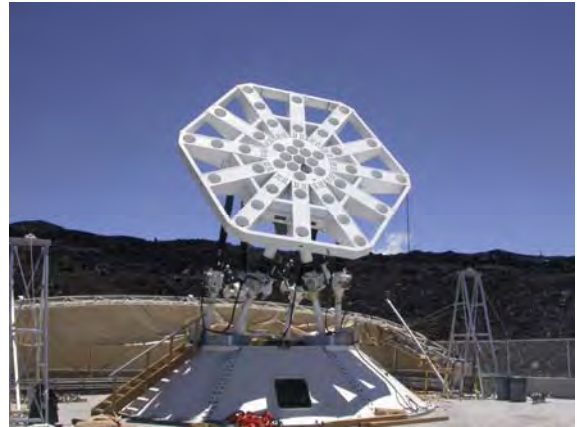


Figure 14.3.11. 6m AMiBA platform on site at Mauna Loa. CFRP plate structure built at CMA



Figure 14.3.12. One of several 0.4 m optical telescopes fabricated at CMA. The mirrors and the OTA (optical tube assembly) are fabricated completely with CFRP.



Figure 14.3.13. CMA vacuum coating chamber for large mirrors.

14.3.3.2 Comments to the CCAT Baseline Specifications

In a June 20, 2005 document supplied to the CCAT, CMA commented on the initial specifications (as required in the contract). CMA finds the preliminary specifications document (contract appendix) to be a good starting point and useful information for the panel feasibility study. There are two areas in which CMA recommended further discussion and/or modification.

I.) The surface error specification: The preliminary specification document discusses the surface error requirements in sections 4.1.4 and 4.5.1 through 4.5.5. Unfortunately, these specifications are not self consistent and do not properly constrain the manufacturing to the advantage of CCAT's performance specification. We understand the intended use of the telescope operation and have discussed some of these error constraints with Tom Sebring and Simon Radford at our kick-off meeting (5/19/2005). We propose the following revision to the surface error specification.

a) The surface reflective coating requirements should be specified separately from the panel surface error requirements. The final reflectivity of the panel is, of course, the product of these two efficiencies. But specifying the final product confuses the issues involved. The separate specification matches the manufacturing processes involved and are numbers which can be verified during manufacture.

b) The surface coating should have a reflective efficiency of 98% or better at wavelengths of 3 mm - 250 μm . The surface coating reflective efficiency should be better than 90% (95%??) at a wavelength of 10 μm . These reflective values refer to normal incidence.

c) The surface error of the mirror panel can be characterized by a Gaussian distribution (ie, applies to all size scales). The rms of this distribution should be better than 3 μm (5 μm ?). This will indicate an (Ruze error) efficiency of 97% (94%?) at 250 μm (Ruze, 1966). [Note: Do not specify a peak to valley error in addition to the rms error. The characterization of a Gaussian distribution fully specifies the error allowed.]

d) For a panel sub-aperture of 300 mm (and smaller) the rms surface error must be less than 0.35 μm . This will result in $\lambda/30$ surface quality for sub-aperture observations at 10 μm wavelength. The resulting surface error efficiency (excluding coating) at 10 μm wavelength would be 84%.

e) For the surface error in item (d), there may be a defect content of 5% by surface area.

f) Correlated surface errors must account for less than 5% of the error. The spatial distribution of surface error must not deviate from a Gaussian distribution by more than 5%.

II.) Sections 4.7 and 4.8 - Operating Conditions: Several of these specifications are not relevant to the surface panels. We believe that this is understood by everyone already but it should, perhaps, be noted in the document or in some written communication. This is a minor point.

14.3.4 Approach and Key Tradeoffs

The feasibility of producing reflector/mirror panels to the CCAT specifications is proven by previous projects and current development underway at CMA. The challenge is to produce the panels at a reasonable cost and time scale.

Our optical telescope mirrors use all CFRP, complex core structures. This provides the stiffness required for holding the optical telescope figure. However, it is an expensive process due to the material costs and the labor time involved. Alternately, we have considered a thin (meniscus) mirror panel bonded to a space frame structure to hold the figure. This would be light weight but would be fairly labor intensive.

Our approach for the CCAT panel design is to follow a similar design to previous submm radio telescope projects. We will fabricate sandwich panels with carbon fiber (CFRP) face sheets and honeycomb aluminum core. The

panels will be replicated on glass molds. This approach is proven technology, as discussed in the background section of this report. Our approach is a refinement and reasonable extension of those 15-20 year old developments. The technical feasibility of producing a CFRP mirror panel meeting the specifications has been established to a relatively high degree. Processes are well in hand, that are traceable to producing 5 μm panels at an areal density of $\leq 10 \text{ kg/m}^2$. Producing over 60 mirrors from a single mandrel has been demonstrated and contributes to the cost effective nature of surface transfer or replication process. Amortizing the cost of the mandrels over high numbers of parts/mandrel creates a low non-recurring engineering, NRE, when compared to the overall project cost. Although the mandrels are not part of the panel production costs discussed in this study, it is useful to keep those costs in mind in this study report.

Our technological approach has low, acceptable risk. Similar products have been field tested in various environmental conditions. Manufacturing using this technology has been successful.

The challenge for the CCAT panel concept study is “value engineering”. How can we maximize the performance, reduce the cost, and reduce the overall weight.

14.3.5 Baseline Panel Concept and Design

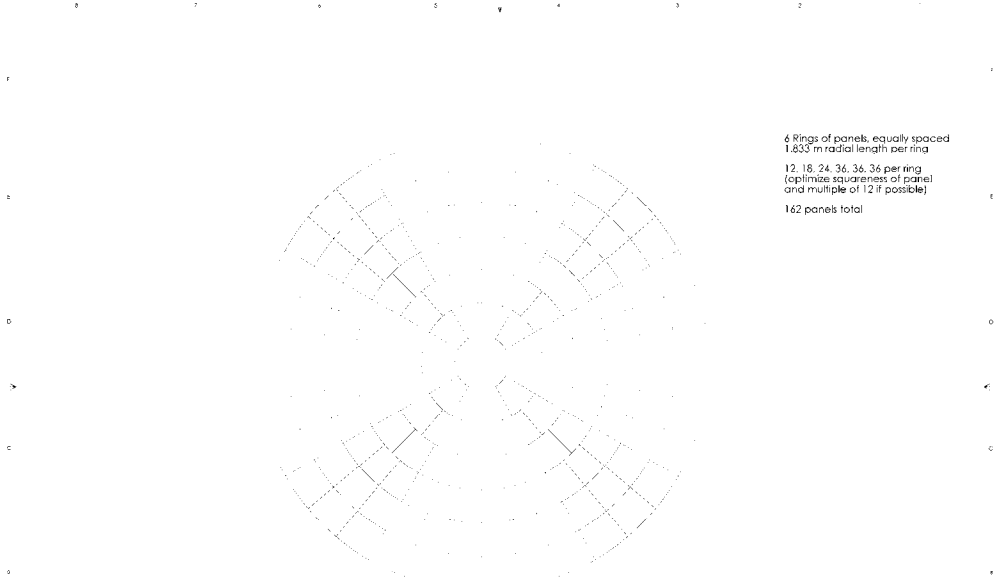
14.3.5.1 Segmentation Scheme

The contract asks that we review and comment on the primary mirror segmentation scheme. This is important for the panel design. The panel size and shape will be particularly important for the panel support points, panel thickness, areal density, performance and cost.

In Drawing CS01 and Drawing CS02 we illustrate segmentation schemes for 6 and 7 rings of panels. For these layouts, we have aimed (a) to have the panel shape aspect ratio symmetric when possible and avoid long narrow panels, (b) keep panel dimensions under 2 m in size, and (3) maintain 12-fold symmetry in the layout when possible. We understand that there is some preference for a 6 ring segmentation scheme. We investigate other panel shapes and sizes to investigate those influences on performance and cost.

The layout for 7 rings of panels leads to panel shapes which are slightly better in aspect ratio. The sizes of 6-ring segmentation are 1.83 m radial and those of 7-ring segmentation are 1.57 m radial. The 7-ring panels are all less than 1.5 m (60") in width. We expect that there will be some significant tooling expenses associated with handling panel sizes with widths over 1.5 m (60"). The availability of key machines (coating chambers, CMM machines, etc) decreases as one crosses the 1.5 m (60") boundary. For example, the availability of a coordinate measuring machine (CMM) up to 60" \times 80" is good for the Tucson and Phoenix area, but larger sizes require a specialty shop. We know of only one such shop in Phoenix and none others in all of Arizona. CMM measurements may be a good approach to verifying the final panel shapes, so this is a important example.

For a comparison in panel shapes, we have also generated a hexagonal segmentation layout in Drawing CS03. The 3 point support requirement for the panels leads one to naturally investigate panel shapes with 3-fold symmetry rather than 4-fold symmetry. Thus, we also have briefly investigated this panel shape.



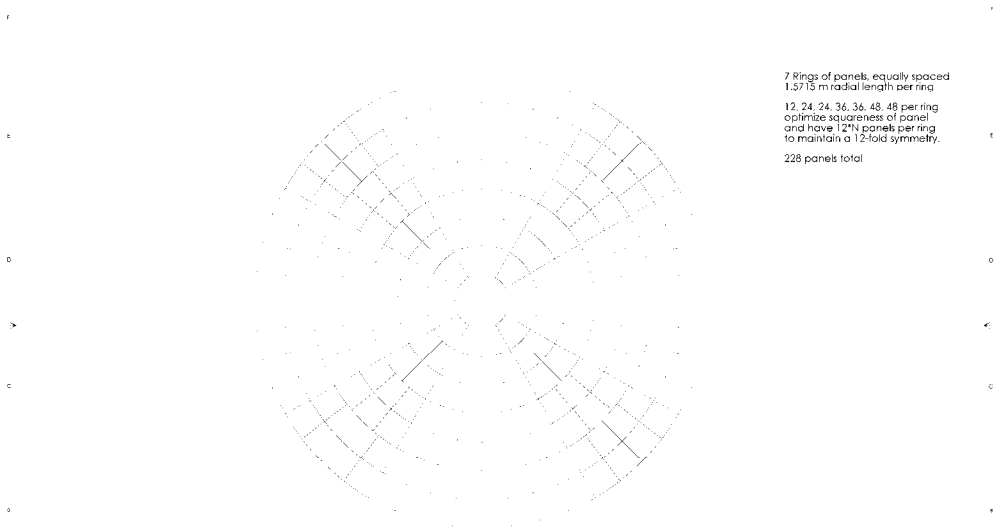
6 Rings of panels, equally spaced
 1.633 m radial length per ring
 12, 18, 24, 30, 36, 42 per ring
 (optimize squareness of panel
 and multiple of 12 if possible)
 162 panels total

6 Ring Segmentation Layout

Composite Mirror Applications

TYPE: GCA* 6 Ring Pane Layout

| | |
|-------|-----------|
| REV | 1 |
| DATE | 03/02 |
| BY | CSJ |
| CHKD | CSJ |
| SCALE | 1" = 100' |
| SHEET | 1 OF 1 |



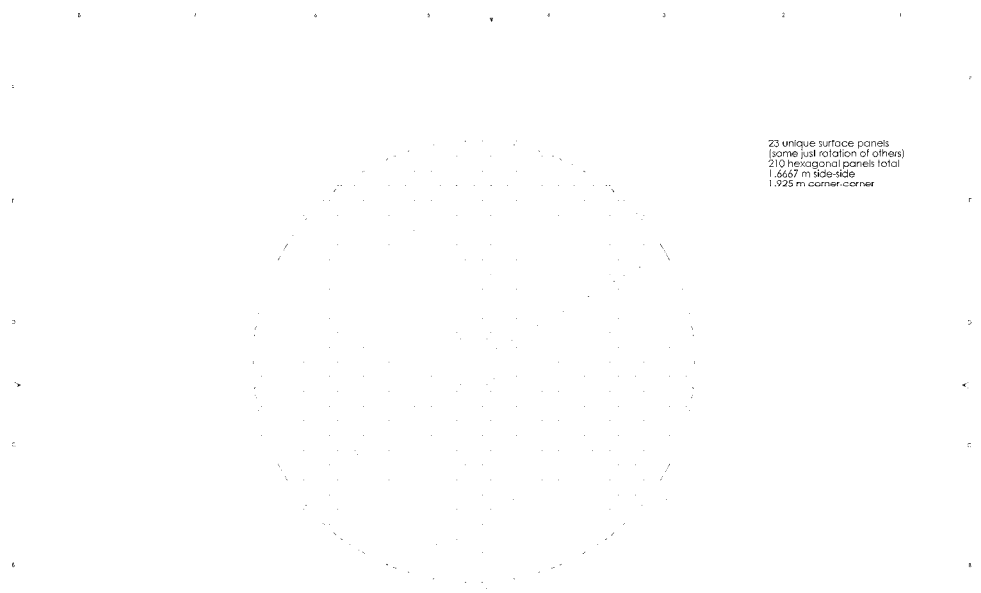
7 Rings of panels, equally spaced
 1.5715 m radial length per ring
 12, 18, 24, 30, 36, 42, 48 per ring
 optimize squareness of panel
 and have 12N panels per ring
 to maintain a 12-fold symmetry.
 228 panels total

7 Ring Segmentation Layout

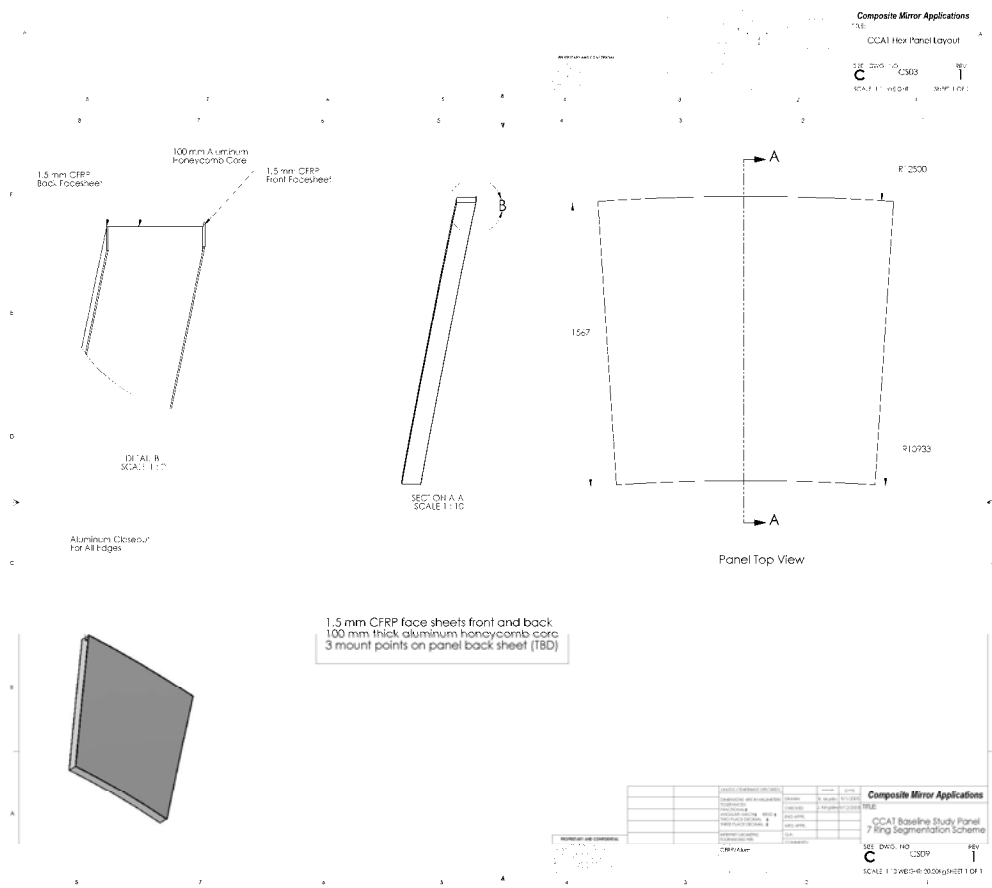
Composite Mirror Applications

TYPE: GCA* 7 Ring Pane Layout

| | |
|-------|-----------|
| REV | 1 |
| DATE | 03/02 |
| BY | CSJ |
| CHKD | CSJ |
| SCALE | 1" = 100' |
| SHEET | 1 OF 1 |



Hexagonal Segmentation Layout



14.3.5.2 Panel Design

Drawing CS09 shows our baseline panel concept for a 7-ring panel. Both the front and back surfaces of the panel will be curved and concentric. The front face sheet will be slightly larger than the core and back face sheet. This will provide close continuity of the front surface while allowing clearance for tip tilt adjustment of the individual

panels without mechanical interference with adjacent panels. Face sheets of 1.5 mm thickness will be used for both the front and rear surfaces. For the CFRP face sheets, we have chosen 63712/EX-1515 high modulus carbon fibers with a cyanate ester resin system (Bryte Technologies). This unidirectional prepreg will be layed up as a 12 ply sheet using [0/60/-60]_{2s} layup schedule. This will yield a quasi-isotropic sheet in x,y with high stiffness. Material choice is critical for the face sheets. We have chosen a high modulus fiber and one that is a pitch based fiber rather than a PAN based fiber (such as M55J or M46J). There is currently a supply shortage of PAN based fibers due to some major defense projects. The industry expects this shortage to continue for some years. We have chosen CFRP materials which we can be assured of a supply and which are cost effective for the application. In addition, we have experience with this material in other project applications

The 5056 aluminum honeycomb core will use 1/4" cell size and 0.001" foil. Aluminum 5056 is chosen over 5052 or commercial grade because of its higher stiffness and strength. This is the material of choice for critical applications in the aerospace industry (5052 is used for less critical aerospace applications). In our design, this choice will allow us to create a design with lower areal density (highest stiffness for lowest density). We will use a vented core configuration. The aluminum will be pre-treated for corrosion. Plascore and Hexcel are both suppliers of this material. A core tag of NB-101 glass reinforced film adhesive, 0.06" (Newport Composites) will be used between the aluminum core and the CFRP face sheets to prevent galvanic corrosion. The thickness of the aluminum core layer will depend on the panel size, shape and attachment points. This is discussed further in the next sections.

Our fabrication utilizes a unique fabrication of the final surface over the glass, polished mandrel. The result is a precise large scale figure accuracy and nearly 1:1 surface roughness replication. For the symmetric, optical mirrors being fabricated at CMA, there is not astigmatism or other large scale error induced during the replication process.

14.3.5.3 Mirror Coating

Candidate coatings for the mirrors are available for the panels, including aluminum and gold thin films. Over-coatings must be investigated thoroughly to yield the required reflectivity across the entire wave band of interest. SiO and SiO₂ over-coatings are likely to meet the requirements for durability and antireflection. CMA has facilities to apply vacuum sputter coating to large mirrors (chamber inside diameter of 1.8 m and 4 m long). CMA has developed considerable experience in applying coatings to glass and polymer surfaces. Aluminized coatings have been applied to several of the CMA projects discussed in Section 14.3.2.2.

14.3.6 Initial Finite Element Analysis (FEA)

14.3.6.1 Parametric Analysis

CMA does the modeling and drafting in *SolidWorks*, a 3D design software. The FEA analysis is done with *Cosmos*, a package which integrates with *SolidWorks*. A key element of the FEA analysis is using the accurate material properties. This is especially critical and difficult for composite material design projects since the CFRP material properties can be highly dependent on the layup schedule and the fabrication. The values we have used in our analysis do have basis in testing done with past projects. In addition, we are currently doing extensive materials testing on another CMA project. We have fabricated CFRP and sandwich composite samples which are currently being tested at Northern Arizona University. NRL (Naval Research Lab) is the funding agency for these studies. The results of these tests will be known in late Fall 2005 and will be used in further at a later, detailed design phase.

Our initial baseline model was a panel for the 6 ring segment configuration. We have used a panel from the 5th ring (second to outside ring). This was chosen for its near square aspect ratio. For this panel we have optimized the location of the 3 point mount. The primary deviations under gravity are the inside corners where there is only

support from single support point along the central axis. This is to be expected. We have investigated reinforcement with support beams on the back side but this is not a recommended solution. Simply making the panel thicker with the core material is the most direct means of creating a stiffer panel.

This is also the most cost effective solution consistent with mass production manufacturing. The result is that a panel can be made which meets the technical requirements. Figure 14 is a representation of the panel under gravitational distortion for a 140 mm thick core panel. These distortions would be acceptable for specified use at submm wavelength and the masked, sub-aperture observations at IR wavelengths. This panel would have an areal density of 9.75 Kg/m² (excluding mounting point hardware defined and supplied CCAT).

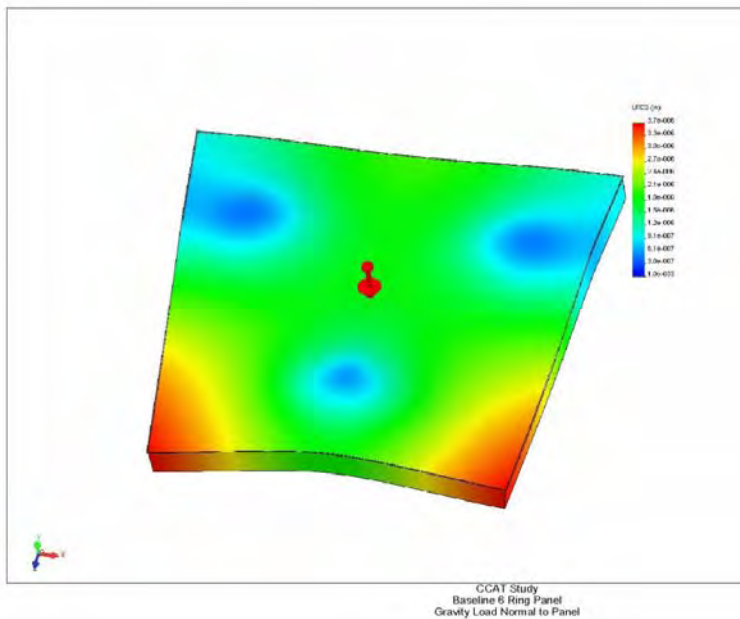


Figure 14.3.14. Deformations of 6 ring segmentation panel under gravitational loading. Panel uses 140mm thick core. Plot scale is 0 to 3.7 μm .

We do not expect thermal loading to be a great concern for our panel design. The low CTE CFRP material will control the main figure of panel surface. The z-displacement will be significant due to the aluminum core. But this can be mitigated by choosing a mounting point through the panel and closer to the front face sheet. We have been informed by the CCAT project that this concern can be ignored for now since the panel will be under active control in use. There are economical solutions to the z-direction thermal expansion if one wishes to implement them. For the current analysis, we have not taken thermal effects into consideration.

The CTE (coefficient of thermal expansion) of the CFRP sheets is similar to pyrex glass. However, CFRP has a much higher thermal conduction (between aluminum and steel in value). The result is that CFRP will thermalize

The CTE (coefficient of thermal expansion) of the CFRP sheets is similar to pyrex glass. However, CFRP has a much higher thermal conduction (between aluminum and steel in value). The result is that CFRP will thermalize

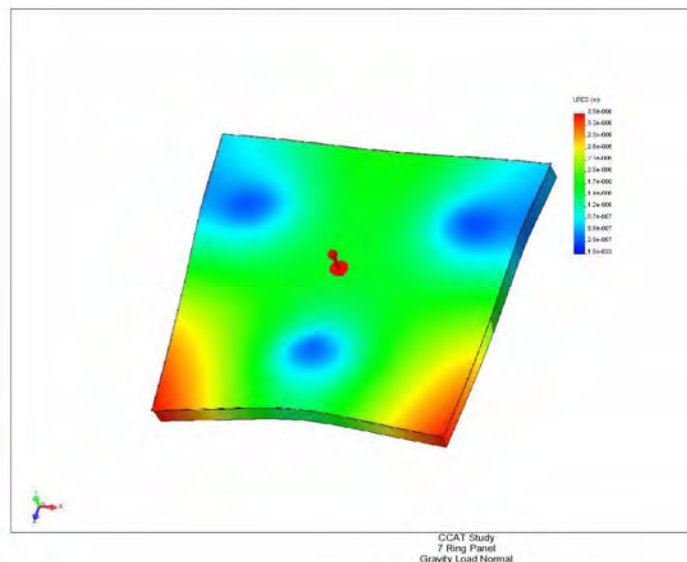


Figure 14.3.15. Deformations of 7 ring segmentation panel under gravitational loading. Panel uses 100mm thick core. Plot scale is 0 to 3.5 μm .

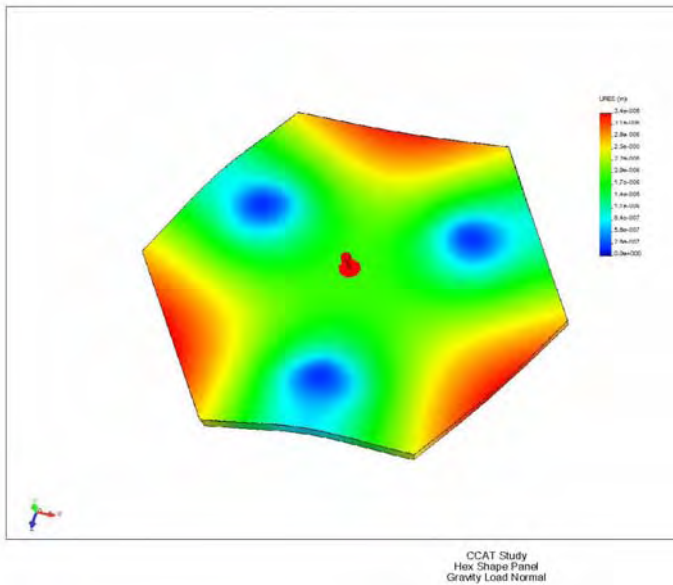


Figure 14.3.16. Deformations of hexagonal segmentation panel under gravitational loading. Panel uses 65mm thick core. Plot scale is 0 to 3.4 μm .

for that analysis since it is the most difficult case. A panel of performance similar to the baseline panel can be fabricated more easily. A core thickness of 100 mm can be used, with a resulting areal density of 8.25 kg/m^2 for the panel. Figure 15 illustrates the deformations under gravity loading.

A second alternate panel of hexagonal shape was also analyzed. The three point mount leads one to consider this shape. It is not surprising that this panel shape performs better than the trapezoidal shaped panels. To obtain the equivalent performance with this panel shape, we can reduce the panel core thickness to 65 mm. This results in an areal density of 7 Kg/m^2 . Figure 16 illustrates this panel under gravitational loading. We are aware that a hexagonal segmentation scheme is not viewed favorably because of the large number of independent panel shapes. But this issue can be mitigated by a judicious choice of molds for the fabrication shapes. We believe that we can reduce the number of molds needed for this segmentation scheme to roughly 8 shapes (of oversized molds).

To further investigate the baseline (6-ring) panel design, we have tried constraining the panel at more than 3 points. A five point mounting system would do a much better job of supporting the trapezoidal shaped panel than a 3 point mount. In such a case, the panel thickness could then be reduced to about 100mm core thickness (and 8.25 Kg/m^2 areal density) for the large, 6-ring trapezoidal panels. The support then relies on the backup structure or active control.

14.3.6.2 Design Conclusions

A panel which meets the design constraints can be fabricated for any of the segmentation sizes and configurations considered. But the size and shape of the panels do have consequences in other areas. These consequences may influence other areas of the primary mirror design.

1) By reducing the panel size using 7 rings instead of 6 rings, it is possible to reduce the areal density by more than 15%. Further, a hexagonal panel scheme could reduce the areal density by 28% over the baseline 6 ring design. This could be a significant factor for the weight on the primary mirror truss structure and the dynamical performance of that primary mirror. A 2 Kg/m^2 difference in areal density of the panels results in a total weight change of 1 metric ton for the segmented primary mirror panel system.

rapidly. With the CFRP and aluminum core panel structure, we do not expect that there will be a significant thermal gradient across the panel under normal load conditions. This fact, combined with the low CTE, results in a structure which is relatively insensitive to thermal effects. Due to these considerations, we have not done an extensive analysis of the panel under thermal (gradient) loading at this stage. This complex analysis is left for later stages in the development. We also feel that it is more effective to test a sample panel under thermal load conditions rather than only analyze the predicted behavior with computer models.

After optimizing the baseline panel, we have analyzed alternate panel sizes and shapes (the two alternate segmentation schemes). The first alternate case is a 7-ring panel. We chose the outermost panel

- 2) The costs of these various panel configurations will scale similarly to the areal density. There is a greater material cost and there is greater difficulty in fabricating a thicker panel. Additionally, the handling of larger panels requires more people (and labor cost), particularly when the total panel weight increases.
- 3) Molds for a 7-ring segmentation scheme would be of lower cost than for the 6-ring configuration due to the lower area of glass to be cast, handled, and polished.
- 4) Improved performance for the trapezoidal panel shapes can be achieved by using 4 or 5 points for support rather than 3 point supports. This is not as critical for the hexagonal panel shape. We are aware that 3 point mounts are strongly favored. There is a tradeoff between panel weight and performance versus more mounting points. The panel deformation errors are small and there would not be large stresses induced by the panels onto the backup structure in configurations of more than 3 mounting points. This is a design philosophy issue. Namely, whether to treat the backup structure and panels as an integrated structure or to treat them as separate elements (with the panels overly rigid on their own).
- 5) Costs will be higher for larger panel sizes (per area costs) because of the greater risks involved during fabrication of each panel component.
- 6) The hexagonal panel segmentation scheme offers some advantages in weight, symmetry to mounting points, and potential cost savings. It is worthwhile reviewing this option in the context of the rest of the reflector structure. It, of course, has large implications in other design areas.
- 7) The panel distortion plots (figures 14-16) indicate that it may be difficult to pick a representative position for edge sensors when trapezoidal panel shapes are used with 3-point mounts. This is understandable, given the mismatch between the panel shape and the support geometry. The hexagonal panel shape, however, offers clear choices on locating the edge sensors. This may be an important consideration if edge sensors are a key component to the primary mirror surface measuring and active control system.

| Summary of Design Conclusions | | | |
|-------------------------------|----------------------------------|----------------------------------|--------------------------------|
| Panel Segmentation Scheme | | | |
| | 6 ring trapezoidal | 7 ring trapezoidal | hexagonal |
| number of panels | 162 | 228 | 210 |
| areal density | 9.8 Kg/m ² | 8.3 Kg/m ² | 7.0 Kg/m ² |
| total reflector mass | 4740 Kg | 4010 Kg | 3390 Kg |
| shape & aspect ratio | worse | acceptable | good |
| attachments * | unnatural match to 3-point mount | unnatural match to 3-point mount | natural match to 3-point mount |
| performance | acceptable | better | better |
| cost | baseline +20% | baseline cost | baseline -10% |

* Multiple (>3) attachment points will improve performance and reduce the areal density for trapezoidal shaped panels (see text).

14.3.6.3 Error Budget

Based on our studies to date, we can estimate an error budget for our panel design as follows.

Error budget for all size scales greater than roughly 200 mm

| <u>Item</u> | <u>rms (μm)</u> |
|----------------------|--|
| Mold | 1 |
| Replication | 1.5 (<i>TDC for these panel shapes, see risk table item 1</i>) |
| Gravitational | 2 |
| Wind (5 m/s) | 1 |
| Absolute temp change | 1 |
| Thermal gradient | 0.5 |
| Aging | 0.5 |
| Total RSS | 3.1 |
| Current CCAT spec | 5 |

Error budget for sub-aperture of less than 200mm diameter

| <u>Item</u> | <u>rms (μm)</u> |
|------------------|---------------------------------------|
| Mold | 0.05 |
| Replication | 0.10 |
| Thermal gradient | 0.20 |
| Aging | 0.30 |
| Total RSS | 0.38 |

For the sub-aperture use, we have assumed that z-adjustment errors of the panels will be accounted for with active control. Thus, the errors due to gravity, wind and absolute temperature change were not relevant. For the small sub-panel aperture, there will not be a gradient across the sub-aperture. It is anticipated that active panel adjustment will be used to compensate for those errors.

CMA has extensive optical test equipment to verify the panels after manufacture. For the local surface roughness (size scales less than 10mm), a WYCO TOPO 3D surface profiler will be used on small samples produced by the same replication techniques. The large scale panel shapes and errors can be verified with a HASO32 wave front sensor (Hartmann wave front sensor manufactured by Imagine Optic) or other optical testing tools. This unit has a large dynamic range for measuring off axis surface segments. Alternately, a CMM facility can be used to verify the panel figure.

14.3.6.4 Other Design Concerns

Based on the experience of the SMT project, there is a concern about possible, large scale panel figure error during replication. The SMT panels showed a very slight warping of the panels after removal from the mandrels. These errors were small in all cases, of the order of 10-30 μm , and do not introduce hazardous residual forces or moments in the panel (or back up structure). For the SMT, this slight, large scale error is removed by supporting the panels on five or six adjustors (attached to the CFRP back-up structure) and the adjustment removes the warping error.

For a trapezoidal shaped panel, the weakest resistance to distortion will be a warping motion just like that observed in the SMT panels. It is difficult for us to computer model such warping which may result during the replication process. The CCAT specifications call for panel support at only 3 points, so removal of any potential warping is not possible with the support points. The CMA replication process is different than that used by MAN for the SMT panels. And, CMA has avoided these sorts of large scale errors during fabrication of other, large mirrors. However, the potential for slight, large scale warps is a concern for trapezoidal panels which should be explored further. We propose that a next step in development would be to fabricate a panel of similar shape using

an existing mandrel to verify the CMA process for trapezoidal shapes. We discuss this further in section 14.3.8.



Figure 14.2.17. WYCO TOPO 3D surface profiler at CMA

We have an additional concern about the backup structure to which the panels are attached. Although this is not within the scope of work for this panel study, it does have an indirect bearing on the panels and how they are deployed. We understand that the CCAT is planning on using a steel truss structure for the backup structure. This will result in deformations due to thermal loading conditions, which are difficult to characterize and predict. These will be corrected with an active surface control system (and measuring system). For the panels, there must be sufficient clearance to allow for panel re-adjustment

during operation. CCAT has allowed up to 5 mm for the panel gaps. This represents almost 1% of the reflector surface and it will allow radiation to be seen through the reflector surface. This may be a source of interference for sensitive measurements. In addition, there will be a large thermal coefficient mismatch between the CFRP panels and the steel structure which must be handled by the attachment and actuators. Any errors due to this thermal mismatch must be accounted for in the total error budget of the reflector surface.

We recommend that CCAT carefully consider the decision to use a steel backup structure. Presumably, the attraction is the lower cost. However, this will result in higher costs in other areas and may limit the ultimate performance of the surface. Virtually all other submillimeter telescope projects of the last 2 decades have used CFRP in the backup structure to handle the thermal concerns, even when the reflector surface panels were metal. A partial list of these telescopes includes the IRAM 15 m, SEST 15 m, SMT 10 m, SMA 6 m, ALMA 12 m, APEX 12 m, U. Cologne 3 m, Japan's ASPE 10 m, 10 m South Pole Telescope.

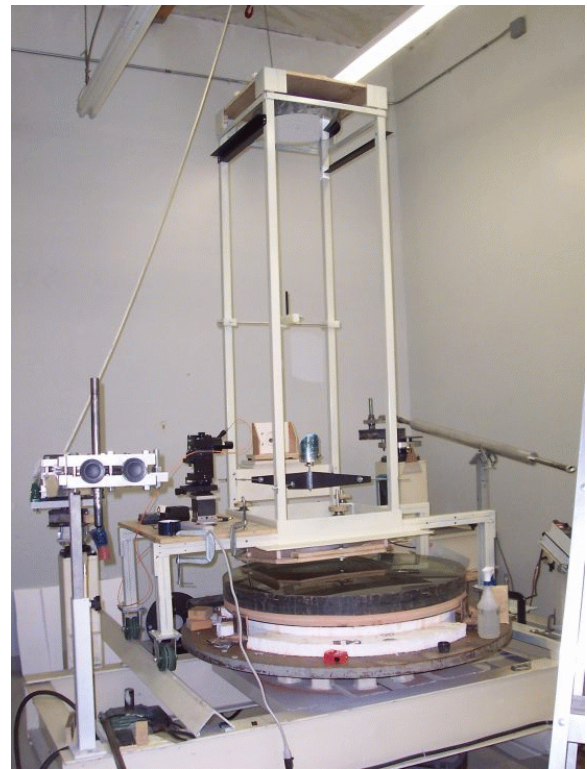
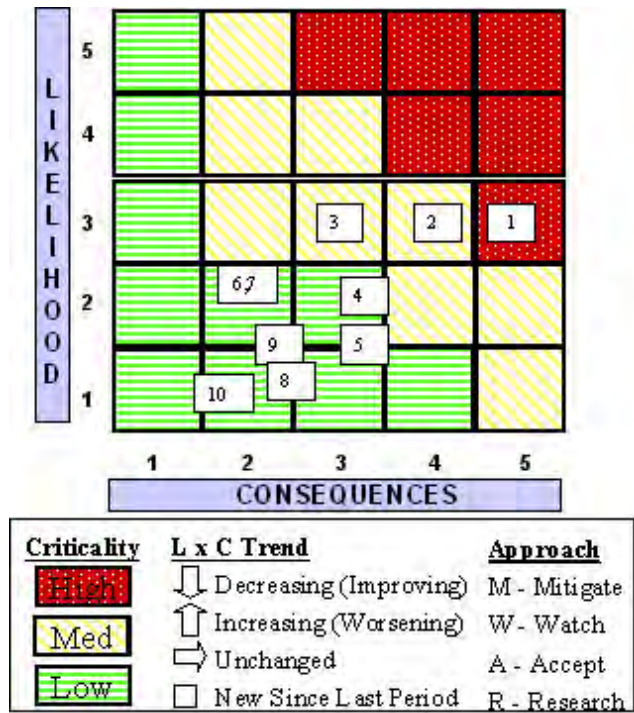


Figure 14.2.18. Optics tower for verification of 1m convex pyrex mandrel under fabrication at CMA. Haso32 wavefront sensor is being used at the test focal plane.

When the CCAT reaches the detailed design phase for the primary mirror system, it is important that there is a close interaction between the backup structure designer/fabricator and the surface panel designer/fabricator. The primary mirror system should be designed as an integrated structure if optimal performance is to be achieved.

14.3.7 Critical Risk Assessment

We tabulate the various risks in the following pages. The table below summarizes the risk in a matrix form. Items 1-3 are the main items to monitor and we have presented approaches to mitigate these risks. These steps are elaborated on in recommendations for further development.



| Level | Likelihood of Occurrence | Consequences of Occurrence |
|-------|----------------------------------|----------------------------|
| 5 | Very high, almost certain | Very high |
| 4 | High, more likely than not | High |
| 3 | Moderate, significant likelihood | Moderate |
| 2 | Low, unlikely | Low |
| 1 | Very low, very unlikely | Very low |

| Rank & Trend | Risk ID | Risk Description | Approach & Plan | Status |
|------------------------------------|---|--|---|---|
| 1 Criticality: High | <u>CMA-1</u> Planned closure: PDR | <u>Potential Trapezoidal Panel Warp using 3-point mount</u> <ul style="list-style-type: none"> • There may be some residual warp in the trapezoidal panels due to lay-up and core design; this is not easy to computer model. • Trapezoidal panels are not optimal with 3-point mounts. | Mitigate <ul style="list-style-type: none"> • Make test panels in next design phase to investigate for potential problems. • Use alternate panel shapes with 3 fold symmetry. • Or, use more attachment points so that constraint symmetry matches panel symmetry | Propose test panels using existing mandrels which are similar in shape. |
| 2 Criticality: Medium | <u>CMA-2</u> Planned closure: Complete fabrication with mandrels | <u>Handling of Glass Mandrel</u> <ul style="list-style-type: none"> • Potential for breakage in use and handling. Manufacture of mandrels is expected to be >12 month delivery and has a potential for significant delays (1 year). • Potential for damage in shipping of mandrel to panel manufacturer. | Mitigate <ul style="list-style-type: none"> • Care and adherence to procedures. • Propose alternate double replication approach which must be confirmed on a demonstrator or prototype panel. Potential cost saving on molds. | Propose evaluation panel to research alternate approach. |
| 3 Criticality: Medium | <u>CMA-3</u> Planned closure: Delivery of panels | <u>Durability of Surface</u> <ul style="list-style-type: none"> • Probable that a new coating is needed compared to past submm panel projects. Similar to glass optical coating technology. Durability not known. | Mitigate <ul style="list-style-type: none"> • Study problem with tests in the prototype phase of the panel study. • Characterize durability of coatings. | Propose testing plans for next phase. |
| 4 Criticality: Low | <u>CMA-4</u> Planned closure: Delivery of Panels | <u>Production Time and Schedule</u> <ul style="list-style-type: none"> • Delays due to delivery of mandrels and starting production. • Compressed time scale of production. | Mitigate <ul style="list-style-type: none"> • Start production as mandrels become available. • Investigate alternate double replication scheme to speed production. | Implemented in the program plan. |

| Rank & Trend | Risk ID | Risk Description | Approach & Plan | Status |
|--|---|--|---|---|
| <u>5</u> Criticality: Low | <u>CMA-5</u> Planned closure: PDR | <u>Long Term Panel Stability</u> <ul style="list-style-type: none"> Risk to be fully characterized on the surface layer. | Mitigate <ul style="list-style-type: none"> Further study at prototype stage. Additional information is being gathered on this with other, optical mirror projects at CMA. | Other CMA development projects; prototype or evaluation panel will address issue. |
| <u>6</u> Criticality: Low | <u>CMA-6</u> Planned closure: Material delivery | <u>Material Availability and Supply</u> <ul style="list-style-type: none"> Supply of CFRP has been unpredictable for some types, especially PAN based. | Mitigate <ul style="list-style-type: none"> Concentrate design on CFRP materials which are readily available and not subject to supply problems. Not a compromise in design. Plan material delivery at start of manufacture contract; payment milestones to cover material delivery. | Continue design activity. |
| <u>7</u> Criticality: Low | <u>CMA-7</u> Planned closure: Panels delivered to site & installed | <u>Shipping</u> <ul style="list-style-type: none"> Damage of final product in shipment to site (remote). This has been a problem in several previous astronomical telescope projects. | Mitigate <ul style="list-style-type: none"> Ship in batches as production is being completed and not all at once. Package container size that can be handled easily and use air freight. Keep panel sizes within limits of air freight dimensions. | Being designed into CMA program. |
| <u>8</u> Criticality: Low | <u>CMA-8</u> Planned closure: Site installation | <u>Handling and Potential Breakage in Field Use</u> <ul style="list-style-type: none"> CFRP is very robust. However, damage is possible in field since the site is both remote and high altitude where human performance is compromised. | Mitigate <ul style="list-style-type: none"> Adhere to handling procedures. On-site staff training and education. Smaller panel size would reduce risk and reduce replacement costs in case of an event. Plan for spare panels during production. | Supply handling procedure document at delivery. |

| Rank & Trend | Risk ID | Risk Description | Approach & Plan | Status |
|--|---|---|--|---|
| 9 Criticality: Low | <u>CMA-9</u> Planned closure: PDR | <u>Galvanic Corrosion</u> <ul style="list-style-type: none"> • Common concern with CFRP when it contacts metal component. | Mitigate <ul style="list-style-type: none"> • Strict adherence to procedures. • QA procedures. ISO certification underway at CMA. | In progress; design and handling procedures reflect concerns. |
| 10 Criticality: Low | <u>CMA-10</u> Planned closure: PDR | <u>CFRP/Honeycomb Core Technology</u> <ul style="list-style-type: none"> • Proven technology (SMT trapezoidal panels, 6 micron rms & 1.55m radial side). In field use for more than 1 decade. Need to scale moderately: up to 1.83m radial side (depending on layout configuration) and 1-5 micron rms. | Mitigate <ul style="list-style-type: none"> • Challenge is to optimize performance versus cost. | Working through design and analysis. |

14.3.8 Proposed Next Steps for Development Work

As a next step in the development, we recommend that a prototype (or demonstration) panel be fabricated using the same process anticipated for the CCAT panels. Ideally, this should be a full size panel with similar curvature to the anticipated CCAT surface. The cost of a mandrel for such a prototype would be too expensive. Instead, we propose to fabricate a panel using existing mandrels which we have access to. We have mandrel choices which are very close to the panel shape, size and accuracy requirements of the CCAT.

A prototype panel will do more than just verify the CMA fabrication process. The concerns about possible panel warpage can be studied. If necessary, the design could be modified to address any problems. Dynamic and static load testing of the panel will be compared with the FEA modeling and verify (and confirm) the design.

We recommend that additional, small sample panels be fabricated for environmental tests. These samples can be deployed in a test setup at the potential site in Chile. Additional samples can be subjected to accelerated aging tests. The surface layer treatment is of particular concern for this testing, not the fundamental panel structural integrity.

In light of possibly high production rate requirements, as can be anticipated for the number of outer-ring panels, additional cost saving measures are possible. A alternate fabrication method using double replication is possible. In this scheme, secondary mandrels (for fabrication) are made from an original glass master. The glass is then the final panel shape (concave) rather than the mating surface (convex). The secondary (replicated) mandrels are CFRP tools, and more than one set can be made from the master. There is the additional benefit that the master surface is easier to test and polish since it is now concave. This fabrication scheme would have to be tested for the panel accuracy required by CCAT before it could be used for fabrication. It would require a moderate, short development program to verify the feasibility.

14.3.9 References

- Baars, J.W.M., Hooghoudt, B.G., Mezger, P.G., & de Jonge, M.J., 1987, *A&A*, **175**, 319.
- Baars, J.W.M., Martin, R.N., Mangum, J.G., McMullin, J.P., and Peters, W.L., 1999, *Pub. Astron Soc Pac*, **111**, 627.
- Chen, P.C., Bowers, C.W., Content, D.A., Marzouk, M. & Romeo, R.C. “Advances In Very Lightweight Composite Mirror Technology”, *Optical Engineering*, 39(9), 2320-2329, September 2000.
- Martin, R.N., Kingsley, J S., 2000, *10-m Platform Array Telescope Design for the AMIBA Project*, Proc. SPIE Vol. 4015, p. 552-558, Radio Telescopes; Harvey R. Butcher; Ed.
- Philippe A. Raffin, Robert N. Martin, Yau-De Huang, Ferdinand Patt, Robert C. Romeo, Ming-Tang Chen, Jeffrey S. Kingsley, 2004, *CFRP Platform and Hexapod Mount for the Array of Microwave Background Anisotropy (AMiBA)*, Proc. SPIE, Vol. 5495, p. 159-167, Astronomical Structures and Mechanisms Technology; Joseph Antebi, Dietrich Lemke; Eds.
- Romeo, R.C., Meinel, A.B., Meinel, M.P., Chen, P.C., “Ultra-lightweight and Hyper-Thin Rollable Primary Mirror for Space Telescopes”, *Astronomical Telescopes and Instrumentation 2000, Large Space Optics*, SPIE, Munich, March 2000.
- Romeo, R.C., Chen, P.C., “Ultra-Lightweight 4-meter segmented composite mirrors for extremely large telescopes”, *Astronomical Telescopes and Instrumentation 2002*, SPIE Highly Innovative Space Telescope Concepts Waikoloa, HI. August 2002.
- Romeo, R.C., Chen, P.C. “CFRP composite thin-shelled mirrors for the future space telescopes”, *Astronomical Telescopes and Instrumentation*, 2002, SPIE Highly Innovative Space Telescope Concepts Waikoloa, HI, August 2002.
- Ruze, J. 1966, *Proc. IEEE*, **54**, 633.
- Stark, A.A., et al., 2001, *Pub of the Astron Soc Pacific*, **113**, 567.
- Tong, C.E., Kawamura, J., Hunter, T.R., Papa, C., Blundell, R., Smith, M., Patt, F., Goltsman, G., & Gershenzon, G., 2000, Proc. 11th Space THz Symposium, Ann Arbor, MI, pp. 49-59.

14.4 Mandrel Manufacturing

Report prepared by Goodrich



14.4.1 Introduction

The CCAT telescope is a 25 m Ritchey-Chrétien telescope that will operate at sub-millimeter wavelengths. The proposed design for the primary mirror is a segmented system of six concentric rings for which mandrels are used in the replication of each optical segment.

Thomas Sebring of Cornell University requested that Goodrich supply the CCAT team with a rough order of magnitude (ROM) cost estimate for eight Primary Mirror (PM) convex mandrels (two mandrels for each outer ring and one mandrel for each of the four inner rings). Goodrich is pleased to respond to the RFI, specifically as it pertains to the grinding, polishing, testing and delivery of the mandrels as specified in this document.

14.4.2 Scope

Included in this ROM cost estimate response is 1.) The assumption on which the estimate was generated, 2.) The nominal configuration of mandrel and support mounts, 3.) An overview of the fabrication and testing process, and 5.) Cost and schedule.

14.4.3 Assumptions

In the assessment of cost and schedule for the mandrels the following assumptions and specifications were used.

- The primary mirror (PM) is a 25 m f/0.6 parent, paraboloid
- Six mandrels are defined by equal width annular rings. (There are two mandrels for each of the outer two rings.)
- The PM segments are keystone shaped and each fits within a 2.2 by 2.2 m square. The mandrels each fit within a square 2.5 by 2.5 m square with approximately 0.2 m thickness (plano-convex)
- Mandrel material is a borosilicate glass provided as customer furnished material (CFM) and generated to a best fit asphere of 30 μm .
- Mandrels are tested and delivered on three kinematic points coupling them to a support/handling fixture.
- The required quality is tested at room temperature
- Each mandrel is polished to 1 μm , rms (spatial sampling TBD) and a specular, having a 3 μm microroughness.

14.4.4 Nominal Configuration and Concept View

Each mandrel is nominally 4500 lbs. Each unit is kinematically supported on three points (Figure 14.4.1) for test, fabrication, and during the replication process. Note the self weight deflection (estimated sag) of a 2.5 by 0.2 m disk is about 7 μm peak-to-valley and 1.6 μm , rms. The stress on the points is less than 100 psi.



Figure 14.4.1. Mandrel on 3-Point Supports plus Mounting Plate

Handling and transportation is performed with the support plate.

14.4.5 Process for fabrication and testing

The following process flow is routinely employed on other large optics in Goodrich and will be repeated for the CCAT mandrels.

1. Receive the rough mandrel in its re-useable shipping container, inspect and prep for 3 point mount.
2. Install the mandrel on the 3-point mount.
3. Transport the mandrel to the test station
4. Perform initial measurements
5. Transport the mandrel to fabrication station
6. Grind with computer controlled system (Arboga)
7. Polish specular surface
8. Transport to test station
9. Perform measurements
10. Repeat steps 5 through 9 until convergence to desired surface requirements

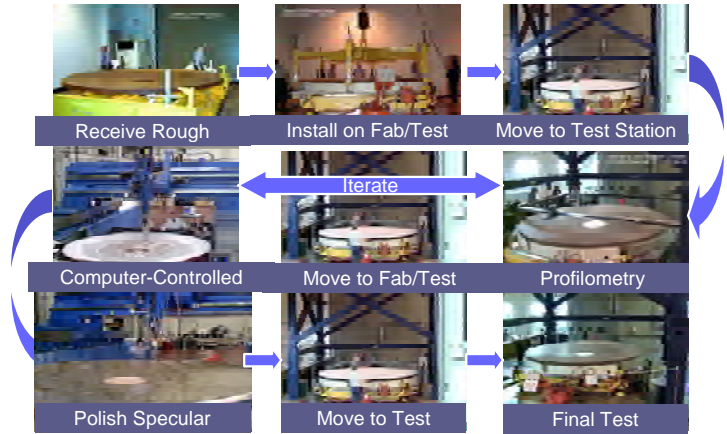


Figure 14.4.2 displays a pictorial version of the process flow with the SOAR mirror.

Figure 14.4.2. Process for Fabrication and Test of Large Optics

Rapid convergence and measurement turn-around time in the test and fabrication process is the key driver to cost and schedule. Essential to rapid convergence in the manufacturing process are the efficient and accurate measurements of a large convex surface. The measurement system must also provide for adequate spatial sampling. Goodrich has experience with an internally-developed large profilometer (Surfitek) as well as experience with commercial profilometers. As example of profilometry measurement of a large optic, figure 3 shows surface error of the SOAR M1 delivered from Corning, as measured by the Goodrich Surefitek profilometer.

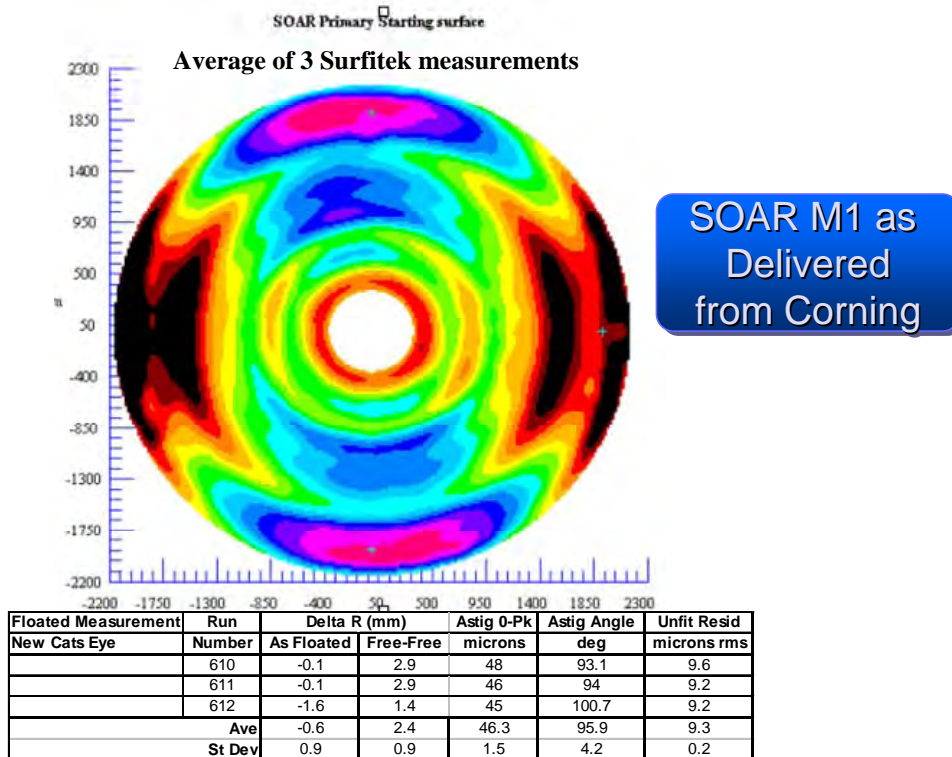


Figure 14.4.3. Surefitek Measurements of the SOAR Primary as delivered from Corning

The actual optical surfacing convergence time for the 4 m SOAR M1 down to 1 micron rms, was consistent with the predicted timeline as displayed in Figure 14.4.4. We have used these optical fabrication models to estimate the cost and schedule for fabrication the CCAT Mandrels. We have examined two alternatives; use of our existing Surefitek profilometer and purchase and use of larger versions of commercial profilometers we routinely use on smaller optics. The advantage of this latter approach is the more rapid measurement and data reduction timelines as well as more accurate and deterministic data. Our schedule estimate uses the latter scenario.

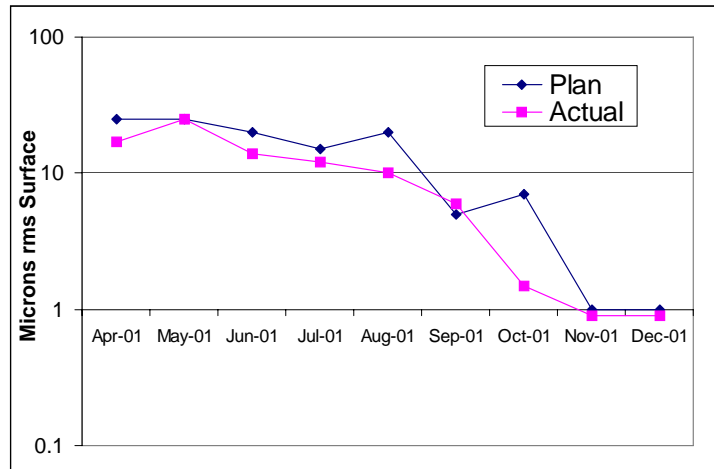


Figure 14.4.4. Predicted and Actual Optical Surfacing Convergence

While the profilometer verifies the convex surface, subaperture sampling with testplates and the use of the Wyco give information on the surface microroughness.

Optical surfacing of the mandrels will be performed with the existing Arboga 5-axis CNC machine which was also used for the SOAR PM. (The SOAR mirror was ultimately ground and shined to 30 Angstroms surface roughness.)

In summary, Goodrich’s production experience and large optic facility make it fully qualified to complete the manufacturing of the CCAT mandrels in a predictable controlled manner.

14.5 Primary Panel Alignment Positioning Systems

14.5.1 Overview

The concept for kinematic segments mounting suggests a simple way to react panel lateral loads is with the actuators rather than an independent mechanism such as used with multiple point whiffletree mirror supports (Keck, HET, SALT). Preliminary error budgeting (Section 9) and the design tolerance analysis (Section 8) suggested the likely required precision and accuracy of actuators. The following draft specification was developed and multiple vendors were contacted. Two vendors appeared likely to be able to meet the requirements, Danaher Precision Motion of Hudson, NH, and Polytec PI of Auburn, MA. Visits were made to both vendors. Although no documentation was received from Danaher, we believe they would be willing to bid on this system. Polytec PI, who is well known to the astronomical community, provided briefings (Section 14.6) that provide conceptual application of a near-stock actuator and provide data on actual tests under lateral and axial load conditions performed without cost to CCAT. The conclusion we reach is the actuators are likely to be available from at least one and probably more vendors as a turn-key system including actuators, wiring, electronics, and controls. The performance appears to meet our initial criteria and this does not appear to be a high risk area of CCAT Design.

14.5.2 Primary Mirror Actuator System (PMAS) Draft Specification

14.5.2.1 Introduction

This section provides initial specifications for mirror panel actuators for the CCAT. The specifications are provided to support concept design by contractors who may provide the actuator subsystem for the Project. These specifications are subject to change, and are intended as a working baseline for discussion and evolutionary change.

14.5.2.2 Background

The CCAT employs a 25 m diameter primary mirror comprised of multiple replicated segments. The segments are specified to be self supporting, meeting the dimensional requirements for surface figure over the full range of gravity variation (from zenith to 15 degrees above the horizon) when supported on three points. These three points are anticipated to be bipod flexures, design such that they introduce minimal moment loads into the facesheets. The bipods in turn, are attached to the Primary Mirror Actuators that are installed in the Primary Mirror Truss. The Primary Mirror Truss is a steel space frame, anticipated to be similar to the Mero brand truss employed in the Hobby Eberly Telescope. This truss is anticipated to have three nodes per panel on the top surface and actuators are anticipated to mount through these top surface nodes.

The Actuators must include a coarse adjustment for initial alignment and positioning of segments. Segments are arranged in six concentric rings and all segments within each ring are identical. A total of 165 panels are currently anticipated. Destination commands for each actuator will be provided to the PMAS by the CCAT Telescope Control System (TCS) via fast Ethernet connection.

14.5.2.3 Scope

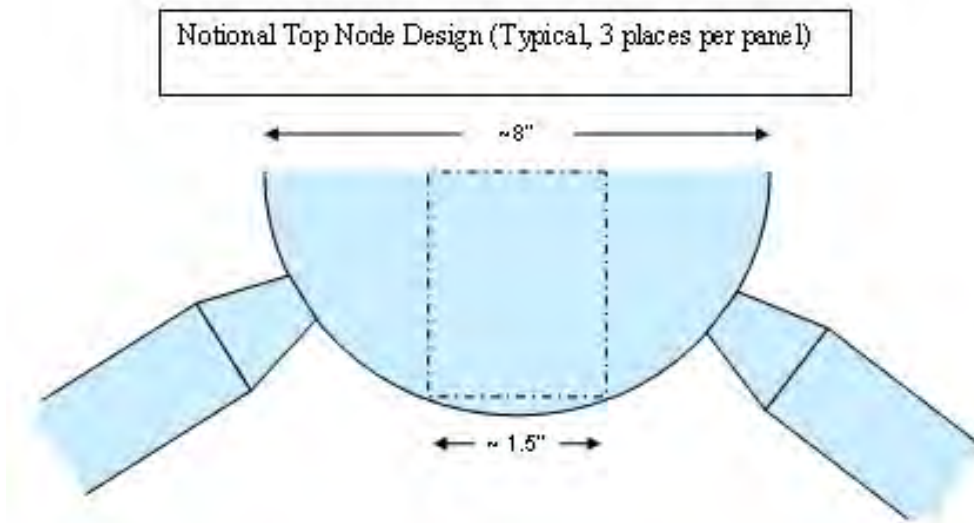
The PMAS consists of the actuators, cabling, electronics, and PC based system controller necessary to effect actuation of the entire suite of actuators. Commands for position are provided to the system as is power. All other required elements are considered part of the PMAS.

14.5.2.4 Requirements

The following are requirements for actuators:

- Mechanical:
 - Length: Not more than 50 cm overall.
 - Diameter: Not more than 25 cm (protrusions possible but must not interfere with truss)

- Weight: Not more than 10 kg/actuator
- Mounting: Anticipated to be mounted through holes in top surface nodes of the primary mirror truss. Diameter of these through holes is anticipated not to exceed 4 cm. A diagram is provided showing a notional hemispherical top layer truss forged steel node joint. The region illustrated with a dotted line shows the area available for a through hole. The manufacturer is permitted to define the nature of this hole and the top and bottom surfaces of the node in the region of the hole. For example, the hole might be threaded to facilitate coarse adjustment.



- Coarse Adjustment: Actuators will provide >20 mm of total manual adjustment range using simple hand tools. This is intended to accommodate the full range of possible variation in truss top node location and panel front surface to panel mounting location dimensional variation.
- Actuator Range of Motion: Actuators will be capable of >10mm total range of travel under motorized computer control.
- Actuator Minimum Step Size: Actuators will be capable of a minimum step of 0.1 μm anywhere in the controlled range of travel.
- Maximum Lateral Motion: Actuators shall exhibit not more than 2 μm of lateral movement of panels when the telescope is moved from the zenith to horizon pointing direction.
- Actuator Stiffness: > 10^6 lbs/in (TBD to resist wind buffeting)
- Actuator Loads:
- Axial Loads: Actuators will each support 15 kg in panel weight axially when the telescope is in the zenith pointing direction.
- Lateral Loads: Actuators will each support 15 kg panel weight in the lateral direction when the telescope is in the horizon pointing direction.
- Electrical & Controls:
 - Actuator System will operate from provided 60 cycle 120 VAC power and include any required power conditioning and transforming equipment.
 - Actuator System will include all electronics, wiring, controls, and software necessary for operation.
 - Cable Lengths: Cable lengths for actuators will be as required.
 - Termination: High reliability quick disconnect termination will be provided for all cabling required to connect actuators and other electrical/electronic modules. All cables will be provided terminated to the correct lengths.
 - Electronics Modules: As required, electronics modules may be mounted within the PM truss.

- Control Computer: Control computer will be a PC running Linux OS. Control software will be National Instruments Labview. The control computer will be located on the telescope azimuth stage and connect to the actuator network through the elevation cable wrap.
- Connection to Telescope Control System: Connection to the CCAT Telescope Control System will be via fast Ethernet.
- Position Commands: The actuator system is not responsible for calculation of any actuator commands, but is responsible for effecting commands provided by the Telescope Control System.
- Actuator Data: The actuator system is responsible for reporting to the TCS the following data: Actuator position via local position encoders provided in each actuator, Commanded vs. Achieved position for all actuators following commanded position changes, results from comprehensive system self-check routines.
- Life Cycle
 - MTBF: 20×10^6 actuations over 10 years (1 position change/cycle \times 1 cycle/10 seconds \times 60sec/min \times 60 min/hour \times 16 hours/day \times 365 days/year \times 10 years = 21,024,000)
- Quantity of Actuators

The system shall be capable of providing and controlling between 500 and 750 actuators, the actual number TBD prior to detailed design.

14.5.2.5 Comments on Design Approach

Designs that use commercially available components to meet all requirements are preferred as are approaches that minimize part count, machining operations, and complicated assembly and adjustment processes.

14.6 Primary Segment Actuators

Report prepared by Polytec PI

14.6.1 Introduction

Polytec PI has undertaken a first look and some preliminary testing of actuators for CCAT. The major requirements are the ability for fine actuation and the ability to accommodate side loads implied by horizon pointing of the telescope. The following is a brief report on a standard product which meets a substantial fraction of the requirements imposed by CCAT and is likely to fully meet all requirements with minimum modifications.

14.6.2 Background and Corporate History

PI has provided world class solutions for industry, OEM and research for several decades. PI (Physik Instrumente) L.P., is the U.S. operation of Physik Instrumente (PI) GmbH & Co. KG. The PI family of companies employs more than 350 people world wide. PI is known throughout the high-tech world for its leadership in the design and manufacture of Nanometer-Level Motion Control Products, Piezo Ceramics and NanoActuators, Hexapod 6DOF Positioning Systems and Micro Robots. ISO 9001 certified since 1994. PI (Physik Instrumente) L.P. Head Office (Auburn, MA)



The actuator proposed is a modification based on a standard model. The proposed actuator is designated PI (Physik Instrumente) M-235K High Load Linear Actuator

- Design derived from PI standard product M-235 DC Servomotor Linear Actuator (used on SALT telescope primary mirror segments)
- M-235K design is optimized for the higher axial and radial loads of CCAT requirements
- M235K design utilizes larger fine pitch precision ball screw and more robust linear roller bearings actuator rod guides for high axial and radial load capacity
- High MTBF design
- Design also incorporates ball bearing actuator rod detrotator mechanism
- General Specifications of the standard product M-235 actuator are as follows:
 - Diameter - 35 mm
 - Length – 200 mm
 - Motorized Stroke – 25 mm
 - Unidirectional resolution - 0.13 μm (0.1 μm can be achieved with linear scale
 - encoder as opposed to motor mounted encoder)
 - Axial Load Capacity - 40 kg
 - Lateral Load Capacity - 15 kg
 - Manual adjustment 20 mm



- DC servo-motor with rotary encoder
- 0.016 $\mu\text{m}/\text{count}$ design resolution at encoder
- 29.6:1 Zero Backlash Gearbox
- Ultra-low-friction, heavy-duty, high-speed ballscrew construction, 1mm/rev pitch
- Non-rotating shaft
- Low-friction guidance ball bearings for shaft extension
- Scalable Design
- Modified M-235K Actuator includes the following modifications:
 - DC servo-motor with linear glass scale encoder
 - 0.020 $\mu\text{m}/\text{count}$ design resolution at encoder
 - 29.6:1 Zero Backlash Gearbox
 - Ultra-low-friction, heavy-duty, high-speed ballscrew construction, 1mm/rev pitch
 - Non-rotating shaft
 - Low-friction guidance
 - ball bearings for shaft extension
 - 200 lb axial and radial load capacity
 - Testing to start in Q1 2006

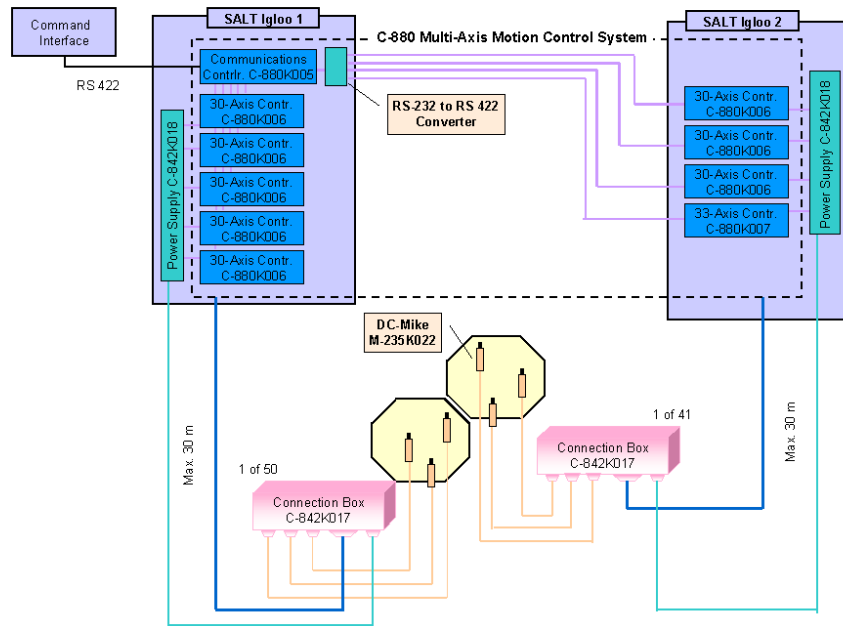
14.6.3 M235 Actuator Features - Summary

| Feature | Typical competitor | PI | Benefit |
|----------------------|------------------------------------|--|--|
| Shaft type | Rotating or non-rotating | Non-rotating | Addresses torque which confers unwanted motion to load. Facilitates sophisticated couplings including push-pull |
| Drive type | Leadscrew driving shaft in bushing | Ballscrew driving shaft in rolling bearing | Low friction design optimizes minimum-incremental-motion (resolution), bi-directional repeatability, reversal error, lifetime, stability including creep from lubricant flow, duty cycle, top and bottom speeds, binding |
| Encoder interface | Single-ended | Differential | Facilitates longer cables and noise immunity |
| Switches integrated | None, or limits only | Limit and Reference switches | Limit switches protect mechanism; Hall effect reference switch also indicates home direction upon power up |
| Intended load | Spring-loaded | Push-pull or spring-loaded (preload not needed) | PI actuators pull as well as they push; require no external spring preload to reduce backlash. <i>Data presented here</i> includes springless unloaded stage (magnetically coupled to actuator tip)—the most severe possible configuration and highly loaded actuator data to simulate in telescope loading. |
| Astronomy experience | Little to none | Extensive | Decades of successful applications like SALT yield deep engineering understanding and proven products |

14.6.4 Actuator Control System

Polytec proposes to provide a complete turnkey system including all actuators, cabling, electronics, and software required to provide full operational capability. The control architecture proposed is:

- Proposed system similar to SALT using standard product C-880 Controllers configured for 30 axes each.
- Fast Ethernet interface as required by CCAT
- Actuators individually addressable
- Connection/ line driver boxes mounted on mirror support trusses for each group of 3 actuators.



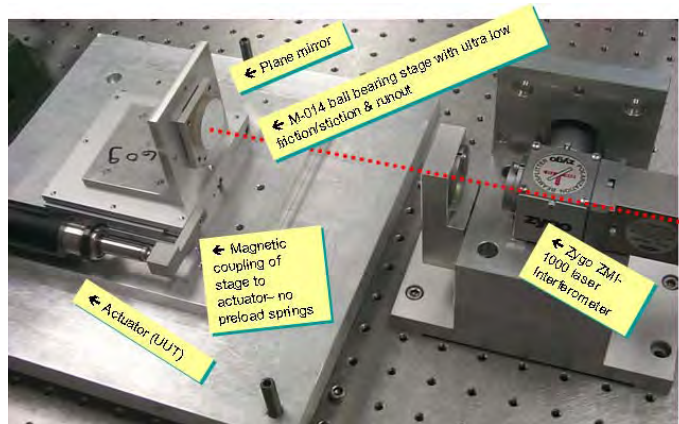
14.6.5 Actuator Testing Program

In order to provide an initial demonstration of the ability of the proposed actuator system to meet CCAT requirements, Polytec PI performed laboratory testing of an actuator similar in construction to that proposed. The following section describes this test process and the results obtained:

14.6.5.1 Test Set Up

The following test setup was used:

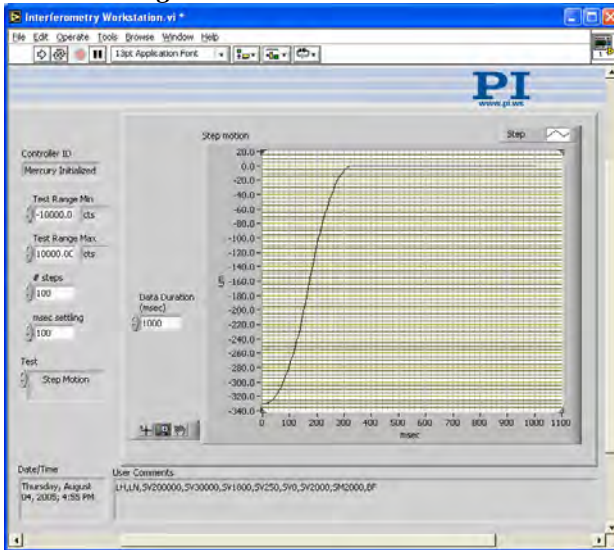
- Zygo ZMI-1000 Plane-mirror Interferometer
- M-235.5DG Actuator driving M-014.00 ball-bearing stage on isolation table
 - Magnetically preloaded bearings for ultra-low friction, runout
 - Magnetic coupling to actuator--no spring preload against actuator
 - Plus 10 & 20 lb force axial load
 - Plus 10 & 50 lb side loading
- GPIB & RS-232 interfacing
- Multifunction interferometry workstation constructed in LabVIEW
 - Step/settle
 - Minimum incremental motion
 - Backlash
 - Bi-directional repeatability
 - Classical “beehive” test
 - Tougher fully-randomized test



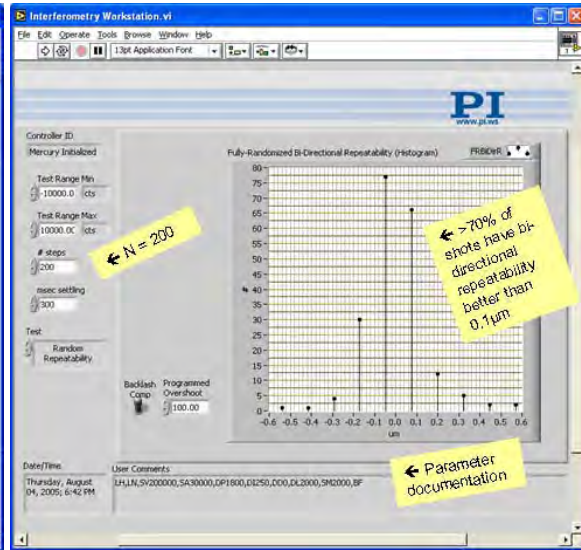
14.6.5.2 Step Motion Test

- C-862 “Mercury” controller used
 - Based on popular National Semiconductor LM629 PID servo chip
 - Robust and serviceable but by no means PI’s best controller.
 - Results presented here should be readily reproducible with any good controller.
 - Integrated amplifier drives motor with PWM

- RS-232 connectivity with networkability, macro capability
- **Results/Interpretation: Good classical PID step/settle performance seen in interferometry capture using nominal settings**



Step Motion Test



Bi-directional Repeatability - Unloaded

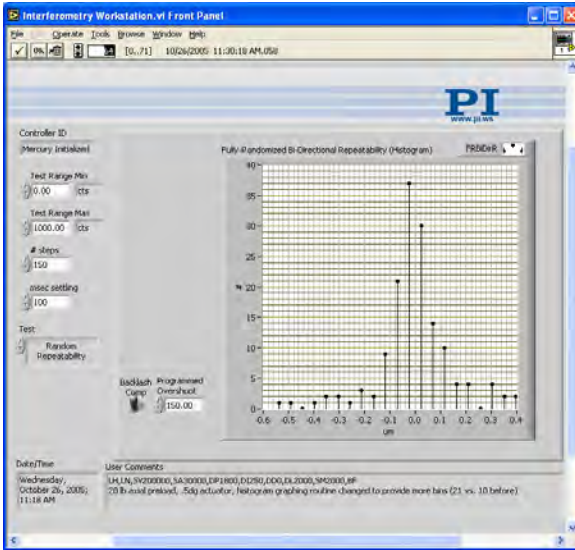
14.6.5.3 Bi-directional Repeatability – Unloaded – Fully Randomized

- **Toughest test of motion performance**
 - Move to random position
 - Read interferometer
 - Move to another random position
 - Return
 - Take reading; calculate difference
 - Repeat N times, randomizing each time
 - Plot statistics
- Note each data point includes a direction reversal
- Programmed-overshoot eliminates backlash
- Zero-motion run shows $<0.1\mu\text{m}$ noise floor
- **Results/interpretation:**
 - **Histogram FWHM $<0.2\mu\text{m}$,**
 - **$>70\%$ better than $0.1\mu\text{m}$**
 - **Backlash is consistent and compensatable**

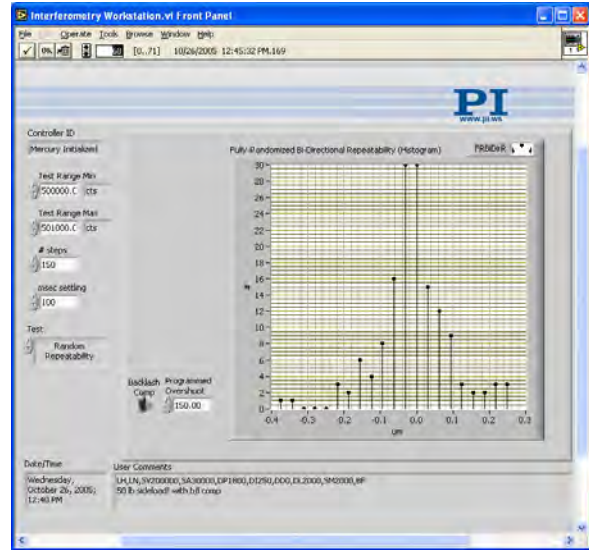
14.6.5.4 Bi-directional Repeatability = 20 lb Axial Load – Fully Randomized

- **Same test of motion performance**
 - Move to random position
 - Read interferometer
 - Move to another random position
 - Return
 - Take reading; calculate difference
 - Repeat N times, randomizing each time
 - Plot statistics
- Note each data point includes a direction reversal
- Programmed-overshoot eliminates backlash
- Zero-motion run shows $<0.1\mu\text{m}$ noise floor
- **Loaded results/interpretation:**

- *Histogram still shows FWHM <0.2μm,*
- *And >70% better than 0.1um*
- *Backlash is consistent and compensatable with high axial load of 20lbs*



Bi-directional Repeatability – 20 lb Axial Load



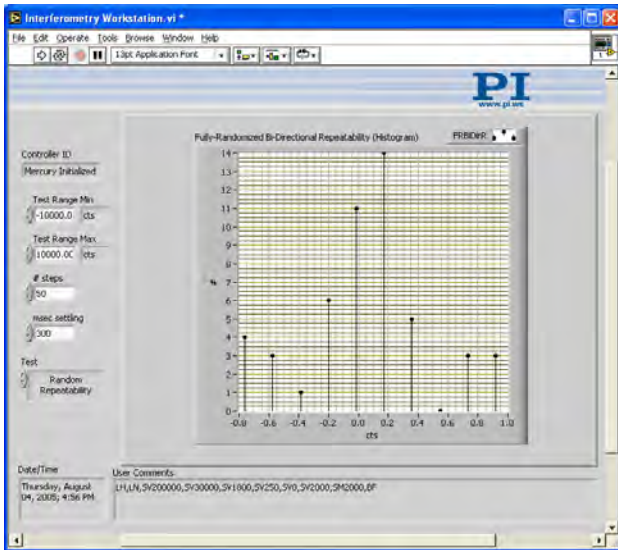
Bi-directional Repeatability – 50 lb Radial Load

14.6.5.5 Bi-directional Repeatability – 50 lb radial load – Fully Randomized

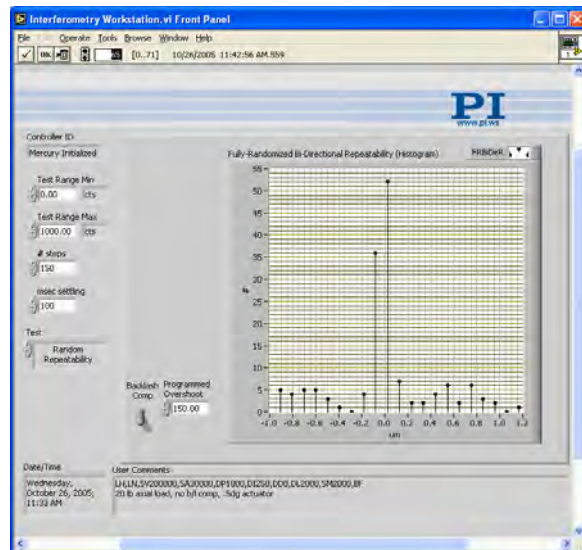
- *Same test of motion performance*
 - Move to random position
 - Read interferometer
 - Move to another random position
 - Return
 - Take reading; calculate difference
 - Repeat N times, randomizing each time
 - Plot statistics
- Note each data point includes a direction reversal
- Programmed-overshoot eliminates backlash
- Zero-motion run shows <0.1um noise floor
- **High radial loaded results/interpretation:**
 - *Histogram still shows FWHM <0.2μm,*
 - *And >70% better than 0.1um*
 - *Backlash is consistent and compensatable with high radial load of 50lbs*

14.6.5.6 Repeatability without Backlash Compensation – Unloaded

- Same test, N=50, backlash compensation turned off to reveal raw mechanical performance
- **Results/Interpretation:**
 - *Data demonstrates submicron backlash*



Repeatability without backlash compensation – unloaded



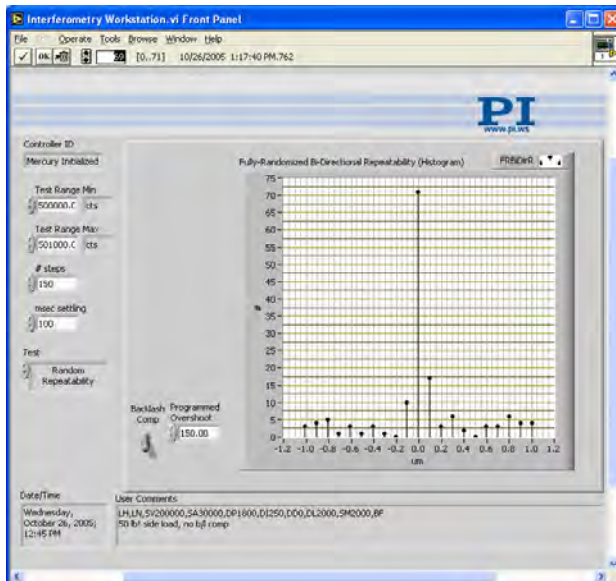
Repeatability without backlash compensation – loaded 20 lb axial

14.6.5.7 Repeatability without Backlash Compensation – Loaded 20 lb Radially

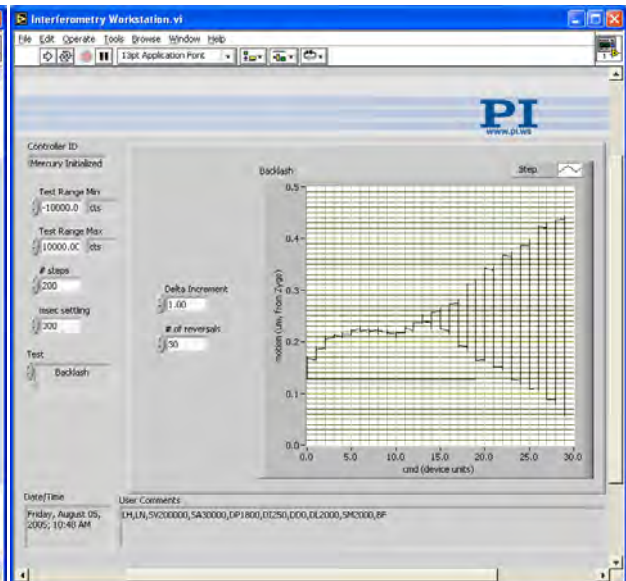
- Same test, N=150, backlash compensation turned off to reveal raw mechanical performance
- **Results/Interpretation:**
 - *Data demonstrates submicron backlash*

14.6.5.8 Repeatability without Backlash Compensation – Loaded 50 lb Radially

- Same test, N=150, backlash compensation turned off to reveal raw mechanical performance
- **Results/Interpretation:**
 - *Data demonstrates submicron backlash*



Repeatability without backlash compensation – loaded 50 lb radially



Minimum Incremental Motion & Backlash

14.6.5.9 Minimum Incremental Motion & Backlash

- Gradually increasing step size with back-and-forth motion reveals true backlash

- **Results/Interpretation:**

- *Backlash ~13-15 counts (@ 0.016 μ m/ct)*

14.6.6 Summary

Polytec PI has provided a first indication that a near stock actuator can meet requirements for CCAT. We have provided an initial cost estimate for a turnkey system including all cabling, electronics, and actuators. A summary of the performance and characteristics of our proposed actuators is as follows:

- High MTBF, low-friction design yields superb motion performance with high relative loads.
- Field-proven design has excelled in professional astronomical active-optic applications and industrial OEM product integrations
- Non-rotating tip facilitate rigid, stable coupling to mechanical interfaces
- True 0.1 μ m motion transducers even in push-pull applications
- Exotic motion controllers or technologies not required for optimum performance
- Compatible with simple, classical programmatic backlash-compensation techniques
- Design has been scaled for higher loads with equivalent motion performance

15 CCAT Telescope Alignment and Guiding

15.1 Introduction

One of the more challenging aspects of the Cornell Caltech Atacama Telescope is the control of active optics to meet image quality requirements. There are two components to this problem, measurement for calibration of optics alignment errors and maintenance alignment sensing and control. These capabilities are provided by a suite of subsystems selected from technologies implemented on current radio and optical telescopes and from emerging technologies. Taken as a group they provide confidence a feasible approach to obtaining and maintaining required image quality as related to mirror positioning can be developed. The challenging tracking requirements suggest that some method of telescope guiding is also important.

15.1.1 Background

For current segmented optical and radio telescopes initial segment and the overall telescope is accomplished in several ways. Initial alignment is done mechanically in most cases. This is followed by star stacking or Hartmann screen testing for optical telescopes and by photogrammetry for radio telescopes. Final alignment is accomplished by center of curvature based Hartmann testing or shearing interferometry for the spherical primary optical telescopes (HET and SALT) and by shearing interferometry, curvature sensing, or phase diversity approaches for Keck. Radio telescopes have typically used holography or interferometry using either distant ground based sources, artificial satellite sources, or astronomical sources such as distant planets. These techniques have varied in success. Typically they are time consuming, noisy, and labor intensive in the early days of operation of new telescopes but mature so they can be used routinely and can be accomplished in a few hours or less.

During operation active segmented telescopes control segment position and M1/M2 alignment via a variety of ways that must not interfere with observing. The segmented optical telescopes use edge sensors based on either capacitance or inductance to measure segment to segment piston displacement. Depending on the telescope and type of sensor, they may or may not be able to measure dihedral angle between segments or segment-to-segment in plane gap changes. Actively controlled radio telescopes have used lookup tables to control segment position based on calibration runs over variations in gravity driven by telescope elevation angle. Others have also used distributed temperature measurements and modeling to derive deformations of the front surface and calculate the correct actuator positions to correct them. This prior work provides CCAT with a substantial toolbox of segmented array control options. We have also added some additional ideas, including use of absolute distance measuring interferometers being developed by JPL for large segmented mirrors in space and the possible use of opto-electronic devices as edge sensors.

15.1.2 Scope

Alignment for CCAT encompasses all stages of mirror and telescope alignment from initial installation through operation. It includes mechanical gages, calibration sensors, alignment maintenance sensors, and wavefront sensing guider/s as well as wiring and controls necessary to acquire data, calculate responses, and transmit the appropriate commands through the Telescope Control System.

15.1.3 Introduction to Subsystems

The following subsystems have been considered and studied with respect to concept and feasibility for this study.

15.1.3.1 Initial Segment Mechanical Alignment

Assembly of the primary mirror will be conducted from the center out and segments will be fabricated and arrive in this order. This will permit initial operations and debug at partial stages of completion with complete apertures without gaps. Installation of the first ring of panels will likely be a bit fussy, and we anticipate initial alignment using gauging tools such as a Hamar laser profilometer that can provide precisions to better than 30 μm over the entire array. As successive panels are added a mechanical spherometer can provide additional edge to edge piston

gauging down to the 1 μm level with the dihedral angle well controlled via the laser profilometer. This should get panels within range of the calibration sensor. Edge sensors will be installed as panels are added to the array.

15.1.3.2 Initial M1/M2 Alignment

We anticipate using a traditional autocollimation technique to establish M1/M2 alignment at the time of installation. For further optimization M1/M2 alignment will be derived from the calibration wavefront sensor.

15.1.3.3 Alignment Calibration Wavefront Sensor (CWS)

The CSO primary mirror surface is measured with a shearing interferometer that uses a single element detector and scanned over the entire aperture. This was developed prior to the current availability of extended area multi-pixel detectors for submillimeter wavelengths. Gene Serabyn of JPL, who was instrumental in development of this sensor, has provided a brief study extrapolating the CSO approach to CCAT, using extended area detectors and verifying the precision that can be obtained using planets is sufficient. Based on these results we plan to advance this technique further in the next phase of CCAT development. This sensor is intended to rapidly align all segments and M1/M2, providing the baseline setting for the maintenance sensors and calibration information as required over ranges of elevation and temperature.

15.1.3.4 Maintenance Alignment Sensor System

There are several elements in the Maintenance Alignment Sensor System. We have chosen a suite of sensors based on the proven performance of edge sensors and the requirement for supplemental sensors to address the performance shortfalls of edge sensors alone.

15.1.3.5 Edge Sensor System: Issues Affecting Edge Sensor Efficacy

Among the design elements that can affect the ability of a suite of edge sensors to provide sufficient information to control the parent mirror figure are:

- **Segmentation:** It is known edge sensors work acceptably for nearly identical hexagonal segments, but concerns have been raised they may not work as well with other segmentation schemes, (such as the concentric rings of segments we propose for CCAT). There are several variations possible for the proposed segmentation scheme.
- **Degrees of Freedom Sensed:** Keck edge sensors have the capability to measure both relative piston movement between segments and changes in the dihedral angle. SALT measures piston and distance between segments, deriving global radius of curvature information from the gap variation. This is not true of HET, which measures relative piston displacement of segments at each sensor location and segment gap. Note for TMT, it has been proposed that capacitance sensors be used as on Keck but with the plates attached to the sides of segments, depriving the system of dihedral angle measurement. TMT proposes to use low order wavefront sensing guiding to provide information on the low order modes not well measured by single DOF sensors.
- **Error Magnification:** Edge sensor noise is correlated with low singular values in the sensor matrix resulting in poor control of some spatial modes. In the case of Keck, the ability to measure both piston errors and dihedral angle alleviates this problem to some degree. This effect is also affected by the segmentation scheme and locations of sensors.
- **Environmental Sensitivity of Edge Sensors:** Capacitance sensors depend on the dielectric constant of the air between them. It has also been demonstrated on SALT that condensation on the segment edges in proximity to the sensors can create errors. On HET the readout electronics exhibited significant temperature dependence that requires careful calibration.
- **CCAT Approach:** For CCAT we have contacted the two commercial vendors of edge sensors, Fogale Nanotech and Blueline Engineering. We have requested early concept design of systems suitable for use with the CCAT primary mirror, including definition of sensors, number and distribution of sensors, identification of cabling, electronics, and data acquisition needed for a stand-alone system, and a ROM cost estimate. As both companies provide these sensors as commercial products and have successfully implemented them for higher precision optical segmented telescopes, we feel the risk for implementation in

CCAT is not great. We also have identified the possible use of lateral effect photodiodes as edge sensors. These may offer a much lower price provided the required range and precision can be obtained. These opto-electronic devices produce current variations depending on location of a laser spot on an extended sensor surface. Current catalogue offerings provide sufficient range or resolution but not both. Variations of the readout electronics may increase the range vs. resolution capabilities.

15.1.3.6 Absolute Distance Measuring Interferometer System

At the inception of the CCAT study, JPL's Metrology and Optics group were already at work on an absolute distance measuring interferometer based system for application with large segmented mirror arrays in space. This system operates in the visible wavelengths, but as CCAT observes in the submillimeter, there are no noise issues as there might be with an optical telescope. This system, described in Section 15.3, has the following advantages:

- **Absolute Distance Measurement:** This system can provide a precise starting point for initial operation that has the potential to obviate the need for initial mechanical alignment after periods of complete shutdown.
- **Aligns Panels to M2:** As the system works from panels to retroreflectors on the periphery of M2 it provides M1/M2 alignment data simultaneously.
- **Not Subject to Degeneracy and Noise Amplification:** As the system measures each panel position independently to the retro-reflectors, it is not subject to the error propagation problems of edge sensors alone.
- **Issues:** As this is a new system, we will be carefully studying all potential sources of problems, such as propagation path index issues, drift, alignment, etc.

15.1.3.7 Shack Hartmann Panel Sensing System

Another technique for segment alignment maintenance sensing has been provided in a white paper from Adaptive Optics Associates of Cambridge, MA. This system operates from a hole in the center of M2 and uses simple and inexpensive components to measure segment tilt by deflection of visible light beams reflected from small mirrors mounted on each segment.

This system has a potential difficulty because radio telescopes usually have a deflecting cone at the center of M2 to eliminate the resonant cavity formed between the instrumentation and the vertex of M2. Hence some detailed analysis will have to be done. It will also be important to assess whether the use of bandpass filters to improve signal to noise ratio for daylight operation will be successful.

The benefits of the system are that it achieves M1/M2 alignment while measuring segment alignment and the cost of components is quite low. The system is also relatively immune to optical path index variations, particularly as it is possible to average over time to obviate any air path driven beam deflections.

This system will be investigated along with the JPL distance measuring interferometers in the next phase of work.

15.1.3.8 Wavefront Sensing Guiding

The pointing precision required for CCAT is determined by the 2 arc sec resolution at 200 μm wavelength. This has led to specifications such as 0.2 arc sec drift over a 1 hour observation and 0.2 arc sec offset pointing. This is state of the art performance for smaller modern optical telescopes, and it may be most easily attained by CCAT with optical guiding. Guiding in the submillimeter is not likely possible because of the extended and amorphous nature of the images and scarcity of suitable guide objects. The telescope has been specified with specular surfaces in the IR partially for sparse aperture interferometry as a science goal, but this also supports IR guiding. Jamie Lloyd of Cornell has provided a brief report (Section 15.5) on a wavefront sensing guiding technique that also provides low order aberration information, including focus, to assist in the overall control of primary mirror segment and M1/M2 alignment.

15.1.4 Plans for the Next Phase

We have proposed and studied several systems for alignment and operation of CCAT. These clearly need to work together. In addition there are many questions including but not limited to detailed design and engineering of the

CWS, optimal segmentation pattern for the PM, distribution of edge and laser sensors, and the effect of contributions to the control scheme from the wavefront sensing guider. JPL is undertaking a broad systems study as well as the development of each of these subsystems with exception of the commercial edge sensors and the wavefront sensing guider, which Jamie Lloyd will continue to develop. They intend to build a full system model so we can investigate the effects of variations in design and environmental effects such as panel edge droop and thermal deformations.

15.1.5 Summary

We have made substantial progress in definition of a suite of sensors which will enable CCAT to attain and maintain panel and overall telescope alignment. This is anticipated to be one of the higher risk areas of the Project, but the success of three segmented optical telescopes and a number of submillimeter telescopes along with our somewhat redundant approach leads us to believe that the risk is manageable and within our technical capabilities as the Project progresses.

15.2 Calibration and Wavefront Sensing

15.2.1 Introduction

For radio and submillimeter telescopes, the normal metric for telescope performance is the “main beam efficiency,” the fraction of the telescope’s response which falls within the main lobe of the telescope’s diffraction pattern. The main beam efficiency, η , is given by $\eta = \exp(-\phi^2)$, where ϕ is the root-mean-square phase error across the telescope aperture. From this it can be seen this single parameter provides a measure of the surface accuracy only in a root-mean-square sense. Without knowledge of the detailed shape of the wavefront in the telescope pupil, however, the surface cannot be adjusted to the correct shape. Likewise, a metrology system as envisaged can be used to stabilize and maintain a given shape, but it cannot be used to determine the absolute shape of the surface because the small-scale metrology fiducials are all offset from the large-scale surface that reflects the submillimeter waves. Thus metrology by itself also can not provide the necessary corrections to apply to the telescope surface to achieve an ideal surface shape. Neither of these indicators thus provides a direct measure of the actual surface shape of the telescope reflector. Of course, a mechanical model of the telescope deformations (vs. elevation angle) will also prove useful but, again, such a model ultimately needs to rely on measured reference points, as was shown in the case of the Caltech Submillimeter Observatory¹ (Figure 15.2.1)

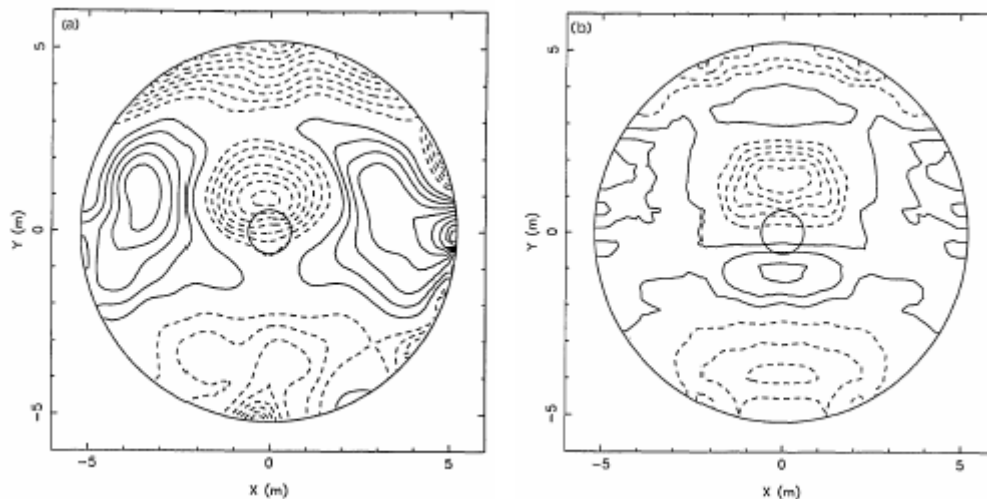


Figure 15.2.1. Comparison of interferometrically measured surface deflections (left) with the original dish model (right) for the CSO. The measured deflections were about twice those predicted. The contour interval is 10 μm .

To provide an actual map of the telescope surface deformations, wavefront sensing (WFS), i.e., a direct measurement of the shape of the wavefront reflected by the telescope at a typical observing frequency is required. Wavefront sensing has been carried out previously from the radio to the optical/infrared (OIR) regimes, but the techniques vary tremendously. In the OIR, WFS is typically a high-speed (kHz), active-control measurement technique used in conjunction with large format detector arrays and adaptive optics correction systems. In the submillimeter, by contrast, the atmosphere is much more stable so WFS is instead envisioned as an “occasional” technique (few times per year) used to provide a well-calibrated measurement of the relatively static surface map that will serve primarily as a reference to calibrate the metrology gauge reference frame. To date, submillimeter WFS has relied largely on single-pixel detectors or small bolometer arrays.

15.2.2 Submillimeter Wavefront Sensing

Because the submillimeter lies between the infrared and radio regimes, wavefront sensing techniques from either domain might conceivably find applicability in this transitional regime. Wavefront measurement techniques in the two domains have tended to be quite disparate however, because of the vastly different photon statistics and applicable technologies. In particular, until recently long-wavelength techniques have largely relied on single

pixel detectors, while in the OIR large format detector arrays have long been available. With the advent of large-format submillimeter arrays, however, it is finally possible to consider directly transferring successful wavefront sensing approaches from the OIR to the submillimeter. Indeed, new OIR methods of wavefront sensing are emerging quite regularly. In this new environment, the appropriate question is then how to optimally sense the telescope wavefront using large-format submillimeter arrays. The immediate goal here is then to identify a technique capable of delivering the needed measurement accuracy of the surface (vertical resolution of a few, e.g., 1-3 μm , with a sub-panel lateral resolution) on a reasonably short timescale (i.e., over an acceptably small elevation angle range). The desired accuracy is a factor of three or more beyond the best accuracies which have been achieved to date. As a reference point, we have the successful application of “shearing interferometry” at the Caltech Submillimeter Observatory (CSO), which was an early interferometric approach based on a single pixel detector^{1,2} that achieved a measurement accuracy of 9 μm and needed 1 to 2 hours per 15×15 to 21×21 point map.

One can measure the quality of the telescope by measuring the field distribution either in the focal plane or the pupil plane. Focal plane sensing is desirable because the astronomer is ultimately interested in the quality of the focal plane diffraction point spread function (PSF). On the other hand, a map of the pupil directly gives the surface deviations. In theory these two fields are related by a Fourier transform relationship and in practice this is true as well if one is careful not to allow non-common path errors to creep in. Because of this theoretical equivalence, no attempt is made here to pick sides – the goal is instead to simply provide an existence proof that one technique possesses adequate sensitivity to meet the needs of the project. Indeed, the temporal stability of the atmosphere at these long wavelengths allows consideration of a number of interferometric wavefront sensors. In particular, the focal plane electric field can be sensed with a single-pixel detector with shearing interferometry¹, or with a variety of array-based interferometers, such as the point-diffraction interferometer (PDI). In the pupil-plane, one can consider classical phase-shifting interferometers based, for example, on a PDI as well. Representative interferometers in each of these three categories are illustrated in Figure 15.2.2.

Since only one of these approaches has ever been applied in the submillimeter, the most crucial question is the ultimate sensitivity attainable with submillimeter WFS. Here we consider only broadband “direct” or “homodyne” detection because the other choice, coherent “heterodyne” detection, is intrinsically narrowband and loses in sensitivity as the frequency increases. In any case, the goal is an existence proof.

The ultimate sensitivity of WFS approaches is well understood for the case of the OIR, but it turns out that to date this topic has not been explored in the submillimeter. However, there are only two essential steps. If one considers a wavefront measurement in the pupil plane, the achievable phase accuracy, ϕ , is given by the well-known relationship, $\phi = 1/\text{SNR}$, where SNR is the signal-to-noise ratio in the detected photon stream in the beam area under consideration (and where factors of order unity arising from a number of detailed measurement issues have been ignored). The second step is then to calculate the SNR per resolution element on the telescope aperture. Here the novelty lies in the fact that at long wavelengths, the photon noise is not given by the square root of the photon counts, as in the OIR, but is instead given by Bose-Einstein statistics as $\Delta n = \sqrt{n(n+1)}$, where n is the number of photons per mode of the radiation field. At the same time, because the submillimeter flux reaching the detector is dominated by thermal background radiation, an accounting for the number of background modes illuminating the detector pixels is needed. The final issue in the SNR calculation is, of course, the incident flux from the source, which raises the question of the existence of suitable astronomical sources.

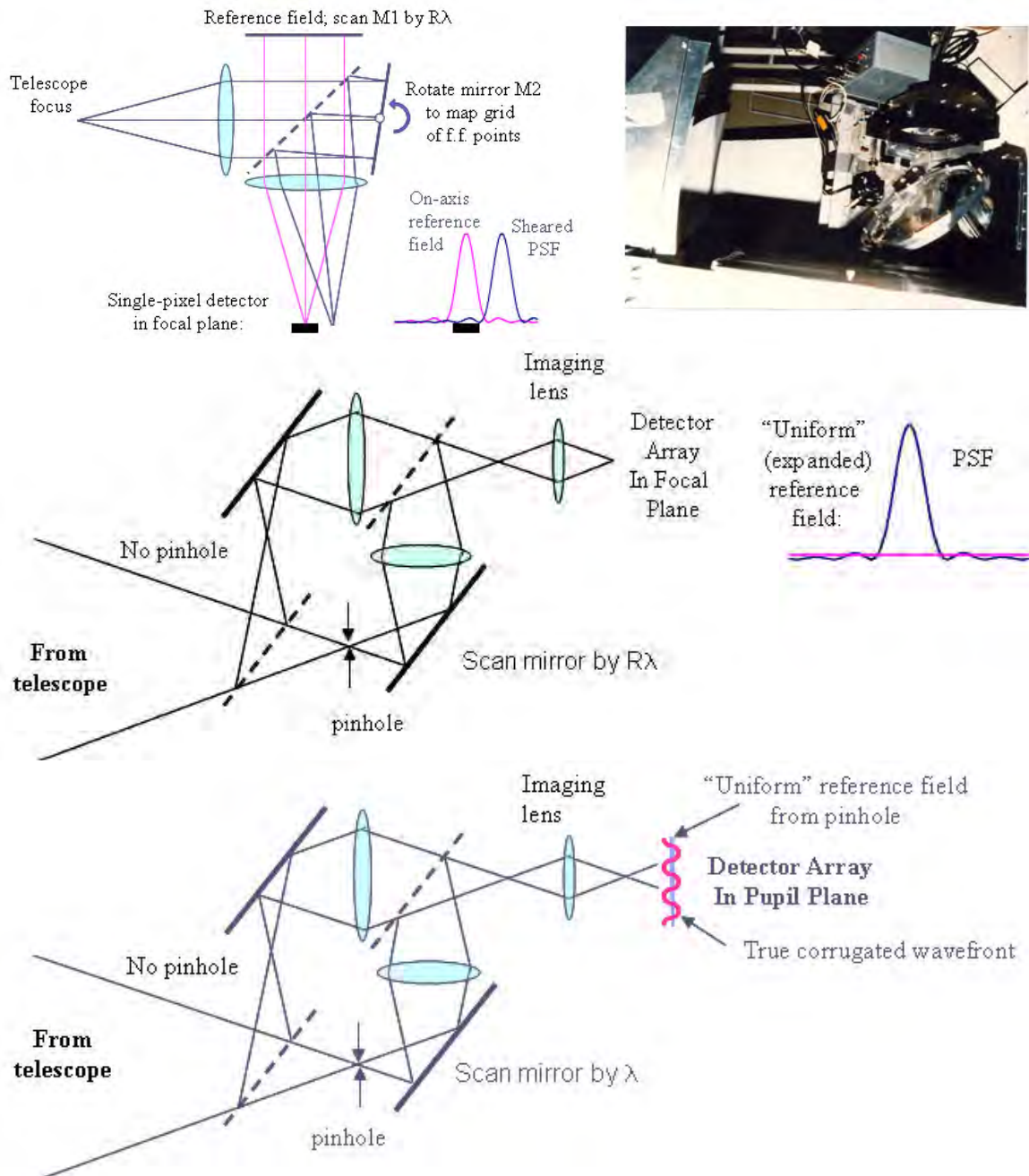


Figure 15.2.2. Top) The shearing interferometer layout used at the CSO. The original CSO interferometer is shown in the right hand image. Middle) A focal plane point-diffraction interferometer. The pinhole in one arm provides a uniform reference field across the final focal plane. Bottom) A pupil plane point-diffraction interferometer. The pinhole now provides a uniform reference field in the final pupil plane.

15.2.3 Sources for Submillimeter Wavefront Sensing

To acquire dish measurements out to the periphery of the aperture, the requirement on the source is its angular diameter be smaller than the diffraction beam width. As the frequency increases, source diameters must narrow. Indeed, for a telescope as large as CCAT, the number of appropriate sources at the high end of the frequency range is actually quite small, given that high brightness is also required to yield a high SNR. Here the size of the aperture doesn't actually help, as it is the size of the measurement cell, or subaperture that is important. Indeed, the planets Mars, when near conjunction, and Uranus and Neptune at any time are satisfactorily small, but the latter two are quite a bit fainter than Mars because of their lower temperatures and, in the case of Neptune, its

smaller angular diameter. In addition, none of these sources is available throughout the year. Thus the number of appropriate sources is fairly small, but on the other hand, wavefront-sensing should not be necessary very often.

15.2.4 Fundamental Sensitivity

Using Mars, which during its orbit ranges in angular diameter from about 3.5 to 20.5 arc seconds, as a test case, its incident submillimeter flux when its angular diameter is small (assuming here that the diameter of Mars is chosen to match the diffraction beamwidth at the selected measurement frequency), is on the order of 10^8 photons/s/m² in a 10% spectral resolution element. On the other hand, the background in the same resolution element is of order 10^{12} photons/s/m². Using Bose-Einstein statistics for the background fluctuations as discussed above, the ultimate theoretical wavefront measurement sensitivity can then be shown from the aforementioned equations to be given approximately by the relationship

$$\Delta x \approx \frac{\lambda}{100T\sqrt{t}},$$

where t is the measurement time, T is the atmospheric transmission, and a conservatively small throughput for the pinhole in the PDI case has been assumed (10%). The resultant sensitivity is approximately proportional to the wavelength, in rough accord with naive expectations (i.e. $\phi = 2\pi x/\lambda$). Taking two “extreme” wavelengths as test cases, a measurement sensitivity of 1 μm (1- σ) can be reached in about 25 sec at $\lambda = 350 \mu\text{m}$ (assuming $T = 0.7$), and in about 4 min at $\lambda = 1500 \mu\text{m}$ (using $T = 0.97$). It is thus clear shorter wavelengths provide higher accuracy wavefront sensing.

For comparison, the CSO shearing interferometry system achieved a measurement accuracy of about 9 μm at $\lambda = 1.5 \text{ mm}$ in a map that took on the order of 2 hours to acquire. In the CSO case, the far-field points were measured sequentially, so the total on-source integration time was actually on the order of 10 - 15 minutes (twice that if the “off” measurements are included). The efficiency set by the duty cycle of the motion-control stages and data transfers was thus quite low. The conclusions are then three-fold. First, the well-characterized CSO shearing interferometer can likely be improved significantly, simply by making measurement efficiency improvements and by moving to shorter wavelengths (at a better site such as the Atacama), to the point where it would be sufficiently accurate for the needs of CCAT. Second, by using shorter wavelengths during periods of high transmission, the measurement accuracy of the detector-array based approaches should approach the theoretical limit given above because the entire pupil plane or focal plane is measured simultaneously, eliminating systematic errors arising from time variations. Indeed, the pupil-plane PDI has the additional advantage that the scanning mirror need only move by λ , instead of $R\lambda$, where R is the spectral resolving power. Given all of these factors, the ultimate measurement sensitivity achievable with an interferometric approach should then be of order 1 μm and this should be achievable in well under an hour.

15.2.5 The System

What might such a WFS system look like? It turns out all three of the potential approaches shown in Figure 15.2.2 can be combined into a single versatile instrument. In particular, except for the position of the submillimeter camera, the instruments in the middle and bottom panels are identical. In addition, the approach shown in the top panel can also be realized by the instrumentation in the middle panel if the pinhole is left out and the second mirror (opposite the scanning one) is made into a rotatable mirror. Thus, all three of the approaches can be realized with a single optical system. Note this hybrid system greatly reduces risk, because the known approach is included as one of the options. This also makes it unnecessary to pick a single optimal realization at this point, so that the strawman system for this stage of the design study is the hybrid shown in Figure 15.2.3. Note to further reduce risk one could consider building and testing such a flexible WFS instrument for an existing submillimeter telescope well before the CCAT WFS system is needed.

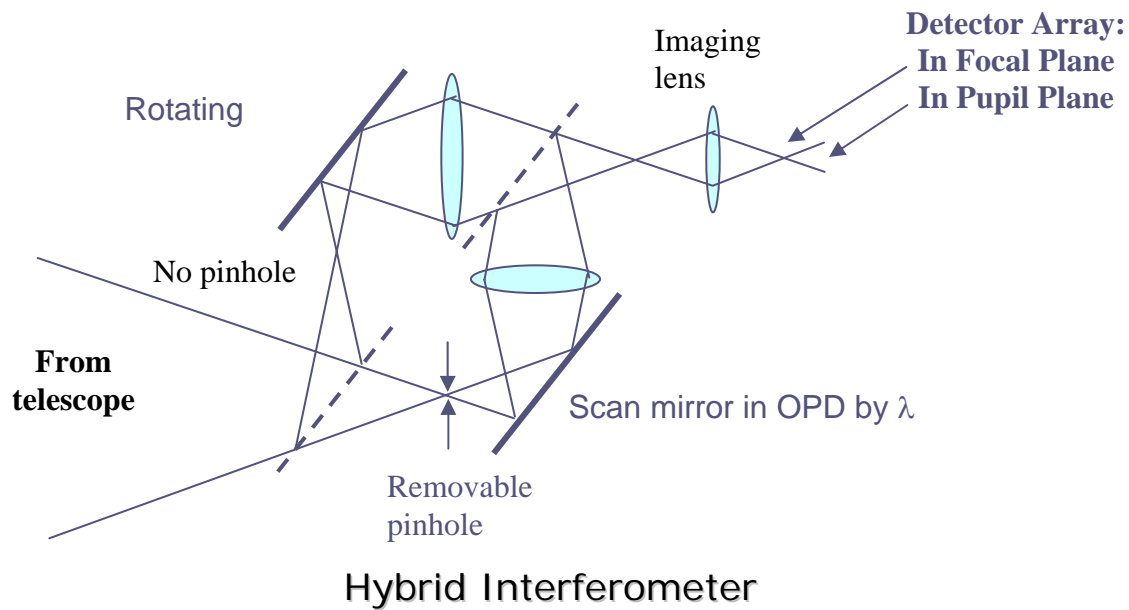


Figure 15.2.3. A hybrid interferometer that provides all three capabilities seen in Figure 15.2.2. By moving the detector array, one gets either version of the PDI and by removing the pinhole and rotating the rotating mirror, one returns to the shearing interferometer.

The cost for such a WFS system would not be excessive; assuming the submillimeter camera to be used is supplied by the facility. Indeed, the major hardware expense would be for up to three large off-axis mirrors (of order 1 to 2 m in size). With these costing roughly \$100 k each and the remainder of the optical, mechanical, and actuation hardware costing \$300 k, the equipment cost would be approximately \$600k. The rest of the cost would be labor. Assuming a duration of two years due to final design time and mirror lead times, and including a project manager (2×0.3 FTE), a system lead (2×0.3 FTE), an optical designer/modeler ($0.5 + 0.3$), an optical engineer ($0.3 + 0.5$), a mechanical engineer ($0.3 + 0.5$), a controls engineer (0.5×2), and a software engineer (0.5×2), the net labor costs, including overhead are approximately \$1.3M. With travel to the collaboration and the telescope included, this leads to a total cost of roughly \$2.0 M.

15.2.6 Conclusions and the Next Steps

In this stage of the design study, the goals have been to establish an existence proof based on general physical principles. While this section has provided a short summary of the basic conclusion that it should be possible to reach the needed CCAT wavefront measurement accuracy, of order a few μm , with an interferometric wavefront sensor of the type described, space constraints here have not allowed a presentation of the detailed physical derivation of this result. This basic result will thus need to be formalized and published separately. At the same time, a detailed comparison of all potential submillimeter wavefront sensing approaches is needed, in order to make sure the optimal approach has in fact been identified. However, as discussed above, by using the CSO shearing interferometer as a starting point, one is already within a factor of about three of the desired goal, albeit with a measurement timescale that is too long for CCAT purposes. Because this long timescale resulted mostly from inefficiencies in the motion control and data transfer steps implemented close to 20 years ago, however, it is a safe bet all of these steps can be made much more efficient with modern hardware.

As to the next phase of the design, it will of course be necessary to flesh out the basic physical approach in a number of directions. These include a more detailed throughput and sensitivity analysis, an aberration sensitivity analysis, and a numerical analysis of the availabilities of the limited number of sources that are both bright enough and small enough to be useful. These steps should provide a solid basis for more accurately estimating the usable field of view (in the focal plane case) and the obtainable lateral and vertical surface resolution vs.

integration time in the various cases and so lead to a downselect to the optimal system. This can then be followed by a detailed optical design and packaging analysis.

References:

- 1 – Serabyn, E., Masson, R. C., Phillips, G. T., “A New Technique for Surface Measurements of Radio Telescopes.” *Submillimetre Astronomy, Proceedings of the Kona Symposium on Submillimetre Astronomy*, held at Kona, Hawaii, October 3-6, 1988, Dordrecht: Kluwer, 1990, edited by Graeme D. Watt, and Adrian S. Webster. *Astrophysics and Space Science Library*, Vol. 158., p.41
- 2 – Woody, D., Serabyn, E., Schinkel, A., “Measurement, modeling, and adjustment of the 10.4-m-diameter Leighton telescopes.” 1998, *Proc. SPIE 3357*, p. 474.

15.3 Laser Metrology

15.3.1 Introduction

One of the technical objectives for CCAT is to devise a system for measuring the shape of the primary mirror. Other segmented telescopes have used a variety of measurement technologies for monitoring the primary mirror such as LVDTs, capacitance sensors, and shadow sensors, collectively known as edge sensors. All of these involve measuring the displacement of one mirror edge relative to its neighbor, so they do not directly measure the positions of the segments.

The laser metrology group at the Jet Propulsion Laboratory is developing solutions for absolute metrology – a technique for measuring the distance from the secondary mirror to a constellation of points on the primary, with both precision and accuracy. Originally conceived to support programs like SIM, TPF, SAFIR, and other space missions, JPL’s laser metrology systems routinely provide high speed, large distance measurements with picometer resolution.

The term *laser metrology* describes techniques that use laser interferometers to measure distances. The particular type of interferometer that would be useful for CCAT is the Common Path Heterodyne Interferometer (CoPHI) developed at JPL.

This interferometer uses two laser beams (red and green, Figure 15.3.1) where the difference in frequencies between the beams is known. Emanating from the *beam launcher* (yellow box), the red beam projects onto the corner cube at distance d . This corner cube has a hole drilled through the middle of it, so that part of the red beam passes through it.

The outer annulus of the red beam reflects off the corner cube at distance d , while the inner portion of the red beam reflects off the further corner cube at distance, x . As both paths of the red beam return the beam launcher, they separate, and each interferes with light from the green beam, which has never left the beam launcher.

When the interference patterns shine onto photodiodes, they produce two sinusoidal electrical signals with the same frequency, but different phases. The difference in phase between these signals is proportional to $(x - d)$, the distance between the two corner cubes.

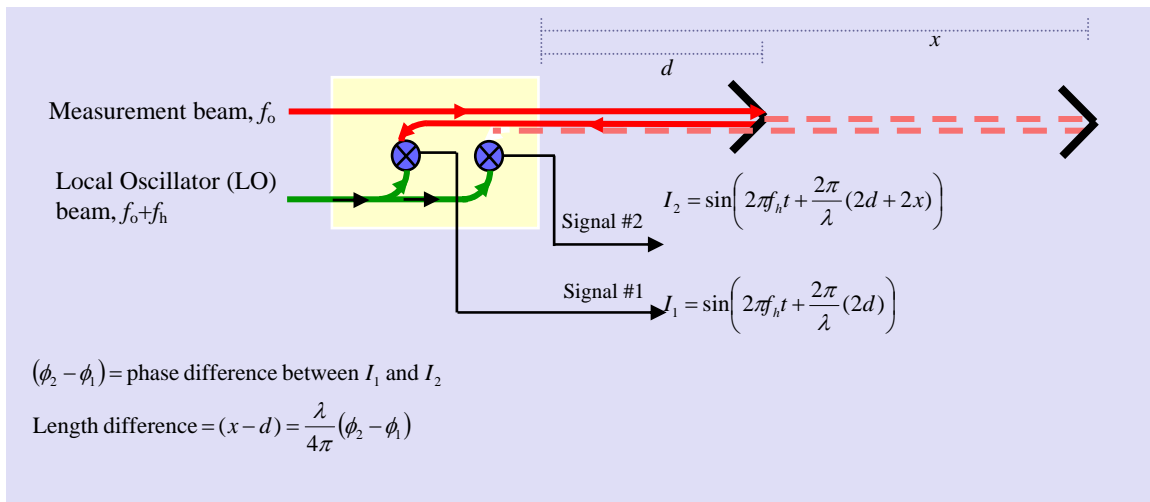


Figure 15.3.1. Schematic layout of a CoPHI (Common Path Heterodyne Interferometer)

A *phasemeter* converts two sinusoidal signals to square waves, and uses a high-speed clock to measure the time delay between them. The phasemeter detects fringe wrapping and extends the CoPHI's dynamic range to a few kilometers, with precision limited by the clock's stability.

CCAT would use a trio of CoPHIs to monitor a cluster of primary mirror panels, with all the shared far corner cubes located near the secondary mirror. The near corner cubes, the beam launchers, and phasemeters would all be beside or behind the primary mirror segments. Figure 15.3.2 is a ray trace diagram for a different telescope having a total of six CoPHI beams, all using corner cubes near the secondary mirror as mechanical reference points.

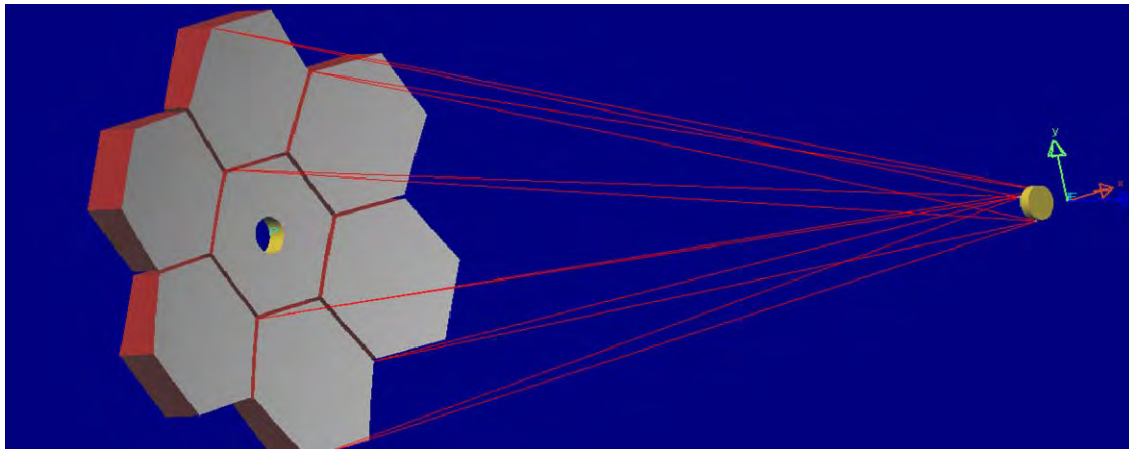


Figure 15.3.2. A conceptual diagram of a segmented telescope showing CoPHI beams for metrology.

CCAT will need a laser metrology system with two operating modes. First, it needs to know the exact path length along each CoPHI until the mirror segments are in their proper positions. In this mode, each CoPHI measurement takes about a second. Once the shape of the telescope stabilizes, the second operating mode comes into play. The CoPHIs switch into a high-speed mode so that the laser metrology system can measure relative motion of each CoPHI to feed back to the primary mirror's active control system.

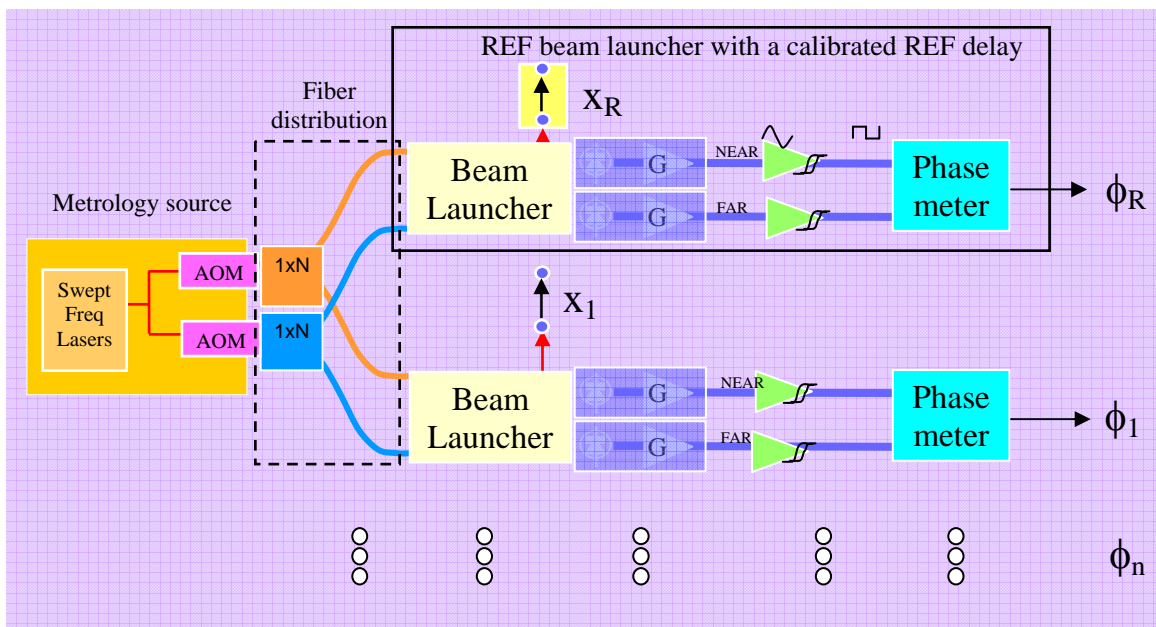


Figure 15.3.3. CCAT would use a single, calibrated, reference delay line (X_R), plus several metrology beams deployed on the telescope (X_1, \dots).

Recall that a single CoPHI on its own only measures changes in distance between two corner cubes. To measure absolute distance, we use one more CoPHI to measure a calibrated delay line of length x_{REF} (Figure 15.3.3). While continually changing the laser frequency (Δf_o), we obtain the phase change $\Delta\phi_{REF}$ from the reference delay line in addition to those $\Delta\phi_n$ from the several interferometers deployed on the telescope. Combined, these determine the unknown distances, since $x_n = x_{REF}\Delta\phi_n / \Delta\phi_{REF}$, where $\Delta\phi_n = 4\pi x_n \Delta f_o / c$ and $\Delta\phi_{REF} = 4\pi x_{REF} \Delta f_o / c$.

Each absolute distance measurement lasts about a second, limited by the time it takes to change the laser frequency by a reasonable amount. Relative distance measurements, however, can run continuously at speeds of up to a few kHz.

15.3.2 Requirements

The laser metrology system should provide absolute measurement with resolution on the order of 10^{-6} meters over a temperature range of -25° to $+20^\circ$ C (-13° to $+68^\circ$ F) and relative humidity from 0% to 95%.

For purposes of cost estimation, we assume that CCAT will need 60 CoPHI beam launchers deployed on the telescope, plus one reference delay line in the control center. Equipment located on the primary mirror truss should be lightweight, and require a minimum amount of power and cabling

15.3.3 Implementation plan

We estimate the incremental cost of each metrology beam to be about \$10,000. Instead of instrumenting all 162 CCAT mirror segments with 3 CoPHIs each, we propose to use 3 laser metrology beams for a cluster of 9 telescope mirrors (Figure 15.3.4). These 3 beams can measure the tip, tilt, and piston displacement of a cluster while conventional, low-cost edge sensors (capacitance, inductance, or shadow) between adjacent panels of a cluster would keep the surface continuous within the cluster.

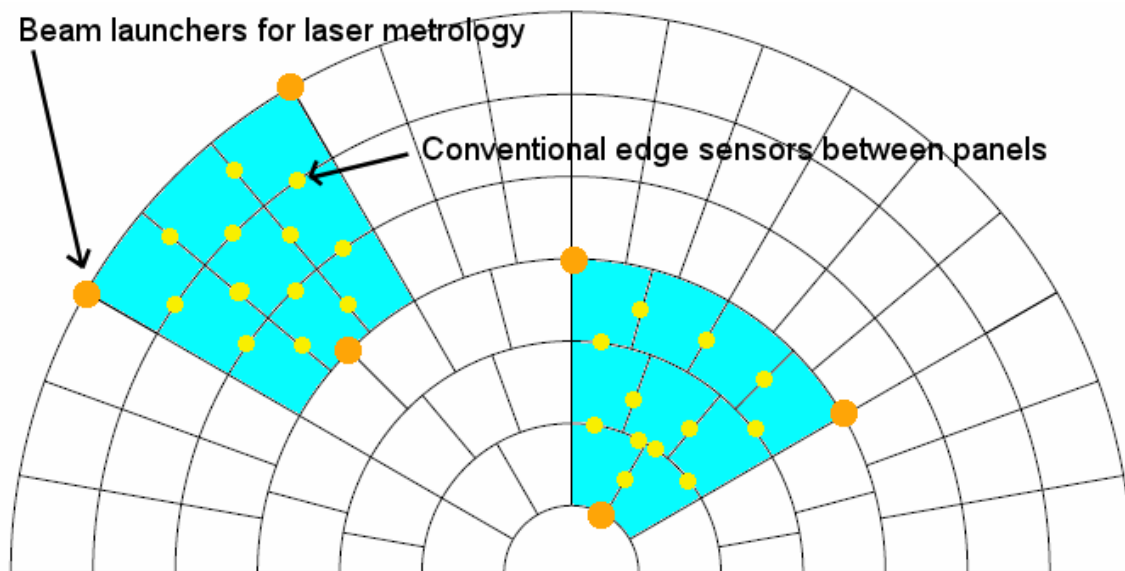


Figure 15.3.4. This conceptual plan for CCAT metrology suggests using 3 CoPHI beams for a cluster of 9 mirrors, plus conventional edge sensors along edges within the cluster. The exact location of the edge sensors and CoPHI beams is recommended for further study.

The beam launchers are behind the primary mirror segments. These project laser light toward the secondary mirror. Figure 15.3.5 shows six beam launchers on a mirror segment – CCAT will only need three beam launchers to measure the tip, tilt, and piston degrees of freedom to form an optical tripod. A steering mirror and near corner

cube are be mounted on the primary mirror support truss for each degree of freedom. The attachment of the corner cube presents the only tight mechanical stability requirements for this system. This suggests the corner cube, between 13-26 mm in diameter, be attached directly to a primary mirror segment.

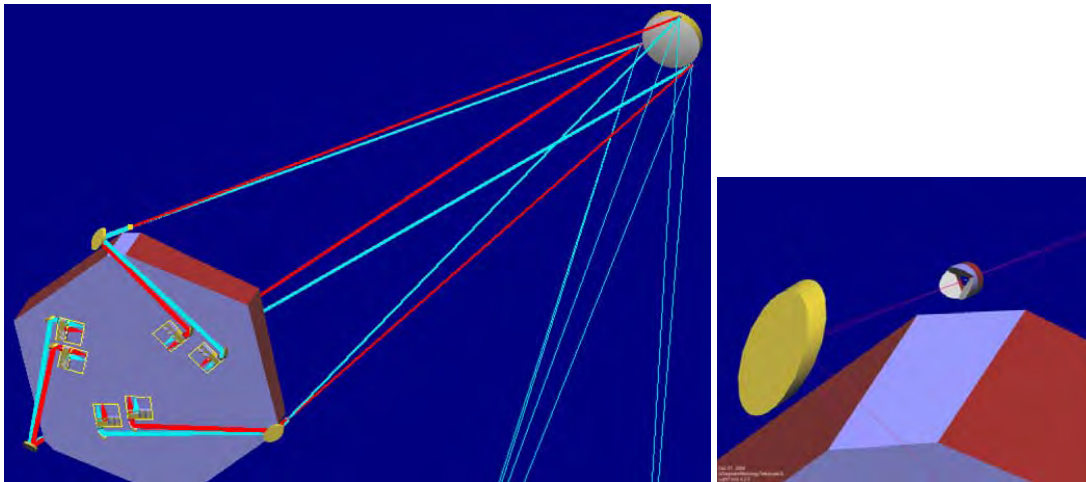


Figure 15.3.5. Left: A schematic design of a monolithic mirror segment with 6 CoPHI beams. CCAT would only need 3 beams for tip, tilt, and piston degrees of freedom. Right: A corner cube (13-36 mm) and steering mirror must be mechanically referenced to the primary mirror segments. Possible strategies range from using a precision machined interface jig to drilling a hole through a primary mirror segment and bonding the corner cube inside. Since a corner cube retroreflects, only its position, and not its alignment, is critical.

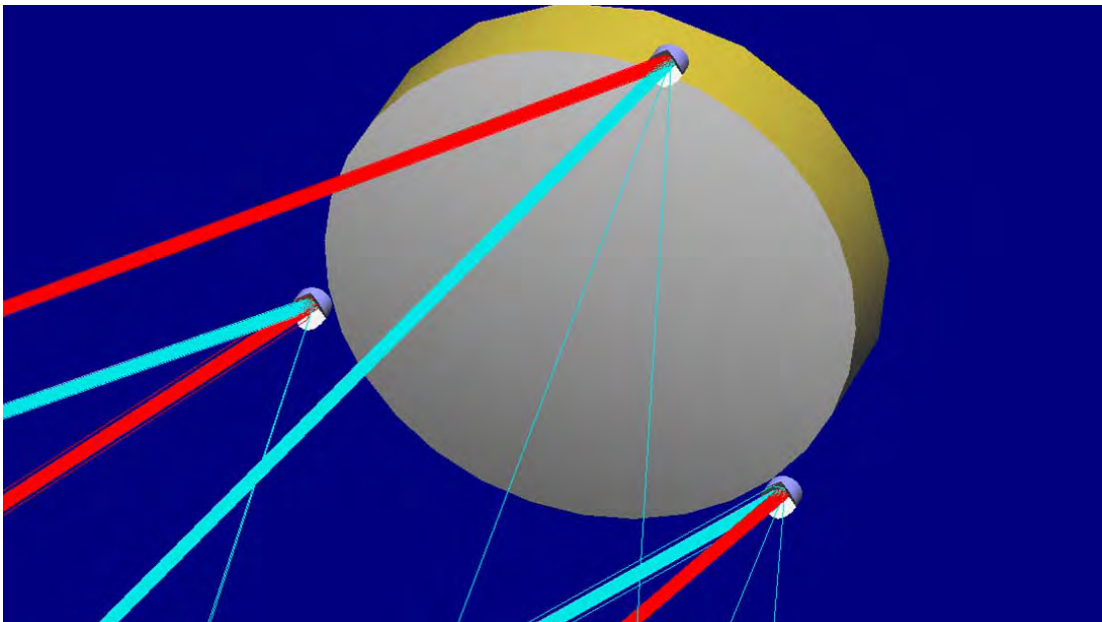


Figure 15.3.6. A close-up of the secondary mirror shows how three corner cubes are the reference points for all the interferometers on the primary mirror.

The phasemeters we are building for other JPL projects are inexpensive and lightweight. The analog electronics for a cluster of mirrors fits onto a single 6-U VME card, while the digital phasemeter electronics can be as simple as a FPGA chip wired to a few connectors (Figure 15.3.8).

Each cluster of mirrors, with three CoPHIs, would have an analog electronics card and a digital phasemeter card. Since the cabling and power requirements are modest (6 optical fibers and approximately 8 low-current wires), it's reasonable for the electronics to be distributed throughout the telescope truss. This choice allows us to

eliminate two expensive fiber aligners from each beam launcher, by replacing them with photodiodes. This is a significant savings in cost and complexity.

We envision a star network topology (Figure 15.3.7), in which each of the 18 mirror clusters is wired independently to the control center.

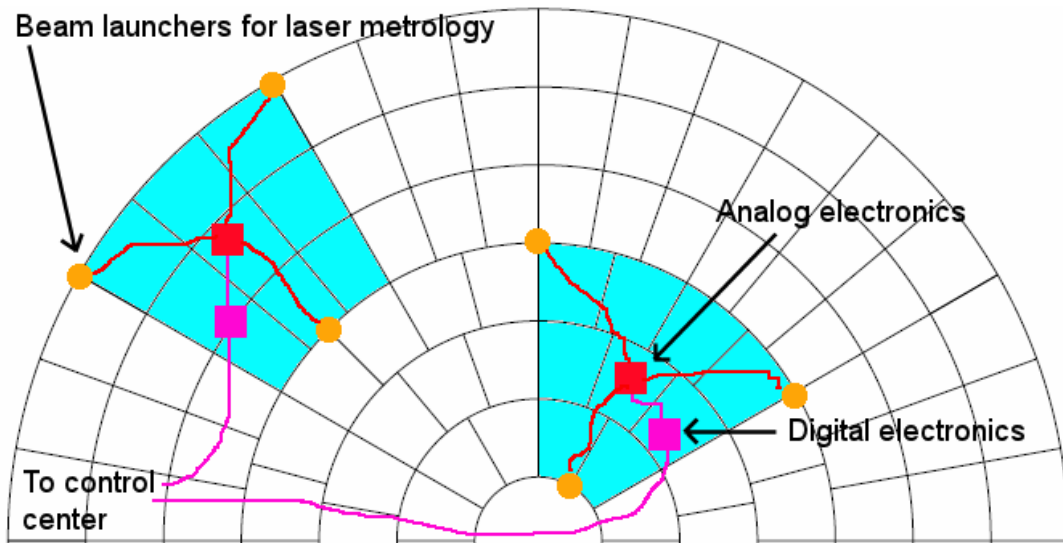


Figure 15.3.7. Star network. A cable harness (6 fibers and ~8 wires) connects the control center to each mirror cluster. Two fibers provide light for each beam launcher. The wires provide power, frequency reference, and network connectivity to the phasemeter electronics.

Each phasemeter card sends ethernet packets to the control center at a fixed rate of around 1 kHz. The control center needs a 20-port ethernet switch to demultiplex the incoming data onto a private network. JPL is developing C and LabView interfaces (Figure 15.3.9) to allow CCAT to integrate the phasemeter data into the telescope control systems.

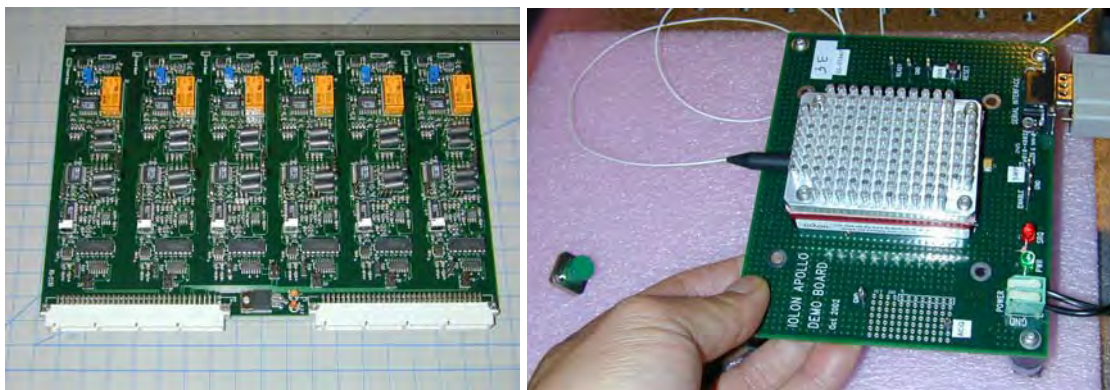


Figure 15.3.8. Left: Analog electronics for three metrology beams (one cluster of 9 mirrors). Right: The tunable laser that drives a constellation of CoPHI beams.

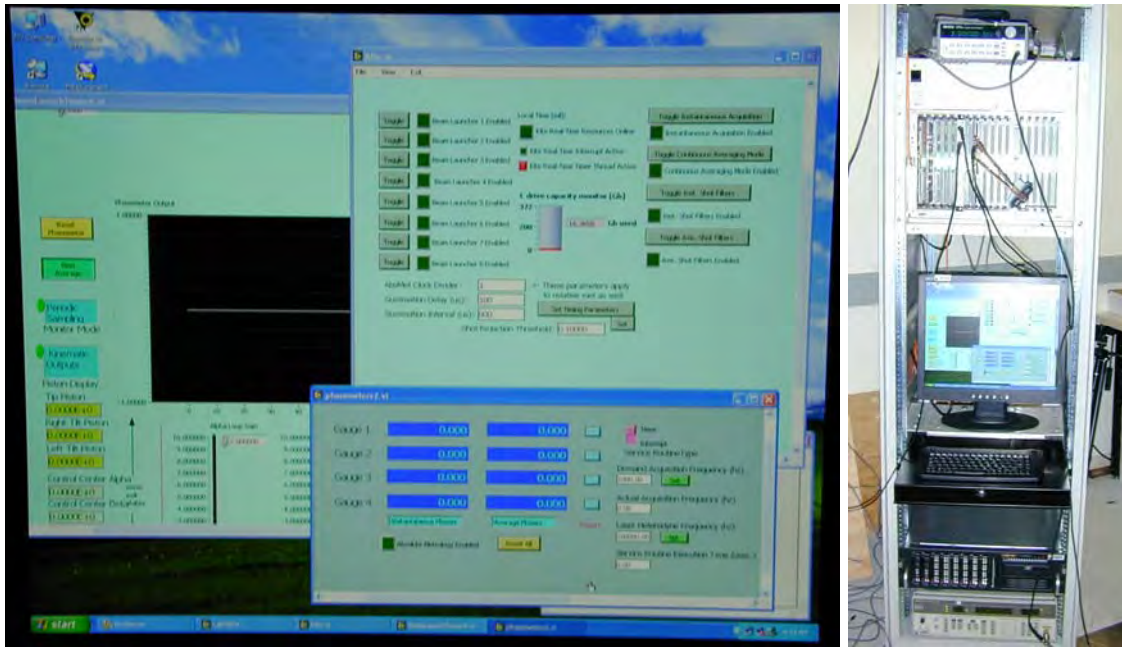


Figure 15.3.9. Left: Software interface to a CoPHI. Right: Instrument rack for testing and debugging the metrology system at JPL.

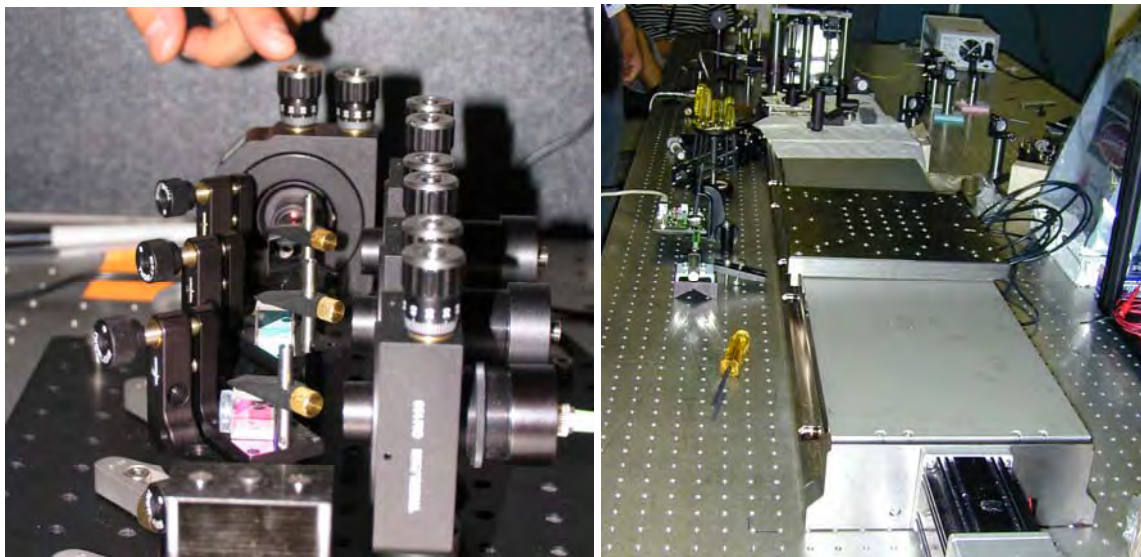


Figure 15.3.10. Left: A beam launcher set up on a breadboard. The third beamsplitter mount holds a triangular prism with a hole drilled through it. Right: Linear translation stage and laser metrology lab for calibrating the reference delay line. The large parabolic mirror at the top center is for collimating a white light beam.

15.3.4 Manufacturing approach

JPL would deliver detailed mechanical drawings and parts lists suitable for CCAT to manufacture and assemble the laser metrology system. CCAT can expect to realize some cost savings by using simplified versions of mechanical parts designed for use in space vehicles.

The beam launcher designed for JPL's space mission has two fiber inputs, and two fiber outputs, the latter carrying the modulated optical signals toward photodiodes. Figure 15.3.11 shows a beam launcher, consisting of four fiber aligners (triangles), four collimators (tubes), an aluminum housing, and four optical components (blue). It may be possible to lower the per-unit cost by about \$2,000 by eliminating two of the fiber aligners. Other options may be available, depending on the thermal analysis of the design.

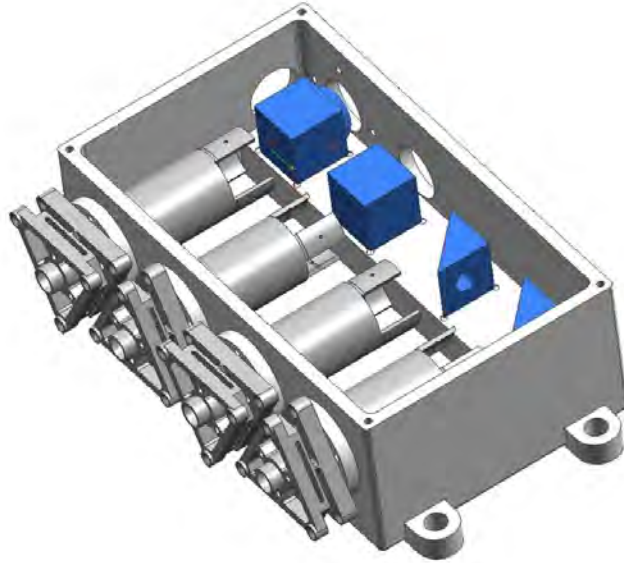


Figure 15.3.11. JPL beam launcher developed for space missions. CCAT can make simple alterations to lower its cost and complexity. A beam launcher masses approximately 250 grams.

Beam launchers are designed to be aligned once, as part of the manufacturing process. Since it's fairly time consuming to align the fiber beams, we suggest omitting the last two fiber aligners (shown on the right in the picture below). Instead, the measurement photodiodes could be attached directly to the beam launcher, which requires placing the phasemeters nearby. This tradeoff drives our recommendation for distributing the metrology electronics throughout the telescope truss.

15.3.5 Performance

Precision and accuracy can be affected by misalignment and laser signal strength. This issue requires further study.

The difficulty of aligning the system depends on the width of the metrology beams at the secondary mirror, presently expected to be ~4 mm. The line formed by each beam launcher and near corner cube must fall near the center of a far corner cube.

- The initial alignment of the beam launchers needs to be accurate to within a few tenths of a milliradian (4 mm/25 m). This will need further study to develop a suitable assembly and registration process that is unique to CCAT.
- The transverse capture range at the secondary mirror is the beam width, 4 mm.
- For a 32-bit word length, the longitudinal capture range of a CoPHI is on the order of 10^3 m, vastly in excess of the size of CCAT.

The laser metrology system is to first order insensitive to fluctuations in the speed of light, so long as the air in the reference delay line is the same as the air between the primary and secondary mirrors.

15.3.6 Environmental Effects

We expect large variations in the humidity and air temperature at Atacama. This will cause variations in the index of refraction of the air, which will affect the distance measured by a CoPHI. The obvious strategy for mitigating this problem is to place a reference delay line in a vacuum chamber. Then, the CoPHIs deployed on the mirror will measure the true optical path length between the primary and secondary. A future study should identify whether the difference in atmospheric index between the science wavelengths and the metrology wavelengths

would warrant a second reference delay line in air, with a weather station. These additional instruments would provide enough information to compensate for chromatic dispersion.

Air turbulence can be treated similarly – refractive index variations within the servo bandwidth will be detected and compensated for by a CoPHI system running in relative distance mode. In absolute measurement mode, the turbulence will be averaged over several seconds. JPL plans to simulate and measure the effect of air turbulence as part of its R&D program.

Light scattering from dust on the corner cubes may couple light from one metrology beam into another. We believe that this is a very, very small effect. In interferometer systems, noise power scales with the square root of the scattered light. To affect a neighboring CoPHI, scattered light would have to pass through a 5 mm^2 hole over a $\sim 10 \text{ m}$ distance. We expect this effect to lead to a length-equivalent error much smaller than a nanometer.

The diffracted CoPHI beam returning to the near corner cube will have a beam width on the order of 10 mm. For beam launchers spaced apart on the order of 10 cm, diffractive crosstalk is negligible.

15.4 Shack Hartmann Alignment Sensor, Adaptive Optics Assoc.

Report prepared by Adaptive Optics Associates

15.4.1 Introduction

This document briefly describes a concept for an optical sensor to be mounted at the secondary of the CCAT telescope that will provide primary mirror segment position measurements to allow maintenance of the primary figure during operation.

The CCAT primary mirror consists of concentric rings of panels each of which is an off-axis asphere. The panels must be aligned with each other to form a single phased optical surface at the operational wavelength of the CCAT. The sensor system described here uses an array of simple geometric sensors, one for each panel, to measure the alignment of the panels and provide error signals for the panel positioning subsystem.

The basic approach is based on the classical Hartmann test that has been used for over a century for the testing of large telescope mirrors. It is a geometric technique that measures the local tilt of the mirror segments. This concept is closely related to the segment alignment sensor provided by AOA to the Southern African Large Telescope (SALT). SALT has an 11m aperture segmented primary that is sensed from a tower located at the center of curvature of the spherical primary. The AOA sensor is described in a paper attached as an appendix to this document (Proc. SPIE Vol 5489, p. 892, 2004).

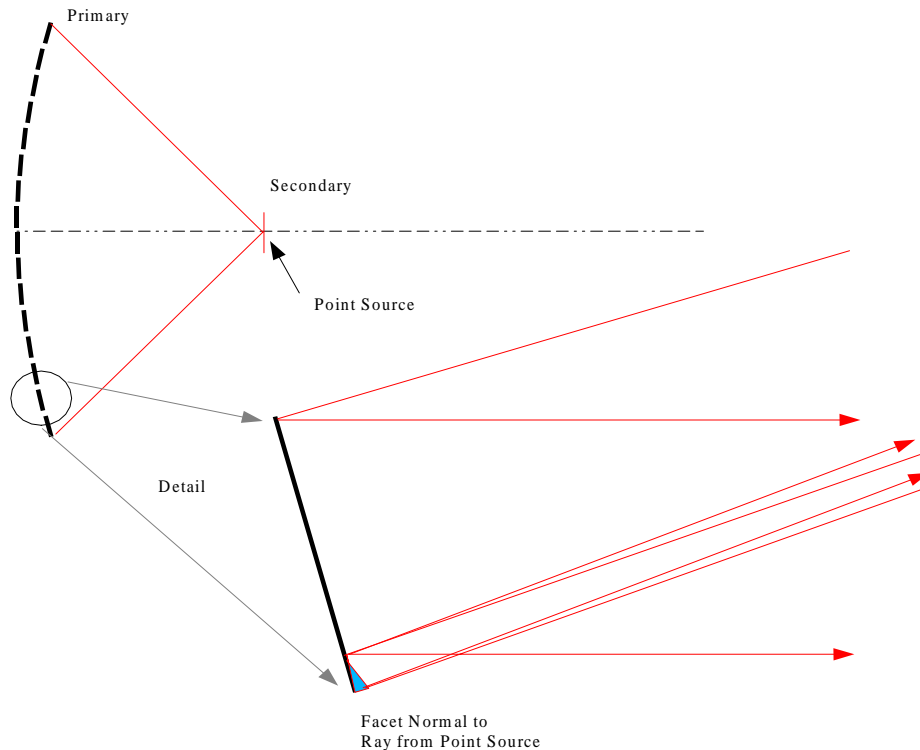


Fig. 15.4.1. Arrangement of the source and segment facets

Because the CCAT has a hyperbolic primary and there is no access to the center of curvature a somewhat different optical layout is required. Rather than looking at the light reflected by the surfaces of the segment, each segment is provided with a small, flat mirror facet that is aligned approximately normal to the line from the segment to the center of the secondary. The angle of these facets would be adjusted once the segments were brought into alignment and then locked in position. To probe these facets, the sensor is provided with a point source of light close to the center of the secondary. This source will illuminate the full surface of the primary. The vast majority of the light will be reflected by the segments in a roughly collimated 25 m beam. The light that strikes the facets, however, will be reflected back toward the source as though they were sparse segments of a spherical mirror. This is shown schematically in Figure 15.4.1.

The facet size must be sufficiently large so that the sensor is still within the near field of the ray bundle produced by the facet. For operation at 633 nm facets in the range of 0.5 to 1.0 cm would be sufficient. The sensor itself consists of a reimaging

lens and an array of tilt sensors. The lens also acts as a “collimator” for the ray bundles coming from the facets. This is the same optical arrangement that is used in the SALT sensor. The camera lens is positioned with its front focus close to the nominal point where the ray bundles cross the optical axis. It forms a good image of the primary mirror on the array of tilt sensors. For this design concept a wide angle large format camera lens was chosen that provides about a 100:1 demagnification of the primary to the image plane. At the same time the tilt angles of the ray bundles are magnified by a factor of 100X. Because the tilt sensors are located at the image plane the mapping of segments to sensors is fixed. This is shown in Figure 15.5.2.

In the SALT sensor system the segment tilt sensors were essentially 91 independent Hartmann style sensors but implemented using a single large detector array. For the CCAT that is not easily achieved. Because of the large size of the primary and its high optical speed the image of the primary is larger than most detector arrays. This is also driven by the requirement that the “collimating” lens have an aperture large enough to accept the ray bundles from segments at the largest anticipated tilts. For the lens shown here the tilt capture range is about ± 0.8 mrad. This aperture size and the optical speed of the wide angle lens required to cover the primary drive the focal length of this lens.

The proposed tilt sensors consist of a lens that forms an image of the point source on a small CMOS focal plane array. The tilt sensors would be held in a single mechanical structure that places their input lenses at the image plane of the primary mirror formed by the reimaging lens. Each sensor unit also has all the data capture and processing electronics required to convert the spot image into a tilt estimate. The array of tilt sensors communicate the tilt information via some standard bus (e.g. USB, Ethernet, etc.) to a central processor that interfaces to the primary mirror control system. These sensors have the advantages of large tilt measurement range, low cost, easy replaceability, and small size.

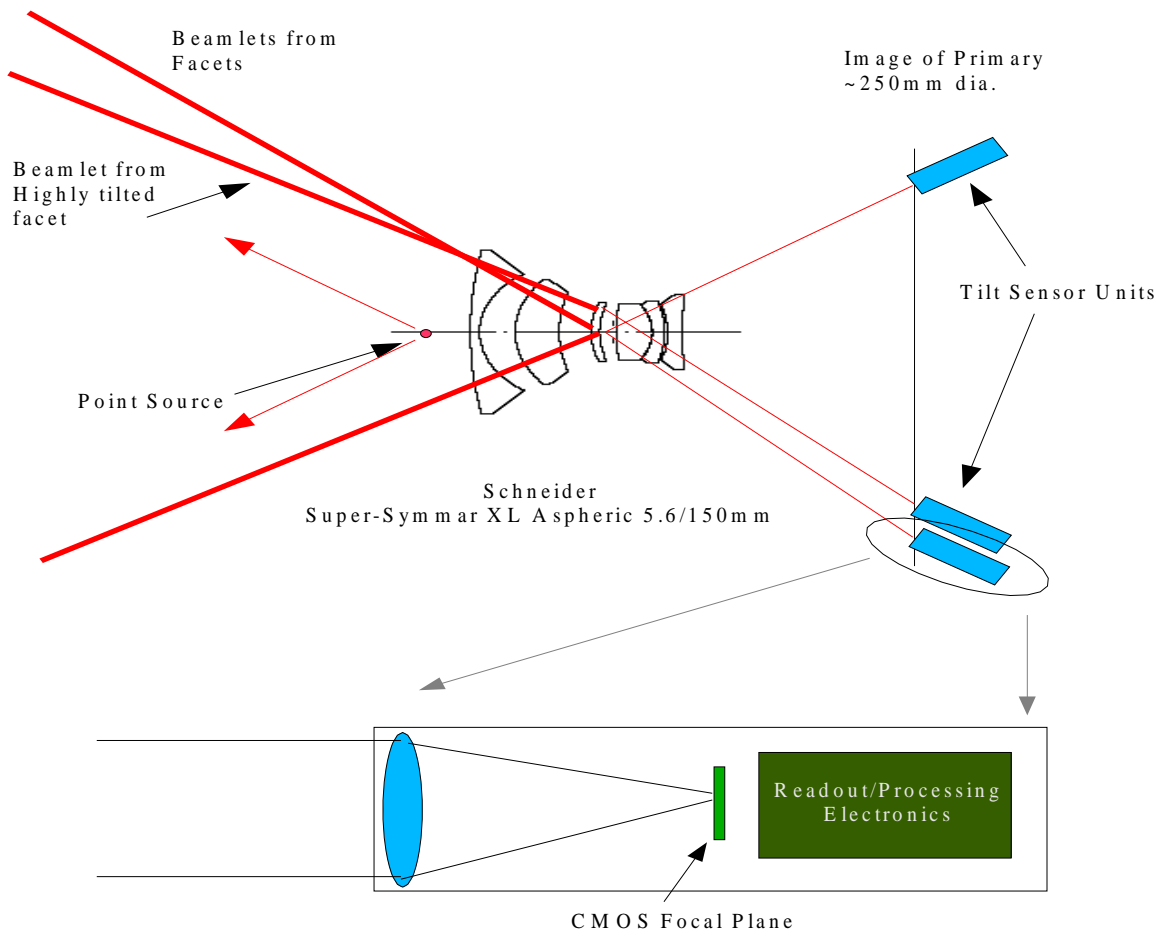


Fig. 15.4.2

Because of the magnification of the segment tilts by the reimaging lens the tilt sensitivity of the system is good. Tilt noise is estimated to be less than $1 \mu\text{rad}$. Because the areal fill factor of the facets is only about $1/40,000$, the light source must be

reasonably bright. Initial analysis indicates that a high brightness LED source would be suitable giving an SNR of better than 50:1 for the anticipated detector noise and integration time.

Figure 15.4.3 shows a schematic of the electronic system within each tilt sensor package. Each sensor would have a CMOS Focal Plane Array (FPA), a Field Programmable Gate Array (FPGA) that collects the image data from the FPA and calculates the spot position. This data is then passed to a micro-processor (CPU) that handles the transmission of the data via Ethernet to the primary mirror control system. The CPU also provides all startup, diagnostics, and health monitoring for the tilt sensor.

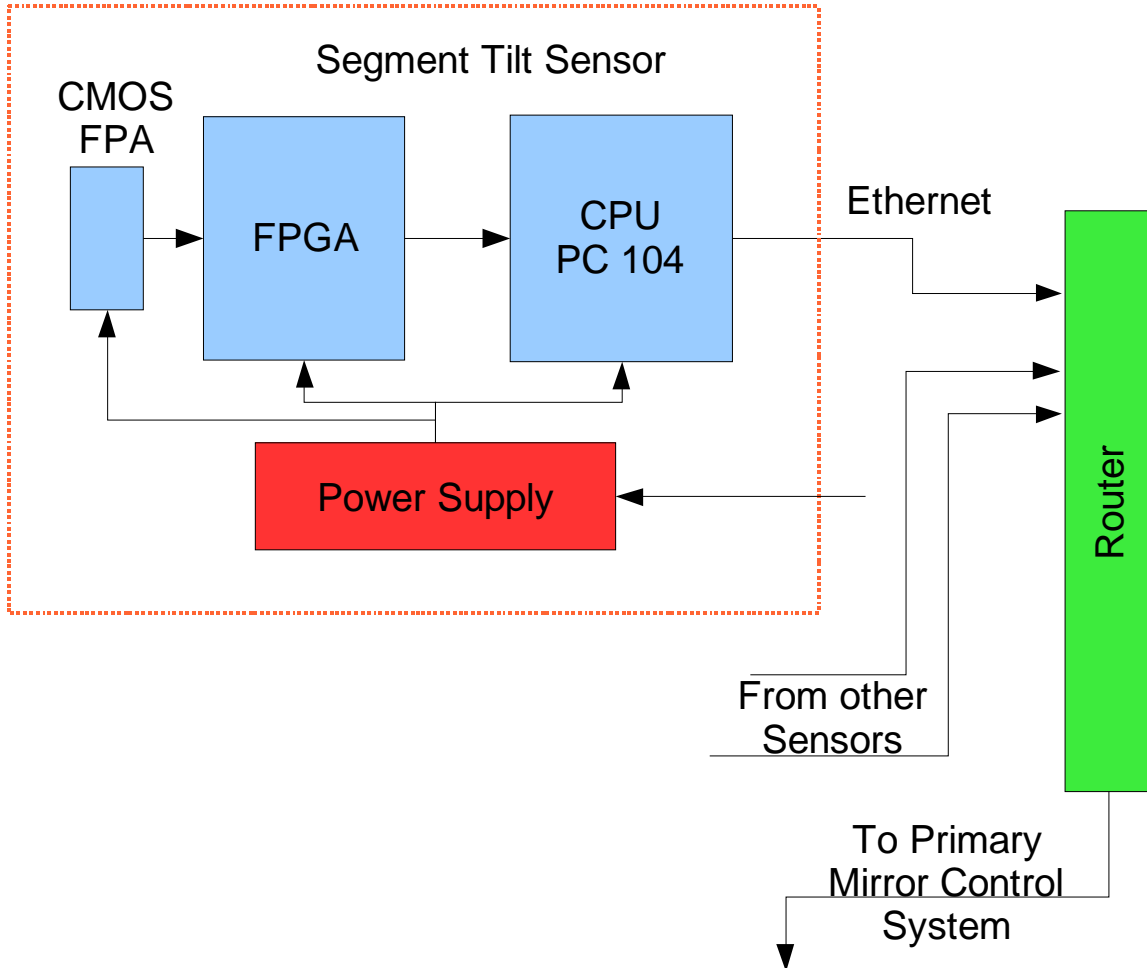


Fig. 15.5.3. Tilt Sensor Electronics

15.5 Optical Guiding with CCAT

15.5.1 Introduction

Historically, pointing and tracking of radio telescopes has been achieved with open loop pointing models. Because of its large aperture and short wavelength operation, the pointing and tracking requirements for CCAT substantially exceed those of prior radio telescopes, and are comparable to the requirements for optical telescopes. Optical telescopes rarely achieve the requisite pointing and guiding to acquire and track astronomical objects to a small fraction of an arcsec for periods of hours without active correction. CCAT bridges the boundary between the conventional domains of optical and radio telescopes. Although certain aspects of the design for CCAT remain in the design envelope of radio telescopes, others (e.g., field of view) cross over into the design parameter space more typical of optical telescopes.

15.5.2 Background



Figure 15.5.1. Edwin Hubble guiding a photographic exposure on the Hooker 100" telescope.

Maintenance of the tracking of optical telescopes has always required active tracking. In one of the most famous images of any astronomer at work, Edwin Hubble is frequently pictured with actively guiding the 100" telescope at Mt. Wilson. Hubble was reputed to be a superb guider with remarkable patience and precision to acquire the deep exposures of galaxies necessary to measure the expansion of the universe. The advent of electronic detectors allowed the implementation of auto-guiding on optical telescopes [7,8]. All large astronomical telescopes routinely employ optical guiding and with the commercial availability of low noise CCD detectors autoguiding is frequently employed by amateur astronomers. In the current generation of large optical instrumentation for 8 m class telescopes, the role of the guider is clearly expanding, driven by two issues: the large size of instruments results in serious differential flexure between instruments and off-axis guiders and the increasing prevalence of queue scheduled observations results in the maintenance of data quality being seen increasingly as an observatory functionality. The Gemini 8 m telescope project addresses these issues by requiring all instruments to incorporate an “on instrument

wavefront sensor” that records in common mode with the instrument focal plane not only the image pointing center but also focus [4,5,6]. The Gemini telescope primary mirror active optics are sensed with a prime focus wavefront sensor [2]. The TMT telescope project plans to implement a wavefront sensing guider to control the mirror modes that are difficult to sense with edge sensors.

15.5.3 Scope

Ideally, guiding would be accomplished within the design wavelength of the telescope, 350-850 μm . However, the high sky background and distribution of astronomical objects at these wavelengths do not permit guiding with any substantial temporal bandwidth the primary consideration is the suitable wavelength range for guiding. Although the sky brightness drops at longer wavelengths, the distribution of bright sources does improve and telescope diffraction limits the angular precision of a guider. At shorter wavelengths, stars become suitable sources for guiding, but the sky brightness does not significantly improve until the wavelength is significantly shorter than the blackbody peak of the telescope, $\sim 10 \mu\text{m}$. Certain candidate mirror technologies for CCAT offer the possibility of specular reflection at IR wavelengths. If this is the case, then it opens up the possibility of “optical guiding” – that is guiding the telescope by sensing the pointing origin of the telescope with starlight and

providing closed loop corrections. For a guider bandwidth of $> 1\text{Hz}$, consideration of the sky brightness and astronomical source counts result in the conclusion that there is a dramatic break in sensitivity and density of suitable targets at $\sim 2.5\ \mu\text{m}$. At $\lambda < 2.5\ \mu\text{m}$ the flux from stars is rapidly rising and the blackbody emission from the telescope is rapidly dropping.

15.5.4 Technical Discussion

Sensitivity for guiding is critically dependant on the size of the point spread function (PSF). The short wavelength PSF can be estimated by Fourier optical calculations of telescope aberrations or by assuming the wavelength is short enough for geometric optics to apply. In both cases, the estimated short wavelength PSF can be surprisingly large compared to the $2''$ PSF at $200\ \mu\text{m}$, as large as $30''$ - $60''$.

2MASS source counts at the Galactic pole [3] yield a density of sources brighter than $K=16.2$ of 1 per 4 square arcmin, or ~ 80 per $20'$ CCAT field of view. Such sources are easily bright enough for CCAT guiding if a compact PSF can be maintained.

Correction of the wavefront errors with a deformable mirror internal to the guider is possible, but would likely require far more actuators than are readily available in conventional deformable mirrors. Liquid crystal spatial light modulators are an alternate technology with very high density of elements, but would likely require multiple pass operation to correct the amplitude of wavefront errors expected with CCAT resulting in a potentially complex instrument.

The apparently simplest approach would be to sample the CCAT aperture with sub-apertures small enough to result in compact images at the guiding wavelength. This can be accomplished by re-imaging the pupil onto a lenslet array, which then forms sub-images from the individual pieces of the pupil. If the subapertures are sufficiently small the wavefront error across the subaperture is reduced to a tolerable level, then a compact PSF will result and the local tilt of the wavefront across the subaperture displaces the spot. Such a layout is commonly used as a Shack-Hartmann wavefront sensor.

It is attractive, therefore, to implement the guider as a Shack-Hartmann wavefront sensor. The S-H sensor provides local tilt for each lenslet and global tilt by averaging the spot positions. The local tilts can be integrated to provide wavefront measurements of all wavefronts up to the Nyquist sampling limit of the lenslet array.

The choice of the appropriate number of subapertures for the lenslet array depends on the segment aberrations of CCAT. It is likely that if the segments meet a $5\ \mu\text{m}$ rms wavefront error budget, then on some fraction of a segment scale, the wavefront error will be sufficient for imaging at $2\ \mu\text{m}$ wavelength. For example, with $25\ \text{cm}$ subapertures, a 100×100 Shack-Hartmann sensor would be needed for CCAT. This is large compared to wavefront sensors that have operated on telescopes but certainly feasible and within the range of devices used for optical metrology.

The conclusion, therefore, is a near-IR wavefront sensing guider is feasible to provide both pointing corrections and higher order wavefront sensing. There are likely to be sufficient natural guide stars available for continuous operation of a wavefront sensor during telescope operations.

If a wavefront sensing guider were implemented with high spatial resolution on the primary it is possible to use such a wavefront sensor not only for maintenance of the mirror figure at low order modes, but also for initial phasing. For pure piston errors of a segment, however, Shack-Hartmann wavefront sensing is inefficient and it would be desirable to implement a phase diversity or curvature sensing mode that is more sensitive to segment edge effects [1].

15.5.5 Strawman Design

The guider requires a pickoff mirror and relay optics to sample a few arcsec field of view of the CCAT focal plane. The patrol field of the guider pickoff can be outside the field of view of the first light instruments but would occult part of the entire telescope focal plane and so could impact future instrumentation with very large format focal plane arrays. The required patrol field of view for the guider is a function of the brightness of the guide star and, therefore, guiding temporal bandwidth. If fast guiding is not required, faint guide stars are not required and only a small patrol field is necessary.

15.5.6 Risk Assessment

The primary risk is the reflectance of the telescope mirrors and the cost of maintenance of the mirror surface. Since optical guiding requires significant transmission of the telescope at $\lambda \sim 2 \mu\text{m}$, guiding is not possible if the telescope does not deliver specular reflection at this wavelength.

Secondary risks include maintaining rigid connection from the guider pointing origin to the instrument pointing origin.

The wavefront sensing guider can mitigate risks associated with primary mirror calibration, telescope alignment, and edge sensor performance.

15.5.7 Cost

The hardware cost for an IR guider will be driven by the focal plane array cost. The development of low noise astronomical focal plane arrays has been focused on the development of very large format low noise arrays for several years. 2048×2048 arrays are available with exquisite noise performance and rapid readout capabilities designed for JWST for \$500k. Rockwell has been developing smaller format low noise arrays for IR wavefront sensing that would be lower cost, but has failed to deliver functioning devices. Although the large format may not be necessary for the CCAT guider, the low noise performance of the state of the art arrays may be required. The guider field of view will further need to be large enough that the blind pointing of the telescope will be sufficient to acquire the guide star. Smaller format focal plane arrays may be available with adequate performance and a likely minimum cost of \$50-75k. The focal plane array cost for the guider will be driven by two requirements: temporal bandwidth and acquisition field of view. A cryostat and control electronics for the guider is estimated at \$50k. The guider requires at a minimum two axes of precision motion to acquire guide stars. Rough order of magnitude cost is \$50k per axis. The cost of the software and integration and test of the guider may also be significant.

15.5.8 References

- [1] Wavefront curvature sensing on highly segmented telescopes. G. A. Chanan. In *Future Giant Telescopes*. Edited by Angel, J. Roger P.; Gilmozzi, Roberto. Proceedings of the SPIE, Volume 4840, pp. 367-377 (2003), pages 367–377, January 2003.
- [2] Gemini prime focus wavefront sensor. J. Sebag, D. M. Walther, P. Gigoux, J. M. Oschmann, and C. P. Cavedoni. In *Proc. SPIE Vol. 4007*, p. 452-460, *Adaptive Optical Systems Technology*, Peter L. Wizinowich; Ed., pages 452–460, July 2000.
- [3] 2MASS All-Sky Catalog of Point Sources (Cutri+ 2003). R. M. Cutri, M. F. Skrutskie, S. van Dyk, C. A. Beichman, J. M. Carpenter, T. Chester, L. Cambresy, T. Evans, J. Fowler, J. Gizis, E. Howard, J. Huchra, T. Jarrett, E. L. Kopan, J. D. Kirkpatrick, R. M. Light, K. A. Marsh, H. McCallon, S. Schneider, R. Stiening, M. Sykes, M. Weinberg, W. A. Wheaton, S. Wheelock, and N. Zacarias. *VizieR Online Data Catalog*, 2246:0–+, June 2003.
- [4] The Gemini-North Multi-Object Spectrograph: Performance in Imaging, Long-Slit, and Multi-Object Spectroscopic Modes. I. M. Hook, I. Jørgensen, J. R. Allington-Smith, R. L. Davies, N. Metcalfe, R. G. Murowinski, and D. Crampton. *PASP*, 116:425–440, May 2004.

- [5] The Gemini Near-Infrared Imager (NIRI). K. W. Hodapp, J. B. Jensen, E. M. Irwin, H. Yamada, R. Chung, K. Fletcher, L. Robertson, J. L. Hora, D. A. Simons, W. Mays, R. Nolan, M. Bec, M. Merrill, and A. M. Fowler. *PASP*, 115:1388–1406, December 2003.
- [6] Near-infrared integral-field spectrograph (NIFS): An instrument proposed for Gemini. P. J. McGregor, P. Conroy, G. Bloxham, and J. van Harmelen. *Publications of the Astronomical Society of Australia*, 16:273–87, December 1999.
- [7] The Lick Observatory TV autoguider. R. Kibrick and L. Robinson. *PASP*, 99:1014–1021, September 1987.
- [8] Application of Image Dissector Photomultipliers. A. A. Hoag, W. F. Ball, and D. E. Trumbo. *Publications of the Royal Observatory of Edinburgh*, 8:71–+, 1971.

16 Secondary and Tertiary Mirror Systems

16.1 Overview

In addition to the primary mirror, the CCAT optics include secondary and tertiary mirrors. To maintain the optical alignment of the telescope and to direct the telescope beam to the active instrument focus, these mirrors require positioning systems. This chapter describes concept designs for the mirror positioners. Introductory remarks are followed by a report of a funded concept design study performed by CSA Engineering of Mountain View, California.

16.1.1 Background

Both the hyperbolic secondary mirror, M2, and the flat tertiary mirror, M3, will be made of a high stiffness, thermally stable, lightweight (10 kg m^{-2}) material, possibly using the same technology as the primary mirror. Because of their size, about 3.3 m diameter for M2 and $2 \text{ m} \times 3 \text{ m}$ for M3, these mirrors likely will be made in segments. When mounted on three points, each segment will meet the dimensional requirements for surface figure under the full range of gravity conditions (zenith to 15° above the horizon) and thermal variations. These three attachment points will be bipod flexures, designed so they impose minimal moment loads on the mirror segments.

The Secondary Mirror Support, Nutator, and Positioner subsystems have three functions. First, the Support structure holds the secondary mirror segments and maintains optical alignment under all operating conditions. This support structure includes an adjustment mechanism for the relative alignment and positioning of the mirror segments. Second, on command the Nutator nutates, or wobbles, the secondary mirror to switch the telescope beam through a small angle on the sky. Third, the Positioner moves the entire Secondary Mirror assembly, including the Support structure and the Nutator, on command to maintain the optical alignment of the entire telescope. Five motions are required: displacement along the optic axis (focus), translations in both directions perpendicular to the optic axis, and tilts in both directions from the optic axis. Limited rotation about the optic axis is beneficial, but not required.

The Tertiary Mirror Positioner has two functions. First, the Positioner supports the tertiary mirror segments to maintain optical alignment under all operating conditions. The Positioner includes an adjustment mechanism for the relative alignment and positioning of the mirror segments. Second, the Positioner rotates the mirror on command to direct the telescope beam in any of four directions, toward either of the two Nasmyth foci on opposite sides of the elevation axis or to either of two Cassegrain foci ninety degrees apart.

16.1.2 Scope

The secondary and tertiary mirror positioning systems consist of the mechanisms, motors, cabling, electronics, system controller, and any other components necessary to support, align, and position the secondary and tertiary mirrors. Commands are provided by a local control system to the various actuators. Any and all other required elements are considered part of the Positioners. The mirror segments themselves are not part of the Positioners. The telescope structure will include suitable flanges for mounting the Positioners.

16.1.3 Secondary Mirror System Concepts

Two concepts were considered for the secondary mirror subsystems. In the first concept, the three functions are realized in separate, stacked mechanisms. Mirror segments are mounted to the Support structure and manually adjusted to the correct locations. The relative segment positions are not routinely adjusted or changed. The Nutator acts on the mirror and Support assembly and the Positioner acts on the combined mirror and Nutator.

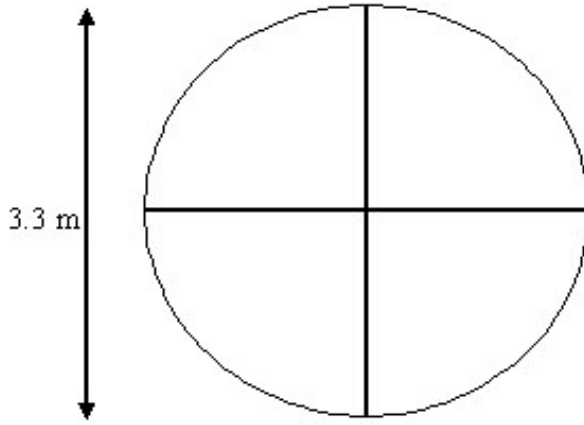
In the second concept, some or all of the functions are combined in one set of mechanisms. Mirror segments are mounted to the support structure with linear actuators. These allow wide bandwidth active control of the mirror segment positions for image jitter control, fine pointing, and secondary mirror nutation.

Both of these concepts were explored in the design study performed by CSA Engineering.

16.1.4 Design Overview

16.1.4.1 Secondary Mirror Mechanism

The secondary mirror is a hyperboloid, about 3.3 m diameter, and is segmented in quarters. The assembled mirror will exhibit $< 5.0 \mu\text{m}$ rms total wavefront error.



The secondary mirror is mounted about 15 m in front of the primary mirror surface. The mirror segments are mounted to the Support structure, a single space frame truss, with bipod flexures or actuators. Adjustment mechanisms permit the relative alignment and positioning of the mirror segments. Both passive and active systems were considered. The overall adjustment range is ≈ 5 mm and the minimum step size at each segment mounting point is $0.5 \mu\text{m}$.

The Nutator switches the telescope beam by $\pm 2.5'$ on the sky at a 1 Hz repetition rate with 100 ms transitions. Smaller beam displacements and proportionally faster transition times are possible. During the dwell phases, the

Nutator maintain the telescope pointing within $0.1''$. The nutation axis coincides with the mirror's center of mass. The Nutator mechanism minimizes dynamic structural loads on the telescope by using a reaction canceling design.

The Positioner provides displacement along the optic axis (focus), translations in both directions perpendicular to the optic axis, and tilts in both directions from the optic axis. The tilt pivot is the vertex of the secondary mirror. The motions are summarized in the table. The range limits refer to the quadrature sum of the orthogonal components. Positioner motions are coordinated so each axis can be driven smoothly without affecting the other axes.

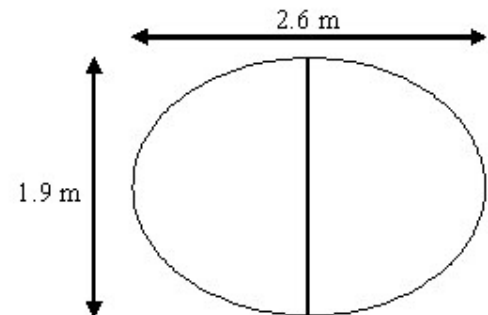
| | Range | Precision | Speed |
|-------------|---------------|------------------|--------------------------|
| Focus | ± 20 mm | $18 \mu\text{m}$ | $300 \mu\text{m s}^{-1}$ |
| Translation | ± 10 mm | $65 \mu\text{m}$ | $150 \mu\text{m s}^{-1}$ |
| Tilt (M2) | $\pm 1^\circ$ | $1''$ | $30'' \text{ s}^{-1}$ |

16.1.4.2 Tertiary Mirror Mechanism

The tertiary mirror is flat with an ellipsoid outline and is divided in two halves. The assembled mirror will exhibit less than $5.0 \mu\text{m}$ rms total half wavefront error.

The center of the tertiary mirror is mounted 3 m behind the primary mirror vertex. The mirror segments are mounted to a space frame truss with bipod flexures. Passive adjustment mechanisms permit the relative alignment and positioning of the mirror segments. The overall adjustment range is ≈ 5 mm and the minimum step size at each segment mounting point is $0.5 \mu\text{m}$.

The Positioner rotates the tertiary mirror about the telescope optic axis to direct the telescope beam to either of the two Nasmyth foci on the elevation axis or to the one or two bent Cassegrain foci ninety degrees from the elevation axis. In 2 min, the Positioner can rotate the tertiary mirror through 180° , i.e., from one Nasmyth focus to the other.



The tertiary mirror is inclined 45° to the telescope axis. The Positioner supports the entire tertiary mirror assembly to maintain the telescope beam on the sky within $0.2''$. This implies holding the tertiary mirror alignment within $5''$ tolerance. This alignment is maintained for all mirror rotations.

16.1.5 Concept Design Study

CSA Engineering undertook a concept design study of these mechanisms under contract to CCAT. The following section reports the results of the study. As part of the study, CSA reviewed the CCAT requirements, developed concept designs, made basic analyses for specification and sizing of the major components, identified the interfaces, and developed cost and risk estimates. The study indicates both concepts for the secondary mirror mechanism are feasible with similar cost.

16.2 Secondary and Tertiary Mirror System

Report prepared by CSA Engineering

16.2.1 Summary and Introduction

This document summarizes work done on concept designs for CCAT subsystems, including:

- Secondary mirror positioner,
- Secondary mirror nutator
- Integrated secondary mirror positioner and nutator, and
- Tertiary mirror positioner.

Using information available for the overall telescope concept, and experience with other similar systems, we identified the driving design considerations and developed design concepts. These concepts are detailed only in their expected overall performance. We made assumptions about the secondary (4 parts) and tertiary (2 parts) segmentation. While the positioning and nutation concepts require electronic and software elements, these were not considered in any detail. They can be addressed subsequently by drawing on previous experience, and they do not affect other telescope subsystems or performance as directly as, for example, hexapod positioner resolution.

A primary consideration in the concept study for secondary mirror (M2) control was the desire to realize separate functions: initial alignment, positioning (mainly to counter gravity-induced deformations), and nutation. The major difference in these positioning requirements is timescale, from adjustment over minutes or even days during installation, to seconds as the telescope azimuth angle changes during operation, to fractions of a second for nutation. The desire was to accommodate these separate but related requirements with the right level of integration or overlap.

The following pages describe a design with the secondary mirror positioner (for both segment alignment and positioning during operation) being distinct from the nutation, with a separate means of actuation. A more integrated design is discussed next. Finally, a concept for tertiary mirror positioning is summarized.

16.2.2 Baseline Design for M2: Separate Positioning and Nutation

The nominal secondary mirror positioner, nutator, and adjustment mechanisms are shown in Figure 16.2.1. An active hexapod is used to position the mirror and nutator with low bandwidth (sub-Hertz) response. The hexapod uses roller screw actuators to provide the force, range, stiffness, and resolution required as described below. Nutation is achieved using two voice coil actuators and a gimbal ring. Figure 16.2.1 shows only one axis of nutation for simplicity, though two-axis nutation is possible. Fine alignment of each mirror segment is accomplished with a passive, manually-adjustable hexapod (four total) using acme lead screw struts.

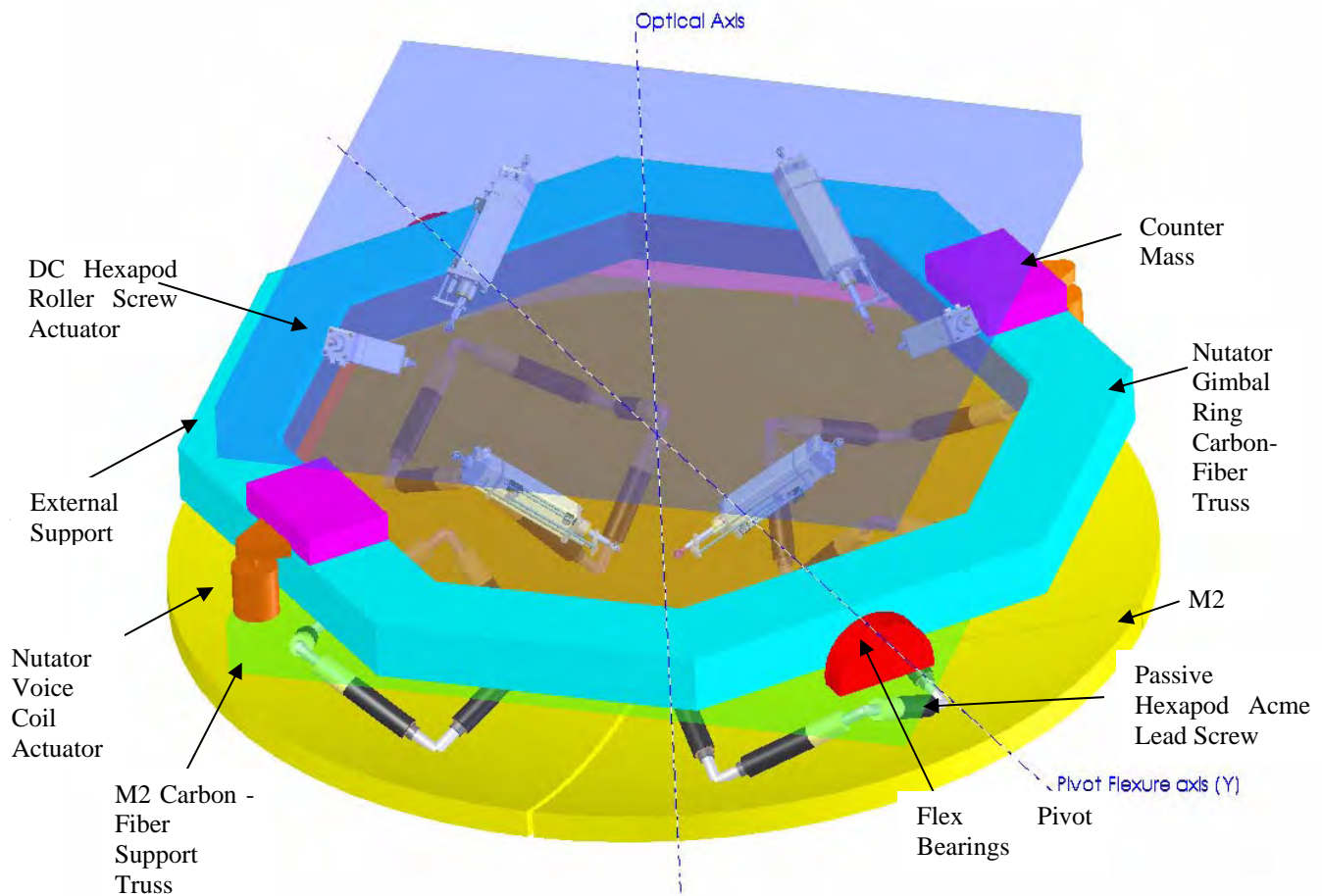


Figure 16.2.1. Concept secondary mirror positioning system

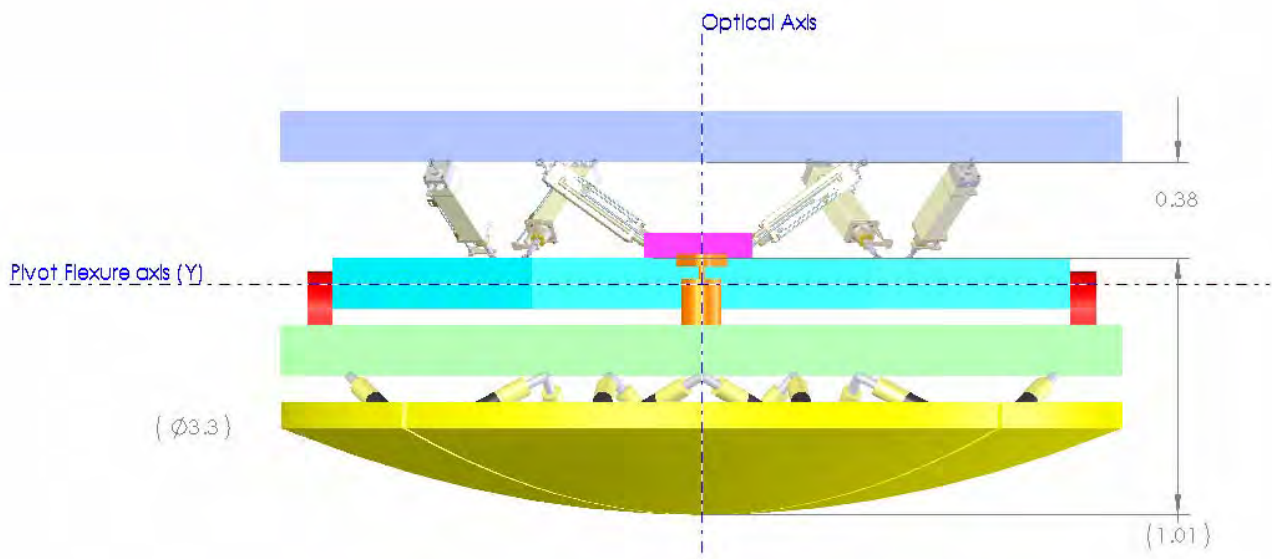


Figure 16.2.2. View of M2 positioner along X axis

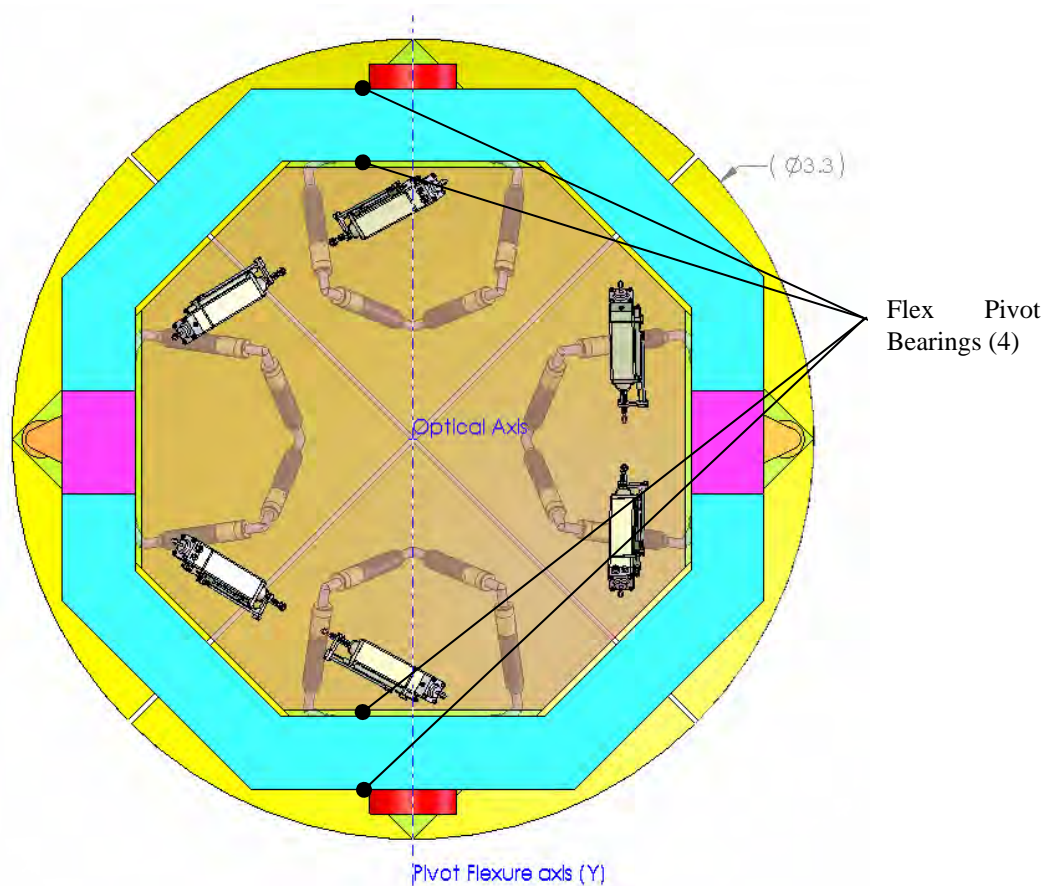


Figure 16.2.3. View of M2 positioner along optical (Z) axis without support

16.2.3 Active Positioning Hexapod

Design of this hexapod was informed by previous experience with other hexapods, including a 3 m-diameter system used to position a large wavefront sensor. Precision, expressed here as resolution, emerged as the key design consideration. With the preferred realization using motor-driven screws, range can be added, up to a point, without dramatic compromise in resolution.

The geometry and the actuator resolution of the positioner were optimally chosen based on the size constraints and the required resolution in each degree of freedom. The size constraints were based on mirror size, and concept drawings of the M2 support structure and dome. To determine the best geometry within these constraints, a cost function was evaluated. The cost function was based on the average error in resolution, standard deviation in resolution, and the maximum force required when pointed at the horizon.

In order to estimate the resolution, the secondary positioner was stepped in each degree of freedom in increments equal to the desired resolution values. At each step, the actuator lengths were determined and then quantized based on the actuator resolution. The position of the secondary positioner was then determined based on these quantized actuator values. Table 16.2.1 shows the resolution results of the chosen geometry shown above. The resolution values were based on 40 commanded steps in the positive direction starting from the nominal position. A required actuator strut resolution of 3 micrometers was assumed.

Table 16.2.1. Estimated resolution for the secondary positioner implementing actuators with 3-micrometer resolution (1 μrad is approximately 0.2 arcseconds)

| Axes – Resolution Spec μm or μrad | Average Resolution μm or μrad | Standard Deviation μm or μrad | Maximum Step μm or μrad |
|---|---|---|---|
| X - 65.0 | 65.0 | 1.66 | 67.6 |
| Y - 65.0 | 65.0 | 1.86 | 69.4 |
| Z - 18.0 | 18.0 | 1.36 | 18.6 |
| Ox - 4.85 | 4.84 | .567 | 7.29 |
| Oy - 4.85 | 4.84 | 1.26 | 8.41 |
| Oz - N/A | 9.60 | 2.84 | 11.7 |

In addition to the resolution, the static force values were calculated assuming the telescope was pointed at the horizon. In this case, the static forces will be the largest since the positioner will react not only the payload weight, but also a moment. In order to calculate these forces, the payload was assumed to have a mass of 220 kg, consisting of 80 kg for the mirror, 40 kg for the truss and 100 kg for the nutator. The center of mass was assumed to be 500 mm in the direction of focus from center of the actuator nodes that attach to the nutator. This location is also the geometric center of the payload. The maximum static force required in any actuator, given the geometry above, was found to be 1.23 kN.

During the concept study, resolution was the more demanding specification. Therefore, efforts were concentrated on resolution specifications and not on range. Typically, if more range is required, an actuator can be chosen with more range. However as range is increased typically the resolution will decrease thus affecting the overall resolution and design of the positioner. The range for the geometry chosen above was determined by simultaneously moving the positioner to the extent of its range in each degree of freedom. Every possible combination of range was tested as the minimum and maximum actuator strokes were recorded. Based on the specified range, ± 10 mm in translation, ± 20 mm in focus, ± 0.5 degrees in tip and tilt, the maximum total stroke for any actuator was 78.4 mm.

All of the requirements can be met with a roller screw actuators similar to the Exlar GSX series, which are shown in the figures. These actuators should have a pitch of 2.54 mm or less, with a pre-loaded nut for minimum backlash, and 75-150 mm of total stroke. The feedback sensor of choice is the absolute rotary encoder with 2048 counts per revolution or higher and revolution counter. An option for dc absolute positioning is the LVDT, which is shown in the figures. The kinematic joints on each end of the struts are gimbaled using pivot flexures.

16.2.4 Passive Alignment Hexapods for Initial Alignment

Initial alignment of the four secondary segments is accomplished through the use of four flexure mounted hexapods. This technique allows for alignment of the four mirror segments each in six degrees of freedom while satisfying the mounting needs of the mirror segments. Each hexapod is connected through a set of flexures to a rigid base. The base is constructed from carbon fiber and aluminum honeycomb sandwich board or carbon fiber tube truss. This entire assembly is then connected to the active hexapod motion platform through pivot flexure bearings.

The hexapod struts consist of a carbon-fiber barrel approximately three inches in diameter. Bonded in each end of the barrel are the nuts of right handed acme lead screws (Figure 16.2.4). The lead screws have a 2 inch root diameter with 4 threads per inch in one end and 5 threads per inch in the other. Using this combination of threads in the same direction will yield 0.050 inches of displacement for each revolution of the barrel. On one end of the strut fixed to the acme thread is a bezel. This stationary bezel slips over the end of the barrel and has incremental marks to aid in positioning.

The barrel and bezel are approximately 3 inches in diameter, which should allow for a total of 100 marks around the circumference. Furthermore, these marks could be subdivided another 10 times using a vernier scale yielding

a total of 1000 divisions. The struts are estimated to have a resolution of approximately 50 micro inches or 1.3 μm . A computer program will be provided to allow the users to quickly determine the necessary strut lengths based on a required mirror motion. The approximate mass of each strut in the segment alignment assemblies is 8.3 kg.

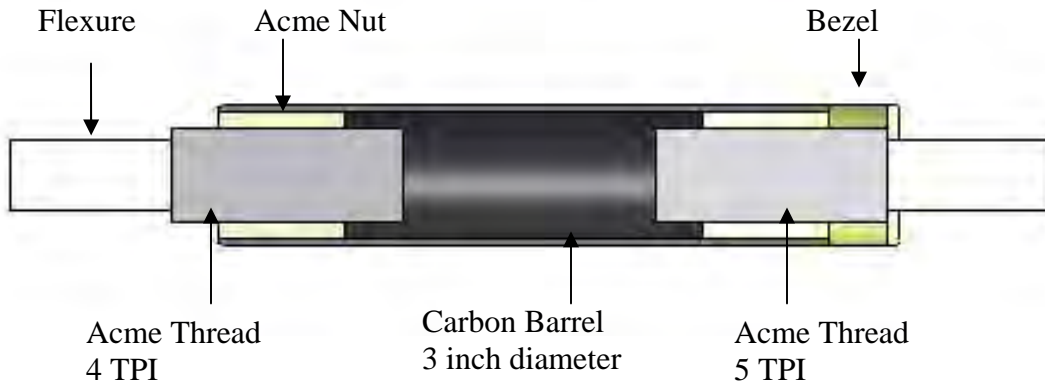


Figure 16.2.4. Cross section drawing of a manual strut used to align the tertiary mirror segments

16.2.5 Nutation

The baseline concept design assumes electromagnetic voice coil actuation will be used to control nutation. Two linear actuators are required for one axis, and a minimum set of 3 is required for two axes. The design concept assumes a total of four actuators will be used for two-axis nutation. The actuators will have linear feedback devices for measurement of relative angular motion, which summed with a gimbal ring angular measurement sensor results in total angular motion of the mirror.

The estimated requirements for nutation actuation in the voice coil actuators were approximately $\pm 1.5\text{mm}$ stroke and $\pm 50\text{N}$ force. This calculation assumed an 84 kg mirror with $114 \text{ kg}\cdot\text{m}^2$ mass moment of inertia, plus an additional $115\text{kg}\cdot\text{m}^2$ to account for the inertia of the passive hexapods. The peak acceleration of 0.7 rad/s^2 allows 5 arcmin of nutation in 100 ms. The nominal actuator would be designed based on CSA Engineering’s SA series actuators (Figure 16.2.5, left) or another high force unit developed for specialized testing (Figure 16.2.5, right). The pivot flexure bearing supports will have some stiffness which will control the dc rotational positioning of the mirror. However, the nominal goal of nutating about the center of inertia of M2 is difficult to achieve in this configuration, and the nutation axis would likely lie close to or in line with the pivot axis for the counteracting inertial mass (see Figure 16.2.2).



Figure 16.2.5. A version of CSA Engineering’s SA10 voice coil actuator and custom high-force unit

One of the design considerations for the actuation will be heat generation. Coil properties can be tailored for the preferred voltage-current mix, and an analysis of heat transfer into the telescope structure would set limits on total heat load per unit time.

16.2.6 Alternative Design: Integrated Secondary Mirror Positioner/Nutator

A more compact and lower-weight package is desired for the secondary mirror assembly. Combining multiple positioning functions in one actuator set is a means to that end. A concept design for the M2 positioner that includes gross static positioning, alignment positioning, and nutation in a single mechanism is shown in Figure 16.2.6. The positioning system uses four active hexapods, each attached to and controlling a single mirror segment. A single hexapod may be used to eliminate mirror alignment errors, compensate for gravitational changes, and nutate the mirror about either of two axes. Each hexapod will be independently controlled with an outer control loop that coordinates the motions such that global nutation is achieved in the desired axes.

Reaction forces from nutation are minimized with the use of a dual axis gimbal truss structure, which also serves as the interface between the rigid support and the hexapods. Pivot flexure bearings on the zero-CTE trusses allow low amplitude dynamic rotary motion while retaining dc positioning capability. The center of gravity of the entire nutating mass will be designed to lie at the intersection of the two nutating pivot flexure axes, which will eliminate any static torques due to gravitational loads on the pivot flexures. Nutation about the mirror center of inertia is achievable in this configuration in two orthogonal axes.

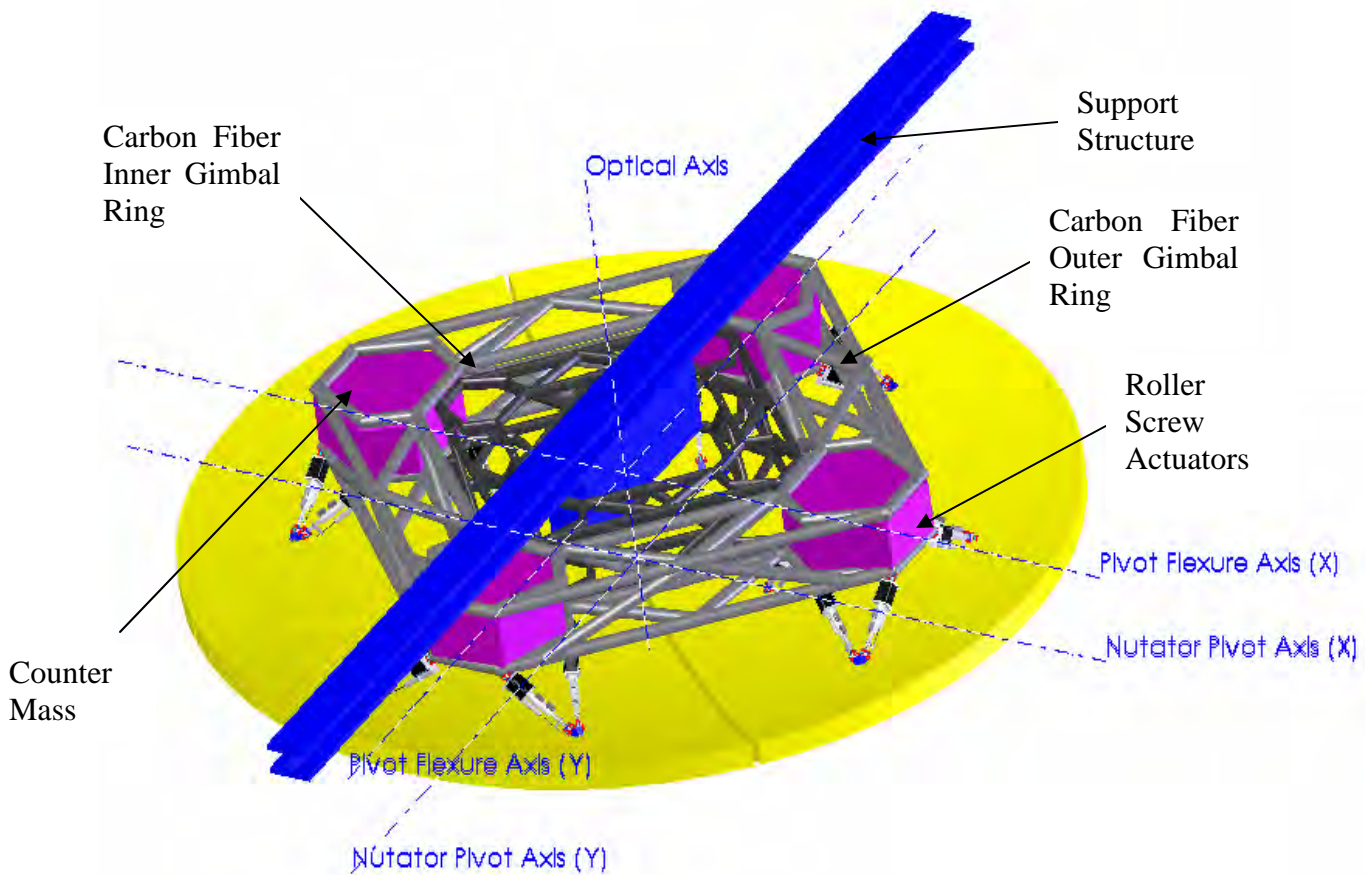


Figure 16.2.6. The concept integrated M2 positioner and nutator uses active hexapods on each mirror segment. Hexapod geometry shown is non-optimal

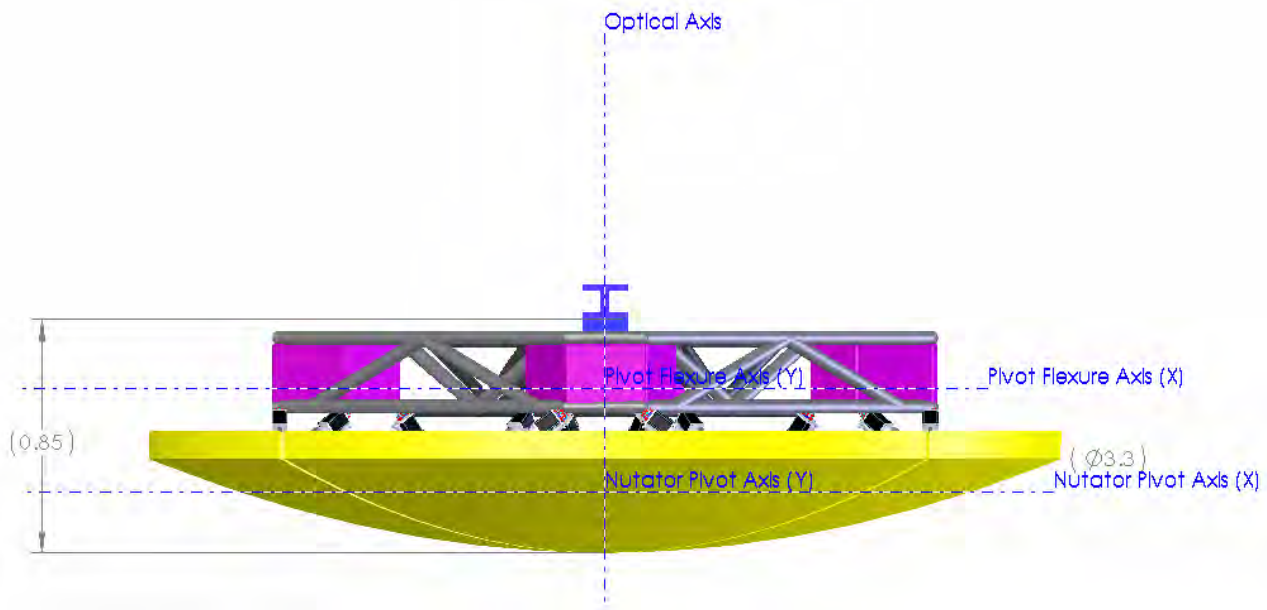


Figure 16.2.7. Integrated M2 positioner along Y axis

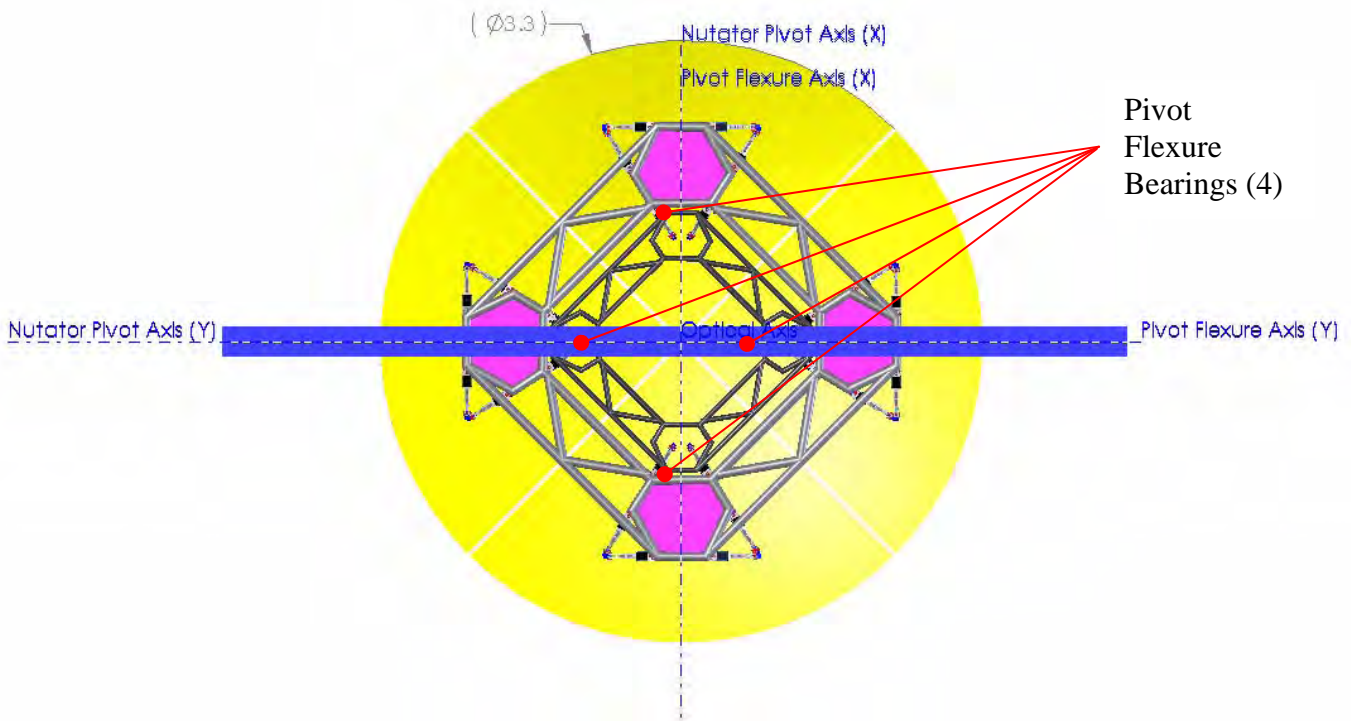


Figure 16.2.8. View of integrated positioner along optical (Z) axis

We again used the method described for the nominal M2 positioner (above) to determine the optimal geometry and required actuator resolution to achieve the desired positioner resolution. With the integrated design, the resolution about one of the tip axes became more demanding causing the need for a finer actuator resolution.

One beneficial geometric feature when rotation is about a given axis is that some of the actuators are located an appreciable distance from this axis. The longer the distance or lever arm, the more the actuator has to move to achieve a given angle, and the resolution of the system is improved. One advantage of the nominal design was some of the actuators were located a long distance from the tip axes. The integrated design consists of four

hexapods and each hexapod has a tip or tilt axis directly through its center. In addition, in the design with four hexapods, each hexapod has a smaller in diameter. The end result was that one of the tip axes had a shorter lever arm so the actuator had to have better resolution to achieve the same results. It was determined that a one micrometer actuator resolution was needed, which yielded the estimated resolution shown below in Table 16.2.2, once again assuming 40 commanded steps in the positive direction, starting from the nominal position.

Table 16.2.2. Estimated resolution for the optimal secondary positioner implementing actuators with 1 micrometer resolution

| Axes – Resolution Spec $\mu\text{m} / \mu\text{rad}$ | Average Resolution $\mu\text{m} / \mu\text{rad}$ | Standard Deviation $\mu\text{m} / \mu\text{rad}$ | Maximum Step $\mu\text{m} / \mu\text{rad}$ |
|---|--|---|---|
| X - 65.0 | 65.0 | 0.86 | 66.7 |
| Y - 65.0 | 65.0 | 1.25 | 66.6 |
| Z - 18.0 | 18.0 | 0.90 | 19.3 |
| Ox - 4.85 | 4.84 | 0.95 | 6.71 |
| Oy - 4.85 | 4.84 | 1.86 | 8.67 |
| Oz - N/A | 4.86 | 0.53 | 5.32 |

The static forces were calculated when the telescope was aligned with the horizon. For the force calculations a payload of one mirror segment was assumed to have a mass of 21 kg. The center of mass was assumed to be 34 mm in translation and 170 mm in focus from the center of the node locations location where the actuators attach to the mirror segment. The maximum static force in any actuator was found to be 107 N.

The range for the geometry chosen above was determined by simultaneously moving the positioner to the extent of its range in each degree of freedom. Every possible combination of range was tested as the minimum and maximum actuator strokes were recorded. Based on the specified range, ± 10 mm in translation, ± 20 mm in focus, ± 0.5 degrees in tip and tilt, the maximum total stroke for any actuator was 70.1 mm.

Since the mirror segments are actuated independently and the nominal “X” configuration with respect to gravity creates unequal inertial forces between segments, the worst case motion was assumed for the calculation of required strut forces and speeds for nutation. For 0.72 rad/s^2 maximum acceleration and a rotational inertia of $24 \text{ kg}\cdot\text{m}^2$, the additional strut forces required for nutation are in the range of 5-10 N, insignificant compared to the static positioning forces. Speeds reach approximately 75 mm/s.

The range, force, resolution, speed, and lifetime (30 million cycles) can be met with an acme screw actuator such as the Ultramotion Digit (as shown in the figures) or roller screw actuator such as the Exlar GSX series, with approximately 2 mm/rev pitch and 100 mm stroke. The metrology and flexure-based kinematic joints are similar to those discussed in the nominal M2 positioner design above.

16.2.7 Tertiary Mirror Positioner

The tertiary positioner is located three meters behind the primary mirror and has two functions. One function is to align the two mirror segments of the tertiary mirror relative to one another. The other function is to rotate the tertiary mirror and direct the beam to either of the two Nasmyth foci located on opposite sides of the elevation axis or to either of the Cassegrain foci, which are located 90 degrees from the Nasmyth foci. After initial alignment, the mirror must be positioned precisely to one of the four angles.

Alignment of the two tertiary mirror segments is accomplished through the use of two flexure mounted hexapods (Figure 16.2.9). This technique allows for alignment of the two mirror segments in six degrees of freedom while satisfying the mounting needs of the mirror segments. Each hexapod is connected through a set of flexures to a rigid base. The hexapod struts are similar to those discussed under the nominal secondary mirror positioner design above (Figure 16.2.4). The base is constructed from carbon fiber and aluminum honeycomb sandwich board keeping its weight to only 61 kg. This entire assembly is then connected to the telescope base through a commercial off the shelf, COTS, rotary table.

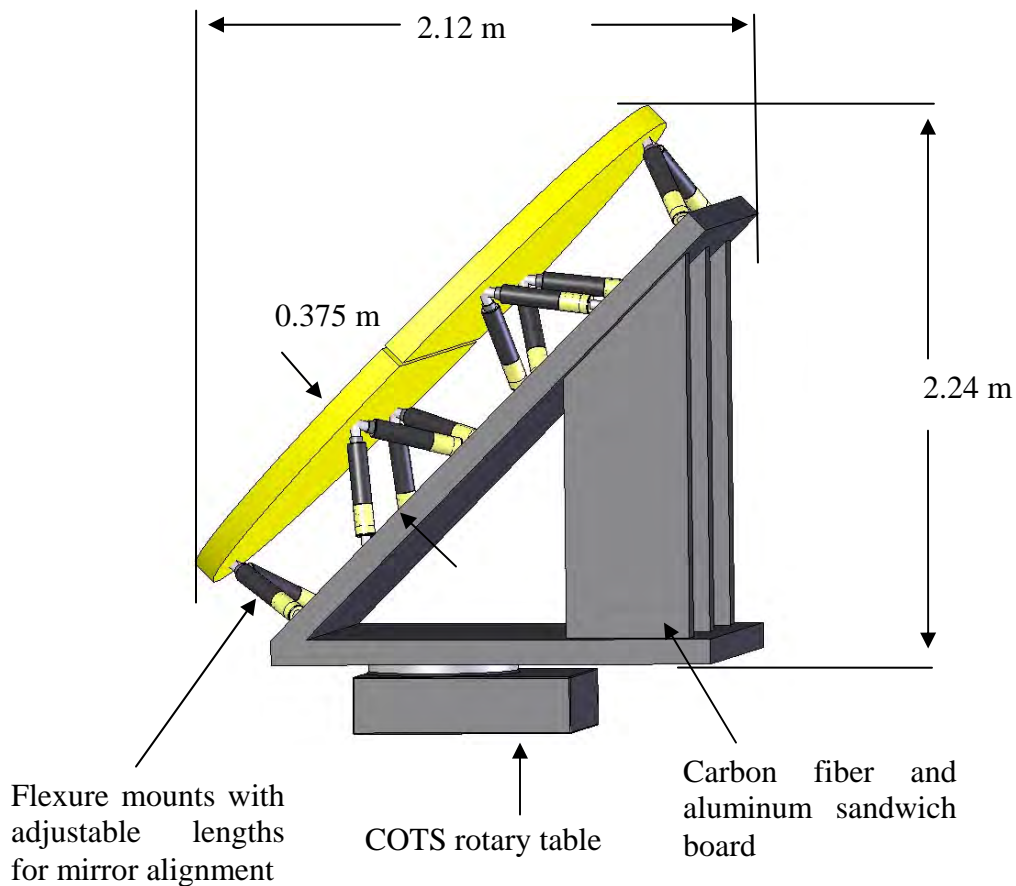


Figure 16.2.9. Concept drawing for the tertiary mirror alignment and positioning

The Troyke NC-30-A rotary table is one candidate COTS item capable of 4053 N m of torque. The unit weighs 630 kg and has a load capacity of 1813 kg in the horizontal direction and 906 kg in the vertical direction. The unit has a resolution of 0.001 degrees and an angular accuracy of ± 3.6 seconds with a repeatability of ± 1 second.

The control system for the rotary stage will require 230 Volts AC. The controller can be located at the base of the telescope; however, a power and feedback cable must be run to the rotary stage. In addition to the power, a 120 psi airline must be run to the rotary stage to operate the brake.

16.2.8 Critical Risk Assessment

Currently the resolution requirements in tip and tilt appear to be driving the design. The necessary actuator resolution for the nominal design needs to be less than $3 \mu\text{m}$, while the integrated design requires a resolution less than $1 \mu\text{m}$. While the integrated actuators are much smaller, both of these resolution requirements are quite demanding and could drive the cost. These resolutions can nominally be met with off-the-shelf or semi-custom microstepping actuators, but dynamic repeatability, deadband, and accuracy troubles could add up to effectively demand a custom actuator.

The integrated design provides many benefits over the nominal design, as the number of linkages (pivoting joints) is reduced, the overall structural stiffnesses are larger, the masses are lighter, the actuators are smaller, no manual alignment is required, and the nutation axis is about the inertial center of M2 (resulting in nominally lower power required). Drawbacks include increased complexity of the control system and possibility of mirror section contact

during periods of partial blackout or system instability. Increased wear will occur in isolated locations in each actuator since nutation will cause much more travel, but over a smaller range, than alignment or gravitational positioning. This may cause an increase in actuator backlash over time. Further study into wind loading is also required.

Electronic systems and software are not the subject of this document. However, these systems will be less likely to degrade over time. Obviously software design, review and extensive testing will be required to ensure low likelihood of failures.

The tertiary mirror positioner is considered to be lower risk. Weight is less of a concern, and the functions required are similar to those required in certain industrial applications. Use of commercially-available products, or customized versions of the same, is likely to be the most direct path to a successful M3 positioner.

To meet the 10 year lifetime requirement some maintenance may be required. In particular, since the nutation range is limited and screws are not likely to be lubricated properly, actuator lubrication is necessary but may take the form of redistribution from a long range move.

17 Observatory Control System

17.1 Introduction

The observatory control system includes all software, computers, and communications hardware needed for control of the telescope, instruments, and supporting systems. Although the control system was not extensively addressed during the CCAT Feasibility Study, this section presents an overview of the technical approach anticipated.

17.2 Scope and Functional Requirements

The major control system functions include, but are not limited to:

17.2.1 Telescope Control

- Pointing and tracking
- Primary mirror active surface control
- Secondary mirror positioning and active figure control
- Tertiary mirror pointing
- Optics alignment
- Safety interlock monitor

17.2.2 Enclosure Control

- Pointing and tracking
- Shutter open and close
- Safety interlock monitor

17.2.3 Environmental Monitoring

- Site meteorology
- Dome and telescope temperature monitors
- Weather forecasts

17.2.4 Instrument Control

- Configuration, tuning, etc.
- Observing synchronization
- Diagnostics, e.g., cold stage temperatures
- Data readout and storage

17.2.5 Observations Control

- GUI and scripted observations
- Remote observing
- Queue scheduling and autonomous observations
- Instrument data quick look display

17.2.6 Data Management

- Instrument data archiving, cataloguing, retrieval, and distribution
- Operations logging
- Maintenance logging and scheduling

17.2.7 Communications

- Inter-process
- Inter-system, i.e., between the telescope and the instrument
- Inter-site, i.e., between the mountain facility and the remote observer
- Both machine (data) and human communications

Although some control system components may be embedded in various subsystems, the overall architecture must account for them all. Each subsystem will require software for configuration, control, diagnostics, and engineering work. Safety systems, such as fire alarms will be supplied by certified vendors and monitored by the control system. Instruments will have specific internal software developed with the instruments but will use a common interface to the observatory control system. Scientific data reduction software, i.e., AIPS, Class, etc., are not included in the control system although computer hardware to support data reduction is included.

17.3 Design Guidelines

In the past, many different combinations of software environments, operating systems, hardware platforms, and communications protocols, have been used successfully for astronomical telescope control systems. These choices may have widely different development and maintenance costs. Although the underlying principles remain stable, specific implementations of information technology change much faster than many other aspects of technology. Hence for CCAT, it is important to choose a flexible system architecture that can be economically supported for most of the life of the telescope. These considerations lead to the following design principles.

- Use existing, well developed solutions when practical.
- Implement transparent distributed control for remote operations.
- Implement efficient user interfaces for both scripted and direct observations.
- Ensure instrument and subsystem developers are able to contribute useful code without relying on software engineers.
- Construct a mostly homogenous system to reduce maintenance costs but allow some variations in order to most efficiently integrate other practical solutions.
- Use software and hardware systems with broad industry support, cross platform capability, and the likelihood of continued support in the future.
- Use applications software environments that are simple, well known, stable, and easily documented.
- Use well known operating systems available for a variety of hardware platforms.
- Use communication protocols with adequate bandwidth and wide compatibility with different devices.
- Use robust, cost effective hardware with a wide range of available “plug-in” accessories, including motion controllers, data acquisition cards, GPS timing hardware, etc.

17.4 Strawman System

For the purpose of the current Feasibility/Concept Design Study, we suggest a system using the following:

- Subsystems, as appropriate, from existing telescopes, including the CSO, Arecibo, SOAR, and others.
- Pointing and telescope control kernel from Pat Wallace (Rutherford Appleton Laboratory).
- PC hardware platforms. These are cost effective, are easily built or modified to provide specific capabilities where needed, are available in numerous configurations from many vendors, have well understood architectures, and are capable of operating either Windows or Linux.
- Linux operating system on most nodes. Selected nodes may run Windows depending on contractor or developer preferences and required capabilities.
- National Instruments LabVIEW for applications development. This graphic programming environment was developed specifically for instrument, process, and machine control. It permits the rapid development of GUIs, integration of legacy code, implements transparent distributed control, and is available for several platforms.
- Ethernet communications with multiple backbones to separate data traffic from control and support communications.
- A separate timing bus, IRIG-B, for synchronization.

The overall system architecture is shown in the figure. Because of the rapid pace of change of IT systems, these detailed choices are subject to change.

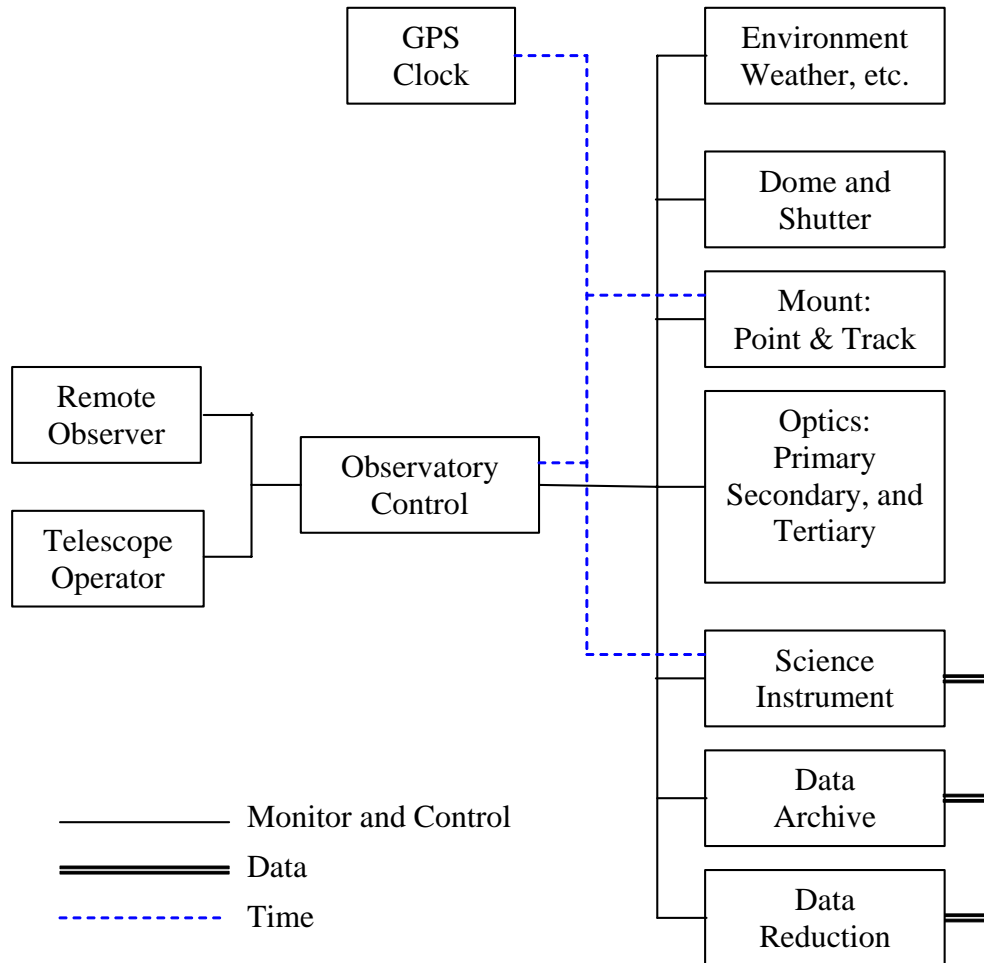


Figure 1. Functional block diagram of observatory control system. Different busses isolate monitor and control, high bandwidth data, and synchronization signals

17.5 Next Phase

During the next design phase, the observatory control system will be addressed more formally. A control and software engineer will be hired to design the system in detail and manage its implementation. Activities during this phase will include:

- Use case definition.
- Detailed requirement and specification definition.
- Interface identification and definition.
- Software development methods and standards choice.
- Data rates, bandwidth, processor capacity, etc., specification.

18 Integration Plan

18.1 Introduction

This section provides an initial plan for integration and commissioning of the Cornell Caltech Atacama Telescope. In general it addresses the stepwise development of the site and facility, integration and assembly of major subsystems, initial operation, and commissioning of the telescope.

18.2 Background

The ease with which the development of site infrastructure, general construction, and the subsequent installation and debugging of the major subsystems can be accomplished is strongly dependent on planning and preparation during the earliest stages of a project. The integration of CCAT is particularly challenging owing to its size, precision, and the extreme environment of a peak over 5000 m in the remote Atacama region of Chile.

Most telescope subsystems will be developed in the US or elsewhere so delivery to the site will require both land and sea transportation. Because of the size of the telescope and space and handling limitations, this implies major subsystems must be designed from the outset to be compatible with shipping.

Labor in the Atacama region for such tasks as general construction, steel erection, trades, and support to telescope subsystems is available, but the logistics of housing, feeding, and transporting personnel also require good planning. The concurrent development of ALMA in the same region may provide some opportunity for collaboration and will be investigated.

Assembly and alignment of major technical components such as the dome, telescope mount, and primary reflector assembly require both large handling equipment and precision alignment processes. Large construction cranes are expensive, both to transport to the site and to keep there on a daily basis, so it will be important to arrange work to minimize the time they are required on site. Specialized equipment and tools will need to be shipped to the site and early identification and procurement of these will be important.

The proliferation of electronics and computer control throughout the observatory implies a good deal of complex wiring, optical fiber, and intermediate control electronics. While Project personnel will have engineering responsibility for these, it may be useful to hire some appropriate support personnel to assist in pulling and terminating wire, running conduit, and other trade work.

After first light and during commissioning the telescope requires development support from the engineers and the scientific staff. The need to prepare for handover to operations must also be addressed. Preparation for this stage must begin even as the initial Project Team is chosen to find individuals who have hands on as well as theoretical and analytical experience. The first members of the operations staff will come on board during integration to become familiar with all the telescope systems and to minimize loss of momentum during transition to operations.

It is the objective of the Integration Plan to identify strategies to meet the full range of anticipated requirements and to ensure that the integration and commissioning of the telescope is accomplished as efficiently as possible.

18.3 Scope

This plan provides initial concepts for approaches to Integration and Commissioning. Integration begins with initial on-site development, including early site work and establishment of relationships with organizations and companies who will assist in various aspects of integration. It also addresses manpower, equipment, support services, and other assets required to assemble, debug, and optimize the observatory. This is an initial plan which will be refined during the next phase of CCAT development.

18.4 Technical Approach to Integration

The following are identified as key elements in our approach to integration and assembly of CCAT:

18.4.1 Site Preparation and General Construction

During site preparation and general construction, the capability of the Project Team to work in Chile is being developed. Sources for all required labor, tools, hardware, and of key services such as steel fabrication, machining, and trades will be identified. On site Project personnel will be chosen for their ability to support all phases of development, not just general construction. During these early phases of on-site activity, the site manager and first mechanical technician will be added to the team. It will be highly desirable to seek Chilean people to fill these positions as the ability to work closely with local laborers, contractors, trades people, etc. will be important.

18.4.2 Subsystem Design and Contract Requirements for Integration

The major subsystems of the telescope will be specified in order to optimize the efficiency and precision of integration. Elements of this are:

18.4.2.1 Modular Design

To the extent possible, each subsystem will be subdivided into modules that can be easily assembled. Modules should be chosen to minimize the number of parts that need to be assembled on site and so complex subassemblies remain assembled for shipping. Provisions for handling these modules will be engineered into them as well as any alignment interfaces.

18.4.2.2 Trial Assembly of Subsystems

Trial assembly of telescope subsystems will be performed at the manufacturers' facilities to ensure to the maximum degree that no problems will be encountered on site. The modular design referred to above also aids efficiency in the trial assembly process. Once complex modules are assembled at the manufacturers, they will not need to be disassembled completely but rather only at the modular level for shipping.

18.4.2.3 Fit Checking

Interfaces between the subsystems and the facility or other telescope subsystems will be checked prior to assembly. This will be achieved by use of templates or other fixtures. For example, if a subsystem requires a certain pattern of anchor bolts in the foundation, the vendor of the subsystem will be required to supply a fixture that holds the bolts in the right pattern as they are cast into the foundation. Mylar templates might also be used.

18.4.2.4 Alignment Fixtures and Tooling

Any specific features, fixtures, or tooling required to accurately assemble the subsystem will be designed and provided by the contractors. The Project will provide standard alignment tools such as contractor's levels, transits, measuring instruments, and a laser level. To the extent possible, the subsystems will use features such as pinning to ensure that components can be re-assembled to the correct positions in assemblies without alignment.

18.4.2.5 Shipping and Handling

Contractors developing major telescope subsystems will be required to prepare shipping and handling plans as part of their initial design work. These plans will take into account the sizes of standard shipping containers and pallets used for overseas transport. Individual packages will to the extent possible be compatible with standard shipping sizes to minimize cost. Larger pieces that might need to be deck loaded for ocean transport must still be compatible with over-the-road transport from the manufacturer to the embarkation port and from Antofagasta or other deep water port to the site. Contractors will be responsible for shipping to the closest deep water port, at which point CCAT will take responsibility for the remaining shipping.

18.4.2.6 Integration and Test Plans

The contractors will be required to provide detailed, step-by-step plans for assembly and integration of their subsystems. This will include identification of required tools, materials, and instruments, step-by-step instructions, listing of all in process tests and values, illustrations and drawings, and any other information required. These plans will be deliverable items of the contracts provided six weeks prior to shipping for review and will require Project approval.

18.4.2.7 Technical Support to Integration

As a part of their contracts, major subsystem contractors will be required to provide technical support for integration. This can vary from a single engineer to a complement of personnel ranging from a field foreman to a controls engineer to a software technician and may vary as the stage of integration of the subsystem progresses. We do not intend to purchase full installation of subsystems as a part of each contract as each contractor would then need to identify the requirements for working in Chile, find labor sources, transport large numbers of personnel and tools to Chile, and would inevitably implement large bid contingencies to make up for their lack of experience working at the remote site.

18.4.2.8 Control System Interface

Subsystems will each be purchased complete with internal control systems. Interface to the CCAT Telescope Control System (TCS) will be first enacted at the contractor's facility during development and proper operation through the TCS will be a part of final acceptance testing. This will be accomplished by the Project providing the appropriate control code and computer to the manufacturer and Project personnel working with the contractor's engineers and technicians to debug the interface. This will ensure minimum complications when the subsystem is tied into the TCS on site.

18.4.3 Preparations for Integration

During facility construction in Chile preparations will be made for the integration phase. The following steps will be taken:

18.4.3.1 Facility Inventory

Project personnel will develop a full inventory of required tools, materials, equipment, hardware, and supplies. This list will be built on existing lists for other telescopes and by taking inventory at existing telescopes. All required items will be purchased by the Project Office, put together into one or more standard shipping containers and shipped to the facility to arrive just prior to completion of general construction. When the facility is at an appropriate stage of completion, these items will be installed to prepare the facility as a base for integration activities. These stores will be comprehensive. The intent is to minimize any work stoppages that might result from lack of tools or components.

18.4.3.2 Supplementary Tools

We plan to hire a Chilean construction company to provide labor for subsystem integration. The majority of the assistance required falls into the category of lifting and erecting heavy components, repetitive installation of truss elements, and grinding, welding, cutting, etc., to adapt to any problems. It is typical for these contractors to provide the majority of their own tools including safety harnesses and lines, hand tools, welding, cutting, and grinding equipment, some rigging equipment, compressors, etc. Other equipment needed only during integration and not for subsequent operation of the telescope will be provided via this contract or rental from vendors.

18.4.3.3 Cranes and Hoists

The design of the CCAT dome incorporates a light duty dome crane. This will be of sufficient capacity to lift panel segments, scientific instruments, and smaller components (≤ 2 tons). Construction cranes will be required for many aspects of general construction and integration. Owing to the use of concrete for much of the facility and the relatively small size of the structural steel, only small truck based cranes will be required at that stage. During installation of the mount and dome, a very large crane will be required. Because of the height of these

elements any crane of sufficient height will most likely have adequate load capacity. Crane availability and cost are often issues so it will be necessary to survey the range of available cranes in Chile as the time approaches, select the best alternative, and have a contract in place well prior to the need. Cranes cost both by the day on site (paid by the hour of operation with a minimum of some hours per day or week) and also by the travel distance to get them to the site and return to their base. This will motivate us to concentrate the use of the crane into the shortest possible time and may lead to parallel integration of the telescope mount and dome.

18.4.3.4 Manlifts, Hoists, and Scaffolding

CCAT will purchase a manlift capable of reaching most or all the way to the upper reaches of the telescope structure and dome. This will be a gasoline or diesel powered lift, the only type available at the reach required. Because the observing floor is slab on grade, the lift can roll about the facility and outside on rubber tires. This lift will be purchased and available at the onset of integration. Other lifts and material handling equipment will be either bought or leased depending on whether the need is transient or continues into operations.

18.4.3.5 Construction Housing

We will need to plan housing for construction workers as well as Project personnel. ALMA has offered as a possibility that they might have sufficient capacity in their construction camp for CCAT contractor personnel. We will closely monitor this. If necessary, we will investigate the possibility of housing personnel in trailers at an appropriate site (TBD) or of daily bus transport from and to Calama.

18.4.3.6 Meals

It will be necessary to provide meals for both Project personnel and contractors during general construction and integration. We will seek a local contractor who will undertake this task and who has the capability to bring hot meals to the construction site. If ALMA has sufficient capacity as noted in Section 18.4.3.5, this would include provision of meals as well.

18.4.3.7 Emergency Medical Planning

From the inception of activities on site it will be extremely important to have emergency medical plans in place. At the point when general construction begins, it will be necessary to have the ability to treat minor injuries on site or nearby and to be able to rapidly evacuate more seriously injured or ill personnel to appropriate medical facilities. We plan on working toward sharing cost of such capabilities with ALMA provided our chosen site is close enough. If this is not possible, we will need to ensure that an appropriate number of our staff are trained emergency medical technicians, that appropriate supplies and equipment are on hand, and that a suitable vehicle and driver for emergency transport are always at hand.

18.4.3.8 Staging

Prior to the inception of integration a site plan will be developed that identifies the areas that will be used for staging components and equipment, where cranes will be located, and what the geometry of the most challenging lifts will be. Ideally the site plan would not require frequent moving of the crane. We must ensure that we have adequate equipment on site at all times to unload containers and trucks as they arrive.

18.4.4 Manpower

Three major sources of manpower have been identified to support integration and commissioning:

18.4.5 Project Personnel

At the inception of on-site activities a site manager will be hired. He will be joined by a mechanical technician shortly thereafter. As general construction nears completion, other major subsystems will arrive. Over the next year, CCAT Project personnel will move to Chile from the location of the Project Office. There they will be located at a suitable urban center and will work at the site on turno shifts. As contractor development of subsystems nears completion, more of the staff will move to Chile. By the time integration of the dome is nearly

complete and the mount is seriously underway, the substantial majority of personnel will be in Chile. The Project will designate an Integration Manager responsible for directing integration activities on a daily basis.

18.4.5.1 Contractor Support to Integration

As identified above, the contracts for the major subsystems will require advisory personnel be supplied to assist in integration. In many cases these will be the same personnel who supervised trial erection and test of the subsystems at the contractors' facilities. These advisors will collaborate with the integration manager to develop approaches to each day's work and to any problems encountered.

18.4.5.2 Contracted Labor

We plan on retaining a subset of the general construction contractor's labor force during the integration phase. As we can observe the capabilities of the individuals during general construction, we have the ability to pick individuals who have both the technical skills and work ethics to best address integration tasks. The contractor will also supply a foreman who will direct the worker's activities as requested by the Project Integration Manager.

18.4.5.3 Local Trades

Periodically we will have need of carpenters, plumbers, electricians, etc. during integration. The general contractor may well use local tradesmen or subcontractors for this work during general construction. We will hire these people as needed to support work during integration.

18.4.6 Stages of Integration

Integration begins with completion of general construction and assumes that the preparations for integration identified in Section 18.4.3 have been completed. The following stages of integration are planned.

18.4.6.1 Dome Integration

Integration of the dome is largely erection work, with the major challenge being the height. We will likely build some scaffolding, use the CCAT provided manlift, and work with a small crane until the height becomes too challenging. The heavy layers are the azimuth rotation layer with bogeys, ways, and drives. This is handily at the base of the dome. The inclined rotation layer is possibly the most challenging integration tasks. The upper cap, particularly if it ends up being aluminum, will be quite light and can, perhaps, be assembled in sections on the ground and lifted in bigger pieces to the top of the dome. Panels will need to be installed, but fit of these is not problematic. We may be able to design scaffolding that rolls on tires on the side of the dome and is lowered by cables to enable workers to reach all elevations while the crane lifts panels to them. This arrangement has been used at several observatories to paint domes. Rotation of the observing space will be enabled as soon as each stage is installed to provide additional flexibility to the assembly process. Interior finishes of the dome will be specified as compatible with direct exposure to the elements, so no further construction work will be required after the dome is weather tight.

18.4.6.2 Mount Integration

The mount will have much heavier individual pieces that will require heavy cranes. The installation of the azimuth bearing and lower azimuth structure can begin in parallel to the dome, subject to safety of dome work going on overhead. Azimuth rotation will be enabled shortly after installation of the bearings and drives to simplify integration. Mount components can be installed through the dome opening once the dome can rotate. Following the installation of the major heavy parts and when the interior of the dome is weather tight, small components like motors, encoders, brakes, stow pins, wiring, etc., will be installed. The more sensitive components such as encoders will be installed by Project personnel.

18.4.6.3 Primary Mirror Truss

Following mount installation, the primary mirror truss will be installed. The truss has been specified as a bolted design that obtains precision through accuracy of components and does not require welding or metrology. Nodes and struts can be lifted by the dome crane and installed by workers who climb in the truss, working from the

mount interface up and the center out. In addition, the manlift easily reaches the truss. The secondary quadripod will be installed at the appropriate stage of truss installation. Following installation of the PM truss, we will be finished with the contracted labor support to integration.

18.4.6.4 Primary Mirror Installation

Project personnel will begin installation of actuators, edge and laser alignment maintenance sensors, and panels of the primary mirror working from the center out. Procurement of panels will specify delivery in this order. Panels can be lifted by the dome crane and installed by workers in the manlift and climbing in the truss. Primary mirror panel installation continues while the following integration activities are performed.

18.4.6.5 Secondary and Tertiary Mirror Installation

Project personnel will install the secondary and tertiary mirror assemblies. These will be assembled on the ground and lifted into place using the dome crane. Covers will be provided for these assemblies so that they can be protected until needed.

18.4.6.6 Telescope Control System Integration

The TCS will be installed during dome installation. The software will be developed in stepwise fashion, with substantial completion shortly after general construction is complete. Initial tasks will include establishing external communications and control of facility systems such as HVAC. As each major subsystem is integrated, the control interface for that system will be enabled and debugged while the next system is being integrated.

18.4.6.7 Installation of Calibration Wavefront Sensor

A CWS will be installed to enable sensing of panel alignment.

18.4.6.8 Installation of First Light Camera

A simple instrument, perhaps taken from an existing instrument telescope, will be used for first light. The initial operation of the telescope is sufficiently challenging to make debugging in parallel with a new science instrument undesirable.

18.4.6.9 Engineering First Light

With the primary mirror partially complete, the mount and dome capable of operation, and M2, M3, and the first light instrument in place, initial tests of mirror control, pointing, and tracking will take place. This will not represent true first light, as the telescope will not be delivering the specified image quality of the full diffraction limited aperture. As the image quality improves, a management decision can be made as to the nature and timing of formal first light.

18.4.7 Commissioning

The Integration Phase will culminate in a system test to validate that all major systems meet requirements to a substantial degree. At some time in close proximity, observations will occur that can be considered “First Light.” The telescope may not fully meet all requirements, but will be at a stage of development where it is felt that scientific operations in conjunction with final engineering optimization will yield the best results. This period of operation is Commissioning. The anticipated work will alternate between observations and improvements.

18.4.7.1 Observations

The operations staff will have been added over the course of integration and will now be at sufficient strength to pursue initial observations. These will, at first, most likely be somewhat halting and abortive. The Operations team working with the science and engineering members of the Project Team will address performance shortfalls in the order of severity of their impact on operations. Once observing is fairly robust, the operations staff will document performance shortfalls daily.

18.4.7.2 Improvements

It will be the responsibility of the remaining Project personnel to rectify the problems encountered during observations. Some staff overlap is anticipated to ensure communication of problems is effective and both groups work as one team.

18.4.7.3 Installation of Science Instruments

The entire team will collaborate with the science instruments' principal investigators to install these as available. Engineering support to initial operations will be provided as required.

18.4.7.4 Operational Statistics

Formal operation of statistics documenting image quality, commanded versus attained positions or tracks, hours spent on sky, and others will be developed as benchmarks of telescope performance. These will be maintained regularly and reported to Project management. This will evolve into the system that tracks telescope performance and efficiency as a long term diagnostic.

18.4.7.5 Problem Log

A software problem log will be set up that allows anyone who observes a shortfall in telescope performance or other problem with the observatory to document the problem. These will be accessible to everyone working on the Project and can be reviewed on a daily basis to see the progress realized. The database can be queried for a report on a weekly or monthly basis to assist in identifying repetitive problems and assess efficacy of the commissioning effort.

18.4.8 Hand-Over

Commissioning will culminate in a comprehensive performance test of the telescope and validation that the established requirements are met, that reliability meets operational levels, and that the level of operation is scientifically acceptable. At this point the telescope will be formally handed over to the Operations Team and considered fully commissioned.

18.5 Integration Risk Assessment

Risk during Integration and Commissioning falls into a few broad categories.

18.5.1 Technical Risk

The risk that subsystems will not fit or perform as specified on site. This risk is mitigated by requiring trial erection and test of major subsystems at the contractor's facility prior to shipping. The requirement for fit checks and templates to validate interface configurations is another safeguard. Risk of failure of individual subsystems to meet specification is addressed in their design sections. Some degree of rework is fair to anticipate, but through the plans identified, this should be small and consistent with capabilities available in Calama or Antofagasta. The Project will have sufficient technical resources to deal with engineering issues that arise.

18.5.2 Cost and Schedule Risk

It is not unusual for a telescope Project to lose schedule during integration resulting in cost overruns. In most cases this is due to the problems in assembly generated by poor fit, subsystems that require extensive field alignment, welding, or in-place machining, or lack of sufficient labor force to meet the planned pace of development. The process we have outlined should minimize these risks.

18.5.3 Health and Safety Risk

The extreme altitude and remote nature of the site combine with work that involves climbing, large crane lifts, and use of machine and hand tools implies a significant risk. The procedures we have outlined above provide adequate preparation in the event of accidents or sickness. Prevention of them is also imperative. We anticipate screening personnel for work at the altitude with an appropriate medical examination. The requirement that all personnel use supplementary oxygen is under serious consideration as we believe it would result not only in better

safety but also higher efficiency. We will investigate in the next stage of work whether we could expect Chilean contractors and workers would accept such a requirement and whether we can identify equipment that is sufficiently not-intrusive so it will not interfere with activities.

18.6 Summary

This Integration Plan is a preliminary plan. It will be updated during the next, Engineering Concept Design Phase of CCAT, when additional contractor information regarding configuration and integration requirements for the major systems is available. The plan will continue to be refined during the Development phase of the Project and contractors are charged with writing specific integration plans for subsystems. The objective is to succeed with minimum risk and maximum efficiency.

19 Operations Concept

19.1 Introduction

Operating a telescope in Chile will require a cadre of resident staff, either local recruits or US expatriates, as well as support facilities and other infrastructure. The scientific observations will involve visiting observers, scientists, and engineers, all of whom will require support. Providing this support introduces interrelated logistical and financial considerations that need to be understood, analyzed, and resolved to the mutual satisfaction of the partners. This section describes a feasible operations model that is based on the experience of the telescopes operating in the Atacama. Although it is perhaps not the only possible operations model, it provides a basis for discussion and improvement.

19.2 Operations and Observations

The primary goal of CCAT operations is to support the scientific and technological interests of the Project partners. Operational flexibility will be essential to support the diversity of scientific interests, both present and future. Operations must support effective use of the telescope consistent with providing a safe work environment at a high altitude (> 5000 m) site where meteorological conditions may change rapidly. The impact on the fragile environment of the surrounding area must be minimized. The telescope and the instruments must work together in a fully coordinated fashion. The ability to switch observing programs rapidly in response to changing atmospheric conditions will be essential to achieve the telescope's full scientific potential. Telescope and instrument systems should be designed to:

- Permit rapid instrument changes in response to dynamic scheduling;
- Minimize the time required for instrument configuration;
- Minimize the global overhead in target selection;
- Allow the telescope to rapidly acquire the target source; and
- Ease the burden of data acquisition and storage.

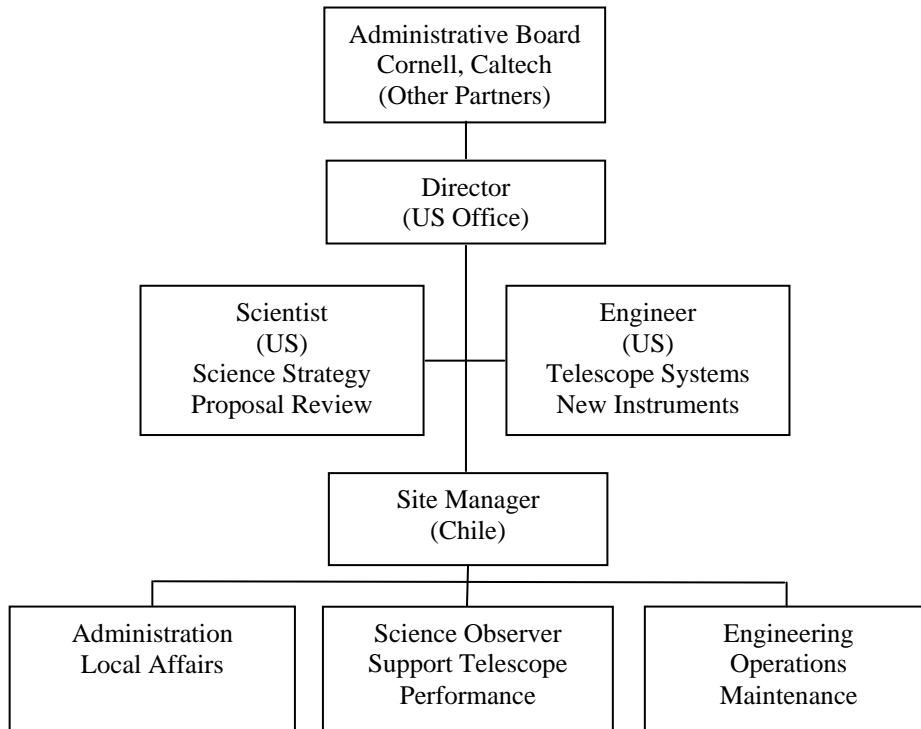
19.3 Operations Model

Several telescopes are now operating or under construction in the vicinity of San Pedro de Atacama, including the CBI, APEX, ALMA, and others. APEX, a 12 m telescope operated by a European consortium, shares many characteristics with the CCAT and for this reason we have used APEX as a baseline. The CCAT operations model embodies these premises:

- Operation of the CCAT will be a joint responsibility of the partners; the CCAT operations staff members will be employed by one of the partner institutions or by a legal entity jointly created to operate the consortium facility. Scientific instruments for the telescope, and the software systems for instrument control and data analysis, will be designed and built at the partner institutions.
- The CCAT operations staff will be based at a support facility near San Pedro de Atacama. This local staff will include astronomers, engineers, telescope operators, technicians, and maintenance and administrative workers. General telescope operations policy, instrument development, proposal evaluation, data processing and selection, etc., will be responsibilities of the partner institutions and will be done in the U.S. The CCAT staff in Chile will have primary responsibility for telescope operations.
- Only those staff members directly involved with the telescope and its instruments will routinely work at the high altitude telescope site. These personnel will maintain the telescope, install or adjust instruments, and service the access road and other facilities. As a rule, they will commute daily from the support facility. Except in unusual circumstances, no one will sleep at the telescope.
- San Pedro de Atacama is a small isolated rural village. Experience at other telescopes shows it will be hard (or impossible) to recruit staff, particularly skilled staff, who will live there full time. Hence most of the staff will work on a *turno* basis, commuting weekly to San Pedro. CCAT operations must provide, therefore, dormitories, food service, and recreational facilities for the staff while they are residing at the support facility. The staff will also need transportation to and from San Pedro for their *turno* commute.

19.3.1 Operations Organization

This structure shows the division of responsibilities between the telescope staff in Chile and those at the US partner institutions.



19.3.2 Observing Modes

Because of the range of scientific objectives and interests of the CCAT Project partners, the telescope must support a variety of observing modes, but the CCAT will normally not provide full service observing as might be appropriate for a national facility. As a University based facility, the telescope will provide an important training ground for students and young scholars so it is important some of those observing modes facilitate “hands-on” access. The following list of observing modes illustrates representative operations. In all cases, it is a requirement that remote astronomers be able to direct and monitor the observations over the Internet (with proper authorization).

19.3.2.1 Telescope Control

During observations, there are two distinct responsibilities: operating the telescope and directing the observations. Telescope operation includes monitoring the electrical and mechanical systems, etc., to ensure safe and correct operation. Directing the observations includes ensuring the scientific integrity of the data. These responsibilities are normally assigned to different parties. The local CCAT staff is responsible for telescope operations and the academic investigators are responsible for directing the observations.

When the CCAT is in routine operation, the telescope operator normally will be stationed at the base facility and control the telescope through a communications link. The operator will have the ability to override the remote observer if necessary. Under special circumstances, for instance during the initial commissioning of the telescope or a new instrument, the operator may be stationed in a local control room adjacent to the telescope. Any visiting astronomer present in Chile to direct the observations normally will be stationed in the same place as the telescope operator.

19.3.2.2 On Site Observing

During telescope commissioning or maintenance or the installation and commissioning of new instruments, observations likely would be carried out at the telescope. Instrument teams would travel to the telescope to install and commission new instruments and to train the local staff in their operation and maintenance. The telescope will be controlled from a local control room. Members of the instrument team will be responsible for the data integrity. During their visits, instrument teams will stay at the base facility or elsewhere in San Pedro.

19.3.2.3 Remote Observing

Much observing will be done remotely over the Internet from the observers' home institutions. Although the local staff will supervise the telescope operation, the remote astronomer will direct the observations and take responsibility for the scientific integrity of the data.

19.3.2.4 Service Observing

When remote observers cannot be available to direct their observations, the resident staff astronomers will be responsible for the observations and the data integrity as well as for supervising the telescope operation. This mode can only work if the scheduled astronomers fully specify the observations. Service observing places additional burden on the resident staff and this has corresponding financial implications.

19.3.2.5 Survey Observing

Surveys are a major component of the CCAT science objectives. These programs will typically involve extended periods of observing. Depending on the particular circumstances, any of the aforementioned observing modes may be used. The staffing level (Section 19.5.4) is sufficient to support service observing for much, although not all, of the surveys.

19.3.3 Observing Fractions

For planning, this table shows a preliminary estimate of the fractions of observations carried out in the different modes and the expected number of visitors present at the support facility.

| Mode | Fraction | Visitors | Comments |
|---------|----------|----------|-------------------------|
| On-site | 20% | 4 | instrument team present |
| Remote | 40% | 0 | includes surveys |
| Service | 40% | 0 | includes surveys |
| Survey | 60% | | remote or service mode |

The basis for this estimate is the nature of the initial instruments planned for the telescope. These instruments, bolometric arrays, are designed for the survey and mapping projects that are the major scientific objectives of the community of researchers at the partner institutions. Hence these priorities are reflected in the preliminary estimates of telescope usage.

19.3.4 Telescope Scheduling

Especially for short wavelength observations, atmospheric conditions will determine which programs can be carried out with the telescope. To adapt to the changing conditions, the CCAT will use a form of dynamic queue scheduling. Once or twice a year, proposals will be evaluated, ranked, and accepted by committees based at the partner institutions. More frequently, the local CCAT staff will select a short list from the pending approved observing programs and will notify the investigators to expect their observations to be made during the upcoming period. Both technical criteria, such as instrument availability or weather forecasts, and logistic criteria, such as partial program completion, time in the queue, or the availability of the remote observer, may be used to select the short list. On a daily basis, primary and backup programs will be selected and any remote observers alerted. Although observing blocks will have no fixed length, the minimum scheduling block will be an hour or so. When atmospheric conditions change, the local staff will have the authority, and the discretion, to switch to another approved observing program.

19.4 High Altitude Mitigation

Telescope operation at high altitude (> 5000 m) presents special risks. Hypoxia reduces human cognitive and physical capabilities and may cause acute disorders, high altitude pulmonary edema and high altitude cerebral edema that are extremely serious if left untreated. Risk mitigation measures include having a minimum two people (or none) at the telescope at any time, using portable supplemental oxygen for work outside, on the telescope, etc., and using oxygen enrichment in the control room and offices. Because of its cost, oxygen enrichment is only practical in limited parts of the facility. The CBI has pioneered these strategies successfully and other telescopes in the vicinity have adopted them subsequently. For advice on these issues the CCAT Project is consulting with John West, MD (UCSD), a leading expert on high altitude physiology.

19.5 Personnel

For several decades, international astronomical observatories have operated in Chile with largely Chilean staff. Technicians and support staff are available. Good Chilean engineers can be recruited, but will likely require specialized, on the job training in the particular skills needed for telescope operation. Although not a forgone conclusion, senior management and scientific positions may be filled by US expatriates. In order to operate and maintain a complex telescope in a remote location with a minimum staff, cross training will be essential for the technical staff.

The labor pool in San Pedro de Atacama itself is very limited. Although junior staff may be recruited from Calama, Antofagasta, and other cities in northern Chile, candidates for senior staff likely will be found only in Santiago or the US. Chilean salaries, with benefits, are somewhat lower than US salaries. US expatriates will expect an expatriation bonus and other allowances.

Although CCAT will benefit from proximity to other observatories in the vicinity of San Pedro de Atacama, CCAT also will have to compete with those same observatories for a limited labor pool. Hence to retain good staff CCAT must match the employment conditions offered by the other observatories, notably ALMA which is ten times larger.

19.5.1 *Turno* System

In Chile, staff is frequently employed on a *turno* system when facilities are far from population centers. This arrangement is common in the mining industry and has been adopted by many observatories. It complies with Chilean labor laws, which set a 45 hour work week. Details of this system vary between different industries and employers. For CCAT, the other observatories in Chile provide instructive examples. Because its observatories are close enough to La Serena to permit daily commuting, AURA does not use *turnos* often. Carnegie, on the other hand, uses *turno* shifts for telescope and facility operations staff at Las Campanas. ESO uses *turno* shifts extensively for its remote observatories at Paranal and La Silla. ALMA, located near San Pedro de Atacama, will use *turno* shifts for most personnel.

At ESO, a typical *turno* shift for technical operations staff is 8/6, meaning an employee works eight days followed by six days off. Seven nights are spent at the facility followed by seven at the employee's residence. ESO provides board and lodging while employees at the observatory and transportation to and from designated pick up locations. In each *turno* period, there are 80 work hours but Saturdays are counted at 1.5 time and Sundays and holidays at 2.25 time. After hours call outs to repair a telescope system are counted as overtime. Transportation time is not counted as working hours. At ESO, these details are defined by collective bargaining agreements. As an example, an employee arrives at the observatory at midday on Tuesday and works that afternoon, works full days for the next six days (Wednesday through Monday), works the morning of the following Tuesday, and departs at midday. Accounting for holidays, vacation, and sick leave, ESO estimates about 2.4 employees are required for each position to provide uninterrupted daily coverage with 8/6 *turnos*. Another variation, more typical for office staff, is a 5/2 *turno*. In this case, Monday and Friday are split between travel and work and Tuesday, Wednesday, and Thursday are full work days.

Variations of the *turno* system can be arranged to fit the CCAT requirements. Continuity of operations, for example, can be maintained by mixing Tuesday *turnos* with Thursday *turnos*. Coordination meetings after the incoming staff arrive and before the departing staff leave would be used to convey information about the current observatory status. Because of budget limits, on the other hand, CCAT might fill positions with only two employees and accept the interruptions in coverage caused by holidays and vacations

19.5.2 Population Centers

San Pedro de Atacama is a very small village, with less than 5000 inhabitants including outlying hamlets in the area. Its rustic character is a major part of its attraction to tourists, who visit in great numbers, perhaps 50,000 per year. Although some modern conveniences have reached the village over the last decade, major development seems unlikely as it would destroy its attraction. The village has no hospital and only elementary schools. Although San Pedro may appeal to some, it holds limited attraction for many long term employees.

Beyond San Pedro, there are three Chilean cities where CCAT staff might be expected to live: Calama, Antofagasta, and Santiago (and to a lesser extent centers such as Copiapo, La Serena, etc.).

- Calama, about 100 km from San Pedro, has about 120,000 inhabitants. The major activity is support of the Chuquibambilla and other mines, until recently the world's largest open pit copper mine. Like much of Chile, it has experienced rapid development over the past decade. Although it has hospitals, good schools, and a retail mall, other amenities such as recreation or cultural opportunities are quite limited and there is no international school. There are flights to and from Santiago several times a day, both direct and connecting through Antofagasta.
- Antofagasta, with close to 300,000 inhabitants, is the regional seat of government and a major port supporting mining activity throughout northern Chile. It is a 3.5 hour drive from San Pedro. Antofagasta has hospitals, three regional Universities, an international school with instruction in English, and some other amenities. Popular beaches are some distance out of town. There are flights to and from Santiago several times a day.
- Santiago is the capital of Chile with over five million inhabitants. It is a major city with corresponding amenities, including national Universities, international schools, and cultural, recreation, and entertainment opportunities. The executive branch of the Chilean government has its offices in Santiago. All international flights arrive in Santiago. US flag carriers have daily direct service to Atlanta (Delta) and to Miami and to Dallas (both American). Traveling from Santiago to San Pedro involves a two hour direct flight to Calama followed by a one hour drive. This is similar to the time required to drive from Antofagasta to San Pedro. In Santiago, AURA has a small liaison office, ESO has a major office, and ALMA and AUI/NRAO have offices.

19.5.3 Expatriates

Observatories in Chile have successfully recruited expatriate astronomers to staff observatories for many years. Although access to unique observing opportunities is appealing for professional development, quality candidates will only be interested if the employment conditions are financially attractive and recognize the dislocation inherent in moving and working overseas. Among the inducements offered by other observatories are expatriation allowances, relocation of family members and household belongings to and from Chile, family vacation travel allowances, school tuition allowances, language courses, and assistance with orientation and learning how to live in Chile. In order to attract and retain excellent staff, CCAT will need to offer similar inducements.

19.5.4 CCAT Operations Staff

The CCAT operations staff will work from the base facility near San Pedro de Atacama. This table, based on the APEX experience, illustrates the minimum staff complement needed to operate the telescope 16–20 h per day and to direct some of the survey observations. It does not include visiting scientists. Because of the *turno* shifts, only half of the staff would be present at the base facility at any one time.

| Position | Number | Shift [d] | | Home Base (Putative) | Hire |
|-----------------------|--------|-----------|-----|-------------------------|----------|
| | | On | Off | | |
| Site Manager | 1 | 8 | 6 | Santiago | US/Chile |
| Administrator | 1 | 8 | 6 | Santiago | Chile |
| Astronomer, Telescope | 2 | 8 | 6 | Santiago | US/Chile |
| Astronomer, Survey | 2 | 8 | 6 | Santiago | US/Chile |
| Operator | 5 | 8 | 6 | Calama | Chile |
| Engineer, instrument | 2 | 8 | 6 | Santiago | Chile |
| Engineer, software | 2 | 8 | 6 | Santiago | Chile |
| Engineer, telescope | 2 | 8 | 6 | Santiago | Chile |
| Technician, elec-mech | 2 | 5 | 2 | San Pedro | Chile |
| Catering | 1 | | | | Contract |
| Housekeeping | 2 | | | | Contract |
| Total | 19+3 | | | | |

19.5.5 Job Descriptions

These brief descriptions illustrate the range of skills necessary to operate the CCAT. At this point, these job classifications are strictly schematic and subject to change and refinement.

- Site Manager: Responsible for all CCAT operations in Chile, both technical and administrative. Represents CCAT to the Chilean government.
- Administrator: Responsible for all CCAT business functions, including services, contracts, legal issues, human resources, import and export, shipping, and travel arrangements. Serves as deputy to the site manager.
- Astronomer, Telescope: Oversees the scientific aspects of telescope operations, including forecasting, scheduling, data archiving, calibration, pointing, and active control systems.
- Astronomer, Survey: Directs survey observations and preliminary data analysis.
- Operator: Responsible for the safe operation of the telescope whenever observations are made. In particular, they pay attention to the fundamental mechanical, electrical, and control aspects. An operator will be required whenever the telescope is observing.
- Engineer, instrument: Responsible for maintenance and repair of science instruments. Requires expertise in cryogenics, optical, and electronic systems. Participates in instrument deployment and commissioning.
- Engineer, software: Responsible for maintenance and repair of observatory software. Requires expertise in control system and scientific software. Participates in deployment and commissioning.
- Engineer, telescope: Responsible for maintenance and repair of telescope and dome. Requires expertise in mechanical, electrical, and electronic systems. Participates in telescope commissioning.
- Technician, elec-mech: Assists engineers in maintenance and repair of mechanical and electrical systems. Participates in deployment and commissioning.

19.5.6 Santiago

In Santiago a representative may be necessary for government relations, import and export, and other business functions. To some extent, it may be possible to contract these services from another organization, such as AURA or AUI.

19.5.7 Travel

For *turno* employees, CCAT operations will have to provide transportation to San Pedro. From Calama, Antofagasta, and other cities in northern Chile, bus service is adequate. Frequent commercial air service connects Santiago to Calama with subsequent shuttle bus service to San Pedro. For expatriates, travel costs will include family relocation and annual vacations in addition to professional travel for CCAT business, conferences, etc.

19.6 Facilities

To contain the construction and operations costs, the facilities will be kept to the minimum necessary. This is an outline of the facilities. More details are provided in Section 11.

19.6.1 Telescope Facility

This high altitude facility provides the necessary infrastructure for the operation and maintenance of the telescope and associated instrumentation. In addition to the telescope itself and the dome, this facility includes:

- The control room;
- Office workspace;
- Instrument laboratory for routine maintenance and simple repairs;
- Electronics room to house the signal processing equipment and initial data storage hardware; and
- Equipment room for electrical generators, power conditioning and other support equipment.

19.6.2 Base Facility

This facility, at a lower altitude (≈ 2500 m) in the vicinity of San Pedro, provides the base for supporting telescope operations. It includes offices, laboratories, workshops, warehouses, a cafeteria, and dormitories. Although the baseline CCAT concept includes an independent facility, there may be a possibility for co-location with one of the other observatories in the vicinity, such as ALMA.

19.6.3 Santiago Support Office

A small support office in Santiago may be necessary for government relations, import-export, and other business. Limited facilities may be needed if staff astronomers wish to pursue personal research when they aren't working in San Pedro. Appropriate facilities can be rented, either on the commercial market, from a Chilean University, or from another observatory. A University link might have useful, intangible benefits.

19.6.4 US Support Offices

Adequate facilities at the partner institutions are required for remote observing, observatory administration, and instrument development.

19.7 Logistics

As far as possible, support services will be contracted. These services include catering, housekeeping, and vehicle, generator, and road maintenance. It may be possible to contract administration services. A small vehicle fleet will be needed at the support facility in San Pedro for transport to and from the telescope.

19.7.1 Technical Maintenance

The resident CCAT staff will carry out preventive maintenance and other technical work during daily visits to the telescope. Allowing 90 minutes each way for travel between San Pedro and the telescope site and one hour for lunch and other breaks, about six hours of work at the telescope are possible in a ten hour shift. Each work team will comprise at least two people in the interest of safety.

19.7.2 Equipment and Supplies

Maintenance parts, expendables, cryogenes, gases, and other supplies will be purchased in Chile as available. Oxygen gas is needed for high altitude mitigation. When necessary or financially advantageous, specialty materials and supplies will be purchased in the US and shipped to Chile.

19.7.3 Utilities

Domestic services, such as water supply and sewage and garbage disposal, will be contracted from local companies. Telecommunications services for the San Pedro support facility will be contracted from the Chilean companies. Telecommunications services between the support facility and the telescope must be provided by a dedicated link included in the capital equipment budget.

No local commercial source can supply electricity for CCAT in adequate amounts. Hence electricity at both the telescope and the support base must be generated. If the support base is collocated with the ALMA facilities, then it may be possible to obtain electricity from ALMA. Likewise, if the telescope is located near the ALMA antennas, it may be possible to connect the telescope to the ALMA power system. In any case, the cost of electricity generation and equipment maintenance is included in the operations budget.

19.7.4 Import, Export, and Shipping

Following established precedent, the CCAT can expect to enjoy the same privileges as other international observatories in Chile, including relief from import duties and local taxes. The legal implications of possible arrangements are under study and will depend on whether a revision of the current disposition of the “Astronomy Law”, now dormant in the Chilean Senate, is passed in the near future.

19.8 Operations Budget Estimate

The operations budget estimates the costs of operating the CCAT in Chile. It does *not* include the costs of providing support at the partner institutions in the US. In particular, this estimate includes the salaries of the resident CCAT staff in Chile, transportation for the resident staff and within Chile for long term visitors, board and lodging for staff and visitors at the base facility near San Pedro, utilities, contract services, and materials. This estimate does *not* include the salaries of visitors, either short term or long term, accommodations for visitors in Santiago or elsewhere other than the base facility near San Pedro, instrument development or shipping to Chile, or data reduction or analysis at the partner institutions in the US. The budget estimate is included in an attached spreadsheet.

20 Project Plan

20.1 Introduction

This Project Plan was developed to fulfill a requirement of the Cornell-Caltech MOU. It is provided for the consideration of the current and future partners and as the basis for assessment of feasibility and risk consistent with the objectives of the current Feasibility/Concept Study.

20.2 Background

The Cornell-Caltech MOU establishing the CCAT study phase calls for a “proposed management structure for the Atacama telescope during the construction, testing, and operational phases.” The Project Plan was developed to address this requirement

It is possible that other institutions will join Cornell and Caltech in development of CCAT so the Project Plan must provide for equitable representation of all partners and for decision making methodologies that are unambiguous and even handed. The Project is in a Feasibility/Concept Study Phase until mid-summer 2006. After that, an Engineering Concept Design Phase would extend another year. Then the Project will be sufficiently certain of full funding to go ahead with full staffing and Project office development, detailed design, general construction, contracting of major subsystems, and subsequent integration and commissioning. Transition to operations is a critical phase in telescope development programs and the plan takes this into account.

20.3 Scope

This plan details the organizational structure and decision making processes of the Project, discusses potential business models, identifies staffing requirements and organization, and identifies concepts for engineering development and contract management. Methods for cost estimation, allocation, and tracking are defined together with an approach to the transitions from engineering development to integration and subsequently to commissioning and operations.

20.4 Project Plan

20.4.1 Phases of Development

The Project is divided into distinct phases of development, each with specific objectives and structured to provide progressive engagement of the participating institutions.

20.4.1.1 Feasibility/Concept Study

This phase was begun in late 2004 and will be complete in mid-2006. The major objectives of this phase of work are: identification of science goals and requirements, definition of the initial suite of instruments, derivation of the telescope requirements, development of an initial concept design, investigation of feasibility and critical risks, and development of an initial cost estimate.

20.4.1.2 Engineering Concept Design

This phase will begin in mid-summer 2006 and will last one year. The major objectives of this phase are: refining requirements and flowdown to subsystem requirements, development of concept designs for telescope and subsystems, engineering analysis to support concept design, and developing a highly detailed and accurate cost estimate.

20.4.1.3 Development Phase

This phase will begin in mid-2007 and will last approximately five years. During this phase documentation and contracts for all major subsystems will be developed and employed in contracting suitable vendors to provide detailed design and manufacture of major telescope subsystems. General construction at the telescope site will be followed by integration of subsystems as completed. This phase will culminate in first light.

20.4.1.4 Commissioning

Following first light, the Project Team will remain intact for one year to optimize telescope performance and to train the operations staff prior to the start of full-time scientific operations. Limited scientific observations will occur during commissioning.

20.4.2 Project Governance

Although the actual Project organization and governance structure will be determined by negotiations between the partners, it is useful to describe a governance mode that has been used for a number of successful telescope projects.

20.4.2.1 CCAT Board and Directors

A governing board of representatives of the partner institutions will oversee the Project activities. It is recommended that Board members constituency strike a balance between scientific, technical, financial, and legal expertise. A Project Director will respond to the Board and be a non-voting member of the same. The Project Director will coordinate activities between Project Manager, Project Scientist and Instrumentation Scientists, and will provide an interface between CCAT consortium members and Project activities. A weighted voting scheme may be used to reflect any differences in the financial commitments of the partners. In practice, most Board decisions are unanimous and reflect the consensus of the full partnership.

20.4.2.2 CCAT Project Manager

The Project Manager reports to the Project Director. He is responsible for:

- Definition and development of the Program Plan by which the Project will be executed.
- Decomposition of the Project into sub-projects, tasks, and sub-tasks that are functional and of reasonable size to be addressed.
- Development of a Project Team, including job descriptions, hiring, and management of personnel sufficient to perform all required tasks in accordance with the Project Schedule.
- Development and execution of a cost management process that ensures accurate initial estimates, allocations sufficient to complete all aspects of the program, and cost tracking processes sufficient to ensure timely knowledge of financial status of the program with regard to plan.
- Definition and implementation of a technical development process that will ensure compliance with all performance objectives and provide the maximum scientific benefit within constraints of cost and schedule.
- Maintaining a consistent vision for the entire Project Team and fostering a team spirit and ethic that will maintain motivation, foster creativity, and provide a positive working environment.

20.4.2.3 CCAT Project Scientist/s

The Project Scientist reports to the Project Director. His/her responsibilities are to:

- Ensure the scientific quality of the Project, making sure the CCAT achieves maximum performance relative to the astronomy objectives within constraints of cost and schedule.
- Serve as an interface to the astronomical community for the Project. A source of information and a place where the user/customers of the Project can discuss performance, plans, and status.
- Lead the efforts to commission the telescope, including formation of the commissioning team and development and prosecution of plans to achieve initial observations and to optimize performance.
- Chair specific committees during the Project, including a Science Working Group, Technical Review Committee, etc., as deemed desirable during development.

20.4.2.4 CCAT Instrumentation Scientist(s)

One or more teams will be assembled to develop the first light instruments that will operate on CCAT. One Instrumentation Scientist will lead each of those teams and be responsible for their scheduling and completion. The Instrumentation Scientists report to the Project Director, and work in close coordination with the Project Manager and the Project Scientist.

20.4.3 Business Model

A variety of business models may be applied and the actual approach will depend on the ultimate constituency and desires of the Project partnership. Models that have been used successfully include: formation of a not-for-profit corporation to own the telescope and to provide a business entity with the ability to let contracts; joint ownership by the partner institutions; and ownership by one or more of the partners with observing time owed to minor partners. In any event, the Project will most likely need to be housed and operate under the auspices of one of the Partner institutions. The Project is probably not large enough to justify separate establishment of capabilities that can be provided by a host institution, such as personnel, purchasing, legal services, bookkeeping, facilities maintenance, etc. Operation of the telescope in Chile will also affect the choice of a business model because of issues such as permission to use the telescope site, importation of equipment into Chile, and other aspects of relations with the Chilean government. Specifics regarding choice of a business model will be addressed during the next, Engineering Design phase of the Project.

20.4.4 Development of Project Office

The location of the Project office will be determined by the Board. The chosen site must provide:

- Contiguous office spaces for up to 10 Project staff,
- Space and services for meetings including both small, working meetings and large, annual review meetings,
- Office services including phone, high speed internet connection, etc.,
- Financial services necessary to bank partner contributions and make necessary disbursement for payroll, accounts payable, etc.,
- Bookkeeping services with the ability to provide quarterly reports detailing all expenditures,
- Human resources support for hiring, benefits, payroll services, etc.,
- Purchasing services including support for procurement, contracting, legal consulting, etc., and
- Acceptable overhead rates and provision for interest generating deposit of partnership funds.

The Project will provide the necessary furniture, office equipment, computers, etc. for Project staff.

20.4.5 Organization & Personnel

An initial assessment of required staffing for the Project is:

- Project Manager
- Deputy Project Manager
- Administrative Assistant
- Project Engineer
- Site Manager
- Administrative Manager
- Optical/RF Engineer
- Electrical Engineer
- Mechanical Engineer (2)
- Control Engineer
- Software Engineer
- Software Technician
- Mechanical Technician (2)
- Electronic Technician (2)
- Scheduler/Planner
- Administrative Specialist

This is 19 people, with a maximum of 10 employed at the US Project Office and the remainder located in Chile. It is assumed that the Project Director will be a member of the academic staff of one of the partner institutions and will operate on a part-time basis for the Project.

20.4.6 Integrated Product Teams (IPT)

Development of the telescope will be divided into subsystems and components. Integrated Product Teams will be established to address development of each area. Each team will consist of a team leader and members drawn largely from within the Project organization according to the technical content of the task to be addressed. In some cases staff members will lead and in others they will participate as IPT members. This approach fosters interdependence between team members and gives each member of the staff the opportunity to manage a subsystem or task as leader. Progress of each IPT will be monitored by the Project and Deputy Project Managers.

20.4.7 Approach to Engineering Development

A semi-formal design process will be put in place, consisting of staged development with review at critical points.

20.4.7.1 Specifications & Requirements

Prior to design process inception, a full and formal statement of performance requirements and specification of general configuration and interfaces will be established. The Project Scientists and Project Managers will review these specifications. The Project Office will develop change control procedures to ensure orderly project development.

20.4.7.2 Concept Design

Conceptual design will proceed from the general to the specific, with initial “brainstorming” activities to identify potential approaches followed by parametric trade studies to assess the relative merits of competing approaches. Concept design will culminate in a Concept Design Review where the specifications and requirements, potential design approaches, trade studies, and resulting chosen conceptual design are presented for peer review.

20.4.7.3 Preliminary Design

Following successful Concept Design activities, Preliminary Design will provide more detailed design of systems, subsystems, and components. Assembly drawings will be used to define dimensions, interfaces, components, and layouts and to specify full assembly level design. Detailed part drawings will be completed as necessary to adequately verify the viability of the overall design approach. Preliminary Design review will take place with approximately 10% drawing completion level. This review will address trades, analysis, drawings, and projected subsystem performance.

20.4.7.4 Critical Design

Following successful Preliminary Design, detailed design will commence. This includes detailed component and part drawings as well as detailed assembly level drawings to ensure fit and function. A Critical Design Review will take place at approximately the 75% drawing completion level and will examine all drawings, analysis, calculations, and performance projections.

20.4.7.5 Design Review Participants

Design Reviews will be formal and will be attended by: Project Director, Project Manager, Project Scientist, appropriate CCAT Project Team personnel, appropriate members of the Science Working Group, and as required, external experts in applicable technologies and similar systems.

20.4.8 Approach to Contracting

Because the CCAT Program will most likely be performed within the business system of one of the Partner institutions, contractual procurements and purchases will adhere to the processes in place at that institution.

20.4.8.1 Major Contracts

Contractors will be selected primarily on the basis of competitive procurements. Such procurements will adhere to the guidelines established by the Federal Acquisition Requirements (FAR). In general such contracts will be solicited on the basis of a Request for Proposal (RFP) including a Statement of Work (SOW) that governs the work content, schedule, defines reviews and progress payments, and in general controls the contractor’s activities.

The RFP will also include a Specification, that defines sub-system or component performance, configuration, interfaces, and any other data required to define the subsystem or component to meet the CCAT Project requirements. In general it is our intention to utilize firm fixed price contracts throughout the program.

20.4.8.2 Sole Source Purchases and Contracts

In the event a sole source procurement is required, a sole source justification will be provided as stipulated within the terms of the FAR, subject to approval of the host institution. In the event that sufficient sole source justification does not exist, competitive procurement will take place.

20.4.8.3 Authorizations for Purchases

The following rules shall apply:

- **Purchases Over \$25,000**
Purchases and contracts over \$25,000 may require approval of the CCAT Director and, at his/her discretion, approved by the Board. The Project Manager will solicit this via e-mail, with printed messages archived at the Project Office.
- **Purchases Under \$25,000**
The CCAT Project Manager shall be authorized to initiate purchases and contracts up to a maximum value of \$25,000. The Board will be informed of any substantial purchases within this range that may be controversial or imply a strategic decision.

20.4.9 Cost Estimation

Cost estimates will be developed during the initial Feasibility/Concept Study and refined during the Engineering Concept Design phase. At the culmination of the ECD, any likely error in the cost estimate should be less than the reserved contingency.

20.4.9.1 Cost Estimation Process

The following are elements of the cost estimation process:

- **Quotations from Subsystem Vendors**
Contractors studying the major subsystems of CCAT will be tasked with providing detailed cost estimates as part of their work. This serves a variety of purposes, among them, identifying what subsystems and which elements of the subsystems bear the greatest cost concentration, calibration of the contractors with respect to our planned cost for subsystems, and sufficient visibility within the corporations to avoid large contingencies in quoted prices.
- **Identification of Purchased Equipment and Components**
Significant items to be purchased by the Project over the entire duration of the project, including computers and communications equipment, furniture, tools, vehicles, etc. will all be identified by comparisons with inventories of existing observatories. Catalogue prices or quotations will be used to identify appropriate cost allocations for all purchases as part of the estimate.
- **Standard Estimating Processes**
General construction is typically estimated by use of established processes (e.g., Means Construction Estimating process). This works fairly well, but important adjustments must be applied for construction in other countries or in difficult locations, such as the high peaks of the Atacama region in Chile. We will use the results of bids on similar work as received by ALMA, for example, to adjust our expectations of construction cost.
- **Personnel Costs**
Detailed estimates of personnel costs on a monthly basis for the duration of the Project will be established, with appropriate additions for annual salary increases, relocation costs, salary enhancements for Chilean deployment, and appropriate costs for benefits and overhead. This will provide an accurate estimate of the personnel costs for the duration of the Project

- **Anticipated Accuracy**
Experience shows the above steps, when applied to previous projects, yield an estimate within 10% of final cost. Provision of a 10% contingency is anticipated at the inception of the Development Phase. An accurate cost estimate at the inception of the Project is the best defense against overruns.

20.4.10 Cost Tracking and Projection

Having an accurate cost estimate at the inception of detailed design and construction is the first key to bringing the project in within budget. The second element is knowing at all times where the project stands with respect to prior expenditures, current balances of funds, and cost to complete from the current position. For CCAT we anticipate project expenditures will be tracked both by the Project and by the host institution's bookkeeping department. A detailed spreadsheet system will be applied to cost tracking and projection for CCAT. The system has the following elements:

20.4.10.1 Organized by Months of the Project and WBS

The spreadsheet system allocates funds by month over the duration of the project by Work Breakdown Structure element. Initially allocations from the cost estimate are used but as actual quotations are received and contracts are awarded, the actual scheduled payments are entered in the appropriate months. This is also performed with personnel, with each individual identified by position initially with anticipated salaries and updated with actual names and salaries as team members are hired. All purchases are also entered in the months in when the anticipated costs are incurred.

20.4.10.2 Reconciliation with Host Institution Books

On a quarterly basis, the spreadsheet system is reconciled with the records of the Institution's bookkeeping system. Working together, the administration and Project representatives review all expenditures and enter actual values on the actual dates. Any schedule payments that have not been made are rescheduled so the total values of contracts remain correct. As time goes on, more of the spreadsheet system reflects actual expenditures and less allocations toward completion.

20.4.10.3 Cost to Complete

At any given time the amount of expenditures allocated in the future are the cost to complete. When summed with the actual expenditures, this becomes the total project cost. Hence on a quarterly basis immediately following resolution with the host institution's books and following re-allocation of expenses for the remainder of the Project, a well established cost-to-complete will be at hand.

20.4.10.4 Cash Flow Projections

The spreadsheet system can incorporate the contribution schedules as well as providing monthly anticipated expenditures. This enables the cross correlation of cash inflow and expenditures to ensure that adequate funds are always on hand. This also permits an ongoing estimate of revenue generation from interest bearing accounts where contributions are held prior to use.

20.4.10.5 Response to Problems

This system allows reprogramming future expenditures to remain within the overall established budget. It is of particular importance to recognize problems early in order to have the opportunity to reallocate budget while there are still sufficient degrees of freedom to find a solution. This system provides that capability.

20.4.10.6 Semi-Annual Budget Reports

Printouts from this spreadsheet system when combined with commentary provides easily understood reports on prior expenditures, current balances, anticipated contributions, and allocations leading to the cost to complete. This report will be part of the Semi-Annual Status Reviews provided for the Project Board.

20.4.11 Integration Management

The remote nature of the site, the fact that work is being done in a culture foreign to the US, and the extreme altitude all combine to make management of integration of the observatory and base support facility a challenge. A more detailed Integration and Commissioning Plan is provided in Section 18, but in general the plan includes:

20.4.11.1 Project Personnel

Job descriptions for each member of the Project Team will require deployment to Chile for up to 3 years as a part of the integration effort. In addition, efforts will be made to recruit an appropriate fraction of the staff from Chile in the interest of having people who will stay with the telescope after construction.

20.4.11.2 Integration with Operations

Operations staff will be added during the integration phase so we avoid as best possible any lag in staff capabilities when Project personnel return to the US. During the year scheduled for Commissioning, the full Operations staff will work alongside the Project staff to optimize telescope performance.

20.4.11.3 Contractor Subsystems

CCAT will maintain responsibility for installation of all major subsystems. Contractors will be required to provide manuals for installation, lists of equipment and tools required, and technical support to integration of their subsystems. This approach allows us to use one labor pool for the entire integration phase, likely drawn from personnel who participated in general construction of the facility. It avoids having each subcontractor figure out how to do business in Chile, hiring its own labor force, and including large cost contingencies because of their concern and lack of knowledge of these things. It also permits us to manage the work to achieve best results.

20.4.12 Transition to Operations

As mentioned above, the Operations Team will be ramped up as integration of the major telescope subsystems is performed. This permits a somewhat expanded labor force and ensures that the Operations personnel are as familiar with the observatory as possible when they take over. It will be important to start early to identify people who have the necessary skills and a willingness to work in the remote location. We anticipate a large number of Chilean operations personnel. Experience shows such people are available in Chile but it may take some time to identify them and bring them on board.

20.4.13 Reporting

At the point when the Project enters the Development Phase, we will begin regularly scheduled reporting. This will include:

20.4.13.1 Monthly Progress Reports

These will include activities, travel and meetings, publications, and discussions of critical issues and objectives for the next month. They will be distributed to all involved members of the Project partnership.

20.4.13.2 Semi-Annual Status Reviews

There will be two progress reviews per year. These will alternate between the hosting institution and the partner institutions, with every other review at the hosting institution. This enables the Project Team members to individually report on their specific areas of responsibility and subsystems progress and issues. At the reviews at the Partner institutions, the Project Director, the Project Manager, Deputy Project Manager, and Project Engineer will make presentations. Each review will include a review of budgetary status and plans.

20.5 Schedule

We plan to use Microsoft Project Manager to plan and track project activities in detail. A preliminary schedule (which is found in the back of the report) meets the major objectives of the Project including time to first light and full science operations. The subsystems are staggered in their starts and durations to enable the Project Team to develop procurements in successive groups and for the products of contracts to arrive at the site in the proper

order identified in the Integration and Commissioning plan. The current critical path runs through panel development, with the actual physical completion of the telescope controlled by the delivery of the final panels. This does not limit progress, however, as the telescope will be functional at sub-full aperture configurations for debug and optimization as well as early science.

The schedule is located at the end of this report.

20.6 Risk Assessment & Mitigation

The phases established for the project provide for early identification of potential risks associated with the Project. In general, risks fall into two categories, technical risk and management or cost risk.

20.6.1 Technical Risk

A philosophy has been established that seeks to keep the telescope and its associated systems within the current state of the art. We have carefully reviewed the technologies and approaches utilized successfully in a wide range of radio and optical telescopes and have attempted not to break new ground where it is not required. That said, there are some areas, most notably primary mirror panel manufacture and overall telescope alignment control, that require additional development because of performance, cost, or both. This report includes critical risk assessment and mitigation for each subsystem studied. In general, we have avoided development by the Project staff of subsystems for the telescope, favoring instead commercial vendors with track records of success. During the ongoing development of the telescope we will closely track progress at the contractors and individuals or groups at the partner institutions developing telescope systems. Identification of technical risk at the earliest opportunity will be met with increased management participation, development of mitigation plans, and activities of appropriate urgency required to address the problems.

20.6.2 Management Risk

While there are a wide range of possible management issues in development of CCAT, the major risk in this area is cost overrun. This can happen through a variety of mechanisms: contracts coming in higher than budgeted, failures to identify cost bearing elements of development, overly optimistic schedules, or problems that drag out development with attendant additional cost. The processes which have been developed and will be utilized to achieve accurate and comprehensive cost estimates and provide daily insight into cost status and cost to complete enable the reallocation of resources early on to ensure that the Project will remain within budget. During the next Phase of CCAT development, these detailed systems and estimates will be developed and implemented. Prior history indicates these systems have served to keep costs within budget when implemented and executed with discipline.

20.7 Summary

This Project Management plan is subject to revision as the CCAT Partnership develops. The specific business approach, nature of project governance, siting of the Project office, and associated business conditions all await more formal definition of the partnership. The approaches recommended here have worked successfully for other projects. As the partnership becomes more fully defined and such decisions on how to proceed are undertaken and resolved by the Partners, this plan will be revised.

21 Summary and Next Steps

The following is an assessment of the state of development of each of the areas of the report along with initial plans for follow on development during the next Project phase: Engineering Concept Design

21.1 CCAT Science

A compelling case for the development of CCAT has been presented. This telescope can achieve astronomical research that no other ground or space based system can accomplish. The science which has been proposed is seminal, cutting edge, and congruent to the development of ALMA. During the Engineering Concept Design, the Project Scientists and the Science Committee will continue development of the science case, review and revise telescope instrument requirements and closely monitor the engineering development to ensure that CCAT will optimally serve the science mission.

21.2 Instrumentation

After careful consideration of the various alternatives, a pair of imaging instruments aimed at rapid exploitation of CCAT's wavelength regimes and field of view have been identified. These represent only the first suite of instrumentation and it will be an objective for CCAT during the next phases of development to identify future instrumentation and routes to funding. At the same time, exercising the full capability of CCAT depends on further development of large focal plane arrays to for operation at submillimeter wavelengths. The Instrument Committee will continue to interact with the developers of such arrays and look to leverage development activities at Cornell, Caltech, and JPL. During the Engineering Concept Design phase the concepts for the two imagers will be further developed and integrated with the telescope to ensure compatibility and to allow an integrated instrument/telescope design to provide optimal performance at the lowest cost. Principal Investigators and instrument teams for the two instruments will be identified and detailed plans for development written and reviewed. Analysis to establish the performance levels which will be attained will be performed and a final report provided as a part of the Engineering Concept Design Report and Final Review.

21.3 CCAT Top Level Requirements

A good initial set of requirements has been established and reviewed. That said, there are a fair number of "TBDs" yet included which need to be resolved quickly. The Engineering Concept Design phase will begin with an in-depth review of requirements. Among the key issues to be studied are whether a faster telescope can help reduce the size of the dome, whether different delivered f/ratios can reduce the scope of re-imaging system requirements, and what are the minimum site and base facilities which can meet scientific and operational requirements. The goal will be a definitive set of top-level requirements which can be agreed to by all partners and will serve to prevent "feature creep" and progressive increases in scope which can threaten Project budgets and schedules.

21.4 Optical Design

Analysis of the telescope design indicates that the desired image quality can be delivered with acceptable alignment and component tolerances. Immediately following the review of this study work will begin to identify what variations in the optical prescription and conjugates can provide the most efficient telescope with respect to size, manufacturability, and achievable alignment tolerances. Optical system modeling will be expanded to include re-imaging systems and instruments as well as the major telescope optics. Delivered image quality at the focal plane will be modeled and investigation of effects of misalignment and component degradation on performance will be analyzed. At the culmination of the Engineering Concept Design phase the definition of all optics will be very firmly established and will not be changed for the remainder of the program without substantial rationale.

21.5 Systems Engineering

We have provided a substantial amount of parametric analysis and a first cut at an image quality error budget. Analysis of the effect of edge sensor error magnification and degeneracy makes clear that we will need to pay special attention to the implementation of a telescope and mirror segment alignment architecture. During the next phase we will develop detailed image quality, alignment, and emissivity budgets for the telescope and instruments. Throughout the Project these budgets will be maintained and as actual data characterizing surfaces, alignment, coatings, etc. are received they will be incorporated ensuring that performance objectives will be met. Discussions with JPL indicate that they will likely develop a system model which incorporates edge sensors and other alignment sensors to determine the efficacy of the overall calibration and alignment systems. This model will be exercised to determine the most practical and cost effective suite of sensors to achieve robust operation.

21.6 Site Testing and Evaluation

Significant progress has been realized in characterizing Atacama sites over the past several years. We have obtained a substantial fraction of that data to add to that garnered by Cornell and Caltech's efforts. During the course of this study, though we marshaled all the necessary equipment and developed approaches to characterizing the sites of interest, changes in procedures granting site access in Chile stymied our efforts to acquire specific data from the peaks we find most attractive. Early in 2006 we intend to implement a site testing campaign with an initial goal to determine whether or not Cerro Chajnantor meets our expectations for transparency at the wavebands of interest and if meteorological conditions are within acceptable parameters. Given appropriate initial indications we will extend the testing to provide the maximum baseline for changing seasons. If, for some reason, Chajnantor fails to meet expectations, then we will commence testing on other peaks as required to determine the optimal site within our candidates. We will also continue to closely monitor all site testing activities in the region to better understand the ranges of possible conditions and opportunities to attain optimal scientific performance.

21.7 Site, Architecture and Civil Engineering

An excellent start on site development, infrastructure, architecture, and cost estimation has been provided by the current study. The estimated price for development has significantly exceeded our target price and a primary order of business in the next phase will be to investigate ways to reduce development costs in this area. We have already identified areas in which optimization of the facility can help reduce cost such as lowering the facility to minimize volume of concrete required. Several other issues will need resolution during the next Project phase. Among these are: Investigation of actual local prices for road development, Determining whether road costs can be shared with other parties interested in Chajnantor (notably the Japanese astronomical community), Investigation whether ALMA might permit use of their Observatory Support Facility for CCAT rather than developing our own base facility, Revisiting summit requirements to determine whether a reduction in capabilities and attendant space can reduce costs, Investigation of ALMA's ongoing development of approaches to obtaining power to see if we can be included as a part of their total requirement, and Revisiting architectural approaches to see if some simpler and more cost effective approach can be identified.

21.8 Enclosure Dome

An initial concept for a dome has been developed following parametric analysis considering three alternative designs. This must be considered a high risk area of the Project owing to the fact that a large dome of this type has never been built. That said, the alternative approaches considered offer substantially reduced structural efficiency, much higher variation in loads on rotation systems, large shutter loads, larger motors and higher operating power requirements, and arguably more complex mechanisms. The initial investigation has provided a first cut at an engineering concept design and as such has clearly identified the areas which will need significant attention during the next Project phase. These areas include:

21.8.1 Overall Structure

"Geodesic" type structures offer structural and manufacturing efficiency and are particularly well suited to transport and erection at the challenging site altitude. We need to investigate the optimal design (e.g. truss

members versus wide flange type beams) and hope to implement a commercially available system such as Temcor's which has been demonstrated over a wide variety of applications and can save substantial weight and cost.

21.8.2 Mechanisms

Azimuth rotation is not particularly challenging, however careful attention must be paid to load distribution, flatness, bogey loads, alignment, and other issues which can create premature wear of components. Access for inspection and repair must also be considered. The inclined calotte axis is probably the most challenging aspect of dome development and substantial effort will be put into validating and further development of the design.

21.8.3 Other Developments in ELT Domes

We will continue to keep our attention focused on development at TMT and GMT to keep abreast of developments in domes of comparable size by other projects. As we have to date, we will continue to share the results of our studies with the other Extremely Large Telescope projects. Toward that end, we will conduct a dome review early in the Engineering Concept Design phase with invitations extended to each of the major ELT projects to participate.

21.8.4 Industrial Engineering and Cost Reduction

While the current estimate for the calotte dome for CCAT is about the same as the cost of each Gemini or Keck dome despite its larger size, we hope to trim the cost by applying industrial engineering principals and establishing routes to mass production of standardized structural elements and rotations system components.

21.9 Telescope Mount

Work in this phase has provided a sound concept for the telescope mount. The combination of hydrostatic bearings for the high load azimuth bearing and rolling element bearings for the more lightly loaded elevation bearings and proven drive and encoder concepts provides a high confidence approach. The current concept illustrates two cylindrical instrument payloads, but in the next phase we will integrate CCAT instruments along with the required reimaging optics to provide additional detail. Work in the next phase will include:

21.9.1 Engineering for Structural Efficiency

The current mount design is extremely robust. Since we have made efforts to kept the PM assembly as light as possible, it seems that we might reasonably expect to significantly lighten the lower mount structure. Finite element modeling will be applied to identify structural modes and design of the structure will be simplified and made more structurally efficient.

21.9.2 Industrial Engineering

The design will be reviewed to identify approaches to minimize the number of machining operations and identify the most efficient way to manufacture components and piece parts. Concurrent engineering via interface with potential suppliers will be performed.

21.9.3 Joint Design

The mount is intended to be assembled via bolting on site. This requirement, given the size of the mount, implies that attention must be paid to where and how joints will be made and ensuring that the resulting piece parts are compatible with shipping and handling to get them to the site. Approaches to alignment such as pinning during trial assembly will be considered.

21.9.4 Pointing and Servo-Control Analyses

Telescope pointing and scanning requirements are challenging and during the next phase of work additional work will be performed to couple FEM and servo-control models to analyze the likely delivered performance.

21.9.5 Manufacturing Plan

During the next phase of work the process for making all piece parts will be considered as they are designed. An overall plan for manufacture, trial assembly, and packing/shipping will be developed.

21.10 Primary Mirror System

The PM system is perhaps the most challenging system for CCAT. We have identified three prospective panel systems: Media Lario's electrodeposited Ni/Al composite, ITT's precision molded lightweight borosilicate glass, and CMA's CFRP replicated panels. There are other vendors who might also offer the last approach. Our objective, of finding panels which were stiff enough to permit mounting kinematically on three points has been validated by analysis. The replication processes employed by all three imply manufacturing efficiency and the cost of these approaches appears to be close to the acceptable range. While our approach appears valid, much work remains prior to the actual procurement of components and subsystems which make up the PM.

21.10.1 Truss Design

We have in hand a quotation from VRSI to make the PM truss which meets our cost target. Our intention, however is to pursue a bolted truss which can be very easily shipped to the site and meets dimensional and structural requirements via precision of the components rather than on-site metrology and adjustment. During the Engineering Concept Design phase we will contract with a noted consultant to develop a truss design with the correct front node pattern for mirror mounting and back mounting to the mount elevation structure. This design will be analyzed and can then be sent to several potential manufacturers for bid.

21.10.2 Continued Panel Development

Little work was done with the Media Lario panels owing to some miscommunication with their technical personnel. We will investigate them further during the next phase of work and elect to fund some continued development contracts for each of the potential panel approaches. This is part of our intention to qualify multiple panel technologies and spawn cost competition between the providers. Panel design will be further advanced, suitable demonstrations performed, and methods for implementation of mounting and metrology will be incorporated. Accelerated life cycle testing for some panels may be required.

21.10.3 Actuator System

We have an acceptable concept from Polytec PI. In pursuit of cost reduction, we will seek alternate vendors while working with Polytec to identify a more cost effective approach. The overall architecture of the actuator system including electronics and cabling will be further developed. Interface between actuators and truss will be conceptually worked out.

21.10.4 Panel Coating

We have included a rough estimate for a DC Magnetron coating system. Some panel types such as Media Lario may not require coating, and should it be determined that CCAT does not require panels which are specular in the IR, a permanent coating for the Submm might be applied at the manufacturers. This could eliminate the need for a coating chamber.

21.10.5 Integrated Structural/Thermal Model

We will develop an integrated model of the panel/actuator/truss system to enable identification of dynamic structural performance and alignment/figure under varying thermal, gravitational, and acceleration (scanning) conditions.

21.11 Telescope Alignment

We have identified a wide range of options toward the eventual definition of a system capable of initial alignment calibration of the telescope and subsequent maintenance alignment during operation. Each subsystem is discussed along with plans for the next phase.

21.11.1 Edge Sensor Systems

We have identified two commercially available edge sensor systems in addition to the system being developed by TMT. We have also identified the possibility of using lateral effect photodiodes as an edge sensor system which JPL is currently working on. In the next phase we will perform trade studies between these systems, with the objective to identify the most robust and cost effective alternative. Qualifying more than one of the commercially available systems could help in cost containment by way of competitive procurement.

21.11.2 Calibration

Our report presents an extended focal plane version of a shearing interferometer approach developed by JPL and implemented on the CSO. This system appears to be larger and more expensive than we would like, and in the next phase of work we intend to investigate whether a smaller system can be devised, using either a single pixel, smaller array, or alternate approach (such as a Shack Hartmann sensor.) Capabilities of this sensor will be incorporated into the JPL mirror alignment model identified in Section 21.5.

21.11.3 Alignment Maintenance System

We have identified two approaches, one being the absolute distance measuring system studied by JPL and the other being a Shack Hartmann type sensor represented by a white paper from Adaptive Optics Associates. During the next phase of work additional work will be done on each to investigate their performance and any concerns regarding implementation or performance. This system is required to supplement the edge sensor system.

21.11.4 Wavefront Sensing Guider

The study includes an initial proposal for a low order wavefront sensing guider provided by J. Lloyd. This system operates in the IR in order to find enough guide objects and to support daytime operations. The potential drawbacks of this system are the requirement for specular mirror surfaces of sufficient accuracy to deliver adequate images for centroiding. We will further investigate this system as it could provide the telescope guiding necessary for the 0.2 arc sec tracking/pointing precision required while meeting the need for an alignment maintenance system as identified in section 21.12.3.

21.11.5 Alternate Guider

Should the wavefront sensing guider not prove feasible, we intend to investigate the use of a co-mounted guide telescope operating at 10 microns. This could be a commercial small astronomical telescope provided that the necessary pointing requirements can be met. Guide object availability statistics for the smaller aperture and FoV will need to be investigated before we move further in this direction.

21.12 Secondary and Tertiary Mirror Systems

Two concepts for a secondary mirror system were identified. Should our investigation of a faster telescope prove successful, the secondary mirror may become small enough that it no longer needs to be a segmented optic. This would require further investigation of fabrication approaches which we would perform. The more novel of the two approaches, which uses high bandwidth positioning of each of the segments to achieve correlated motion for nutation, offers very low part count and mass. We intend to further develop this approach as mass is critical at the M2 location. The tertiary mirror rotation system has been identified as a commercially available turntable system. This will be more critically assessed and a determination made whether we need a custom system to achieve the required stability and positioning.

21.13 Telescope Control System

Relatively little work was done on the actual selection of platforms, operating system, communications protocols, software environment, and system architecture. Investigation of a number of existing observatory control systems revealed that most mature systems employ relatively dated hardware and software owing to the rapid pace of development in this industry and the time required to develop an observatory control system. While we can make additional progress during the next phase of work, it is not deemed strictly necessary that we make these decisions early. We will do a more in-depth investigation of the options preparatory to the selection of approach and the

conceptual definition of the actual system. It seems prudent to await the appointment of the software manager prior to finalizing this decision.

21.14 Plans and Schedules

During the Engineering Concept Design phase additional detail will be provided for the Integration and Commissioning Plan, Operations Plan, and Project Plan. These will be reviewed by the Project Committees and administrations of the Partner institutions. The objective will be to have definitive approved plans by the culmination of the phase. A much more detailed Project Schedule will also be provided, updated with information from subsystem providers to include their projected rates of development.

21.15 Cost Estimate

As an adjunct to this report we have developed a cost estimate (not included owing to the proprietary and competition sensitive nature of contractor estimates.) This is a good initial estimate and indicates the areas where we need to pay additional attention to development of cost effective approaches. By the end of the Concept Design Phase this estimate will be over 90% supported by contractor quotations, catalogue prices, standard estimating practices, and comparison with other recent systems. The error should be less than 10% by that time and an equivalent contingency established.

| ID | Task Name | Duration | Start | Finish | Predecessors | 2005 | | | | 2006 | | | | 2007 | | | | 2008 | | | | 2009 | | | | 2010 | | | | 2011 | | | | 2012 | |
|----|--|------------|--------------|--------------|--------------|------------|----|----|----|------|----|----|----|------|----|----|----|------|----|----|----|------|----|----|----|------|----|----|----|------|----|----|----|------|----|
| | | | | | | Q1 | Q2 | Q3 | Q4 | Q1 | Q2 | Q3 | Q4 | Q1 | Q2 | Q3 | Q4 | Q1 | Q2 | Q3 | Q4 | Q1 | Q2 | Q3 | Q4 | Q1 | Q2 | Q3 | Q4 | Q1 | Q2 | Q3 | Q4 | Q1 | Q2 |
| 1 | Concept/Feasibility Study | 13.5 mons | Mon 1/3/05 | Fri 1/13/06 | | [Task Bar] | | | | | | | | | | | | | | | | | | | | | | | | | | | | | |
| 2 | C/F Study Review | 0 mons | Fri 1/13/06 | Fri 1/13/06 | 1 | | | | | | | | | | | | | | | | | | | | | | | | | | | | | | |
| 3 | Engineering Concept Design | 13 mons | Thu 6/1/06 | Wed 5/30/07 | 2 | | | | | | | | | | | | | | | | | | | | | | | | | | | | | | |
| 4 | Concept Design Review | 0 mons | Wed 5/30/07 | Wed 5/30/07 | 3 | | | | | | | | | | | | | | | | | | | | | | | | | | | | | | |
| 5 | Development Phase | 44 mons | Thu 5/31/07 | Wed 10/13/10 | 4 | | | | | | | | | | | | | | | | | | | | | | | | | | | | | | |
| 6 | | | | | | | | | | | | | | | | | | | | | | | | | | | | | | | | | | | |
| 7 | FACILITIES CONSTRUCTION | 32.95 mons | Fri 12/1/06 | Wed 6/10/09 | | | | | | | | | | | | | | | | | | | | | | | | | | | | | | | |
| 8 | Support Facility Construction | 24.45 mons | Fri 12/1/06 | Wed 10/15/08 | | | | | | | | | | | | | | | | | | | | | | | | | | | | | | | |
| 9 | Prepare Bid Documents | 3 mons | Fri 12/1/06 | Thu 2/22/07 | | | | | | | | | | | | | | | | | | | | | | | | | | | | | | | |
| 10 | Procurement | 3 mons | Fri 2/23/07 | Thu 5/17/07 | 9 | | | | | | | | | | | | | | | | | | | | | | | | | | | | | | |
| 11 | Sign Construction Contract | 0 mons | Wed 5/30/07 | Wed 5/30/07 | 10,4 | | | | | | | | | | | | | | | | | | | | | | | | | | | | | | |
| 12 | Occupy Site | 2 mons | Thu 5/31/07 | Wed 7/25/07 | 11 | | | | | | | | | | | | | | | | | | | | | | | | | | | | | | |
| 13 | Ground Breaking | 0 mons | Wed 7/25/07 | Wed 7/25/07 | 12 | | | | | | | | | | | | | | | | | | | | | | | | | | | | | | |
| 14 | Site Preparation & Excavation | 2 mons | Thu 7/26/07 | Wed 9/19/07 | 13 | | | | | | | | | | | | | | | | | | | | | | | | | | | | | | |
| 15 | Concrete Work | 2 mons | Thu 9/20/07 | Wed 11/14/07 | 14 | | | | | | | | | | | | | | | | | | | | | | | | | | | | | | |
| 16 | General Construction | 12 mons | Thu 11/15/07 | Wed 10/15/08 | 15 | | | | | | | | | | | | | | | | | | | | | | | | | | | | | | |
| 17 | Occupy Support Facility | 0 mons | Wed 10/15/08 | Wed 10/15/08 | 16 | | | | | | | | | | | | | | | | | | | | | | | | | | | | | | |
| 18 | | | | | | | | | | | | | | | | | | | | | | | | | | | | | | | | | | | |
| 19 | Telescope Facility Construction | 32.95 mons | Fri 12/1/06 | Wed 6/10/09 | | | | | | | | | | | | | | | | | | | | | | | | | | | | | | | |
| 20 | Site Development | 12.45 mons | Fri 12/1/06 | Wed 11/14/07 | | | | | | | | | | | | | | | | | | | | | | | | | | | | | | | |
| 21 | Prepare Docs | 3 mons | Fri 12/1/06 | Thu 2/22/07 | | | | | | | | | | | | | | | | | | | | | | | | | | | | | | | |
| 22 | Procurement | 2 mons | Fri 2/23/07 | Thu 4/19/07 | 21 | | | | | | | | | | | | | | | | | | | | | | | | | | | | | | |
| 23 | Sign Contract | 0 mons | Wed 5/30/07 | Wed 5/30/07 | 22,4 | | | | | | | | | | | | | | | | | | | | | | | | | | | | | | |
| 24 | Develop Road | 3 mons | Thu 5/31/07 | Wed 8/22/07 | 23 | | | | | | | | | | | | | | | | | | | | | | | | | | | | | | |
| 25 | Level Site | 1 mon | Thu 8/23/07 | Wed 9/19/07 | 24 | | | | | | | | | | | | | | | | | | | | | | | | | | | | | | |
| 26 | Install Utilities & Trailers | 2 mons | Thu 9/20/07 | Wed 11/14/07 | 25 | | | | | | | | | | | | | | | | | | | | | | | | | | | | | | |
| 27 | Site Ready | 0 mons | Wed 11/14/07 | Wed 11/14/07 | 26 | | | | | | | | | | | | | | | | | | | | | | | | | | | | | | |
| 28 | Facility Development | 30.75 mons | Thu 2/1/07 | Wed 6/10/09 | | | | | | | | | | | | | | | | | | | | | | | | | | | | | | | |
| 29 | Prepare Docs | 6 mons | Thu 2/1/07 | Wed 7/18/07 | | | | | | | | | | | | | | | | | | | | | | | | | | | | | | | |
| 30 | Procurement | 3 mons | Thu 7/19/07 | Wed 10/10/07 | 29 | | | | | | | | | | | | | | | | | | | | | | | | | | | | | | |
| 31 | Sign Contract | 0 mons | Wed 10/10/07 | Wed 10/10/07 | 30 | | | | | | | | | | | | | | | | | | | | | | | | | | | | | | |
| 32 | Occupy Site | 2 mons | Thu 11/15/07 | Wed 1/9/08 | 31,27 | | | | | | | | | | | | | | | | | | | | | | | | | | | | | | |
| 33 | Excavation | 2.5 mons | Thu 1/10/08 | Wed 3/19/08 | 32 | | | | | | | | | | | | | | | | | | | | | | | | | | | | | | |
| 34 | Concrete Work | 3 mons | Thu 3/20/08 | Wed 6/11/08 | 33 | | | | | | | | | | | | | | | | | | | | | | | | | | | | | | |
| 35 | Erect Steel | 3 mons | Thu 6/12/08 | Wed 9/3/08 | 34 | | | | | | | | | | | | | | | | | | | | | | | | | | | | | | |
| 36 | Exterior Finishes | 3 mons | Thu 9/4/08 | Wed 11/26/08 | 35 | | | | | | | | | | | | | | | | | | | | | | | | | | | | | | |
| 37 | Trades | 4 mons | Thu 11/27/08 | Wed 3/18/09 | 36 | | | | | | | | | | | | | | | | | | | | | | | | | | | | | | |
| 38 | Telescope Room Complete | 0 mons | Wed 3/18/09 | Wed 3/18/09 | 37 | | | | | | | | | | | | | | | | | | | | | | | | | | | | | | |
| 39 | Interior Finishes | 3 mons | Thu 3/19/09 | Wed 6/10/09 | 37,38 | | | | | | | | | | | | | | | | | | | | | | | | | | | | | | |
| 40 | Telescope Facility Complete | 0 mons | Wed 6/10/09 | Wed 6/10/09 | 39 | | | | | | | | | | | | | | | | | | | | | | | | | | | | | | |
| 41 | | | | | | | | | | | | | | | | | | | | | | | | | | | | | | | | | | | |
| 42 | DOME DEVELOPMENT | 35 mons | Thu 5/31/07 | Wed 2/3/10 | | | | | | | | | | | | | | | | | | | | | | | | | | | | | | | |
| 43 | Prepare Docs | 3 mons | Thu 5/31/07 | Wed 8/22/07 | 4 | | | | | | | | | | | | | | | | | | | | | | | | | | | | | | |
| 44 | Procurement | 2 mons | Thu 8/23/07 | Wed 10/17/07 | 43 | | | | | | | | | | | | | | | | | | | | | | | | | | | | | | |

Project: Project Schedule 02nov05
Date: Wed 12/14/05

| | | | | | | | | | |
|---------------|--|----------------|--|-------------------------|--|-----------------|--|------------------|--|
| Task | | Milestone | | Rolled Up Critical Task | | Split | | Group By Summary | |
| Critical Task | | Summary | | Rolled Up Milestone | | External Tasks | | Deadline | |
| Progress | | Rolled Up Task | | Rolled Up Progress | | Project Summary | | | |

Acronyms

| | |
|---------------|--|
| ACT..... | Atacama Cosmology Telescope |
| ADRs..... | Adiabatic Demagnetization Refrigerators |
| AGN..... | Active Galactic Nuclei |
| ALMA..... | Atacama Large Millimeter Array |
| AMiBA | Array for Microwave Background Anisotropy |
| APEX | Atacama Pathfinder Experiment |
| APEX-SZ | APEX Sunyaev Zel'dovich |
| ASIAA | Academic Sinica Institute of Astronomy & Astrophysics |
| ASPE..... | American Society for Precision Engineering |
| ASTE..... | Atacama Submillimeter Telescope Experiment |
| AU..... | Astronomical Unit |
| AzTEC | Astronomical Thermal Emission Camera |
| BICEP | Background Imaging of Cosmic Extragalactic Polarization |
| BIMA | Berkeley Illinois Maryland Array |
| Caltech | California Institute of Technology |
| CARMA..... | Combined Array for Research in Millimeter-wave Astronomy |
| CBI..... | Cosmic Background Imager |
| CCAT | Cornell-Caltech Atacama Telescope |
| CCC..... | Cold Cloud Core |
| CFHT | Canada France Hawaii Telescope |
| CFRP..... | Carbon Fiber Reinforced Plastic |
| CII | Ionized Carbon |
| CL | Confusion Limit |
| CMB..... | Cosmic Microwave Background |
| CO..... | Carbon Monoxide |
| COBE..... | Cosmic Background Explorer |
| CONADI..... | Corporación Nacional de Desarrollo Idigena |
| CONICYT..... | Comisión Nacional de Investigación Científica y Tecnológica de Chile |
| CoPHI | Common Path Heterodyne Interferometers |
| CSO..... | Caltech Submillimeter Observatory |
| CTE..... | Coefficient of Thermal Expansion |
| ESS..... | Edge Sensor System |
| Far-IR..... | Far Infrared |
| FEA..... | Finite Element Analysis |
| FIR | Far Infrared |
| FNFW | First Null Full Width |
| FoV | Field of View |
| FPA | Focal Plane Array |
| FPGA | Field Programmable Gate Array |
| FTS..... | Fourier Transform Spectrometer |
| FWHM | Full Width Half Maximim |
| G..... | Goal |
| GBT..... | Green Bank Telescope |

GLIMPSEGalactic Legacy Infrared Mid-Plane Survey Extraordinaire
 GOODS-SGreat Observatories Origins Deep Survey - South
 GPSGlobal Position System
 GUIGraphic User Interface
 HDTVHigh Definition Television
 HEMTHigh Electron Mobility Transistor
 HPFWHalf Power Full Width
 HVACHeating, Ventilation, Air Conditioning
 ICM.....Intra Cluster Medium
 IRAMInstitut de Radio Astronomie Millimétrique
 ISOInfrared Space Observatory
 JCMTJames Clerk Maxwell Telescope
 JPLJet Propulsion Laboratory
 JWST.....James Webb Space Telescope
 KBOs.....Kuiper Belt Objects
 kSZ.....kinetic Sunyaev-Zel'dovich
 LANLocal Area Network
 LMTLarge Millimeter Telescope
 LVDTsLinear Variable Differential Transformers
 LWCam.....Long Wavelength Camera
 M3Tertiary Mirror
 M3M3 Engineering and Technology Corporation
 MAMBOMax Planck Millimeter Bolometer
 MATMobile Anisotropy Telescope
 MBMegabyte
 MINTMillimeter Interferometer
 MKIDS.....Microwave Kinetic Inductance Detectors
 MNRASMonthly Notices of the Royal Astronomical Society
 MOUMemorandum of Understanding
 MPIfRMax-Planck Institut für Radioastronomie
 MSXMidcourse Space Experiment
 NAIC.....National Astronomy and Ionosphere Center
 NEC.....National Electrical Code
 NEFDNoise Equivalent Flux Density
 NII.....Ionized Nitrogen
 NIST.....National Institute of Standards and Technology
 NRL.....Naval Research Lab
 OINeutral Oxygen
 OIII.....Doubly Ionized Oxygen
 OIR.....Optical Infrared
 OSHA.....Occupational Safety & Health Administration
 OSSOptics Support Structure
 OVROOwens Valley Radio Observatory
 PAN.....Polyacrylonitrile
 PWV.....Precipitable Water Vapor
 QUADQ and U Extragalactic Submm Telescope

RCRitchey Chretien
RLTReceiver Lab Telescope
RMSRoot Mean Square
SAFIRSingle Aperture Far Infrared Observatory
SCUBASubmillimetre Common User Bolometer Array
SCUBA-2.....Submillimetre Common User Bolometer Array 2
SDBCBare Stranded Copper
SEDSpectral Energy Distribution
SESTSwedish-ESO Submillimetre Telescope
SHARC-2.....Submillimetre High Angular Resolution Camera 2
SHARP.....SHARC-II Polarimeter
SLLSide Lobe Level
SMASubmillimeter Array
SMTSubmillimeter Telescope
SOAR.....Southern Astrophysical Research Telescope
SPICASupport Program for Instructional Competency in Astronomy
SPIEInternational Society for Optical Engineering
SPT.....South Pole Telescope
SQUIDSuperconducting Quantum Interference Device
SuZIESunyaev-Zel'dovich Infrared Experiment
SWCam.....Short Wavelength Camera
SZ.....Sunyaev-Zel'dovich
TCSTelescope Control System
TESTransition Edge Superconductor
TF.....Telescope Facility
TMTThirty Meter Telescope
TNOTrans-Neptunian Objects
tSZ.....thermal Sunyaev-Zel'dovich
UPSUninterruptible Power Supply
VACVolts Alternating Current
VLBA.....Very Long Baseline Array
WaFIRS.....Waveguide Far-IR Spectrograph
WFEWave Front Error
XMM.....X-Ray Multi-Mirror Mission
ZEUS.....High-redshift (Z) and Early Universe Spectrometer

